MECHANISMS OF OXIDATION OF ALLOY 617 IN He-CO-CO_2 ENVIRONMENT WITH VARYING CARBON AND OXYGEN POTENTIALS

by

Deepak Kumar

A dissertation submitted in partial fulfillment
of the requirements for the degree of
Doctor of Philosophy
(Materials Science and Engineering)
in The University of Michigan
2010

Doctoral Committee:

Professor Gary S. Was, Chairman
Professor Michael Atzmon
Professor J. Wayne Jones
Professor Tresa M. Pollock

To my parents.

ACKNOWLEDGEMENTS

I would like to thank my advisor Dr. Gary S. Was, for his guidance and assistance in completing this work. I would also like to thank the members of my dissertation committee, Dr. Atzmon, Dr. Jones, and Dr. Pollock for their helpful insight as I completed this thesis.

I would also like to thank my colleagues and friends Raghavendra Adharapurapu, Zhijie Jiao, Kun-Dar Li, Jun Zhu, Gaurav Gupta, Micah Hackett, Elaine West, Pantip Ampornrat, Anne Campbell, Janelle Wharry, Michael McMurtrey, Cheng Xu, Gokce Gulsoy, and Kale Stephenson for their assistance in the lab and helpful discussions.

Finally, I want to thank my parents' patience, understanding, and support they have given me throughout the years.

This work was supported by Department of Energy under the contract number DE-FG07-07ID14894.

TABLE OF CONTENTS

DEDICATION……....ii

ACKNOWLEDGEMENTS……iii

LIST OF FIGURES vii

LIST OF TABLES xvii

LIST OF APPENDICES……...xix

ABSTRACT…….xxi

CHAPTER

1. INTRODUCTION 1

2. BACKGROUND 8

2.1 Microstructure and precipitate stability in alloy 617 8
2.2 Mechanism of growth of Cr_2O_3 film 11
2.3 Oxidation of Ni-Cr-Al alloys 14
2.4 Oxidation of Ni-Cr alloys in impure helium 18
2.4.1 Characteristics of impure helium 18
2.4.2 Gas/metal surface reactions in impure helium 19
2.4.3 Oxidation behavior of Ni-Cr alloys based on the Cr-stability diagram 21
2.4.3.1 Cr-stability diagram 21
2.4.3.1.1 Definition and representation 22
2.4.3.1.2 Cr-stability diagram and prediction of oxidation behavior of Ni-Cr alloys 25
2.4.4 Definition of critical temperature 27
2.4.5 Influence of impurity concentration on critical temperature 28
2.4.6 Decarburization mechanisms 30

3. EXPERIMENTAL PROCEDURE 55

3.1 Alloy description 55
3.2 Controlled-Impurity Helium Flow System 56

3.2.1 Description of the facility 57
3.2.1.1 Gas mixing section 57
3.2.1.2 Exposure section 58
3.2.1.3 Gas analysis section 59
3.2.2 Characterization of the facility 62
3.2.2.1 Temperature uniformity inside the 7 quartz tubes 62
3.2.2.2 Calibration and repeatability of gas analysis through DIDGC 63
3.2.2.3 Control of gas chemistry in the reaction zone 65
3.2.2.4 Verification of adsorption and desorption of CO and CO_2 by the quartz tubes 66
3.2.2.5 Determination of minimum flow rate to avoid starvation of reactants 66
3.3 Exposure experiment parameters 68
3.4 Exposure experiment procedure 70
3.4.1 Preparation of samples for corrosion tests 71
3.4.2 Preparation of the facility for corrosion tests 72
3.4.2.1 Baking and establishment of target CO and CO_2 concentrations in the tubes 72
3.4.2.2 Insertion of the samples in the hot zone and start of the exposure experiment 73
3.4.2.3 Pulling out of the samples from hot zone after the exposure 75
3.5 Post exposure analysis of the samples 75
3.5.1 Measurement of weight change in the sample 75
3.5.2 X-ray analysis 76
3.5.3 SEM imaging 77
3.5.4 TEM imaging 80
3.5.4.1 Sample preparation using FIB 80
3.5.4.2 TEM imaging conditions 81
3.5.4.3 Indexing of the diffraction pattern 82
3.5.5 Electron Micro-Probe analysis (EMPA) 83
3.6 Error analysis procedure 84

4. RESULTS 115

4.1 CO and CO_2 behavior vs. time over 850°C -1000°C 116
4.2 Weight gain 118
4.2.1 Weight gain vs. time 118
4.2.2 Weight gain vs. temperature 120
4.3. Microstructure examination 120
4.3.1 As-received alloy 617 121
4.3.2 Samples exposed in environment 1 (CO/CO_2 = 9) 123
4.3.2.1 Surface microstructure 123
4.3.2.2 Bulk microstructure 126
4.3.3 Samples exposed in environment 6 (CO/CO_2 = 1272) 126

4.3.3.1 Identification of phases formed during oxidation 127
4.3.3.2 Microstructure examination 129
4.3.3.2.1 Surface microstructure..... 130
4.3.3.2.2 Bulk microstructure at 900°C..... 135
4.3.3.3 Weight of oxygen in the Cr_2O_3, Al_2O_3 and weight of carbon in the form of Cr_7C_3 in samples oxidized at 900°C..... 137
4.4 Pre-oxidation experiment..... 138
4.5 Short term experiment in environment 6 (CO/CO_2 = 1272) at 900°C 141

5. DISCUSSION..... 239

5.1 Establishment of reactions governing carburization and decarburization..... 239
5.1.1 Establishment of oxidation and carburization at 900°C..... 240
5.1.2 Establishment of decarburization at 1000°C..... 243
5.2 Determination of the critical temperature range..... 248
5.2.1Critical temperature in environment 1 (CO/CO_2 = 9) 249
5.2.2 Critical temperature in environments 2 (CO/CO_2 =150) to 6 (CO/CO_2 =1272)..... 250
5.2.3 Comparison of the critical temperature with literature..... 252
5.2.4 Calculation for activity of Cr in alloy 617..... 253
5.3 Decarburization Mechanism..... 256
5.3.2 Rate limiting step for decarburization of as-received alloy at 1000°C ... 263
5.3.3 Role of Aluminum in decarburization..... 266
5.4 Carburization mechanism 269

6. CONCLUSIONS..... 312

7. FUTURE WORK..... 315

APPENDICES…….317

BIBLIOGRAPHY..... 328

LIST OF FIGURES

Figure

1.1 A schematic of the VHTR [4] 7

2.1 A typical microstructure for alloy 617 35

2.2 Weight fraction of precipitates in alloy 617 by THERMOCALC® [9] 36

2.3 Time-temperature-precipitation diagram for $M_{23}C_6$ and M_6C carbide in alloy 617 [9] 37

2.4 Oxygen-18 profile showing the growth mechanism of chromia on Ni-25Cr alloy [46].. 38

2.5 Oxide map for Ni-Cr-Al alloys[49] 39

2.6 Representative microstructure of group I alloy in the oxide map [49] 40

2.7 Representative microstructure of group II alloy in the oxide map [49] 41

2.8 Representative microstructure of group III alloy in the oxide map [49] 42

2.9 Comparison of the oxidation kinetics of Ni-Cr-Al alloys [53] 43

2.10 Schematic diagram illustrating the oxidation mechanism of Ni-Cr-Al alloys [49] 44

2.11 Microstructure of Ni-20Cr-3Al alloys oxidized at 1200°C in 1 atm oxygen. The alloy lies on the border of the group II and III alloys and shows heterogeneous oxidation. Locally it shows oxidation behavior which is typical of the group II and III alloys in the Ni-Cr-Al oxide map [49] 45

2.12 Schematic of Cr-stability diagram showing three critical parameters, $P^*_{O_2}$, a^*_C, and P^*_{CO}. 46

2.13 Predication of oxidation behavior of a Ni-Cr alloy based on Cr-stability diagram. 47

2.14 Explanation of critical temperature based on Cr-stability diagram. 48

2.15 Procedure for experimental determination of critical temperature [74] 49

2.16 Plot of critical temperature as a function of CO concentration in the environment for alloy 617. Critical temperature increases with CO concentration in the environment [74,78,83]..... 50

2.17 Plot of critical temperature as a function of CO concentration in the environment for alloy 230 [84]..... 51

2.18 Influence of hydrogen on the critical temperature for alloy 617. Hydrogen does not influence the critical temperature [83] 52

2.19 Influence of water vapor on the critical temperature for alloy 617. Critical temperature decreases with increase in water vapor concentration [83]. 53

2.20 Schematic of mechanism of decarburization of alloy 617 in impure helium as proposed by Brenner et al [26,60,75]..... 54

3.1 Schematic of the controlled-Impurity-Flow system. 91

3.2 Photograph of the assembled Controlled-Impurity-Flow system. 92

3.3 Photographs of custom fabricated quartz push rod to move the specimen from the hot zone to cold zone of the furnace without breaking the seal of the system 94

3.4 Schematic of the flow path of the carrier gas during analysis of an unknown gas mixture..... 95

3.5 A representative chromatogram obtained for a gas mixture containing 2 ppm of CO_2, H_2, Ar, O_2, CH_4, and CO in helium 97

3.6 (a) Cross-sectional view of the furnace showing the arrangement of the seven quartz tubes inside it, and (b) temperature profiling of the furnace in each quartz tube. The location of the corrosion coupons inside the furnace is marked in the figure. 99

3.7 Calibration curve for the (a) carbon dioxide, (b) hydrogen, (c) oxygen, (d) methane, and (e) carbon monoxide. A linear calibration curve was obtained for in all the cases. 102

3.8 Plot of the percentage deviation of CO_2 at the inlet of the quartz tube over 500 hours of exposure duration..... 103

3.9 Plot of the percentage deviation of CO at the inlet of the quartz tube over 500 hours of exposure duration..... 104

3.10 Plot of the percentage depletion of CO vs. time at different gas flow rates for a gas mixture consisting of 70 ppm CO and 0.7 ppm CO_2 105

3.11 The equilibrium carbon and oxygen potentials in the helium gas superimposed on the Cr-O-C stability diagram for alloy 617 at 850°C. The activity of Cr for alloy 617 is assumed to be 0.72 106

3.12 The equilibrium carbon and oxygen potentials in the helium gas superimposed on the Cr-O-C stability diagram for alloy 617 at 900°C. The activity of Cr for alloy 617 is assumed to be 0.72 107

3.13 The equilibrium carbon and oxygen potentials in the helium gas superimposed on the Cr-O-C stability diagram for alloy 617 at 950°C. The surface activity of Cr for alloy 617 is assumed to be 0.72. 108

3.14 Figure 3.14 The equilibrium carbon and oxygen potentials in the helium gas superimposed on the Cr-O-C stability diagram for alloy 617 at 1000°C. The surface activity of Cr for alloy 617 is assumed to be 0.72..... 109

3.15 Cross-sectional view showing the placement of a corrosion coupon inside the quartz tube. Top and bottom of the 6.5 mm x 6.5 mm x 1.5 mm corrosion coupons resting on the walls of the quartz tube were exposed to the flowing helium gas mixture. 110

3.16 A typical fluctuation of the furnace temperature due to opening and closing of the furnace during insertion and pulling out of the corrosion coupons. 111

3.17 Procedure for measuring the area fraction of Cr_2O_3, Al_2O_3, and Cr_7C_3 from microstructure 112

3.18 Procedure for measuring the area fraction of bulk carbides using Adobe Photoshop® software from Adobe, Inc. 113

3.19 Schematic of the cross-sectional TEM sample preparation using FIB. 114

4.1 (a) Plot of CO out – CO in vs. time in environment 1(CO/CO_2 = 9) over 850°C - 1000°C. (b) portion of the plot showing the consumption/evolution behavior in first 150h of oxidation..... 161

4.2 (a) Plot of CO out – CO in vs. time in environment 2(CO/CO_2 = 150) over 850°C - 1000°C. (b) portion of the plot showing the consumption/evolution behavior in first 150h of oxidation..... 162

4.3(a) Plot of CO out – CO in vs. time in environment 3(CO/CO_2 = 291) over 850 - 1000°C. (b) portion of the plot showing the consumption/evolution behavior in first 150h of oxidation..... 163

4.4(a) Plot of CO out – CO in vs. time in environment 4(CO/CO_2 = 453) over 850 - 1000°C. (b) portion of the plot showing the consumption/evolution behavior in first 150h of oxidation..... 164

4.5 (a) Plot of CO out – CO in vs. time in environment 5(CO/CO_2 = 900) over 850°C - 1000°C. (b) portion of the plot showing the consumption/evolution behavior in first 150h of oxidation..... 165

4.6 (a) Plot of CO out – CO in vs. time in environment 6(CO/CO_2 = 1272) over 850°C - 1000°C. (b) portion of the plot showing the consumption/evolution behavior in first 150h of oxidation..... 166

4.7 Plot of CO_2 out – CO_2 in vs. time in environment 1(CO/CO_2 = 9) over 850 - 1000°C 167

4.8 Plot of CO_2 out – CO_2 in vs. time in environment 2(CO/CO_2 = 150) over 850 - 1000°C. 168

4.9 Plot of CO_2 out – CO_2 in vs. time in environment 3(CO/CO_2 = 291) over 850 - 1000°C. 169

4.10 Plot of CO_2 out – CO_2 in vs. time in environment 4(CO/CO_2 = 453) over 850 - 1000°C. 170

4.11 Plot of CO_2 out – CO_2 in vs. time in environment 5(CO/CO_2 = 900) over 850 - 1000°C. 171

4.12 Plot of CO_2 out – CO_2 in vs. time in environment 6(CO/CO_2 = 1272) over 850°C - 1000°C..... 172

4.13 Weight gain vs. time in the six tested environments at 850°C. 173

4.14 Weight gain vs. time in the six tested environments at 900°C. 174

4.15 Weight gain vs. time in the six tested environments at 950°C. 175

4.16 Weight gain vs. time in the six tested environments at 1000°C. 176

4.17 Weight gain vs. temperature in environment 1 (CO/CO_2 = 9). 177

4.18 Weight gain vs. temperature in environment 2 (CO/CO_2 = 150). 178

4.19 Weight gain vs. temperature in environment 3 (CO/CO_2 = 291). 179

4.20 Weight gain vs. temperature in environment 4 (CO/CO_2 = 453). 180

4.21 Weight gain vs. temperature in environment 5 (CO/CO_2 = 900). 181

4.22 Weight gain vs. temperature in environment 6 (CO/CO_2 = 1272). 182

4.23 Microstructure of the etched as received alloy 617 183

4.24 (a) Transmission electron image of the carbide along a grain boundary in the as received alloy 617 (b) Diffraction pattern from the grain boundary carbide. In this pattern, the larger spots (encircled spots) are reflections from γ matrix and the small spots are reflections from the carbide. 184

4.25 X-ray diffraction pattern of the as received alloy 617. 185

4.26 (a) Low magnification and (b) high magnification BSE image of the sample exposed in environment 1(CO/CO_2 = 9) at 850°C for 100h..... 186

4.27(a) Low magnification and (b) high magnification BSE image of the sample exposed in environment 1(CO/CO_2 = 9) at 850°C for 500h..... 187

4.28 (a) Low magnification and (b) high magnification BSE image of the sample exposed in environment 1(CO/CO_2 = 9) at 900°C for 100h..... 188

4.29 (a) Low magnification and (b) high magnification BSE image of the sample exposed in environment 1(CO/CO_2 = 9) at 900°C for 500h..... 189

4.30 (a) Low magnification and (b) high magnification BSE image of the sample exposed in environment 1(CO/CO_2 = 9) at 900°C for 750h..... 190

4.31 Plot of the thickness of the Cr_2O_3 film as a function of time for samples exposed in environment 1(CO/CO_2 = 9) at 900°C. 191

4.32 (a) Low magnification and (b) high magnification BSE image of the sample exposed in environment 1(CO/CO_2 = 9) at 950°C for 100h..... 192

4.33(a) Low magnification and (b) high magnification BSE image of the sample exposed in environment 1(CO/CO_2 = 9) at 950°C for 375h..... 193

4.34 (a) Low magnification and (b) high magnification BSE image of the sample exposed in environment 1(CO/CO_2 = 9) at 950°C for 750h..... 194

4.35 Plot of the thickness of the Cr_2O_3 film as a function of time for samples exposed in environment 1(CO/CO_2 = 9) at 900°C and 950°C. 195

4.36(a) Low magnification and (b) high magnification BSE image of the sample exposed in environment 1(CO/CO_2 = 9) at 1000°C for 100h. Surface Cr_2O_3 film was not observed..... 196

4.37 Surface XRD of the sample exposed in environment 1(CO/CO_2 = 9) at 1000°C for 100h. The expected positions of the high intensity peaks of Cr_2O_3 are marked on the plot with the diamond symbol in red color. 197

4.38 Concentration profiles of Cr, Ni, Mo, and Co measured by EMPA. The sample was exposed in environment 1(CO/CO_2 = 9) for 100h. 198

4.39 (a) BSE image of the sample exposed in environment 1(CO/CO_2 = 9) for 375 h at 1000°C. The surface microstructure was non-uniform 199

4.40 BSE images of the sample exposed in environment 1(CO/CO_2 = 9) at 1000°C for 500h. The surface microstructure was non-uniform 200

4.41 SEM image of the (a) sample exposed at 900°C for 375 h in environment 1(CO/CO_2 = 9), and (b) as received alloy 617. 201

4.42 SEM image of the sample exposed at 950°C in environment 1(CO/CO_2 = 9) for (a) 100h, and (b) 375h. 202

4.43 SEM image of the sample exposed in environment 1(CO/CO_2 = 9) at 1000°C for (a) 100h, (b) 375h 203

4.44 (a) Low magnification (b) high magnification back scattered electron image (BSE image) of the sample exposed at 1000°C for 100h in environment 6 (CO/CO_2 = 1272). 204

4.45 (a)-(f) Back scattered electron image and the corresponding x-ray map of the sample exposed in environment 6 (CO/CO_2 = 1272) for 100h at 1000°C. 205

4.46 X-ray diffraction pattern of the sample exposed in environment 6 (CO/CO_2 = 1272) at 1000°C for 100h. 206

4.47(a) High angle annular dark field image (HAADF), (b)-(f) corresponding x-ray map of chromium, oxygen, aluminum, carbon, and nickel. This sample was exposed at 850°C for 225h in environment 6 (CO/CO_2 = 1272). 207

4.48 (a) Bright field TEM image of the sample oxidized at 850°C for 225 h in environment 6 (CO/CO_2 = 1272), (b) and (c) are diffraction patterns taken from the location marked as “A” and “B” in the figure (a). A is Cr_7C_3 and B is Cr_2O_3. 208

4.49 (a) Low magnification and (b) high magnification BSE images of the sample exposed in environment 6 (CO/CO_2 = 1272) at 850°C for 100h 209

4.50 (a) Low magnification and (b) high magnification BSE images of the sample exposed in environment 6 (CO/CO_2 = 1272) at 850°C for 375h. 210

4.51(a) Low magnification and (b) high magnification BSE images of the sample exposed in environment 6 (CO/CO_2 = 1272) at 850°C for 500h. 211

4.52 (a) Low magnification and (b) high magnification BSE images of the sample exposed in environment 6 (CO/CO_2 = 1272) at 900°C for 100h 212

4.53 (a) Low magnification and (b) high magnification BSE images of the sample exposed in environment 6 (CO/CO_2 = 1272) at 900°C for 225h. 213

4.54 (a) Low magnification and (b) high magnification BSE images of the sample exposed in environment 6 (CO/CO_2 = 1272) at 900°C for 375h 214

4.55(a) Low magnification and (b) high magnification BSE images of the sample exposed in environment 6 (CO/CO_2 = 1272) at 900°C for 500h 215

4.56(a) Low magnification and (b) high magnification BSE images of the sample exposed in environment 6 (CO/CO_2 = 1272) at 900°C for 750h 216

4.57(a) Low magnification and (b) high magnification BSE images of the sample exposed in environment 6 (CO/CO_2 = 1272) at 950°C for 100h 217

4.58(a) Low magnification and (b) high magnification BSE images of the sample exposed in environment 6 (CO/CO_2 = 1272) at 950°C for 375h 218

4.59 Low magnification BSE images of the sample exposed in environment 6 (CO/CO_2 = 1272) at 950°C for 500h 219

4.60 (a) Low magnification and (b) high magnification BSE images of the sample exposed in environment 6 (CO/CO_2 = 1272) at 1000°C for 100h 220

4.61(a) Low magnification and (b) high magnification BSE images of the sample exposed in environment 6 (CO/CO_2 = 1272) at 1000°C for 375h 221

4.62 Low magnification BSE images of the sample exposed in environment 6 (CO/CO_2 = 1272) at 1000°C for 500h 222

4.63 Bulk microstructure of the as received alloy 617 223

4.64 (a) Bulk microstructure of the sample oxidized in environment 6 (CO/CO_2 = 1272) at 900°C for 100h. (b) high magnification image of the area boxed in (a). 224

4.65 (a) Bulk microstructure of the sample oxidized in environment 6 (CO/CO_2 = 1272) at 900°C for 375h, and (b) high magnification image of the area boxed in (a). 225

4.66 (a) Bulk microstructure of the sample oxidized in environment 6 (CO/CO_2 = 1272) at 900°C for 500h, and (b) high magnification image of the area boxed in (a). 226

4.67 The measured area fraction of the $M_{23}C_6/M_6C$ carbides (where M is Cr, Mo) in the bulk of the alloy for as received alloy 617 and the samples oxidized in environment 6 (CO/CO_2 = 1272) for 100h, 375h and 500h at 900°C. 227

4.68 Plot of the depth of denuded zone vs. time for samples exposed in environment 6 (CO/CO_2 = 1272) at 900°C. 228

4.69 Plot of the calculated weight of oxygen in the form of Cr_2O_3 and Al_2O_3 and weight of carbon in the form of the surface Cr_7C_3 as a function of time. CO/CO2 = 1272, Temperature = 900°C 229

4.70 Plot of the difference in CO concentrations at the outlet and inlet as a function of exposure time during pre-oxidation step at 900°C and decarburization at 1000°C. 230

4.71 Change in the weight of the sample as a function of exposure duration during the decarburization step at 1000°C 231

4.72 (a)Low magnification and (b) high magnification BSE image of the sample pre-oxidized at 900°C for 150 h. 232

4.73 (a)Low and (b) high magnification BSE image of the sample after the 100h of decarburization step 1000°C..... 233

4.74 Microstructure of the sample pre-oxidized at 900°C for 150h. 234

4.75 Bulk microstructure of the samples (a) decarburized for 15h at 1000°C, and (b) decarburized at 1000°C for 100 h. 235

4.76 Concentration profile of Cr in samples pre-oxidized at 900°C for 150h and decarburized for 5h and 100h at 1000°C 236

4.77 (a)XRD of the surface film formed after 1h of oxidation at 900°C in environment 6 (CO/CO_2 = 1272), (b) zoomed in portion of the XRD. 237

4.78 BSE image of the sample exposed in environment 6 (CO/CO_2 = 1272) for 1 h at 900^{o}C..... 238

5.1 Bulk microstructures of (a) as received alloy, and (b)pre-oxidized sample at 900°C for 150h in environment 1 (CO/CO_2 = 9). 289

5.2 Bulk microstructures of (a) sample pre-oxidized at 900°C for 150h, (b) decarburized at 1000°C for 15h, and (c) decarburized at 1000°C for 100h in environment 1 (CO/CO_2 = 9). 290

5.3 Weight of carbon produced during exposure at 1000°C; Pre-oxidation experiment..... 291

5.4 SEM/EDS spectrum of the quartz tube used in exposing samples in environment 1 (CO/CO_2 = 9) at 1000°C. Chromium peak was not observed suggesting that chromia was not volatile in the present case..... 292

5.5 Weight of carbon produced during exposure of as-received sample at 950°C and 1000°C during decarburization of as received sample..... 293

5.6 Bulk microstructures of (a) as received alloy 617, (b) sample oxidized at 900°C for 375h, (c) sample oxidized for 375h at 950°C, and (d) sample decarburized at 1000°C for 375h. Environment1 (CO/CO_2 = 9)..... 294

5.7 Bulk microstructure of (a) as-received alloy, (b) sample decarburized in environment 1 (CO/CO_2 = 9), (c) sample oxidized in environment 2 (CO/CO_2 = 150), and (d) sample oxidized in environment 6 (CO/CO_2 = 1272). Temperature =1000°C, time = 375h..... 295

5.8 Plot of critical temperature as a function of CO concentration in impure helium with range of critical study from present study. 296

5.9 Schematic diagram showing the decarburization of the as received alloy at 1000°C in environment 1 (CO/CO_2 = 9) with 15 ppm of CO and 1.7 ppm CO_2 in helium. 297

5.10 Weight gain vs. time for as-received sample exposed at 1000°C..... 298

5.11 Bulk microstructure of the (a) as-received alloy, and as-received sample decarburized in environment 1 (CO/CO_2 = 9) at 1000°C (b) for 100h, and (c) for 375h..... 299

5.12 Plot of the mass fraction of carbon remaining in the sample as a function of time.. 300

5.13 Surface microstructure of the sample decarburized in environment 1 (CO/CO_2 = 9) at 1000°C for (a) 375h and (b) 500h 301

5.14 The CO out – CO in and the weight gain due to oxygen in chromia as a function of time. The sample was decarburized in environment 1 (CO/CO_2 = 9) at 1000°C. 302

5.15 Oxide map for Ni-Cr-Al ternary alloy. Alloy 617, if viewed as, Ni-22Cr-1Al alloy lies in group II and is expected to form internal oxidation of Al at 1000°C. For Ni-22Cr alloys the critical concentration of Al required to form alumina film is ~3wt%. 303

5.16 Alloy/oxide interface more convoluted in region II in comparison to region I. The sample was decarburized at 1000°C for 500h in environment 1 (CO/CO_2 = 9) 304

5.17 Schematic of mechanism of carburization of the as-received alloy in environment 6 (CO/CO_2 = 1272) at 900°C..... 305

5.18 Bulk microstructure of the (a) as-received alloy, and (b) sample carburized in environment 6 (CO/CO_2 = 1272) at 900°C. 306

5.19 Carbon and oxygen potentials in the environment 6 (CO/CO_2 = 1272) superimposed on the Cr-stability diagram at 900°C. 307

5.20 Microstructure substantiation of the nucleation and growth mechanism of surface carbide. 308

5.21 Concentration profile of Cr measured by EMPA. The sample was carburized in environment 6 (CO/CO_2 = 1272) for 100h at 900°C. 309

5.22 The calculated diffusion coefficient of Cr, D_{Cr} superimposed on the bulk diffusivity, D_B of Cr in chromia in the literature. 310

5.23 (a) Plots of (a) a_{Cr}-a_C at 900°C showing the a_{Cr} below which Cr_7C_3 cannot form (point A, a_{Cr} = 0.16) at the gas/scale interface where carbon potential is fixed by the CO/CO_2 ratio in the environment 6 (CO/CO_2 =1272), (b) a_{Cr}- P_{O_2} at 900°C diagram showing that the corresponding to the a_{Cr} = 0.16 (point A) in part (a), the chromia can form near the gas/scale interface. 311

LIST OF TABLES

Table

1.1 Nominal composition of alloy 617 [27] 6

1.2 A typical composition of impure helium as per the NGNP guideline [28] 6

2.1 Impurity content in the helium of experimental reactors [19] 33

2.2 Impurity concentrations, alloy, and corresponding critical temperaturefor alloy 617 [74,78,83] 34

3.1 (a)-3.1 (d) Characterization of the alloy 617 plate obtained from Special Metals, Inc., (a) initial dimensions of the plate, (b) chemical composition of the alloy 617 as provided by Special Metals, Inc., Sherry lab, and EMPA (c) the impurity contents as analyzed by Sherry lab, and (d) room temperature tensile properties..... 85

3.2 Composition of the gas cylinders used to calibrate the DIDGC. 86

3.3 Repeatability of the gas analysis through the DIDGC in the low concentration range of impurities. 86

3.4 Repeatability of gas analysis through the DIDGC in the high concentration range of impurities. 87

3.5 Concentration of CO at the inlet and outlet of the tube at four temperatures through an empty quartz tube over 25°C - 1000°C. 87

3.6 Concentration levels of six He-CO-CO_2 environments established at 850°C, 900°C, 950°C and 1000^{o}C. 88

3.7 Concentrations of the He + x ppm CO and He + y ppm CO_2 type of bottles used, flow rates of the gases from He + x ppm CO (V_1) and He + y ppm CO_2 (V_2), and research grade helium (V_3) type of bottles used to obtain the target concentration levels of CO and CO_2 in each environment 89

3.8 Element, spectrometer crystal, x-ray radiation and material used for calibration in EMPA analysis 90

4.1 Rate constant k and the rate exponent, n, for Eq. (4.1) over 850°C - 1000°C. For each environment the values of k and n were determined by a least square curve fit. 143

4.2 Indexing of the diffraction pattern from carbides in the as received alloy 617 shown in Fig. 4.24 b..... 144

4.3 Identification of peaks shown in XRD pattern from as received alloy 617 (Fig. 4.25). 145

4.4 Identification of peaks shown in XRD pattern from the sample exposed in environment 1 (CO/CO_2 ratio 9) for 100h at 1000°C..... 146

4.5 Summary of surface microstructure in environment 1 (CO/CO_2 ratio 9) over 850-1000°C. 147

4.6 Identification of peaks shown in XRD pattern from the sample exposed in environment 6 (CO/CO_2 = 1272) for 100h at 1000°C..... 148

4.7 Indexing of the diffraction pattern from the precipitate marked “A” in Fig. 4.48..... 149

4.8 Indexing of the diffraction pattern from the precipitate marked “B” in Fig. 4.48..... 150

4.9 Summary of the microstructure observations in environment 6 (CO/CO_2 = 1272) over 850°C-1000°C 151

4.10 Measurement of area fraction of the carbide in the bulk of the alloy. 152

4.11 Calculation of the weight gain due to increased fraction of the bulk carbide. 153

4.12 Measurement of depth of denuded zone in sample exposed in environment 6 (CO/CO_2 =1272) at 900°C. 154

4.13 Calculation of the weight of oxygen (in the form of Cr_2O_3 and Al_2O_3) and carbon (in the form of Cr_7C_3) in the sample exposed at 900°C for 100h in environment 6 (CO/CO_2= 1272). 155

4.14 Identification of peaks shown in XRD pattern from the sample exposed in environment 6 (CO/CO_2 =1272) for 1h at 900°C..... 160

5.1 Calculation for the weight of CO consumed during exposure to environment 1 (CO/CO_2 = 9) at a temperature of 900°C for 150h. 287

5.2 Comparison between the measured loss in weight of the sample and calculated weight of CO from the area under the curve for exposure of pre-oxidized alloy to 1000°C for 100h in environment 1 (CO/CO_2 = 9) (shown in Fig. 4.70) 287

LIST OF APPENDICES

Appendix

I. EMPA data for as received sample exposed to environment 1 (CO/CO_2 = 9) for 100h at 1000°C……317

II. EMPA data for pre-oxidation experiment……...320

ABSTRACT

MECHANISMS OF OXIDATION OF ALLOY 617 IN He-CO-CO_2 ENVIRONMENT WITH VARYING CARBON AND OXYGEN POTENTIALS

by

Deepak Kumar

Chair: Gary S. Was

The oxidation and the resulting degradation in the mechanical properties of the alloy is the major concern in the heat exchangers used in the Very High Temperature Helium-Cooled Reactor. Depending on the alloy composition, temperature, and helium composition the alloy can oxidize, carburize, and decarburize. Oxidation reduces the load bearing cross-section of the component, carburization leads to reduction of creep-rupture ductility, and decarburization reduces the creep strength of the alloy. Therefore, a detailed knowledge of the oxidation mechanisms is required in order to estimate the lifetime of the component.

The objective of this research was to determine the mechanism of decarburization and carburization of the alloy 617 by determining the gas-metal reactions. Simplified binary gas mixtures containing only CO and CO_2 as impurities were chosen to circumvent the complications caused by impurities H_2, H_2O, and CH_4, normally, present

in helium in addition to CO and CO_2; and oxidation tests were conducted between 850°C-1000°C in six environments with CO/CO_2 ratio varying between 9 and 1272.

A critical temperature corresponding to the equilibrium of the reaction

$$2Cr + 3CO \leftrightarrow Cr_2O_3 + 3C_{solution}$$

was identified. Below the critical temperature the alloy reacted with CO resulting in formation of a stable chromia film and carburization, whereas, above the critical temperature the decarburization of the alloy occurred via reaction between the chromia film and carbon in the alloy producing CO and Cr. In environment with CO/CO_2 of 9 the critical temperature was between 900°C and 950°C, whereas, in environment with CO/CO_2 ratio higher than 150, it was greater than 1000°C.

The decarburization of the alloy occurred via two reactions occurring simultaneously on the surface:

formation of chromia

$$2Cr + 3/2O_2 \rightarrow Cr_2O_3 ,$$

and reduction of chromia

$$Cr_2O_3 + 3C_{solution} \rightarrow 2Cr + 3CO.$$

At 1000°C, the rate liming step was the formation of chromia which prevented the growth of chromia film until the carbon in the sample was depleted. The time taken for this to occur was 300h. The depletion of carbon led to the dissolution of carbides in the entire sample, which is expected to reduce the lifetime of the alloy by reducing its creep-strength.

The carburization of the alloy resulted in the formation of porous surface scale consisting of Cr_2O_3 and Cr_7C_3 precipitates. The Cr_7C_3 was a metastable phase which

nucleated due to preferential adsorption of carbon on the chromia surface. The Cr_7C_3 precipitates coarsened at the gas/scale interface via outward diffusion of Cr cations through the chromia scale until the activity of Cr at the reaction site fell below a critical value. Decrease in activity of Cr at the carbide/chromia interface triggered a reaction between chromia and carbide:

$$Cr_2O_3 + Cr_7C_3 \rightarrow 9Cr + 3CO.$$

The CO so produced was transported through the oxide cracks and pores and was released into the environment where it was detected by a gas chromatograph. Chromium diffused outward from the reaction site to the gas/scale interface where it was re-oxidized to Cr_2O_3.

CHAPTER 1

INTRODUCTION

Over the past 25 years, the Very High Temperature Gas-Cooled Reactor (VHTR) has emerged as a leading advanced nuclear reactor concept. High efficiency of electricity production (>50% at 1000°C), combined with a broad range of process heat applications, such as hydrogen production, distinguish it from other "Generation IV" nuclear energy systems[1-3]. A schematic of the VHTR concept is shown in Fig. 1.1[4]. The main parts in this concept are: reactor pressure vessel, core and close-to-core components, gas turbine, intermediate heat exchangers, and hydrogen production unit.

One of the most critical metallic component in this design is the intermediate heat exchanger (IHX)[5], which transfers the reactor heat to the electricity generation and hydrogen production units. Service condition of the IHX is characterized by high temperature (>900°C), low stress (<8 MPa), oxidizing/carburizing/decarburizing helium gas with CO, CO_2, H_2, H_2O, CH_4 as impurities that mainly arise from the reaction between hot graphitic core and in-leaked air from seals/welds, and degassing of fuel and thermal insulating materials; and high lifetime expectancy (~60 years)[5-7]. Under these service conditions, the oxidation of the IHX in impure helium and the resulting degradation in mechanical properties, particularly creep strength[8], is considered as a major problem with respect to the safe operation of the VHTR. The goal of ensuring the structural integrity of the IHX for a service lifetime of 60 years demands that the alloy

have excellent oxidation resistance, microstructure stability, strength, ductility, creep strength, and fatigue strength.

Ni-base alloys have traditionally been used for high temperature applications. Two types of Ni-bases alloys, typically, are used - precipitation hardened alloys and solid-solution hardened alloys. These alloys achieve high strength and creep resistance by virtue of the precipitation hardening caused by ordered γ' or γ'' Ni_3(Al, Ti, Ta, Nb) precipitates (precipitation hardened alloys) , and/or solid-solution hardening caused by refractory elements such as Co, Mo, W, Ru, Ta, Re (solid-solution hardened alloys). The additions of Cr and Al give these alloys high oxidation resistance. The precipitation hardened alloys are precluded from VHTR heat exchanger applications, as at the operating temperature of 900°C-1000°C and service lifetime of 60 years, the γ' or γ'' precipitates are expected to dissolve [9]. On the other hand the solid-solution hardened alloys can maintain their strength at these temperatures for long times [10, 11], and are considered more suitable for the heat exchanger application. Some of the commercial solution hardened alloys which are under consideration are: alloy 617, alloy 230, Nimonic 86, and Hastelloy X.

Alloy 617 is the leading candidate alloy for the heat exchanger application by virtue of its superior creep strength over other Ni-based superalloys, such as Nimonic 86 and Hastelloy X [6, 10, 12]. Nominal composition of the alloy 617 is shown in table 1.1. It is an austenitic alloy based on Ni-Cr with solid solution strengthening caused by cobalt and molybdenum. The Cr and Al provide oxidation resistance. It shows exceptional creep strength [8, 13-15], yield strength [16, 17], and retains toughness after long-time exposure at elevated temperatures and does not form embrittling phases such as σ, μ, or

Laves [9, 13]. Addition of a small amount of carbon (~0.1 wt%) to this alloy results in precipitation of intergranular and intragranular $M_{23}C_6$ and M_6C (where M is mainly Cr, Mo) carbides. The carbides provide additional creep strength and microstructure stability by inhibiting grain boundary sliding and grain growth at elevated temperatures. It has good fabricability and weldability, and can be processed into plate and tube geometries by hot and cold working [12]. It has lower thermal expansion than most austenitic stainless steels imparting high dimensional stability [10].

In spite of the exceptional mechanical properties of the alloy 617, its application in the IHX is questionable owing to its poor chemical compatibility with the CO, CO_2, CH_4, H_2, and H_2O impurities in helium. Low oxygen and carbon potentials arise from the part-per-million (ppm) levels of impurities, which actively corrode the metallic surfaces. Depending on the temperature, impurity concentrations, and alloy compositions; surface or internal oxidation, carburization, and decarburization of the alloy can occur. These oxidation processes can degrade the mechanical properties of the alloy, e.g. internal oxide precipitates has been shown to act as the preferential crack initiation sites in alloy 617[18]. These cracks can develop in surface cracks and can, potentially, decrease the creep and fatigue life of the alloy. A significant reduction in the creep-rupture ductility of alloy 800H[19], alloy 617[20, 21], and Hastelloy X [22] has been reported in carburizing environment in comparison to pure helium and air environment. The loss of ductility in carburizing environment was mainly due to occurrence of cleavage fracture in carburizing gas as opposed to ductile fracture in air. Coarse and continuous network of carbides form along the grain boundaries during carburization of the alloys which act as the preferential crack initiation and propagation paths, and could severely decrease the

operating life of the alloys. Grain boundary migration and sliding has been identified as the dominant creep deformation mechanism in alloys, such as alloy 617 at 1000°C[8, 20, 23, 24], and the dissolution of carbides during decarburization will lead to significant loss of the creep strength as the $M_{23}C_6$ and M_6C carbides pin the grain boundaries. Therefore, there is an impetus on understanding the oxidation behavior and the microstructure degradation of alloys in impure helium.

Considerable oxidation studies have been conducted on various Ni-based superalloys [25-28], Ni-Cr experimental alloys [29, 30], and ODS alloys in impure helium [31]. The focus of these studies ranged from determining the basic chemical reactions involved in the alloy/impurity interaction to the development and modification of alloys, and coatings for better oxidation resistance. The Cr- stability diagram [27] and the Ternary Environmental Attack (TEA) diagram [32] was developed as predictive tools to delinate benign and deterimental helium chemistries. The benign helium chemistries are defined as the impurity concentration ranges in which a slow growing, protective oxide film formed on the alloy, which inhibited the substrate from heavy carburization or decarburization. The detrimental helium chemistries are defined as the impurity concentration ranges in which heavy surface/internal carburization or decarburization was observed. Extensive database on the kinetics of oxidation, carburization, and decarburization of various Ni-based alloys in impure helium exists in the literature [18-25]. However, the literature lacks in the characterization of the time and temperature evolution of the oxides and the bulk microstructure changes in impure helium. Most of the studies in the literature were conducted in complex helium chemistries containing multiple impurities in which the microstructure degradation due to a specific impurity

could not be determined. Further, the mechanisms of oxidation, such as decarburization and carburization, of the alloys have not been determined unequivocally. Two, fundamentally different mechanisms, proposed by Brenner et al. [32] and Christ et al. [26], exist for Ni-Cr alloys, whereas, the mechanism of carburization of the Ni-Cr alloys in impure helium has not been reported in the literature.

The objective of this thesis was to determine the mechanism of carburization and decarburization of alloy 617 in impure helium. Binary gas mixtures containing only CO and CO_2 as impurities were chosen to avoid the complications arising from presence of other impurities in helium, such as H_2, H_2O, and CH_4.The oxidation studies were conducted in six He-CO-CO_2 gas mixtures between the temperature range of 850-1000°C. The CO/CO_2 ratios in the environment were varied systematically in the wide range of 9 to 1272 and the mechanisms of oxidation was determined at low and high CO/CO_2 ratios of 9 and 1272 by characterizing the surface and bulk microstructures changes as a function of oxidation time and temperature. The low CO/CO_2 ratio environment represents the case where alloy 617 is expected to undergo decarburization, whereas the high CO/CO_2 ratio environment represents the case where the alloy 617 was expected to degrade via carburization.

The arrangement of the thesis is following: Chapter 2 provides the background material relevant to the present work. Chapter 3 describes the experimental procedure and the apparatus used in this research. Chapter 4 presents the results of the oxidation experiments conducted over 850°C-1000ºC in six He-CO-CO_2 gas mixtures. Chapter 5 discusses the mechanism of carburization and decarburization. Conclusions from this study are stated in chapter 6 and suggestions for future work are listed in chapter 7.

Table 1.1. Nominal composition of alloy 617[33].

elements	Ni	Cr	Co	Mo	Al	C	Fe	Mn	Si	Ti	Cu
concentration (weight%)	44.5 min	20-24	10-15	8-10	0.8-1.5	.05-1.5	3 max	1 max	1 max	0.6 max	0.5 max

Table 1.2. A typical composition of impure helium as per the NGNP guideline[34]

	H_2	H_2O	CO	CO_2	CH_4	N_2
concentration (ppm)	200	1	20	0.1	10	<5

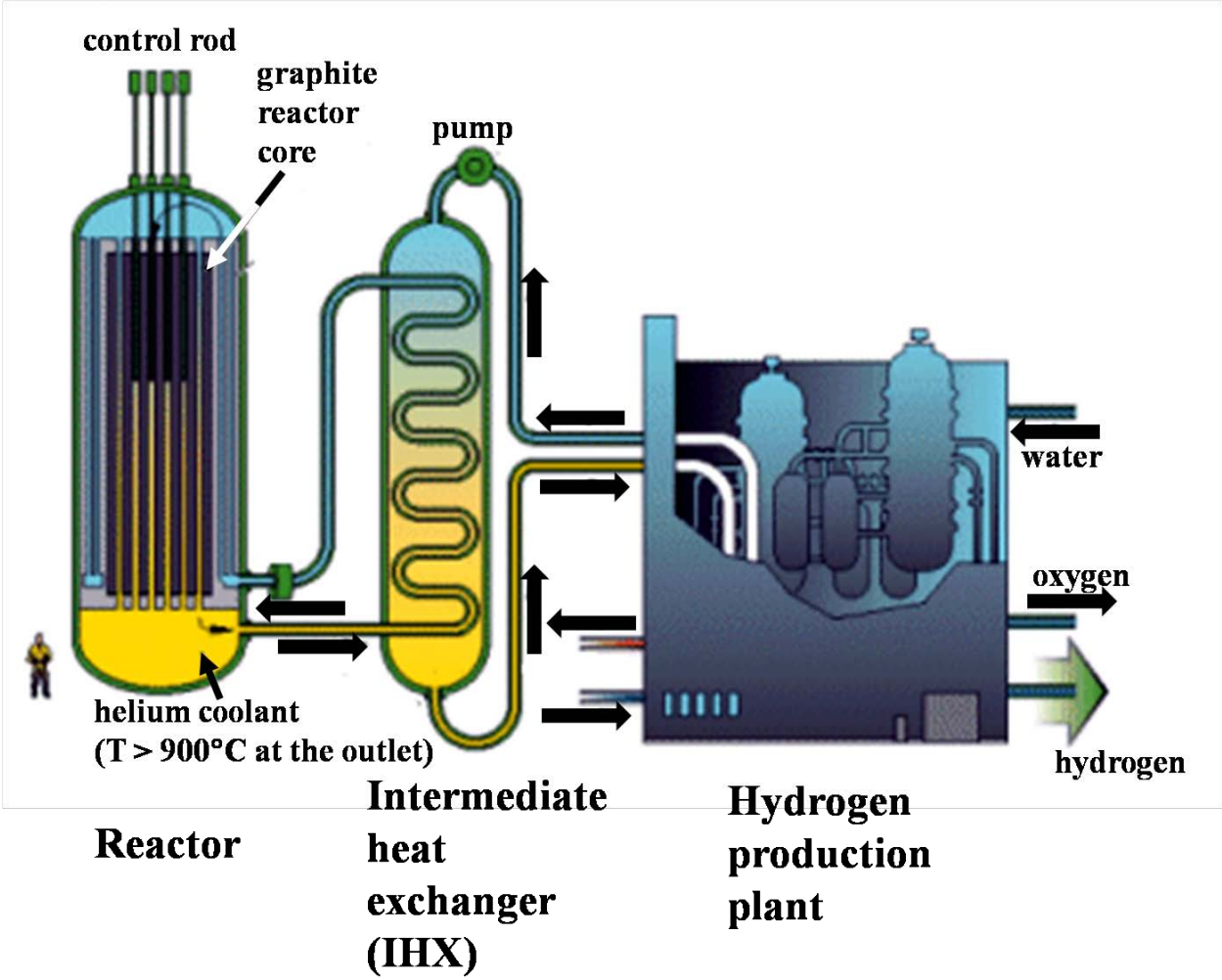

Figure 1.1 A schematic of the VHTR [4]. The outlet temperature of the helium coolant is expected to be higher than 900°C and will contain ppm levels of CO, CO_2, CH_4, H_2, H_2O as impurities.

CHAPTER 2

BACKGROUND

This chapter consists of four major sections. The first section reviews the microstructure and stability of precipitates in alloy 617. The second section reviews the growth mechanism of chromia film on pure Cr and Ni-Cr alloys. The third section discusses the oxidation of Ni-Cr-Al alloy with primary focus on the mechanism of surface and sub-surface oxidation. Finally, the fourth section reviews the oxidation of Ni-Cr alloy in impure helium gas. The Cr-stability diagram is discussed in this section, along with the critical temperature above which the Ni-Cr alloys are observed to undergo decarburization. The influence of gas chemistry on the critical temperature is also discussed. The mechanisms of decarburization of Ni-Cr alloy is discussed in the end of this section.

2.1 Microstructure and precipitate stability in alloy 617

Alloy 617(Ni-22Cr-12Co-9Mo) is a face centered cubic solid solution strengthened wrought alloy, which was developed by Special Metals Corporation, Inc. under the trade name of Inconel® 617 as a material with an exceptional combination of high temperature creep and oxidation resistance [35-37]. It is one of a few materials with allowable design stresses specified by ASME Boiler and Pressure Vessel Code for operation up to 980°C [9, 38]. The alloy is predominantly used in the solution annealed

condition which consists of annealing at 1175°C followed by water quenching or rapid air cooling [39, 40]. Typically, a grain size of ASTM No. 6 (45μm) or coarser is preferred for high creep-rupture strength. A tradeoff exists, however, when fatigue is an issue, as finer grain size is preferred for fatigue resistance [9, 41]. A typical alloy delivered by the mill contains intergranular and intragranular precipitates aligned along the rolling direction, as shown in Fig. 2.1.

A THERMOCALC® [9] prediction shown in Fig. 2.2 indicates that in the temperature range of 600-1400°C the equilibrium precipitates in alloy 617 are M(C,N), $M_{23}C_6$, M_6C, and Ni_3Al (γ'). A small amount (< 0.05wt%) of M(C,N) (where M is mainly Ti) forms from the melt and persists through the entire temperature range of 600°C-1400°C. The M_6C (where M is mainly Cr, Mo) carbide is stable at the solution annealing temperature of 1175°C and is usually observed as globular precipitates at the grain boundaries and in clusters. As much as 1 wt% of M_6C can exist at the solution annealing temperature of 1175°C. Further, as the temperature decreases, the $M_{23}C_6$ (where M is mainly Cr, Mo) starts to form below 1000°C at the expense of M_6C. Approximately 1wt% of $M_{23}C_6$ could be present at 800°C and below. γ'starts to form at ~800°C and its content increases with decreasing temperature down to 600°C where as much as 8wt% could be present in the equilibrium condition.

The predictions of the THERMOCALC® calculation in Fig. 2.2 differ somewhat with the aging studies on alloy 617 performed by Mankins et al. [42]. This study was conducted in the temperature range of 649°C-1093°C on a 19 mm diameter hot rolled bar, solution treated at 1177°C for 1h followed by air cooling. Samples included tensile bars aged for 50h and 1000h and post test creep-specimens from 215h at 1093°C to

beyond 10,000h at 760°C. The major precipitate identified in this study was $M_{23}C_6$, which was present along the grain boundaries and interior of the grains as discrete precipitate, and was stable until 1093°C for up to 10,000h. M(C,N) and M_6C carbides were not observed under X-ray diffraction (XRD) studies, suggesting that these precipitates were present in minor amounts. Approximately 0.6 wt% of γ'was observed in this study at temperatures below 760°C.

Takahashi et al. [43] studied the microstructure stability of the alloy 617 at 1000°C for time ranging between 1h and 1000h. The findings in this study were similar to that of Mankins et al. [42]. The major precipitates present in the alloy were $M_{23}C_6$, followed by M_6C, Ti(C,N), and γ'. Using Electron Micro-Probe Analysis (EMPA), the composition of the $M_{23}C_6$ and M_6C was determined to be $Cr_{21}Mo_2C_6$ and $Mo_3Cr_2(Ni,Co)_1C$.

Recently Ren et al. [9] reviewed the literature on the long term stability of precipitates in alloy 617 and constructed a time-temperature-precipitation (TTP) diagram for the two most abundant precipitates $M_{23}C_6$ and M_6C. Figure 2.3 shows the TTP diagram from this review. The legend lists the time and temperature conditions under which a precipitate was observed or not observed in three references reviewed by them. The open symbols in this figure show condition under which the carbides were observed in the microstructure, whereas the solid symbols show the conditions under which the carbides were not observed in the microstructure. According to this diagram $M_{23}C_6$ is a stable precipitate which persists in the microstructure up to 1050°C and is stable for durations more than 100,000h. The M_6C is stable up to 1000°C, but its stability is limited only till 2000-3000h, after that they transform into $M_{23}C_6$ [44].

Summary

The main precipitates in alloy 617 in order of decreasing abundance are $M_{23}C_6$, M_6C, and γ' (Ni_3Al). According to THERMOCALC calculation (Fig. 2.2) and aging studies [42, 43, 45] the γ' is a low temperature phase which is stable only at temperatures below 800°C. This precipitate is generally too fine to be observed under SEM and optical microscopy. $M_{23}C_6$ is the most abundant precipitate in the alloy and is, typically, observed along the grain boundaries and interior of the grains as discrete particles. It is a Cr, Mo-rich phase with composition of 90at% Cr and 10at% Mo and is stable for more than 100,000h at 1050°C (Fig. 2.3). The second most abundant precipitate in the alloy 617 is M_6C with the average composition of 35at% of Cr, 50at% of Mo, 12.5% of Co and 12.5% of Ni[43]. M_6C carbide are stable until 10,000h at 1000°C after which they tend to transform in $M_{23}C_6$ carbide by rejecting Mo into the matrix[44, 46].

2.2 Mechanism of growth of Cr_2O_3 film during oxidation

The high temperature oxidation resistance of Cr-rich alloys, such as alloy 617 is in practice provided by a barrier layer of chromia scale. As a consequence the defect and transport properties of chromia have been of considerable interest and significant research have been conducted. This section reviews the growth mechanism of chromia scale on pure Cr and Cr-rich alloys.

Caplan and Sproule [47] studied the oxidation of etched Cr and Fe-26Cr alloy in 1 atm oxygen between 980°C-1200°C. While the alloy compositions are much different from alloy 617, some of the results are significant with regard to the growth mechanism of chromia. On etched Cr, the oxide layer grew rapidly on some grains and more slowly

on other grains. The thick oxide was fine grained and developed compressive stress, whereas, the thin oxide was monocrystalline and free of stress due to growth of the film. Their interpretation is that the single crystal grew solely at the free gas/scale interface by outward cation diffusion and hence stress did not develop. The polycrystalline scale grew partly by anion diffusion and formed new oxide within the oxide layer and generated compressive stress. Since compressive stresses arise from anion transport and no compressive stress was observed in the cases where oxide grain boundaries do not exist, it follows that the anion transport must occur via grain boundaries. Thus, they conclude that polycrystalline chromia grows via simultaneous counter-current transport of chromium and oxygen, whereas single crystal chromia primarily via outward diffusion of chromium.

The counter-current diffusion of Cr and oxygen during chromia growth has also been confirmed by Skeldon et al. [48]. In this study, mechanically and electro-polished samples were first oxidized in natural oxygen ($^{16}O_2$) for the time varying between 4 to 268 minutes to form an inner layer of chromia and then in oxygen-18 ($^{18}O_2$) atmosphere for additional 20 to 389 minutes to form an outer layer chromia. The distribution of oxygen-18 was then traced in the inner and outer oxide scale to determine the growth mechanism of chromia. If the chromia had grown exclusively due to outward diffusion of chromium, then new scale would only have formed at the oxide/gas interface and the concentration of the oxygen-18 at the oxide/gas interface would have been 100%. However, authors measured only 80% to 94% of the initial oxygen-18 concentration at the oxide/gas interface suggesting that some of the oxygen had transported in the inner layer of chromia forming fresh oxide at the inner layer grain boundaries. In other words,

the oxide formation was predominantly via outward transport of Cr cations but some inward transport of oxygen also occurred.

Graham et al. [49] also concur with the conclusions of Skeldon et al. [48]. In this study pure Cr was oxidized in 6.6x 10^{-6} atm O_2 at 825°C. The data showed that chromia film grew primarily by outward cation transport with ~1% of the oxide growth occurring via inward oxygen transport along the chromia grain boundaries.

Using oxygen-18 tracer technique, Barnes et al. [50] and Lees et al. [51] studied the growth mechanism of chromia in the temperature range of 850-950°C. They conclude that outward transport of chromium through chromia was the only significant transport at a lower temperature of 850°C. However, at higher temperature the growth of chromia was more complex, and, at 950°C, the oxygen-18 distribution in the chromia scale suggested that some inward transport of oxygen occurred, most likely along high diffusivity paths such as grain boundaries.

Similar conclusions were drawn in the recent study by Zurek et al. [52]. Two stage oxidation experiment using $Ar/^{16}O_2$ followed by $Ar/^{18}O_2$ on Ni-25Cr alloy at 1050°C led to the isotope distribution shown in Fig.2.4 Normalized plots were used to compensate for partial spallation which occurred during cooling. As shown in this figure, the oxygen in the outer scale is nearly exclusively $^{18}O_2$ suggesting that the chromia scale on Ni-25Cr alloy grew predominantly via outward diffusion of Cr.

Summary

In summary the literature suggests that the chromia film grows primarily via outward transport of Cr cations. However, a small amount of oxygen transport does occur, mainly along grain boundaries of the chromia and correspondingly oxide formation takes place at the grain boundaries. The fraction of oxide growth due to inward transport of oxygen through the grain boundaries in chromia varied between ~1% to 20% in different investigations.

2.3 Oxidation of Ni-Cr-Al alloys

This section reviews the oxidation of Ni-Cr-Al alloys. The focus is on understanding the surface microstructure of the alloys and the mechanism of oxidation.

Ni-Cr-Al alloys are typically used for high temperature applications because of their potential for forming stable and slow growing chromia and/or alumina scale which provide oxidation resistance to alloys for temperatures up to 1200°C [46, 53, 54]. Depending on the alloy composition the surface and sub-surface oxidation behaviors of these alloys can be different. An effective and concise way of describing the oxidation behavior of a broad range of Ni-Cr-Al alloys is the, so called, “oxide map” [54-57]. In this map the composition ranges of the alloys are delineated for the formation of different types of oxide scale and the reaction behavior. Note that these maps are not thermodynamically-derived but are rather based on experimental data and are empirical attempts of setting the critical compositions limits of the alloys for the formation of nickel oxide, chromia and/or alumina scale under a given experimental condition[58]. An example of the oxide map is illustrated in Fig. 2.5 for oxidation of Ni-Cr-Al alloys in 0.1

atmosphere oxygen at 1000°C [55]. Three different types of oxide formation and reaction behavior can be delineated in this map:

(i) In dilute alloys (group I) where the concentrations of Cr and Al are not sufficiently high to establish continuous scales of chromia or alumina, the scale consists of NiO and Ni-Cr and Ni-Al spinels, e.g. $Ni(Cr,Al)_2O_4$. In addition, the alloy is internally oxidized. The rate of oxidation is primarily determined by the diffusion of Ni through NiO scale, which is usually observed to be doped with small amount of Cr and Al. Fig. 2.6 is a representative microstructure of alloys in this group.

(ii) For alloys with sufficiently high concentration of Cr and relatively low concentrations of Al (group II), Cr is selectively oxidized, and the scale consists of chromia. In addition, Al is oxidized internally, as shown in Fig. 2.7. Under steady state, the oxidation is primarily determined by the diffusion of Cr cation through the chromia scale.

(iii) For alloys with sufficiently high concentrations of Al (group III alloys), selective oxidation of Al yields a continuous surface scale of alumina, as shown in Fig.2.8. The oxidation is determined by the diffusional growth of alumina scale.

The oxidation kinetics of group I, II and III alloys in the oxide map, in general, follows the trend $K_P(I) > K_P(II) > K_P(III)$ (where K_p is the parabolic rate constant) with oxidation kinetics of each group differing by more than an order of magnitude, as shown in Fig. 2.9[59]. This figure provides an interesting perspective on the comparison of kinetics of (a) pure Ni to group I, (b) Ni-30Cr to group II, and (c) Ni-25Al to group III alloys. The measured higher oxidation kinetics in group I alloys in comparison to pure Ni is believed to be the result of doping of NiO with Cr and Al, whereas, a slower kinetics in group II alloys with respect to Ni-30 Cr alloy is a result of gettering effect of Al which

promotes the growth of protective chromia film. The higher kinetics in group II alloys with respect to Ni-25Al is a result of Cr-gettering effect which promotes the formation of alumina scale[46, 60, 61].

Mechanism of oxidation of Ni-Cr-Al alloys

Pettit et al. [55, 62] studied the oxidation of Ni alloys containing 2 to 30 wt% Cr and 1 to 9 wt% Al at 1000-1200°C in 0.1 atmosphere oxygen environment and demonstrated that the difference in the development of surface and subsurface oxide microstructure in the three groups in the oxide map (Fig. 2.5) is solely due to different processes occurring during the transient state, i.e. the pre-steady state oxidation. Figure 2.10 is a schematic of the mechanism proposed by the authors [55]. As per this mechanism, at the beginning of exposure, rapid initial gas/metal reaction converts the alloy surface to oxide with little diffusion in the alloy and a scale primarily consisting of mixed spinels (labeled "S"), $Ni(Cr,Al)_2O_4$, with isolated grains of NiO form (Fig. 2.10). The exact composition of this layer, however, is determined by the composition of alloys and significant amount of chromia and alumina would also be present in the scale for alloys with sufficiently high Cr or Al contents. In group I alloys, the Al and Cr concentration are low and cannot form a continuous scale, but, get oxidized internally via inward transport of oxygen. Since, the oxygen activity required to oxidize the Al in the alloy is smaller than that required to oxidize Cr, the precipitates of alumina extend deeper into the alloy than the particles of chromia, as shown in Fig. 2.10b. In the external scale the growth rate of NiO is much faster than any other oxide phase that can be present and NiO completely envelops the other phases, as shown in Fig. 2.10c.

In group II and III alloys, due to higher concentration of Cr a more or less continuous scale of chromia forms beneath the outer spinel and NiO scale. This is shown schematically at step d in the Fig.2.10. For group II alloys the flux of oxygen from the duplex scale into the alloy is still sufficient to oxidize Al internally but not the Cr. Cr, therefore, diffuses from the alloy through the duplex scale and reduces the spinel and NiO to form chromia as illustrated in Fig. 2.10e. This process continues until all of the spinel or NiO are reduced and a continuous scale of chromia is formed, after which a steady state is achieved. Once the steady state is achieved the growth of the oxide is determined primarily by the transport of Cr cations through the scale. In the case of group III alloys, since the Al concentration is higher than the group I and II alloys a more or less continuous layer of alumina forms underneath the chromia layer, as shown in Fig. 2.10f. Steady state is established when a continuous film of alumina forms and the oxidation is controlled by the transport through the alumina scale.

One interesting result from the work by Pettit et al. [55] is that the oxidation behavior of alloys whose composition lie on the border of the two groups undergo heterogeneous oxidation and show evidence of the groups bordering them. Figure 2.11 shows example of this behavior by taking the case of Ni-20Cr-3Al alloy oxidized at 1200°C. This alloy composition falls on the border of the group II and group III and locally forms chromia film with internal oxidation which is the oxidation behavior for group II alloys (Fig.2.11a) and chromia film with a thin alumina film underneath the chromia film (Fig. 2.11 b), which is similar to the oxidation behavior shown by group III alloys. A satisfactory explanation for this heterogeneous oxidation behavior is not known

in the literature. Pettit et al. [55] speculate that this heterogeneity could be due to local differences in surface preparation or impurity content.

2.4 Oxidation of Ni-Cr alloys in impure helium

This section reviews the oxidation of Ni-Cr alloys in impure helium. Section 2.4.1 discusses the origin of impurities in impure helium. Section 2.4.2 lists the reactions that govern the oxidation behavior of Ni-Cr alloys in impure helium. Section 2.4.3 introduces the Cr-stability diagram and then explains the interpretation of oxidation behavior according to the stability diagram. The concept of critical temperature and the effect of impurities on the critical temperature are explained in sections 2.4.4 and 2.4.5. Lastly, the two mechanism of decarburization for alloy 617 is explained.

2.4.1 Characteristics of impure helium

Helium gas used in VHTR as coolant inevitably contains impurities. The sources of impurities for instance are air from charge/discharge of fuel elements, water vapor and carbon dioxide from degassing of the core graphite and insulators, and hydrogen from proton diffusion through materials of water-cooled heat exchangers and coolers [63-68]. These primary impurities react with large volumes of the graphitic core where virtually all the oxygen from air is converted in to CO, water vapor is partially converted to hydrogen and CO, any CO_2 is largely reduced to CO, and hydrogen reacts with the graphite to form methane. The major part of the impurities introduced in the helium is removed within a purification unit, but the remaining impurities are transported to the heat exchangers where they react with the metallic materials. Table 2.1 [25] lists the

concentration levels of impurities in heat exchangers of some experimental reactors. As observed in this table, the helium contains hydrogen, carbon monoxide, carbon dioxide, methane and nitrogen ranging from few hundreds to a few parts per million (ppm) range; the water vapor content is extremely low, in the ppm range. In this specific environment, the oxidizing potential is low while carbon activity, set by the carbon bearing species CO and CH_4 could be significant. Furthermore, due to short dwell time as well as the low concentrations of impurities, it is generally accepted that the impure helium is not in thermodynamic equilibrium. Instead, a dynamic balance between the rate of ingress of impurities, the reaction in the core, and the purification efficiency establishes the impurity nature and concentrations in the heat exchanger [32, 68, 69].

2.4.2 Gas/metal surface reactions in impure helium

Although the concentrations of impurities in helium are low, they interact with metallic materials, and typical oxidation behavior observed are surface or internal oxidation, surface or bulk carburization, and bulk decarburization. All of these processes can degrade the mechanical strength of the material, e.g. internal oxides are potential sites for crack nucleation [70], bulk carburization can result in loss in creep-ductility of the alloy[71, 72] and decarburization can reduce the creep strength of the alloy[21, 22, 24, 73-75].

Several authors have attempted to describe the gas/metal reactions that determine the oxidation behavior of Ni-Cr alloys in impure helium gas [32, 64-66, 76-78]. But the most comprehensive description of the gas/metal reactions comes from a series of paper by Brenner et al. [32, 66, 78], Quadakkers et al. [76, 77] and Christ et al. [79]. As per

their study, the oxidation behavior of Ni-Cr alloys can be described by six competing reactions which occur simultaneously on a metallic surface. These reactions are described below by assuming that the Cr is the main element which forms oxide and carbide in the alloy:

Oxidation by water vapor and carbon dioxide

$$2Cr_{solution} + 3H_2O \rightarrow Cr_2O_3 + 3H_2 \quad (2.1),$$

$$2Cr_{solution} + 3CO_2 \rightarrow Cr_2O_3 + 3CO \quad (2.2).$$

Water vapor and carbon dioxide can oxidize Cr and in favorable thermodynamic and kinetic conditions can promote the formation of surface Cr_2O_3 layers which can protect the base metal from severe carburization or decarburization.

Decarburization by water vapor

$$H_2O + C_{solution} \rightarrow CO(g) + H_2 \quad (2.3).$$

Water vapor can oxidize the carbon in the alloy in the form of CO causing decarburization of the metal.

Carburization by methane

$$7Cr_{solution} + 3CH_4 \rightarrow Cr_7C_3 + 6H_2 \quad (2.4),$$

Methane can decompose at the metal surface leading to the formation of metal carbides (Eq. 2.4). With increase in temperature the thermal stability of methane decreases and consequently this reaction becomes dominant at higher temperatures[79].

Oxidation by CO

$$9Cr_{soltuion} + 3CO \leftrightarrow Cr_2O_3 + C_{solution} \quad (At\ T > Tcr) \quad (2.5).$$

The direction of this reaction depends on the temperature. At temperatures below the so called “microclimate”[32, 66, 78] or “critical temperature” (T_{cr}) [77, 80], the reaction 2.5

proceeds in the forward direction resulting in formation of oxide and carbide, whereas, above the critical temperature the reaction 2.5 proceeds in reverse direction resulting in the formation of Cr metal and CO gas:

$$Cr_2O_3 + 3C_{solution} \rightarrow 2Cr_{solution} + 3CO \quad (At\ T > Tcr) \qquad (2.6).$$

The critical temperature at which the reaction 2.5 reverses depends mainly on the CO concentration in the environment [25, 77, 81], which will be discussed in section 2.4.4.

2.4.3 Oxidation behavior of Ni-Cr alloys based on the Cr-stability diagram

As seen from the reactions 2.1 – 2.6, the impurities in helium can be grouped into two categories; oxidizing gases (CO_2 and H_2O: reaction 2.1 and 2.2) which establish an oxygen potential at the metal surface and carburizing/decarburizing gases (CO and CH_4: reactions 2.4 and 2.5), which establish carbon potential at the metal surface. The combined effect of the oxidizing and carburizing/decarburizing gases in a Ni-Cr alloy system can be determined by the theoretical model proposed by Quadakkers et al. [76, 77, 82]. In this model, the carbon and oxygen potential at the alloy surface is determined using the kinetics of the reactions 2.1 – 2.6 and is superimposed on a Cr-stability diagram which delineates the stability regimes of metal, oxide and carbide. In the following section the definition and representation of the Cr-stability diagram is discussed first, followed by its use in prediction of oxidation behavior of Ni-Cr alloys.

2.4.3.1 Cr-stability diagram

Stability diagram, also known as predominance diagram, is a two dimensional graphical representation of the thermodynamic equilibrium between a metal and its

surrounding environment [83]. It is typically used to interpret the reaction of a metal with its gaseous environment containing two oxidants, such as, oxygen and carbon or sulfur and oxygen. Figure 2.12 shows a schematic of the Cr- stability diagram for Ni-Cr alloys, assuming Cr is the only element which can form oxide and carbide in the alloy. In this diagram the oxygen and carbon potentials in the gas and the stabilities of the metal (Cr), oxide (Cr_2O_3) and carbides ($Cr_{23}C_6$, taken as the representative carbide in Fig 2.12) are drawn on the same plot. For the ease of representation the diagram is drawn at a fixed temperature and activity of Cr in the alloy. In this diagram the stability of single phase is shown as area and two phases co-exist only along the boundary lines between two adjacent phases. Further the co-existence of three phases is shown as a point on this diagram where the phase fields of three phases meet.

2.4.3.1.1 Definition and representation [61, 84]

The stability regimes of metal (Cr), oxide (Cr_2O_3), and carbide ($Cr_{23}C_6$) are shown in green, white, and black colors, respectively in the stability diagram in Fig. 2.12. The boundary separating the metal and oxide is the vertical line QA. To the left of line QA, the metal is stable, and to the right is the oxide. Along this line metal/oxide/gas equilibrium exists, and both metal and oxide can coexist on this line. The co-existence of metal and oxide requires an equilibrium partial pressure of oxygen $P^*_{O_2}$ in the gas, which is governed by the reaction:

Line QA: $$4Cr_{solution} + 3O_2 \leftrightarrow 2\ Cr_2O_3 \qquad (2.7)$$

where $Cr_{solution}$ is the Cr in solid solution with the matrix. The $P^*_{O_2}$ is given by:

$$P_{O_2}^{*} = \left[\frac{a_{Cr_2O_3}}{K_{2.7} \times (a_{Cr})^4} \right] \quad (2.8)$$

Where $K_{2.7}$ is the equilibrium constant for the reaction in Eq. 2.7, $a_{Cr_2O_3}$ is the activity of Cr_2O_3, and a_{Cr} is the activity of Cr in the alloy. Assuming the activity of the oxide to be unity:

$$P_{O_2}^{*} = \left[\frac{1}{K_{2.7} \times (a_{Cr})^4} \right]^{(1/3)} \quad (2.9)$$

The boundary line separating the metal and carbide is the horizontal line QB. Above this line carbide is stable and below this line metal is stable. The co-existence of both metal and carbide is possible only on the line QB where the metal/carbide/gas equilibrium exists. The coexistence of metal and carbide requires an equilibrium carbon activity in the environment, a_C^{*} which is given by the reaction:

Line QB: $23Cr_{solution} + 6C_{solution} \leftrightarrow Cr_{23}C_6$ (2.10)

Assuming the activity of the carbide to be unity,

$$a_C^{*} = \left[\frac{1}{K_{2.10} \times (a_{Cr})^{23}} \right]^{(1/6)} \quad (2.11)$$

Where $K_{2.10}$ the equilibrium is constant for the reaction in Eq. 2.10 and a_{Cr} is the activity of Cr in the alloy.

The slanted line QC separates the phase fields of oxide and carbide. To the left carbide is stable, whereas to the right the oxide is stable. Along the line QC oxide/carbide/gas equilibrium exists and both oxide and carbide are stable on this line. The reaction governing the oxide/carbide/gas equilibrium is:

Line QC: $Cr_{23}C_6 + 69O_2 \leftrightarrow 46Cr_2O_3 + 24C_{solution}$ (2.12)

Assuming the activity of the oxide and carbide to be unity, the slanted line is given by:

$$K_{2.12} = \frac{(a_C)^{24}}{(P_{O_2})^{69}} \tag{2.13}$$

where $K_{2.12}$ is the equilibrium constant for reaction in Eq. 2.12. One important point to note in the oxide/carbide/gas equilibrium shown in Eq. 2.12 is that the co-existence of oxide and carbide poses a strict condition on the oxygen and carbon potential in the environment. Where the metal/oxide/gas (line QA) and metal/carbide/gas (line QB) equilibrium is dependent only on either oxygen or carbon potentials in the environment, the oxide/carbide/gas equilibrium (line QC) is dependent on both carbon and oxygen potentials in the environment; the ratio of the two potentials has to be satisfied as per Eq. 2.13 to maintain the oxide/carbide/gas equilibrium. Another point to note about the oxide/carbide/gas equilibrium it is independent of the activity of Cr in the alloy (see Eq. 2.13).

At the triple point Q, the phase fields of metal, oxide, and carbide meet. At this point the metal/ oxide/carbide/gas are in equilibrium and metal, oxide, carbide can co-exist. The chemical reaction governing the co-existence of metal, oxide, and carbide is:

Point Q: $$2Cr_2O_3 + Cr_{23}C_6 \leftrightarrow 27Cr_{solution} + 6CO \tag{2.14}$$

Assuming the activity of oxide and carbide as unity,

$$P^*_{CO} = \left(\frac{K_{2.14}}{a_{Cr}^{27}} \right)^{1/6} \tag{2.15}$$

where $K_{2.14}$ is the equilibrium constant for reaction in Eq. 2.14 and P^*_{CO} is the equilibrium concentration of CO, which is which is often referred as "*critical concentration of CO*" in the literature [76, 77, 82, 85].

Graphically, P^*_{CO} is shown as a slanted line QD with slope -1/2 on the stability diagram which must pass through the triple point, Q, where all the three solid phase metal, oxide, and carbide meet to depict the equilibrium of the reaction in Eq. 2.14. The slope -1/2 arises from the fact that on the stability diagram, which is drawn with the carbon activity and oxygen activity as the two axes, the CO-isobar is represented as a straight line with slope -1/2, according to the relation:

$$2CO \leftrightarrow 2C + O_2 \qquad (2.16)$$

Any point on this line gives rise to same value of P^*_{CO} and the reaction in Eq. 2.14 is in equilibrium. To the left of the line QD the CO concentration in gas is less than the critical concentration of CO, $P_{CO} < P^*_{CO}$, hence reaction in Eq. 2.14 proceeds in the forward direction, i.e. carbide and oxide will react to form CO and Cr. To the right of this line the CO concentration in environment is greater than the critical concentration of CO, $P_{CO} > P^*_{CO}$, and hence the reaction in Eq. 2.14 proceeds in the reverse direction, i.e. Cr will react with CO resulting in simultaneous oxidation and carburization.

2.4.3.1.2 Cr-stability diagram and prediction of oxidation behavior of Ni-Cr alloys

According to Quadakkers et al. [76, 77] the oxidation behavior of a Ni-Cr alloy can be predicted by comparing the oxygen potential and carbon potential at the metal surface established by the impurities with the three critical parameters $P^*_{O_2}$, a^*_C, and P^*_{CO} in the Cr-stability diagrams shown in Fig. 2.13. In order to further illustrate the prediction of oxidation behavior based on the stability diagram, four environments with carbon and

oxygen potential at the metal surface corresponding to points 1, 2, 3, and 4 are labeled in Fig. 2. 13.

- In environment 1, the oxygen potential and carbon potential at the metal surface is lower than required for formation of chromia and carbide. Hence Cr metal is stable and no corrosion is expected in this region.
- In environment 2, the oxygen potential at the metal surface is higher than required for formation of chromia, so oxidation of Cr to chromia is feasible. Also, since the carbon potential is less than required for formation of carbide carburization cannot occur. Further, since the CO concentration in the helium is lower than the critical CO concentration, P^{*}_{CO}, decarburization as per the reaction in Eq. 2.14 is feasible. Thus for potentials lying in this regime decarburization of the alloy is expected.
- The situation in environment 3 is similar to environment 2, except that the CO concentration in the helium is greater than the critical concentration of CO, P^{*}_{CO}. Hence as per reaction in Eq. 2.14, metal can react with CO forming oxide and carbide. However, in practice the Cr-rich alloys have been demonstrated to form chromia film in this regime which by separating the base metal from gas minimizes the carburization of the base metal. Thus in this regime oxidation and slow carburization of Cr-rich Ni-Cr alloy is expected.
- In environment 4, the carbon potential at the surface is greater than required for formation of carbide, hence carburization of the alloy is expected and correspondingly the alloy can be carburized in this regime. Oxidation of the metal can occur if the oxygen potential in the environment is higher than $P^{*}_{O_2}$.

2.4.4 Definition of critical temperature

The boundary lines in the stability diagram constitute a graphical representation of the equilibrium of a set of chemical reactions defined in Eqs. 2.7, 2.10, 2.12, and 2.14. With change in temperature these boundary lines shift as the respective equilibrium constant, K, changes. If we consider the case of increase in temperature then shift in the boundary lines is shown in Fig. 2.14. The stability field of metal expands and that of carbide and oxide shrinks. This results in the movement of the P^*_{CO} line to the right, in other words P^*_{CO} will increase. Consider an environment "E" in this figure. At temperature T1, oxidation potential in the environment is higher than required for the formation of chromia so chromia can form. Further, since the $P_{CO} > P^*_{CO}$ (at temperature T_1) the alloy will react with CO as per the reverse of the reaction in Eq. 2.14. At higher temperature, T_2, the boundaries shifts towards the right and now the environment E lies in region where the reaction 2.14 can proceed in the forward direction, i.e. oxide and carbide will react causing decarburization of the alloy. Thus, due to change in temperature the reaction in Eq. 2.14 can reverse its direction, i.e. the alloy oxidation behavior may change from oxidation + slow carburization to decarburization. Between these two temperatures T_1 and T_2, there will be an intermediate temperature at which the point E will fall on the corresponding P^*_{CO} line where the reaction in Eq. 2.14 will be in equilibrium. The intermediate temperature at which the point "E" would fall on the P^*_{CO} line is referred as the "critical temperature", as at this temperature the reaction in Eq. 2.14 is in equilibrium.

2.4.5 Influence of impurity concentration on critical temperature

The concept of critical temperature was explained based on the Cr-stability diagram in the earlier section. The critical temperature is the temperature at which the reaction in Eq. 2.14 is in equilibrium. A few studies have been conducted to determine the influence of gas composition on critical temperature. The typical procedure used for determination of critical temperature is presented first followed by influence of impurities on the critical temperature for alloy 617 and alloy 230.

The experimental procedure for critical temperature determination was developed by Quadakkers. In this procedure the specimen is slowly heated from a lower temperature to a higher temperature and the behavior of CO is measured continuously, typically using gas chromatograph. The temperature at which the CO production starts is the critical temperature, as below this temperature CO will be consumed as per the reaction in Eq. 2.5, whereas above this temperature a CO production will occur as per the reaction in Eq. 2.6. Figure 2.15 shows an example of this procedure. In this case, alloy 617 was oxidized in a He + 1.5ppm H_2O + 15ppm CO + 20 ppm CH_4+ 500 ppm H_2 gas mixture. At lower temperature the sample reacted with CO as per the reaction in Eq. 2.5 and the surface was passivated by chromia film, as observed by no net consumption of CO. Subsequent continuous heating of the sample to a higher temperature resulted in a sudden CO spike which started at ~920°C (marked as T_{cr} in the Fig. 2.15). The observed amount of CO production of ~18 ppm was higher than that could be accounted by the depletion in water vapor (1.5 ppm) and methane (1 ppm), which led Quadakkers [77] to conclude that the reaction in Eq. 2.5 reversed at 920°C, i.e. the critical temperature for the given mixture is 920°C.

Influence of CO on the critical temperature

Figure 2.16 is a plot which shows the influence of change in CO concentration on the critical temperature for alloy 617. The data for this plot were taken from Quadakkers et al. [77], Chapovaloff et al. [86], and Sakai et al. [81]. Table 2.2 shows the gas composition which was used by the authors to determine the critical temperature. All the references mentioned in this figure have used Quadakkers' method to determine the critical temperature. The key observation from this plot is that the critical temperature is strongly influenced by the CO concentration in the gas mixture. An increase in CO concentration from 6.5 ppm to 105 ppm increased the critical temperature from 900°C to 994°C. Similar behavior was also seen in case of alloy 230 by Cabet et al. [87]. Figure 2.17 is a plot from their paper which shows that the critical temperature increases with increase in CO level.

Influence of hydrogen and water vapor on the critical temperature

Chapovaloff et al. [86] varied the gas composition in a systematic manner and determined the influence of hydrogen and water vapor on the critical temperature for alloy 617. Figs. 2.18 and 2.19 show plots from their paper. As observed from Fig. 2.18, within the experimental uncertainty limit of ±5°C, a change in hydrogen concentration from 30 ppm to 500 ppm does not change the critical temperature for alloy 617. However, water vapor seems to affect the critical temperature slightly. The critical temperature decreased by 20°C by an increase in water vapor concentration from 3 to 16 ppm, Fig. 2.19.

So, in summary it can be stated that the critical temperature is mainly influenced by CO in the gas mixture and is weakly dependent on the water vapor concentration in the environment. Hydrogen does not influence the critical temperature.

2.4.6 Decarburization mechanisms

Oxidation experiments on several chromium containing alloys, e.g. alloy 617 (Ni-22Cr-12Co-9Mo)[81, 88, 89], Nimonic 86[77], Hastelloy X (Ni-22Cr-2Co-9Mo)[77], alloy 230 (Ni-22Cr-15W)[90-92] etc. in impure helium have demonstrated that at temperatures below some critical value, e.g. 900°C, oxidation and carburization of the samples occur. At these temperatures the alloys usually develop a Cr-rich surface oxide scale that protects the alloy from further corrosion. But above a critical temperature, T_A (above 900°C in all cases), these alloys undergo decarburization and the Cr-rich oxide scale is no longer protective.

The exact mechanism of decarburization of alloy 617 is still debatable. There are two models which attempt to explain the decarburization mechanism for alloy 617. The first mechanism was propounded by Brenner et al. [32, 66, 78] according to which decarburization is a microclimate reaction, and second by Christ et al. [80, 85] according to which it is a simple solid-solid reaction that occurs at oxide/metal interface.

Figure 2.20 shows a schematic of the decarburization mechanism proposed by Brenner et al. [32, 66, 78]. It is a two step mechanism which states that decarburization occurs via gas medium in a localized region near the surface of the sample as per the reactions:

$$2Cr_2O_3\ (solid) + 6H_2\ (gas) \rightarrow 6H_2O + 4Cr, \qquad (2.17)$$

$$6H_2O\ (gas) + Cr_{23}C_6\ (solid) \rightarrow 23Cr + 6H_2 + 6CO \quad . \qquad (2.18)$$

It was postulated that hydrogen triggers the reaction by reducing the chromia film to provide water vapor as per the reaction 2.17, which in turn reacts with the carbide to produce CO, Cr, and regenerates the hydrogen as per the reaction 2.18. Thus, the net result is that CO is produced, whilst hydrogen and water vapor, which act as the transfer media, are neither produced nor depleted. In effect, therefore, the net process is seen to be occurring through the medium of gas catalysis at the oxide/metal interface.

The physical size of the zone within which the process occur was assumed to be extremely small and probably at least an order of magnitude less than the thickness of the oxide-hence the term 'microclimate' was used. The Cr released during the reaction is free to migrate, either equilibrating with the underlying matrix or arriving at the oxide/gas interface.

The second model is proposed by Christ et al. [80, 85], who conducted experiments in impure He + 60 ppm CO + 6ppm CO_2 + 10ppm H_2O environment, which was free from H_2, showed that rapid decarburization of alloy 617 occurs at $T \geq 950^{\circ}C$. They conclude that since the hydrogen, which triggers the decarburization is absent microclimate cannot be established and proposed that in this environment decarburization occurred as per the following reaction:

$$Cr_2O_3\ (solid) + 3\ C_{Solution} \rightarrow 2Cr + 3\ CO. \qquad (2.19)$$

i.e. carbon in solid solution and in equilibrium with carbide within the alloy matrix reduces the chromia. This reaction was assumed to be occurring at the oxide/metal interface.

The two models proposed by Brenner et al. [32, 66] and Christ et al. [26, 80] agree that the decarburization occurs via reaction of the surface chromia film with carbon, but they differ on the question of whether the decarburization is a gas mediated reaction (Benner's model) or a solid/solid reaction (Christ's model). In Brenner's model, the chromia and carbide are in solid form and are not required to be in direct physical contact with each other as they are "in contact" through the media, namely, H_2 and H_2O, which locally react with chromia and carbide. In Christ's model, the decarburization is a result of reaction between two reactants solids (chromia and carbon in solution with the matrix) that are in physical contact with each other, and hence, the mediation of any gas medium is not required.

Recently, Cabet et al. [88] and Rouillard et al. [90, 93] also determined the mechanism of decarburization for alloy 230 and experimental NiCrW alloys with and without carbon and showed that decarburization in these alloy occurs without any gas intermediates. So, in essence their result supports the mechanism proposed by Christ et al. They proposed that the reaction 2.19 occurs at the oxide/scale interface and the CO released was transported to the environment via gaseous diffusion through cracks and nano-channels which were assumed to form during the oxide film growth.

Table 2.1. Impurity content (in ppm level) in the helium of experimental reactors[25].

Reactor	H_2(ppm)	H_2O(ppm)	CO_2(ppm)	CO(ppm)	CH_4(ppm)	N_2(ppm)
Dragon	20	1	<0.4	12	3	3
AVR	300	30	100	100		
Peach Bottom	225	<12	-	12	15	12
PNP	500	1.5	-	15	20	5
HHT	50	5	5	50	5	5
HTGR-SC	200	10	<1	20	20	15
Jaeri-type B	200	1	2	100	5	<5

Table 2.2. Impurity concentrations, alloy, and corresponding critical temperaturefor alloy 617.

H_2 (ppm)	H_2O (ppm)	CO (ppm)	CH_4 (ppm)	Alloy	T_{cr} (^oC)	Reference
500	1.5	13	20	617	926	[77]
500	1.5	26	20	617	954	[77]
500	1.5	38	20	617	965	[77]
500	1.5	63	20	617	947	[77]
500	1.5	105	20	617	994	[77]
500	5.5	5.5	0	617	900	[86]
500	26	7	0	617	900	[86]
27	58.6	14.2	0	617	921	[86]
500	14.6	14.2	0	617	908	[86]
113	7	14.4	0	617	908	[86]
112	14.4	14.4	0	617	908	[86]
500	14.4	14.6	0	617	921	[86]
110	60	14.9	0	617	928	[86]
500	14.9	14.9	0	617	928	[86]
500	14.9	15.6	0	617	927	[86]
38	15.6	26	0	617	948	[86]
128	14.2	58.6	0	617	973	[86]
500	14.2	60	0	617	953	[86]
300	3	100	4	617	975	[81]

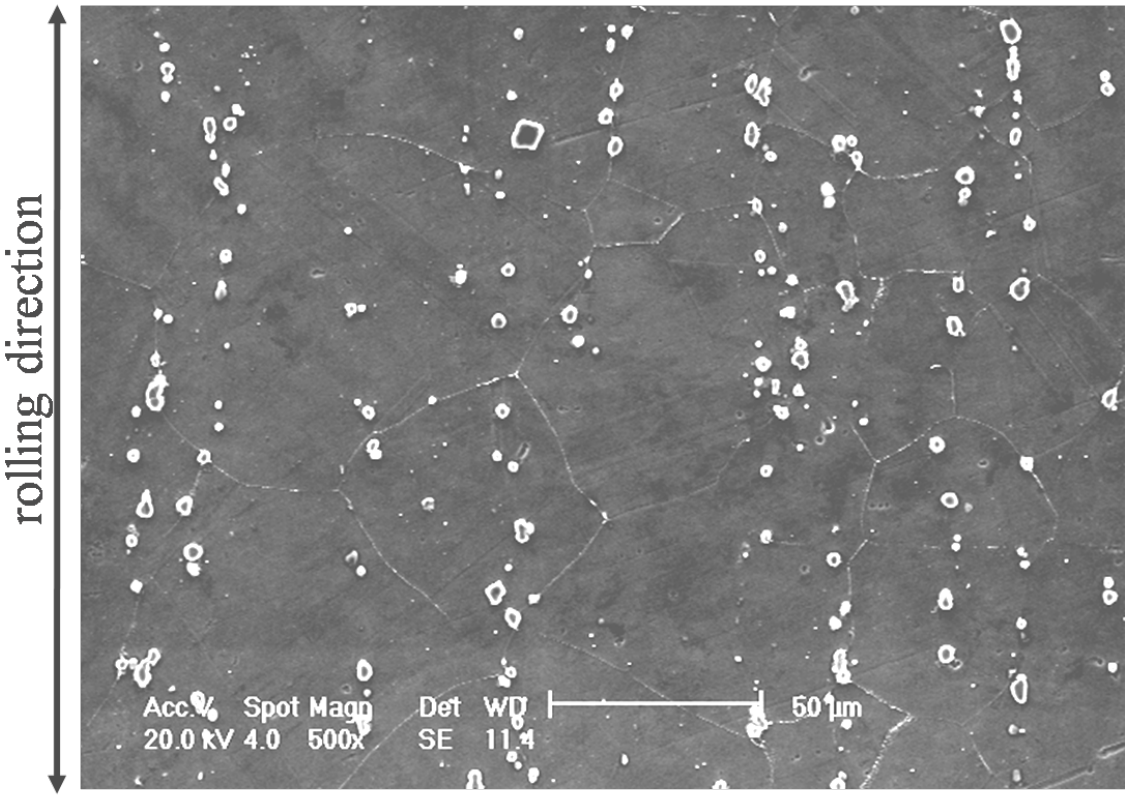

Figure 2.1 A typical microstructure for alloy 617.

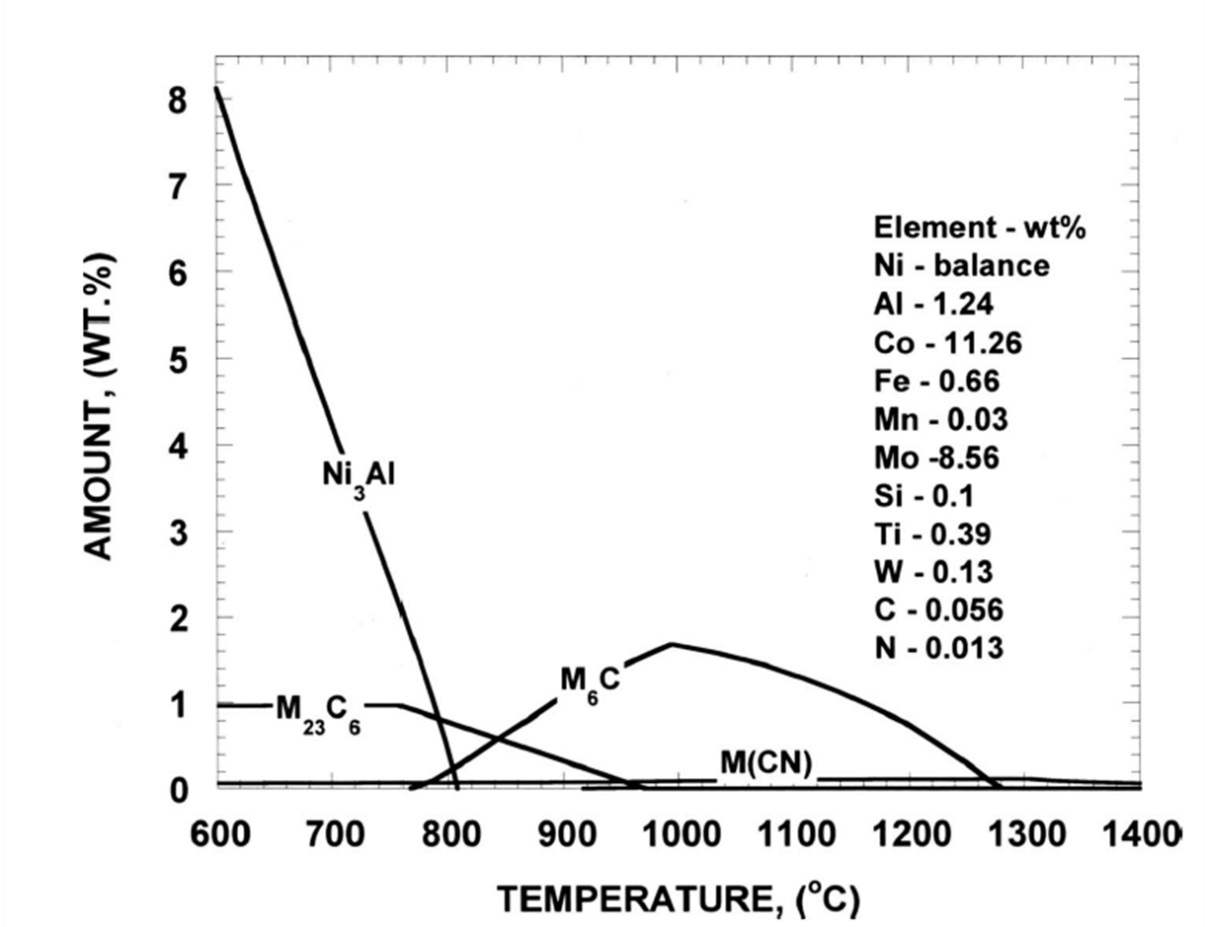

Figure 2.2 Weight fraction of precipitates in alloy 617 calculated by THERMOCALC® [9]. The composition of alloy 617 used for calculation is shown on the plot.

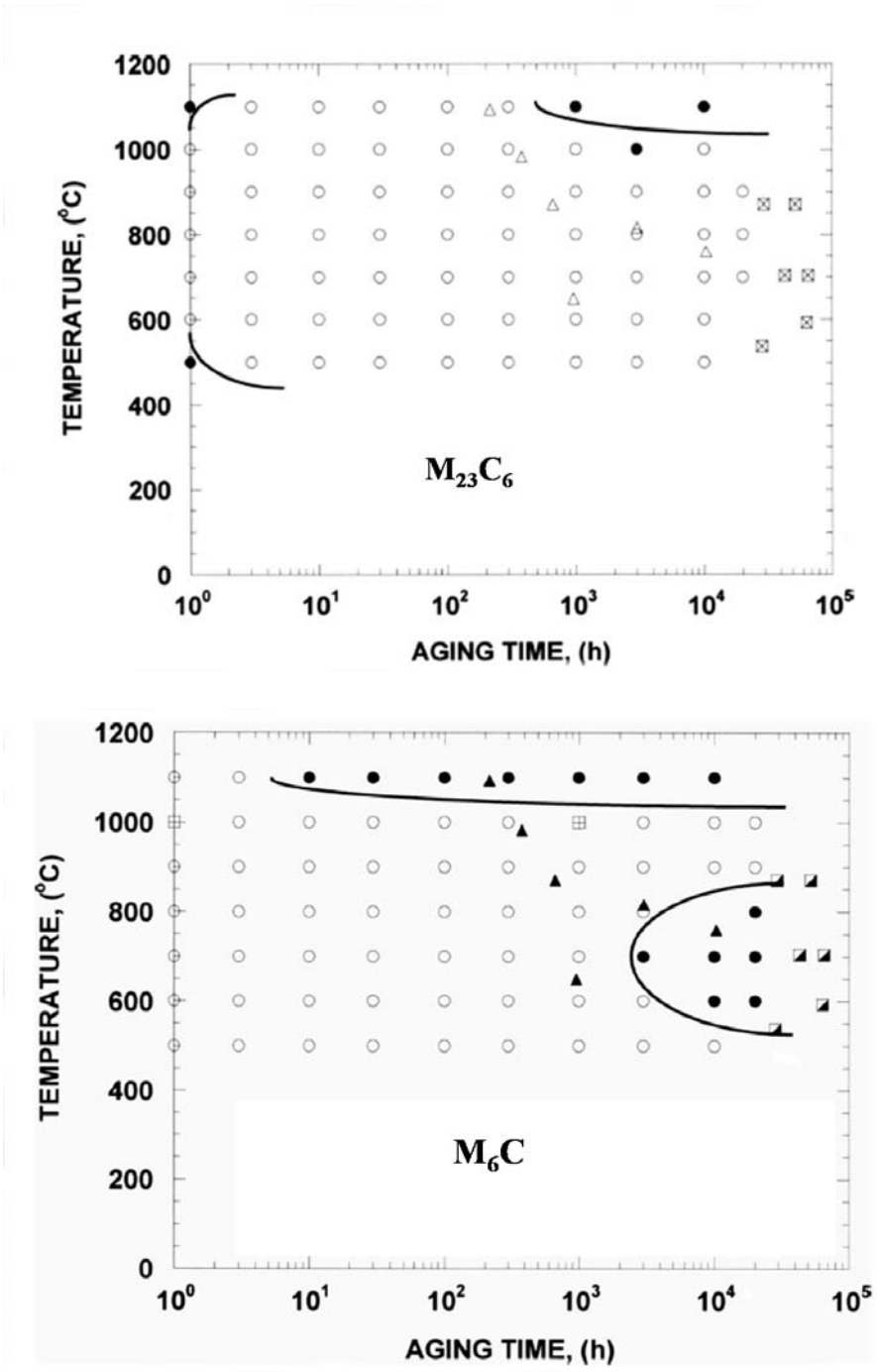

Figure 2.3 (a) Time-temperature-precipitation (TTP) diagram for $M_{23}C_6$ and (b) M_6C carbide in alloy 617[9]. Open and closed symbols denote where the precipitate was observed or not observed, respectively.

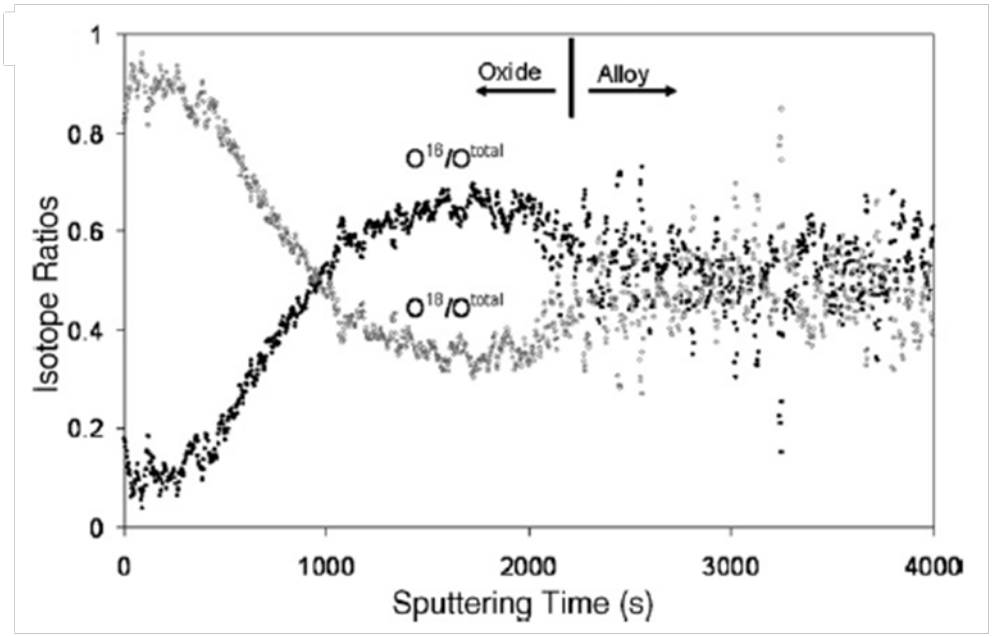

Figure 2.4 oxygen-18 profile showing the growth mechanism of chromia on Ni-25 Cr alloy. The sample was oxidized at 1050°C for 0.5h in Ar-20%$^{16}O_2$ follwed by 2h in Ar-20%$^{18}O_2$[52].

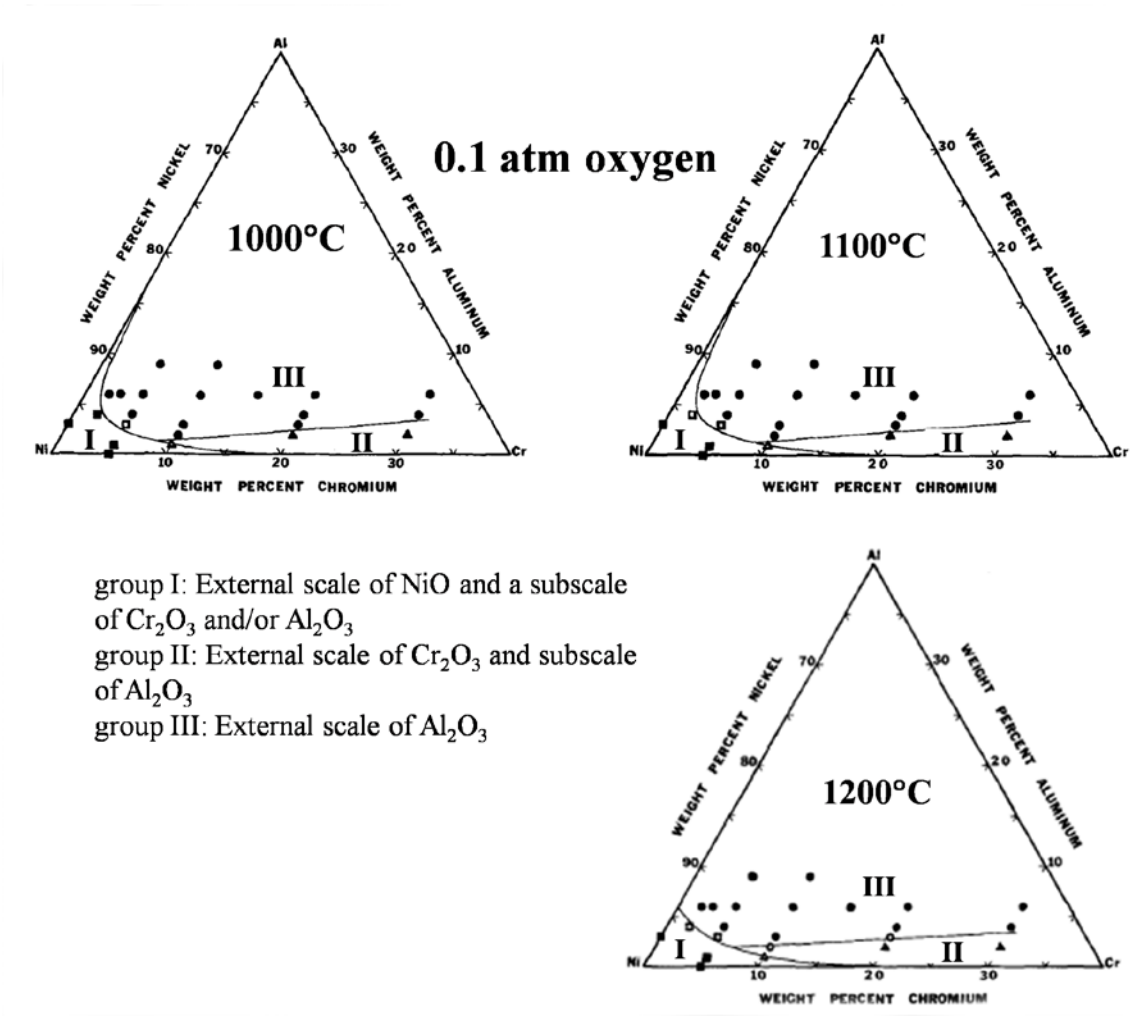

Figure 2.5 Oxide map for Ni-Cr-Al alloys [55].

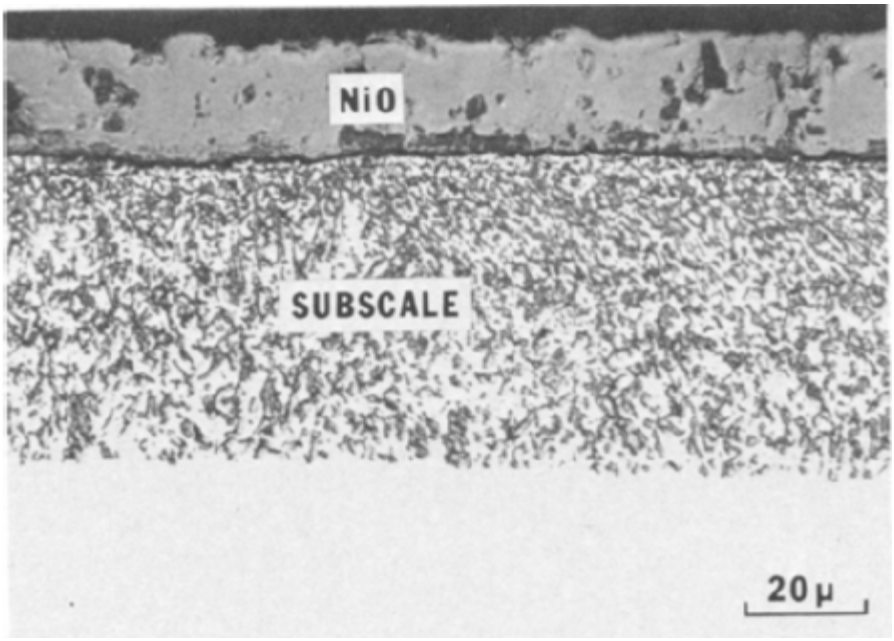

Figure 2.6 Representative microstructure of group I alloy in the oxide map. Alloy: Ni-2Cr-4Al, time= 20h, environment 0.1 atm of oxygen, temperature =1000°C. This structure is [55].

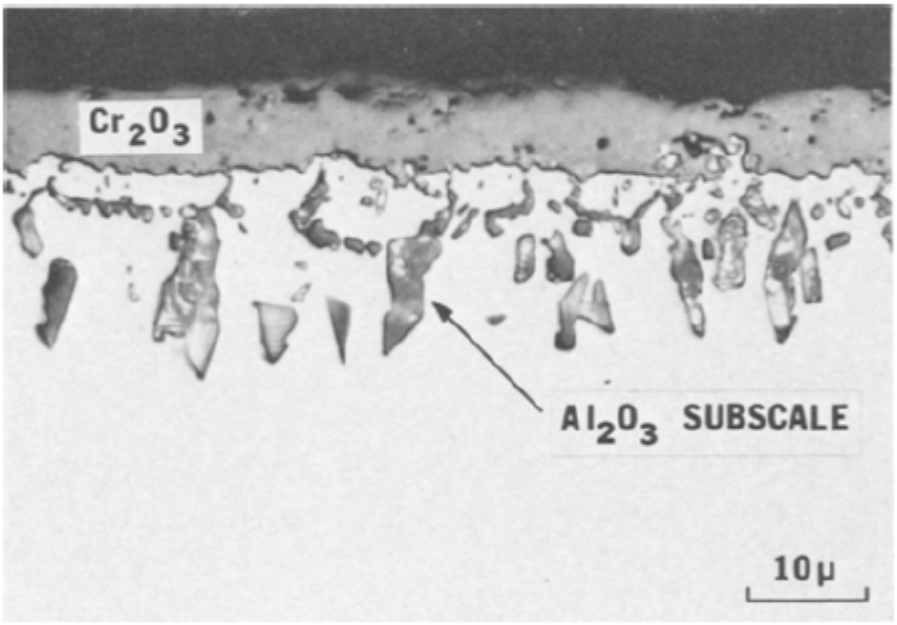

Figure 2.7 Representative microstructure of group II alloy in the oxide map. Alloy: Ni-20Cr-2Al, time = 21h, environment 0.1 atm of oxygen, temperature =1100°C[55].

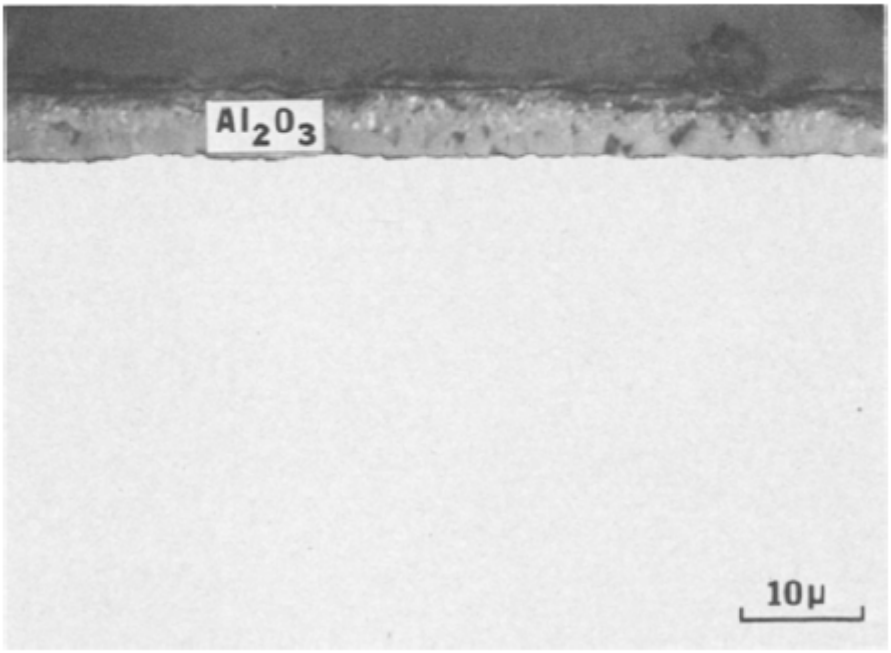

Figure 2.8 Representative microstructure of group III alloy in the oxide map. Alloy: Ni-20Cr-4Al, time = 20h, environment 0.1 atm of oxygen, temperature =1200°C [55].

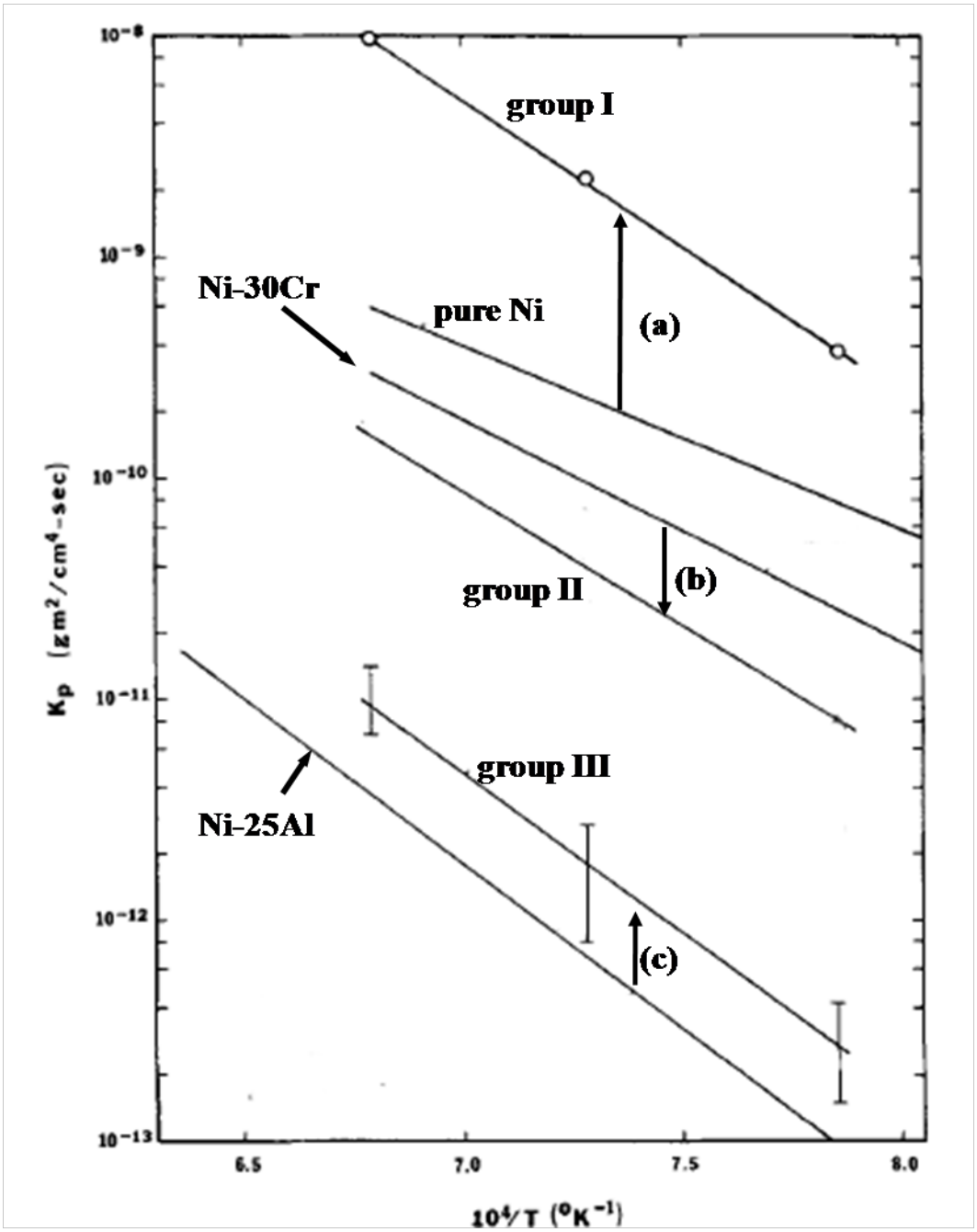

Figure 2.9 Comparison of the oxidation kinetics of Ni-Cr-Al alloys (groups I, II, and III) with pure Ni, Ni-Cr, and Ni-Al alloys; Arrehenius plot [59].

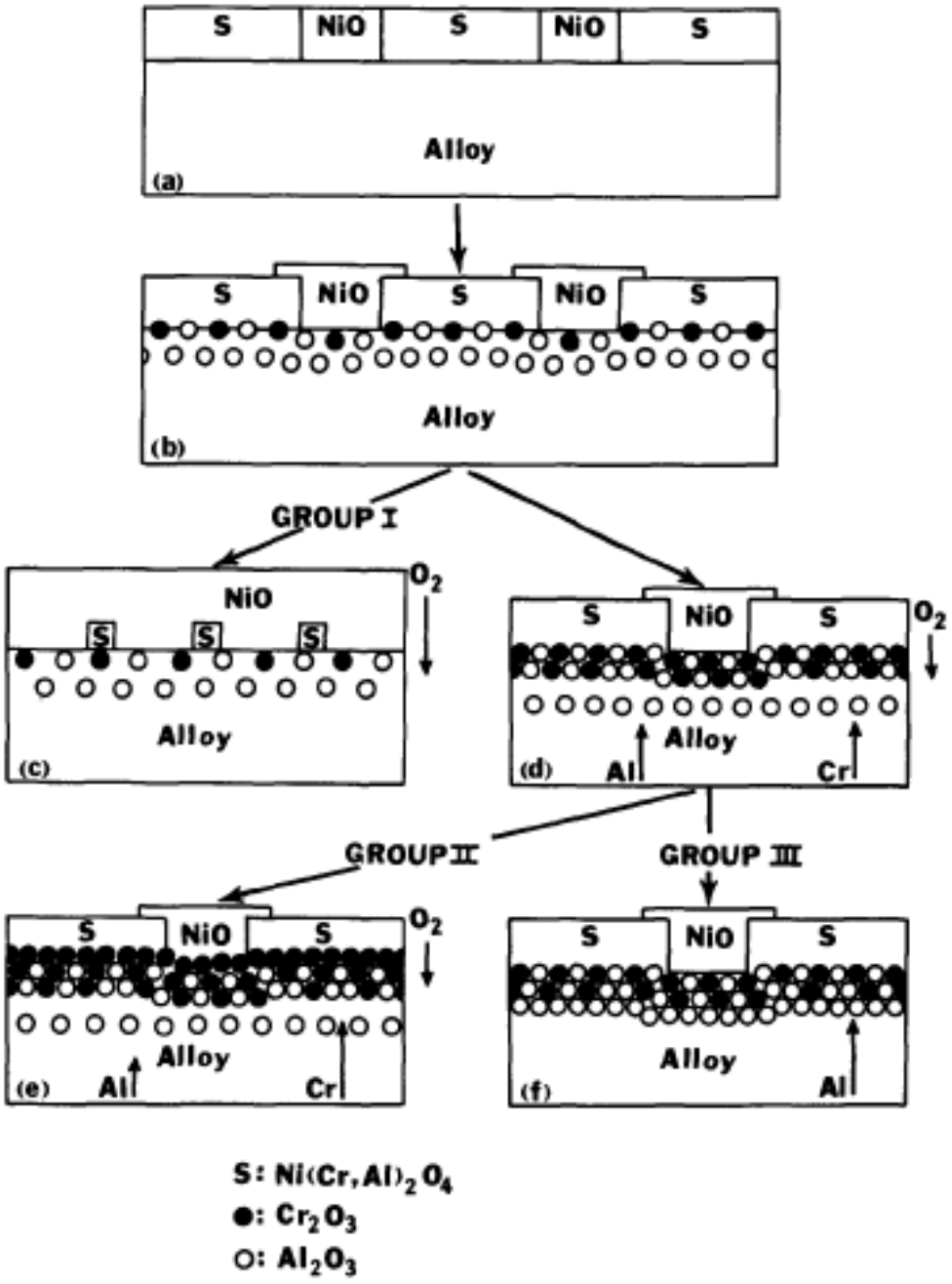

Figure 2.10 Schematic diagram illustrating the oxidation mechanism of Ni-Cr-Al alloys[55].

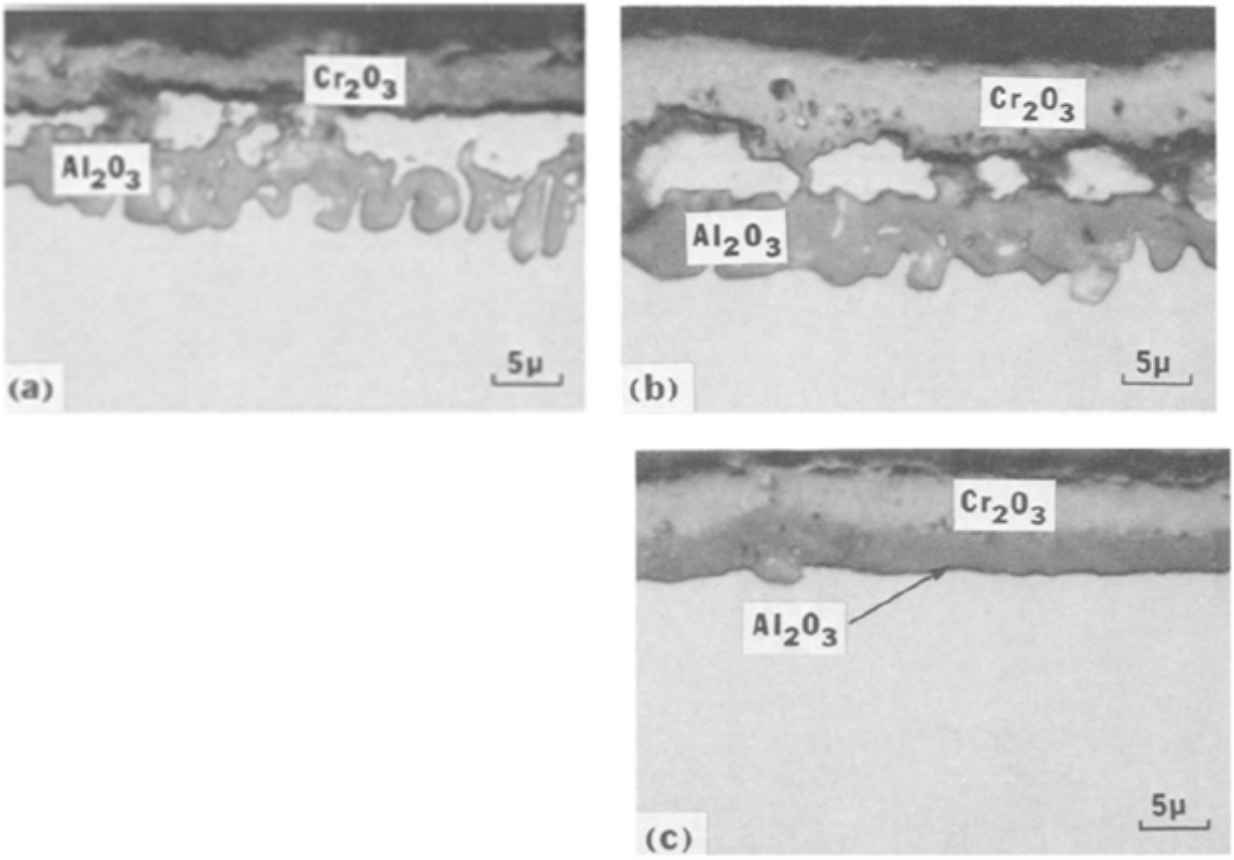

Figure 2.11 Microstructure of Ni-20Cr-3Al alloys oxidized at 1200°C in 1 atm oxygen. The alloy lies on the border of the group II and III alloys and shows heterogeneous oxidation. Locally it shows oxidation behavior which is typical of the group II (Fig. a and b) and III alloys (Fig. c) in the Ni-Cr-Al oxide map [55].

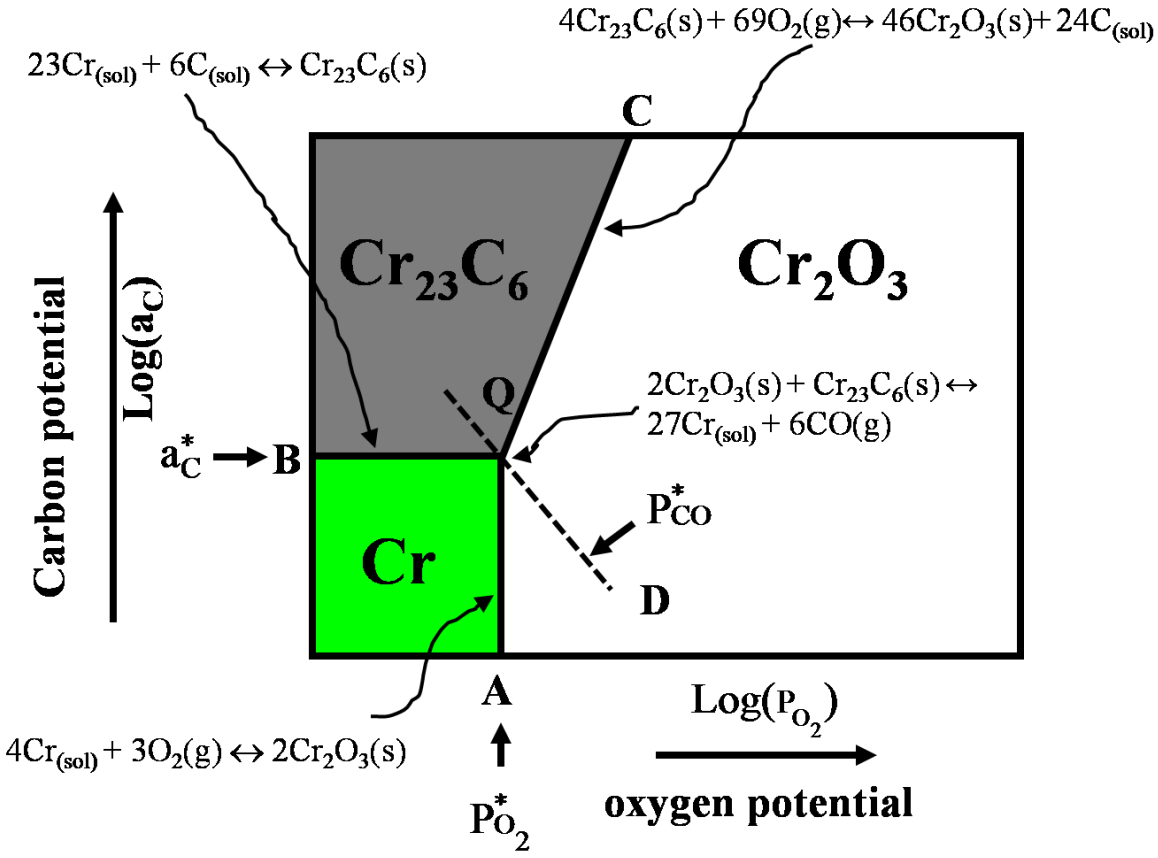

Figure 2.12 Schematic of Cr-stability diagram showing three critical parameters, $P_{O_2}^*$, a_C^*, and P_{CO}^*.

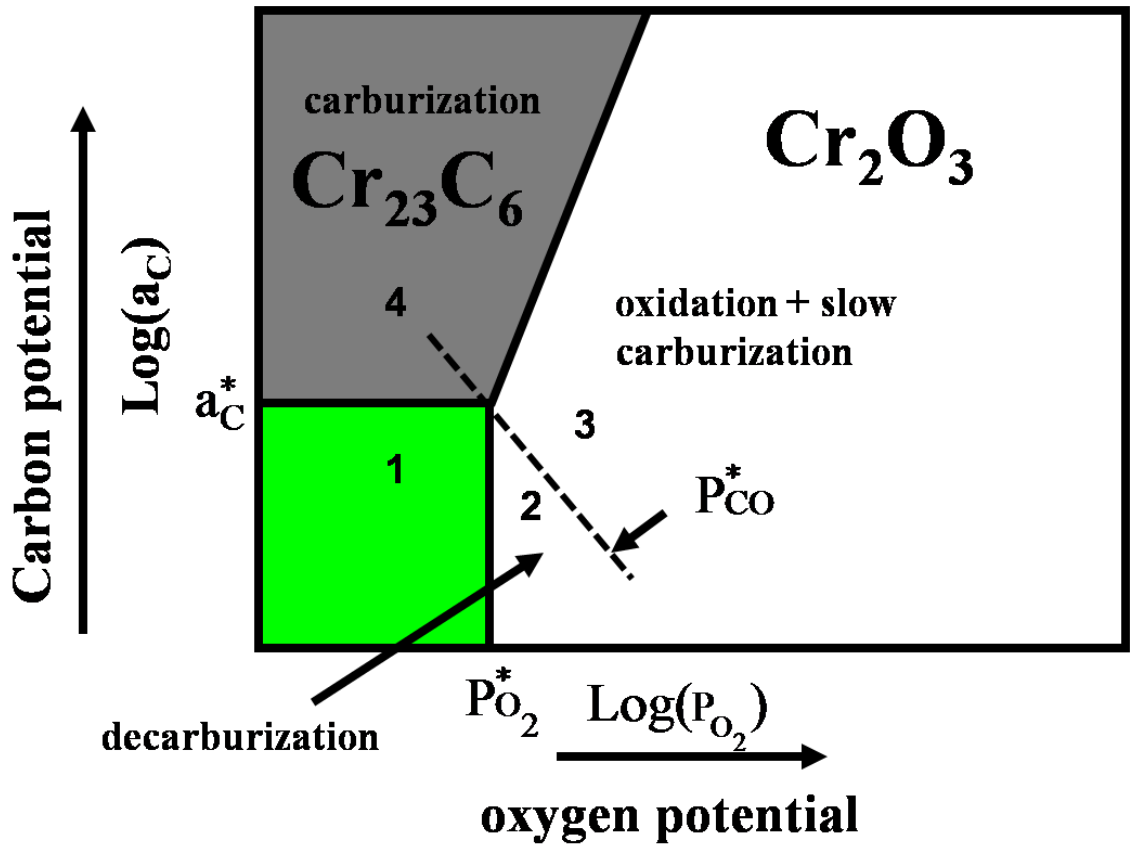

Figure 2.13 Predication of oxidation behavior of a Ni-Cr alloy based on Cr-stability diagram.

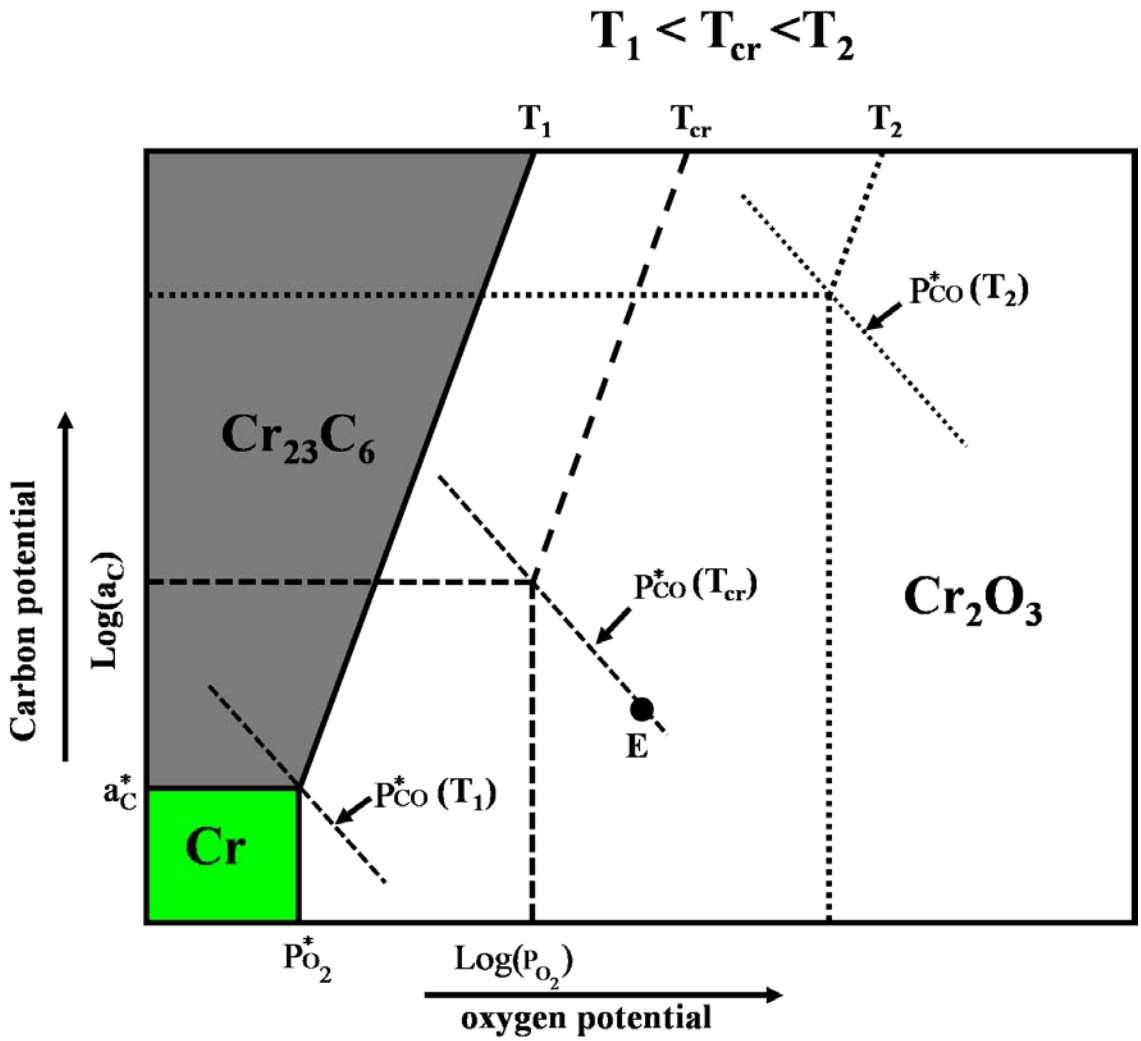

Figure 2.14 Explanation of critical temperature (T_{cr}) based on Cr-stability diagram.

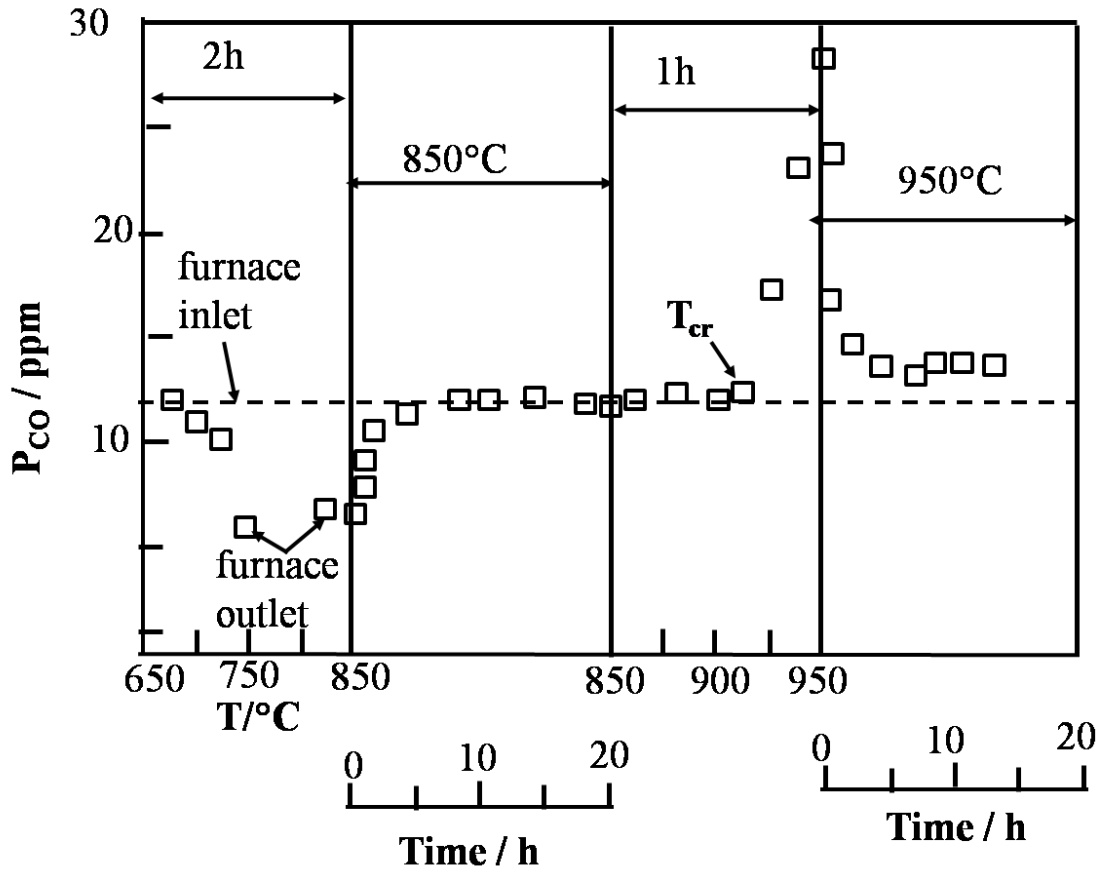

Figure 2.15 Change in CO concentration above and below critical temperature, T_{cr} replotted from [77]. Alloy 617 was heated at low temperature in He + 1.5 ppm H_2O + 12 ppm CO + 20 ppm CH_4+ 500 ppm H_2 gas to form chromia film and in subsequent step heated slowly to higher temperature. The critical temperature is the temperature at which CO evolution just starts (marked as T_{cr} in the figure).

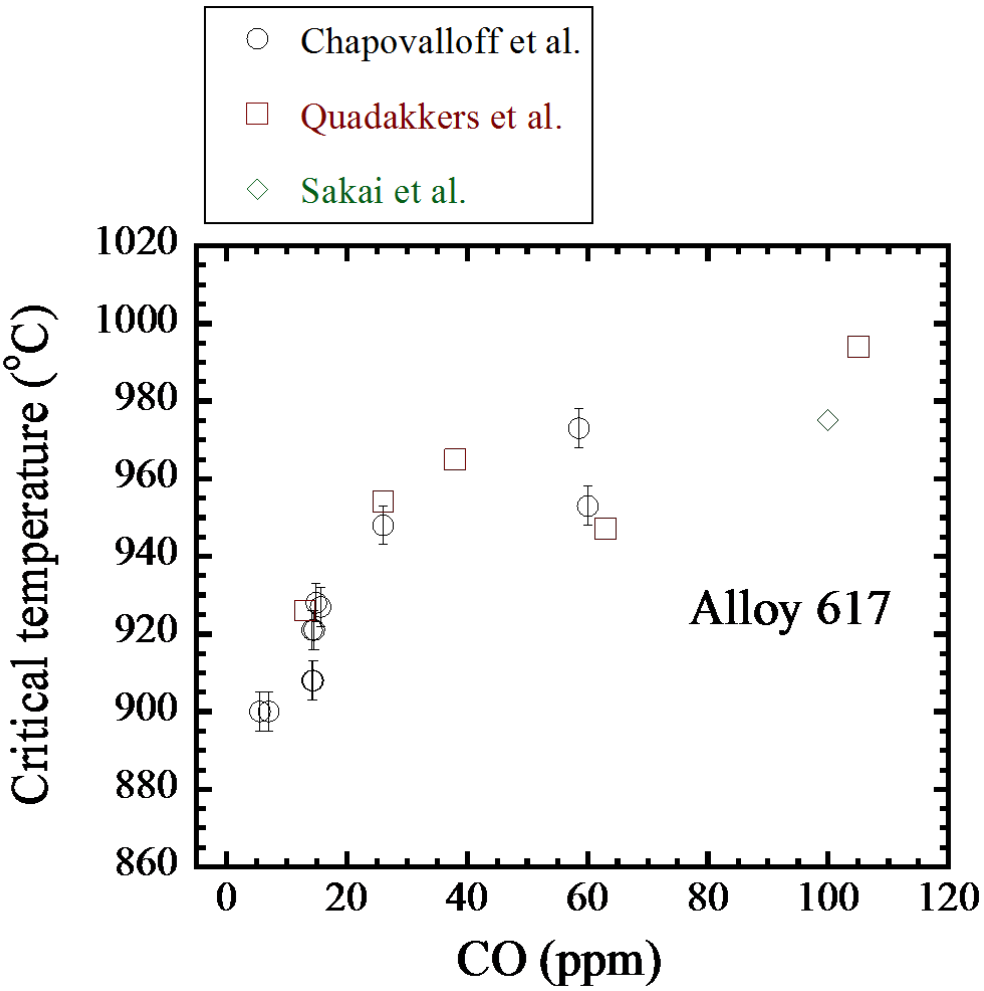

Figure 2.16 Plot of critical temperature as a function of CO concentration in the environment for alloy 617. Critical temperature increases with CO concentration in the environment. The gas composition used by the authors is shown in table 2.2 [77, 81, 86].

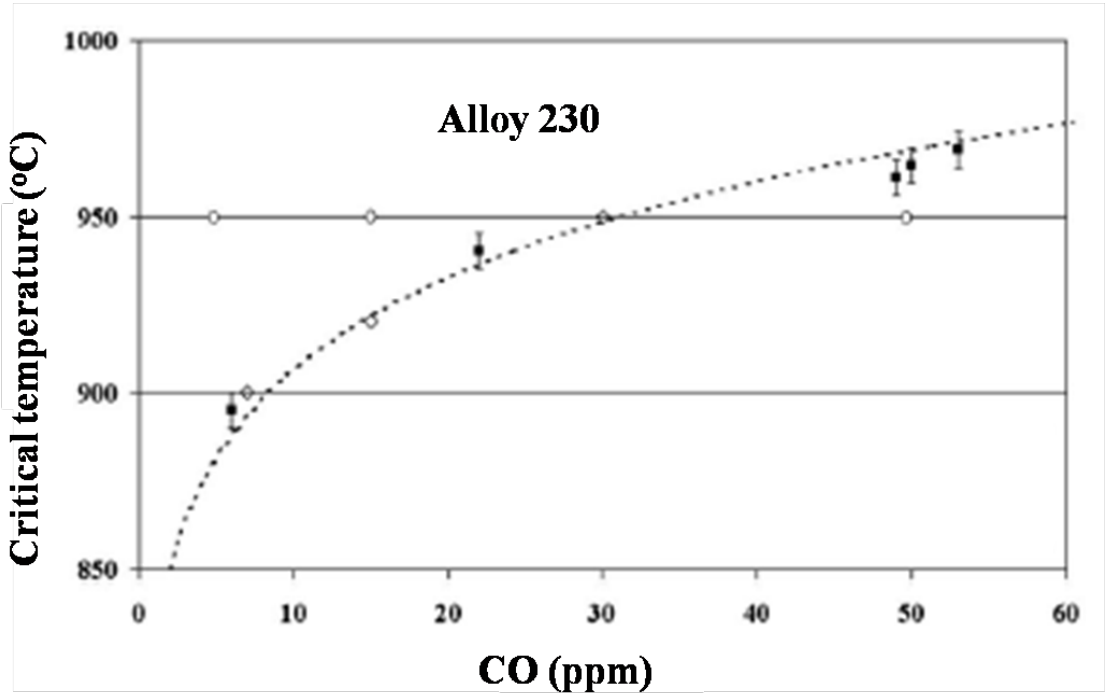

Figure 2.17 Plot of critical temperature as a function of CO concentration in the environment for alloy 230[87].

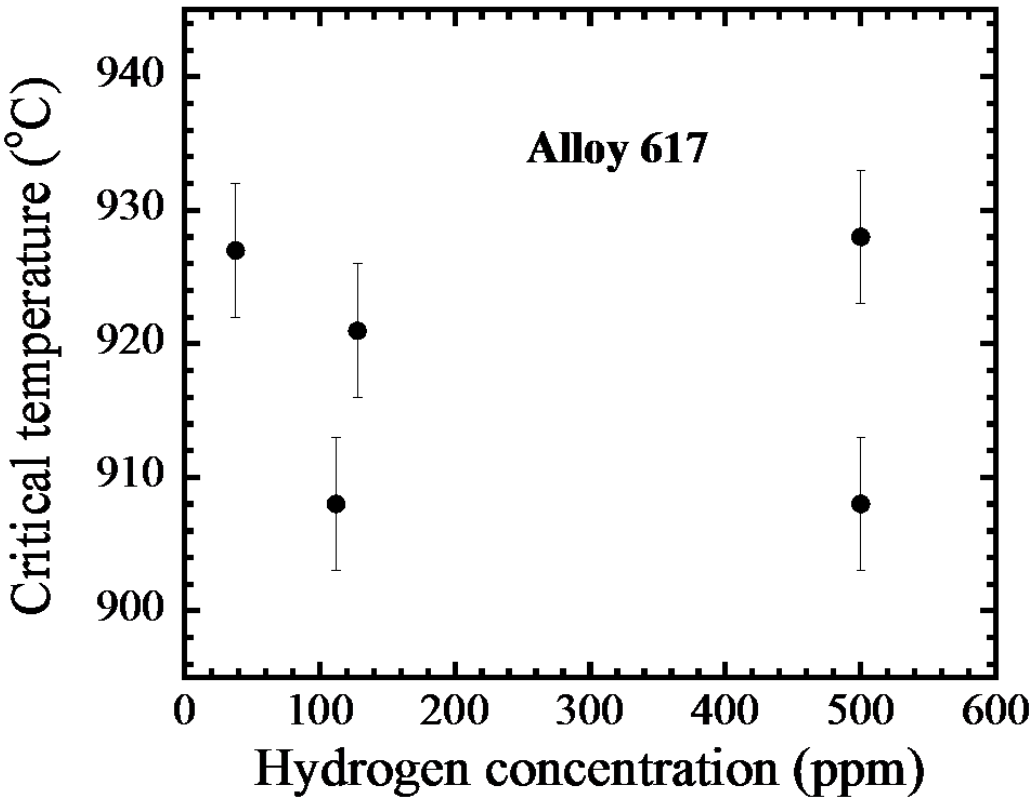

Figure 2.18 Influence of hydrogen on the critical temperature for alloy 617. The gas composition used is shown in table 2.2. Hydrogen does not influence the critical temperature. Redrawn from [86].

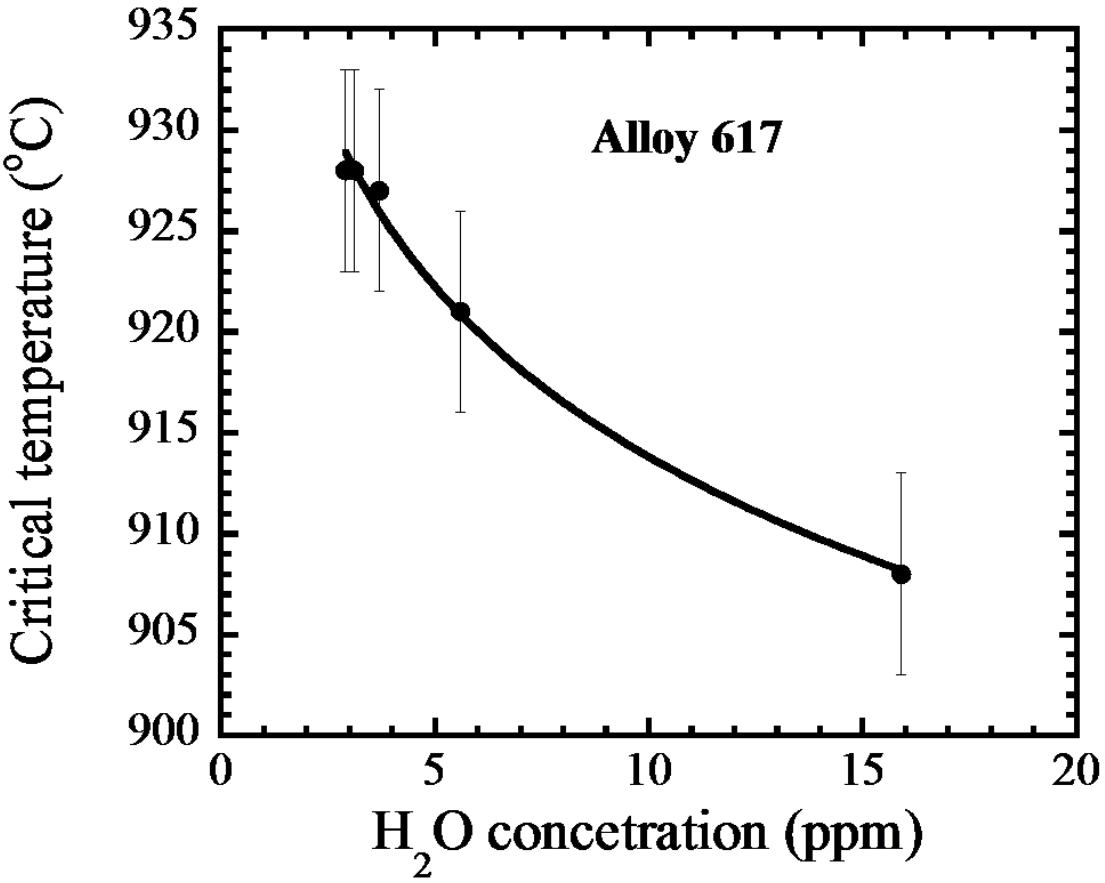

Figure 2.19 Influence of water vapor on the critical temperature for alloy 617. The gas composition used is shown in table 2.2. Critical temperature decreases with increase in water vapor concentration. Redrawn from [86].

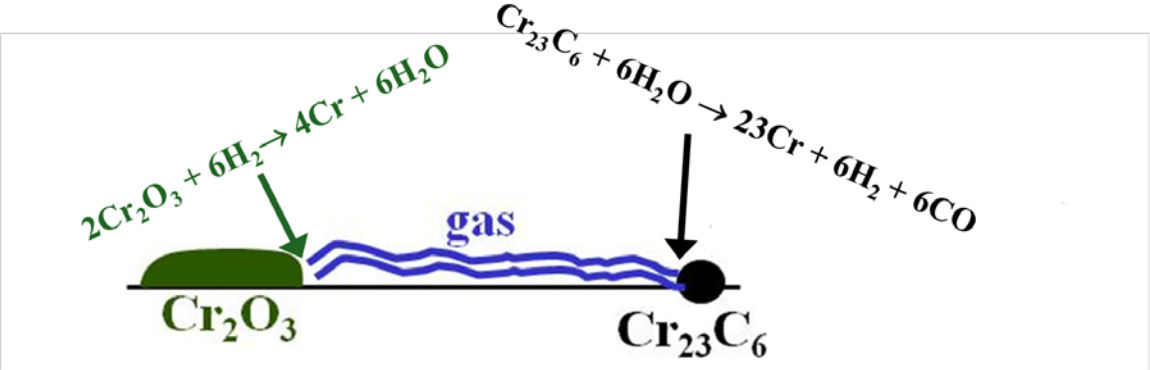

Figure 2.20 Schematic of mechanism of decarburization of alloy 617 in impure helium as proposed by Brenner et al [32, 66, 78].

CHAPTER 3

EXPERIMENTAL PROCEDURE

This chapter presents the experimental procedure, techniques, and analyses used in this research. It has been divided into six major sections. Section 3.1 gives the description of the experimental material, alloy 617. Section 3.2 presents the design and characterization of the facility which was used for the conduction of corrosion tests. Sections 3.3 and 3.4 present the experimental parameters and experimental procedure followed during the corrosion experiments, respectively. Section 3.5 presents the experimental techniques used for post-corrosion microstructural analysis, and lastly, section 3.6 provides a summary of the error analysis procedure.

3.1 Alloy description

The material investigated in this thesis work was alloy 617. It was obtained in the form of a plate from Special Metals, Inc. A solution annealing heat treatment, consisting of heating at 1175ºC and subsequent cooling in air, was given to this plate by the manufacturer. Tables 3.1 a - 3.1d provide information on the alloy 617 as obtained from the supplier, which includes the heat number, dimension of the plate, chemical composition, impurities concentration, and room temperature tensile properties. The chemical composition of the obtained alloy was also verified by Sherry Labs, Inc. Further, the compositions of the key metallic elements, Ni, Cr, Co, Mo, Al, Fe, Ti, Cr, and Mn in the plate was also measured on a representative 6.5 mm x 6.5 mm x1.5 mm

sample cut from the cross-section of the plate by electron microprobe with wavelength dispersive X-ray analysis in the Electron Microbeam Analysis Laboratory, at the University of Michigan. The chemical composition analysis of the alloy 617 from the manufacturer, Sherry Laboratory, and EMPA are presented in table 3.1 b. The composition analysis from the three sources are in excellent agreement with each other with the maximum disagreement being <0.5wt% in the case of nickel. The commercial alloys, usually, contain some impurities, such as, sulfur, phosphorous, oxygen, and nitrogen. The concentrations of these impurities were also analyzed by Sherry Labs and are presented in table 3.1c. The impurities level was < 0.005wt%.

3.2 Controlled-Impurity Helium Flow System

The corrosion experiments were conducted in six He + x ppm CO + 1.5 ppm CO_2 (where x = 15, 240, 465, 680, 1260 and 1908 ppm) environments for durations up to 750 h at 850, 900, 950, and 1000°C. Figures 3.1 and 3.2 show the schematic and the photograph of the Controlled-Impurity Helium Flow System which was built to conduct the corrosion experiments throughout this research. This facility consists of three major sections; a gas mixing section, an exposure section and the gas analysis section. The gas mixing section achieves the desired concentration of CO and CO_2 inside the quartz tube using premixed bottled gases of helium with a given level of one type of impurity and a series of mass flow controllers. The helium with controlled levels of CO and CO_2 was then passed through the exposure section in which the top and bottom of the corrosion coupons resting on the walls of the quartz tubes were exposed to the flowing helium containing varying levels of CO and CO_2. A tee and a needle valve at the furnace

entrance were used to control the flow rate of the gas mixture through this section. The CO and CO_2 levels in helium were analyzed continuously both before and after the entry into the furnace using the discharge ionization detector gas chromatograph (DIDGC) in the analysis section. Experimental variables such as flow rates of gases and concentration levels of impurities were continuously monitored using a personal computer (PC). The following subsection describes each section in detail.

3.2.1 Description of the facility

3.2.1.1 Gas mixing section

The gas mixing section consisted of 7 premixed gas bottles (A1 in Figs. 3.1 and 3.2) and 18 mass flow controllers (A2 in Figs. 3.1 and 3.2). To obtain the gas mixture with the target concentration of each impurity, a pre-mixed gas cylinder of helium with a certified level of one type of impurity, e.g., He + 100 ppm of CO, and a controlled amount of another impurity from a different certified pre-mixed bottle were combined using electronic mass flow controllers from Omega, Inc. If required, the resulting impurity gas mixture was then diluted by mixing it with research grade helium of 99.9999% purity. The electronic mass flow controller used for gas mixing had an accuracy of ±1 ml/min with a full scale operation range of 0 to 100 ml/min, and was capable of withstanding pressure up to 500 PSIG. All the components involved in transporting and mixing the gases were made from 316 stainless steel. Whenever possible, weld fittings were used for connecting lines from different gas bottles to avoid the in-leakage of air.

3.2.1.2 Exposure section

The exposure section consisted of a horizontal 30” long, three-zone tube furnace, housing seven 1/2” outer diameter quartz tubes. Six out of the seven tubes were arranged along the periphery of the process diameter in the furnace, whereas the seventh tube was inserted in the middle. The six tubes arranged along the periphery of the process diameter were attached to the premixed He gas, thus enabling corrosion studies in six separate environments simultaneously. The seventh tube was attached to a research grade purity helium cylinder. The horizontal tube furnace was rated for temperatures up to 1200°C and was a split tube design, which could be opened for easy access to the tubes. The three temperature zones of this furnace were controlled by independent controllers of resolution 1°C. One S type thermocouple was inserted in the middle of each zone for temperature monitoring. The temperature of the three zones could be tuned to obtain a uniform temperature zone of 6” in length, in which the temperature variation, as well as that between tubes, was ±2°C (see section 3.2.2.1). This long uniform temperature zone enabled the exposure of multiple samples in each tube, which were removed from the hot zone to the cold zone of the furnace at different exposure durations. The length of the cold zone was ~8” with temperature ~60°C at a helium gas flow rate of 100 ml/min.

A custom push-rod was used to remove the samples while maintaining an airtight seal to the tubes. The push-rod consisted of a quartz rod with five hooks and an encapsulated steel rod on the end and resided completely inside the quartz tube. A magnet was used to manipulate the push-rod. Figure 3.3(a), (b), and (c) show photograph of the push-rod and the magnet used to manipulate it. The manipulating magnet is marked as “A”, the encapsulated rod is marked as “B”, and the five hooks are marked

with the letters “C” to “G”. The five hook design of the push rod was adopted to overcome the limitation of the small space available for the manipulation of the push rod. The uniform hot zone, where the corrosion coupons were exposed over the temperature range of 850 - 1000°C, lied between 12” to 18” cm from the rear end of the furnace. This required at least 18” of the manipulation space beyond the furnace end so that the corrosion coupons could be pulled out even from the farthest position in the uniform hot zone. However, the length of the cold zone (the distance beyond the furnace end) was only 8”, which was short of the required length of 18” by 10”. The five-hook design in which the hooks were out of phase from each other by 90 degrees, helped in overcoming this limitation. When the sample was at the farthest position from the furnace end, the first hook (marked as “G” in Fig. 3.3) was engaged in moving the sample for 8” after which the second hook (“F” in Fig. 3.3) was engaged in moving the sample for the next 8”. Before the second hook could be engaged, the push-rod was rotated by 90 degrees to disengage the first hook, and engage the second hook. If required, the 3rd and 4th hook was employed in the similar manner to pull the coupons completely out in the cold zone without having to break the seal of the system.

3.2.1.3 Gas analysis section

The third section was the gas-analysis section, which consisted of the DIDGC and the PC (Figs. 3.1 and 3.2). The DIDGC was used to continuously analyze the gas mixture both before and after the exposure section, and the PC was used to control the GC.

The important parts in the DIDGC were columns (K1, K2 and K3 in Fig. 3.4) and the detector (DID in Fig. 3.4). The columns, which were kept in a controlled temperature

oven, separated out the individual components in the gas mixture by first adsorbing them and then later releasing them during controlled temperature ramp. The gas components thus released were then transported to the detector by an inert carrier gas where, by virtue of their characteristic ionization energies; the components were identified and quantified.

Figure 3.4 shows the details of DIDGC used in the facility. It consisted of two sample loops where a total of 0.25 ml of the unknown gas mixture was retained for the analysis, three capillary columns K1, K2, K3 that resided in an oven with temperature control of ±0.1ºC and separated out the individual components in the gas mixture, and a pulsed discharge ionization detector (DID) which identified and quantified the components of the unknown gas mixture. Two pneumatically actuated valves (8-port and 6-port valves in Fig. 3.4) were provided for facilitating the appropriate routing of gases during analysis. Helium gas with total impurity < 10 ppb was used as the carrier gas. The carrier gas with total impurity < 10 ppb was obtained by additional purification of the research grade helium of 99.9999% purity through an impurity trapper (HP2, from Valco, Inc.), which trapped H_2O, H_2, O_2, N_2, NH_3, CO, CO_2, and CH_4 from helium.

The flow path of the carrier gas during analysis of an unknown gas mixture through DIDGC is shown by different colors in Fig. 3.4. The arrows on the diagram show the flow direction of the gases during analysis. First the carrier gas from the bottle was divided into ("T" in Fig. 3.4) two separate parts (colored in blue and green). The blue stream was flowed through the sample loop1 to carry the unknown gas mixture to the columns K1 and K2 via port numbers 1' and 2'. The column K2 was a molecular sieve column where the actual separation of H_2, Ar, O_2, N_2 and CH_4 occurred, whereas, the column K1 acted as a trap which kept the unwanted hydrocarbons from going to column

K2. Column K2 could not separate out the CO_2 from the gas mixture. Hence, another column K3 was used to separate the CO_2 from the gas mixture (Fig. 3.4). The green flow path shows the routing of the carrier gas in the column K3 and the arrows show its flow direction.

Figure 3.5 shows a representative chromatogram obtained from the DIDGC for a gas mixture containing 2 ppm of CO_2, H_2, O_2, N_2, CH_4 and H_2 in helium. The elution of the components from the columns were done by holding the oven at 50°C for the first 5 minutes, followed by ramping to 120°C at 7°C/min until all gases elute completely from columns K2 and K3. The peaks 1 and 2 in this chromatogram correspond to the unresolved gas mixture peak of the helium matrix and the other unresolved trace gases, such as, Ne and heavy hydrocarbons. As shown in the figure, the first peak of interest in this chromatogram was CO_2 followed by H_2, O_2, N_2, CH_4, and CO. The CO_2 and H_2 gases eluted at the oven temperature of 50^oC, whereas, other gases came out during ramping of the oven temperatures. The effect of temperature ramping resulted in the rising of the baseline of the detector's response (Fig. 3.5), however, the quantification of the gases were unchanged as the shape and area of the peaks above the background did not alter.

For good repeatability of the DIDGC, it is important to completely resolve the individual components in the gas mixture. Figure 3.5 (a) shows the separation of the CO_2, H_2, Ar, O_2, CH_4 and CO from each other. The magnified portion of the chromatogram near the CO_2 peak and Ar/O_2 peak is also shown this figure. As is evident from the figure, the peaks 1 and CO_2 were well separated from each other, but the peaks for O_2 and Ar lied very close to each other. Proper care was taken to separate these two peaks,

particular attention was paid on maintaining the constant flow rate of the carrier gas through the columns and the precise controlling of the oven temperature which collectively control the elution of components from the columns and hence their separation.

3.2.2 Characterization of the facility

The soundness of the facility for corrosion experiments in controlled He + x ppm CO + 1.5 ppm CO_2 (where x ranged between 15 ppm to 1908 ppm) gas was determined by measuring the uniformity of temperature in the 7 quartz tubes housed in the furnace, calibration and repeatability of the gas analysis section, variation of CO and CO_2 in the exposure section in a long duration experiment, and inertness of the exposure section. Further, since high temperature corrosion in dilute He + CO + CO_2 gas is subjected to a rapid deletion of the reactive species (CO and CO_2 in present case), which might alter the oxidation mechanism/kinetics, an experiment was conducted to determine the minimum flow rate of the helium gas required to avoid significant depletion of the reactants during an exposure experiment. The following subsection describes the characterization of the facility performed to determine the limitation and resolution of the facility for He + x ppm + 1.5 ppm CO_2 (x varying between 15 ppm to 1908 ppm) corrosion experiments.

3.2.2.1 Temperature uniformity inside the 7 quartz tubes

The temperature profile inside the 7 quartz tubes housed inside the furnace was determined with the aim of determining the optimum location of the corrosion coupons inside each quartz tube. The optimum location of the corrosion coupons inside a quartz

tube is the position where the temperature is uniform along the length of the tube and is same as the target temperature. Further, at this location the helium gas must be heated to the target temperature.

The furnace was set at the target temperature of 1000°C, and the actual temperature at different points along the length of the tubes was recorded using external K-type thermocouples without flowing the helium gas through the tubes. Figure 3.6 shows the arrangement of the seven quartz tubes inside the furnace and the measured temperature profile in the seven tubes. As is evident from this figure, the zone where the actual temperature inside each quartz tube was uniform and was equal to the target temperature of 1000°C lied between 12” to 18” from the entrance of the furnace. In addition, in this zone, the temperature variation among the seven tubes was ±2°C.

Next, research grade helium of 99.9999% purity was flowed through the tubes at 200 ml/min (the maximum flow rate expected during the experiment) and the gas temperature inside the tubes was measured. As shown in the Fig. 3.6 (b), the helium gas reached the target temperature at a distance of 11 inches along the tube. Thus, this zone, which lied between 12 inches and 18 inches from the front side of the furnace, is the optimum location for the corrosion coupons and throughout this thesis work the corrosion coupons were exposed in this zone.

3.2.2.2 Calibration and repeatability of gas analysis through DIDGC

The DIDGC was calibrated for CO_2, H_2, O_2, CH_4, and CO. For this purpose three certified gas cylinders from Matheson Trigas, Inc. were flowed through the DIDGC at a flow rate and temperature of 50 ml/min and 25°C, respectively. The DIDGC’s responses

for the certified concentration of the gases were used to obtain the calibration curve. Table 3.2 shows the composition of the cylinders used to calibrate the DIDGC and the obtained calibration curves for the five gases are presented in Fig. 3.7 (a) – (e). In the calibrated range of concentrations the DIDGC showed linear response for all the five gases.

The repeatability of gas analysis through the DIDGC was determined for CO, CO_2, H_2, O_2 and CH_4 by analyzing the gas mixture from cylinders 1 and 3 (table 3.2) in five separate runs. The temperature and flow rate of the gas mixture during analysis was 25°C and 50 ml/min, respectively. The cylinders 1 and 3 were chosen to quantify the repeatability of the DIDGC, as they represent the low (cylinder 1) and high concentrations (cylinder 2) of the gases used in exposure experiments.

Tables 3.3 and 3.4 present the results of the analysis. In these tables, columns 2 and 3 show the certified concentration of the gases and the average and standard deviation of the five run measured by the DIDGC. The difference between the average of the measured runs and the certified concentration represents the DIDGC's quantification reliability. In ideal case, the average of the runs and the certified concentration value should be the same. Further, the standard deviation of the runs (column 3 in tables 3.3 and 3.4) represent the repeatability of the gas analysis through the DIDGC. As is evident from the tables 3.3, at the low concentration of gases the average concentration measured by the DIDGC is close to the certified concentration demonstrating the reliability of the DIDGC in quantifying the gases. Further, the standard deviations of the 5 runs for various gases are < 1 ppm, suggesting that from practical stand point, the reading from the DIDGC was reliable up to 1 ppm.

Table 3.4 shows the repeatability of the DIDGC at the higher concentrations of gases. As shown in this table, the average concentrations of the five measurements are very close to the certified concentration and also the standard deviation <10 ppm showing that at the high concentrations it was reliable up to 10 ppm.

3.2.2.3 Control of gas chemistry in the reaction zone

The corrosion of alloys in He-CO-CO_2 environment is dependent on the concentrations of the reactants, i.e. CO and CO_2, and it important to maintain the concentration of these reactants throughout the experiment duration. As a measure of the facility's capability in maintaining the concentrations the reactants, the deviation of the CO and CO_2 concentrations from the target value at the inlet of the reaction zone is presented in Figs. 3.8 and 3.9. The target values in this case were 1.5 ppm of CO_2 and 1908 ppm of CO, respectively. As shown in Fig. 3.8, the maximum deviation of CO_2 at the inlet was 0.1 ppm at the target value of 1.5 ppm, which is below the resolution of the DIDGC. The maximum deviation of CO from the target value of 1908 ppm was 3.5%, which corresponds to an absolute deviation of 69 ppm (Fig. 3.9). These results show that in the long exposure duration experiments the CO and CO_2 levels in the reaction zone could be controlled tightly with a maximum deviation of $\pm$ 3.5% from the target value. Corrosion of alloys in impure helium is governed by the oxygen or carbon potentials in the environment (proportional to the CO/CO_2 ratio for a He+CO+CO_2 environment). The maximum deviation of 3.5% of impurities in the reaction zone corresponds to < 10% deviation in the target oxygen or carbon potentials over the exposure duration of 500h.

3.2.2.4 Verification of adsorption and desorption of CO and CO_2 by the quartz tubes

In order to verify that there was no significant adsorption or desorption of gases from the inert surfaces, such as quartz tube, helium gas containing 242 ppm CO and 1.5 ppm CO_2 was flowed through an empty quartz tube and the inlet and outlet concentration of CO at four temperatures; 25°C (room temperature), 900°C, 950°C and 1000°C were measured. Prior to measurements at high temperature the tube was baked at 1050°C under nitrogen gas at a flow rate of 90 ml/min. Table 3.5 shows the average and standard deviation of the measured CO concentration at the inlet and outlet of the tube for each of the four temperatures. At each temperature seven separate measurements were made. As is evident from this table, the variation of the inlet and outlet concentrations at the four temperatures was ~ 3% which is comparable to the repeatability of gas analysis through DIDGC. Thus, baking of the tube at a temperature above that for the experiment ensured that the quartz tube neither added nor removed the gas from the stream.

3.2.2.5 Determination of minimum flow rate to avoid starvation of reactants

Rapid depletion of the reacting species adjacent to the metal surfaces can occur when a reactive metal surface is exposed to a flowing gas mixture containing dilute amount of reactive species (in ppm level) in inert gas[94]. In this case the reaction becomes starved and the oxidation behavior shown by the metal may not be representative of the true oxidation mechanism. A sufficiently high flow rate of gases must be used to avoid a significant depletion of the reacting species in the gas-mixture.

An experiment was conducted to determine the minimum flow rate of the gas mixture required to avoid the significant depletion of the reactants CO and CO_2, which

could cause starvation of the reactant during an experiment. The onset of starvation of reactive species inside the reaction zone was determined by the variation in the degree of depletion (difference in the inlet and outlet concentration) of the reacting species with the flow rate of the gas mixture. The flow rate at which the reactive species at the outlet is depleted by more than 10% from the inlet level was considered to be the onset of starvation and represents the minimum flow rate of the gas mixture that should be maintained in the experiment [95, 96].

A helium gas chemistry of He + 70 ppm CO + 0.7 ppm CO_2 was chosen to determine the starvation limit. A total of seven alloy 617 corrosion coupons, each with dimension 6.25 mm x 6.25 mm x 1.5 mm were exposed at 950°C with the gas flow rate was varied between 24 ml/min and 106 ml/min. Prior to the experiment, the quartz tubes were baked for 30 hours at 1000^{o}C under nitrogen gas at a flow rate of 90 ml/min.

Figure 3.10 is a plot of the percentage depletion of CO at the outlet as a function of exposure duration at different gas flow rates during the experiment. The flow rate of the gas mixture over the specimens was changed in four successive time steps “A”, “B”, “C”, and “D” in the Fig. 3.10. Proper care was taken to ensure that the concentrations of CO and CO_2 at the inlet remained constant, while changing the flow rate in the tube. In time step A, which lasted for the first 56 hours, the gas flow rate of 106 ml/min was maintained over the corrosion coupons, and then in the time step B the flow rate was decreased to 24 ml/min for ~170 hours. In time step C, the flow rate was brought back to initial flow rate of 106 ml/min to replicate the behavior seen in time step A, and finally, in time step D, a flow rate of 52 ml/min was maintained over the corrosion coupons and the inlet and outlet CO concentrations were recorded.

As shown in Fig. 3.10, during time steps A, C and D, where the flow rate of gas mixture was either 106 ml/min or 52 ml/min, the difference in the inlet and outlet concentration of CO was less than 10%. However, in time step B with a gas flow rate of 24 ml/min the inlet and outlet concentration levels differed by more than 10%. Based on the criterion that the environment should not be depleted in CO by more than 10%, the flow rate in region D (52 ml/min, corresponding to flow rate of 6.3 ml/cm^2 surface area) was determined to be the minimum flow rate to avoid starvation. Hence, in this research, the corrosion experiments were conducted at the gas flow rate of 70 ± 10 (ml/min).

3.3 Exposure experiment parameters

The objective of this thesis was to determine the mechanisms of oxidation of alloy 617 in helium with varying carbon and oxygen potentials in the temperature range of 850°C-1000°C. For this purpose exposure experiments were conducted in six He + x ppm CO + 1.5 ppm CO_2 (where x = 15, 240, 465, 680, 1260 and 1908 ppm) gas mixtures for durations up to 750 h. In the He + CO + CO_2 gas mixture the oxygen potential is given by the reactions:

$$2\,CO + O_2 \leftrightarrow 2\,CO_2\,. \tag{3.1}$$

The equilibrium oxygen potential, P_{O_2} in the He + CO + CO_2 environment can be calculated by:

$$P_{O_2} = \frac{(P_{CO_2})^2}{K_{3.1}(P_{CO})^2}\,. \tag{3.2}$$

The carbon potential in the He + CO + CO_2 gas is determined by:

$$C + CO_2 \leftrightarrow 2\,CO. \tag{3.3}$$

The equilibrium carbon potential, a_c, in the gas can be calculated from:

$$a_c = \frac{(P_{CO})^2}{K_{3.3}(P_{CO_2})}, \tag{3.4}$$

where $K_{3.1}$ and $K_{3.3}$ are the equilibrium constants of the reactions in Eqs. (3.1) and (3.3), respectively. CO and CO_2 are the concentrations of the carbon monoxide and carbon dioxide and the P_{O_2} and a_c are the equilibrium oxygen and carbon potentials in the environment. Furthermore, at a given temperature, T, the values of equilibrium constants, $K_{3.1}$ and $K_{3.3}$ are determined by

$$K_{3.1} = \mathrm{Exp}\left(\frac{-\Delta G^{o}_{3.1}}{R \times T}\right) \tag{3.5}$$

$$K_{3.3} = \mathrm{Exp}\left(\frac{-\Delta G^{o}_{3.3}}{R \times T}\right) \tag{3.6}$$

where $\Delta G^{o}_{3.1}$ and $\Delta G^{o}_{3.3}$ are the standard Gibbs free energy for the reactions (3.1) and (3.3), respectively, R is the universal gas constant, and T is temperature.

As shown in Eq. (3.2) the oxygen potential in the environment depends only on the CO/CO_2 ratios, whereas the carbon potential in the environment depends on both the CO/CO_2 ratio and the CO concentration in the gas (Eq 3.4). In this research, various He + x ppm CO + 1.5 ppm CO_2 gas mixtures were designated according to the CO/CO_2 ratio in the environment. Table 3.6 shows the concentration levels of CO, CO_2 and the corresponding CO/CO_2 ratio established in each environment over 850 -1000°C. This table has been arranged in the increasing order of CO/CO_2 ratios in the gas mixture, and correspondingly, the environment with the lowest CO/CO_2 ratio has been named as environment 1 and the environment with the highest CO/CO_2 ratios as environment 6.

Throughout this thesis this nomenclature will be followed, i.e. the environment with higher CO/CO_2 ratio will be designated with the higher environment number.

Figures 3.11 - 3.14 show the carbon and oxygen potentials of the six environments superimposed on the Cr-O-C stability diagram for alloy 617 at 850, 900, 950, and1000°C, respectively. In this diagram, the activity of Cr for alloy 617 has been taken as 0.72 [97]. The stability diagram shown in Figs. 3.11-3.14 is, typically, used to identify the stable phases when a metal is exposed to a gas mixture containing two components which can react with it, such as, a gas mixture containing sulphur and oxygen, carbon and oxygen, nitrogen and oxygen. In this research, alloy 617 samples were exposed to He + CO + CO_2 gas mixtures and the two reactive components were carbon and oxygen. As shown in Figs 3.11-3.14, the oxygen and carbon potentials in the environments 1 (CO/CO_2 = 9) to 6 environment 1 (CO/CO_2 = 1272) lied in the region where, thermodynamically, Cr_2O_3 is the most stable phase and is expected to predominate over other phases, such as Cr_7C_3 or $Cr_{23}C_6$. Further, as the CO/CO_2 ratios in the environment increases, the oxidation potential in the environment decreases, whereas the carbon potential increases, e.g. in the tested temperature range of 850 -1000°C, the environment 1 environment 1 (CO/CO_2 = 9) had the highest oxygen and lowest carbon potential in it, whereas, the environment 6 environment 1 (CO/CO_2 = 1272) with the highest CO/CO_2 ratio had lowest oxygen potential and highest carbon potential in it.

3.4 Exposure experiment procedure

The following subsection presents the experimental procedure followed during the exposure experiments on alloy 617 in He + x ppm CO + 1.5 CO_2 (where x ranged

between 15 ppm and 1908 ppm) environment in the temperature range of 850 – 1000°C. Prior to start of the experiments the corrosion coupons and the facility was prepared as per the description given below.

3.4.1 Preparation of samples for corrosion tests

Rectangular corrosion coupons of dimension 6.5 mm x 6.5 mmx1.5 mm were machined from the alloy 617 plate received from Special Metals, Inc. using Electric Discharge Machine (EDM). The surface of the obtained corrosion coupons were then ground and polished with SiC paper of successively increasing grade up to grit number 800. In one of the experiments, referred as "pre-oxidation experiment" in this thesis, the surface of the coupons were further prepared by 1.0 μm diamond suspension and electro-polishing in 10% perchloric acid in methanol at - 40ºC with an applied voltage of 4V for 30 sec. The two electrodes were the sample (anode) and the platinum (cathode). After electropolishing the samples were washed thoroughly in distilled water and dried with a handheld blower.

Followed by the surface preparation the dimension of the corrosion coupons were measured by a digital micrometer with 0.01mm accuracy. The weights of the samples were then measured by a microbalance with the resolution of 0.01 mg. A total of three weight measurements were performed on each sample. The three weight measurements were then averaged to obtain the weight of the sample. In the final step, the specimens were degreased and cleaned ultrasonically for ~ 15 minutes using a 50% acetone and 50% ethanol mixture.

3.4.2 Preparation of the facility for corrosion tests

Following steps were adopted sequentially to prepare the facility for the corrosion experiments.

3.4.2.1 Baking and establishment of target CO and CO_2 concentrations in the tubes

The quartz tubes were baked at 1025°C for 24 hours under nitrogen gas (99.99% purity) flowing at a rate of 90 ml/min to expel out any adsorbed gases that might be present in the quartz tube. The corrosion coupons with the prepared surface finish were then inserted in the cold zone of the furnace and the quartz tubes were sealed. The temperature of the cold zone was ~ 60°C at the gas flow rate of 90 ml/min. Research grade helium of 99.9999% purity was then flowed through the sealed tubes to flush out the nitrogen and oxygen from the sealed tubes. The concentration levels of oxygen and nitrogen were measured at the outlet and inlet of the tubes through DIDGC every 5 hours, and, after the oxygen level dropped below the detection limit of ~ 1ppm, the furnace was brought down to the experiment temperature. The target concentrations of CO and CO_2 (table 3.6) were then established by further diluting the pre-diluted He + x ppm CO and He + y ppm CO_2 (x, and y are the concentration of the CO and CO_2 in the pre-diluted gas bottle) type of gas bottles with research grade helium of purity 99.9999%. To achieve the target concentration, say 1900 ppm of CO in a tube, V_1 cc/min of gas from He + x ppm CO gas bottle was added to a gas stream of V_2 cc/min from He + y ppm of CO_2 bottle. V_3 cc/min of gas from research grade helium of purity 99.9999% purity was then added to this V_1 cc/min of CO + V_2 cc/min of CO_2 stream. The concentrations of the CO and CO_2 in a tube then can be calculated by the rule of mixture:

$$\text{CO concentration (ppm)} = \frac{V_1 \times \text{CO concentration in the gas bottle (x)}}{V_1 + V_2 + V_3} \quad (3.7)$$

$$CO_2 \text{ concentration (ppm)} = \frac{V_2 \times \text{CO concentration in the gas bottle (y)}}{V_1 + V_2 + V_3} \quad (3.8)$$

Table 3.7 shows the values of x, y , V_1, V_2, V_3, and the calculated values of CO and CO_2 in each environment. Comparing columns 7 and 8 in table 3.7 with columns 3 and 4 in table 3.6, the calculated values of CO and CO_2 were in very good agreement with the CO and CO_2 values measured by the gas chromatograph.

After the establishment of the target CO and CO_2 concentrations, the outlet and inlet concentrations of CO and CO_2 were measured through the empty tubes 5 times. Theoretically, the inlet and outlet concentrations of the CO and CO_2 should be same, however, a difference of 3-8 ppm was noticed for the CO and a difference of 0.2 to 0.5 ppm was noticed for CO_2, which are comparable to the repeatability limit of the GC for these gases (see tables 3.3 and 3.4).

Typically, the baking of the tubes and establishment of the target concentration lasted for 70-80 hours.

3.4.2.2 Insertion of the samples in the hot zone and start of the exposure experiment

After establishing the target concentrations and temperature, the corrosion coupons which were initially placed in the cold zone of the furnace were inserted into the uniform temperature zone of the furnace. Fig 3.15 shows a cross-sectional view (drawn to the scale) of a quartz tube showing the placement of the corrosion coupon inside it. The top and bottom of the corrosion coupons resting on the walls of the quartz tubes were exposed to the flowing helium gas mixture. The location of the sample in the quartz tubes are marked in Fig 3.6 (b). In order to insert the corrosion coupons at the uniform

temperature zone marked in Fig. 3.6 (b), the furnace was opened briefly and the corrosion coupons were pushed in without breaking the seal of the quartz tubes using the custom fabricated push-rod and the magnet (Fig 3.3). The procedure of pushing the coupons in and out of the furnace without having to break the seal of the system is described in section 3.2.1.2. Typically, the insertion of the samples in the uniform hot zone took 3-4 minutes per tube during which the furnace temperature fluctuated from the experiment temperature. Figure 3.16 shows a typical temperature fluctuation in the uniform temperature zone during the insertion of six corrosion coupons in one quartz tube. In this particular case, the experiment temperature was 900°C. A total of ~5 minutes was required to push the samples inside the uniform temperature zone during which the furnace was kept opened followed by which it was closed. An external K type of the thermocouple was inserted in the adjacent quartz tube and the drop/increase in the furnace temperature was recorded every 30 seconds. Figure 3.16 shows the temperature fluctuation thus measured. As shown in this figure the temperature of the uniform temperature zone decreased from the experiment temperature of 900°C to 738°C as a result of the furnace being opened. Immediately after closing the furnace the temperature shot up to a peak temperature of 933°C followed by which it reached the experiment temperature exponentially within ~ 6 minutes of closing of the furnace. Thus it is expected that opening and closing of the furnace disturbs the temperature of the corrosion coupons placed in the uniform temperature zone, the duration of which is ~ 11 minutes, for the first 5 minutes the temperature is less than the experiment temperature and for the next ~ 6 minutes the temperature was higher than the experiment temperature. In a long

experiment duration of100 to 750 hours, the effect of this fluctuation is expected to be negligible.

3.4.2.3 Pulling out of the samples from hot zone after the exposure

After the target exposure durations of 100h, 225h, 375h, 500h and 750h the corrosion coupons were pulled out of the hot zone and were placed into the cold zone of the furnace where they were cooled under the flowing helium gas for ~ 10 hours. The custom fabricated push rod described in the section 3.6 was used to pull the coupons out of the hot zone of the furnace. At the conclusion of the experiment, the quartz tube seal was broken; the corrosion coupons were taken out, inspected visually for any obvious oxide scale spallation, weighed on the microbalance and analyzed for microstructural changes.

3.5 Post exposure analysis of the samples

Post exposure analysis of the coupons was focused on the microstructural examination. The coupons were first weighed on a microbalance, and then analyzed for microstructural changes by XRD, SEM, TEM, and EMPA.

3.5.1 Measurement of weight change in the sample

The weights of the samples were measured before and after the exposure using a microbalance with the resolution 0.01 mg to determine the overall kinetics of corrosion. A total of three weight measurements were performed on each sample. The three weight measurements were then averaged to obtain the weight of the sample. The change in weight of the sample was then determined as per the Eq. (3.7)

$$\frac{\Delta W}{S} = \frac{W_{final} - W_{initial}}{S} \qquad (3.7)$$

Where, ΔW is the change in weight of the sample due to exposure,

W_{final} is the weight of the sample after exposure,

$W_{initial}$ is the weight of the sample before exposure, and

S is the total surface area of the sample calculated as S = 2(L x B+ B x H+ L x H), where L, B, and H are the measured length, width and thickness of the corrosion coupon, respectively.

3.5.2 X-ray analysis

After weight measurements, the selected exposed samples were analyzed by x-ray diffraction to determine the structure of the oxidation products formed on the surface of the samples. A Rigaku rotating anode CuK_α X-ray diffractometer was used in θ - 2θ mode at the operating voltage and current of 40kV and 100 mA, respectively. The choice of scan rate and duration of each XRD was dependent largely upon the range of diffraction angles being measured. A scan rate of 1 degree per minute and wide scan range of 30º - 90º was used to identify all the possible phases that could form under the given exposure conditions. The expected phases were NiO, TiO_2, Al_2O_3, SiO_2, Cr_2O_3, spinels of Ni/Cr/Al, Cr_3C_2, $Cr_{23}C_6$, Cr_7C_3, and Mo-based carbides. The selected range of 30º - 90º encompasses the signals from all the above mentioned phases. Typically present in larger fractions in the surface film, the oxides showed peaks with intensities well above the background level, whereas, the minor phases, such as carbides, showed peaks with low intensities that sometimes were not well resolved from the background. To enhance the intensities of the carbides-peaks a slower scan rate of 0.1 degrees per minute was used in the 2θ range of 30° to 60°, which includes the major peaks from the

chromium carbides. After obtaining the x-ray diffraction pattern, the peaks were indexed using the commercial software package Jade® from Materials Data, Inc[48]. The software matches the position (2θ values) and the relative intensities of the peaks in the diffraction pattern with that of the large database of known crystallographic material to allow determination of each phase.

3.5.3 SEM imaging

The corrosion coupons were examined in the cross-section with the aim of characterizing the morphology and distribution of phases such as oxides and carbides in the surface scale and in the sub-surface zone. A section of the corrosion coupon was cut using a precision diamond cut-off saw and was mounted in a phonelic resin using SimpliMet2 hot mounting press from Buehler, Inc. Mounts were then successively ground using 320, 600, 800, 1200, 2400 and 4000 grit SiC paper and prepared finally with 1μm diamond suspension solution. An electrolytic etching using oxalic acid etch (10% oxalic acid in distilled water) at room temperature and 3V for 10 seconds revealed the distribution of carbides in the bulk of the sample. This etch preferentially etches the carbides. The SEM was operated in the 15-20 KV range and depending on the size of the microstructural features being examined; the spot size was varied between 3 to 5. Typically, a lower spot size was used for a higher spatial resolution. The imaging was done both in back-scattered electron (BSE) and secondary electron (SE) mode. The SE mode was used to characterize the morphology of the film, whereas, the BSE mode was used to identify the distribution of various phases in the coupons. The thickness of the external scale was measured from the BSE images. The grain size was measured using

the linear intercept method [98]. Several lines were superimposed on a micrograph and the number of grains intersected by each line was counted. The grain size was then determined by dividing the total length of the superimposed line by the number of grains intersected.

Calculation of weight of carbon in Cr_7C_3 and oxygen in Cr_2O_3 and Al_2O_3

The oxidation of alloy 617 in high CO/CO_2 environment resulted in the formation of an external scale which consisted of Cr_2O_3 and Cr_7C_3 and a subsurface zone where Al_2O_3 precipitates formed. The weight gain associated with the carbon in the form of Cr_7C_3 and oxygen in the form of Cr_2O_3 and Al_2O_3 were calculated by measuring the absolute areas occupied by each phase in a BSE micrograph of known magnification. Measurement of the area of each phase in a micrograph was done using Scandium® software from Olympus Soft-Imaging Solutions GMBH, Germany [99]. Fig 3.17 shows the procedure for measuring the area of each phase (Cr_2O_3, Cr_7C_3, and Al_2O_3). The areas enclosed by the external scale, Cr_7C_3, and Al_2O_3 were first delineated using a pencil tool in the software. The area Cr_2O_3 was then obtained by subtracting the area of Cr_7C_3 from the total area enclosed by the external scale. Mass of a phase per unit length of the micrograph, M_i, ("i" stands for Cr_2O_3, Cr_7C_3, and Al_2O_3) was then calculated as per the relation:

$$M_i = \frac{\rho_i \times A_i}{L} \qquad (3.8),$$

where ρ_i, A_i, and L are the room temperature density, measured area, and the length of the micrograph used, respectively. The density values used (in mg/mm^3) were 5.2 for Cr_2O_3, 6.9 for Cr_7C_3, and 4.0 for Al_2O_3 [100].

Mass per unit length of the microstructure measured from Eq. (3.8) was then assumed to be the same as the mass per unit surface area of the sample. The weight of carbon in Cr_7C_3, oxygen in Cr_2O_3, and Al_2O_3 was then calculated by the identity that Cr_7C_3 contains 0.09 weight fraction of carbon, Cr_2O_3 contains 0.316 weight fraction of oxygen, and Al_2O_3 contains 0.471 weight fraction of oxygen, i.e.

mass of oxygen in Cr_2O_3, $M_{O/Cr_2O_3} = M_{Cr_2O_3} \times 0.316$ (3.9)

mass of oxygen in Al_2O_3, $M_{O/Al_2O_3} = M_{Al_2O_3} \times 0.471$ (3.10)

mass of carbon in Cr_7C_3, $M_{C/Cr_7C_3} = M_{Cr_7C_3} \times 0.09$ (3.11).

Measurement of the area fraction of carbide in the bulk of the alloy

The area fraction of the carbides in the bulk of the alloy was measured using Adobe Photoshop® software from Adobe, Inc[101]. For this purpose, the brightness and contrast of the image was adjusted manually such that only carbides were visible in the image and not the matrix. This brightness and contrast level was set as the threshold brightness and contrast level. The software then calculates the area fraction of the bright pixels (carbide) with respect to the dark pixel (matrix), by calculating the area of the bright and dark pixels in the image. Figure 3.18 shows a representative bulk microstructure and the brightness/contrast adjusted image finally used to estimate the area fraction of the carbide in the image. In this specific case the area fraction of the carbide was estimated to be 3.2%.

Calculation of weight associated with the carbide in the bulk

The increase in the area fraction of the carbide was calculated by subtracting the area fraction of carbide in the oxidized sample from the as-received sample. The increase in area fraction was then assumed to be the same as increase in volume fraction. This volume fraction was then multiplied with the total volume of the sample to obtain the absolute increase in volume of the carbide. The weight gain due to the carbide was then calculated by assuming that the bulk carbides were all $Cr_{23}C_6$ with density 6.97 mg/mm^3. Since $Cr_{23}C_6$ contains only 5.68% of carbon by weight, the weight gain due to carbon will be weight gain due to carbide x 0.0568.

Procedure for SEM/EDS

X-ray energy dispersive spectroscopy (EDS) was used to examine the chemical composition of the elements near the surface film under SEM. For this purpose, the sample was focused, corrected for astigmatism using the lens stigmators, and the objective aperture of the SEM was aligned to obtain a crisp image of the desired area in the sample. The Z-height of the sample was adjusted to 10mm, the eucentric height of the SEM stage and the EDS spectrum was collected. The Kα lines of Cr, Ni, O, Al and Ti and for Mo Lα were used for the EDS map collection.

3.5.4 TEM imaging

3.5.4.1 Sample preparation using FIB

Cross sectional TEM specimens were prepared by the conventional H-bar technique [7, 102]. A schematic of the sample preparation by this method is shown in Fig

3.19. A small sample of dimension 3 mm x 2mm x 1.5 mm was first cut from the bulk corrosion coupon using a precision diamond cut-off saw. This small sample was further cut into three equal portions of dimension 1 mm x 2 mm x 1.5 mm. A silicon wafer was then glued onto the surface of the sample to protect the oxide surface. The silicon wafer was then transferred onto a U-shaped Mo-TEM grid and polished mechanically to a thickness of ~ 100µm using 1 µm diamond paper. This preliminary thinning step was required to minimize the milling time in FIB. The final thinning was then performed by the Ga^+ ions using FIB. Before the milling by FIB, the area of interest was protected from the beam damage by platinum coating of thickness 2 µm. The voltage and beam current used in FIB varied between 10 - 30 keV and 30 pA – 7 nA. A higher voltage and beam current of 30 keV and 7nA was used for the coarse milling in the initial stages and in the final milling stages a lower voltage of 10 keV and beam current of 10pA was used to minimize the Ga^+ ion interaction with the TEM sample.

3.5.4.2 TEM imaging conditions

Characterization of the TEM sample was conducted on a JEOL2010F analytical TEM. The operating voltage used was 200keV. The gun, electron beam, condenser, and objective lenses were aligned with the optical axis of the TEM according to the procedure outlined in the reference [103]. The feature of interest was then located in the electron transparent region in the TEM sample and was brought to the center of the viewing screen. A suitable objective aperture was then inserted to select the transmitted electron beam and the bright field image of the feature was recorded. Next a suitable selected area

diffraction pattern (SAD) aperture was inserted on the feature of interest, sample was tilted to a zone axis, and the diffraction pattern was recorded at known camera length.

3.5.4.3 Indexing of the diffraction pattern

The diffraction pattern was indexed to identify the phases. For this purpose, the distances of three diffraction spots closest to the transmitted spot(central spot) were measured and the lattice spacing of those three spots were calculated using [104]:

$$Rd = \lambda L, \tag{3.12}$$

where R is the distance of a diffraction spot from the transmitted spot, d is the lattice spacing of a given plane systems, λ is the voltage dependent wavelength of the electron beam (0.02508 A° at the operated voltage of 200 keV), and L is the camera length of the TEM. The calculated lattice spacing was then compared against the known lattice spacing of the expected phase for a possible match. Standard powder diffraction file (PDF) for the expected phase was used for this purpose. A tentative (hkl) value was assigned to each of the spots based on the d-spacing values. The angles between the three tentative (hkl) planes were then measured from the obtained diffraction pattern and compared against the ideal angle between the (hkl) plane from the PDF. The tentative (hkl) value was then retained if the measured angles matched with the ideal angles for the expected phase, otherwise this procedure was repeated until a good match between the measured and ideal angle was obtained. Further, the vector addition method was used and some additional diffraction spots were indexed and their angles were compared against the ideal angles to ensure the consistency of the indexing.

3.5.5 Electron Micro-Probe analysis (EMPA)

The concentration profiles of elements Ni, Cr, Co, Mo, Al, Ti, and Fe were measured using a Cameca SX100 electro-micro-probe analyzer (EMPA). The accelerating voltage and beam current used were 15KV and 10nA, respectively. Elements, spectrometer crystal, characteristic x-ray lines and the calibration standard used for this purpose are listed in table 3.8. Calibration of the instrument for the elements Ni, Cr, Co, Mo, Al, Ti, and Fe was verified by first calibrating the EMPA with the standards shown in table 3.8 and then using the same standard as the unknown. The electron interaction volume of the beam with the Ni-based alloy has been reported to be 1-2μm [105]. A variable step size was used to measure the concentration profiles of the elements in the cross-section of the sample. The step size used was 1.0μm. Three representative concentration profiles were measured in each case, and the average and standard deviations of these three lines were used for further calculations.

The corrosion of alloy 617 resulted in depletion (during oxidation) or enrichment (during decarburization) of Cr/Al/Ni etc. near the alloy/scale interface. The Cr/Al/Ni-concentration profile measured by EMPA was used to calculate the weight of Cr/Al/Ni in the depleted/ enriched due to corrosion. The weight of Cr/Al/Ni in the depletion/ enrichment zone, ΔW_{EMPA}, (mg/mm^2) was calculated by:

$$\Delta W_{EMPA} = \rho_{Alloy} \times \int_0^Z [Cr_{bulk} - Cr(x)]dx , \qquad (3.13)$$

where ρ_{Alloy} is the density of alloy 617 (8.36 mg/mm^3), Cr_{bulk} is the weight fraction of Cr in the bulk, $Cr(x)$ is the weight fraction of Cr content at depth x from the oxide/alloy interface, and

Z stands for the width of the depletion/enrichment zone (in mm) measured from the alloy/scale interface.

3.6 Error analysis procedure

All the weight measurements, microstructure measurements, such as, oxide thickness, depth of carbide free zone, area fraction of Cr_7C_3 in the external scale are reported with the standard deviation, σ, which is defined as

$$\sigma = \sqrt{\frac{1}{N}\sum_{i=1}^{N}(x_i - \mu)^2}\ , \qquad (3.14)$$

where N is the total number of readings, x_i is the value of a particular measurement, and μ is the average of N measurements.

Frequently, the result of an experiment is not measured directly rather is calculated from several physical measurements, each of which has an average value and an error. The resulting error in the final result of such experiment is the propagation of error and was calculated as per the relations shown in table 3.9.

Table 3.1(a)-3.1 (d) Characterization of the alloy 617 plate obtained from Special Metals, Inc., (a) initial dimensions of the plate, (b) chemical composition of the alloy 617 as provided by Special Metals, Inc., Sherry lab, and EMPA (in weight % and atomic%), (c) the impurity contents as analyzed by Sherry lab, and (d) room temperature tensile properties.

(a)Heat number and dimensions of the as received alloy 617 plate received from Special Metals, Inc.

Heat number	Inches	Centimeters
XXX2322 U K	½ x 3 x 19	1.3 x 7.6 x 48.3

(b) Chemical composition of the alloy 617 as obtained from Special Metals, Inc., Sherry Labs, and EMPA at Electron Micro-beam Analysis Lab.

Element	Ni	Cr	Co	Mo	Al	Ti	Fe	Mn	Cu	Si	C
Weight% (from Special Metals Inc.)	54.6	21.8	11.5	9.7	1.1	0.3	0.79	0.03	0.02	0.07	0.09
Weight% (from Sherry labs)	55.1	21.6	11.5	9.4	0.9	0.3	0.68	0.06	0.03	0.08	0.09
Weight% (measured by EMPA)	54.8	21.4	11.5	9.2	1.1	0.3	0.78	0.02	0.02	0.08	not detected

(c) The impurity contents in the alloy 617, test method, and the ASTM standard used for quantification (as obtained from Sherry Labs).

Impurities	Sulfur	Phosphorous	oxygen	Nitrogen
Weight%	<0.005	0.007	<0.0005	0.007
Testing method	CO	XRF	IG	IG
ASTM standard	E1019-03	E-1621-94(1999)	E1019-03	E1019-03

(d) Tensile test results conducted at room temperature on the as received alloy 617

Hardness (Rockwell hardness scale B)	89.1
Yield strength (0.2% offset value)	410.9 MPa
Tensile strength	810.8 Mpa
% Elongation	48.6
% Reduction of area	57.6

Table 3.2 Composition of the gas cylinders used to calibrate the DIDGC.

	CO_2 (ppm)	H_2 (ppm)	CH_4 (ppm)	O_2 (ppm)	CO (ppm)
Cylinder 1	2	50.5	10.1	2	10.1
Cylinder 2	5.1	-	50.2	19.9	999.3
Cylinder 3	20.1	3003.2	199.8	39.3	3012.3

Table 3.3 Repeatability of the gas analysis through the DIDGC in the low concentration range of impurities.

Gas	Certified concentrations (ppm)	Average and standard deviation of 5 measurements by DIDGC (ppm)
CO	10.1	9.9 ± 0.3
CO_2	2.0	2.2 ± 0.1
CH_4	10.1	10.1 ± 0.1
H_2	50.5	48.4 ± 0.9
O_2	2	2.7 ± 0.8

Table 3.4 Repeatability of gas analysis through the DIDGC in the high concentration range of impurities.

Gas	Expected concentration (ppm)	Average of 5 runs (ppm)
CO	3012.3	2998.4 ± 4.6
CO_2	20.1	20.7 ± 0.3
CH_4	199.8	193.1 ± 1.8
H_2	3003.2	3017.5 ± 8.0
O_2	15	16.7 ± 1.26

Table 3.5 Concentration of CO at the inlet and outlet of the tube at four temperatures through an empty quartz tube over 25°C - 1000°C.

Temperature (°C)	Inlet (ppm)	Outlet (ppm)	% change from the inlet
25	241 ± 1.6	243 ± 1.6	0.8
900	241 ± 2.1	242 ± 2.4	0.4
950	243 ± 1.8	237 ± 1.9	2.5
1000	242 ± 1.7	234 ± 2.9	3.3

Table 3.6 Concentration levels of six He-CO-CO_2 environments established at 850°C, 900°C, 950°C and 1000°C. The table has been arranged in the increasing order of the CO/CO_2 ratios and the environment number. The average and standard deviation of the CO, CO_2 and CO/CO_2 ratio for each environment are shown.

Environment no.	(CO/CO_2) ratio	CO (ppm)	CO_2 (ppm)
1	9 ± 1	15 ± 0.3	1.7 ± 0.1
2	150 ± 12	240 ± 3.8	1.6 ± 0.1
3	291 ± 39.5	466 ± 4.9	1.6 ± 0.2
4	453 ± 68	680 ± 11.2	1.5 ± 0.2
5	900 ± 77	1260 ± 17.5	1.4 ± 0.1
6	1272 ± 186	1908 ± 24.2	1.5 ± 0.2

Table 3.7 Concentrations of the He + x ppm CO and He + y ppm CO_2 type of bottles used, flow rates of the gases from He + x ppm CO (V_1) and He + y ppm CO_2 (V_2), and research grade helium (V_3) type of bottles used to obtain the target concentration levels of CO and CO_2 in each environment. The calculated values of CO and CO_2 by the Eqs. (3.7) and (3.8) are given in columns 7 and 8, respectively.

Environment number	Concentration of CO in the He+CO bottle (ppm)	Concentration of CO_2 the He+CO_2 bottle (ppm)	Flow rate from He + CO bottle, V_1 (cc/min)	Flow rate from He + CO_2 bottle, V_2 (cc/min)	Flow rate from research grade helium bottle, V_3 (cc/min)	Calculated value of CO in mixed gas stream (ppm)	Calculated value of CO_2 in mixed gas stream (ppm)
1	He+350 ppm CO	He + 10 ppm CO_2	5.5	21	97	15.5	1.7
2	He+350 ppm CO	He + 10 ppm CO_2	65	14	18	235	1.4
3	He + 2010 ppm CO	He + 10 ppm CO_2	24	12	67	468	1.2
4	He + 2010 ppm CO	He + 10 ppm CO_2	49	18	79	675	1.2
5	He+4500 ppm CO	He + 10 ppm CO_2	42	30	82	1227	1.9
6	He+4500 ppm CO	He + 10 ppm CO_2	44	19	41	1904	1.8

Table 3.8 Element, spectrometer crystal, x-ray radiation and material used for calibration in EMPA analysis. In this table LLIF stands for Large Lithium Fluoride, PET stands for Pentaerythritol, and TAP stands for Thallium Acid Phthalate

Element	Crystal	Line	Calibration standard used
Ni	LLIF	Kα	NiAl
Cr	PET	Kα	pure Cr
Co	LLIF	Kα	pure Co
Mo	PET	Lα	pure Mo
Al	TAP	Kα	NiAl
Ti	PET	Kα	pure Ti
Fe	PET	Kα	pure Fe

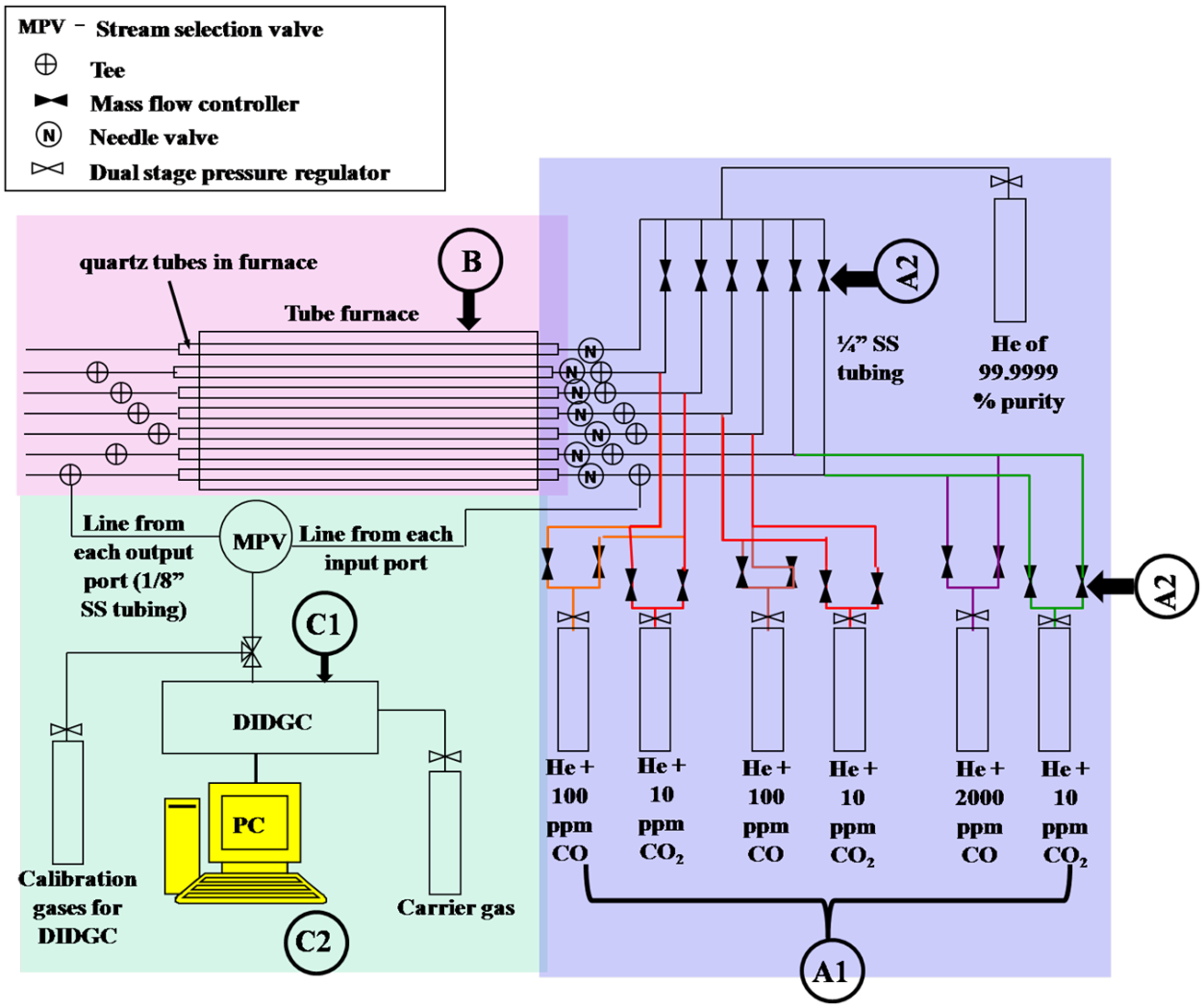

Figure 3.1 Schematic of the controlled-Impurity-Flow system. The three major sections: gas mixing section (A1 and A2), exposure section (B), and the gas analysis section (C1 and C2) are shaded in different colors.

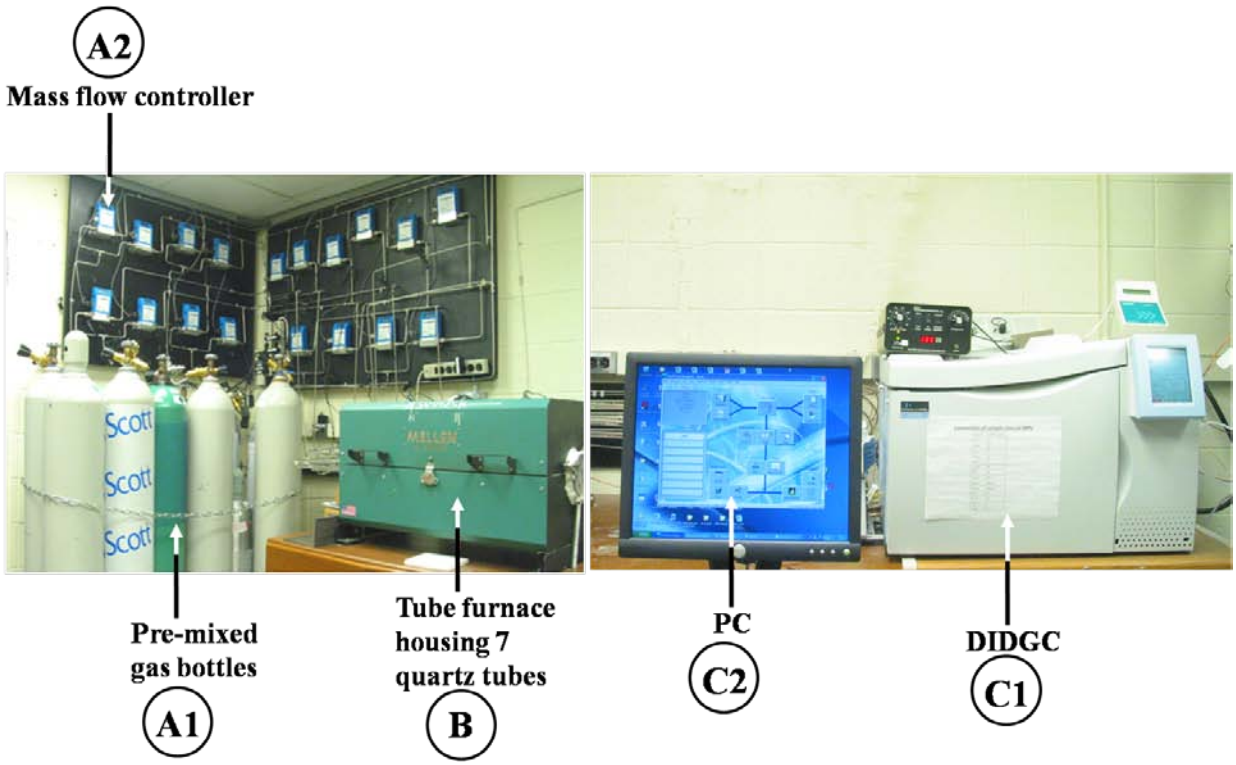

Figure 3.2 Photograph of the assembled Controlled-Impurity-Flow system.

(a)

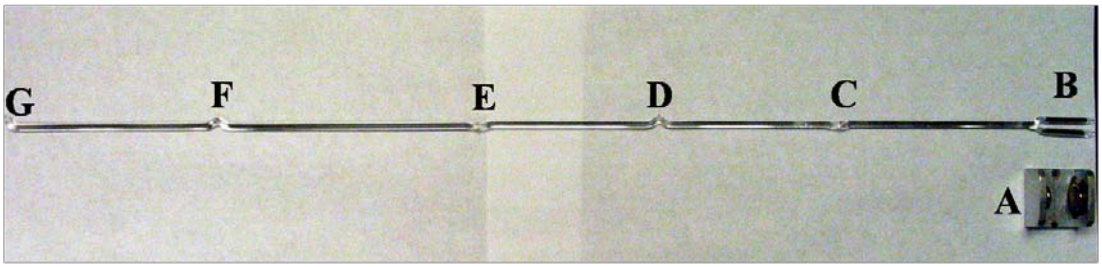

(b)

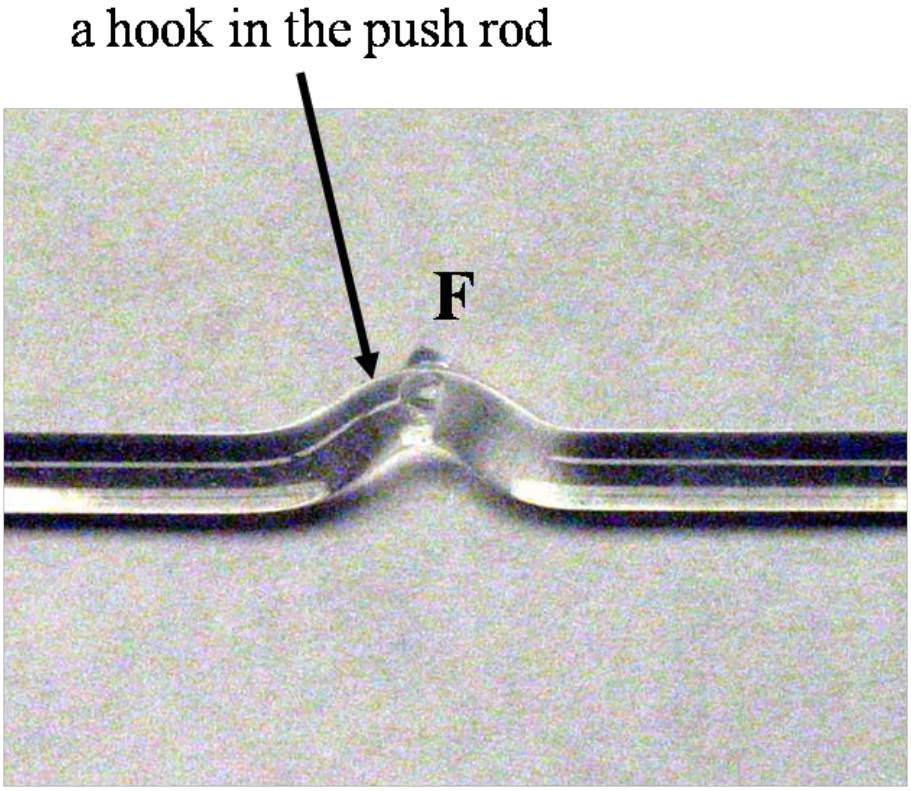

(c)

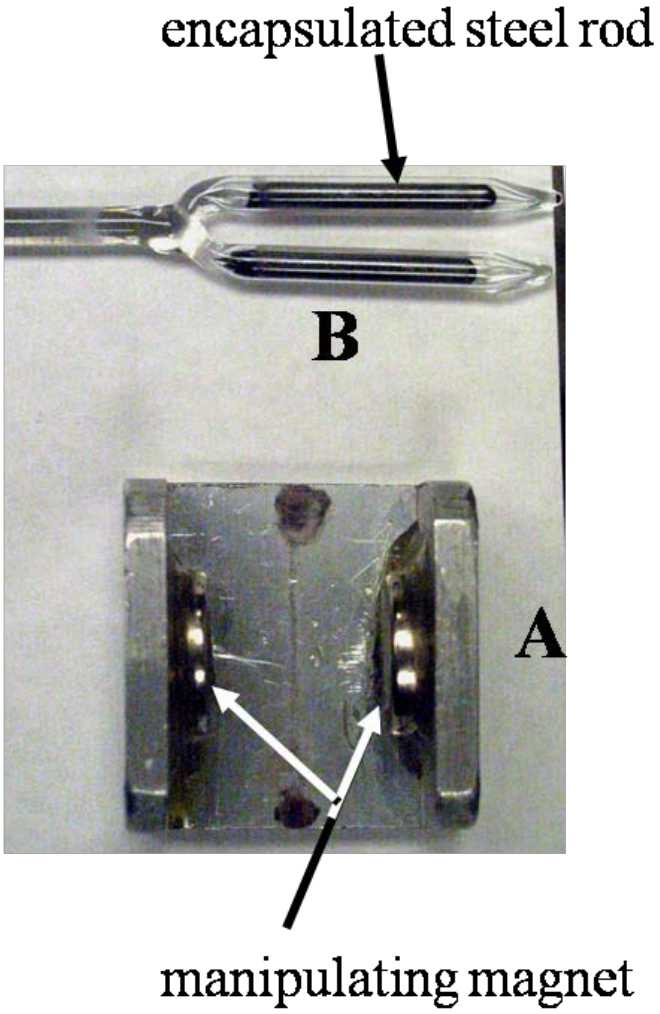

Figure 3.3 Photographs of (a) custom fabricated quartz push rod to move the specimen from the hot zone to cold zone of the furnace without breaking the seal of the system. A is the high strength magnet, B is the encapsulated steel, C, D, E, F, and G are the five hooks used to move the specimens, (b) high magnification photograph of the push rod showing the shape of the hook, and (c) high magnification photograph of the manipulating magnet, and encapsulated rod.

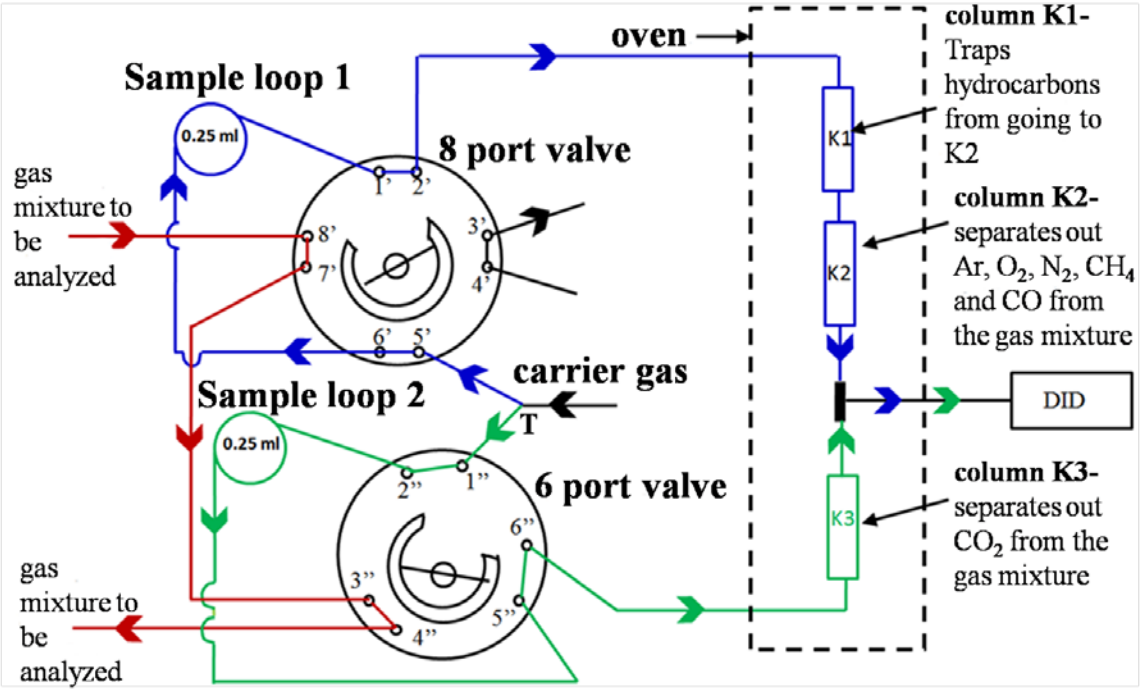

Figure 3.4 Schematic of the flow path of the carrier gas during analysis of an unknown gas mixture. The carrier gas from the bottle splits in two streams at position "T" and flows in the sample loops 1 (colored in blue) and 2 (colored in light green). The separation of Ar, O_2, N_2, and CH_4 occurs in column K2, whereas the column K3 separates the CO_2 from the unknown gas mixture.

(a)

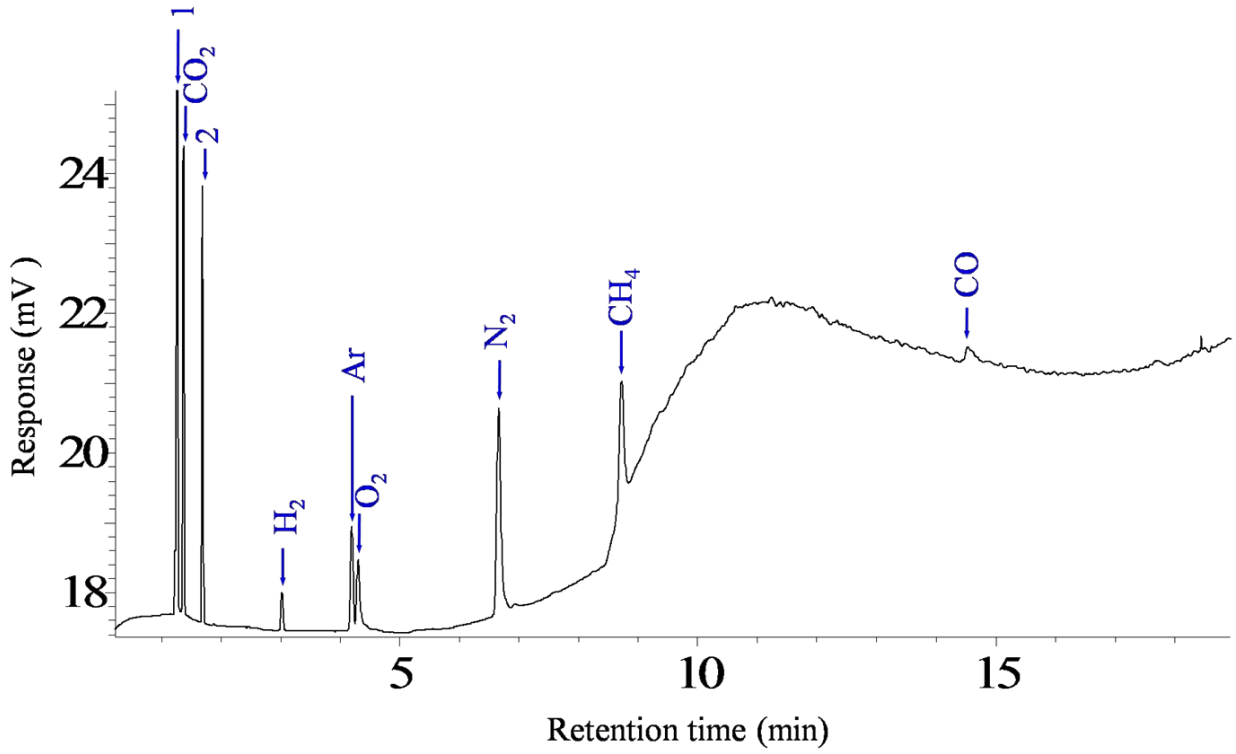
1
CO_2
2
H_2
Ar
O_2
N_2
CH_4
CO
Response (mV)
24
22
20
18
5
10
15
Retention time (min)

(b)

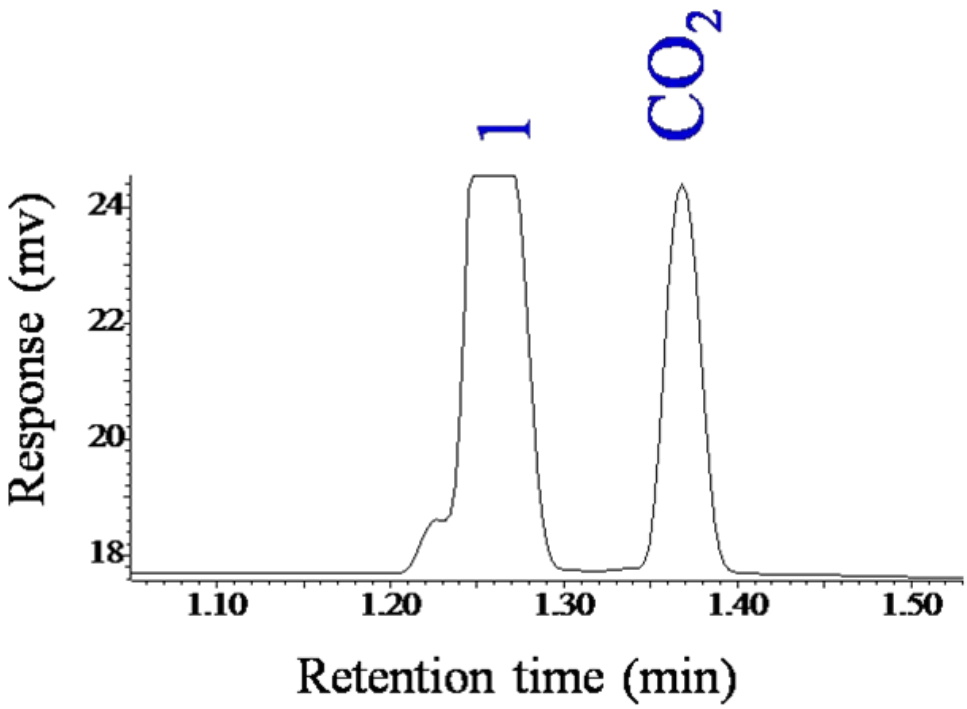
1
CO_2
Response (mv)
24
22
20
18
1.10
1.20
1.30
1.40
1.50
Retention time (min)

(c)

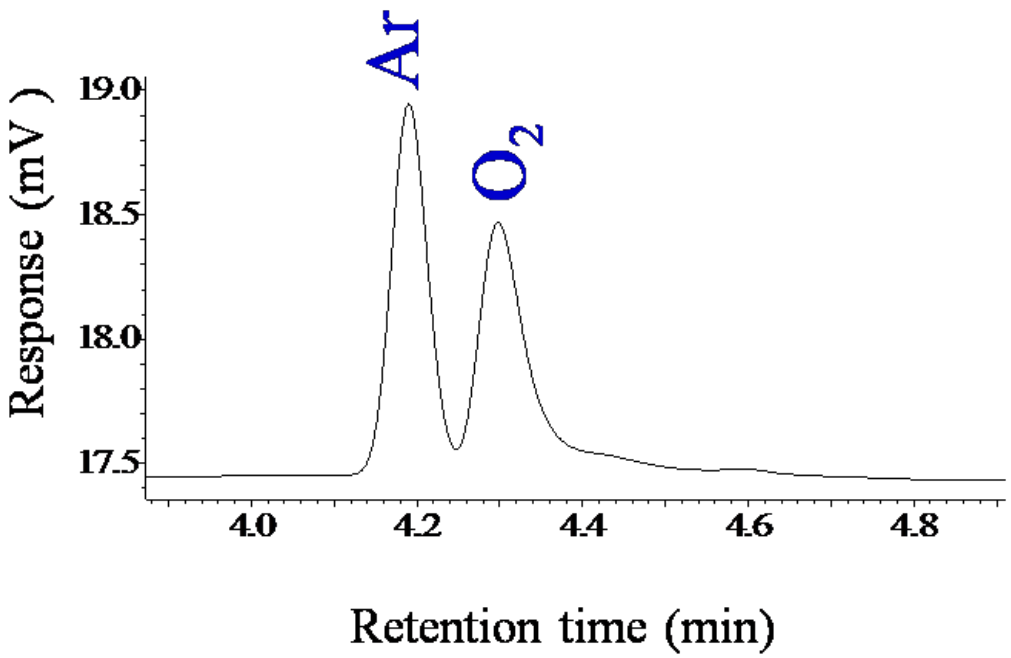

Figure 3.5(a) A representative chromatogram obtained for a gas mixture containing 2 ppm of CO_2, H_2, Ar, O_2, CH_4, and CO in helium. The peaks 1 and 2 are the unresolved gas mixture peaks, (b) portion of the chromatogram showing the peak separation of between the peak 1 and CO_2, and (c) portion of the chromatogram showing the peak separation between Ar and O_2.

(a)

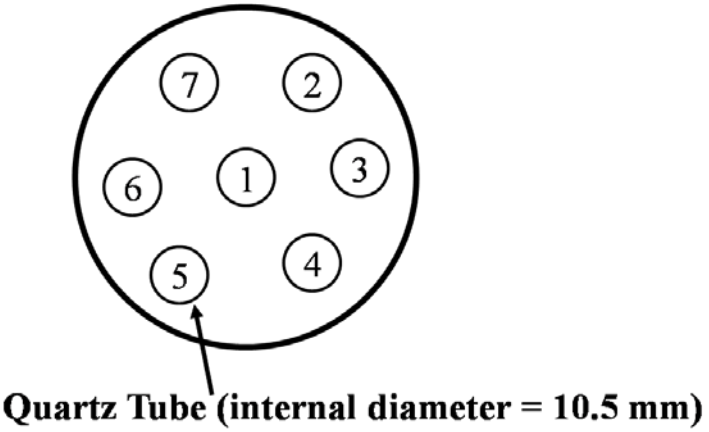

(b)

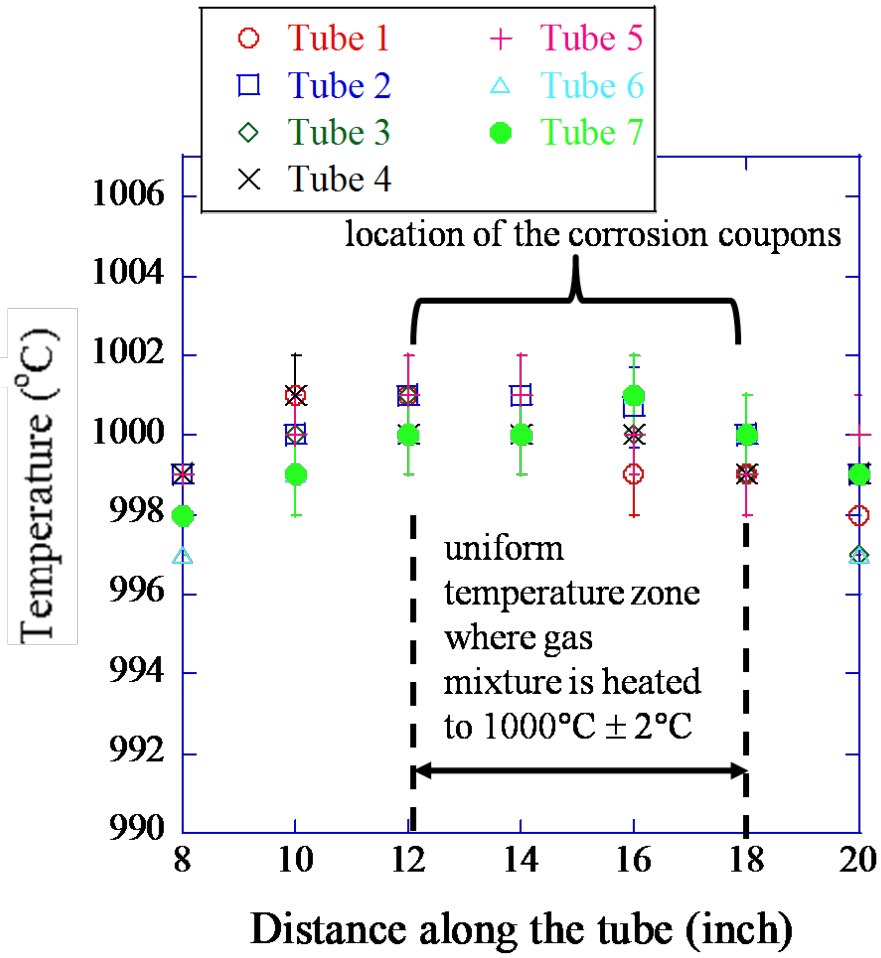

Figure 3.6 (a) Cross-sectional view of the furnace showing the arrangement of the seven quartz tubes inside it, and (b) temperature profiling of the furnace in each quartz tube. The location of the corrosion coupons inside the furnace is marked in the figure.

(a)

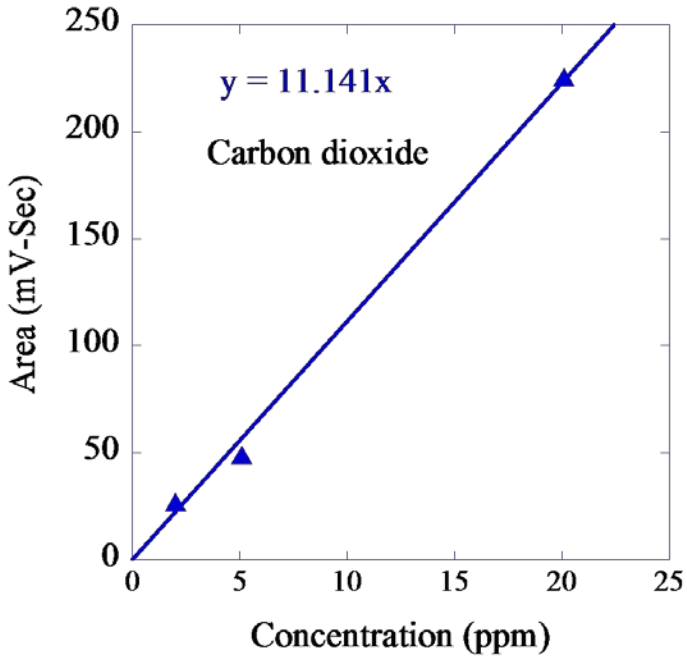
y = 11.141x
Carbon dioxide
Area (mV-Sec)
Concentration (ppm)
0
50
100
150
200
250
0
5
10
15
20
25

(b)

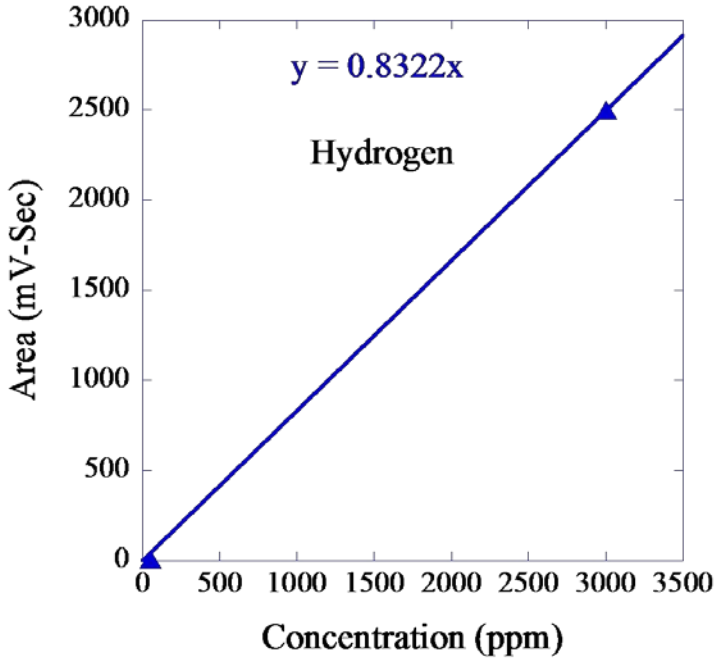
y = 0.8322x
Hydrogen
Area (mV-Sec)
Concentration (ppm)
0
500
1000
1500
2000
2500
3000
0
500
1000
1500
2000
2500
3000
3500

(c)

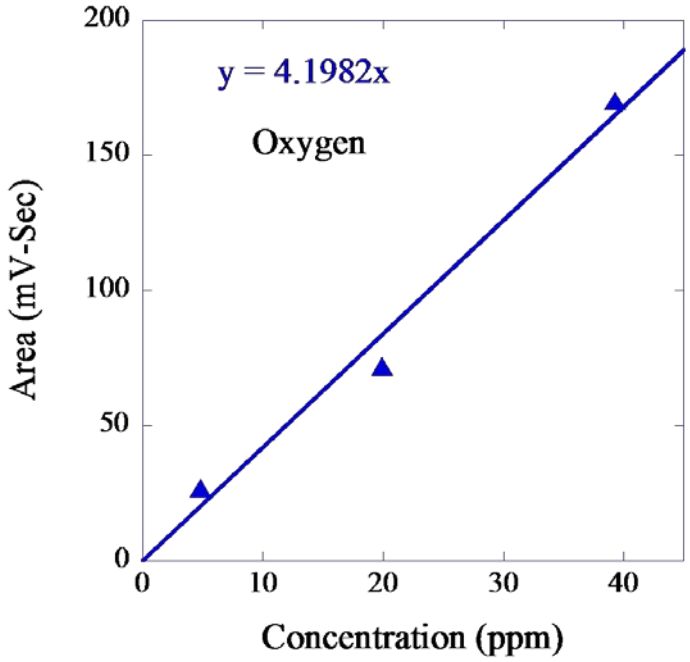
y = 4.1982x
Oxygen
Area (mV-Sec)
Concentration (ppm)
0
50
100
150
200
0
10
20
30
40

(d)

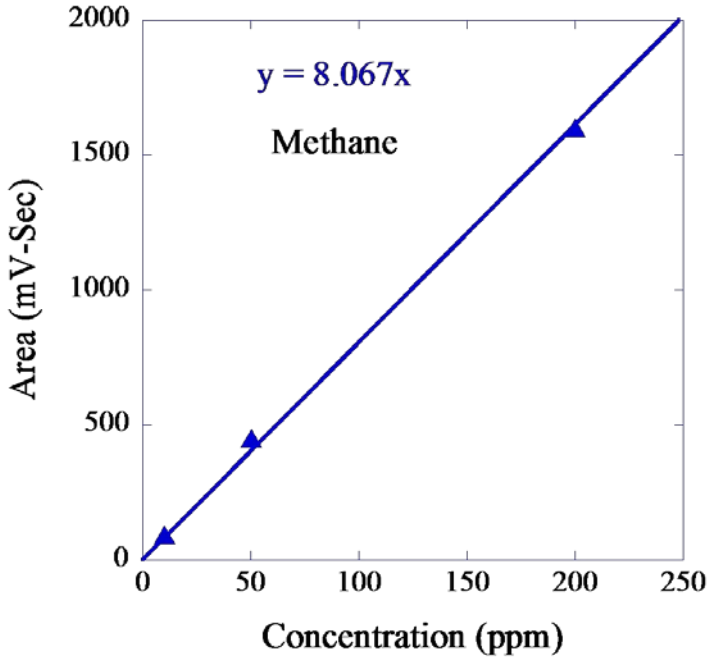
y = 8.067x
Methane
Area (mV-Sec)
Concentration (ppm)
0
500
1000
1500
2000
0
50
100
150
200
250

(e)

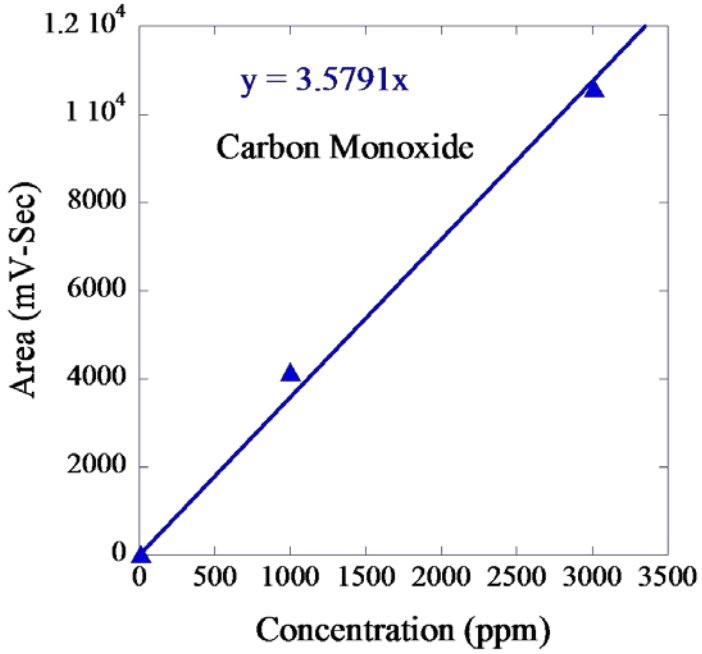

Figure 3.7 Calibration curve for the (a) carbon dioxide, (b) hydrogen, (c) oxygen, (d) methane, and (e) carbon monoxide. Table 3.3 shows the composition of the cylinders used to calibrate the gas chromatograph. A linear calibration curve was obtained for in all the cases.

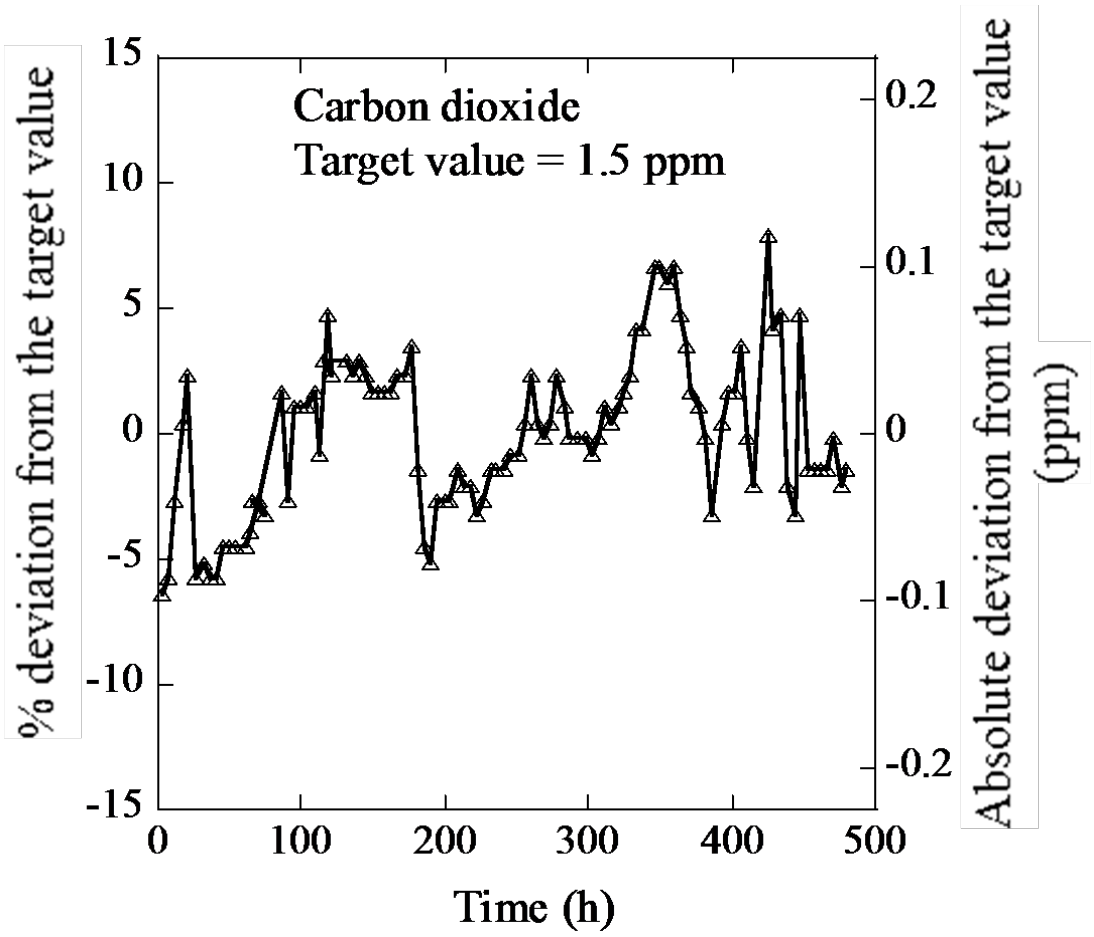

Figure 3.8 Plot of the percentage deviation of CO_2 at the inlet of the quartz tube over 500 hours of exposure duration. The absolute deviation of the inlet concentration is shown on right hand Y-axis. The maximum deviation of concentration form the target value of 1.5 ppm was 8%, which correspond to an absolute deviation of 0.1 ppm.

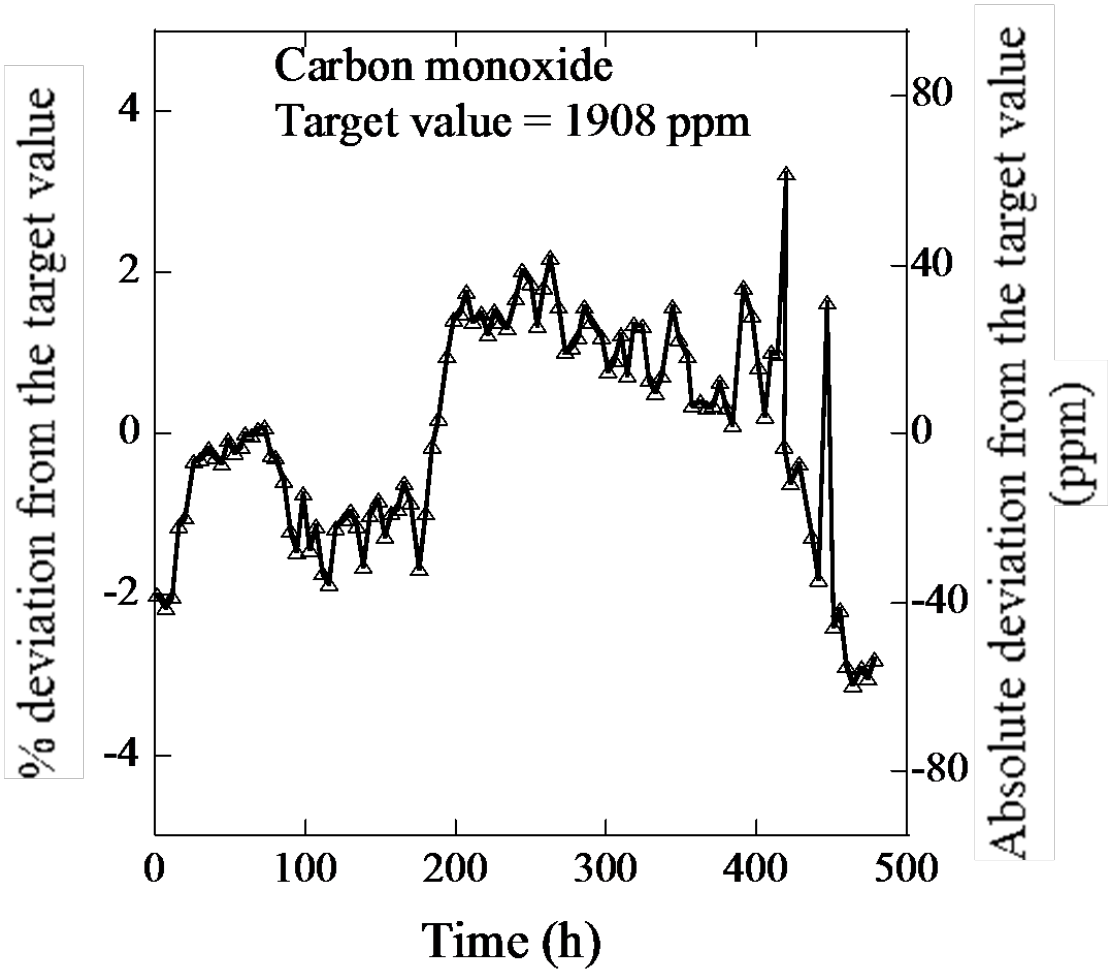

Figure 3.9 Plot of the percentage deviation of CO at the inlet of the quartz tube over 500 hours of exposure duration. The absolute deviation of the inlet concentration is shown on right hand Y-axis. The maximum deviation of concentration form the target value of 1908 ppm was 3.5%, which correspond to an absolute deviation of 69 ppm.

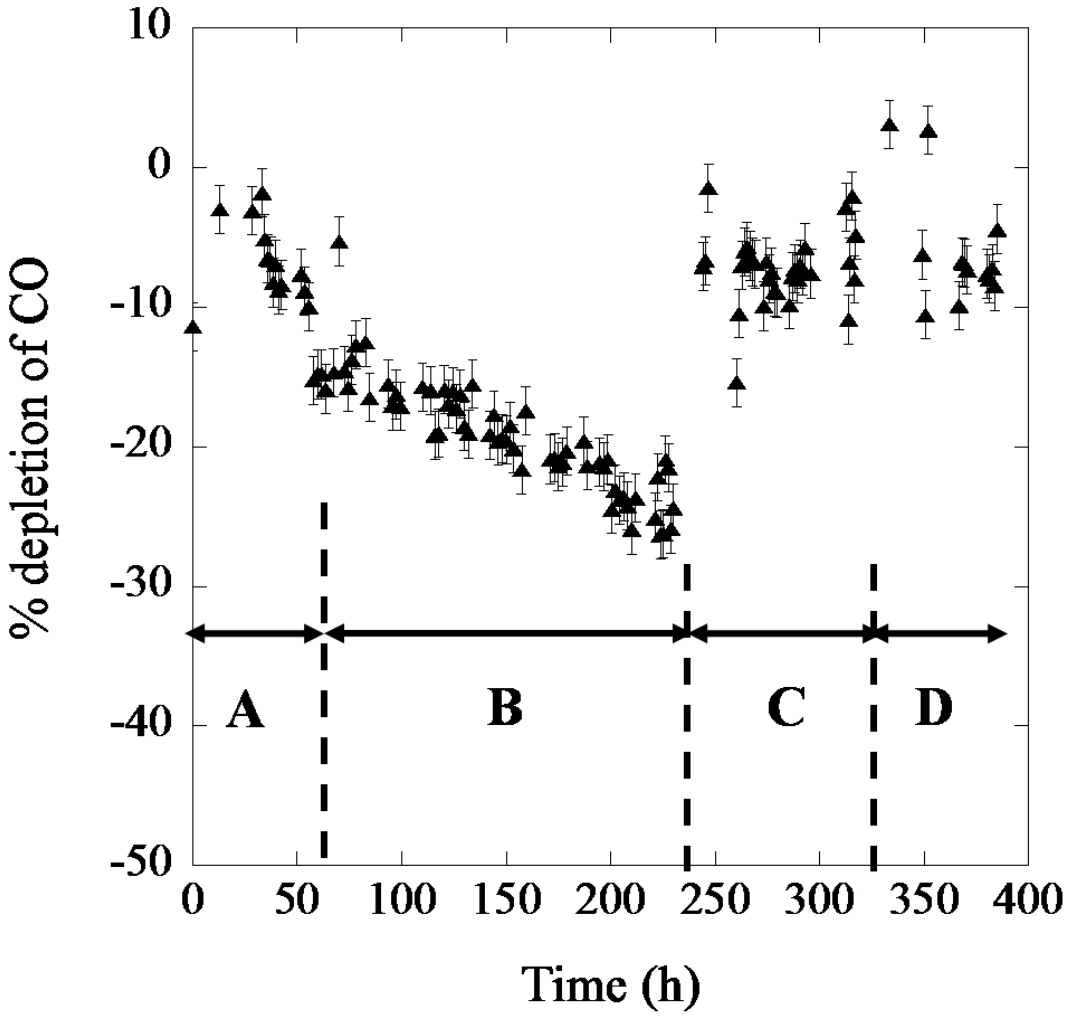

Figure 3.10 Plot of the percentage depletion of CO vs. time at different gas flow rates for a gas mixture consisting of 70 ppm CO and 0.7 ppm CO_2. Flow rate of gas in the tube in time steps A and C was maintained at 106 ml/min, whereas, the flow rate in the time steps B and D was maintained at 24 ml/min and 52 ml/min, respectively.

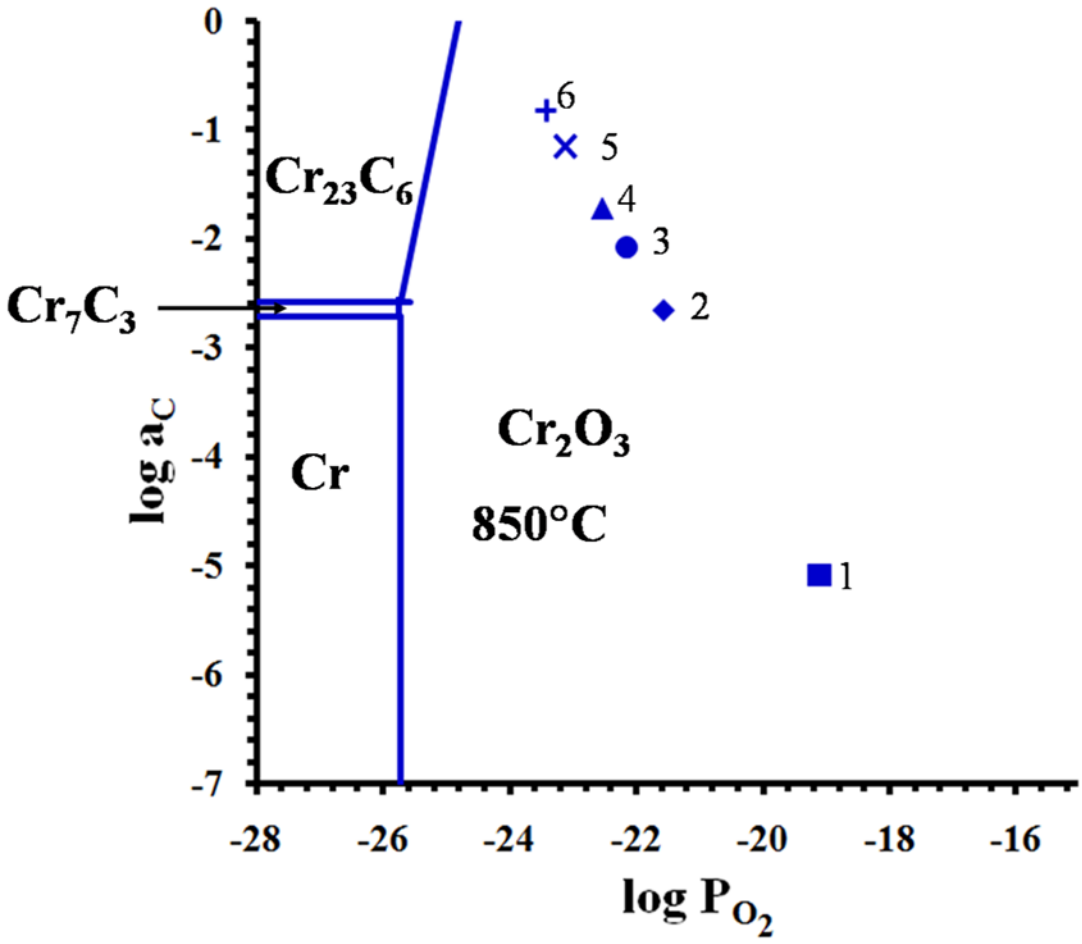

Figure 3.11 The equilibrium carbon and oxygen potentials in the helium gas superimposed on the Cr-O-C stability diagram for alloy 617 at 850°C. The surface activity of Cr for alloy 617 is assumed to be 0.72 [97].

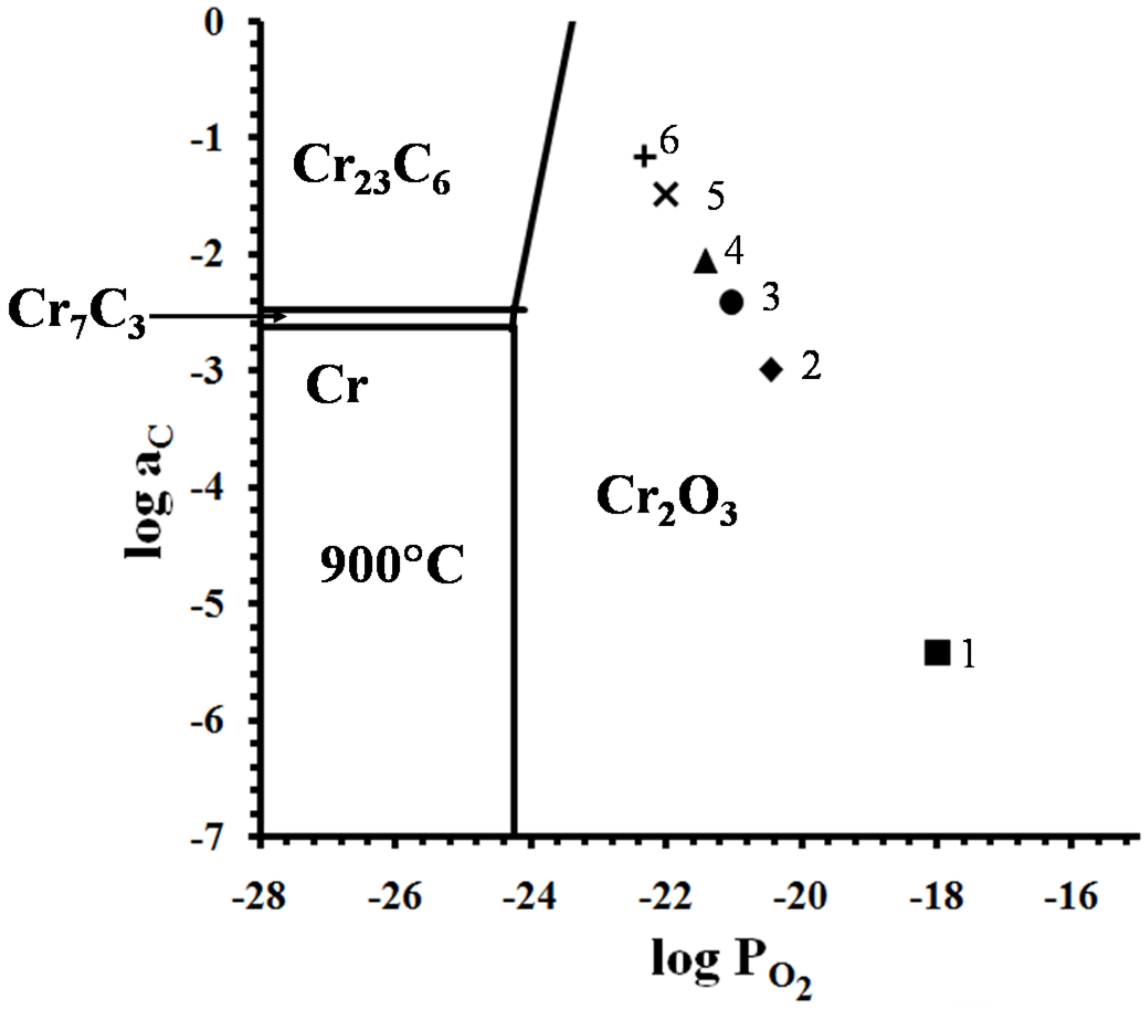

Figure 3.12 The equilibrium carbon and oxygen potentials in the helium gas superimposed on the Cr-O-C stability diagram for alloy 617 at 900°C. The surface activity of Cr for alloy 617 is assumed to be 0.72 [97].

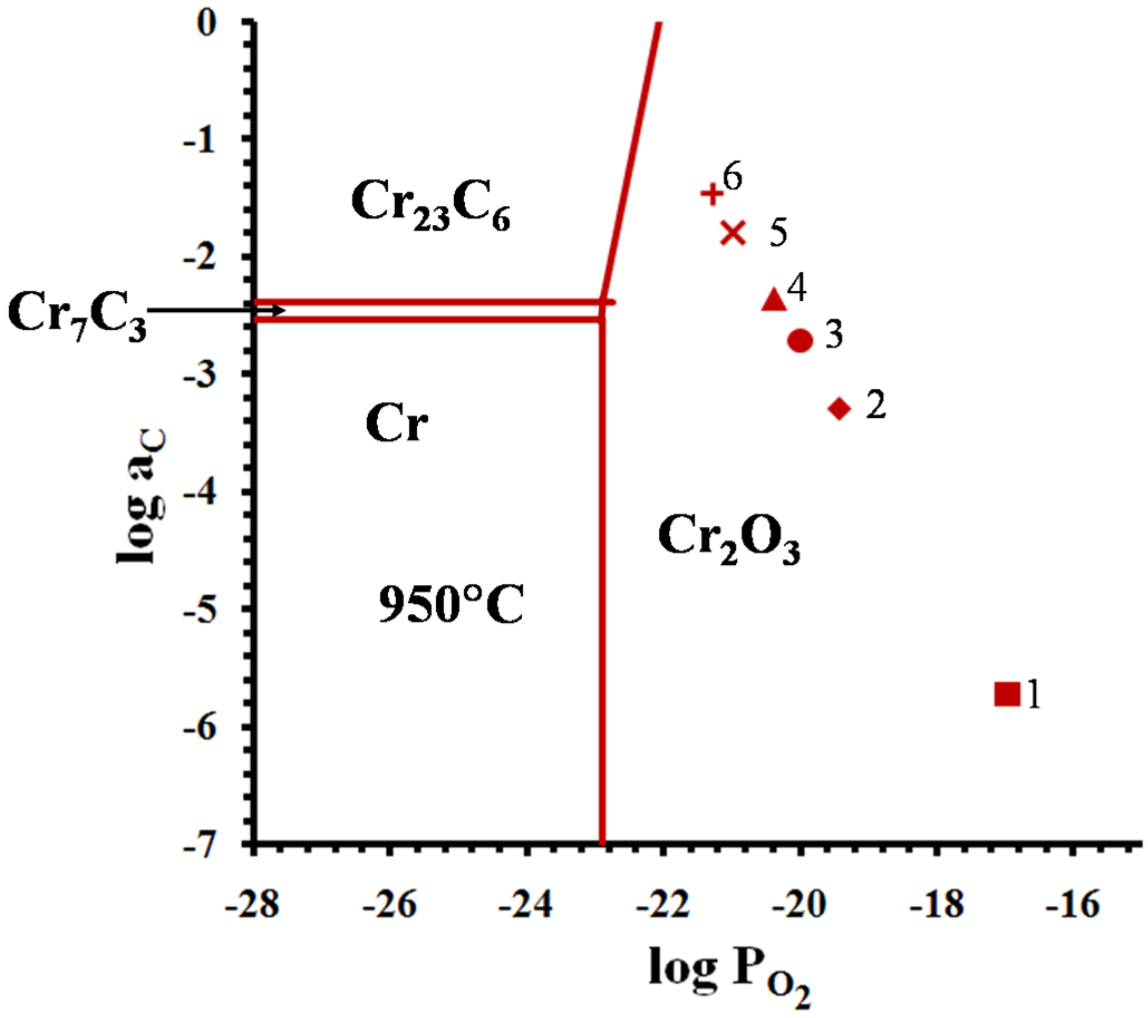

Figure 3.13 The equilibrium carbon and oxygen potentials in the helium gas superimposed on the Cr-O-C stability diagram for alloy 617 at 950°C. The surface activity of Cr for alloy 617 is assumed to be 0.72 [97].

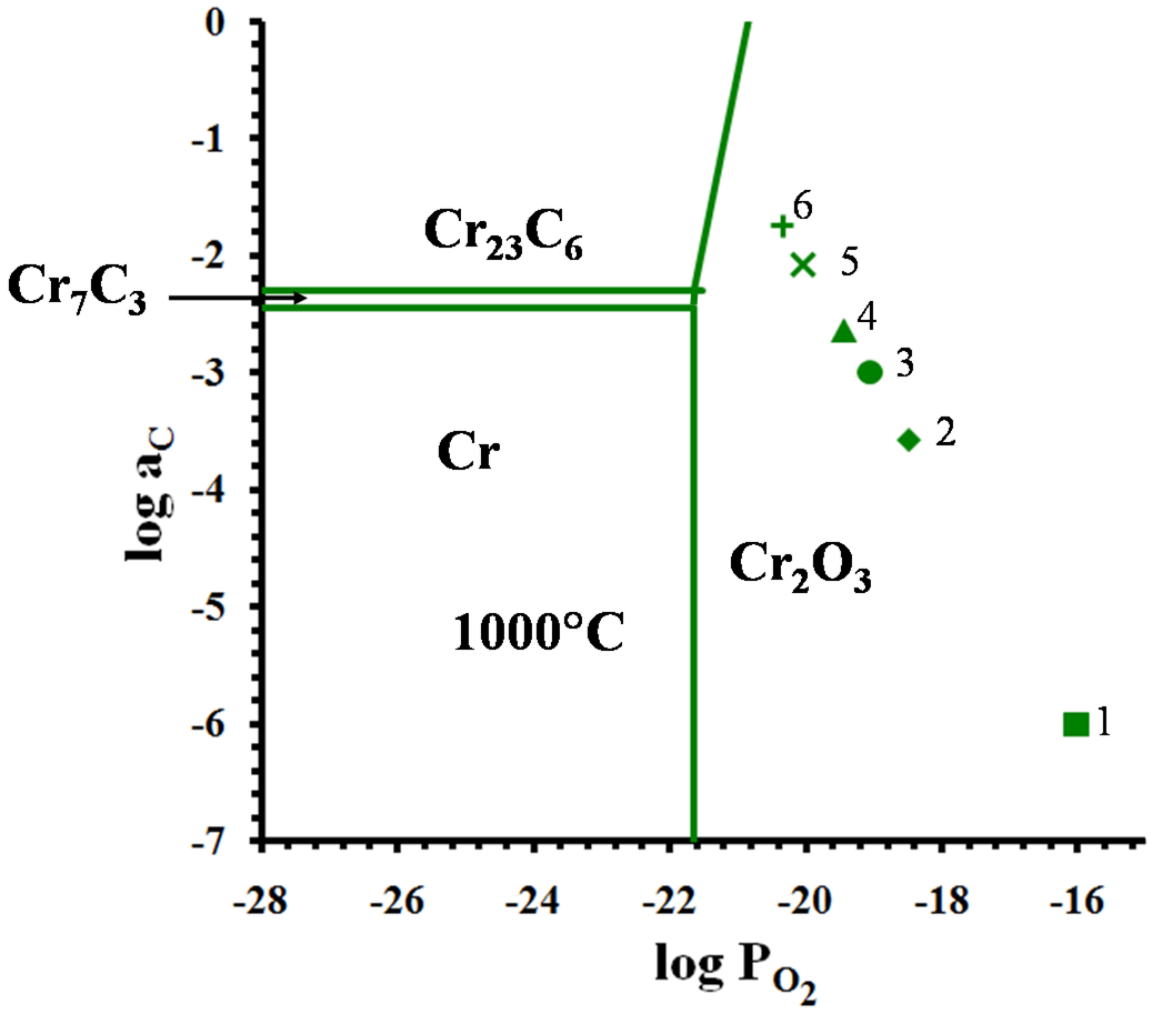

Figure 3.14 Figure 3.14 The equilibrium carbon and oxygen potentials in the helium gas superimposed on the Cr-O-C stability diagram for alloy 617 at 1000°C. The surface activity of Cr for alloy 617 is assumed to be 0.72 [97].

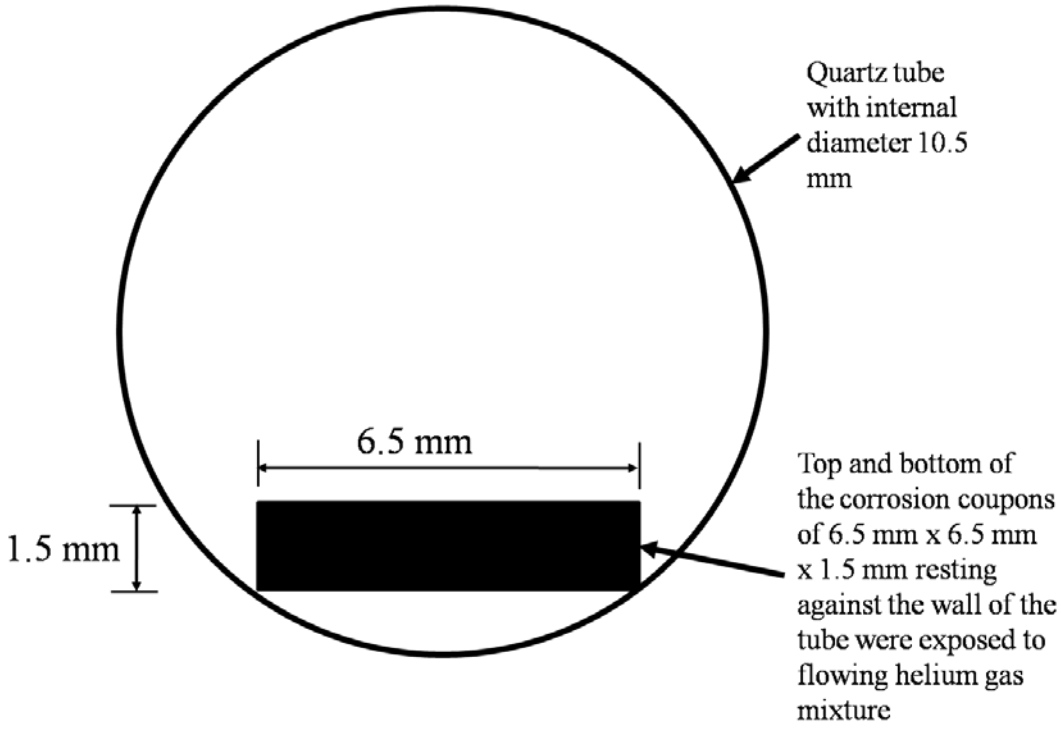

Figure 3.15 Cross-sectional view showing the placement of a corrosion coupon inside the quartz tube. Top and bottom of the 6.5 mm x 6.5 mm x 1.5 mm corrosion coupons resting on the walls of the quartz tube were exposed to the flowing helium gas mixture. The figure is drawn to the scale.

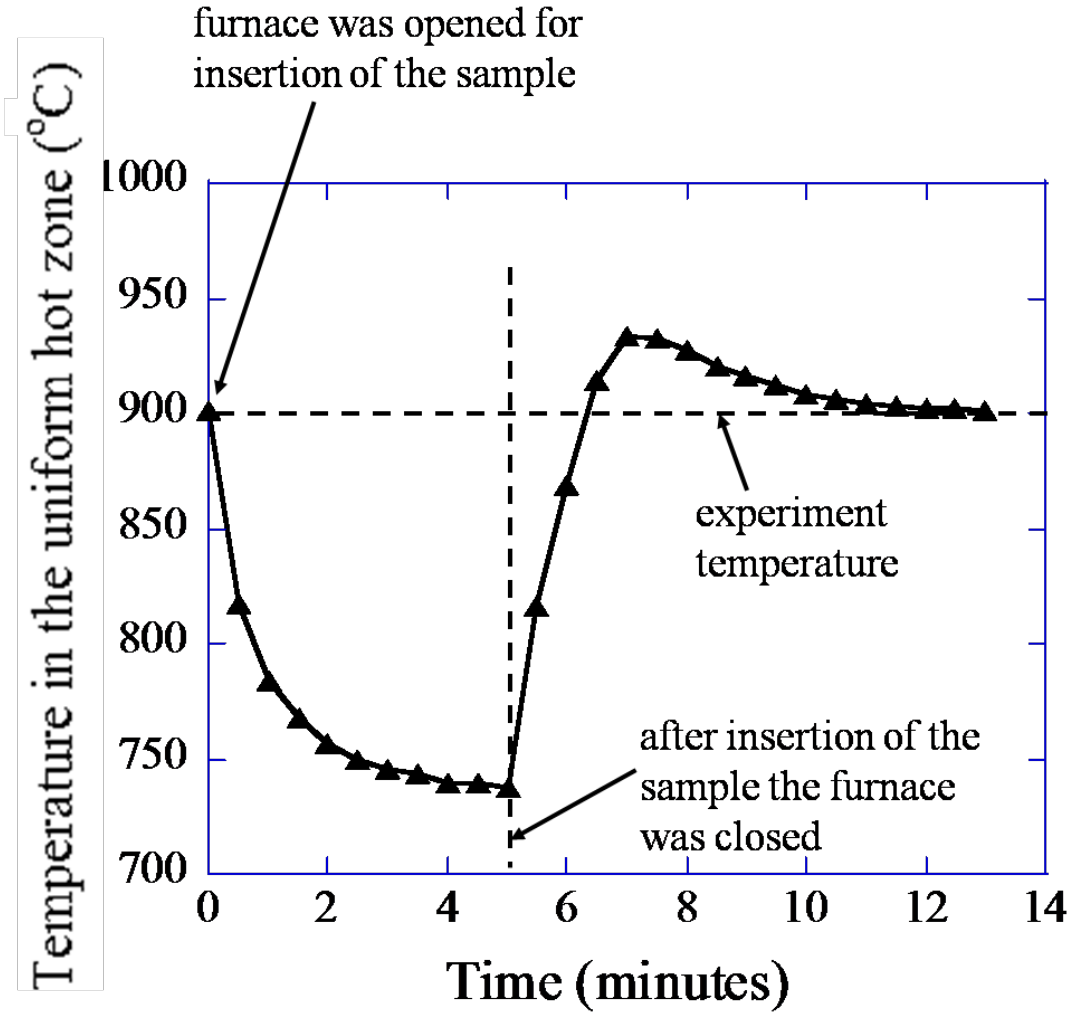

Figure 3.16 A typical fluctuation of the furnace temperature due to opening and closing of the furnace during insertion and pulling out of the corrosion coupons. In this particular case, the experiment temperature was 900°C and the furnace was kept open for 5 minutes to insert the sample in the uniform hot zone in the furnace.

(a)

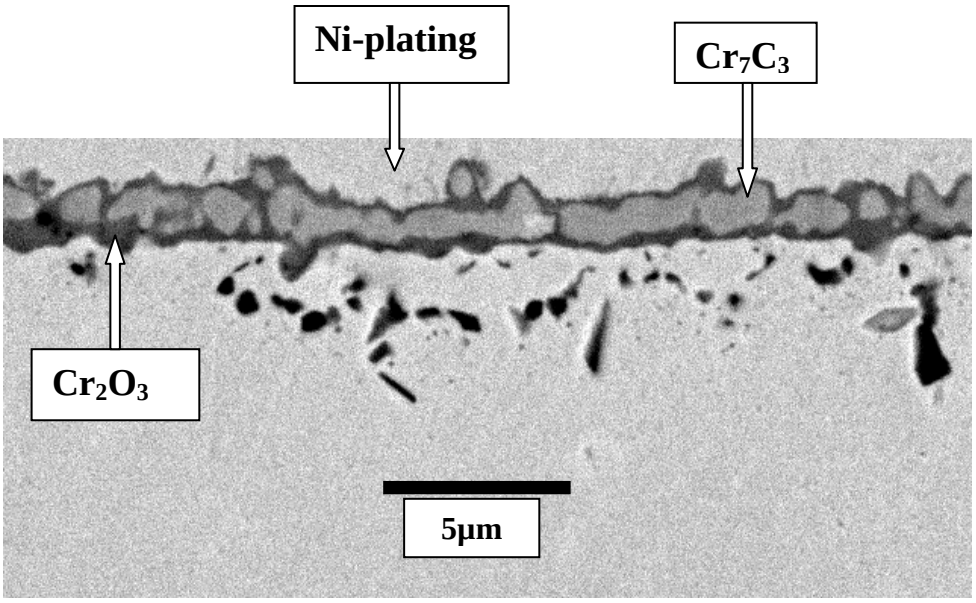

(b)

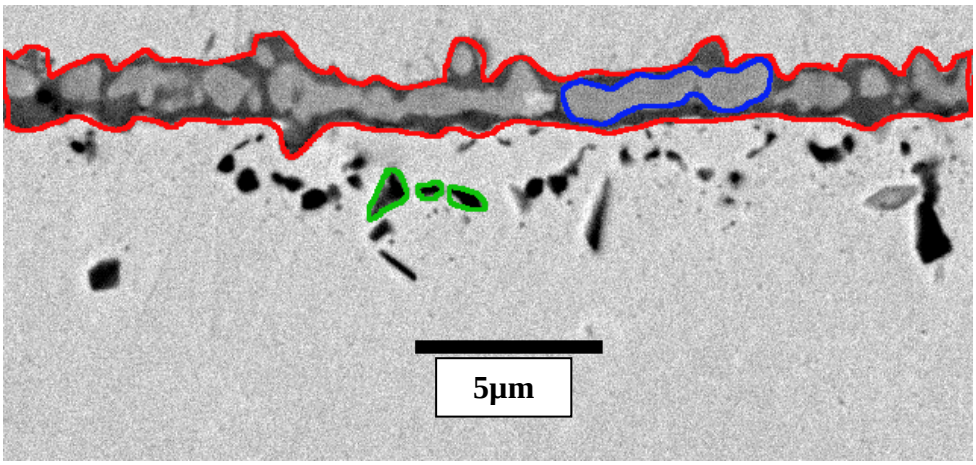

Figure 3.17 (a) A representative microstructure of the sample exposed in environment 6 environment 1 (CO/CO_2 = 1272) at 900°C for 225 hours. The external scale consists of Cr_2O_3 (the dark phase) and Cr_7C_3 (the lighter phase), (b) the procedure for measuring the area fractions the Cr_2O_3, Al_2O_3 and C_7C_3 in the external scale. The area enclosed by the external scale (colored red), Cr_7C_3 precipitate (colored blue, only one carbide particle shown for clarity), and Al_2O_3 (colored green, only few particles are delineated for clarity) was measured by the Scandium® software[99]. Area of the Cr_2O_3 is determined by subtracting the area of the Cr_7C_3 precipitates from the total area of the external scale. was measured by the Scandium® software[99]. Area of the Cr_2O_3 is determined by subtracting the area of the Cr_7C_3 precipitates from the total area of the external scale.

(a)

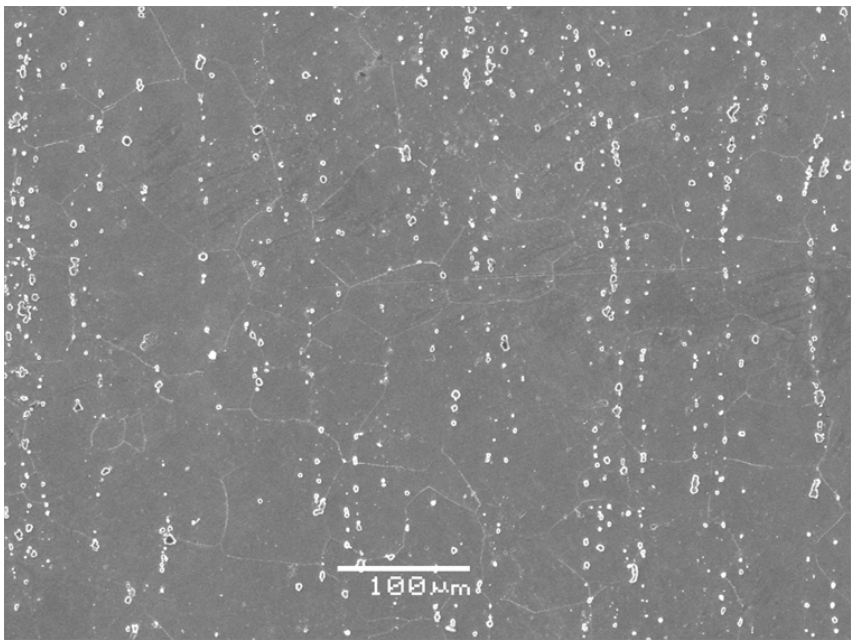

(b)

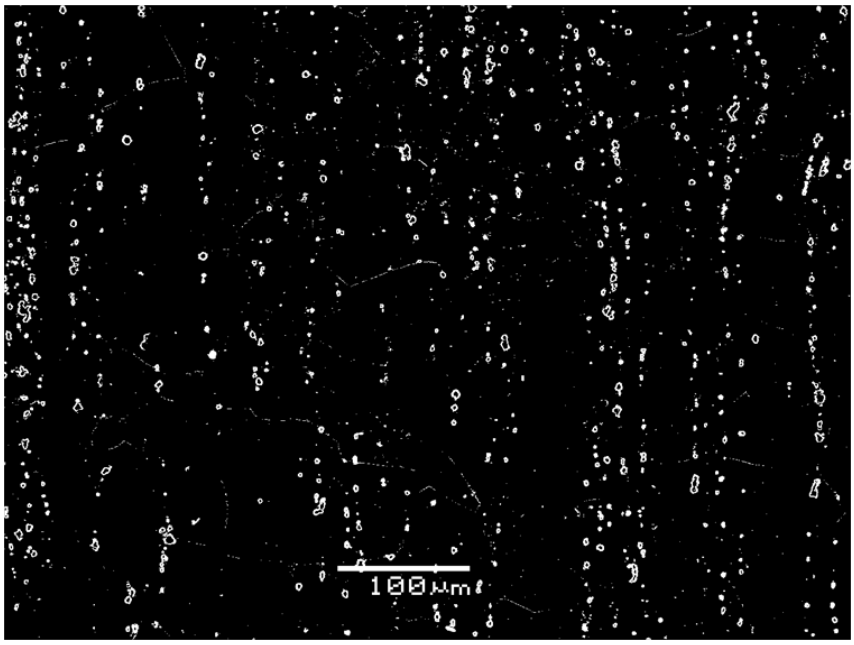

Figure 3.18 (a) The bulk microstructure of the as-received alloys 617, (b) the brightness and contrast of micrograph shown in (a) adjusted by using Adobe Photoshop® software from Adobe, Inc.[101] so that only carbides (bright phase) are seen in the image and not the matrix (dark phase). The software then calculates the area fraction of the carbide in the matrix. The area fraction of the carbide in this particular case was 3.2%.

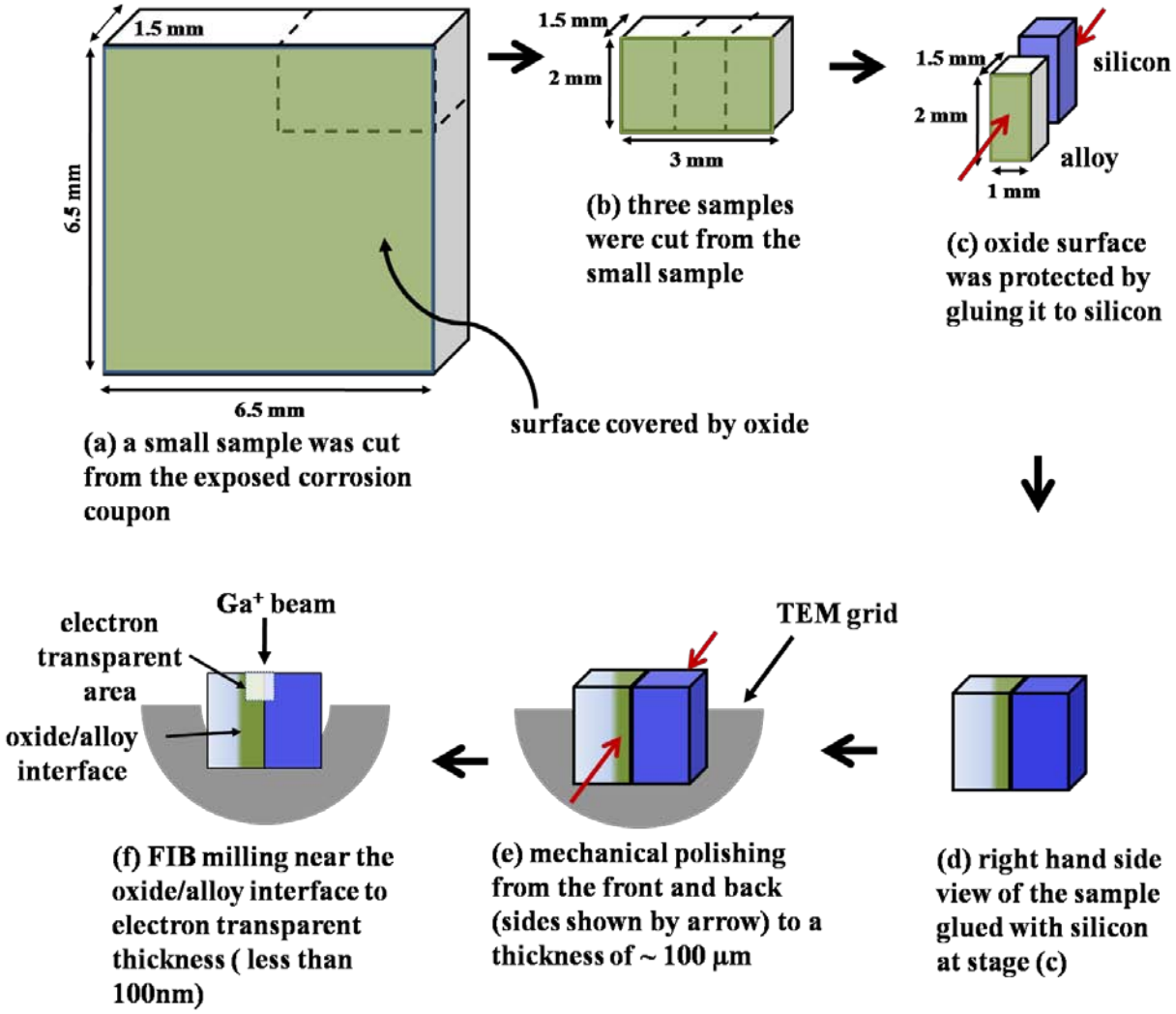

Figure 3.19 Schematic of the cross-sectional TEM sample preparation using FIB.

CHAPTER 4

RESULTS

This chapter presents the results of the experiments conducted in six He-CO-CO_2 environments at 850°C, 900°C, 950°C, and 1000°C. The results are organized based on the types of analyses performed on the samples; (1) analysis of the CO and CO_2 gas at the inlet and outlet of the furnace (gas-phase results), (2) change in weight of the sample due to oxidation (weight gain results), and (3) microstructure analysis of the surface and bulk of the sample. Section 4.1 presents the results of the gas-phase analysis for the six environments over 850-1000°C. Section 4.2 presents the results of the weight gain analysis for the six environments with CO/CO_2 ratio varying between 9 and 1272 over 850-1000°C, and section 4.3 presents the microstructure of two representative environments: environment 1 (CO/CO_2 = 9) and environment 6(CO/CO_2 = 1272), over 850-1000°C. Environment 1 (CO/CO_2 = 9) represents the case of oxidation + decarburization, and environment 6 (CO/CO_2 = 1272) represents the case of oxidation + carburization. The results of the surface and bulk microstructure are presented separately for each environment. Section 4.4 presents the results of the pre-oxidation experiment designed to determine the role of Cr_2O_3 during decarburization. In this experiment the sample was first pre-oxidized at lower temperature and subsequently decarburized at higher temperature. Finally, the results of a short term experiment conducted in environment 6 (CO/CO_2 = 1272) at 900°C for 1 h are presented in section 4.5. This

experiment was deigned to determine the mechanism of formation of surface carbides during carburization of samples in environment 6 (CO/CO_2 = 1272).

4.1 CO and CO_2 behavior vs. time over 850 -1000°C

The results of the CO and CO_2 consumption/evolution in six environments and at four temperatures are presented in this section. In each experiment the concentrations of the CO and CO_2 in helium were analyzed continuously at the inlet and outlet of the furnace every ~5 hours using a gas chromatograph (GC). The difference in the concentration levels of CO and CO_2 at the outlet and inlet, i.e. $CO_{out} - CO_{in}$ and $CO_{2out} - CO_{2in}$ was used to determine the nature of alloy/gas interaction in the experiment. Figures 4.1-4.6 present the $CO_{out} - CO_{in}$ vs. time plots for environments 1 (CO/CO_2 = 9) to 6 (CO/CO_2 = 1272) as a function of exposure duration over 850 to 1000^{o}C. The error bars shown on these plots correspond to the repeatability limit of the GC determined by measuring the difference between the outlet and inlet of the empty tube before starting the experiment. A negative value on these plots denote a net consumption of CO inside the reaction zone, whereas, a positive value denotes a net production of CO inside the reaction zone. The data is presented for the range of temperatures in a given environment, i.e. the difference in CO concentration at the outlet and inlet for a specific environment is plotted at the four tested temperatures in one figure.

Figure 4.1 is the plot of CO out- CO in vs. time for environment 1 (CO/CO_2 = 9). As observed from this figure, at 850°C and 900°C, the amount of CO consumption dropped off to zero in ~80-100h, whereas a net evolution of CO occurred at 950°C and 1000°C from the start of the experiment. Note that the first GC data point was recorded in this environment after ~9h from the start of the experiment at 950°C and 1000°C. The

CO evolution continued up to ~250h at 950°C and up to ~300h at 1000°C. The rate of CO evolution, as indicated by the slope of the CO out – CO in vs. time plots, was approximately linear at both 950°C and 1000°C.

Figures 4.2, 4.3, and 4.4 present the CO out – CO in vs. time plots for environment 2 (CO/CO_2 = 150), environment 3(CO/CO_2 = 291), and environment 4 (CO/CO_2 = 453), respectively. In these environments, CO consumption occurred over the entire temperature range of 850-1000°C. At each temperature the CO consumption dropped off rapidly to zero in ~50 to 80h and no significant change in the CO concentrations at the outlet and inlet was observed in the longer exposure durations, suggesting that the oxidation by CO occurred largely in the first ~50-80h.

Figures 4.5 and 4.6 are the plots of CO out – CO in vs. time for environment 5 (CO/CO_2 = 900) and environment 6 (CO/CO_2 = 1272). As observed in these figures the CO was consumed for ~ 50h - 80h over 850-1000°C followed by which a net evolution of CO occurred in the subsequent exposure time. Within the repeatability limit of the GC (3-5 ppm) the rate of CO evolution, which is given by the slope of the CO out – CO in vs. time plot was constant.

Figures 4.7- 4.12 plot the consumption of carbon dioxide, i.e., CO_{2out} - CO_{2in} as a function of time for environments 1 (CO/CO_2 = 9) to environment 6 (CO/CO_2 = 1272) over 850-1000°C. The error bars shown on these plots correspond to the repeatability limit of ~ 0.1 ppm, which is the minimum detection limit of the GC for this gas. As shown in these plots, the CO_{2out} - CO_{2in} value was negative in every case, i.e. consumption of CO_2 occurred in every environment at each temperature. At a given exposure duration, a higher amount of CO_2 consumption (represented by the area under

the curve) occurred at higher temperature. Again, at a fixed temperature, The CO_2 consumption fell to zero in ~200h - 300h of exposure.

4.2 Weight gain

In this section, the changes in weight of the samples exposed in six environments and at four temperatures are presented. The experiments were conducted for a total duration of 500 hours at 850°C and 1000°C and 750h at 900°C and 950°C. The samples were exposed for 100h, 225h, 375h, 500h and 750h.

4.2.1 Weight gain vs. time

Figures 4.13-4.16 show the plots of the weight gain in the samples exposed in environment 1 (CO/CO_2 = 9) to environment 6 (CO/CO_2 = 1272) as a function of exposure duration over 850 - 1000°C. A least square curve fit of the form

$$w = \frac{\Delta W}{S} = k \times t^n \qquad (4.1)$$

was made to the data, where w is the weight gain per unit area, ΔW is weight gain in the sample (in mg), S is total surface area (in mm^2), t is the exposure duration (in hr), n is the rate exponent, and k is the rate constant (in mg/mm^2hr^n). Table 4.1 presents the values of the rate constant, k, rate exponent, n, and the R^2 of the fitted curve for all environments at each temperature.

As shown in Fig. 4.13, the oxidation rate of alloy 617 at 850°C decreased with the increasing exposure duration, as indicated by the slope of the weight gains vs. time curve. The value of the rate exponent for environments 1 (CO/CO_2 = 9) to 6 (CO/CO_2 = 1272) fell in the range of 0.6 to 0.7 and the rate constant fell in the range of 6.3×10^{-5} to 1.4×10^{-4} mg/mm^2hr^n (table 4.1).

Figure 4.14 shows the oxidation kinetics of the samples exposed at 900°C. The weight gain kinetics decreased with the oxidation time for all environments. A rate law with n varying between 0.6 and 0.7 was shown by each environment. The value of the rate constant, k fell in the range of 8.9×10^{-5} to 2.3×10^{-4} mg/mm^2hr^n (table 4.1). In general, the weight gain in the environment with lower CO/CO_2 ratio (environment 1, ratio 9) was lower than the weight gain in the higher CO/CO_2 ratios in the environment (environment 6, ratio 1272).

Figure 4.15 shows the oxidation kinetics of alloy 617 at 950°C. The weight gain in environments 2 (CO/CO_2 = 150) to 6 (CO/CO_2 = 9) decreased with the exposure duration (observed by the flattening of the curve) and followed a rate law with n varying between 0.6 and 0.7. Environment 1 (CO/CO_2 = 9) showed different oxidation behavior that followed linear oxidation kinetics (n =1).

Figure 4.16 presents the oxidation kinetics at 1000°C. The oxidation kinetics of the samples in environments 2 (CO/CO_2 = 150) to 6 (CO/CO_2 = 9) decreased with the increasing exposure duration. The value of the rate exponent for these environments fell in the range of 0.5 to 0.7, and the rate constant fell in the range of 1.4×10^{-4} to 5.2×10^{-4} mg/mm^2hr^n (table 4.1). The oxidation behavior in environment 1 (CO/CO_2 = 9) at this temperature was distinctly different than that in environments 2 (CO/CO_2 = 150) to 6 (CO/CO_2 = 1272). Within the resolution of the microbalance of 0.01 mg, the samples in this environment showed little or no weight gain for the first 375 hours of exposure, after which there was a rapid increase in the weight. An unusual non-linear rate law (n = 4.3) with a low rate constant value of 2.0×10^{-14} $mg/mm2/h^{4.3}$was exhibited by the samples in this environment (table 4.1).

4.2.2 Weight gain vs. temperature

For a given environment, the weight gain is plotted as a function of time over the range of temperatures in Figs 4.17 to 4.22. To facilitate the easy comparison between different environments a consistent symbol/color scheme is adopted for the different temperatures. Figure 4.17 shows the temperature dependence in environment 1 (CO/CO_2 = 9) between 850 -1000°C. An increase from 850°C to 900°C resulted in increased weight gain over the entire exposure duration. However, an increase in the temperature from 950°C to 1000°C resulted in a decrease in the weight gain in the sample. For the initial 375 h of the oxidation the weight gain at 1000°C was lower than that between 850 - 950°C, but, after 500h of oxidation the weight gain at 1000°C was higher than that between 850-950°C.

Figures 4.18-4.22 present the temperature dependence of the samples exposed in environments 2 (CO/CO_2 = 150) to 6 (CO/CO_2 = 1272) between 850 -1000°C. As shown in these figures, an increase in temperature resulted in increased weight gain over the temperature range 850 -1000°C, and accordingly the rate constant, k, increased with the temperature (table 4.1).

4.3. Microstructure examination

Results of the microstructure examinations are presented in this section. The two extreme environments: environment 1 (CO/CO_2 = 9) and environment 6 (CO/CO_2 = 9) were chosen for microstructure examinations. The choice of these two environments was based on the fact that the weight gain and the gas-phase results showed the oxidation behavior in environment 1 (CO/CO_2 = 9) to be distinctly different than all other environments, i.e. environment 2 (CO/CO_2 = 150) to 6 (CO/CO_2 = 1272). In environment

1 (CO/CO_2 = 9) the oxidation behavior changed with the increase in temperature (between 850 – 900°C, the CO was consumed, whereas between 950 -1000°C, the CO was evolved, Fig. 4.1), whereas, in environments 2 (CO/CO_2 = 150) to 6 (CO/CO_2 = 1272) the, CO was consumed over 850 -1000°C. The environment 6 (CO/CO_2 = 1272) was chosen as the representative of the oxidation behavior in environments 2 (CO/CO_2 = 150) to environment 6 (CO/CO_2 = 1272). For each environment the surface microstructure and the bulk microstructure is presented separately.

The microstructure results presented in this section will be compared against the as-received alloy 617. Hence, the microstructure characterization performed on the as-received sample is presented first followed by the microstructure examinations in environment 1 (CO/CO_2 = 9), and lastly the microstructure examination of the sample oxidized in environment 6 (CO/CO_2 = 1272).

4.3.1 Microstructure of the as-received alloy 617

Figure 4.23 shows representative microstructures of the as-received alloy 617 under secondary electron (SE) imaging (Fig. 4.23a) and back scattered electron (BSE) imaging mode (Fig. 4.23b). As seen from these figures, the microstructure basically consists of a solid solution phase,γ, and inter-granular, and intra-granular carbide precipitates, which are aligned along the rolling direction of the plate, Fig. 4.23a.

Two types of carbides are seen in the microstructure (Fig. 4.23 b) - distinguished by light or dark contrast. TEM and XRD of the as received alloy 617 were performed to determine the structure of the carbides. Figures 4.24 (a) and 4.24 (b) are the TEM image and the selected area diffraction (SAD) pattern of the carbides along a grain boundary in

the as-received alloy. A larger SAD aperture was selected to obtain the diffraction patterns from the matrix as well as the carbides. In Fig. 4.24 (b) the larger spots are the lattice plane reflections from the γ-matrix, and the smaller spots are the lattice plane reflections from the carbides. <111> type six fold symmetry corresponding to a FCC structure (both for γ-matrix and the carbide) can be seen in the image. The diffraction pattern was indexed as per the procedure outlined in section 3.5.4.3 (experimental section). Table 4.2 shows the distances of three diffraction spots (R) (smaller spots from carbides), the calculated d-spacing, (hkl) value of the spot, the d-spacing for $Cr_{23}C_6$ from PDF, the measured angles and the theoretical angle from PDF. As shown in the table both the calculated d-values and the measured angles are in very good agreement with the ideal d-spacing and the angles for $Cr_{23}C_6$. This confirms that the grain boundary carbides observed in the Fig 4.24a are $Cr_{23}C_6$.

XRD of the as received alloy was performed to verify the presence of M_6C carbides. Fig. 4.25 presents the diffraction pattern and table 4.3 shows the comparison between the peaks from the standard powder diffraction files (PDF) for Ni, $(Cr,Co,Mo)_{23}C_6$, and $(Cr,Co)_6C_6$ and the peaks obtained by the XRD. A very good match between the expected 2θ values of the peaks from the PDFs and the XRD patterns confirms the presence of Ni, $M_{23}C_6$ carbides, and M_6C carbides in the alloy 617.

The area fraction of the carbides and the average grain size in the as received alloy 617 was measured as per the procedure described in section 3.5.3 to be 2.9 ± 0.4% and 65μm, respectively.

4.3.2 Microstructure examination of the samples exposed in environment 1 (CO/CO_2 = 9)

This section presents the microstructure examination of the sample exposed in environment 1(CO/CO_2 = 9) over the temperature range 850 – 1000°C. The surface microstructure of the samples is presented first followed by the bulk microstructure.

4.3.2.1 Surface microstructure in environment 1 (CO/CO_2 = 9)

Figures 4.26-4.27 present the cross-sectional BSE images of the sample exposed for 100h and 500h at 850^{o}C. A continuous film of Cr_2O_3 of thickness 0.2±0.05µm formed after 100h of oxidation. Internal oxidation of alumina occurred in a shallow region beneath the Cr_2O_3 scale. With continued exposure the thickness of the chromia film increased to 1.8 ±0.3 µm after 500h.

Figures 4.28-4.30 present the BSE image of the sample exposed for 100h, 500h, and 750h at 900°C. A continuous film of Cr_2O_3 of thickness 0.8±0.2µm formed in 100h of oxidation. The internal oxidation of aluminum occurred beneath the Cr_2O_3 scale. With continued exposure the thickness of the chromia film increased to 2.2 ±0.4 µm (after 500h) and 2.6 ±0.4 µm after 750h. Figure 4.31 shows the measured thickness of Cr_2O_3 film as a function of exposure duration. The measured weight gain in the sample at 900°C is also plotted in this figure. A least square fit of the form given in Eq. 4.1 showed that the growth behavior of the Cr_2O_3 and weight gain was similar.

Figures 4.32-4.34 show the microstructure of the sample exposed at 950°C for 100h, 375h, and 500h. A continuous film of Cr_2O_3 formed on the surface over the entire exposure duration. The thickness of the Cr_2O_3 film was measured as a function of

exposure duration and the result is presented in Fig. 4.35. A least square curve fit of the form given in Eq. 4.1 made to the data showed that the oxide thickness grew according to a linear rate law, which was similar to the oxidation weight gain kinetics.

Figure 4.36 presents the surface microstructure of the sample oxidized at 1000°C for 100h. A few nodules of Al_2O_3 are observed on the surface after 100h of oxidation. Note that after 100h of oxidation at 850°C (Fig. 4.26), 900°C (Fig.4.28) and 950°C (Fig.4.32) a thin surface film of Cr_2O_3 with internal oxidation of Al_2O_3 was observed. XRD of the sample oxidized for 100h at 1000°C was performed. Figure 4.37 shows the obtained x-ray intensities as a function of diffraction angle 2θ. The expected high intensity peaks for Cr_2O_3 are marked in this figure by the solid diamond symbol. These peak positions are marked according to the standard powdered diffraction file number (PDF#) 99-000-1069 from the International Center for Diffraction Data (ICDD) database. As shown in this figure all the high intensity Cr_2O_3 peaks were absent from the XRD pattern. Instead, the XRD pattern showed the peaks from Al_2O_3 and TiO_2 (see table 4.4 for the comparison between the peaks from Al_2O_3 and TiO_2 from standard PDFs and those in Fig 4.37). Thus the XRD result also showed that the Cr_2O_3 film did not exist after 100h of oxidation in environment 1 (CO/CO_2 = 9) at 1000°C. Further, to determine the possibility of in-situ or ex-situ spallation of the Cr_2O_3 scale, the concentration profiles of the major alloying elements (Ni, Cr, Co, and Mo) were measured using EMPA. Appendix I tabulates the results of the measured concentrations of Ni, Cr, Co, and Mo in the alloy as a function of distance from the alloy/scale interface. Three line scans was performed randomly on this sample. Figure 4.38 shows the average concentration profiles of the three line scans tabulated in appendix I. Within the resolution of the EMPA

measurements (<0.1wt%), the concentration profiles of the alloying elements are essentially flat and their concentrations are the same as for the as-received sample substantiating the XRD and SEM result that Cr_2O_3 film did not exist on this sample.

Figure 4.39 shows the surface microstructure of the sample exposed at 375 h at 1000°C. The microstructure was non-uniform in this case and probably depended on the location where the sample was cross-sectioned for SEM examination. SEM examination of the cross-section revealed that at some locations, a thin film of Al_2O_3 of average thickness ~ 0.3μm formed (region I in Fig. 4.39 a), whereas at other locations nodules of Cr_2O_3 formed (region II, Fig. 4.39 b). It is likely that with continuing oxidation the Al_2O_3 nuclei formed after 100h of oxidation grew laterally and joined to form thin Al_2O_3 film locally.

Figure 4.40 shows the surface microstructure of the sample exposed for 500h at 1000°C. The surface microstructure remained non-uniform even after 500h of exposure. Two regions were observed. Region I had a thin film of Al_2O_3 of thickness 0.6μm (region I in Fig. 4.40a) and region II had duplex oxide scale structure with Al_2O_3 film of thickness 0.6μm formed underneath the Cr_2O_3 film of thickness ~1.5μm (region II in Fig. 4.40 b). Another observation from Fig. 4.40 is that the internal oxidation of Al_2O_3 occurred only where there was a surface Cr_2O_3 film, i.e. region II. This locally different oxidation behavior of alloy 617 had also been observed by Christ et. al.[106] during the decarburization study in He+10ppm H_2O + 60 ppm H_2 gas mixture at 1000^{o}C.

A summary of the surface microstructures presented above (environment 1: CO/CO_2 = 9) over the temperature range of 850-1000°C, are given in table 4.5.

4.3.2.2 Bulk microstructure in environment 1 (CO/CO_2 = 9)

Figure 4.41 shows the bulk microstructure of the sample oxidized at 900°C for 375 h. An increased fraction of carbides was observed in this sample (compare it with Fig. 4.41 b; as received alloy 617 sample etched under same condition). The carbides were observed at the grain boundaries, twin boundaries, and the interior of the grains.

Figure 4.42 shows the bulk microstructure of the sample oxidized at 100h and 375h at 950°C. After 100h of oxidation, the carbides near the surface had completely dissolved. The depth of decarburization zone, defined as the region near the alloy surface where the carbides had completely dissolved in the matrix, was ~75μm after 100h of decarburization. Figure 4.42b shows the SEM image of the sample oxidized at 950°C for 375h. The carbides had dissolved from the entire cross-section of the sample, i.e. decarburization zone extended to the middle of the cross-section.

Figure 4.43 shows the SEM image of the sample oxidized at 100h and 375 h at 1000°C. A decarburization zone is observed near the alloy surface. The depth of decarburization after 100h of oxidation was ~100μm, whereas after 375 h of oxidation the depth of decarburization extended to the middle of the cross-section, i.e. the carbides dissolved in the entire cross-section.

4.3.3 Microstructure examinations of the sample exposed in environment 6 (CO/CO_2 = 1272)

Cross-sections of the samples oxidized in environment 6 (CO/CO_2 = 1272) for different exposure temperatures and times were examined in SEM. The focus of this investigation was on determining the evolution of surface and bulk microstructures of the samples as a function of time over the temperature range 850-1000°C. In particular, the

morphological evolution of the surface oxide/carbide and bulk carbides was examined. The identification of the crystal structure of the oxide and the carbide is presented first in section 4.3.3.1, followed by the surface and bulk alloy microstructure in sections 4.3.3.2, and 4.3.3.3, respectively.

4.3.3.1 Identification of phases formed during oxidation

The oxidation of alloy 617 in environment 6 (CO/CO_2 = 1272) resulted in formation of an external scale consisting of oxides and carbides. The structures of each were determined using of SEM/EDS, XRD and TEM. Figure 4.44 shows BSE images of the sample exposed at 1000°C for 100h. The surface scale (Fig. 4.44a) consisted of discrete irregular shaped precipitates residing in the upper part of the scale and a continuous film residing in the lower part of the scale. In the sub-surface area lenticular shaped precipitates are observed (Fig. 4.44 a). Fig.4.45 shows the BSE image and corresponding x-ray maps of chromium, oxygen, aluminum, titanium, nickel, and molybdenum of the same sample. As shown in this image the microstructure had a chromium, titanium, and oxygen rich surface scale. The lenticular shaped internal precipitates were rich in aluminum and oxygen. The irregular shaped precipitates were rich in chromium and were devoid of Ti and Ni. The XRD of the surface film was performed to identify the crystal structure of the chromium + titanium + oxygen-rich continuous scale and the irregular shaped Cr-rich precipitates observed in the EDS map. Fig. 4.46 presents the plot of the x-ray intensities as the function of 2θ. The peaks shown in this figure were identified by comparing them against the standard powder diffraction files for Ni, Cr_2O_3, and Cr_7C_3. Table 4.6 shows this comparison. A very good match

between the expected peak positions from PDFs and the peak positions in the XRD pattern confirms the presence of Cr_2O_3 and Cr_7C_3 at ~10 – 12 μm (the penetration depth of x-rays at 20kV and 100mA in alloy 617 [107]) of depth near the surface of the alloy. Since the as-received alloy did not have Cr_2O_3 and Cr_7C_3 carbides to begin with, these two phases must be present in the surface scale. Further, since in a BSE image, the Cr_7C_3 appears brighter (molecular weight = 400 gm/mol) than the Cr_2O_3 (molecular weight = 152 gm/mole), it can be concluded that the irregular shaped precipitates observed in Fig. 4.44 b are Cr_7C_3 and the continuous film residing in the lower part of the scale is Cr_2O_3. The lenticular shaped aluminum and oxygen rich precipitates observed in the EDS map (Fig. 4.45) were assumed to be Al_2O_3.

The identification of the phases in the oxide film was also determined on a cross-sectional TEM sample prepared by FIB. Figure 4.47 shows a high angle annular dark field (HAADF image) and the corresponding x-ray maps for chromium, oxygen, aluminum, carbon, and nickel. As observed in this image, the external scale consists of irregular shaped precipitates, which were rich in chromium and carbon, (and are devoid of oxygen), and were embedded in a continuous chromium and oxygen rich film. Aluminum and oxygen rich precipitates were observed in the alloy matrix. Figure 4.48 is the bright field TEM image of the same sample. The surface scale consists of discrete and irregular shaped precipitates embedded in a continuous film. One instance of irregular shaped precipitate is marked with a dotted red line and the continuous film is marked with dashed blue line in this image. Diffraction patterns were obtained from the irregular shaped and continuous film. The specific locations of the diffraction patterns in the image are marked as “A” and “B”. Indexing of the diffraction pattern was done by the procedure

outlined in the section 3.5.4.3. The diffraction pattern was indexed as per the procedure outlined in section 3.5.4.3. Table 4.7 (diffraction pattern from "A") shows the distances of three diffraction spots (R), the calculated d-spacing, (hkl) value of the spot, the d-spacing for Cr_7C_3 from PDF, the measured angles and the theoretical angle from PDF for Cr_7C_3. As shown in the table both the calculated d-values and the measured angles are in very good agreement with the ideal d-spacing and the angles for Cr_7C_3. As shown in the table both the calculated d-values and the measured angles are in very good agreement with the d-spacing and the angles for Cr_7C_3. This confirms that the irregular shaped precipitate observed in the Fig. 4.48 is Cr_7C_3. Table 4.8 shows the results pertinent to indexing the pattern indexing from point B. It was indexed as Cr_2O_3 confirming that the continuous film observed in Fig. 4.47 to be Cr_2O_3. Results from the x-ray diffraction pattern shown in Fig. 4.46 were consistent with these.

4.3.3.2 Microstructure examination in environment 6 (CO/CO_2 = 1272)

In this section the stability of the surface oxide/carbide is presented for the samples exposed in environment 6 (CO/CO_2 = 1272) over the temperature range 850 – 1000°C. As will be presented below, the morphological evolutions of the surface oxide/carbide were similar at all temperatures, so 900°C was chosen as a representative temperature for a presentation of the details of the stability of the bulk alloy at 100h, 375h, and 500h of oxidation. The microstructure examinations of the bulk alloy are presented next in this section. The weight of oxygen and carbon in the sample as a function of exposure duration for the chosen representative temperature of 900°C is presented in the end of this section.

4.3.3.2.1 Morphological evolution of surface oxide/carbide in environment 6 (CO/CO_2 = 1272)

The morphological evolution of the surface oxide/carbide is presented as a function of temperature. At each temperature a pair of images is shown to illustrate the microstructure of the sample. These images were recorded in back-scattered electron (BSE) mode to distinguish between the various phases; Cr_2O_3, Cr_7C_3, and Al_2O_3 formed due to oxidation. In BSE mode the Al_2O_3 appears the darkest, and the Cr_7C_3 appears the brightest with the contrast from Cr_2O_3 lying between that of Al_2O_3 and Cr_7C_3. The contrast from voids appears as similar to that from Al_2O_3. However, due to their different shapes (voids are generally spherical and Al_2O_3 is lenticular) they can be easily distinguished. Further, Al_2O_3 precipitates are located beneath the Cr_2O_3 surface scale.

<u>850°C</u>

Figures 4.49-4.51 present the cross-sectional BSE images of the surface scale of the samples exposed at 850°C for 100h, 375h and 500h, respectively. As shown in Fig.4.49 a duplex surface scale with irregular shaped discrete carbide (Cr_7C_3) precipitates residing in the upper part (outer layer) and a continuous oxide (Cr_2O_3) film residing in the lower part of the layer (referred as inner chromia layer). Typically, the size of the carbide precipitates ranged between 0.5 μm and 1.5 μm, although, in many cases, contiguous carbides seem to have combined and appeared larger (Fig. 4.49 a). The average thickness of the inner chromia layer was 0.20 ± 0.03 μm.

Fig 4.50 shows the microstructures of the sample exposed for 375h at 850°C and shows that after longer exposure, a Cr_2O_3 layer formed near the gas/scale interface so that

the external scale morphology changed from alloy/Cr_2O_3/Cr_7C_3 at 100h to alloy/Cr_2O_3/Cr_7C_3/Cr_2O_3 at 375h, i.e. an outer layer of Cr_2O_3 formed near the gas/scale interface. The total thickness of the external scale increased from 0.5±0.1 μm after 100h of oxidation to 1.4±0.1 μm after 375h of oxidation. Note that this increase in the thickness of the external scale occurred mainly due to the thickness of the outer Cr_2O_3 layer as the average thickness of the inner Cr_2O_3 layer (0.2±0.03) μm remained similar to that after 100h. Another observation from comparing the Figs. 4.49 and 4.50 is that the Cr_7C_3 layer became less continuous after 375 h of exposure suggesting the dissolution of the Cr_7C_3 with continuing oxidation time. Few voids were also observed near the carbide precipitates (Fig 4.50).

Fig 4.51 shows the cross-sectional microstructure of the sample exposed for 500h at 850°C. In comparison to oxidation after 375 h, the carbide layer became more discontinuous, and the area fraction of the voids in the external scale increased. These voids were observed mainly near the carbide precipitates. A slight increase in the thickness of external scale occurred. After 375 h, the external thickness was 1.4±0.1 μm, whereas the external scale thickness was 1.7± 0.2 μm after 500h. This increase in thickness was due to increase in the outer Cr_2O_3 layer.

Table 4.9 shows the summary of microstructure observations at 850°C.

900°C

Figures 4.52-4.56 present the surface BSE images of the sample exposed at 900°C for 100h, 225, 375, 500h, and 750h, respectively. An external scale consisting of an outer layer of discrete Cr_7C_3 precipitates and an inner layer of continuous Cr_2O_3 film formed

near the alloy/scale interface (Fig 4.52). The thicknesses of the inner Cr_2O_3 layer was 0.3±0.03 µm. The typical size of the carbide precipitates varied between 1-2µm.

With increased exposure to 225 hr, the morphology of the surface scale changed to alloy/Cr_2O_3/Cr_7C_3/Cr_2O_3 (Fig. 4.53), i.e. a continuous Cr_2O_3 layer formed near the gas/scale interface, which resulted in an increase in the total thickness of the surface scale. Note that the thickness of the inner layer remained largely unaltered (compare Fig. 4.52 b and Fig. 4.53b). Further, in comparison to oxidation at 100h, the carbide layer was less continuous after 225h of oxidation.

Fig. 4.54 presents the BSE image of the sample oxidized for 375 hours. As shown in the image, the Cr_7C_3 precipitates dissolved noticeably (compare with Fig. 4.52). Some voids were also observed in the surface scale, primarily, near the carbide precipitates.

Fig. 4.55 presents the representative microstructure of the sample oxidized for 500h at 900°C. Comparing Figs. 4.52 and 4.55, it is evident that by 500h, most of the carbides observed after 100h of oxidation had dissolved and the resulting external scale was porous. Voids of size 1-2 µm were observed in the external scale at a distance of ~0.2µm from the alloy/scale interface and smaller voids of size < 0.1µm were observed scattered throughout the external scale. The total thickness of the external scale had increased from 1.0±0.2 micron at 100h to 3.1±0.3 µm after 500h. Note that this increase in thickness occurred mainly in the outer part of the surface scale, i.e., the thickness of the inner scale did not change significantly.

Figure 4.56 presents the microstructure of the sample oxidized for 750h. The external scale essentially consisted of only Cr_2O_3 with ~10% porosity. The location of the voids from the alloy/scale interface was similar to the average distance of the carbide

precipitates from the alloy/scale interface. In some instances, the voids were observed near partially dissolved carbide precipitates (Fig. 4.56 b).

Table 4.9 summarizes of the surface microstructure in sample exposed at 900^{o}C.

950°C

Figures 4.57-4.59 present the BSE images of the sample exposed at 950°C for 100h, 375h and 500h, respectively. An outer layer consisting of discrete Cr_7C_3 precipitates and inner layer of continuous Cr_2O_3 film formed. The thickness of the inner Cr_2O_3 layer 0.3± 0.1µm was comparable to the inner layer formed after 100h of oxidation at 850 and 900°C (table 4.9). The typical size of the carbide precipitate was 1-2µm, which was also similar to the oxidation at 850 and 900°C for the same exposure duration. However, in comparison to the oxidation over 850-900°C, the Cr_7C_3 layer at 950°C appeared less continuous.

Figure 4.58 presents the BSE image of the sample oxidized for 375 h. As shown in this figure, the morphology of the external scale was alloy/Cr_2O_3/Cr_7C_3/Cr_2O_3, which is similar to the morphology of the external scale after 375 h of exposure at 850°C and 900°C, with the main difference being a thicker external scale at 950^{o}C (3.5±0.25µm) than at 900°C (2.3±0.3µm, table 4.9) and 850°C (1.4±0.1µm, table 4.9). The voids were observed mainly near the carbides (Fig. 4.58 b).

Figure 4.59 is the BSE image of the sample exposed for 500h. The external scale at this time was comprised of mainly Cr_2O_3, i.e. the Cr_7C_3 had mostly dissolved by 500h of exposure. The Cr_2O_3 scale was porous with voids of size ranging between 1-5µm. The location of the void with respect to the alloy/scale interface was similar to that of carbides

observed after 100h and 375 h of oxidation (~ 0.3μm from the alloy/scale interface). The total thickness of the surface scale was 3.9±0.4μm.

A summary of the microstructure observation at 950°C in this environment is shown in table 4.9.

1000°C

The surface microstructure of the sample oxidized for 100h at 1000°C is shown in Fig. 4.60. An outer layer of discrete Cr_7C_3 precipitates and inner layer of continuous Cr_2O_3 film formed. The thickness of the inner Cr_2O_3 layer was 0.4±0.2μm. A high standard deviation in the inner layer thickness was due to the convoluted nature of the alloy/scale interface. This morphology is similar to the 100h of oxidation over 850 - 950^{o}C, (Fig. 4.49, 4.52 and 4.57) with the main difference of Cr_7C_3 layer being less continuous in comparison to the oxidation at lower temperatures.

Figure 4.61 shows the BSE image of the sample oxidized for 375 h at 1000°C. With continuing isothermal exposure the Cr_7C_3 precipitates dissolved and the total thickness of the surface scale increased from 1.8±0.4μm at 100h to 4.3±0.4μm after 375 h.

Figure 4.62 presents the surface microstructure of the sample oxidized for 500h at 1000°C. The Cr_7C_3 precipitates had mostly dissolved by 500h of oxidation. The voids of size varying between 1-5μm were observed in the Cr_2O_3 scale.

Table 4.9 summarizes the surface microstructure examination over 850 -1000°C.

4.3.3.2.2 Bulk microstructure of the sample exposed in environment 6 (CO/CO_2 = 1272) 6 at 900°C

This section presents the characterization of the bulk alloy exposed in environment 6 (CO/CO_2 = 1272) at 900°C. The extent of carburization/decarburization of the sample was estimated by comparing the surface area fractions of the oxidized sample to that of as-received alloy 617. The representative temperature selected was 900°C and the representative exposure durations selected were 100h, 375h and 500h.

Figures 4.64 - 4.66 show the bulk microstructure of the samples exposed at 900°C for 100h, 375h, and 500h. The bulk microstructure of the as-received alloy 617 is also shown in Fig 4.63. As shown in Fig. 4.64, upon oxidation, from the surface into the bulk, the as-received alloy 617 microstructure evolved into two zones. Near the alloy/scale interface a "denuded zone" is observed, where the carbides no longer exist. Beyond this denuded zone is a "carburized zone" in which the area fraction of the carbide has increased. The morphology and distribution of the carbides are also altered in this zone. The carbides in the as-received sample were observed mainly along the rolling direction (Fig.4.63), whereas, the carbides in the carburized zone (Figs. 4.64-4.66) were observed to decorate the grain boundaries, interior of the grains, and the twin boundaries with no directionality. Note that in the as-received microstructure the carbides were never observed at the twin boundaries (Fig. 4.63).

The surface area fraction of the carbides in the carburized zone was measured using Adobe Photoshop® software from Adobe, Inc. for the as received sample, and the samples oxidized at 900°C for 100h, 375h and 500h. For the oxidized samples, first the carburized zone was selected from the entire bulk microstructure by discarding the

surface and the denuded zone. Brightness and contrast of the carburized zone was then adjusted and the surface carbide fraction was measured using Adobe Photoshop® software from Adobe, Inc. Section 3.5.3 explains this procedure in much detail. In each case a total sample length of 2.5 mm and cross-sectional thickness of 0.6 mm (~extending up to the middle of the cross-section) from the surface was used. Table 4.10 gives the values of the measured area fraction of the carbide in the bulk of the as received alloy 617, and after 100h, 375h, and 500h of oxidation at 900°C. Figure 4.67 is a plot of the results tabulated in table 4.10. The standard deviation in the carbide area fractions taken from different micrographs (table 4.10) are shown as error bars on this plot. As observed from this plot, the area fractions of the bulk carbides after 100h, 375h, and 500h of oxidation at 900°C were similar. Further, the area fraction of carbides in oxidized sample was higher than the as received sample. The weight gain corresponding to increased fraction of carbide in the oxidized sample was calculated by assuming that the area fraction is equal to volume fraction as per the procedure given in section 3.5.3. Table 4.11 shows the results of this calculation.

As stated earlier, the bulk microstructure showed a denuded zone near the alloy surface that was free from carbides. The depth of the denuded zone was measured as a function of exposure duration at 900°C. Table 4.12 shows the measurements of the depth of denuded zone. Figure 4.68 plots this depth of denuded zone as a function of time. A least squares curve fit applied to this measurement showed that the depth of the denuded zone increased according to a parabolic law.

4.3.3.3 Weight of oxygen in the Cr_2O_3, Al_2O_3 and weight of carbon in the form of Cr_7C_3 in samples oxidized at 900°C

The weight of oxygen in the form of Cr_2O_3 (in external scale) and Al_2O_3 (in the form of internal oxide precipitates), and carbon in the form of Cr_7C_3 (in the external scale) was calculated by measuring the absolute area occupied by Cr_2O_3, Al_2O_3 and Cr_7C_3 precipitates in high magnification BSE images. Section 3.5.3 (experimental chapter) details the procedure used for this purpose. Tables 4.13 (a)- 4.13 (e) shows the length of the micrograph used, the area occupied by chromia, alumina and the carbide, and the calculated weights of oxygen and carbon for samples exposed at 100h, 225h, 375h, 500h, and 750h, respectively. Figure 4.69 is a plot of these weights of oxygen and carbon from microstructure measurements as a function of exposure duration at 900°C. The total weight gain measured by the microbalance is also plotted in this figure. The error bars on this plot correspond to one standard deviation between the weights of the oxygen and carbon between the micrographs used (table 4.13 a-4.13 e). Note that this result does not reflect the weight of carbon associated with the bulk carbides (formed due to internal carburization).

As shown in the Fig. 4.69, the weight gain due to oxygen in chromia and alumina increased with the oxidation time, whereas the weight of carbon in the Cr_7C_3 decreased with time. The rate of weight gain due to oxygen in chromia was higher than the weight gain due to oxygen in alumina. Consequently, after a given oxidation time, the weight of carbon in the form of Cr_7C_3, the weight of oxygen in the form of alumina, and the weight of oxygen in the form of chromia were in increasing order, i.e. most of the measured weight gain was present in the form of oxygen in the chromia.

Another observation from this figure is that the calculated weight gain is always less than the measured weight gain. The difference between the two values after 100h, 375h, and 500h are $(1.4\pm0.4)x10^{-3}$ mg/mm^2, $(1.6\pm0.7)\ 10^{-3}$ mg/mm^2, and $(0.9\pm0.6)\ 10^{-3}$ mg/mm^2, respectively, which can be attributed to the unaccounted weight gain from carbon in the form of internal carburization. Considering that the average surface area of the sample was 123 mm^2, the weight gain due to internal carburization after 100h, 375h, and 500h will thus be 0.2±0.05mg, 0.2±0.1 mg, and 0.11±0.07 mg. The weight gain due to carbon in the form of internal carburization was also estimated by measuring the area fraction of the carbide in the bulk in section 4.3.3.2.2 (table 4.11). The agreement between the two methods (section 4.3.3.2.2 and this section) is satisfactory, e.g. after 100h the oxidation at 900°C the weight of carbon due to internal carburization calculated from the area fraction measurement was 0.36±0.1 mg (section 4.3.3.2.2), whereas in this section this value was estimated to be 0.2±0.05 mg.

4.4 Pre-oxidation experiment

Based on isothermal experiments over 850 - 1000°C, it was hypothesized that the surface chromia scale plays a role in decarburization of the alloy over 950-1000°C. To determine the role of chromia during decarburization, a two-step experiment was designed. In the first step a continuous surface chromia film was formed by exposing the sample at 900°C for 150h, referred as the "pre-oxidation" step in this thesis. In the second step the sample was decarburized at 1000°C for 100h, referred as "decarburization" step in this thesis. The surface microstructure, bulk microstructure and the gas-phase analysis was used to determine the role of chromia during decarburization.

The gas chemistry used in both the pre-oxidation and decarburization step was He+15ppm CO + 1.5 ppm CO_2, which is same as the environment 1 (CO/CO_2 = 9).

Figure 4.70 shows the plot of the difference in the concentration levels of CO measured at the outlet and inlet of the tube. A negative value in this figure denotes a net consumption of CO causing the concentration level at the outlet to be below than that at the inlet, whereas, a positive value denotes a net evolution of CO inside the reaction zone as a result of the decarburization of the samples. As shown in the Fig. 4.70, during the pre-oxidation step CO was consumed. However, during the decarburization step, starting with a high amount of CO evolution (~16 ppm) the amount of CO evolution dropped to a steady state value of ~1 ppm after ~50h of the exposure. The total weight of carbon due to decarburization of the samples, $\Delta W_{c,}$, was calculated by the calculating the area under the curve of CO production by the following equation:

$$\Delta W_c = \frac{I \times \dot{V} \times M_C}{V_m \times S}, \qquad (4.2)$$

where I is the area under the curve (in mol-h), $\dot{V}$ is the flow rate of the gas mixture (in liter/h), M_C is the molar weight of carbon (in mg/mol), V_m is the molar volume of the gas (in liters) ($V_m = \frac{R \times T}{P}$, *R* is universal gas constant, T is room temperature taken as 298 K and P is 1 atmosphere) and S is the surface area of the sample (in mm^2). The total mass of carbon produced in the decarburization step was $2.2 \pm 0.4 \times 10^{-3}$ mg/mm^2. The only source of the carbon inside the reaction zone is the sample itself and therefore, the net production of carbon in the form of CO must come from decarburization of the samples.

Figure 4.71 shows the weight change in the corrosion coupons as a function of time during the decarburization step. The initial weight shown in this figure is equal to

the weight gain in the sample during pre-oxidation step. A net weight gain of 3.5±0.4 x 10^{-3} mg/mm^2 occurred during the pre-oxidation step, whereas, a continuous weight loss in the sample occurred during the decarburization step. The weight loss was rapid during the first 15h of decarburization step after which the rate of weight loss was slow. The sample had lost ~70% of the weight gained during the pre-oxidation step in the first 15h of decarburization. The total weight loss in the sample after 100h of decarburization at 1000°C was 82% of the weight gained during the pre-oxidation step.

Figures 4.72 and 4.73 show the cross-sectional image of the sample after the 150h of pre-oxidation at 900°C and the 100h of decarburization at 1000°C, respectively. An external Cr_2O_3 film with thickness of 1.5±0.4 μm had formed during the pre-oxidation step. Few matrix precipitates were also observed entrapped in the oxide scale. Internal oxidation of Al_2O_3 occurred in the sub-surface region. After the 100h of decarburization step, the Cr_2O_3 thickness had decreased to 0.1 ± 0.1 μm (Fig. 4.73). In comparison to microstructure after pre-oxidation step, no marked difference in the internal oxidation of Al_2O_3 was observed in between the pre-oxidized and decarburized samples.

Figures 4.74 and 4.75 show the bulk microstructure of the sample after pre-oxidation and decarburization step (Fig. 4.75 a and b were decarburized for 15h and 100h at 1000°C, respectively). The $M_{23}C_6$/M_6C carbides are observed in the entire cross-section of the pre-oxidized sample, whereas, a decarburization zone is observed near the alloy surface in the samples decarburized for 15h and 100h. In this decarburized zone the carbides existing in the pre-oxidized sample have dissolved in the matrix. Further, the depth of the decarburization zone increased with exposure duration, most likely, because

with the progress of decarburization the carbon was pulled out from a greater depth in the sample.

The concentration profile of the Cr was measured on the sample pre-oxidized at 900°C for 150h and the samples decarburized for 5h and 100h at 1000°C. In each case three line scans were taken from different regions in the sample. Appendix II tabulates the values of the three measured Cr concentration profiles. Figure 4.76 presents the average and one standard deviation of the three profiles as a function of depth in the alloy. In this plot the alloy surface lies to the left of the Y-axis. The Cr concentration in the as-received sample is also plotted in this figure. As shown in this figure, during the pre-oxidation step the Cr-near the surface was depleted. The width of the depletion zone was ~15μm. The Cr-depletion in this zone had established a steep Cr-concentration gradient with the lower Cr concentration (~14 wt%) at the oxide/alloy surface and high Cr-concentration (21.8 wt%, same as the initial concentration of Cr in the alloy 617) in the bulk of the alloy. However, during the subsequent decarburization step there was a partial recovery of the Cr depletion profile by 5 hr and complete recovery by 100h. This recovery of the Cr depletion profile can occur only if there is a Cr-source at or near the alloy/scale interface. Chapter 5 will discuss this aspect in detail.

4.5 Short term exposure experiment in environment 6 (CO/CO_2 = 1272) at 900°C

The objective of this experiment was to determine the mechanism of formation of surface carbides during oxidation of samples in environment 6 (CO/CO_2 = 1272). For this purpose, one corrosion coupon was oxidized in environment 6 (CO/CO_2 = 1272) for 1 hour at 900°C. The surface finish of the sample (grit 800) was same as that for the 750h

isothermal oxidation at this temperature. The weight gain in this sample was $0.39 \pm 0.16 \times 10^{-3}$ mg/mm^2.

XRD of the surface film was performed to characterize the surface phases. A slow scan speed of 0.1 deg per min was used to enhance the signal from the carbides. Figure 4.77 plots the intensities as a function of diffraction angle 2θ. Table 4.14 shows a comparison between the peaks observed in Fig. 4.77 and the PDFs used to identify the peaks. As shown in this table, the peaks in the x-ray spectrum in Fig. 4.77 matched Cr_2O_3, Cr_7C_3, and Ni which comes from the γ-matrix.

Figure 4.78 presents the cross-sectional image of this sample. A gold coating followed by a nickel coating was applied to protect the surface film. As shown in this figure, a continuous thin film of Cr_2O_3 of thickness 70 ± 18 nm formed on the entire cross-section near the scale/alloy interface. The nuclei of Cr_7C_3 formed near the gas/scale interface. The sizes of these Cr_7C_3 precipitates varied between 20nm – 200nm. Note that the carbide density varied from one cross-sectional area to the other. Some internal oxidation of Al_2O_3 also occurred in the alloy substrate.

Table 4.1 Rate constant k and the rate exponent, n, for Eq. (4.1) over 850°C - 1000°C. For each environment the values of k and n were determined by a least square curve fit. The R^2 value for each case is also given in the table.

environment number	CO/CO_2 ratio	850°C			900°C			950°C			1000°C		
		k ($mg/mm^2 h^n$) x 10^{-4}	n	R^2	k ($mg/mm^2 h^n$) x 10^{-4}	n	R^2	k ($mg/mm^2 h^n$) x 10^{-4}	n	R^2	k ($mg/mm^2 h^n$) x 10^{-4}	n	R^2
1	9	0.63	0.6	0.99	0.89	0.6	0.9	0.13	1.0	0.99	$2x10^{-10}$	4.3	0.97
2	150	0.53	0.7	0.99	0.92	0.7	0.99	1.4	0.7	0.99	1.4	0.7	0.98
3	291	0.51	0.7	0.99	4.2	0.6	0.91	2.4	0.6	0.96	2.2	0.6	0.90
4	453	0.51	0.7	0.99	2.3	0.6	0.92	1.9	0.6	0.97	1.6	0.7	0.98
5	900	1.40	0.6	0.98	1.5	0.6	0.98	1.6	0.7	0.98	3.7	0.6	0.93
6	1272	1.40	0.6	0.91	2.3	0.6	0.94	3.1	0.6	0.98	5.2	0.5	0.92

Table 4.2 Indexing of the diffraction pattern from carbides in the as received alloy 617 shown in Fig. 4.24 b. Note that the smaller spots in this image correspond to carbides, whereas, the larger spots correspond to the Ni. The value of λ and L was 0.00252 nm (at 200kV) and 530 mm.

Spot number	distance from the transmitted spot (R) mm	calculated lattice spacing (d), A°	(hkl)	Lattice spacing of Cr_7C_3 (PDF# 00-011-0545 (A°)	measured angles between spot (1, 2) and (1,3) degrees	Ideal angle between the planes (1, 2) and (2,3) degrees
1	3.59	3.76	(02-2)	3.76	between 1 & 2 = 60	between 1 & 2 = 60
2	3.59	3.76	(-202)	3.76		
3	3.59	3.76	(-2-20)	3.76	between 1 & 3 = 120	between 1 & 3 = 120

Table 4.3. Identification of peaks shown in XRD pattern from as received alloy 617 (Fig. 4.25). The peaks were compared against the standard peaks of Ni (shown as γ-matrix in Fig. 4.25), $M_{23}C_6$ (where M = Cr, Co, Mo) and M_6C (where M = Cr, Co). The powder diffraction file number (PDF #) for the each phase is shown in the table.

Peak position in the XRD (2θ), degree	Peak position of Ni (PDF# 04-004-2759) (2θ), degree	Peak position for $(Cr,Co,Mo)_{23}C_6$,(2θ), degree (PDF# 00-011-0545)	Peak position for Ni_3Mo_3C, (2θ), degree (PDF# 01-089-4883)	phase assigned to the peak,(2θ), degree
32.3			32.4	M_6C
35.3			35.4	M_6C
37.5		37.8		$M_{23}C_6$
39.8			39.9	M_6C
41.2		41.4		$M_{23}C_6$
42.4			42.5	M_6C
43.6	43.9			Ni
46.2			46.5	M_6C
47.9		48.3		$M_{23}C_6$
49.4			49.4	M_6C
50.2		50.7		$M_{23}C_6$
50.9	51.2			Ni
53.9		54.4		$M_{23}C_6$
56.8		56.5		$M_{23}C_6$

Table 4.4 Identification of peaks shown in XRD pattern from the sample exposed in environment 1 (CO/CO_2 ratio 9) for 100h at 1000°C. The peaks were compared against the standard peaks of Ni (shown as γ-matrix in Fig. 4.37),TiO_2, and Al_2O_3. The powder diffraction file number (PDF #) for the each phase is shown in the table.

Peak position in the XRD (2θ), degree	Peak position of Ni (PDF# 04-004-2759) (2θ), degree	Peak position for Al_2O_3, (2θ), degree (PDF# 01-073-5928)	Peak position for TiO_2, (2θ), degree (PDF# 98-000-128)	Phase assigned to the peak,(2θ), degree
25.5		25.6	25.4	Al_2O_3+ TiO_2
32.3				unidentified
35.3		35.2		Al_2O_3
37.8		37.8		Al_2O_3
39.8			40.0	TiO_2
42.3				Ni
43.7	43.9	43.4		Al_2O_3
46.3			46.1	TiO_2
47.8			48.0	TiO_2
50.9	51.2			Ni
52.3		52.7		Al_2O_3
57.4		57.6		Al_2O_3

Table 4.5 Summary of surface microstructure in environment 1 (CO/CO_2 ratio 9) over 850-1000°C.

Temperature(°C)	Time (h)	external oxide phase	external oxide thickness (μm)	internal oxidation of Al_2O_3
850	100	Cr_2O_3 film	0.2 ± 0.05	yes
	500	Cr_2O_3 film	1.8 ± 0.3	yes
900	100	Cr_2O_3 film	0.8 ± 0.2	yes
	375	Cr_2O_3 film	2.2 ± 0.4	yes
	500	Cr_2O_3 film	2.6 ± 0.4	yes
950	100	Cr_2O_3 film	0.8 ± 0.1	yes
	375	Cr_2O_3 film	2.1 ± 0.3	yes
	500	Cr_2O_3 film	4.2 ± 0.6	yes
1000	100	Al_2O_3 nodules	no continuous film	no
	375	region I- continuous Al_2O_3 film	0.3 ± 0.06	no
		region II – Cr_2O_3 nodules	not continuous	no
	500	region I – continuous Al_2O_3 film	0.6 ± 0.06	no
		Region II- Cr_2O_3 film over continuous Al_2O_3 film	$Cr_2O_3 = 1.5 \pm 0.4$, and $Al_2O_3 = 0.6 \pm 0.06$	yes

Table 4.6. Identification of peaks shown in XRD pattern from the sample exposed in environment 6 (CO/CO_2 = 1272) for 100h at 1000°C. The peaks were compared against the standard peaks of Ni (shown as γ-matrix in Fig. 4.46), Cr_7C_3, and Cr_2O_3. The powder diffraction file umber (PDF #) for the each phase is shown in the table.

Peak position in the XRD (2θ), degree	Peak position of Ni (PDF# 04-004-2759) (2θ), degree	Peak position for Cr_7C_3, (2θ), degree (PDF# 01-89-7244)	Peak position for Cr_2O_3, (2θ), degree (PDF# 99-000-1069)	phase assigned to the peak,(2θ), degree
36.0			36.2	Cr_2O_3
39.1		39.2		Cr_7C_3
39.6		39.4		Cr_7C_3
40.6		40.5		Cr_7C_3
41.3			41.5	Cr_2O_3
42.6		42.6		Cr_7C_3
43.7	43.9			Ni
44.1		44.2		Cr_7C_3
47.7		47.8		Cr_7C_3
48.5		48.4		Cr_7C_3
49.1		49.3		Cr_7C_3
50.2			50.2	Cr_2O_3
50.8	51.2			Ni
52.0		52.2		Cr_7C_3
54.5			54.8	Cr_2O_3

Table 4.7 Indexing of the diffraction pattern from the precipitate marked "A" in Fig. 4.48. The distances of three spots closest to the transmitted spot was measured and d-spacing was calculated using Eq. (3.12). The value of λ and L was 0.00252 nm (@ 200KV) and 300 mm.

Spot number	distance from the transmitted spot (R) mm	calculated lattice spacing (d), A° using Eq. (3.12)	(hkl)	Lattice spacing of Cr_7C_3 (PDF# 04-004-4542 (A°)	measured angles between the planes (degrees)	Ideal angle between the planes (1, 2) and (2,3) (degrees)
1	2.27	3.31	(-131)	3.22	between 1 & 2 = 72.1	between 1 & 2 = 70.96
2	3.72	2.02	(1-32)	2.03		
3	3.73	1.55	(003)	1.51	between 1 & 3 = 45.9	between 1 & 3 = 44.9

Table 4.8 Indexing of the diffraction pattern from the precipitate marked "B" in Fig. 4.48. The distances of three spots closest to the transmitted spot was measured and d-spacing was calculated using Eq. 3.12. The value of λ and L was 0.00252 nm (@ 200KV) and 250 mm.

Spot number	distance from the transmitted spot (R) mm	calculated lattice spacing (d), A° using Eq. (3.12)	(hkl)	Lattice spacing of $Cr_2)_3$ (PDF# 99-000-1069 (A°)	measured angles between spot (1, 2) and (1,3) degrees	Ideal angle between the planes (1, 2) and (2,3) degrees
1	2.43	2.58	(110)	2.48	between 1 & 2 = 57.8	between 1 & 2 = 59.3
2	2.43	2.58	(2-10)	2.48		
3	1.49	1.49	(300)	1.43	between 1 & 3 = 29.1	between 1 & 3 = 29.0

Table 4.9 Summary of the microstructure observations in environment 6 (CO/CO_2 = 1272) over 850-1000°C.

Temperature (°C)	time (h)	morphology of the surface scale	inner Cr_2O_3 layer thickness (μm)	Total scale thickness (μm)
850	100	alloy/Cr_2O_3/Cr_7C_3	0.2±0.03	0.5±0.1
	375	alloy/Cr_2O_3/Cr_7C_3/Cr_2O_3	0.2±0.02	1.4±0.1
	500	alloy/Cr_2O_3/Cr_7C_3/Cr_2O_3	0.2±0.06	1.7±0.2
900	1	alloy/Cr_2O_3/Cr_7C_3	0.07±0.02	0.07±0.02
	100	alloy/Cr_2O_3/Cr_7C_3	0.3±0.03	1.0±0.2
	225	alloy/Cr_2O_3/Cr_7C_3/Cr_2O_3	0.3±0.05	1.7±0.2
	375	alloy/Cr_2O_3/Cr_7C_3/Cr_2O_3	0.3±0.05	2.3±0.3
	500	alloy/Cr_2O_3/Cr_7C_3/Cr_2O_3	0.3±0.06	3.1±0.3
	750	alloy/Cr_2O_3/Cr_7C_3/Cr_2O_3	0.3±0.08	4.1±0.5
950	100	alloy/Cr_2O_3/Cr_7C_3	0.3±0.1	1.5±0.3
	375	alloy/Cr_2O_3/Cr_7C_3/Cr_2O_3	0.5±0.2	3.5±0.3
	500	alloy/Cr_2O_3/Cr_7C_3/Cr_2O_3	0.4±0.1	3.9±0.4
1000	100	alloy/Cr_2O_3/Cr_7C_3	0.4±0.2	1.8±0.4
	375	alloy/Cr_2O_3/Cr_7C_3/Cr_2O_3	0.6±0.3	4.3±0.4
	500	alloy/Cr_2O_3/Cr_7C_3/Cr_2O_3	0.5±0.2	5.4±0.6

Table 4.10 Measurement of area fraction of the carbide in the bulk of the alloy.

Exposure condition	micrograph number	area fraction of the carbide (in %)	Average ± Standard deviation
as received	1	2.7	2.9±0.4
	2	2.6	
	3	3.2	
	4	3.4	
	5	2.5	
900°C, 100h, environment 6 (CO/CO_2 = 1272)	1	5.6	4.8 ± 0.5
	2	4.8	
	3	4.6	
	4	4.2	
	5	5.1	
900°C, 375h, environment 6 (CO/CO_2 = 1272)	1	3.7	4.2 ± 0.7
	2	5.1	
	3	4.4	
	4	4.5	
	5	3.4	
900°C, 500h, environment 6 (CO/CO_2 = 1272)	1	4.3	4.3 ± 0.6
	2	5.1	
	3	3.7	
	4	4.6	
	5	3.9	

Table 4.11. Calculation of the weight gain due to increased fraction of the bulk carbide.

Time (h)	Increase in volume fraction from the as received sample	Total volume of the sample (mm^3)	Increase in the volume of the carbide (mm^3)	Increase in weight of carbide (mg)	weight gain due to carbon in the bulk (mg)
100	0.017	54.7	0.9	6.5	0.36±0.1
375	0.013	54.7	0.7	4.9	0.3±0.1
500	0.014	54.7	0.8	5.3	0.3±0.1

Table 4.12. Measurement of depth of denuded zone in sample exposed in environment 6 (CO/CO_2 =1272) at 900°C.

Exposure condition	micrograph number	depth of denuded zone (μm)	Average ± Standard deviation
900°C, 100h, CO/CO_2 ratio 1272; environment 6	1	9	7.8 ± 1.3
	2	7	
	3	8	
	4	9	
	5	6	
900°C, 375h, environment 6 (CO/CO_2 = 1272)	1	16	16.8 ± 0.8
	2	18	
	3	16	
	4	17	
	5	17	
900°C, 500h, environment 6 (CO/CO_2 = 1272)	1	22	22.0 ± 0.7
	2	23	
	3	21	
	4	22	
	5	22	

Table 4.13 a. Calculation of the weight of oxygen (in the form of Cr_2O_3 and Al_2O_3) and carbon (in the form of Cr_7C_3) in the sample exposed at 900°C for 100h in environment 6 (CO/CO_2= 1272).

Micrograph number	Length of interface (µm)	Area of Cr_2O_3 (μm^2)	Area of Al_2O_3 (μm^2)	Area of Cr_7C_3 (μm^2)	Area of Cr_2O_3 per unit length of micrograph (µm)	Area of Al_2O_3 per unit length of micrograph (µm)	Area of Cr_7C_3 per unit length of micrograph (µm)	Mass of oxygen in Cr_2O_3 (mg/mm^2) x 10^{-3} calculated as per Eq. (3.9)	Mass of oxygen in Al_2O_3 (mg/mm^2) x 10^{-3} calculated as per Eq. (3.10)	Mass of carbon in Cr_7C_3 (mg/mm^2) x 10^{-3} calculated as per Eq. (3.11)
1	24	12.1	5.6	13.1	0.50	0.23	0.55	0.63	0.44	0.54
2	24	21.3	4.9	12.1	0.89	0.20	0.50	1.26	0.38	0.51
3	24	21.6	3.7	13.5	0.90	0.15	0.56	1.28	0.29	0.55
4	24	22.4	7.4	13.9	0.93	0.31	0.58	1.34	0.58	0.56
5	24	13.2	5.5	13	0.55	0.23	0.54	0.90	0.43	0.54
6	24	9.9	4.1	12.6	0.41	0.17	0.53	0.68	0.32	0.53
7	40	28.1	15.5	19.6	0.70	0.39	0.49	0.96	0.73	0.51
8	40	31	22.5	28	0.78	0.56	0.70	1.08	1.06	0.64
9	40	37.3	14.4	22	0.93	0.36	0.55	1.33	0.68	0.54
10	24	19.5	7.5	14.3	0.81	0.31	0.60	1.24	0.59	0.57
11	24	18.1	7.8	12.4	0.75	0.33	0.52	1.04	0.61	0.52
12	24	16.3	6.5	14.2	0.68	0.27	0.59	1.00	0.51	0.57
13	24	17.8	5.1	14.1	0.74	0.95	0.59	1.00	0.42	0.57
Average ± Standard deviation								1.0± 0.27	0.5 ± 0.30	0.55± 0.03

Table 4.13 b. Calculation of the weight of oxygen (in the form of Cr_2O_3 and Al_2O_3) and carbon (in the form of Cr_7C_3) in the sample exposed at 900°C for 225h in environment 6 (CO/CO_2 = 1272).

Micrograph number	Length of interface (µm)	Area of Cr_2O_3 (μm^2)	Area of Al_2O_3 (μm^2)	Area of Cr_7C_3 (μm^2)	Area of Cr_2O_3 per unit length of micrograph (µm)	Area of Al_2O_3 per unit length of micrograph (µm)	Area of Cr_7C_3 per unit length of micrograph (µm)	Mass of oxygen in Cr_2O_3 (mg/mm^2) x 10^{-3} calculated as per Eq. (3.9)	Mass of oxygen in Al_2O_3 (mg/mm^2) x 10^{-3} calculated as per Eq. (3.10)	Mass of carbon in Cr_7C_3 (mg/mm^2) x 10^{-3} calculated as per Eq. (3.11)
1	60	76.7	17.82	35.5	1.28	0.30	0.59	2.10	0.56	0.53
2	40	32.59	13.2	17.3	0.81	0.33	0.43	1.34	0.62	0.43
3	40	53.5	26.8	22.3	1.34	0.67	0.56	2.20	1.26	0.51
4	40	44.3	12.2	21.6	1.11	0.31	0.54	1.82	0.57	0.50
5	24	25.1	4.3	15	1.05	0.18	0.63	1.72	0.34	0.55
6	40	36.4	14.8	27.5	0.91	0.37	0.69	1.50	0.70	0.59
7	60	78.3	16.23	32.1	1.31	0.27	0.54	2.15	0.51	0.49
8	24	19.2	8.8	10.4	0.80	0.37	0.43	1.32	0.69	0.43
9	40	38.7	28.9	19.3	0.97	0.72	0.48	1.59	1.36	0.46
10	40	49.2	15.4	19.2	1.23	0.39	0.48	2.02	0.72	0.46
Average ± Standard deviation								1.8 ± 0.3	0.7 ± 0.32	0.49± 0.05

Table 4.13 c. Calculation of the weight of oxygen (in the form of Cr_2O_3 and Al_2O_3) and carbon (in the form of Cr_7C_3) in the sample exposed at 900°C for 375h in environment 6 (CO/CO_2 = 1272).

Micrograph number	Length of interface (µm)	Area of Cr_2O_3 (μm^2)	Area of Al_2O_3 (μm^2)	Area of Cr_7C_3 (μm^2)	Area of Cr_2O_3 per unit length of micrograph (µm)	Area of Al_2O_3 per unit length of micrograph (µm)	Area of Cr_7C_3 per unit length of micrograph (µm)	Mass of oxygen in Cr_2O_3 (mg/mm^2) x 10^{-3} calculated as per Eq. (3.9)	Mass of oxygen in Al_2O_3 (mg/mm^2) x 10^{-3} calculated as per Eq. (3.10)	Mass of carbon in Cr_7C_3 (mg/mm^2) x 10^{-3} calculated as per Eq. (3.11)
1	40	82.80	26.70	19.40	2.07	0.67	0.49	3.41	1.26	0.30
2	40	80.20	39.60	28.60	2.01	0.99	0.72	3.30	1.86	0.45
3	24	43.40	19.80	9.60	1.81	0.83	0.40	2.98	1.55	0.25
4	24	36.40	15.80	8.90	1.52	0.66	0.37	2.50	1.24	0.23
5	24	38.60	7.20	13.50	1.61	0.30	0.56	2.65	0.56	0.35
6	24	43.00	4.70	10.70	1.79	0.20	0.45	2.95	0.37	0.28
7	24	43.00	14.80	8.15	1.79	0.62	0.34	2.95	1.16	0.21
8	24	49.40	27.40	11.10	2.06	1.14	0.46	3.39	2.15	0.29
9	24	47.10	14.40	13.01	1.96	0.60	0.54	3.23	1.13	0.34
10	24	55.00	19.90	10.10	2.29	0.83	0.42	3.77	1.56	0.26
Average ± Standard deviation								3.1 ± 0.4	1.3 ± 0.5	0.29± 0.06

Table 4.13 d. Calculation of the weight of oxygen (in the form of Cr_2O_3 and Al_2O_3) and carbon (in the form of Cr_7C_3) in the sample exposed at 900°C for 500h in environment 6 (CO/CO_2 = 1272).

Micrograph number	Length of interface (μm)	Area of Cr_2O_3 (μm^2)	Area of Al_2O_3 (μm^2)	Area of Cr_7C_3 (μm^2)	Area of Cr_2O_3 per unit length of micrograph (μm)	Area of Al_2O_3 per unit length of micrograph (μm)	Area of Cr_7C_3 per unit length of micrograph (μm)	Mass of oxygen in Cr_2O_3 (mg/mm^2) x 10^{-3} calculated as per Eq. (3.9)	Mass of oxygen in Al_2O_3 (mg/mm^2) x 10^{-3} calculated as per Eq. (3.10)	Mass of carbon in Cr_7C_3 (mg/mm^2) x 10^{-3} calculated as per Eq. (3.11)
1	40	96.80	9.50	12.10	2.42	0.24	0.30	3.98	0.45	0.19
2	24	69.70	19.50	7.50	2.90	0.81	0.31	4.78	1.53	0.19
3	24	79.80	11.70	9.20	3.33	0.49	0.38	5.47	0.92	0.24
4	24	92.10	21.20	8.20	3.84	0.88	0.34	6.31	1.66	0.21
5	40	159.90	84.00	13.30	4.00	2.10	0.33	6.58	3.96	0.21
6	60	194.00	69.20	12.10	3.23	1.15	0.20	5.32	2.17	0.13
7	24	73.20	14.20	8.90	3.05	0.59	0.37	5.02	1.11	0.23
8	24	80.40	29.20	6.50	3.35	1.22	0.27	5.51	2.29	0.17
9	24	89.20	23.20	5.40	3.72	0.97	0.23	6.11	1.82	0.14
Average ± Standard deviation								5.5 ± 0.8	1.8 ± 0.8	0.2 ± 0.04

Table 4.13 e. Calculation of the weight of oxygen (in the form of Cr_2O_3 and Al_2O_3) and carbon (in the form of Cr_7C_3) in the sample exposed at 900°C for 750h in environment 6 (CO/CO_2 = 1272).

Micrograph number	Length of interface (μm)	Area of Cr_2O_3 (μm^2)	Area of Al_2O_3 (μm^2)	Area of Cr_7C_3 (μm^2)	Area of Cr_2O_3 per unit length of micrograph (μm)	Area of Al_2O_3 per unit length of micrograph (μm)	Area of Cr_7C_3 per unit length of micrograph (μm)	Mass of oxygen in Cr_2O_3 (mg/mm^2) x 10^{-3} calculated as per Eq. (3.9)	Mass of oxygen in Al_2O_3 (mg/mm^2) x 10^{-3} calculated as per Eq. (3.10)	Mass of carbon in Cr_7C_3 (mg/mm^2) x 10^{-3} calculated as per Eq. (3.11)
1	60	350.4	66.3	0	5.84	1.11	0.00	9.59	2.08	0.00
2	24	111.9	27.8	0	4.66	1.16	0.00	7.65	2.18	0.00
3	30	151.5	31	0	5.05	1.03	0.00	8.29	1.95	0.00
4	60	294	57	17	4.90	0.95	0.28	8.04	1.79	0.18
5	60	318	60	32	5.30	1.00	0.53	8.70	1.88	0.33
6	60	342	78	0	5.70	1.30	0.00	9.36	2.45	0.00
7	40	192	35.6	0	4.80	0.89	0.00	7.88	1.68	0.00
8	40	236	48	0	5.90	1.20	0.00	9.69	2.26	0.00
Average ± Standard deviation								8.7 ± 0.8	2.0 ± 0.4	0

Table 4.14. Identification of peaks shown in XRD pattern from the sample exposed in environment 6 (CO/CO_2 =1272) for 1h at 900°C. The peaks were compared against the standard peaks of Ni, Cr_7C_3, and Cr_2O_3. The powder diffraction file number (PDF #) for each phase is shown in the table.

Peak position in the XRD (2θ), degree	Peak position of Ni (PDF# 04-004-2759) (2θ), degree	Peak position for Cr_7C_3, (2θ), degree (PDF# 01-089-7244)	Peak position for Cr_2O_3 (2θ), degree (PDF# 99-000-1069)	phase assigned to the peak,(2θ), degree
39.1		39.2		Cr_7C_3
39.7		39.2		Cr_7C_3
41.1			41.5	Cr_2O_3
42.4		42.6		Cr_7C_3
43.7	43.9			Ni
46.4		46.2		Cr_7C_3
47.9		47.8		Cr_7C_3
50.2		50.2	50.2	Cr_2O_3
51.0	51.2			Ni
54.5		54.4	54.8	Cr_2O_3

(a)

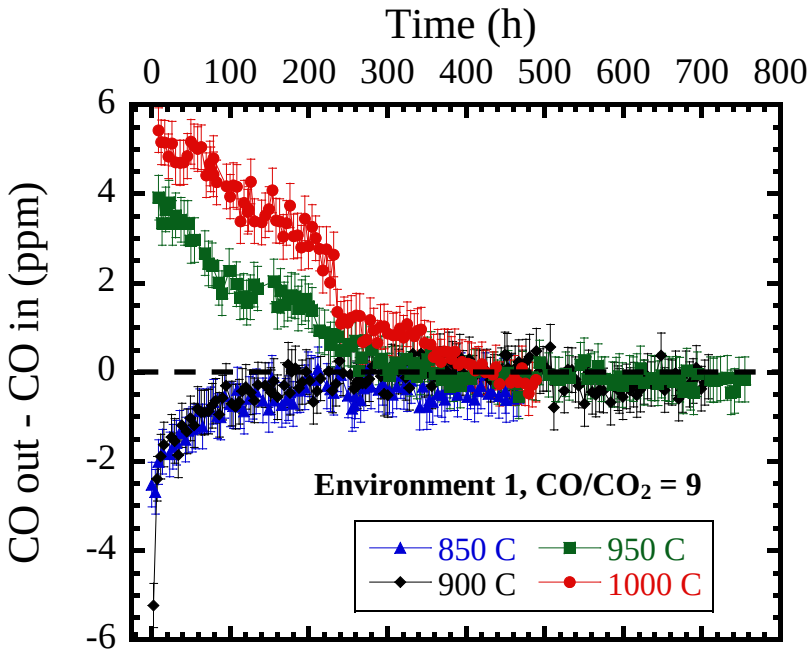

(b)

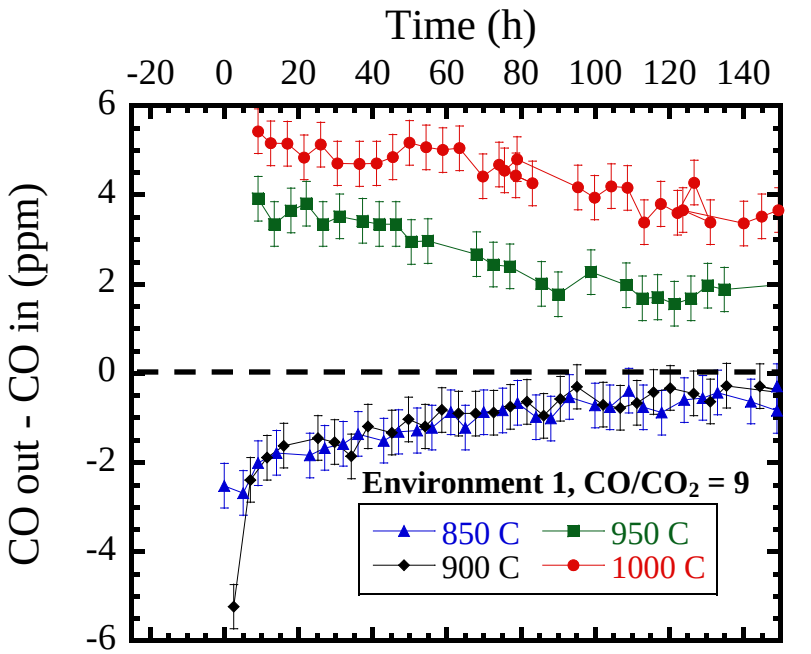

Figure 4.1 (a) Plot of CO out – CO in vs. time in environment 1(CO/CO_2 = 9) over 850 - 1000°C. (b) portion of the plot showing the consumption/evolution behavior in first 150h of oxidation.

(a)

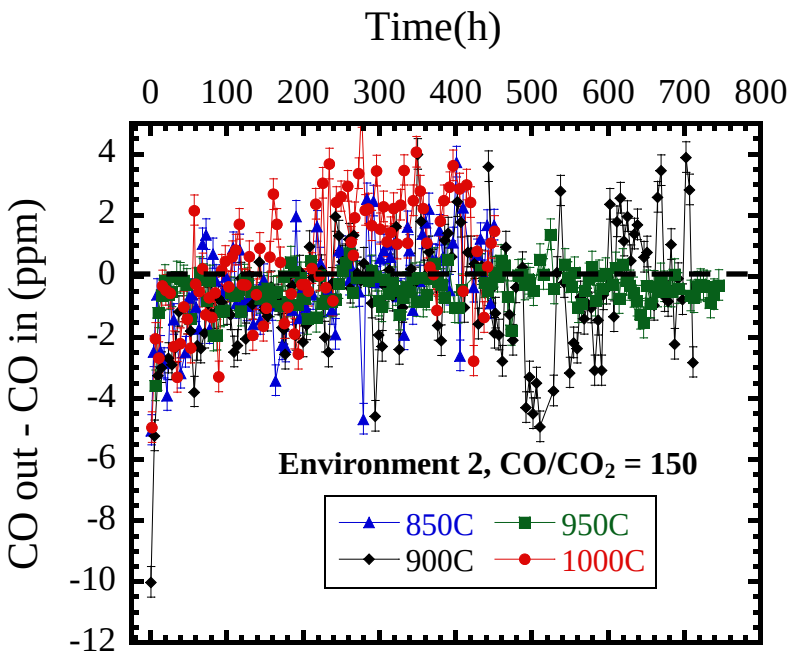

(b)

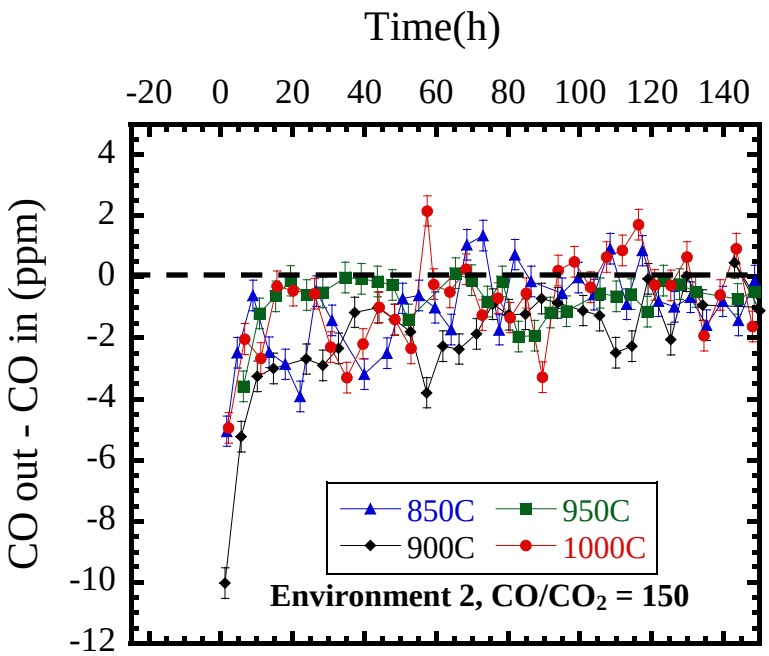

Figure 4.2 (a) Plot of CO out – CO in vs. time in environment 2(CO/CO_2 = 150) over 850 - 1000°C. (b) portion of the plot showing the consumption/evolution behavior in first 150h of oxidation.

(a)

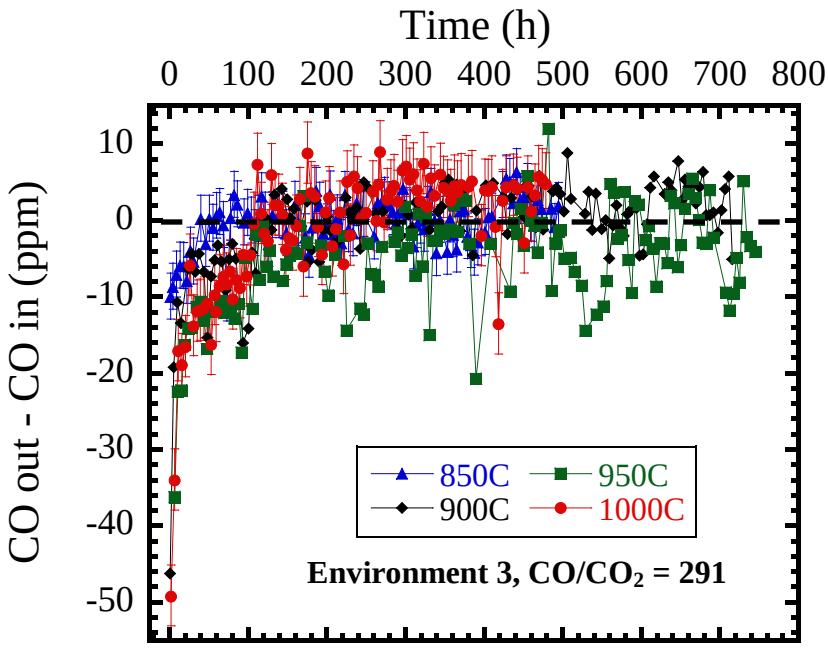

(b)

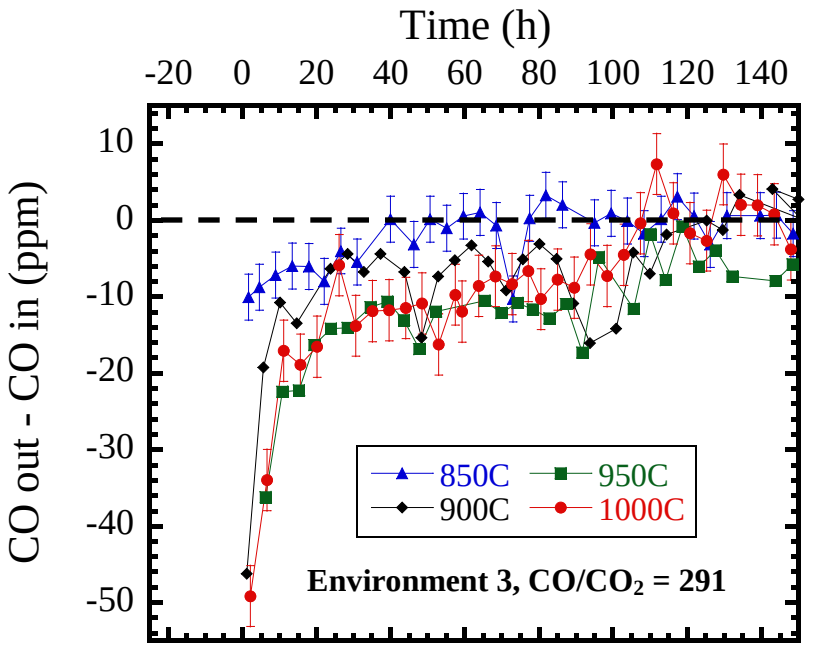

Figure 4.3(a) Plot of CO out – CO in vs. time in environment 3(CO/CO_2 = 291) over 850 - 1000°C. (b) portion of the plot showing the consumption/evolution behavior in first 150h of oxidation.

(a)

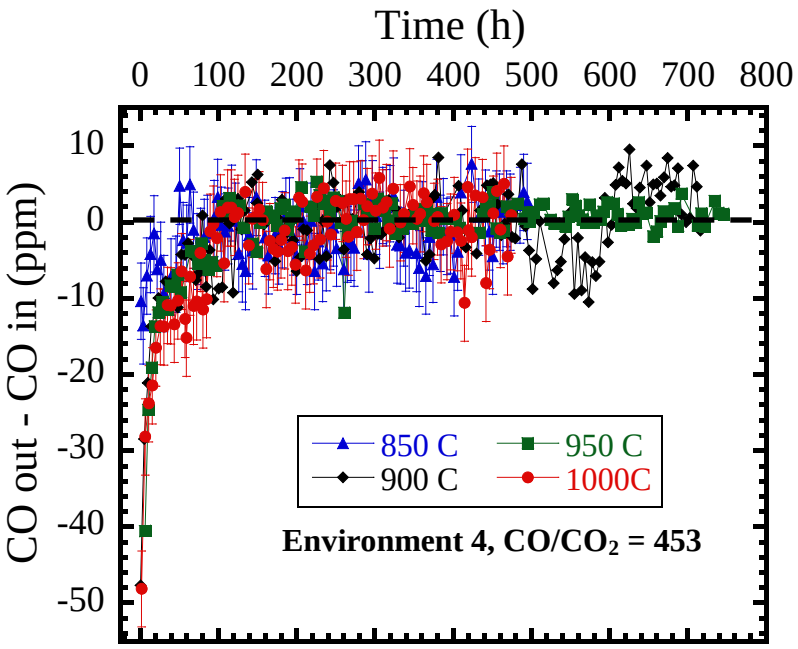

(b)

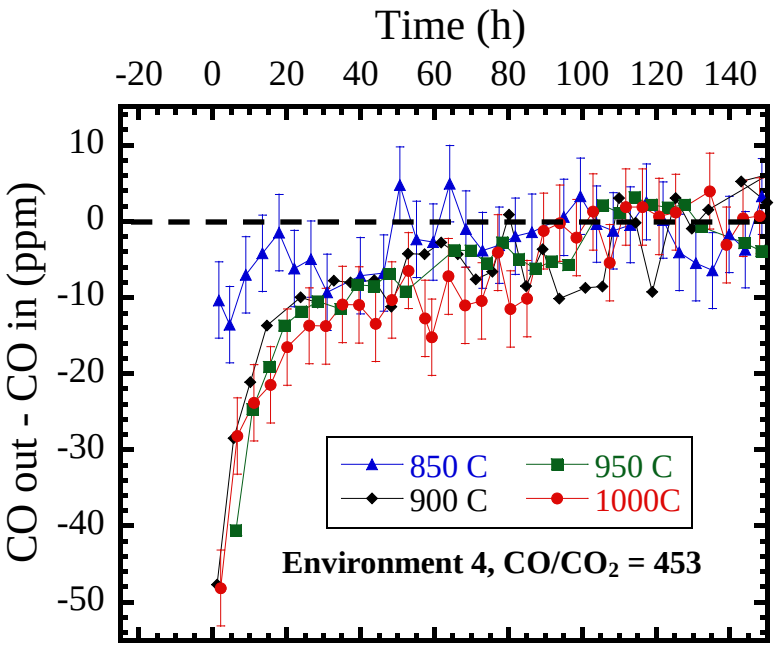

Figure 4.4(a) Plot of CO out – CO in vs. time in environment 4(CO/CO_2 = 453) over 850 - 1000°C. (b) portion of the plot showing the consumption/evolution behavior in first 150h of oxidation.

(a)

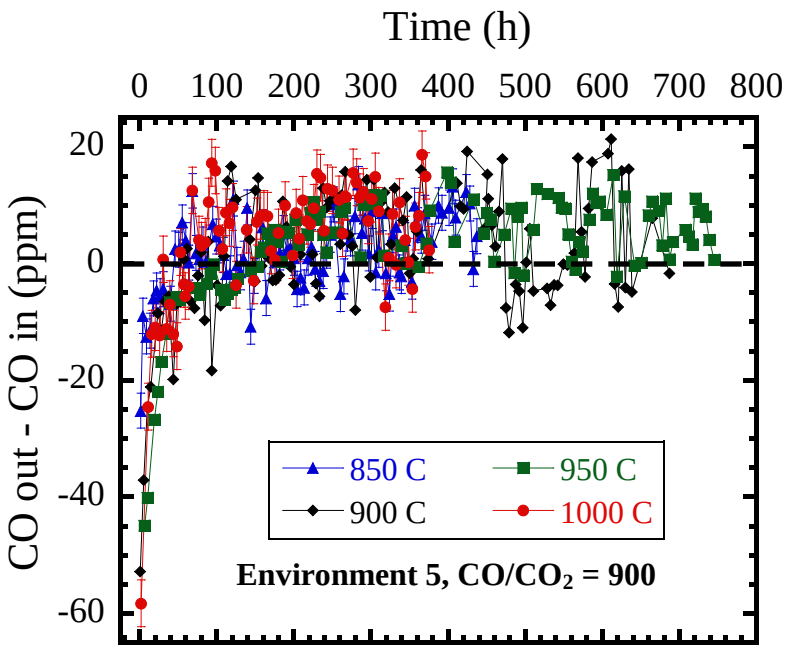

(b)

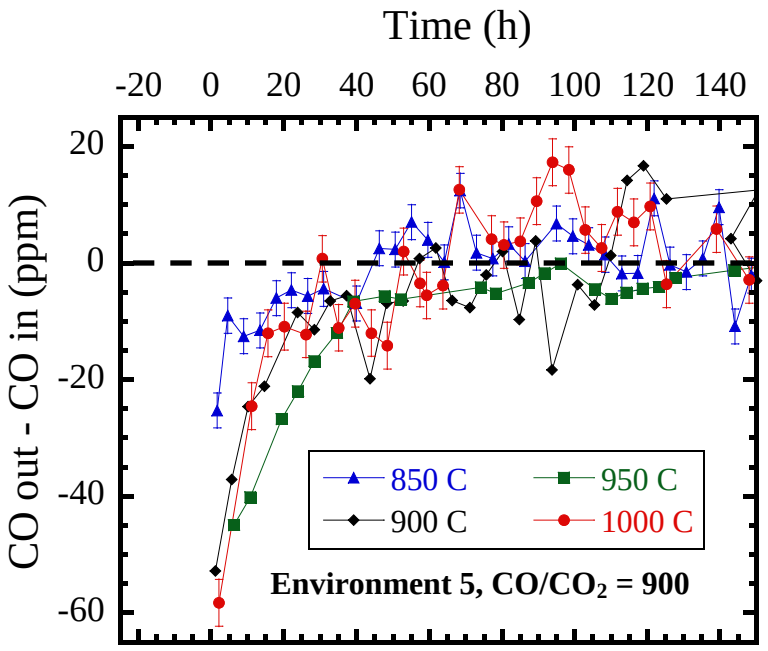

Figure 4.5 (a) Plot of CO out – CO in vs. time in environment 5(CO/CO_2 = 900) over 850 - 1000°C. (b) portion of the plot showing the consumption/evolution behavior in first 150h of oxidation.

(a)

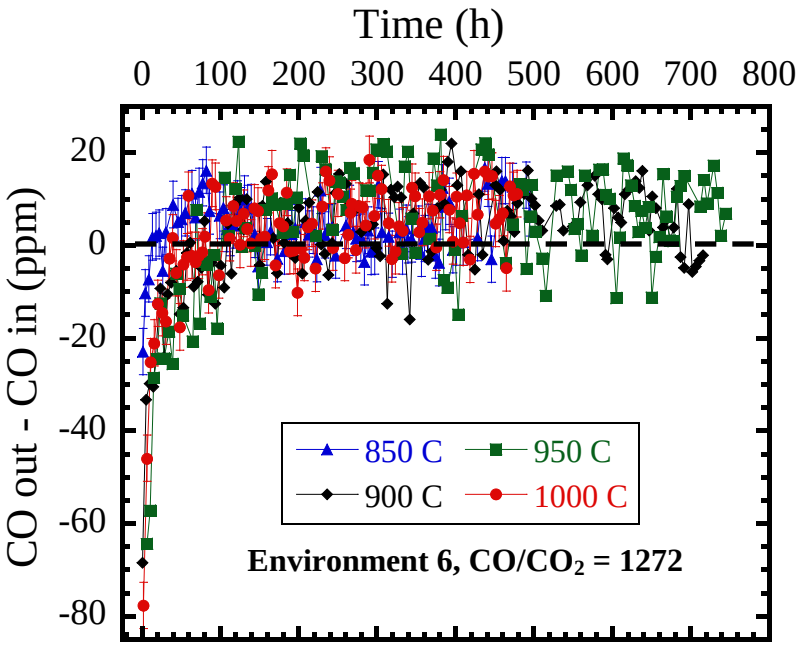

(b)

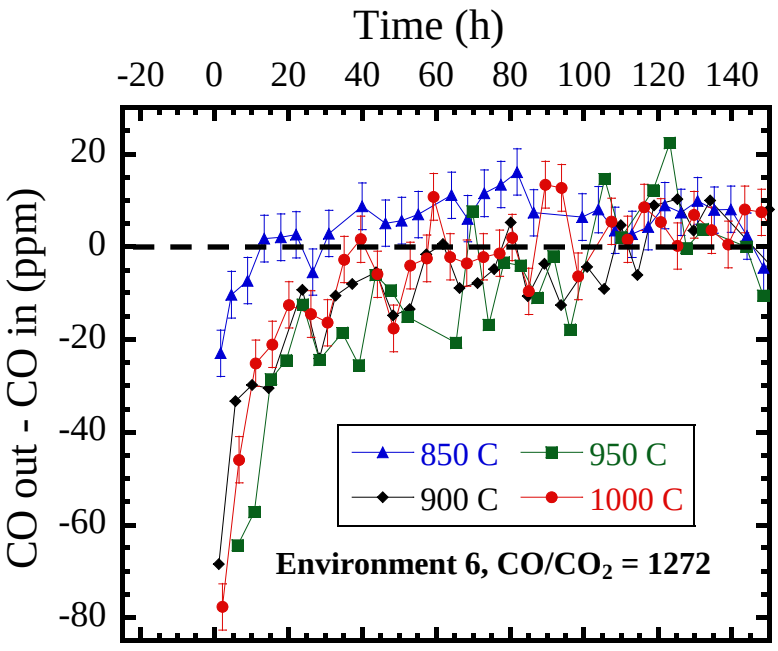

Figure 4.6 (a) Plot of CO out – CO in vs. time in environment 6(CO/CO_2 = 1272) over 850 - 1000°C. (b) portion of the plot showing the consumption/evolution behavior in first 150h of oxidation.

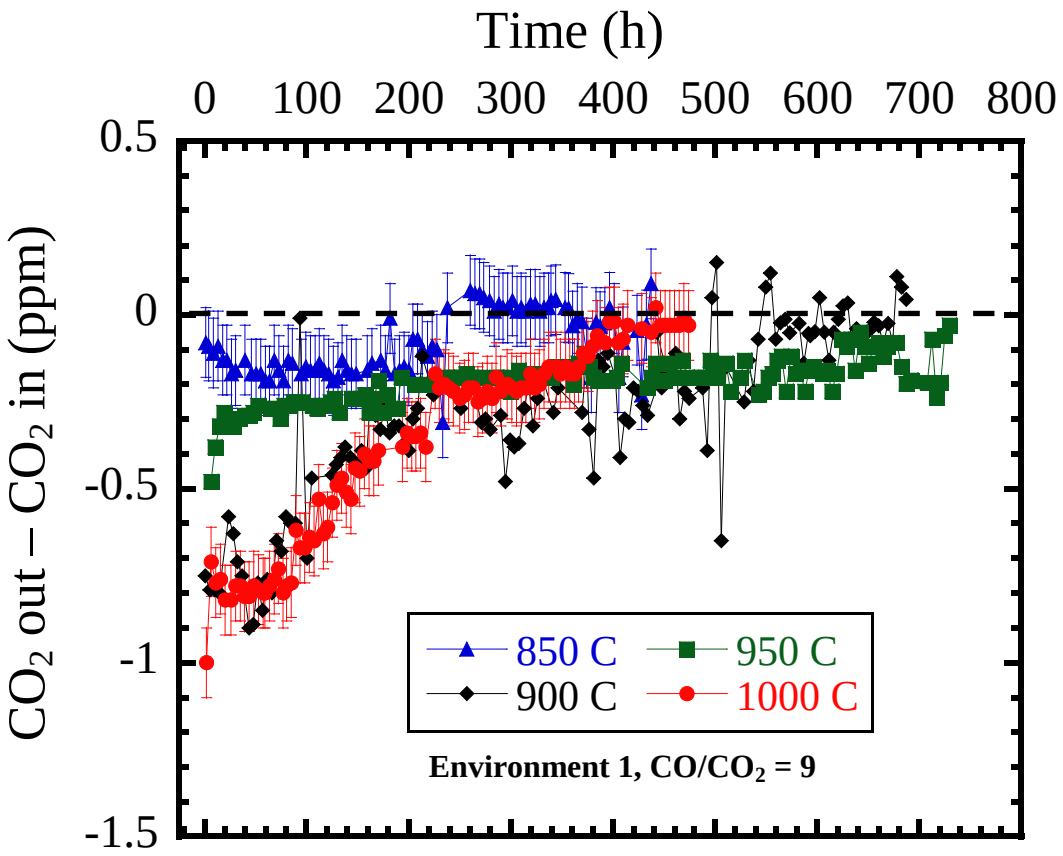

Figure 4.7 Plot of CO_2 out – CO_2 in vs. time in environment 1(CO/CO_2 = 9) over 850 - 1000°C

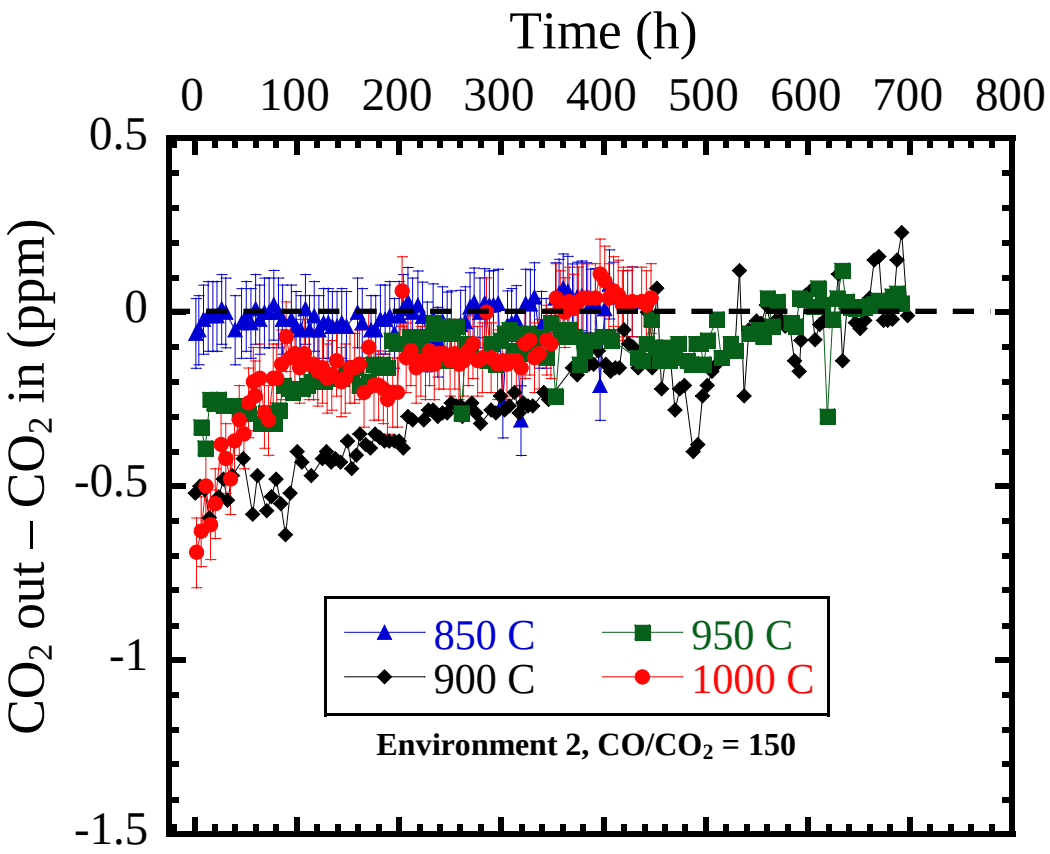

Figure 4.8 Plot of CO_2 out – CO_2 in vs. time in environment 2(CO/CO_2 = 150) over 850 - 1000°C.

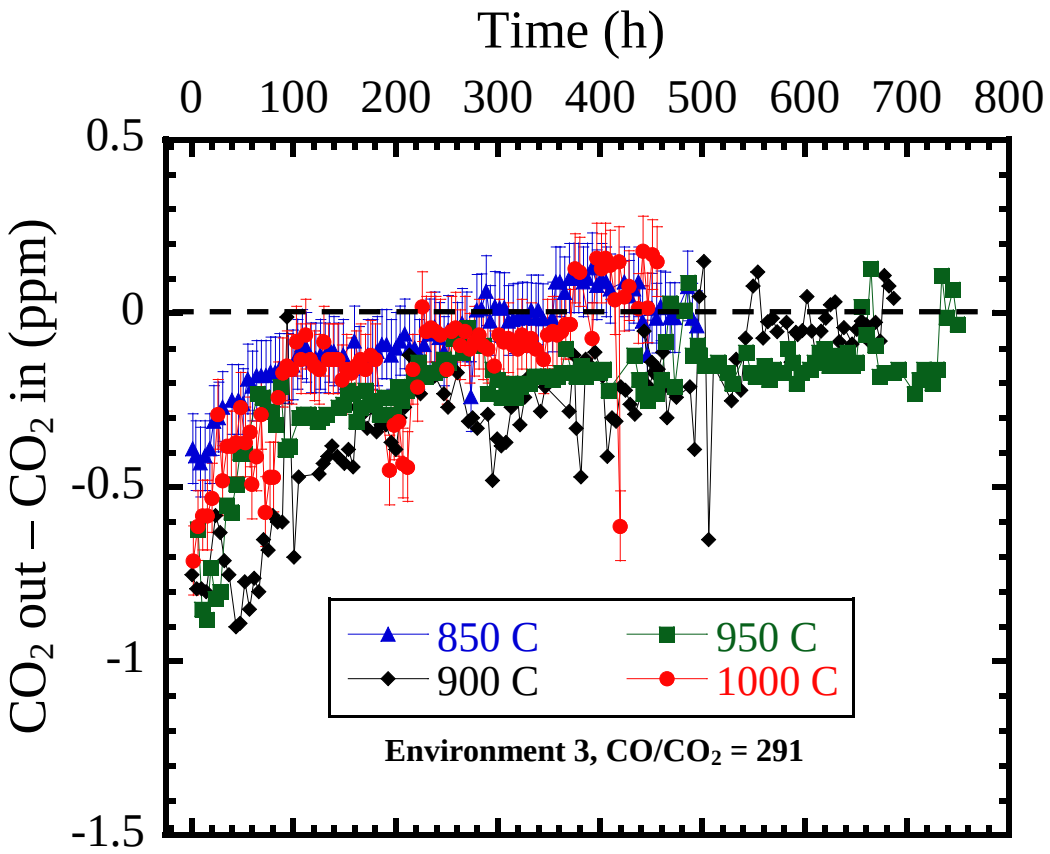

Figure 4.9 Plot of CO_2 out – CO_2 in vs. time in environment 3(CO/CO_2 = 291) over 850 - 1000°C.

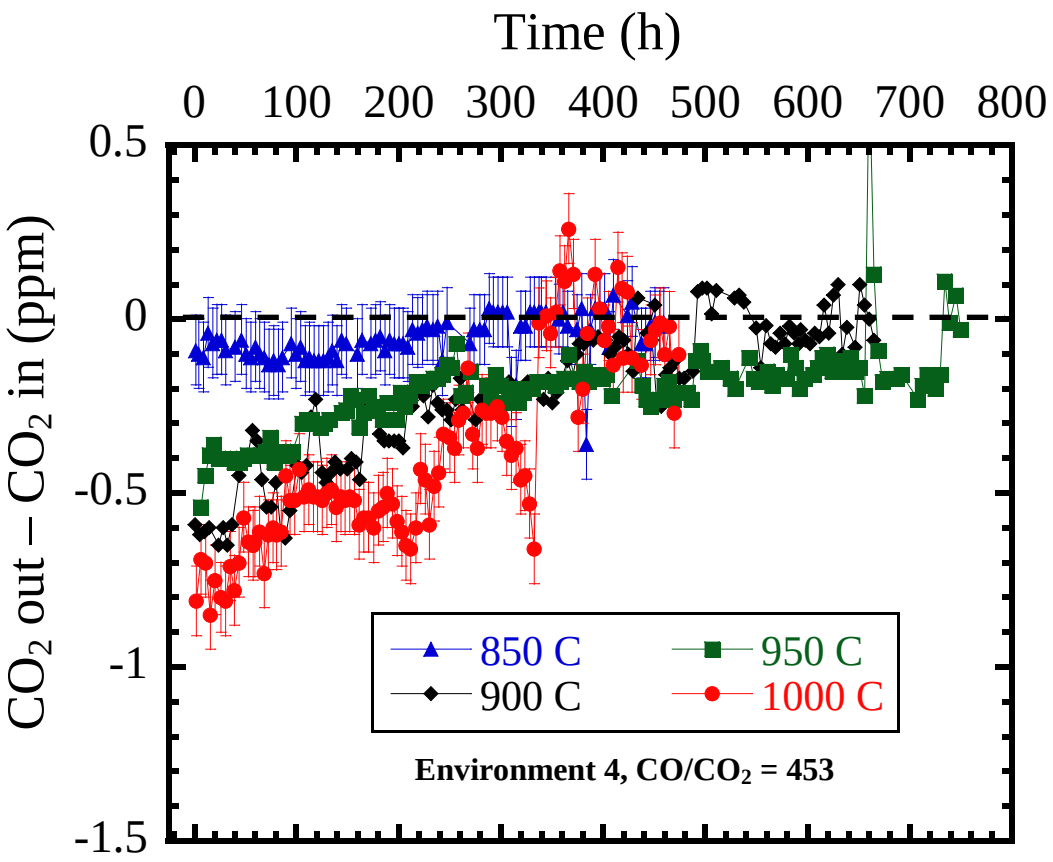

Figure 4.10 Plot of CO_2 out – CO_2 in vs. time in environment 4(CO/CO_2 = 453) over 850 - 1000°C.

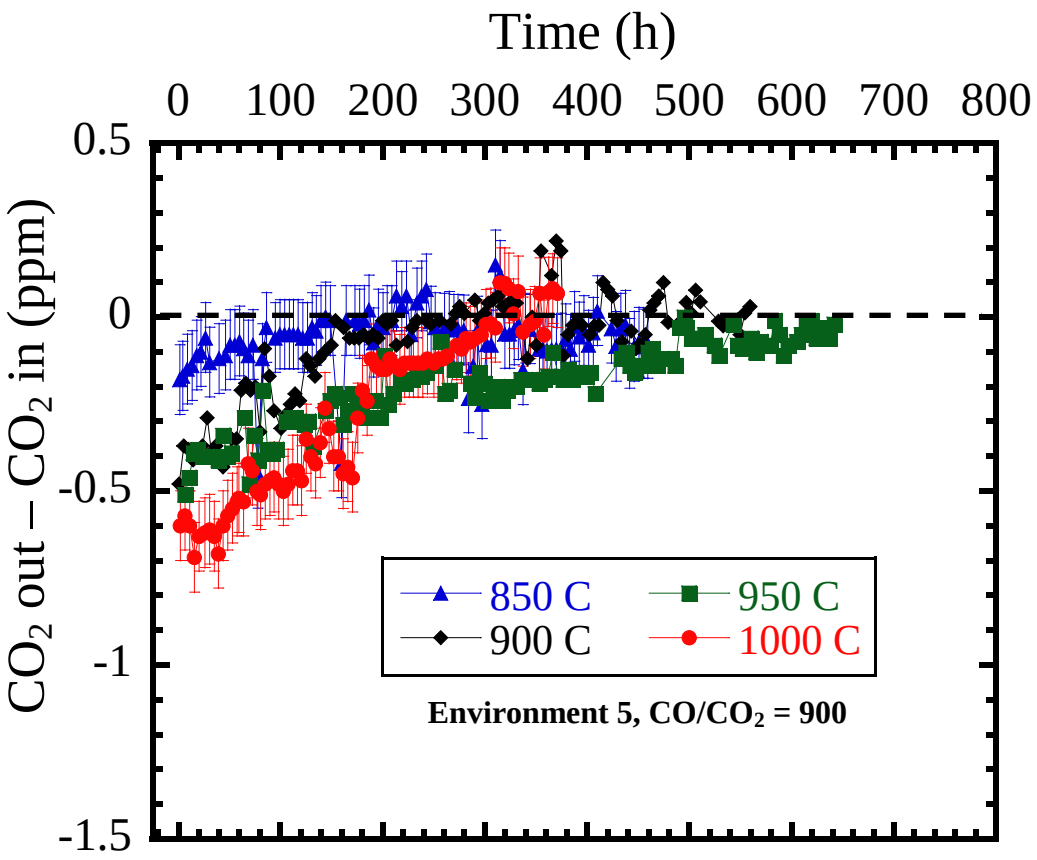

Figure 4.11 Plot of CO_2 out – CO_2 in vs. time in environment 5(CO/CO_2 = 900) over 850 - 1000°C.

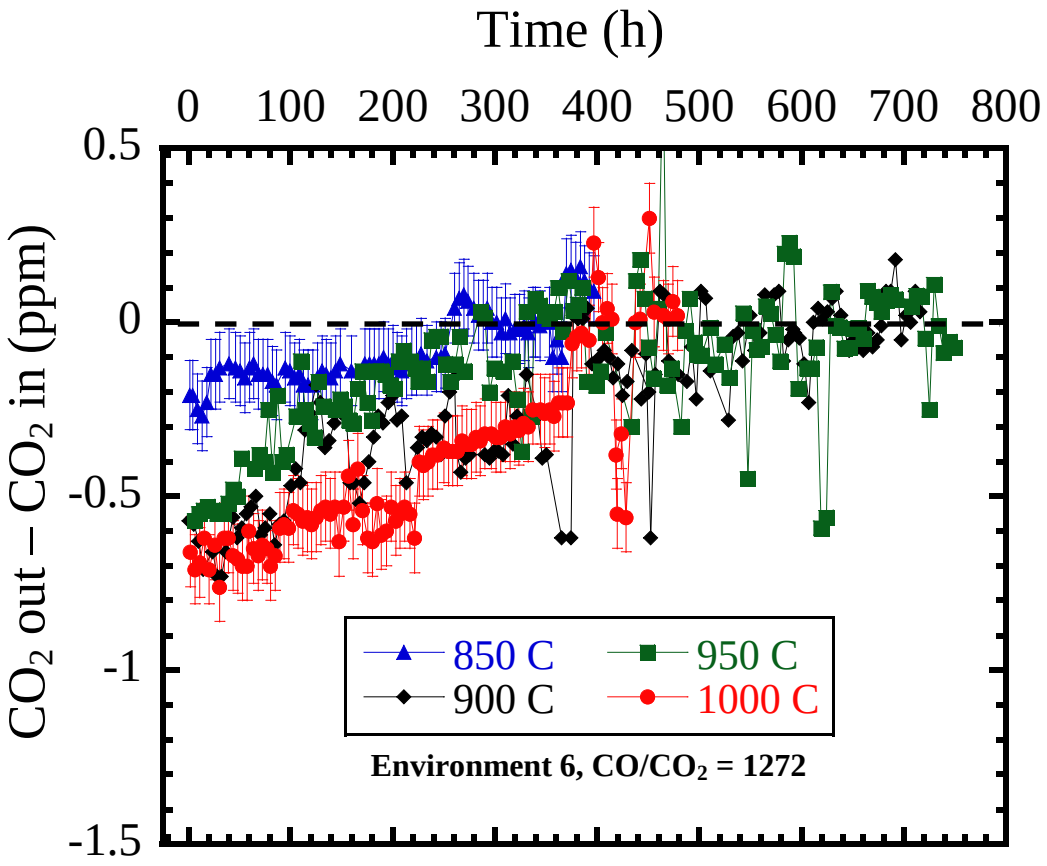

Figure 4.12 Plot of CO_2 out – CO_2 in vs. time in environment 6(CO/CO_2 = 1272) over 850 - 1000°C.

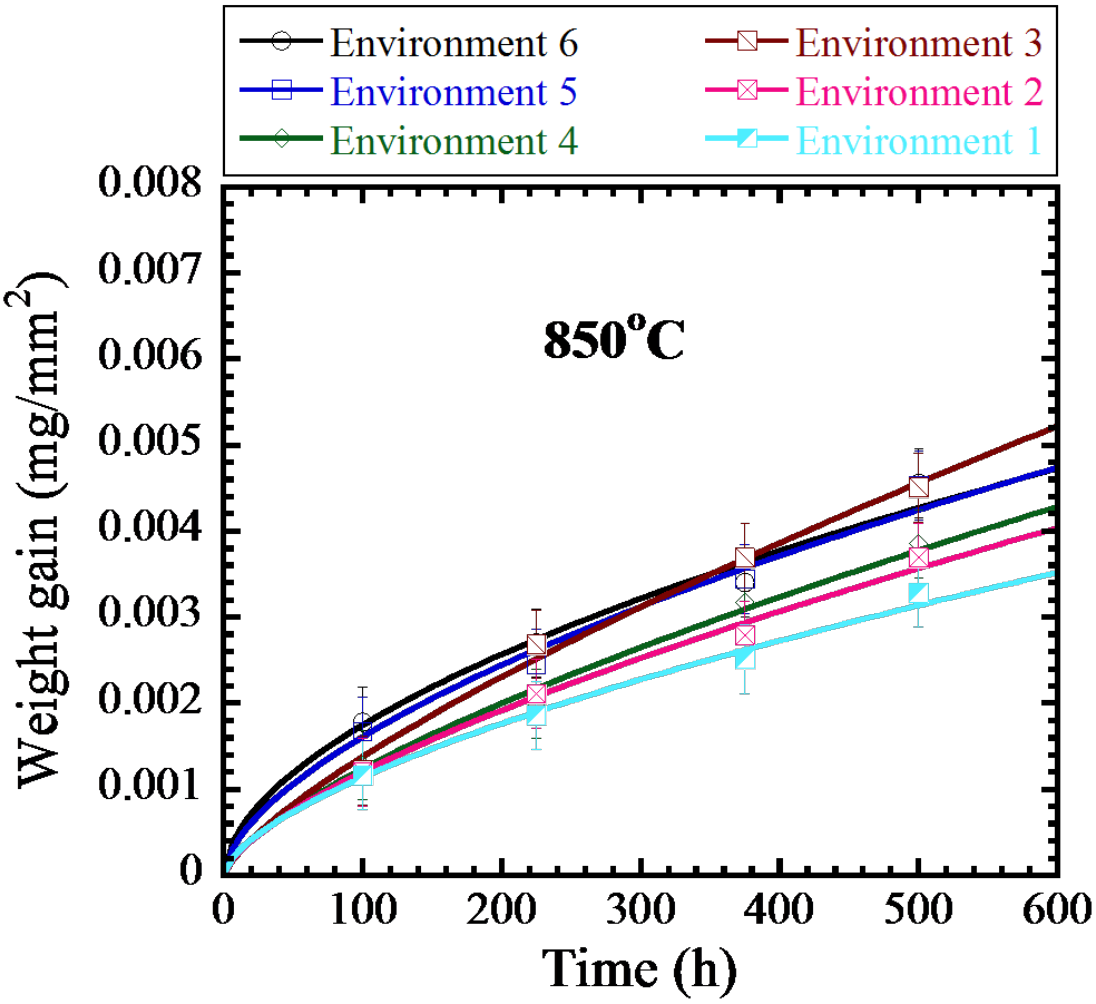

Figure 4.13 Weight gain vs. time in the six tested environments at 850°C.

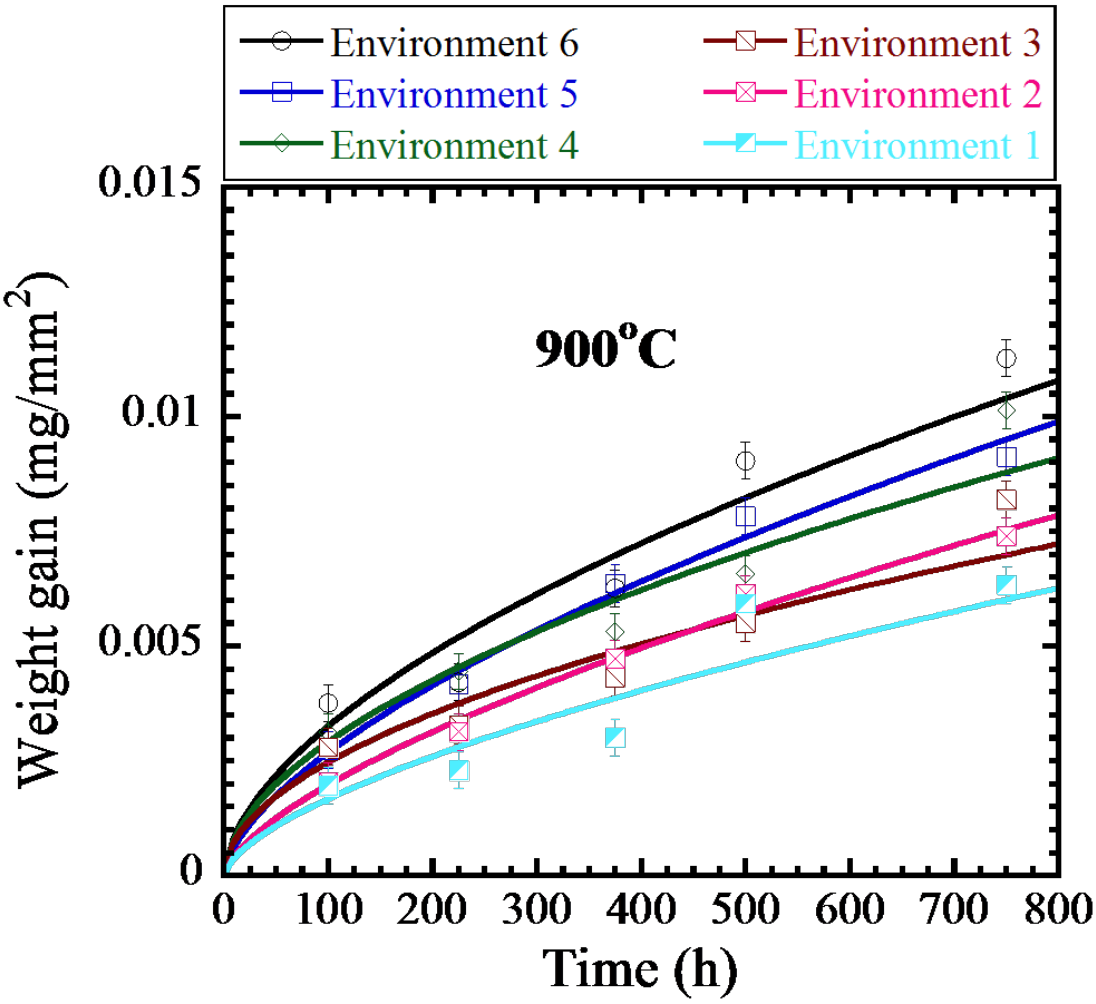

Figure 4.14 Weight gain vs. time in the six tested environments at 900°C.

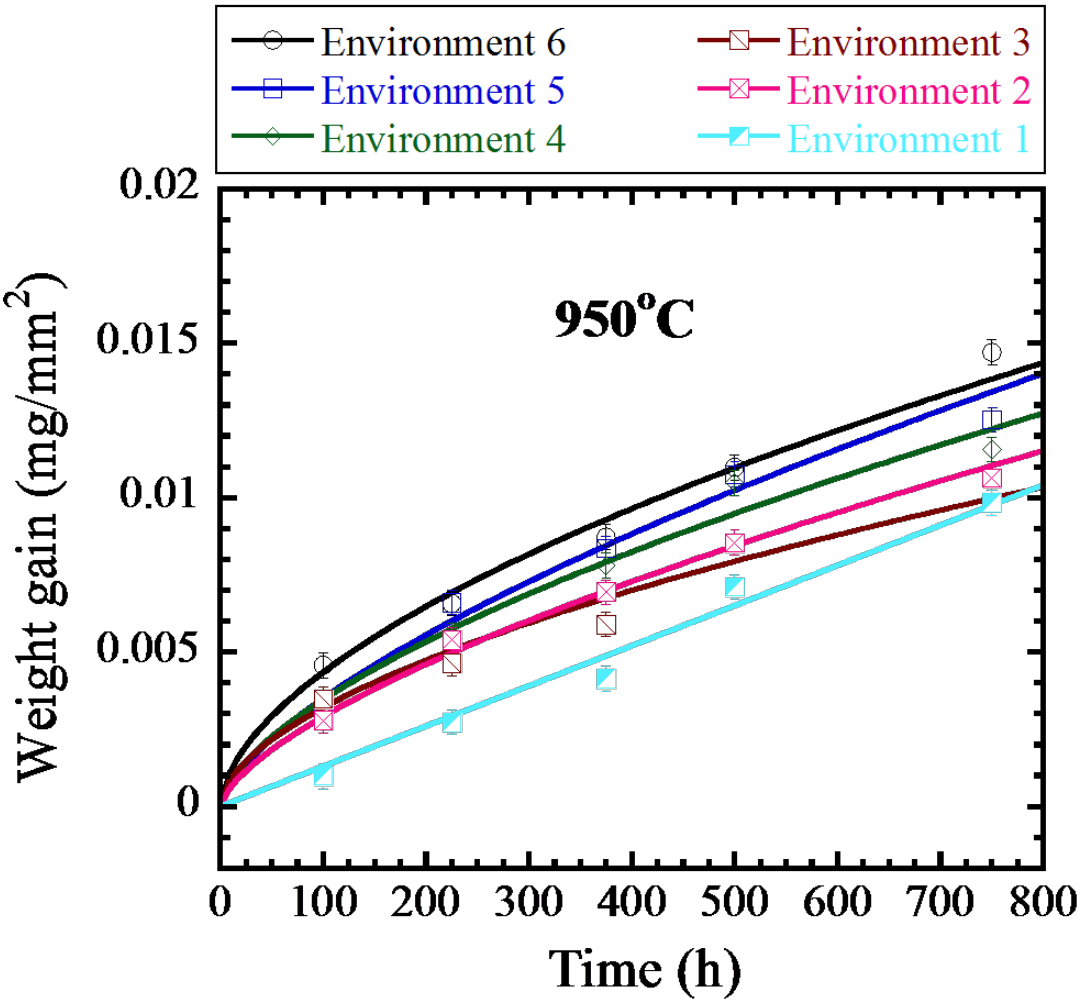

Figure 4.15 Weight gain vs. time in the six tested environments at 950°C.

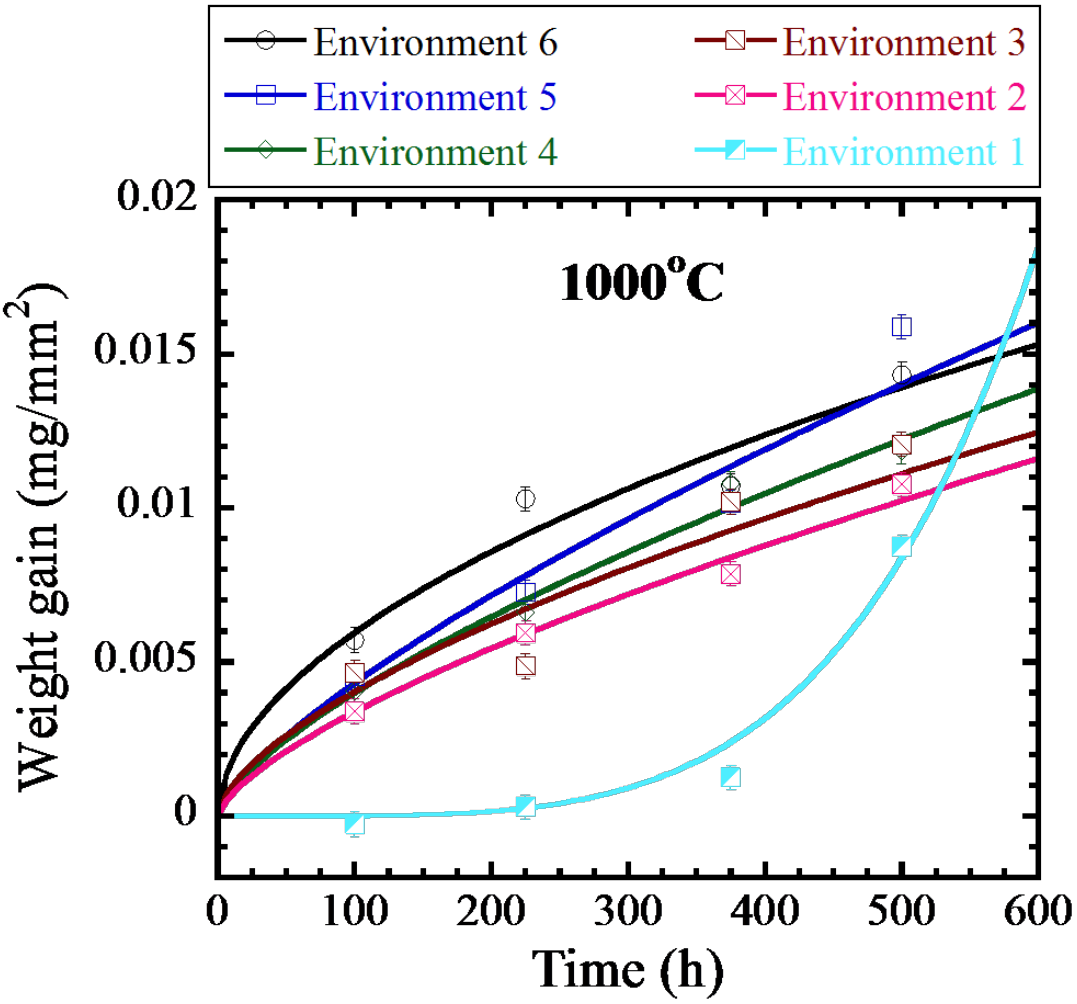

Figure 4.16 Weight gain vs. time in the six tested environments at 1000°C.

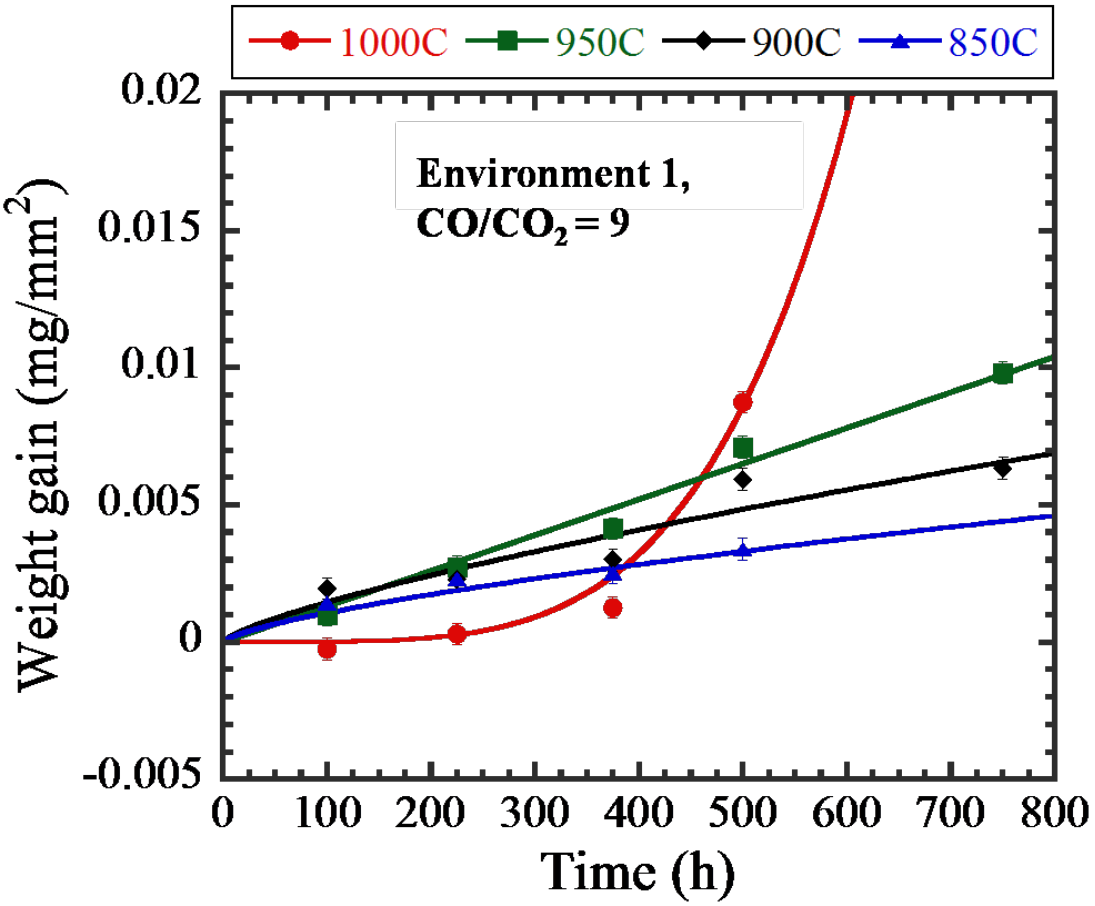

Figure 4.17 Weight gain vs. temperature in environment 1 ($CO/CO_2 = 9$).

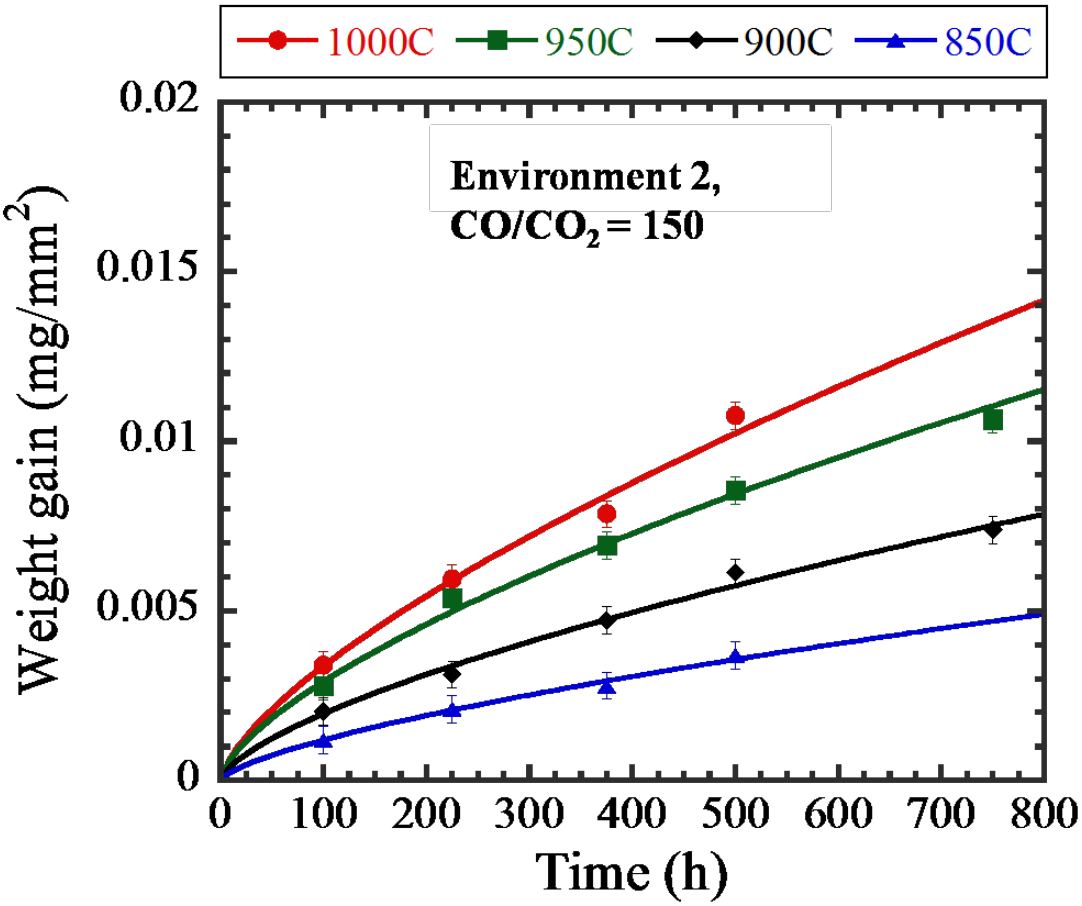

Figure 4.18 Weight gain vs. temperature in environment 2 (CO/CO_2 = 150).

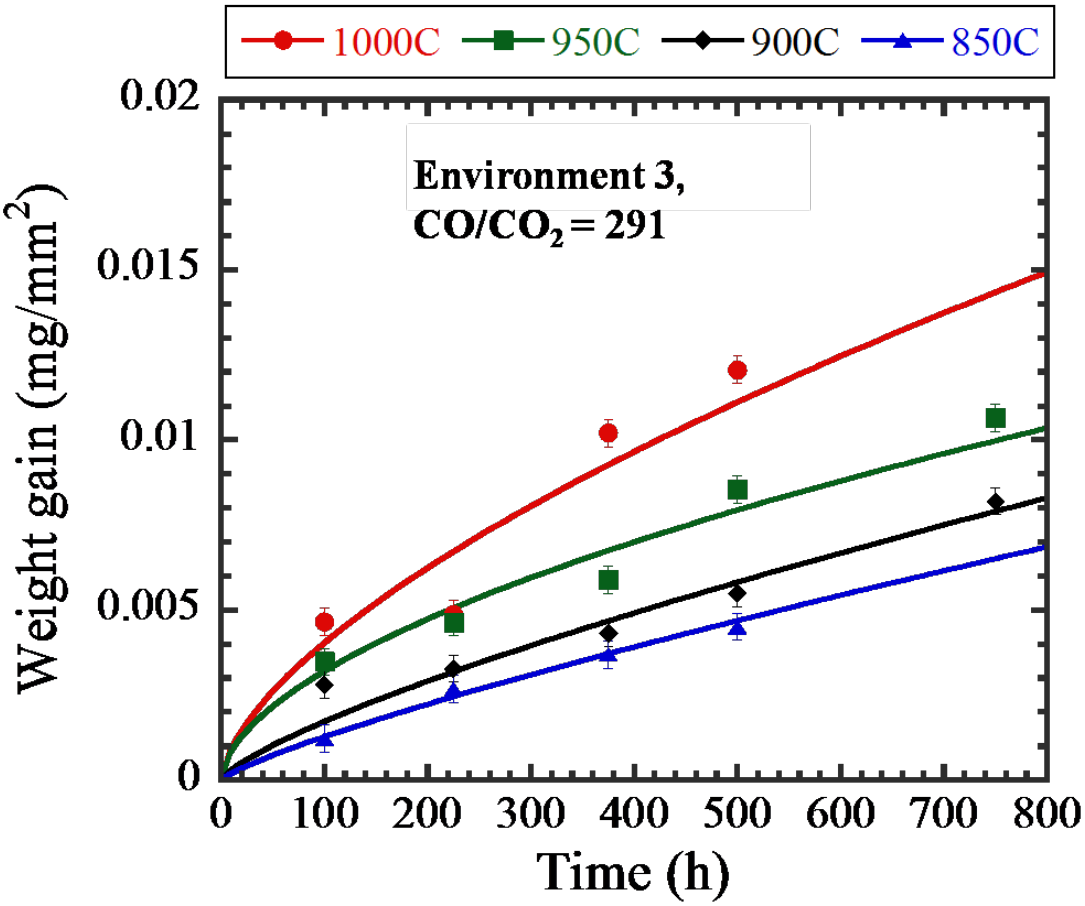

Figure 4.19 Weight gain vs. temperature in environment 3 (CO/CO_2 = 291).

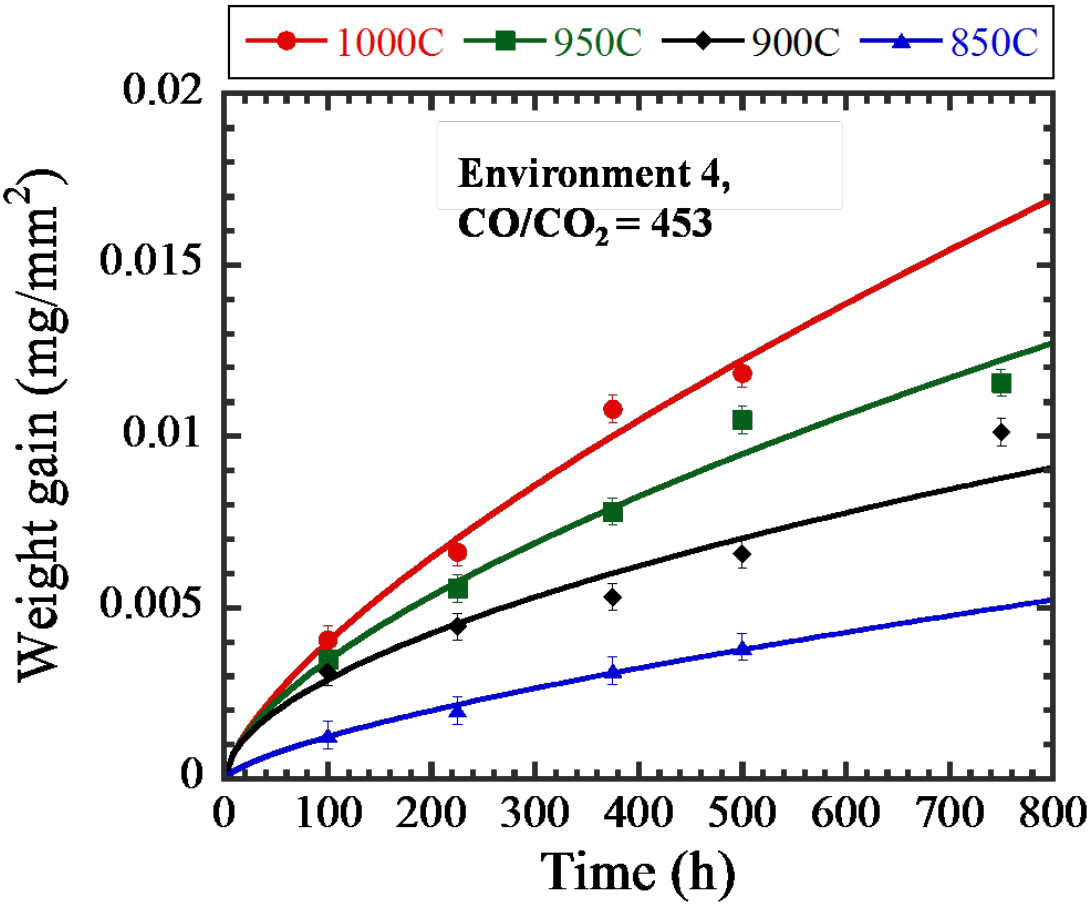

Figure 4.20 Weight gain Vs. temperature in environment 4 (CO/CO_2 = 453).

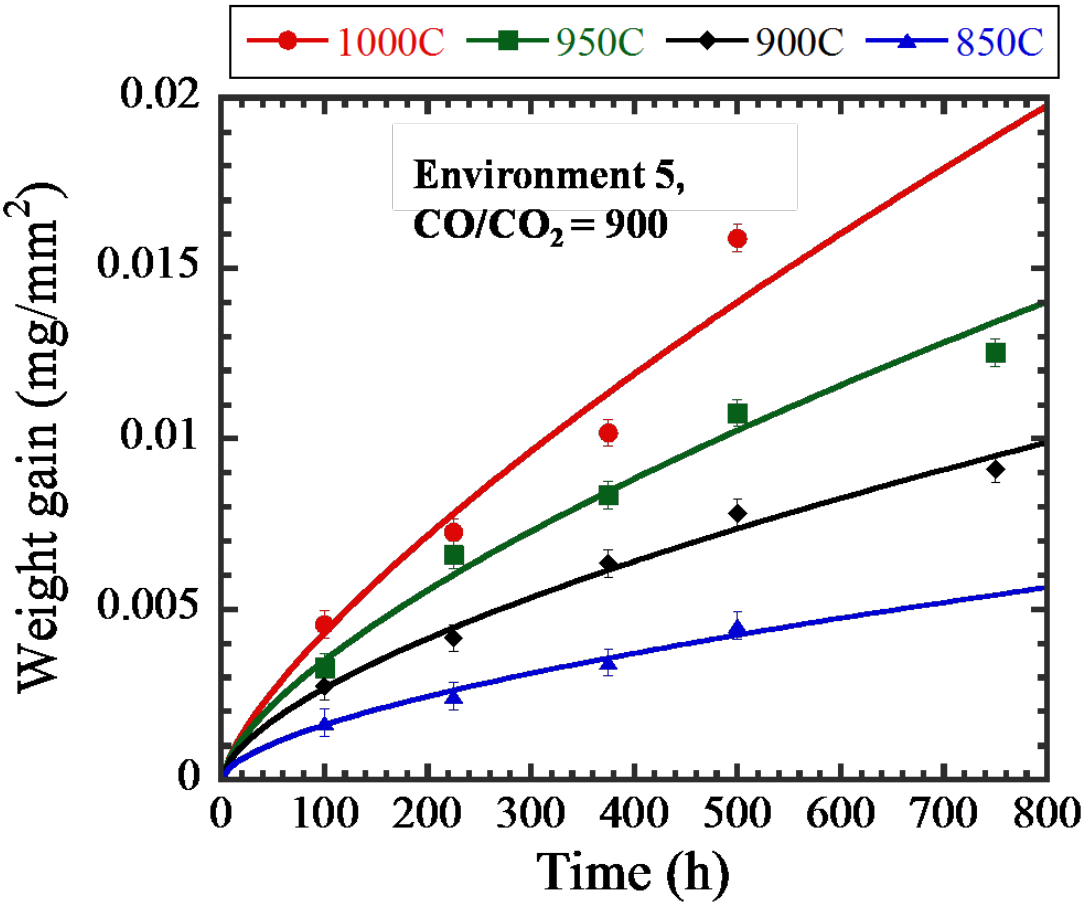

Figure 4.21 Weight gain Vs. temperature in environment 5 ($CO/CO_2 = 900$).

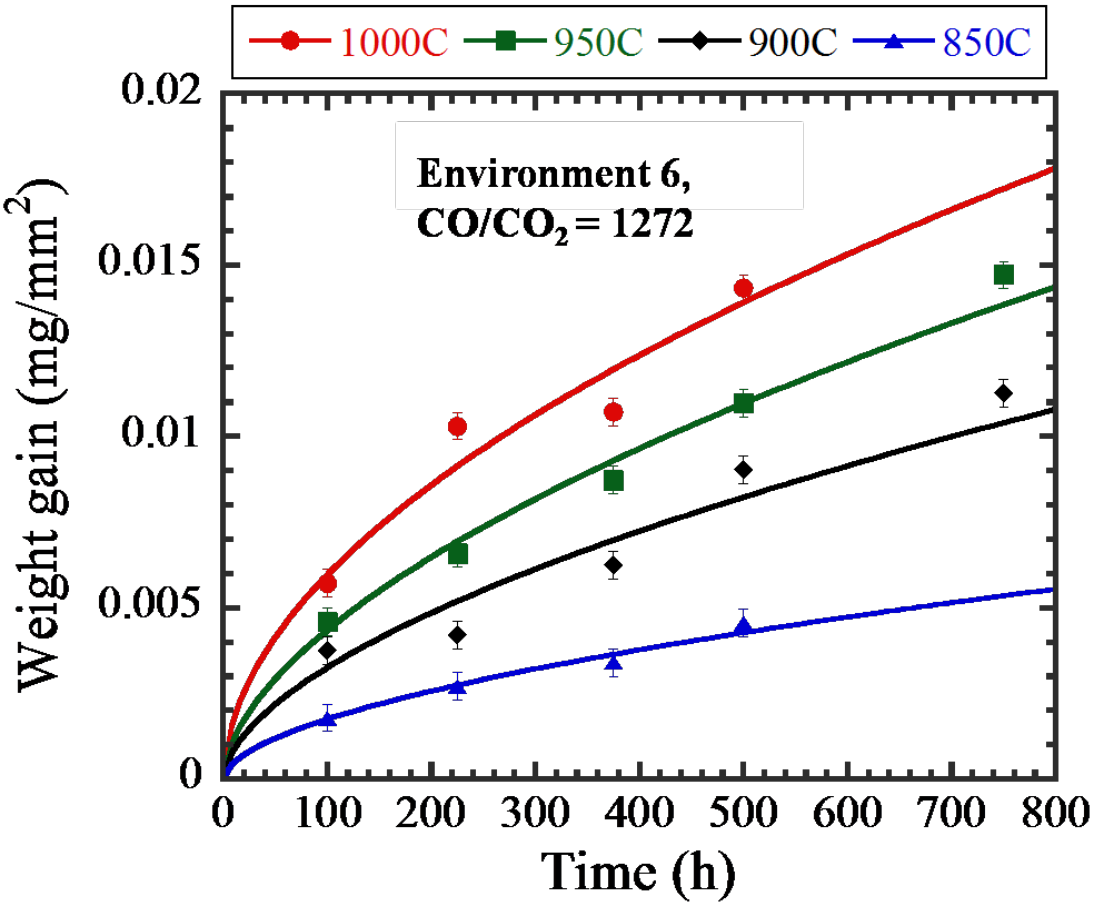

Figure 4.22 Weight gain Vs. temperature in environment 6 (CO/CO_2 = 1272).

(a)

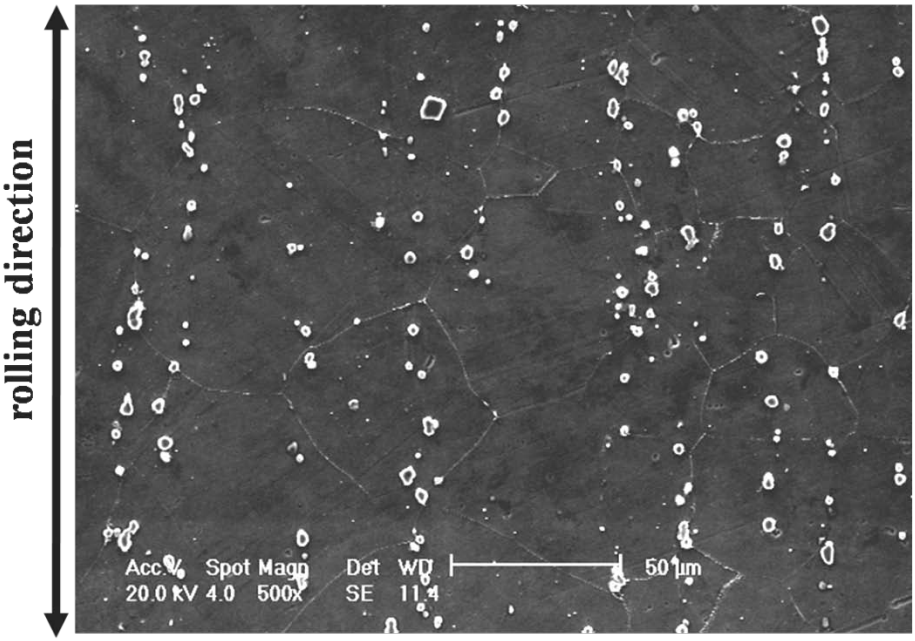

(b)

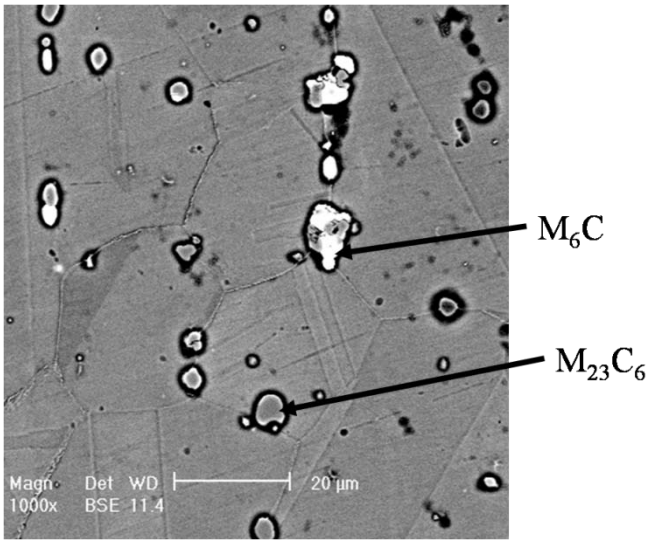

Figure 4.23 Microstructure of the etched **as received alloy 617** (a) secondary electron image showing the stringers of carbides along the rolling direction, and (b) back scattered electron image showing the two types of carbides present. The darker carbides are $M_{23}C_6$ type of carbide, whereas the bright carbides are M_6C type of carbide, where M is Cr, Mo.

(a)

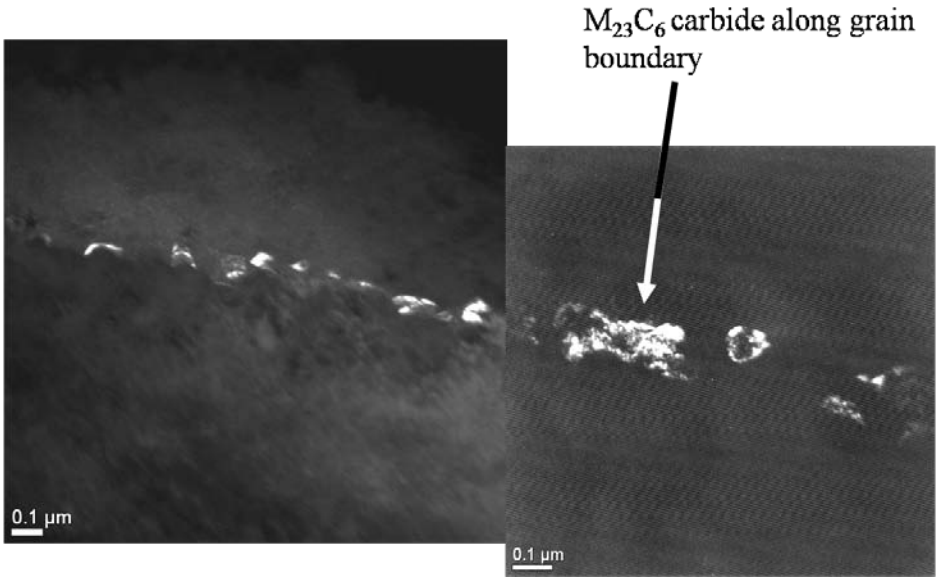

(b)

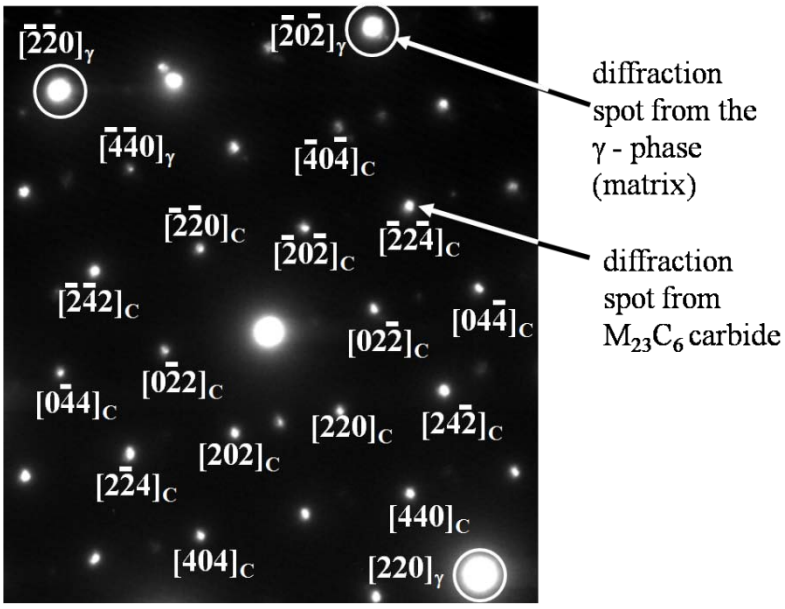

Figure 4.24 (a) Transmission electron image of the carbide along a grain boundary in the **as received alloy 617**.Small precipitates of $M_{23}C_6$ carbides (where M is Cr, Mo) can be seen along the grain boundary. (b) Diffraction pattern from the grain boundary carbide. In this pattern, the larger spots (encircled spots) are reflections from γ matrix and the small spots are reflections from the carbide.

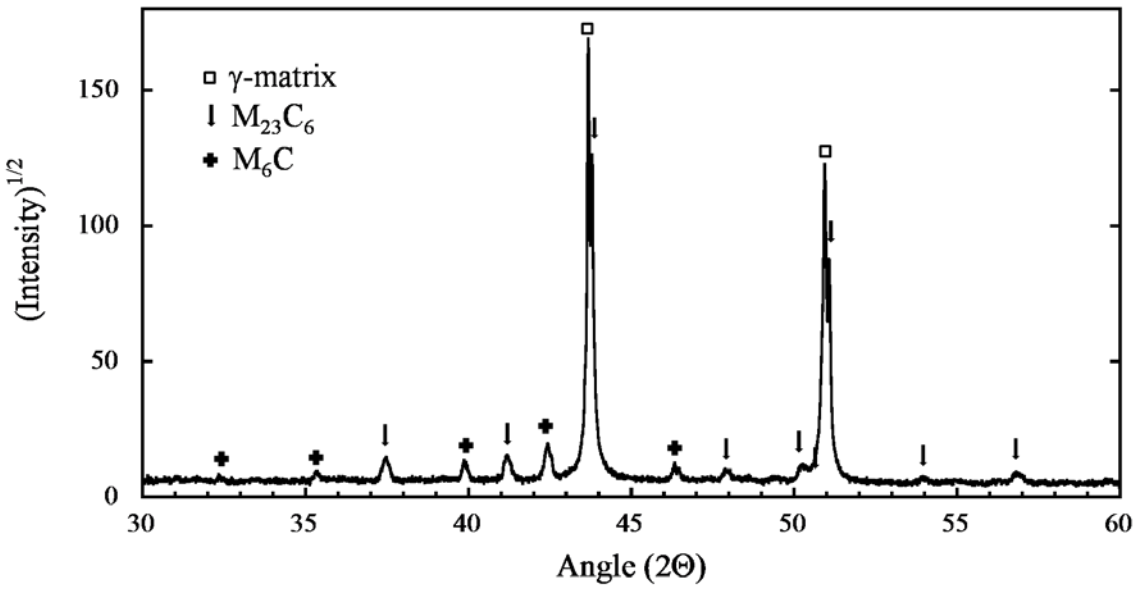

Figure 4.25 X-ray diffraction pattern of the as received alloy 617. The peaks of the γ (matrix), $M_{23}C_6$, and M_6C (where M is Cr, Mo) are marked. The CuKα radiation with of wavelength of 1.540 A°was used to obtain the XRD pattern.

(a)

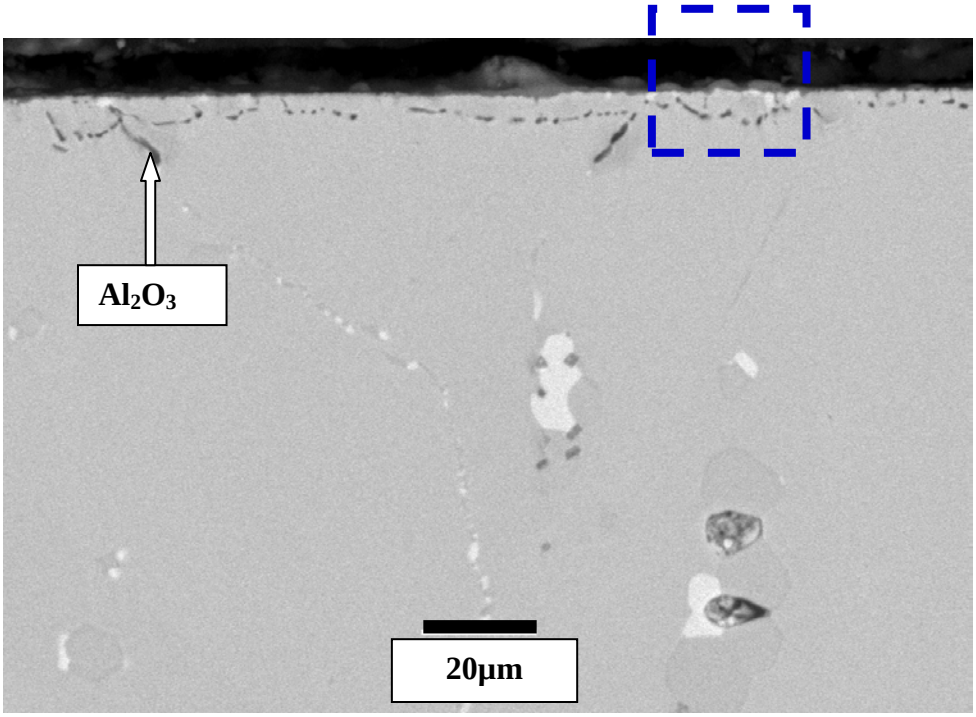

(b)

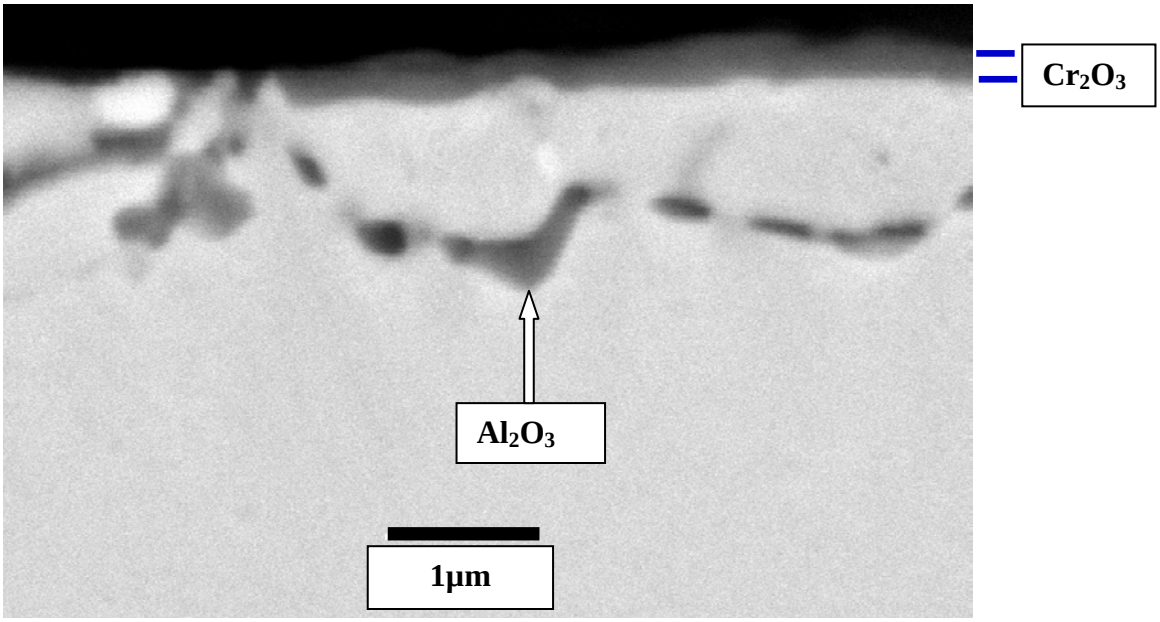

Figure 4.26 (a). Low magnification and (b) high magnification BSE image of the sample exposed in environment 1(CO/CO_2 = 9) at 850°C for 100h

(a)

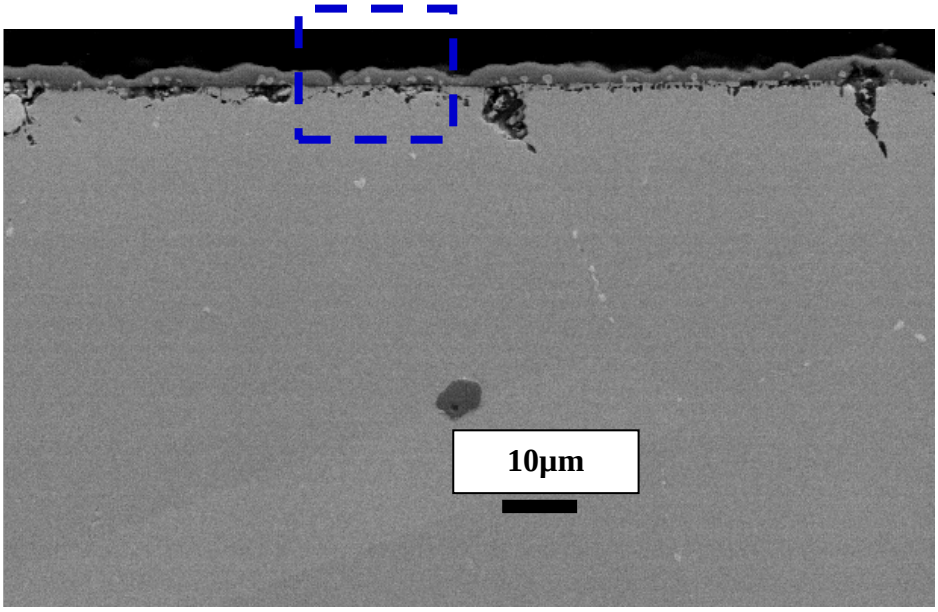

(b)

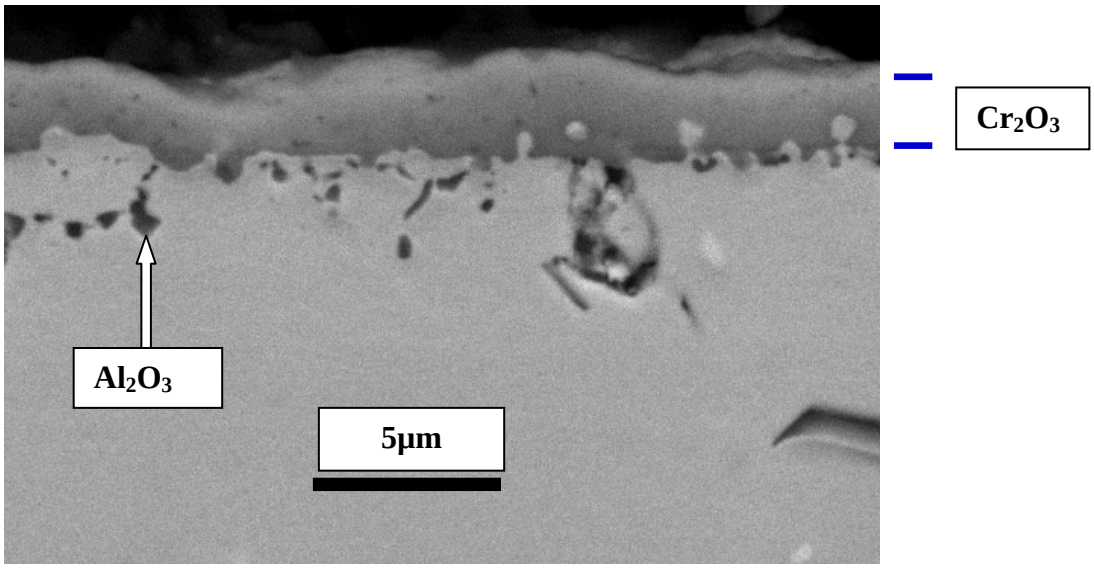

Figure 4.27 a). Low magnification and (b) high magnification BSE image of the sample exposed in environment 1(CO/CO_2 = 9) at 850°C for 500h.

(a)

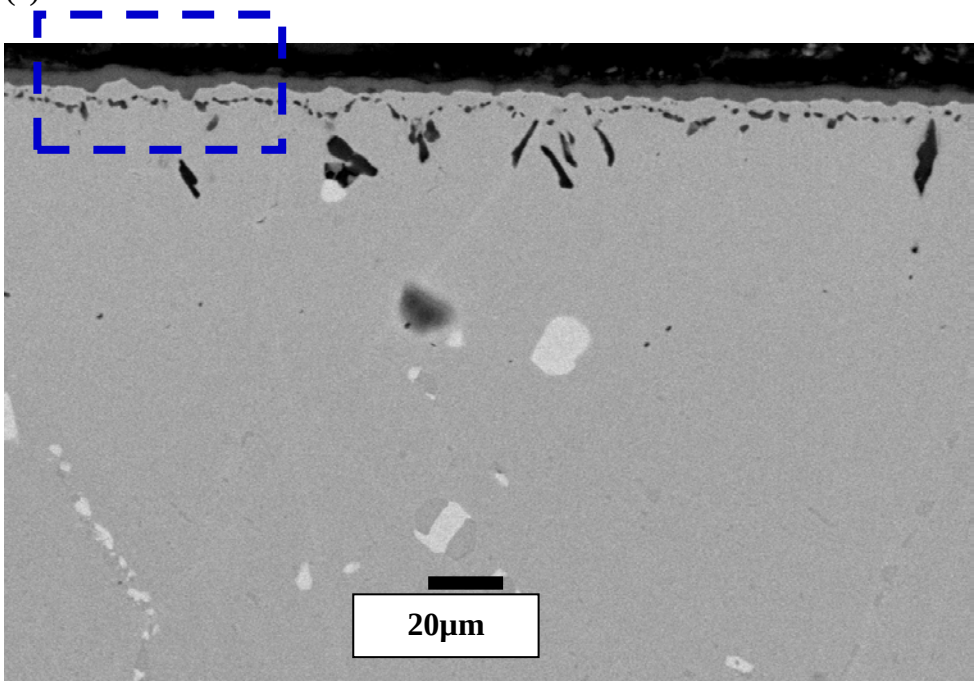

(b)

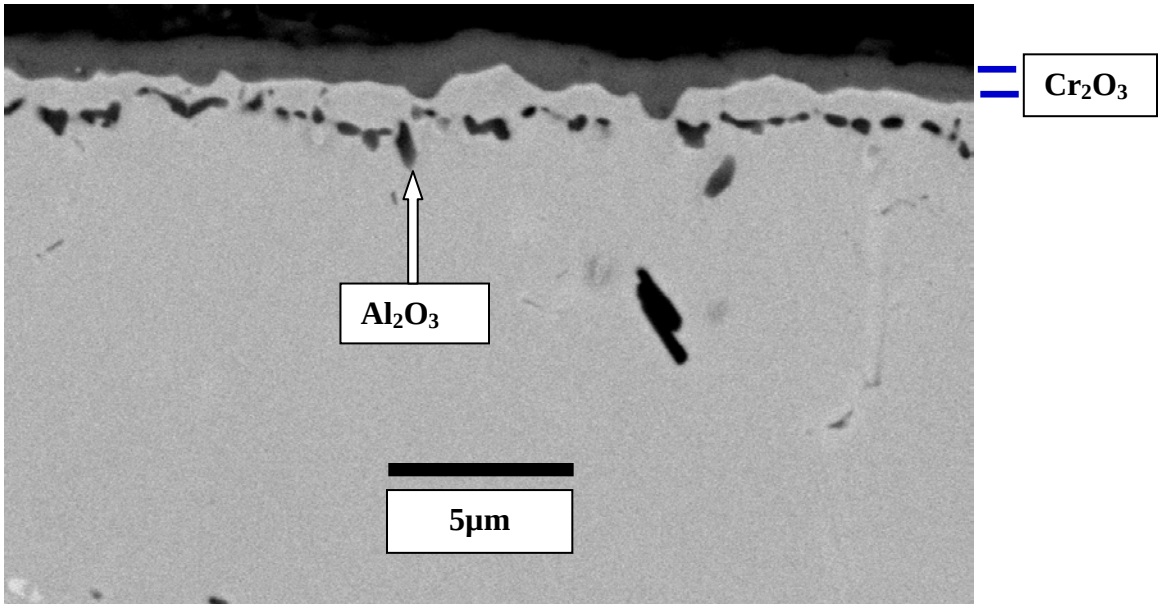

Figure 4.28 (a). Low magnification and (b) high magnification BSE image of the sample exposed in environment 1(CO/CO_2 = 9) at 900°C for 100h.

(a)

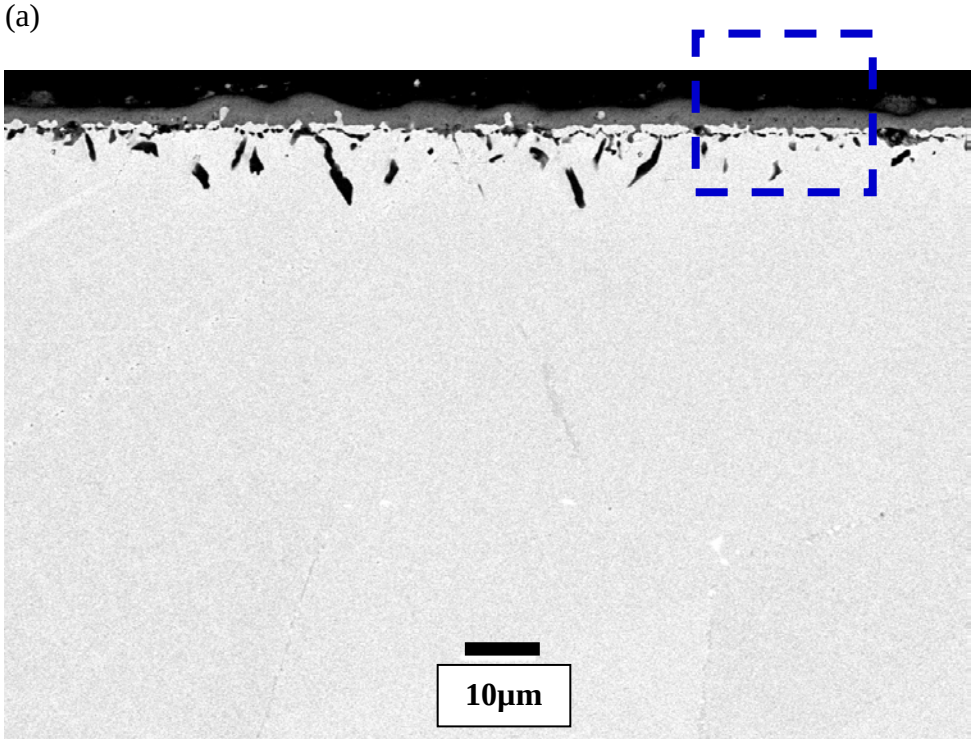

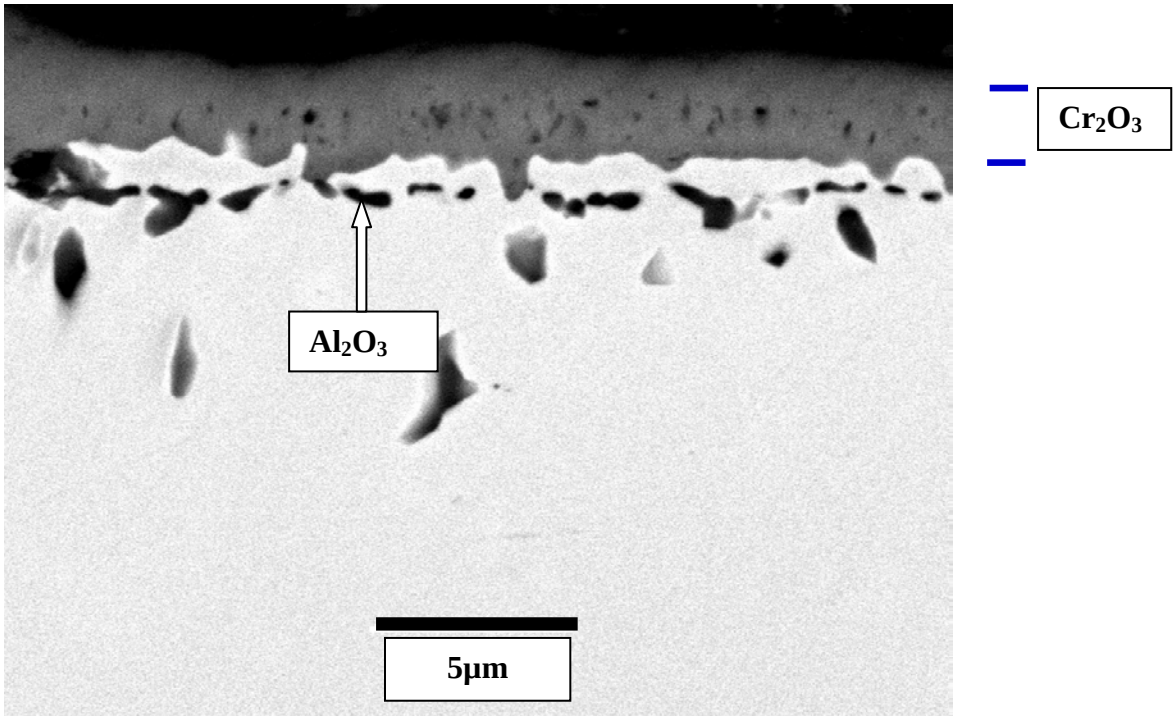

Figure 4.29 (a). Low magnification and (b) high magnification BSE image of the sample exposed in environment 1(CO/CO_2 = 9) at 900°C for 500h.

(a)

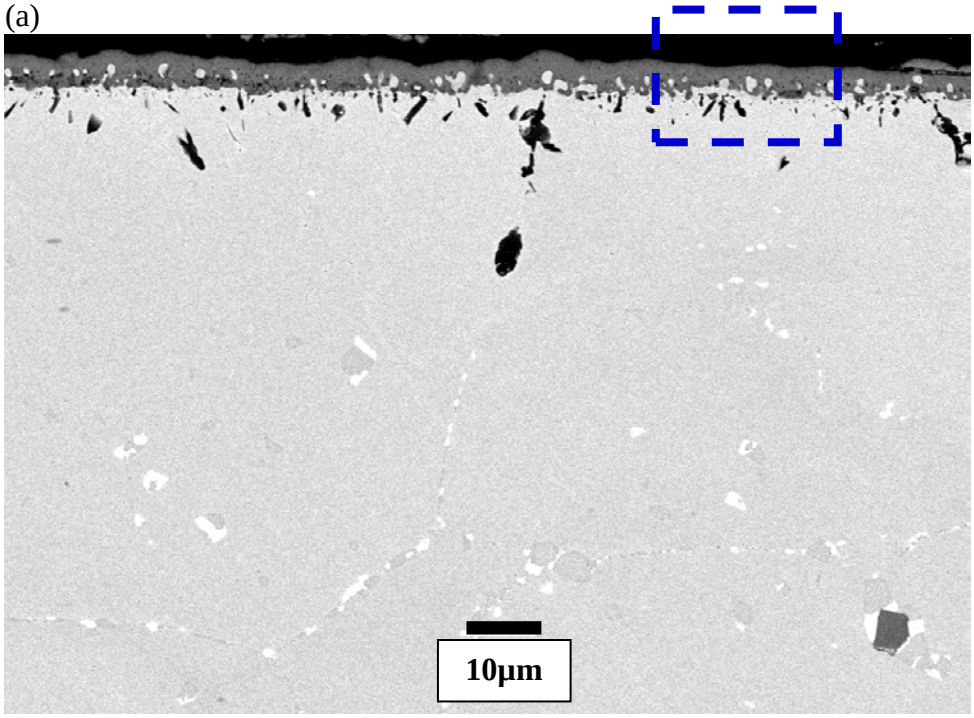

(b)

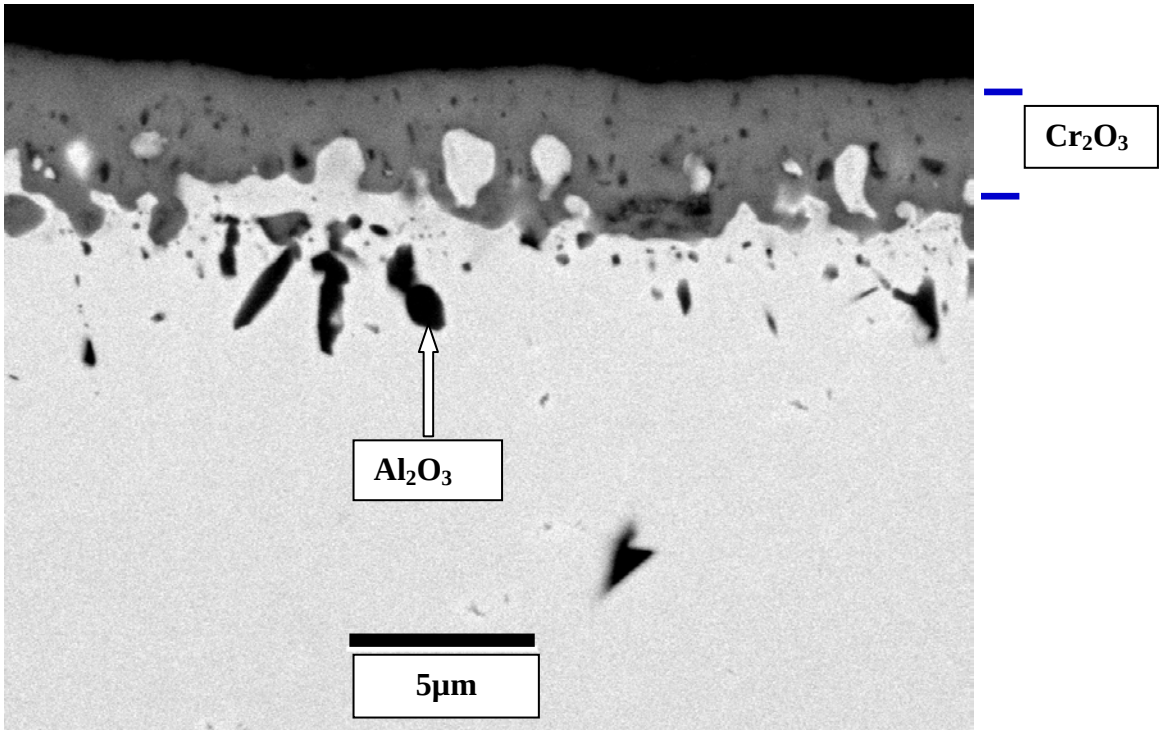

Figure 4.30 Low magnification and (b) high magnification BSE image of the sample exposed in environment 1(CO/CO_2 = 9) at 900°C for 750h.

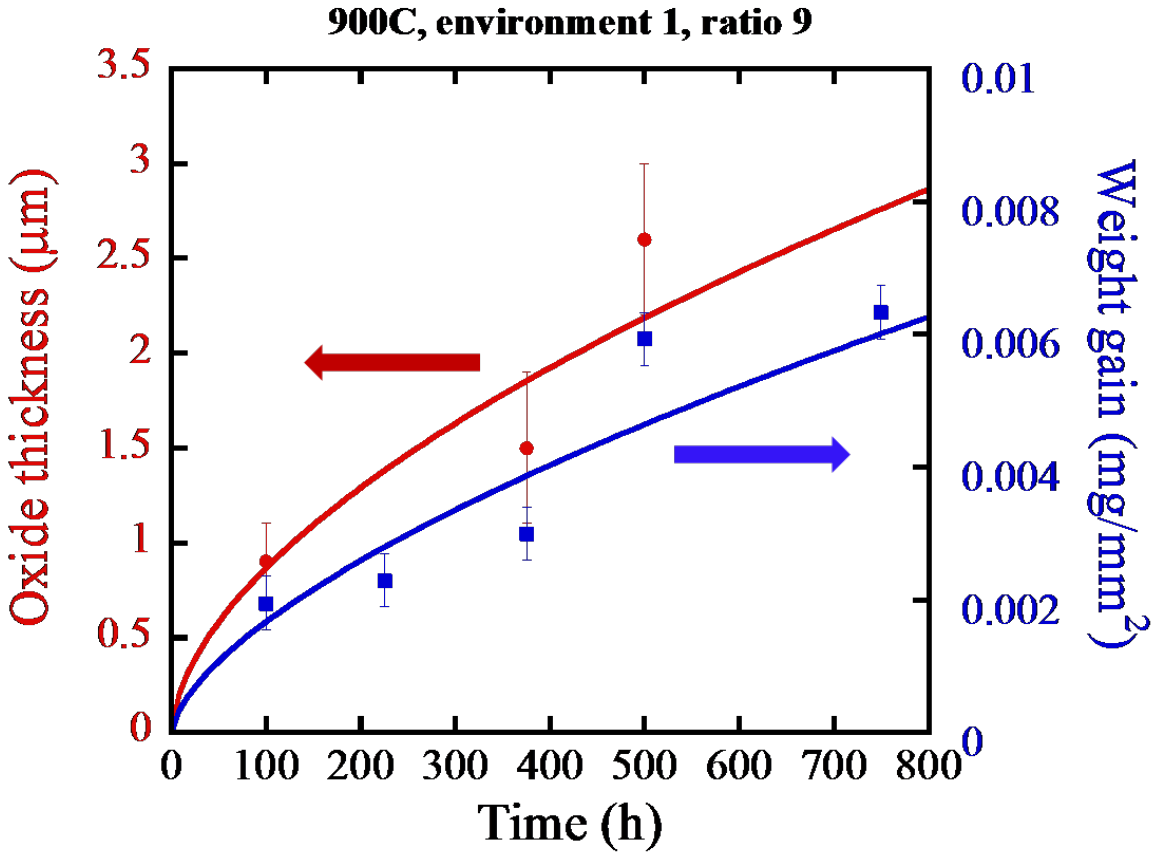

Figure 4.31 Plot of the thickness of the Cr_2O_3 film as a function of time for samples exposed in environment 1(CO/CO_2 = 9) at 900°C.

(a)

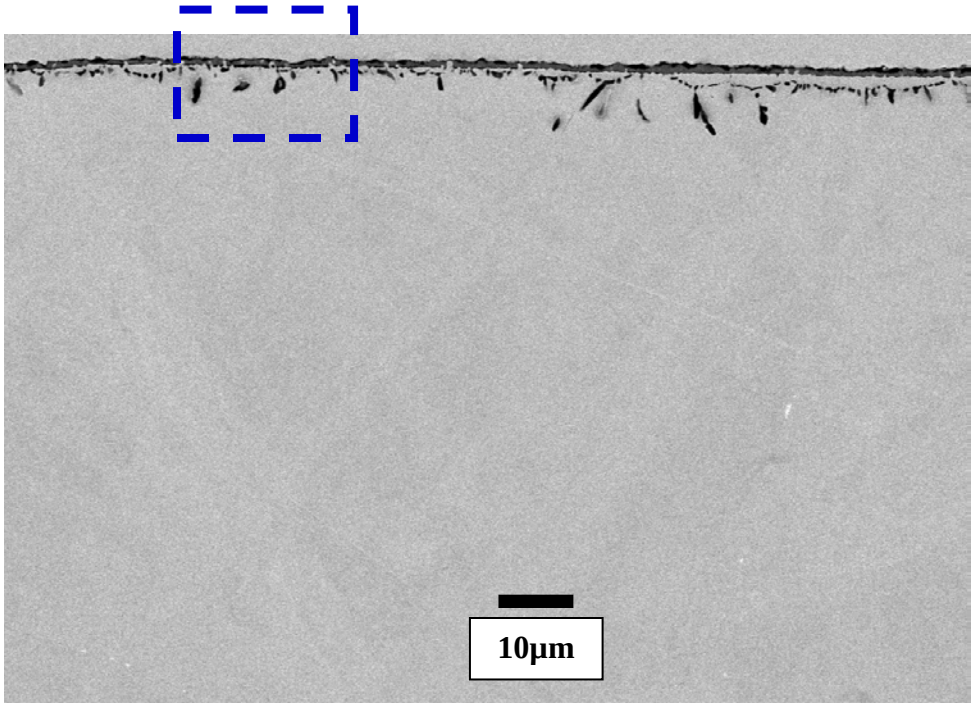

(b)

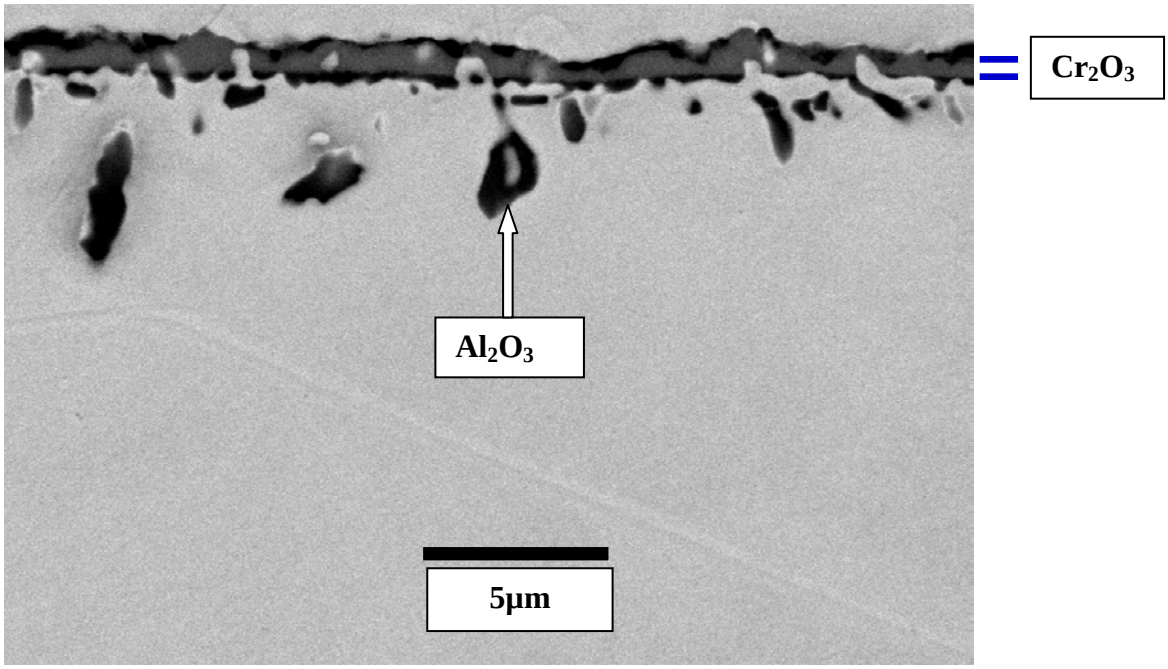

Figure 4.32 (a). Low magnification and (b) high magnification BSE image of the sample exposed in environment 1(CO/CO_2 = 9) at 950°C for 100h.

(a)

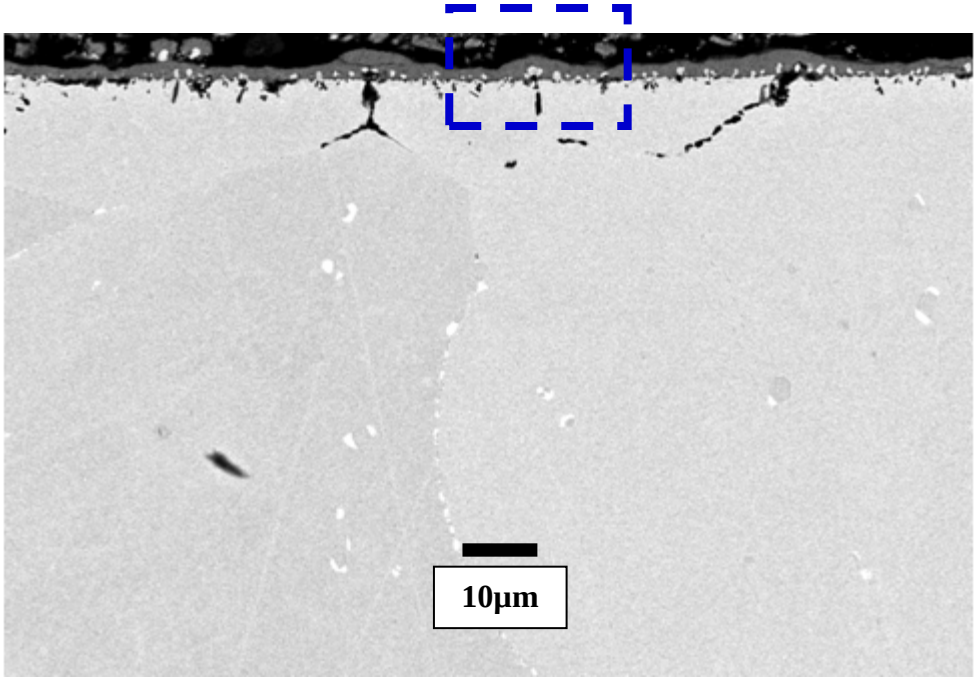

(b)

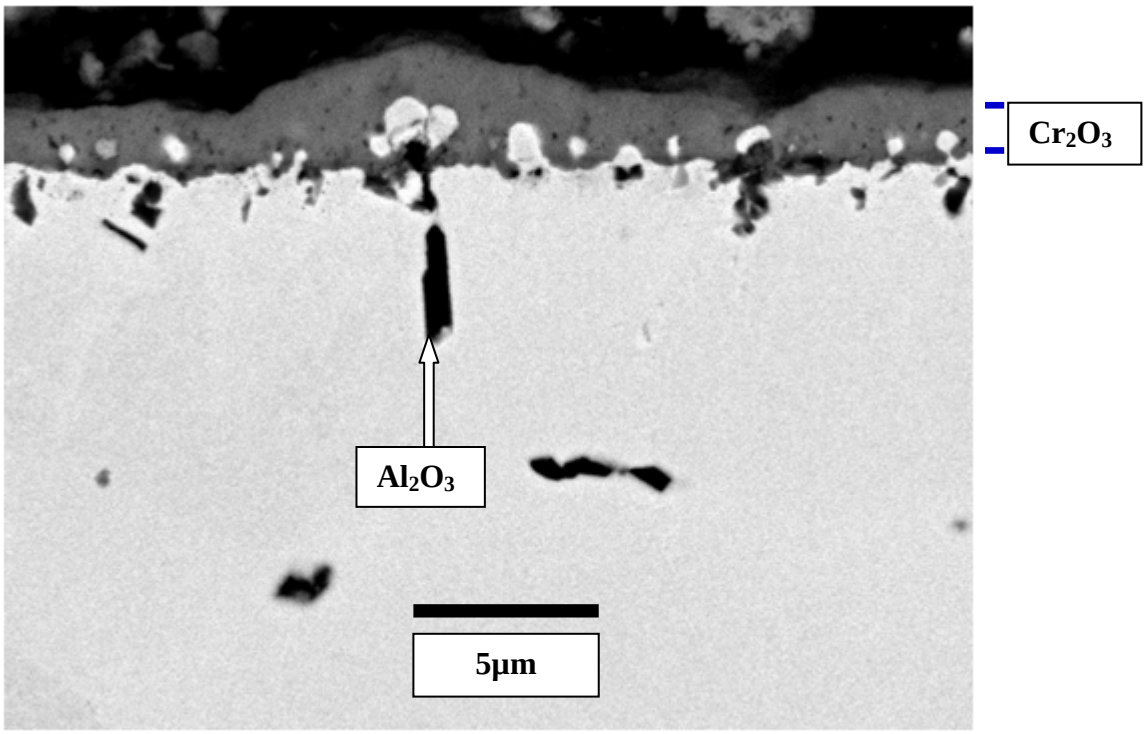

Figure 4.33(a). Low magnification and (b) high magnification BSE image of the sample exposed in environment 1(CO/CO_2 = 9) at 950°C for 375h.

(a)

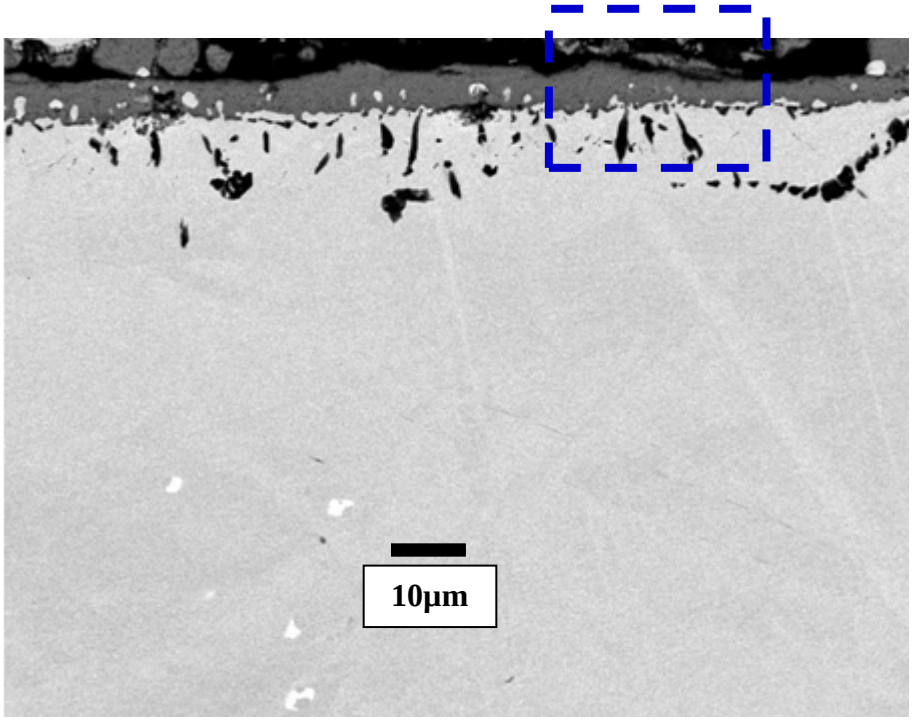

(b)

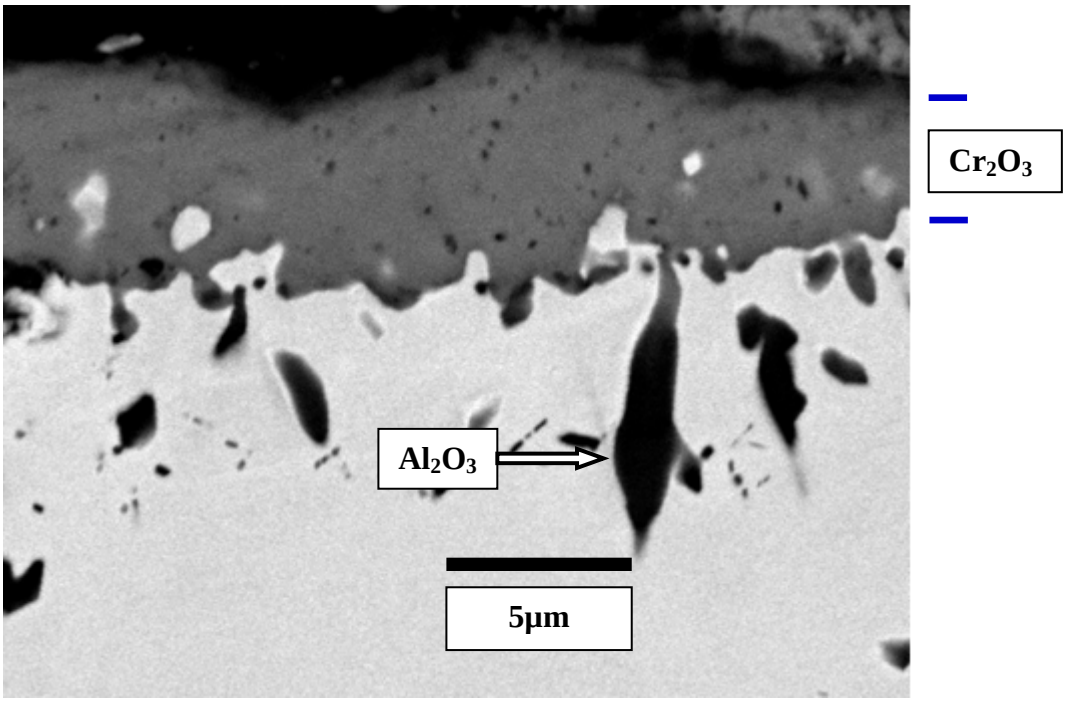

Figure 4.34 (a). Low magnification and (b) high magnification BSE image of the sample exposed in environment 1(CO/CO_2 = 9) at 950°C for 750h.

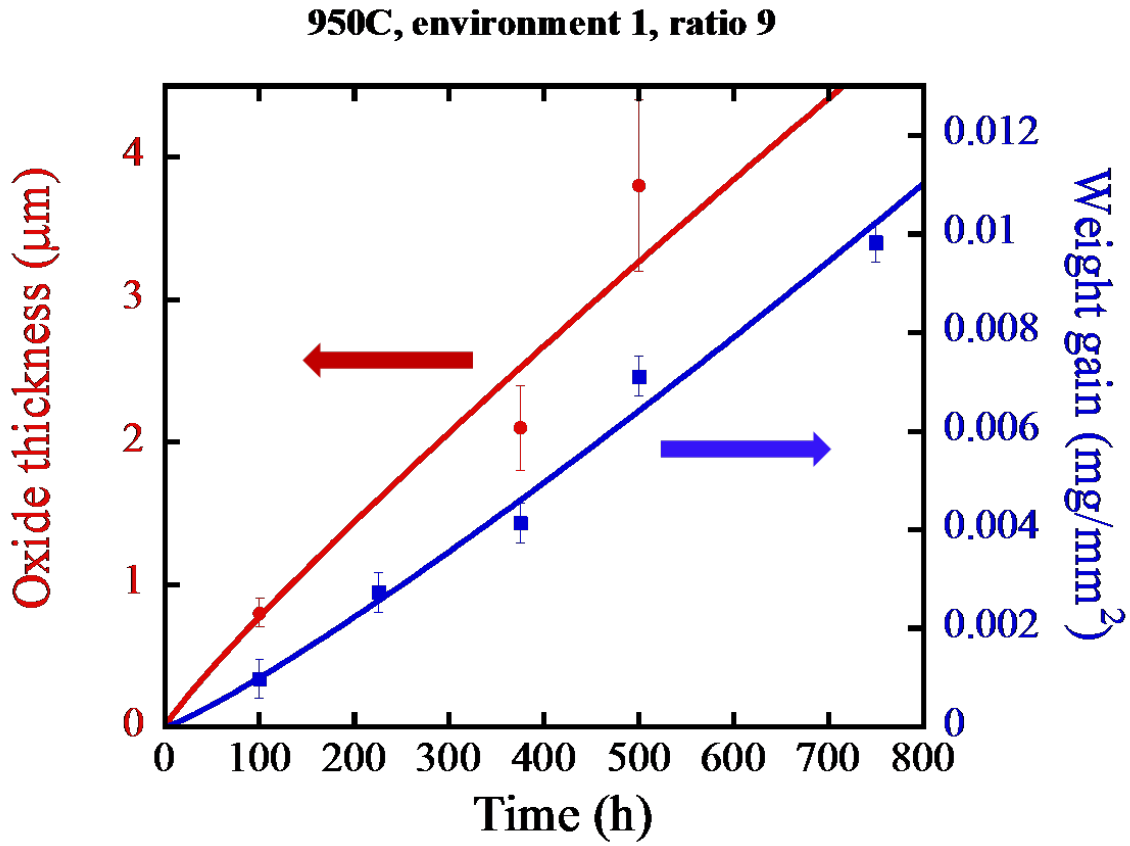

Figure 4.35 Plot of the thickness of the Cr_2O_3 film as a function of time for samples exposed in environment 1(CO/CO_2 = 9) at 900°C and 950°C.

(a)

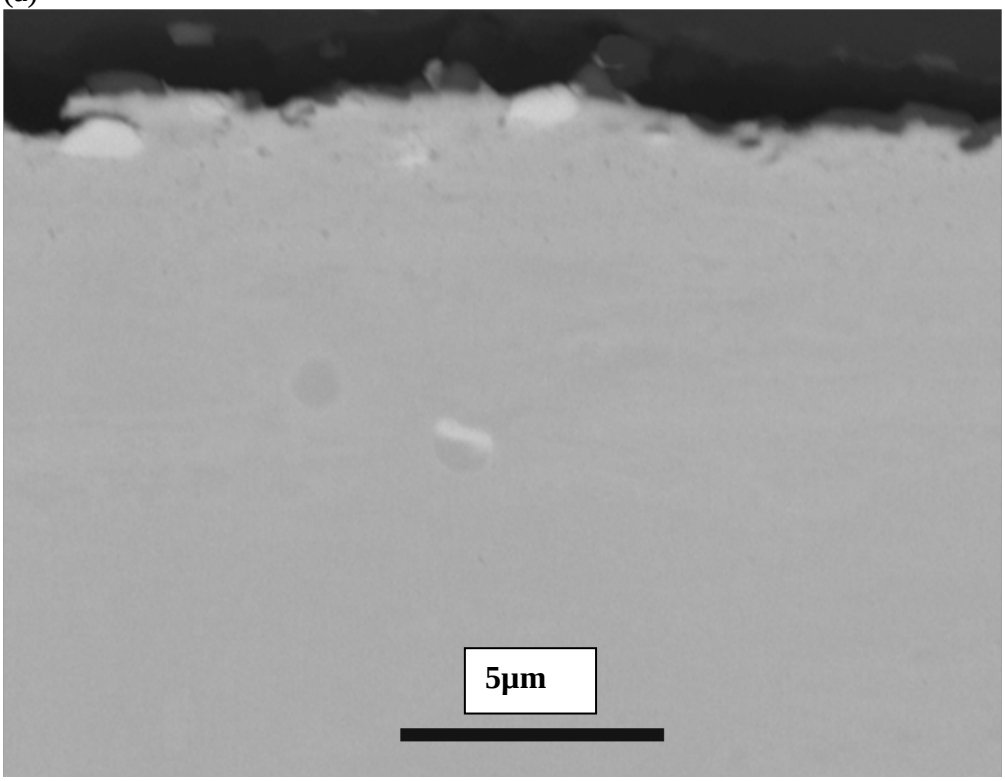

(b)

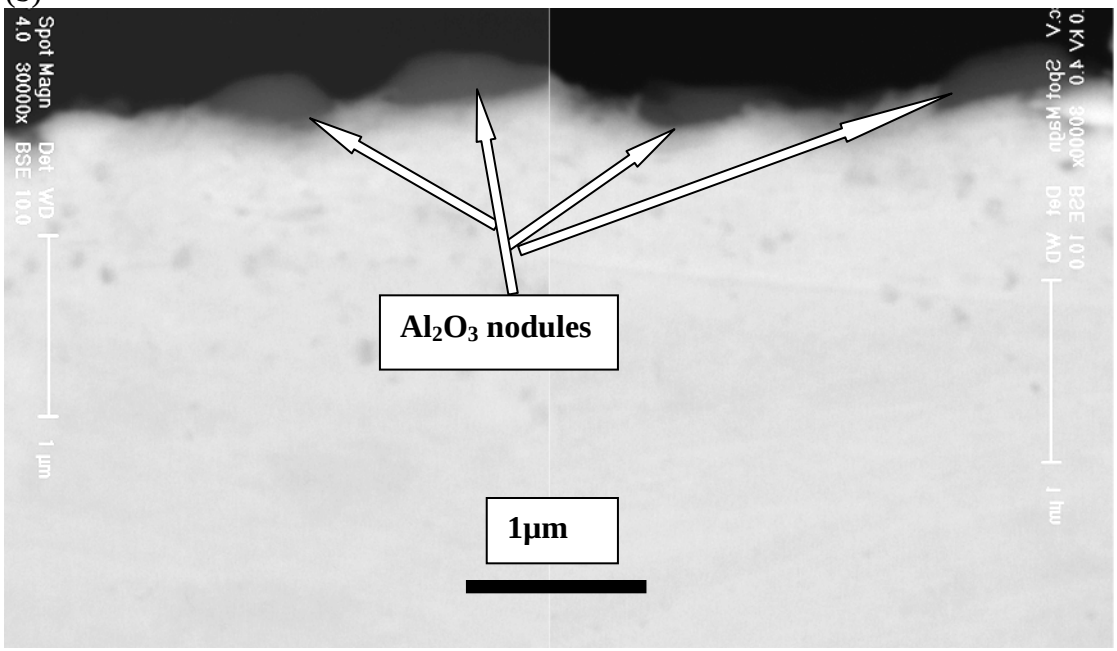

Figure 4.36(a). Low magnification and (b) high magnification BSE image of the sample exposed in environment 1(CO/CO_2 = 9) at 1000°C for 100h. Surface Cr_2O_3 film was not observed.

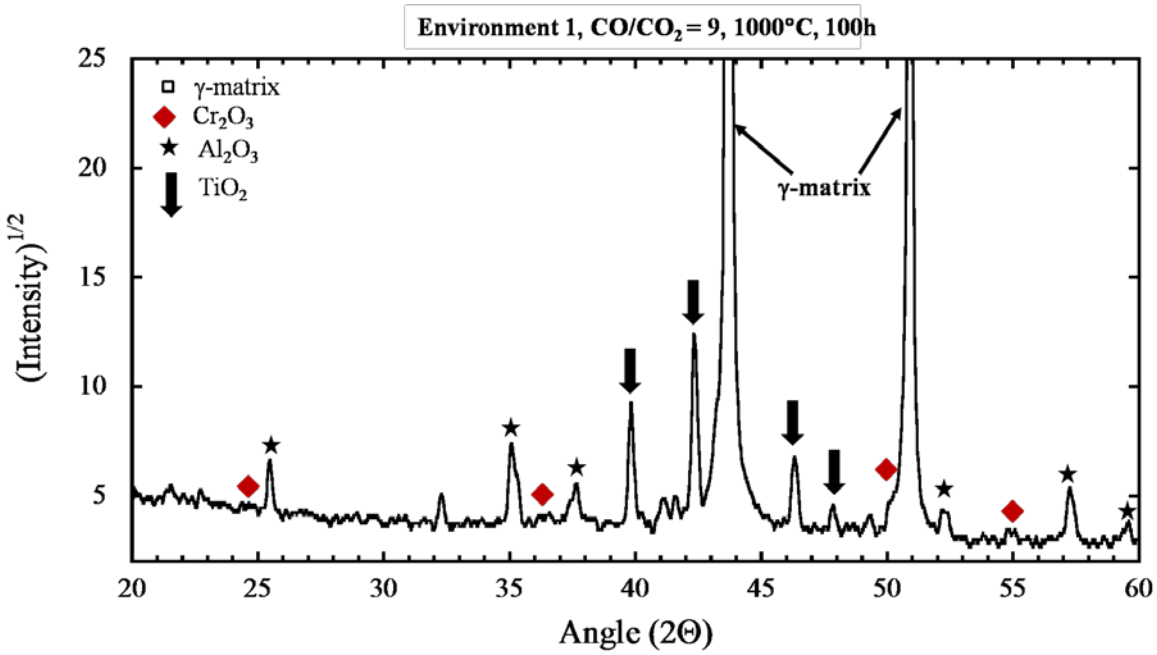

Figure 4.37 Surface XRD of the sample exposed in environment 1(CO/CO_2 = 9) at 1000°C for 100h. The expected positions of the high intensity peaks of Cr_2O_3 are marked on the plot with the diamond symbol in red color. The CuKα radiation with of wavelength of 1.540 A°was used to obtain the XRD pattern.

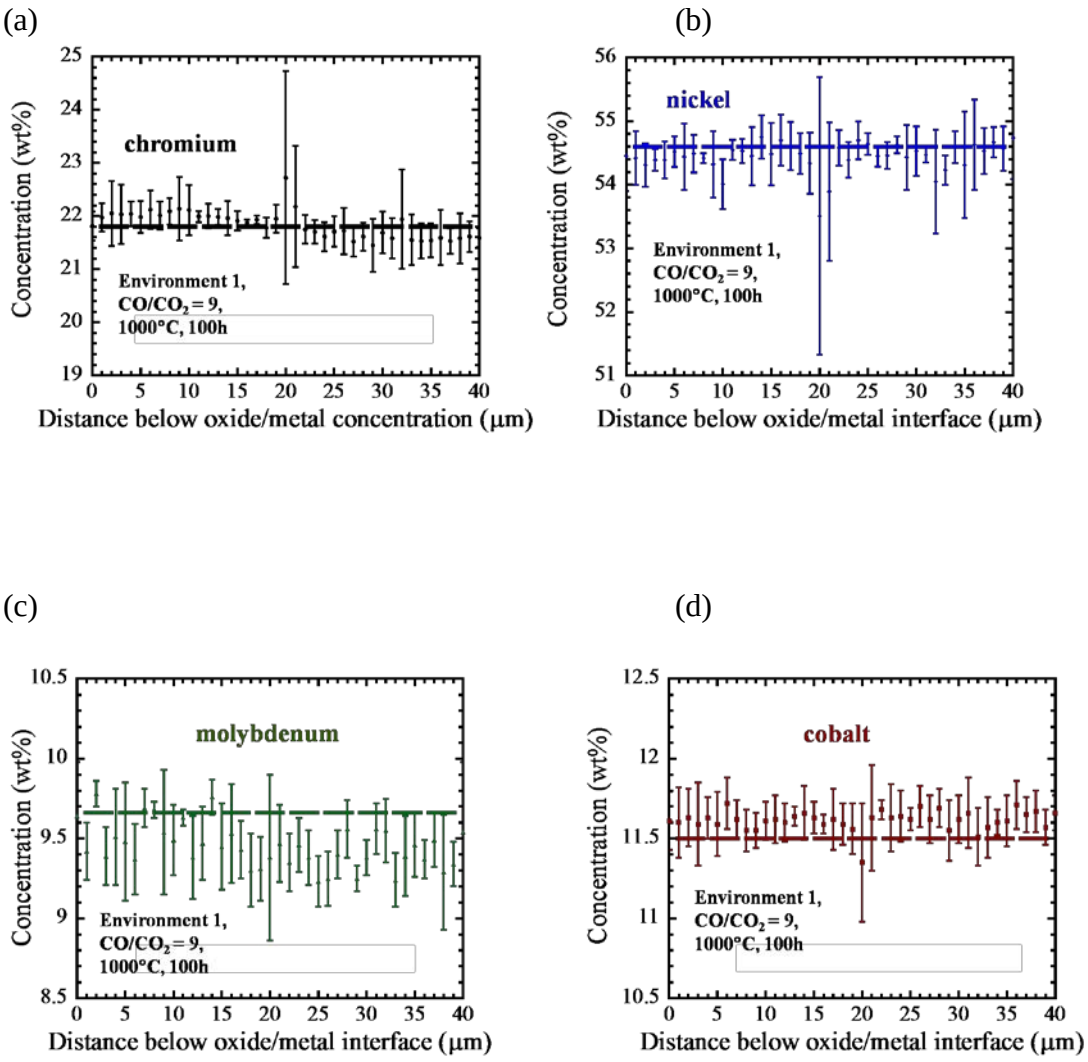

Figure 4.38 Concentration profiles of Cr, Ni, Mo, and Co measured by EMPA. The error bars are the standard deviations between three line scans. The broken lines in (a)-(d) shows the concentration of the elements in the as received alloy. The sample was exposed in environment 1(CO/CO_2 = 9) for 100h.

(a)

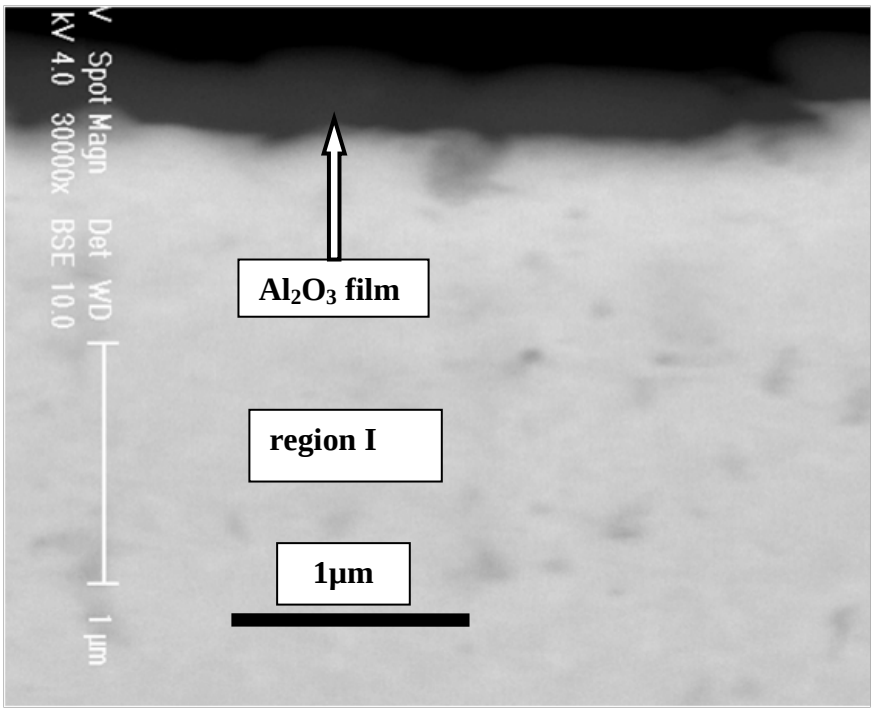

(b)

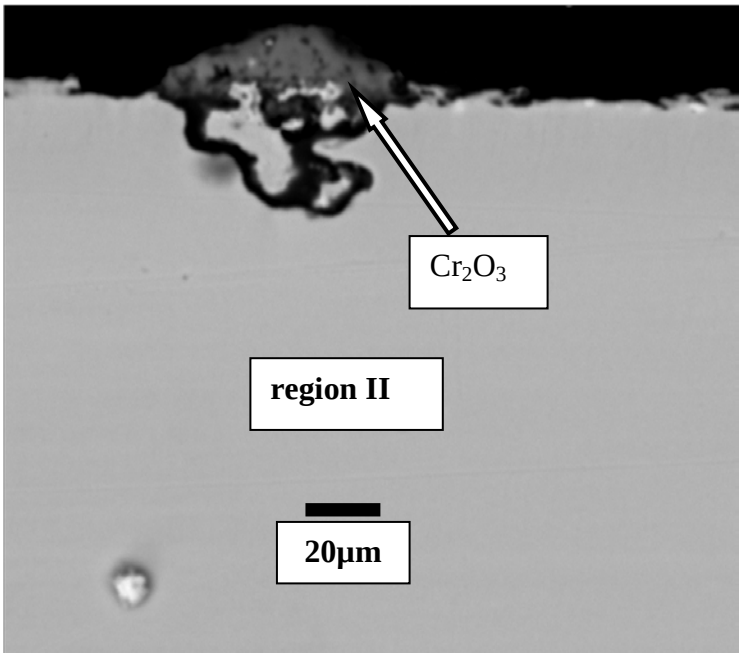

Figure 4.39 (a). BSE image of the sample exposed in environment 1(CO/CO_2 = 9) for 375 h at 1000°C. The surface microstructure was in-homogenous. In region I a thin film of Al_2O_3 was observed (a) whereas in region II nuclei of Cr_2O_3 were observed (b).

(a)

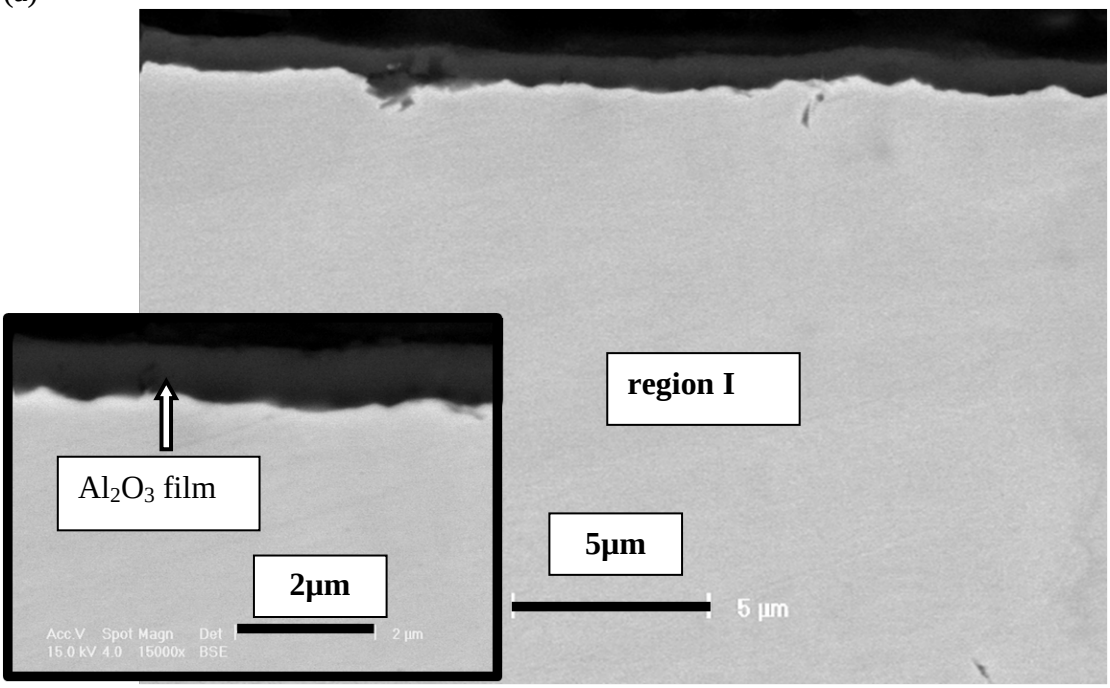

(b)

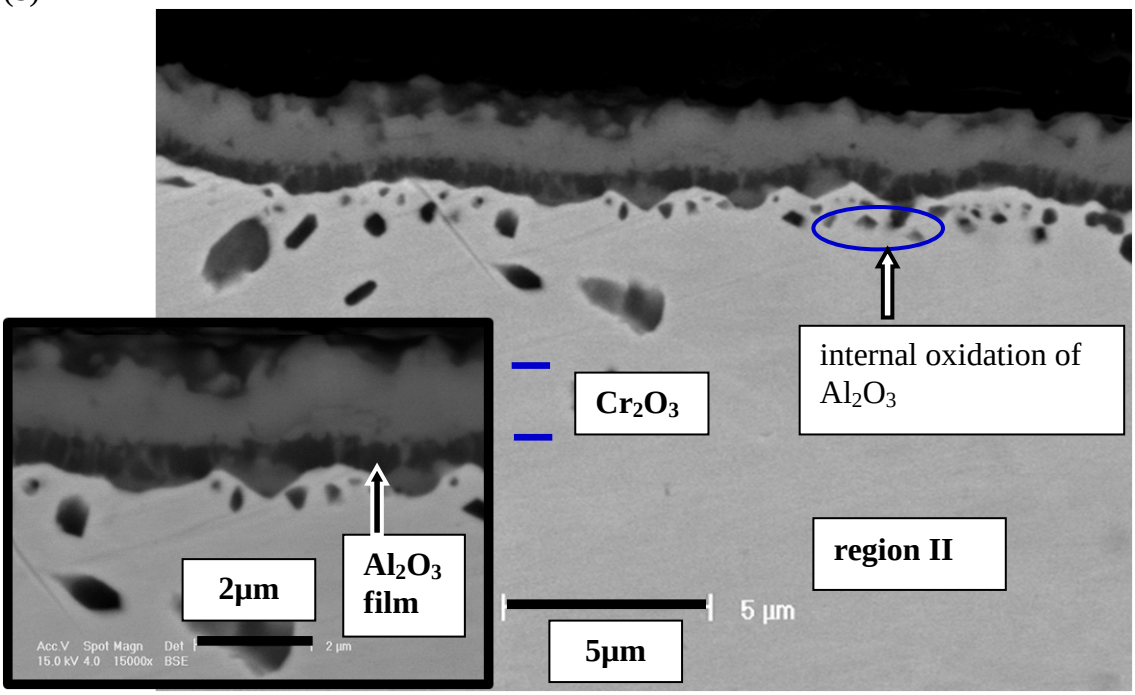

Figure 4.40 BSE images of the sample exposed in environment 1(CO/CO_2 = 9) at 1000°C for 500h. The surface microstructure was heterogeneous. (a) In region I, a thin film of alumina formed and (b) in region II, a duplex scale of chromia on top of alumina formed.

(a)

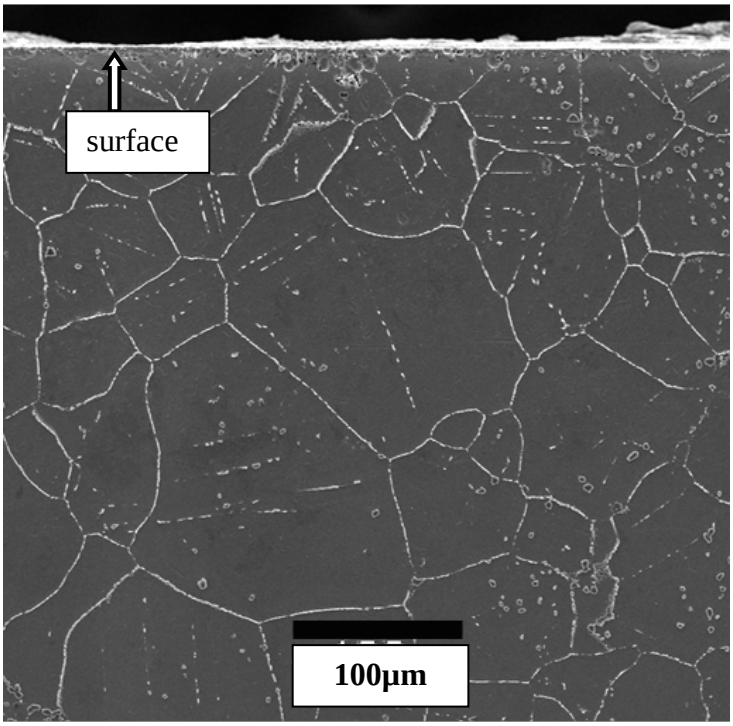

(b)

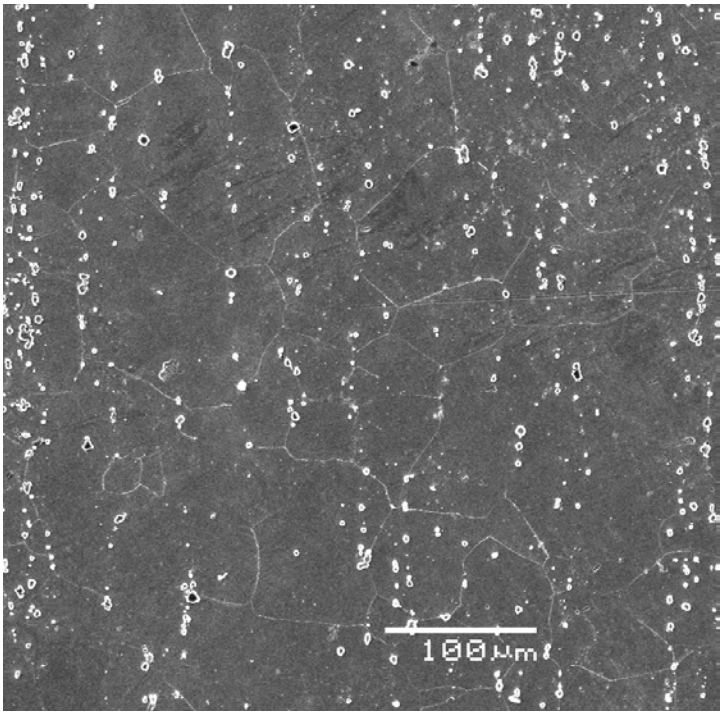

Figure 4.41 SEM image of the (a) sample exposed at 900°C for 375 h in environment 1(CO/CO_2 = 9), and (b) as received alloy 617.

(a)

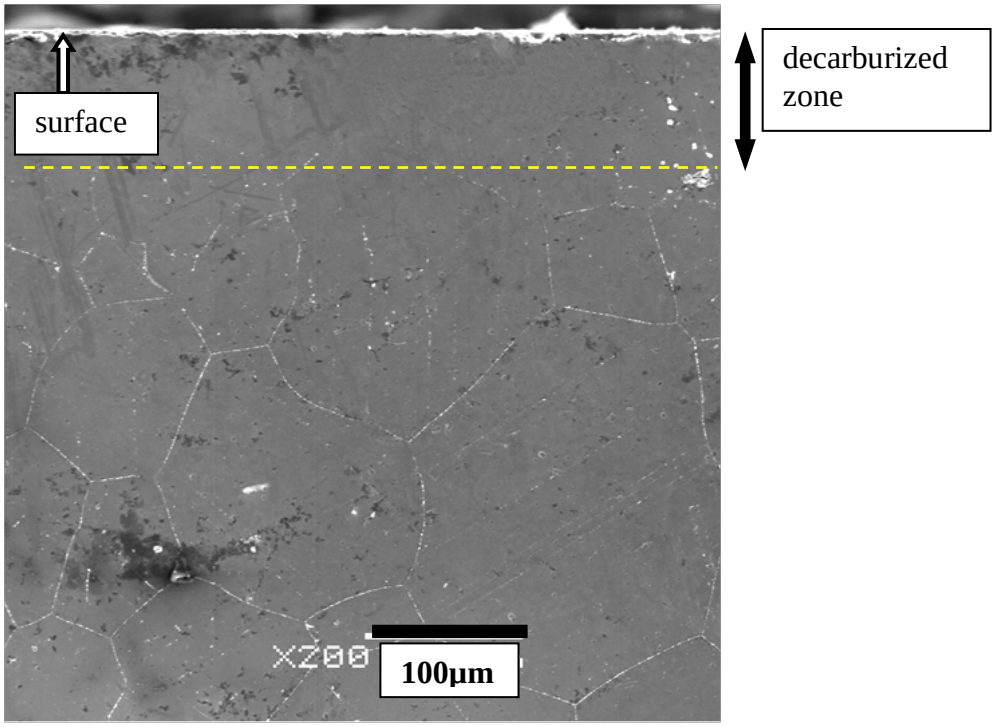

(b)

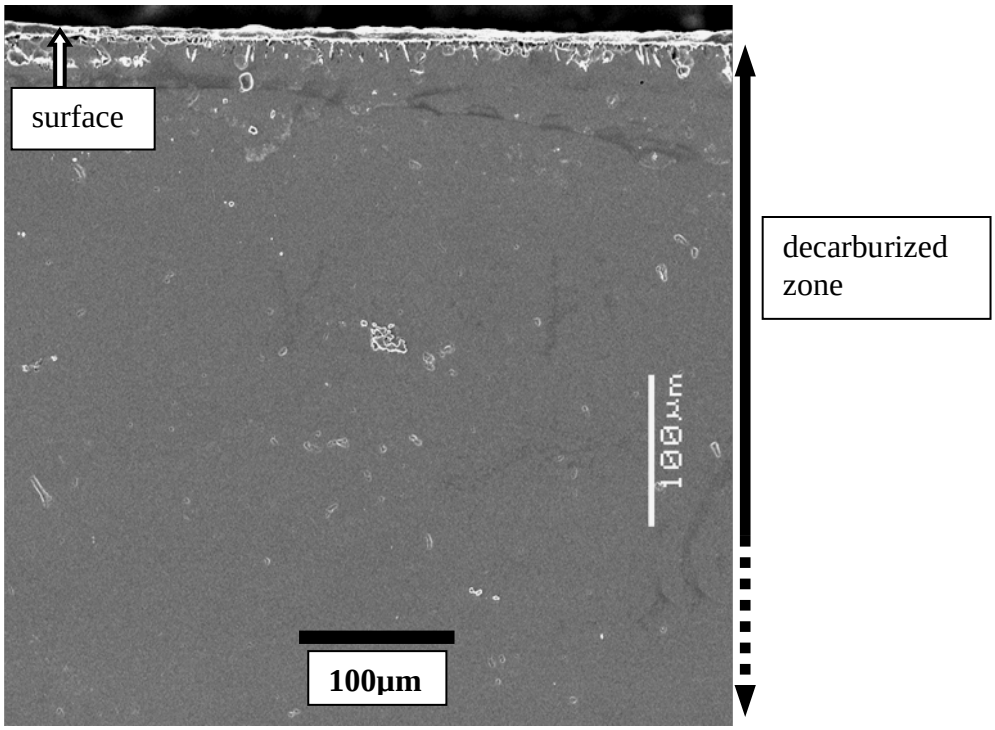

Figure 4.42 SEM image of the sample exposed at 950°C in environment 1(CO/CO_2 = 9) for (a) 100h, and (b) 375h. The decarburization zone extends in the alloy beyond the depth shown in the image (b).

(a)

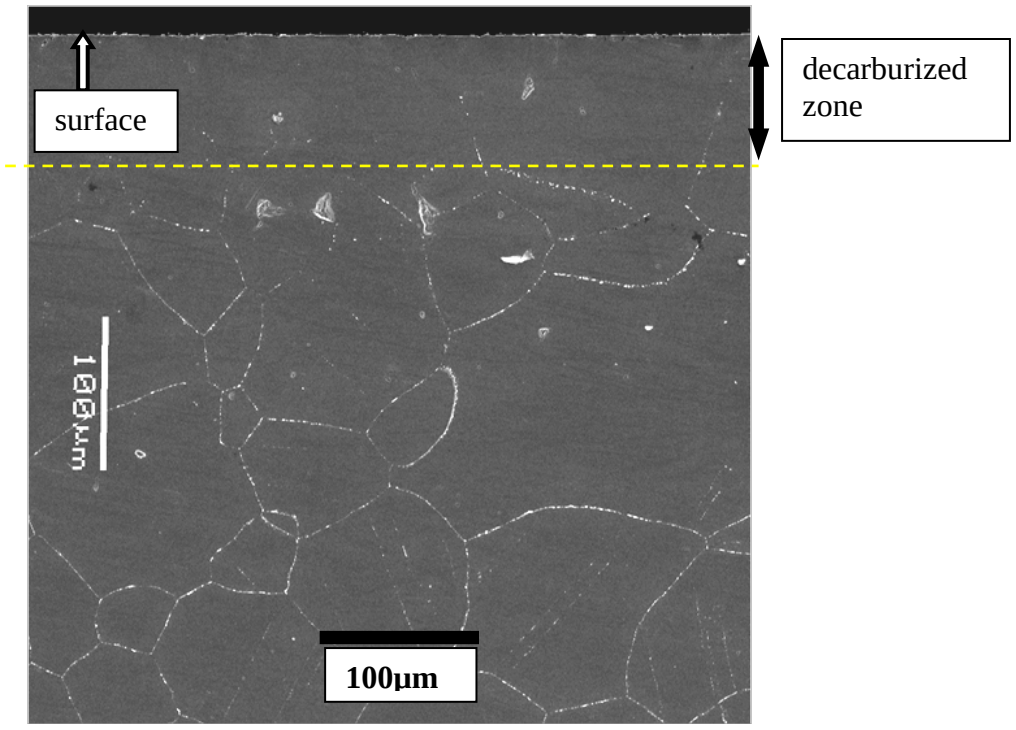

(b)

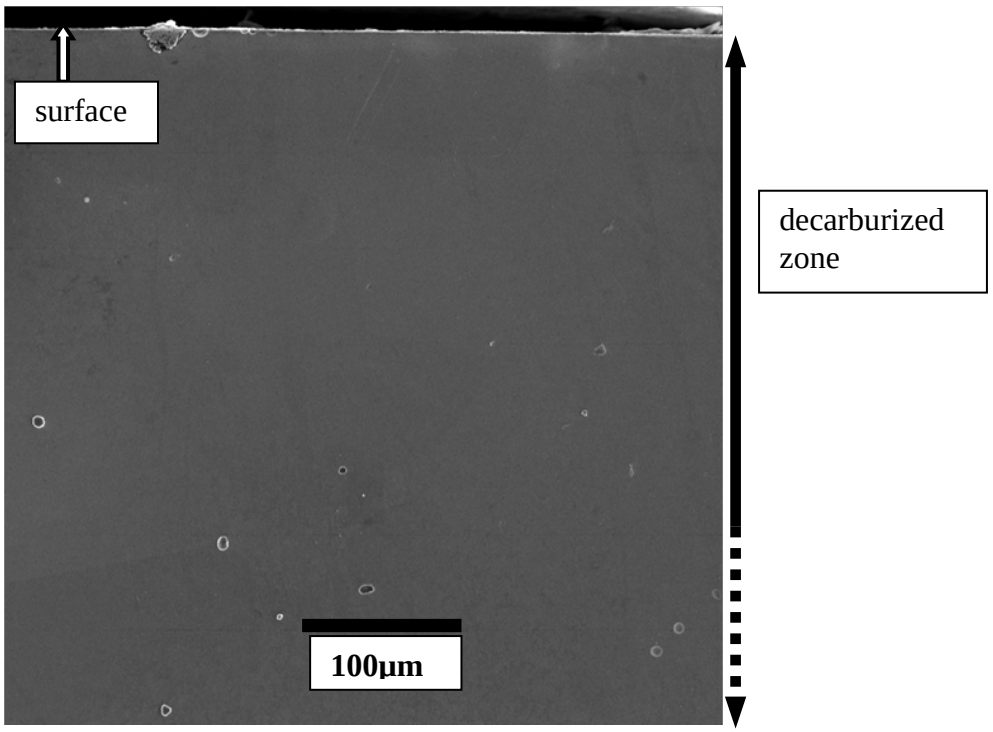

Figure 4.43 SEM image of the sample exposed in environment 1(CO/CO_2 = 9) at 1000°C for (a) 100h, (b) 375h. The decarburization zone extends in the alloy beyond the depth shown in the image (b).

(a)

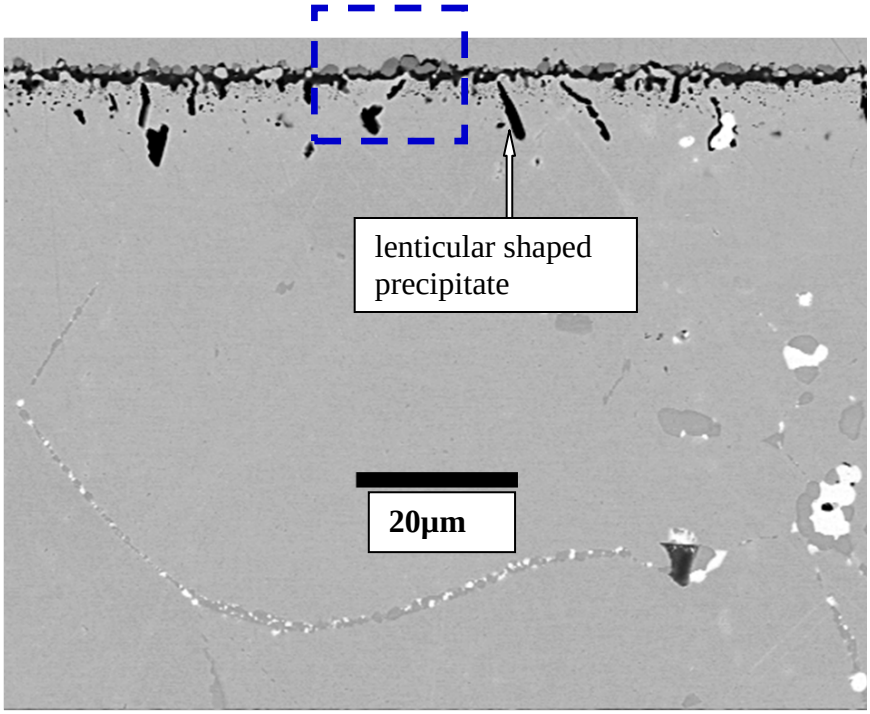

(b)

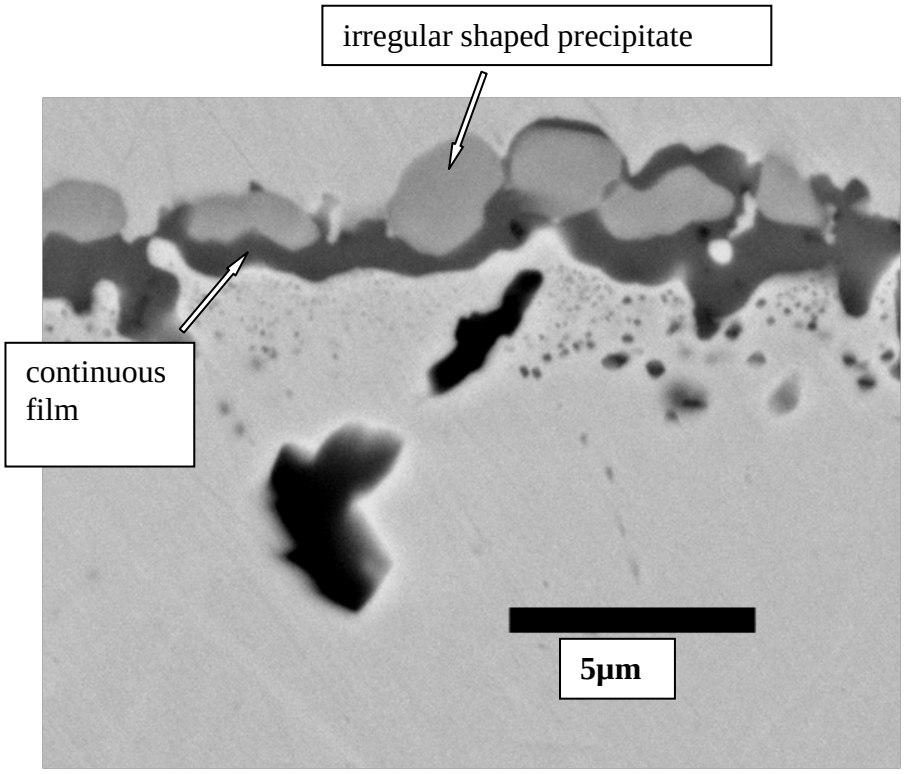

Figure 4.44 (a) Low magnification (b) high magnification back scattered electron image (BSE image) of the sample exposed at 1000°C for 100h in environment 6 (CO/CO_2 = 1272).

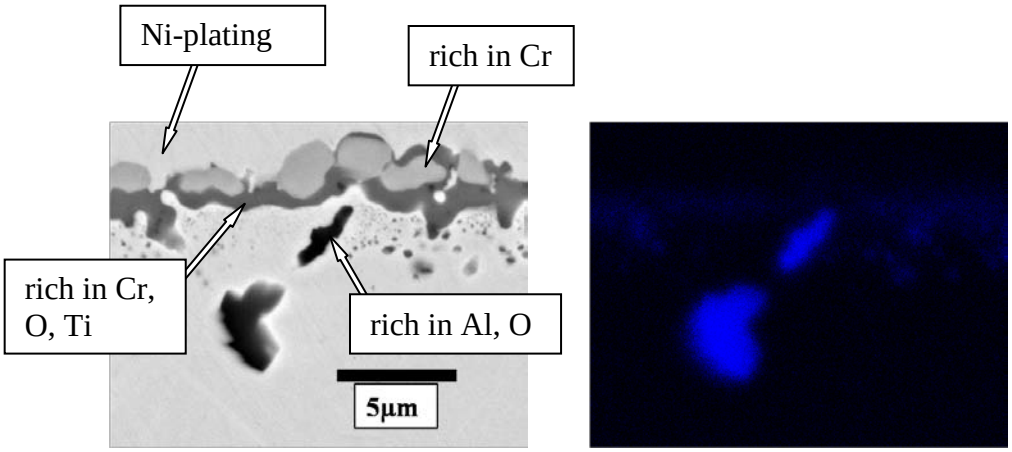

(a) BSE image

(b) aluminum

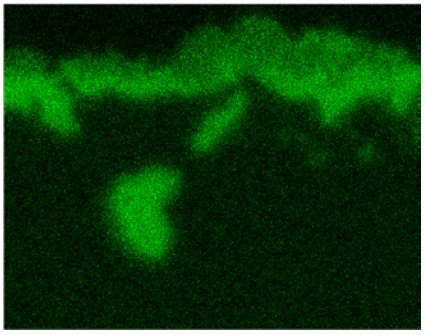

(c) oxygen

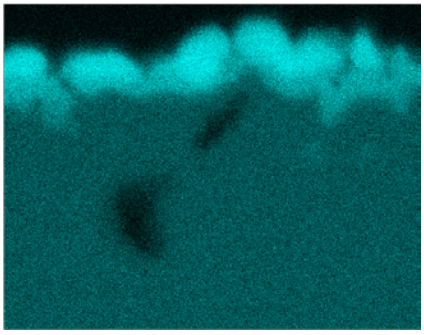

(d) chromium

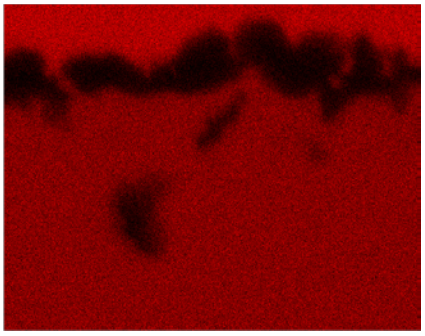

(e) nickel

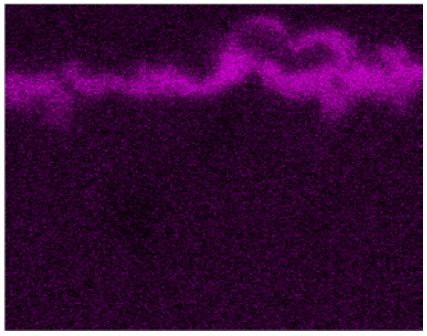

(e) titanium

Figure 4.45(a)-(f). Back scattered electron image and the corresponding x-ray map of the sample exposed in environment 6 (CO/CO_2 = 1272) for 100h at 1000°C.

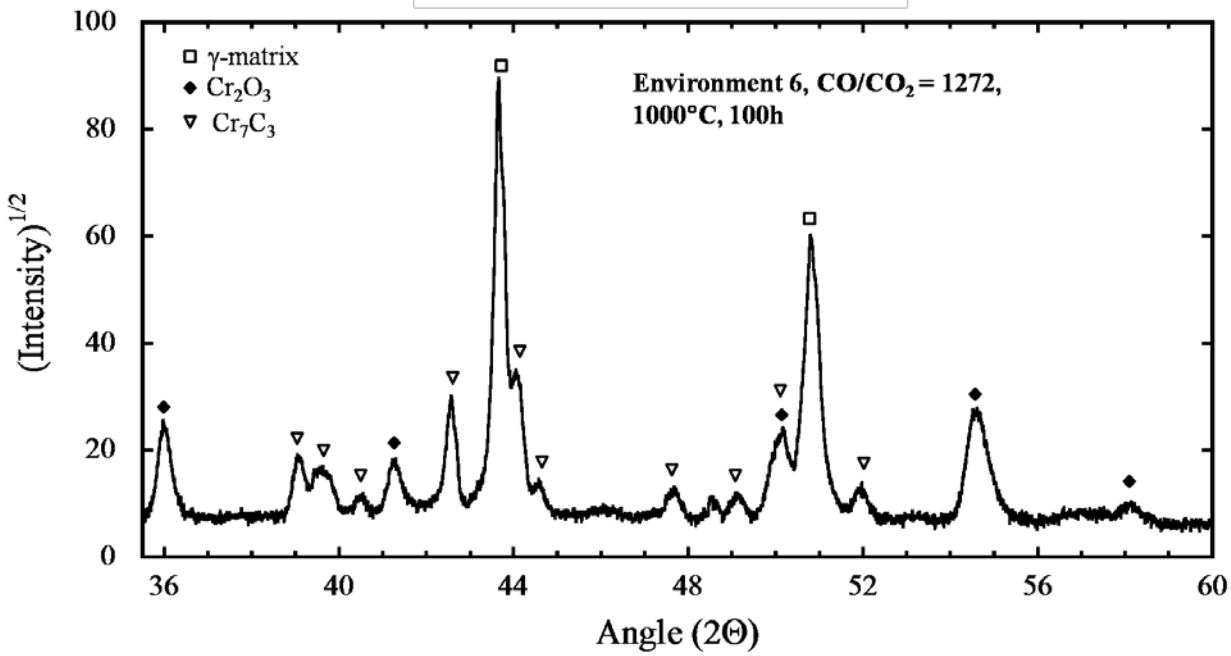

Figure 4.46 X-ray diffraction pattern of the sample exposed in environment 6 (CO/CO_2 = 1272) at 1000°C for 100h. The CuKα radiation with of wavelength of 1.540 A°was used to obtain the XRD pattern.

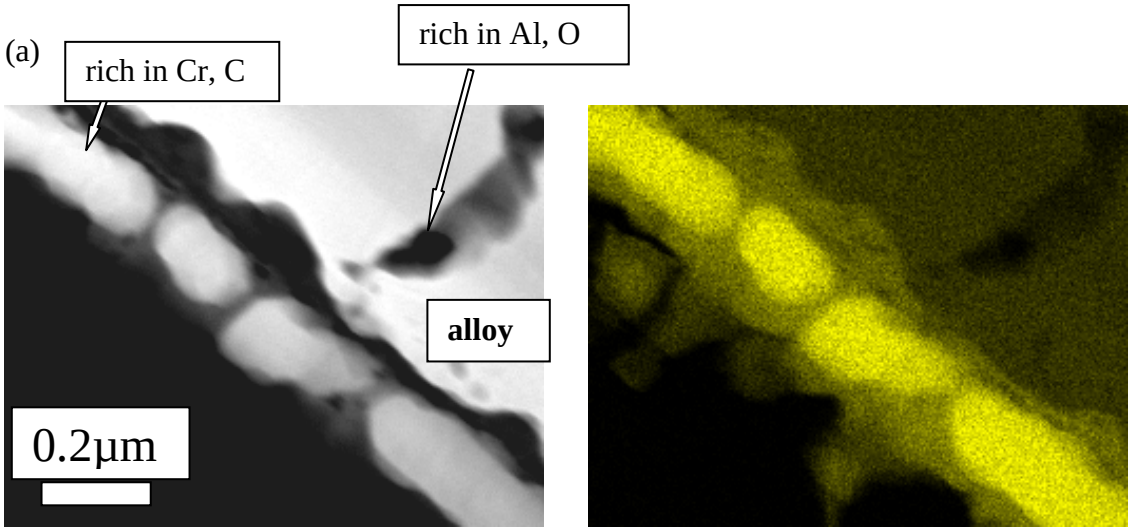

(a) HAADF image

(b) chromium

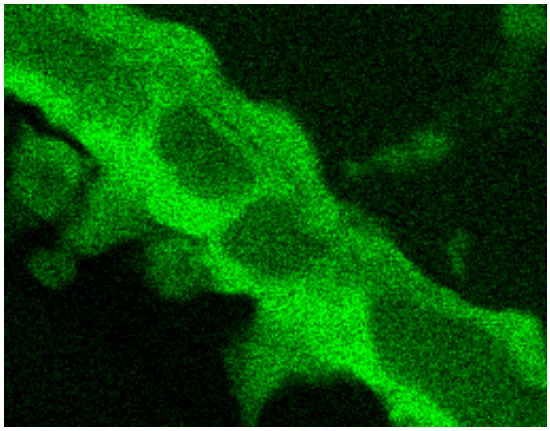

(c) oxygen

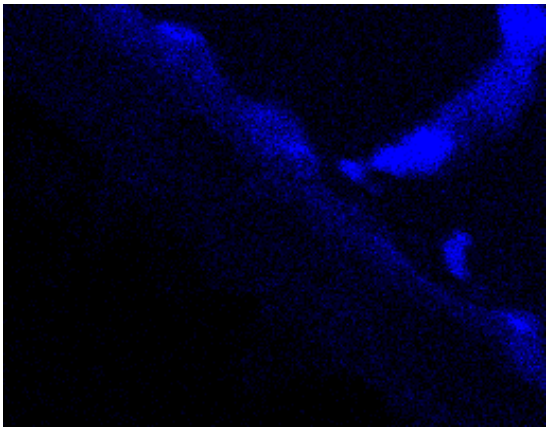

(d) aluminum

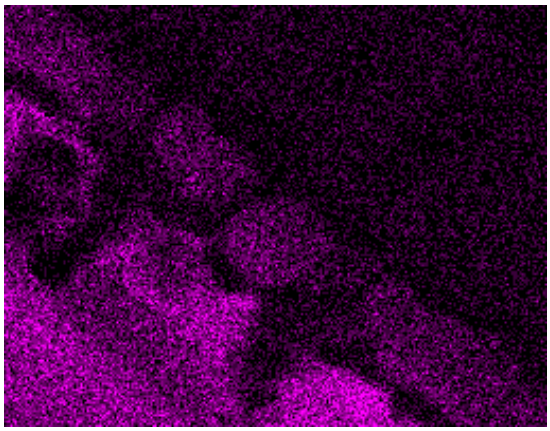

(e) carbon

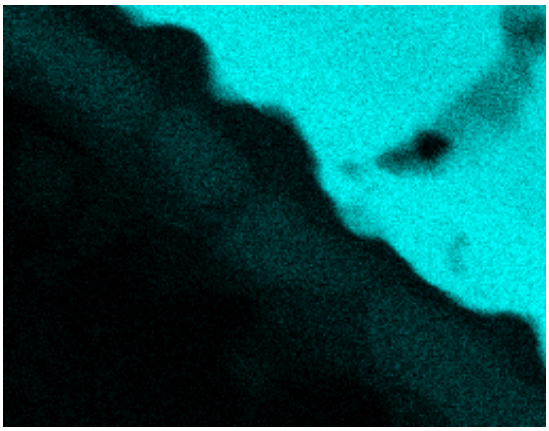

(f) nickel

Figure 4.47(a)High angle annular dark field image (HAADF), (b)-(f) corresponding x-ray map of chromium, oxygen, aluminum, carbon, and nickel. This sample was exposed at 850°C for 225h in environment 6 (CO/CO_2 = 1272).

(a)

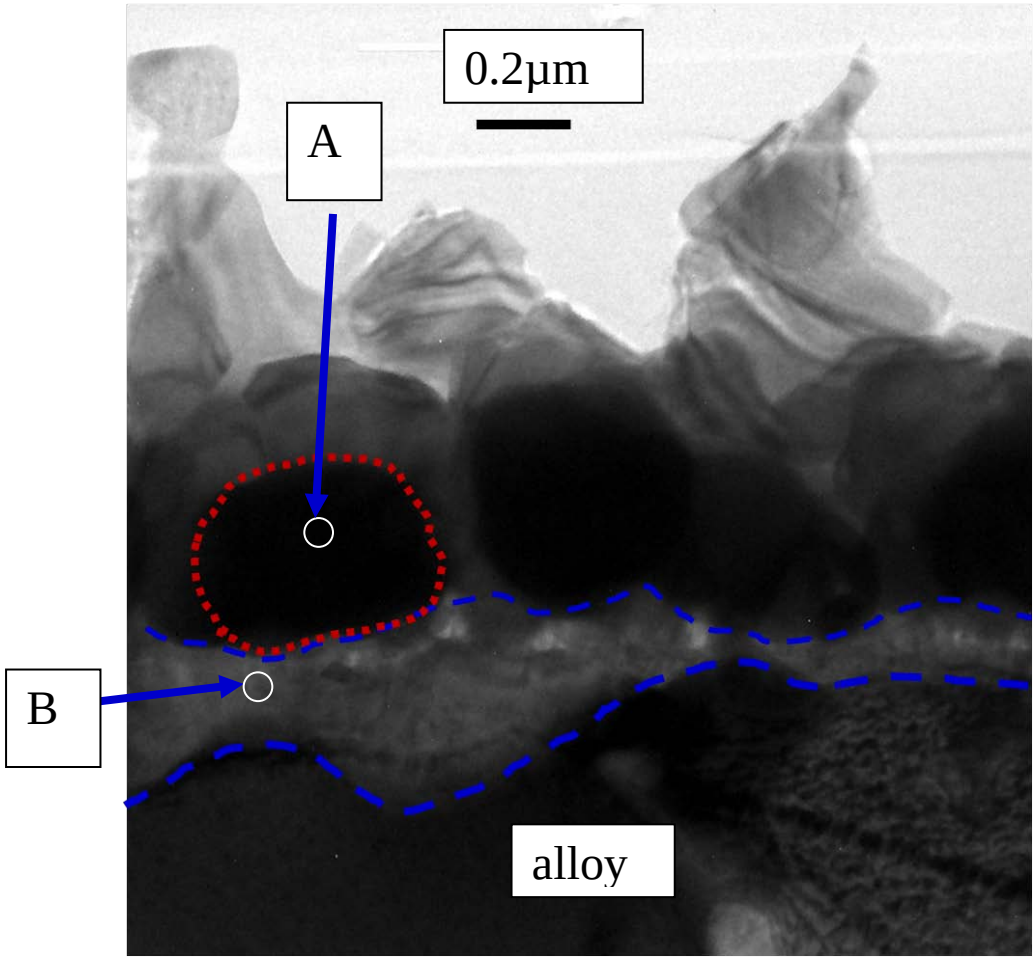

(b)

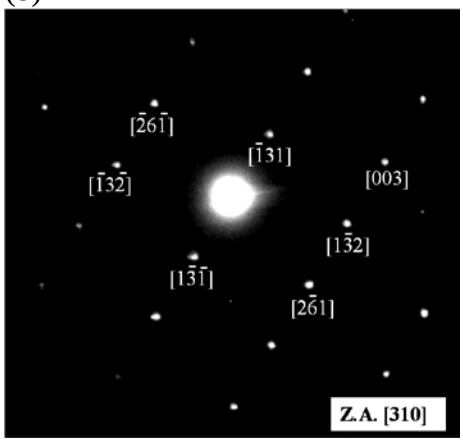

(c)

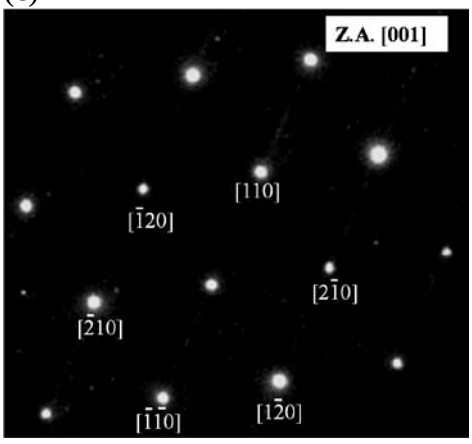

Figure 4.48 (a) Bright field TEM image of the sample oxidized at 850°C for 225 h in environment 6 (CO/CO_2 = 1272), (b) and (c) are diffraction patterns taken from the location marked as "A" and "B" in the figure (a). A is Cr_7C_3 and B is Cr_2O_3.

(a)

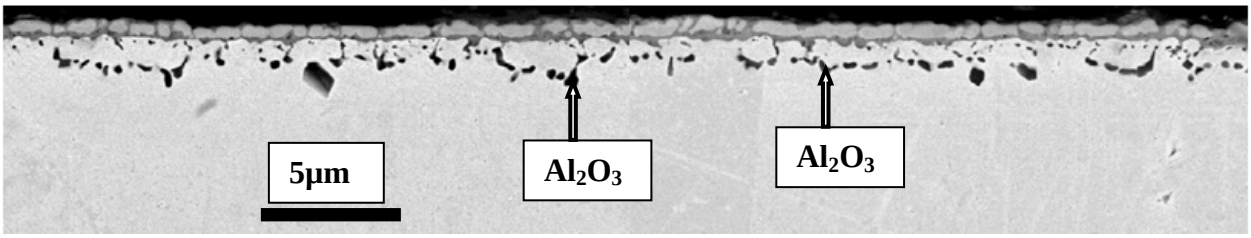

(b)

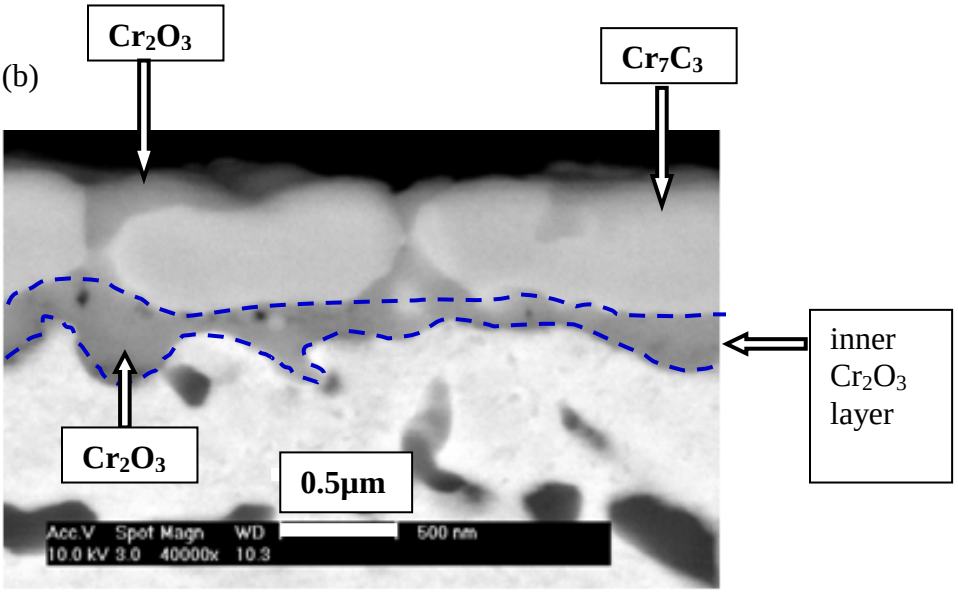

Figure 4.49(a) Low magnification and (b) high magnification BSE images of the sample exposed in environment 6 (CO/CO_2 = 1272) at 850°C for 100h. The continuous Cr_2O_3 layer adjacent to the alloy is defined as inner Cr_2O_3 layer (marked by blue dashed line).

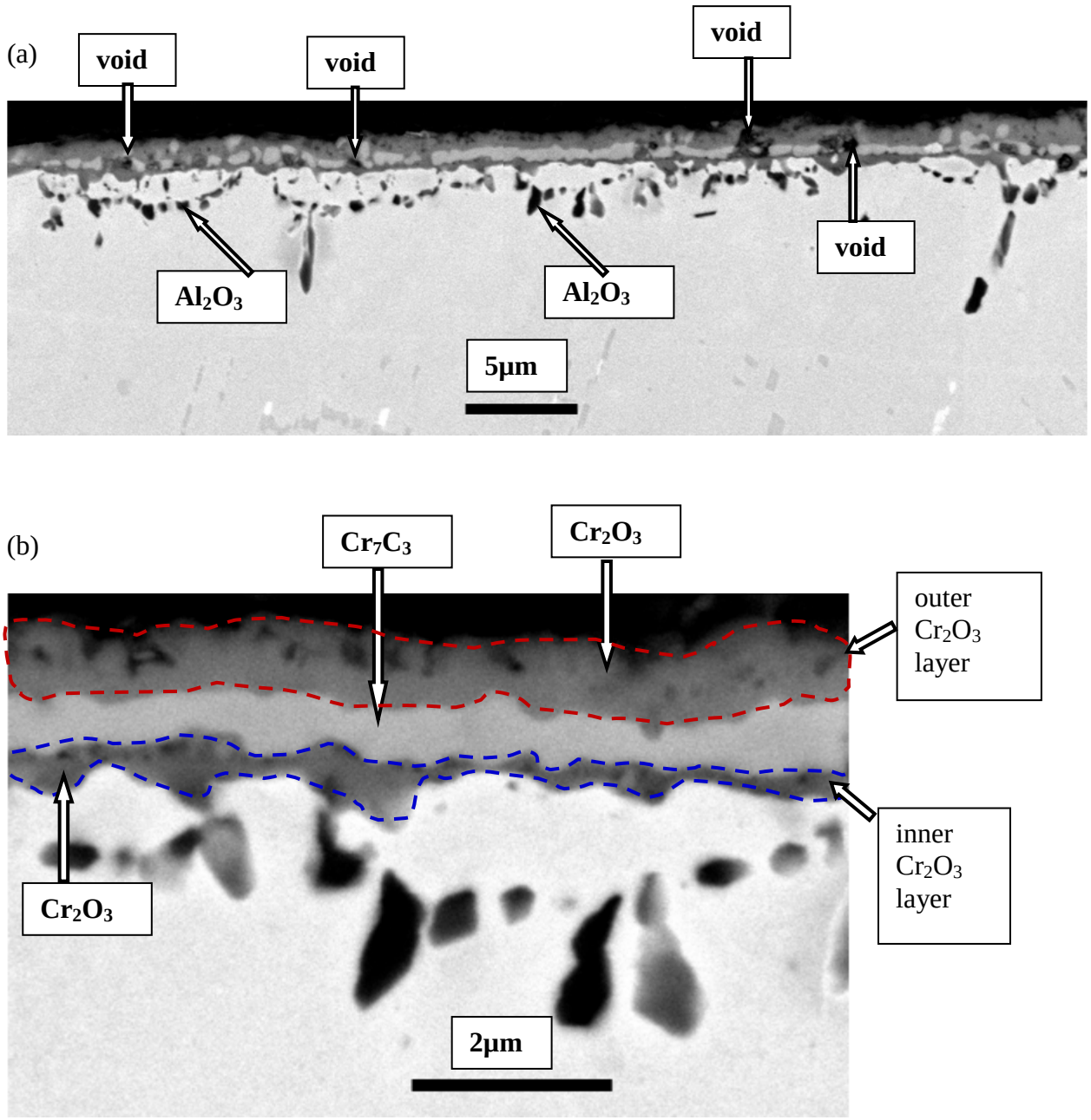

Figure 4.50 (a) Low magnification and (b) high magnification BSE images of the sample exposed in environment 6 (CO/CO_2 = 1272) at 850°C for 375h. The continuous Cr_2O_3 layer adjacent to the alloy is defined as inner layer (marked by blue dashed line). The Cr_2O_3 layer formed near the gas/scale is defined as outer Cr_2O_3 layer (marked with red dashed line).

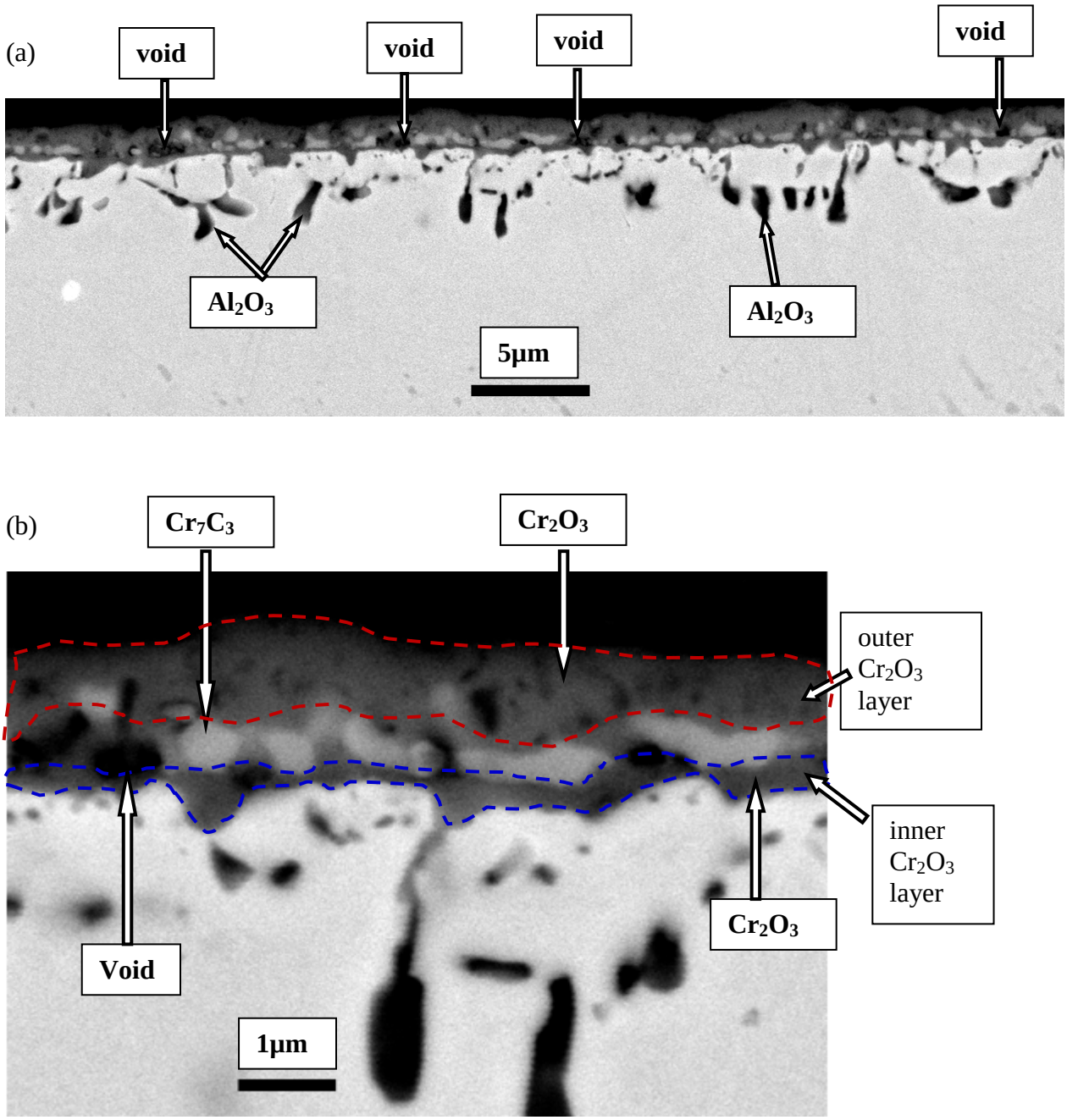

Figure 4.51(a) Low magnification and (b) high magnification BSE images of the sample exposed in environment 6 (CO/CO_2 = 1272) at 850°C for 500h. The continuous Cr_2O_3 layer adjacent to the alloy is defined as inner layer (marked by blue dashed line). The Cr_2O_3 layer formed near the gas/scale is defined as outer Cr_2O_3 layer (marked with red dashed line).

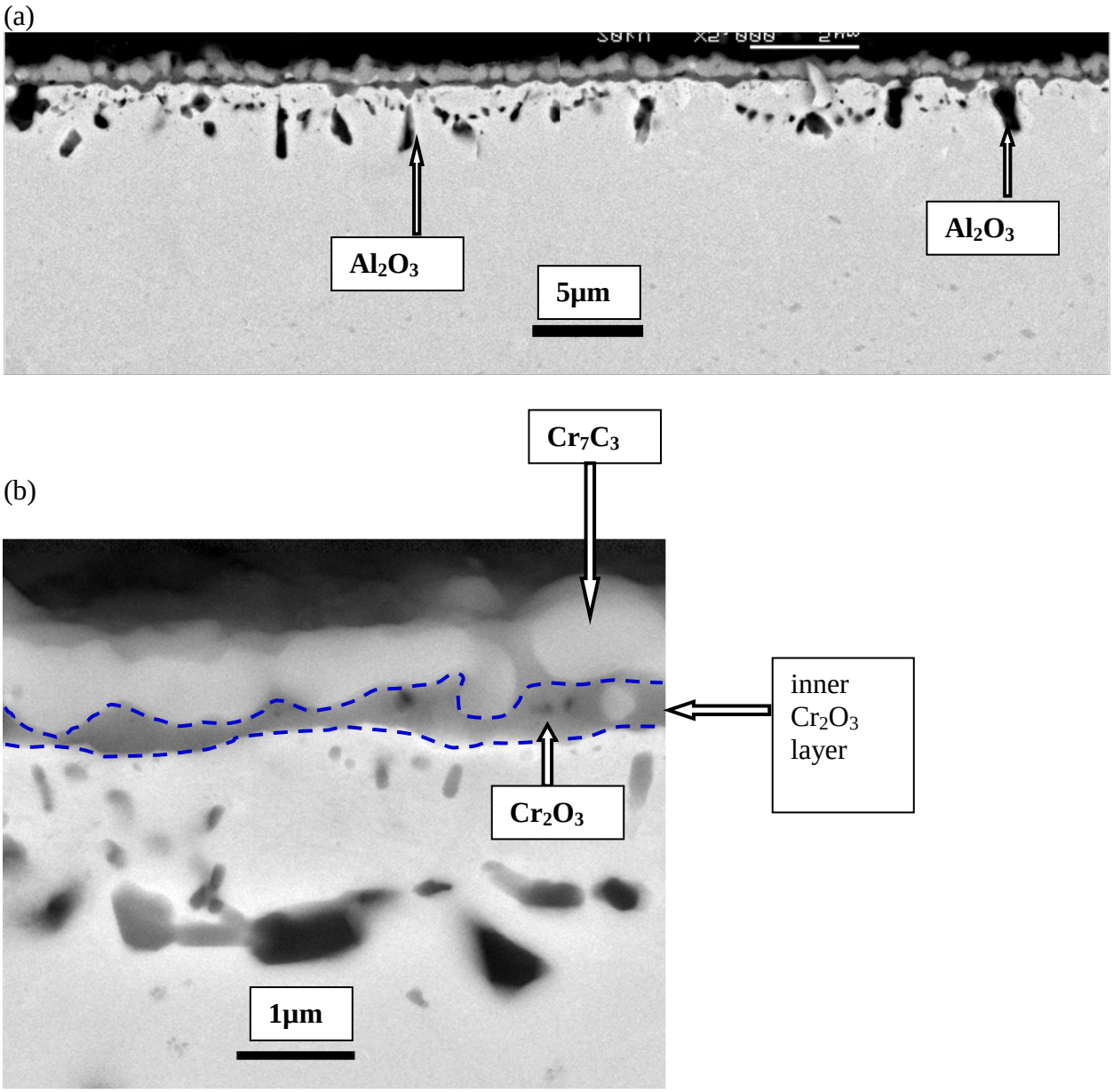

Figure 4.52 (a) Low magnification and (b) high magnification BSE images of the sample exposed in environment 6 (CO/CO_2 = 1272) at 900°C for 100h. The continuous Cr_2O_3 layer adjacent to the alloy is defined as inner Cr_2O_3 layer (marked by blue dashed line).

(a)

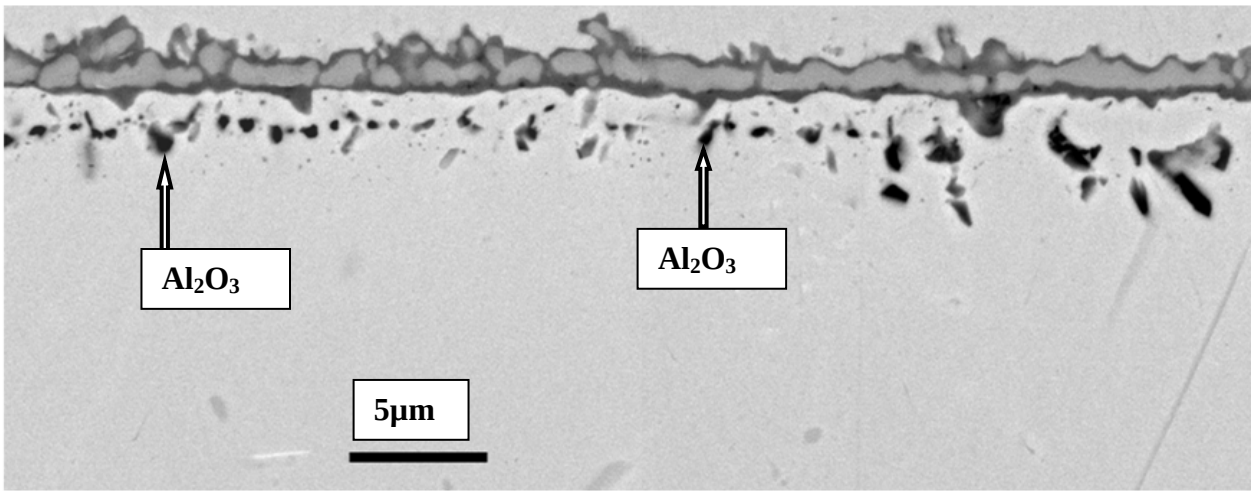

(b)

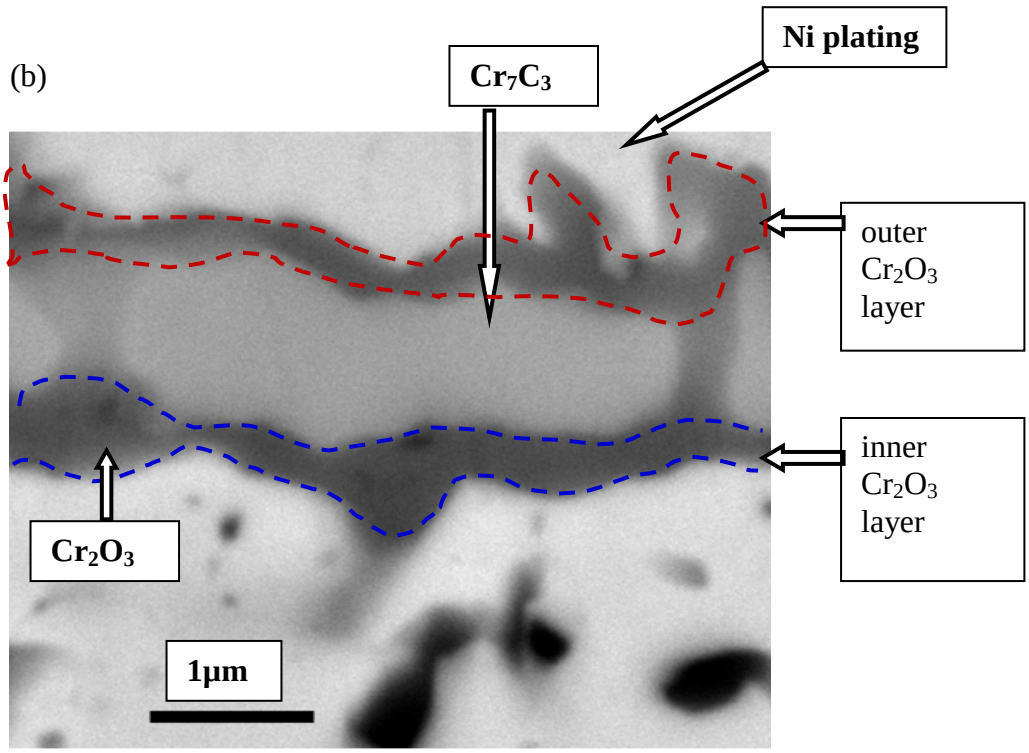

Figure 4.53 (a) Low magnification and (b) high magnification BSE images of the sample exposed in environment 6 (CO/CO_2 = 1272) at 900°C for 225h. The continuous Cr_2O_3 layer adjacent to the alloy is defined as inner layer (marked by blue dashed line). The Cr_2O_3 layer formed near the gas/scale is defined as outer Cr_2O_3 layer (marked with red dashed line).

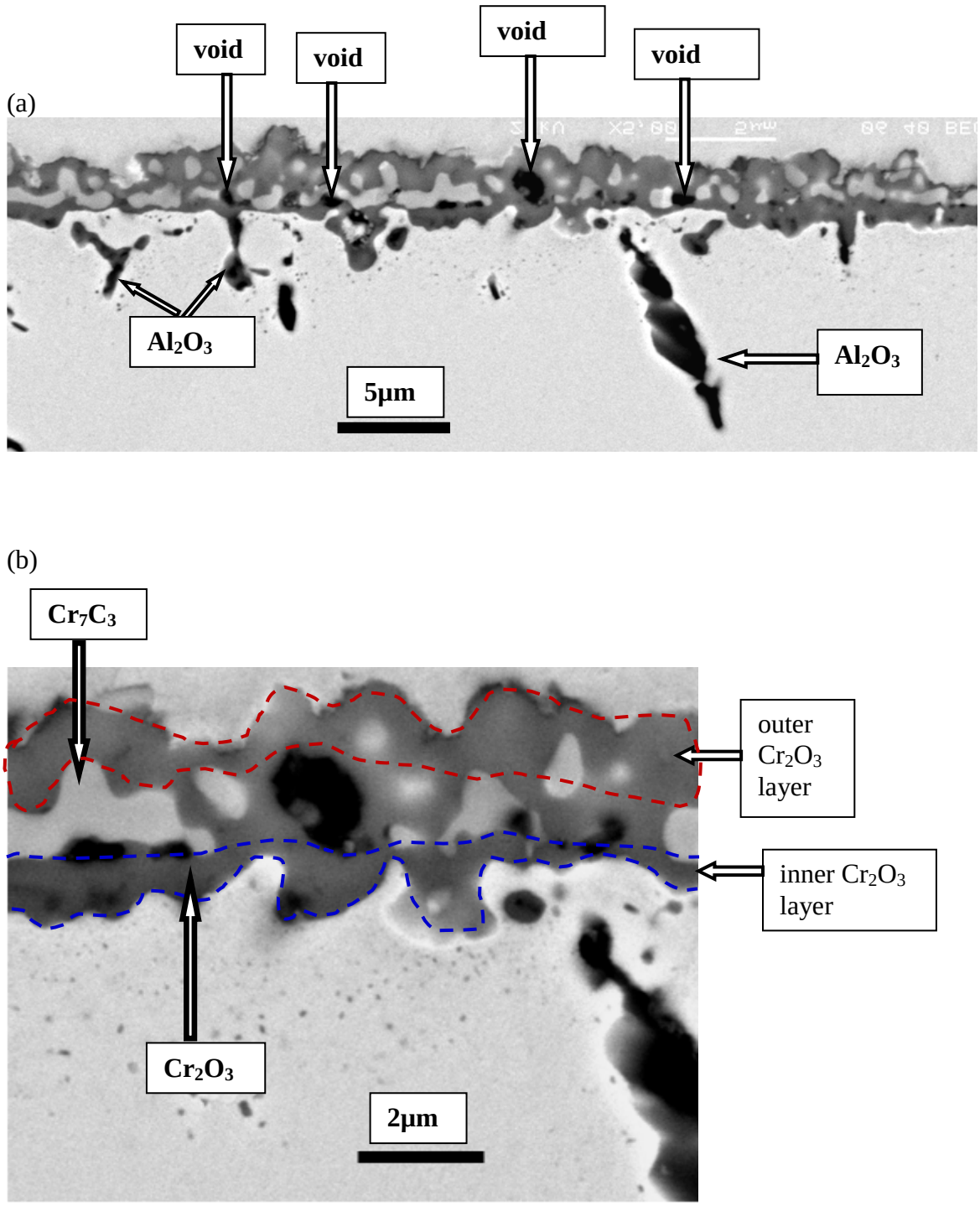

Figure 4.54 (a) Low magnification and (b) high magnification BSE images of the sample exposed in environment 6 (CO/CO_2 = 1272) at 900°C for 375h. The continuous Cr_2O_3 layer adjacent to the alloy is defined as inner layer (marked by blue dashed line). The Cr_2O_3 layer formed near the gas/scale is defined as outer Cr_2O_3 layer (marked with red dashed line).

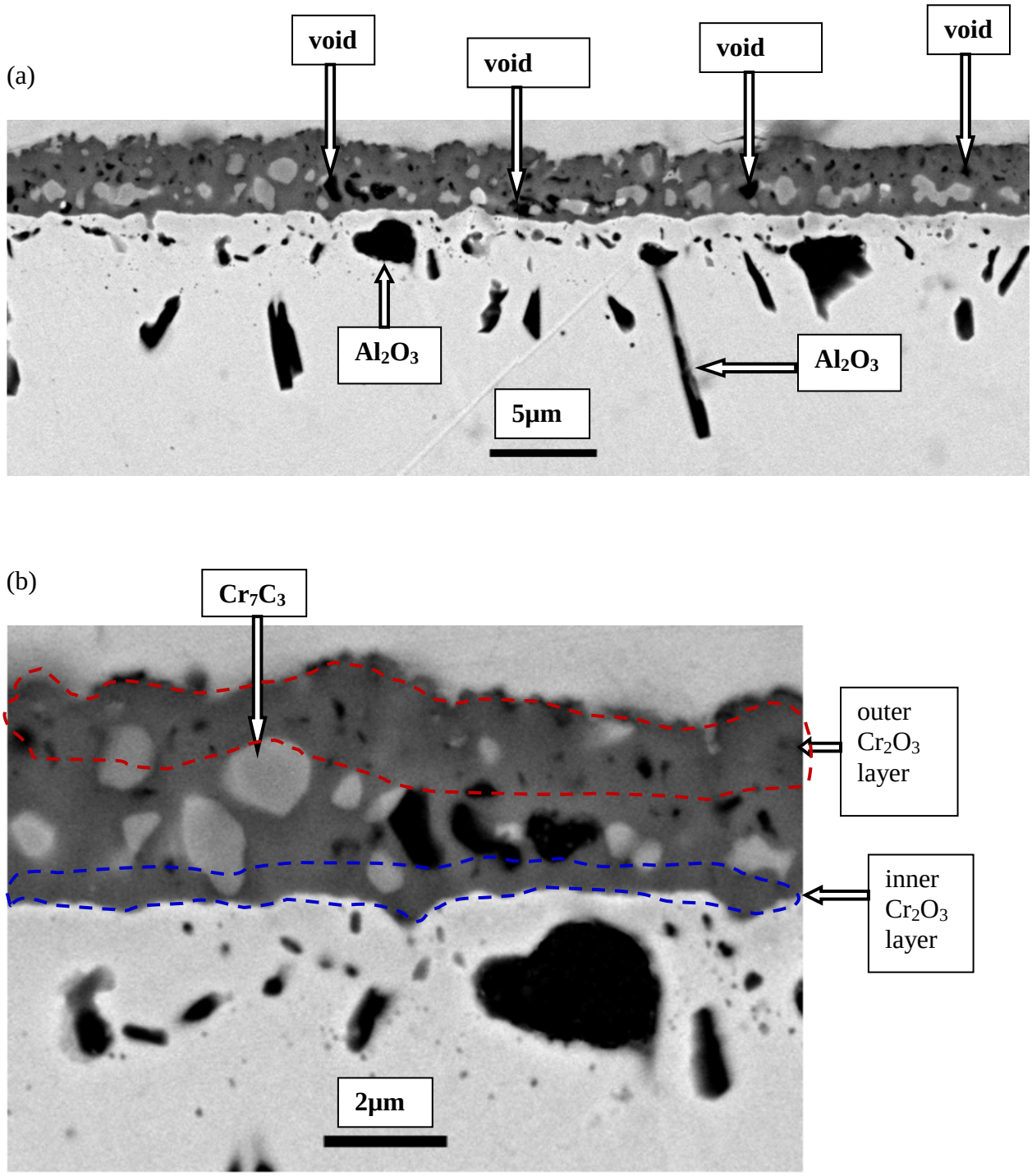

Figure 4.55(a) Low magnification and (b) high magnification BSE images of the sample exposed in environment 6 (CO/CO_2 = 1272) at 900°C for 500h. The continuous Cr_2O_3 layer adjacent to the alloy is defined as inner layer (marked by blue dashed line). The Cr_2O_3 layer formed near the gas/scale is defined as outer Cr_2O_3 layer (marked with red dashed line).

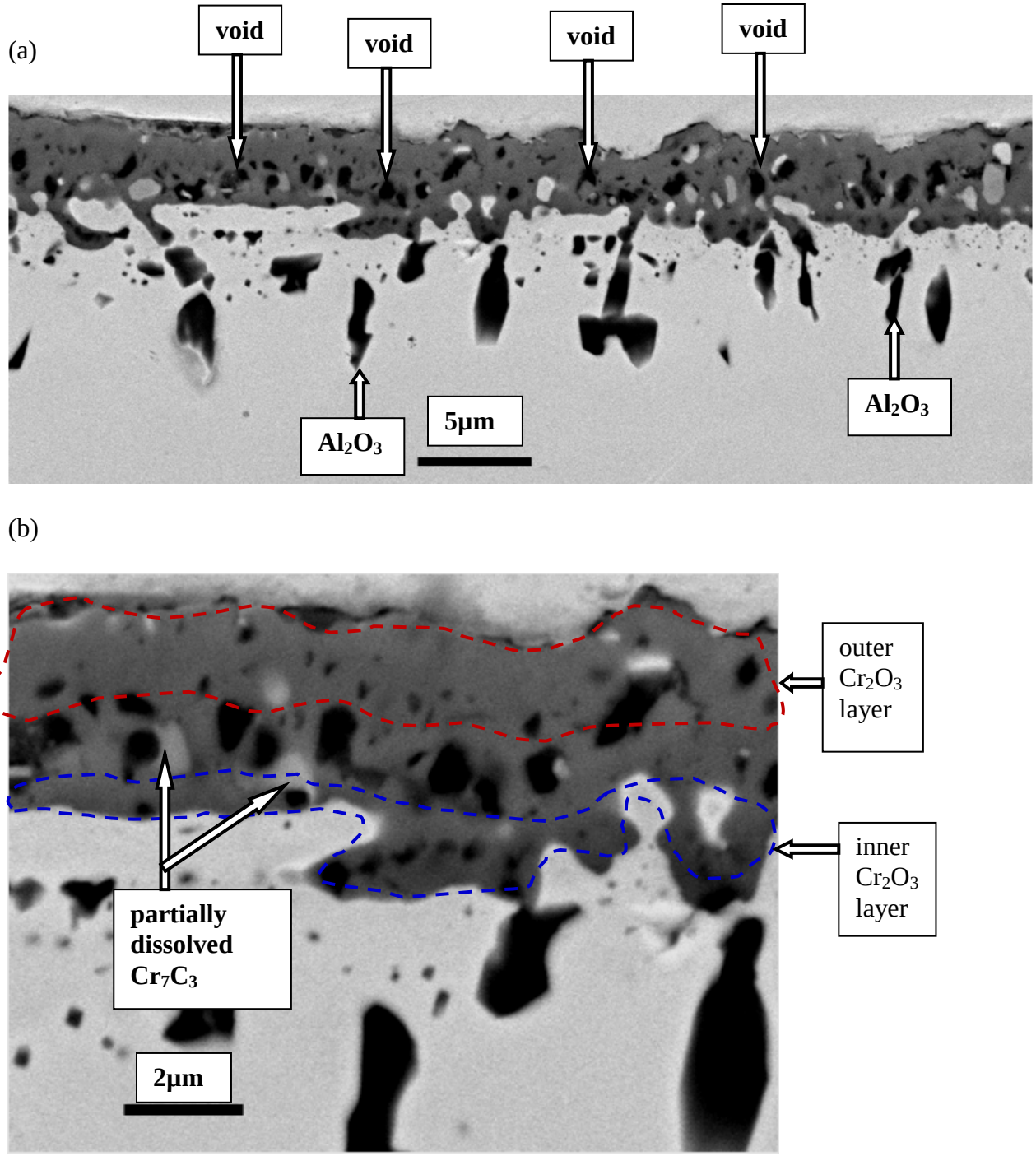

Figure 4.56(a) Low magnification and (b) high magnification BSE images of the sample exposed in environment 6 (CO/CO_2 = 1272) at 900°C for 750h. The continuous Cr_2O_3 layer adjacent to the alloy is defined as inner layer (marked by blue dashed line). The Cr_2O_3 layer formed near the gas/scale is defined as outer Cr_2O_3 layer (marked with red dashed line).

(a)

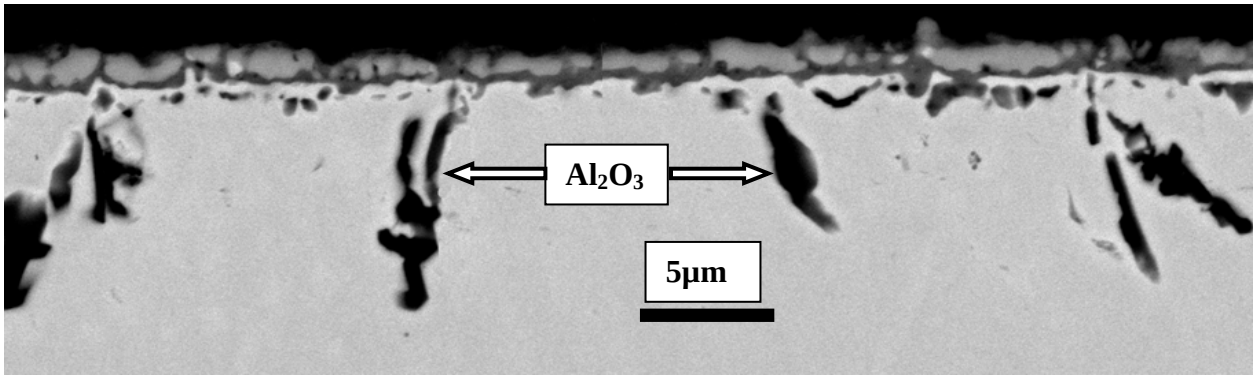

(b)

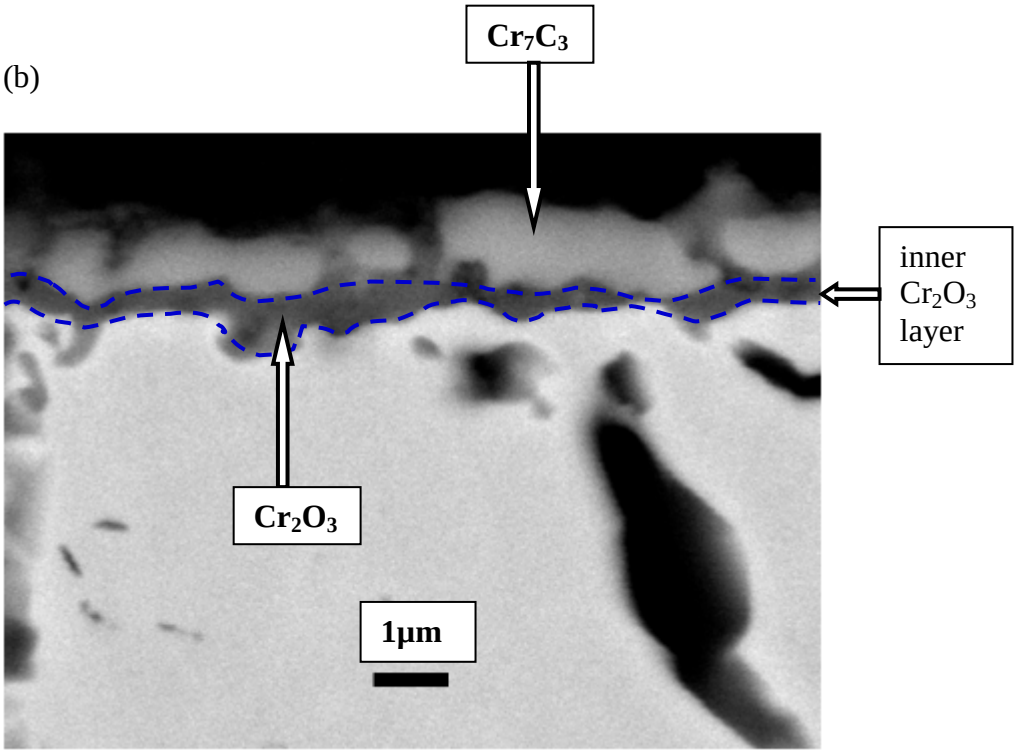

Figure 4.57(a) Low magnification and (b) high magnification BSE images of the sample exposed in environment 6 (CO/CO_2 = 1272) at 950°C for 100h. The continuous Cr_2O_3 layer adjacent to the alloy is defined as inner layer (marked by blue dashed line). The Cr_2O_3 layer formed near the gas/scale is defined as outer Cr_2O_3 layer (marked with red dashed line).

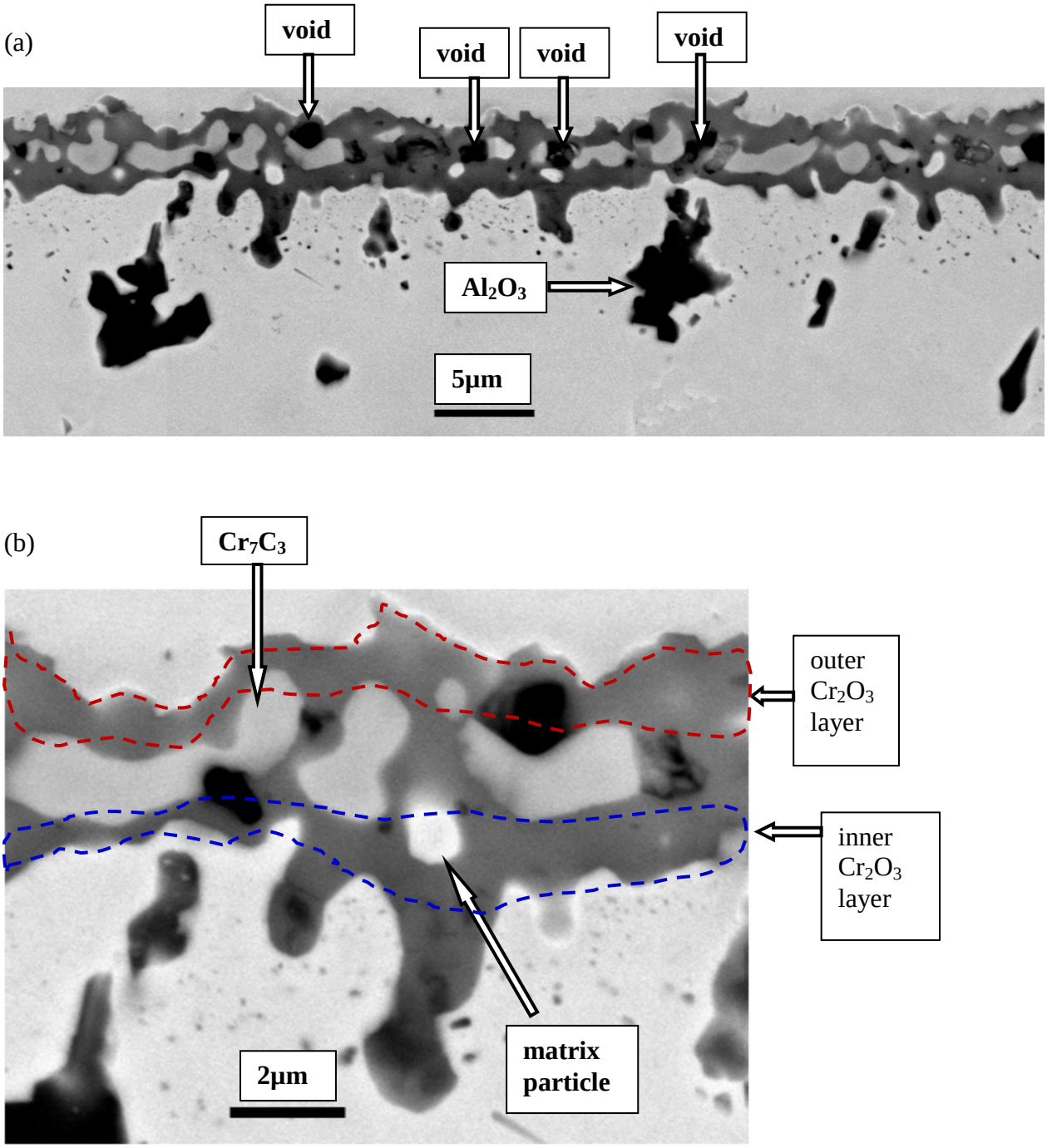

Figure 4.58(a) Low magnification and (b) high magnification BSE images of the sample exposed in environment 6 (CO/CO_2 = 1272) at 950°C for 375h. The continuous Cr_2O_3 layer adjacent to the alloy is defined as inner layer (marked by blue dashed line). The Cr_2O_3 layer formed near the gas/scale is defined as outer Cr_2O_3 layer (marked with red dashed line).

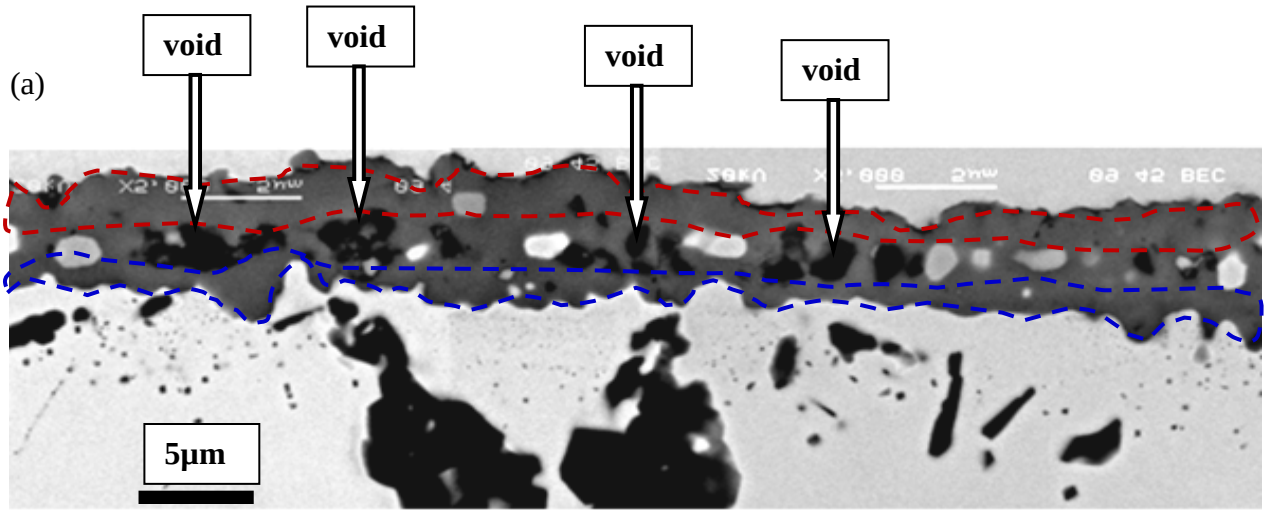

Figure 4.59 Low magnification BSE images of the sample exposed in environment 6 (CO/CO_2 = 1272) at 950°C for 500h. The continuous Cr_2O_3 layer adjacent to the alloy is defined as inner layer (marked by blue dashed line). The Cr_2O_3 layer formed near the gas/scale is defined as outer Cr_2O_3 layer (marked with red dashed line).

(a)

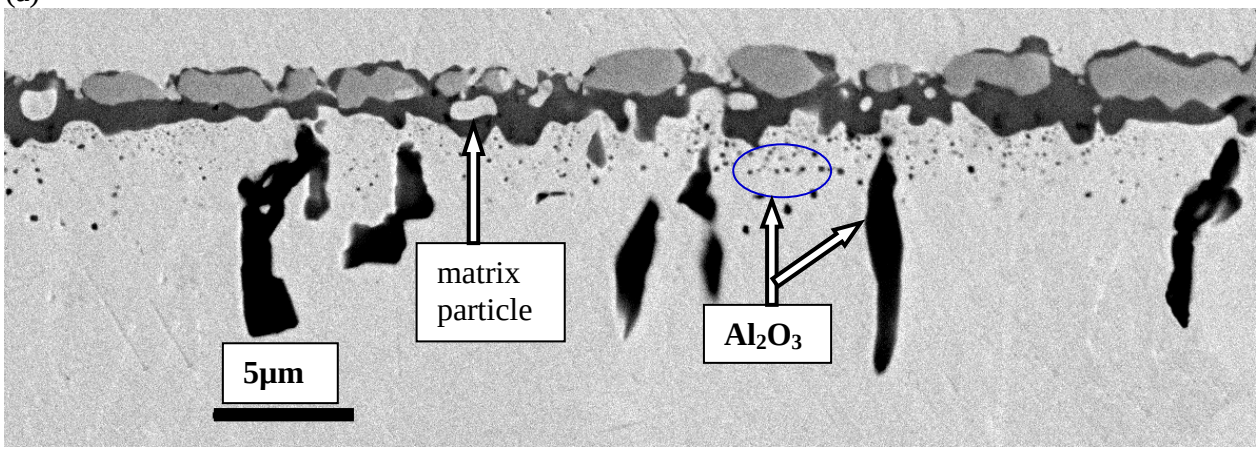

(b)

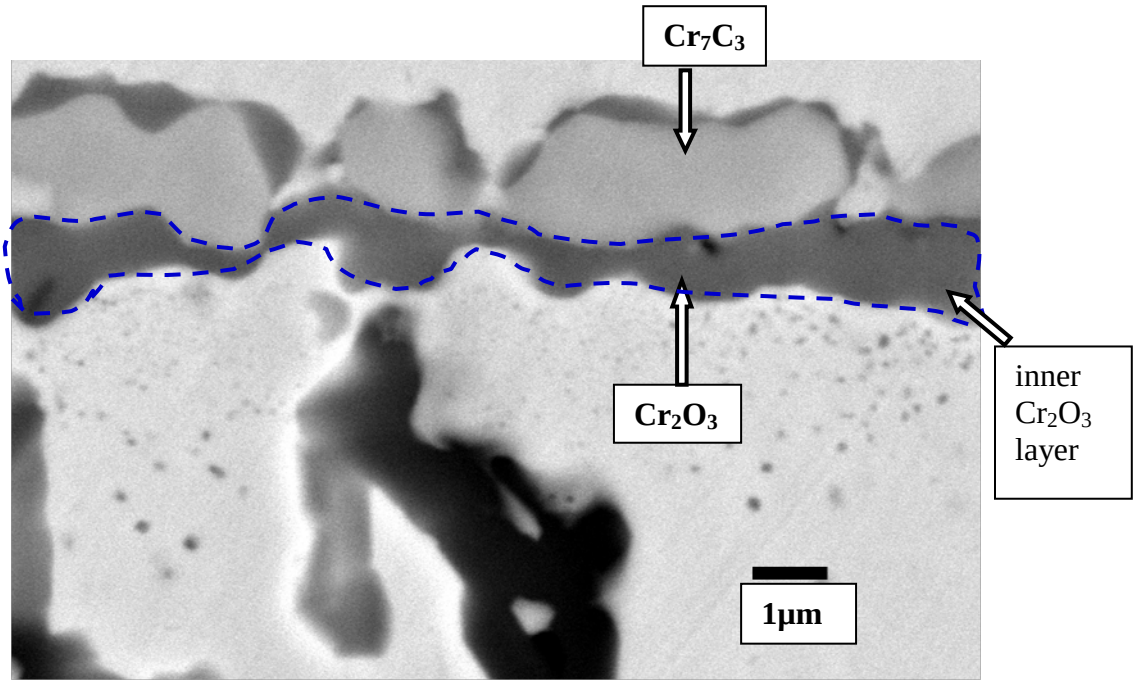

Figure 4.60 (a) Low magnification and (b) high magnification BSE images of the sample exposed in environment 6 (CO/CO_2 = 1272) at 1000°C for 100h. The continuous Cr_2O_3 layer adjacent to the alloy is defined as inner layer (marked by blue dashed line). The Cr_2O_3 layer formed near the gas/scale is defined as outer Cr_2O_3 layer (marked with red dashed line).

(a)

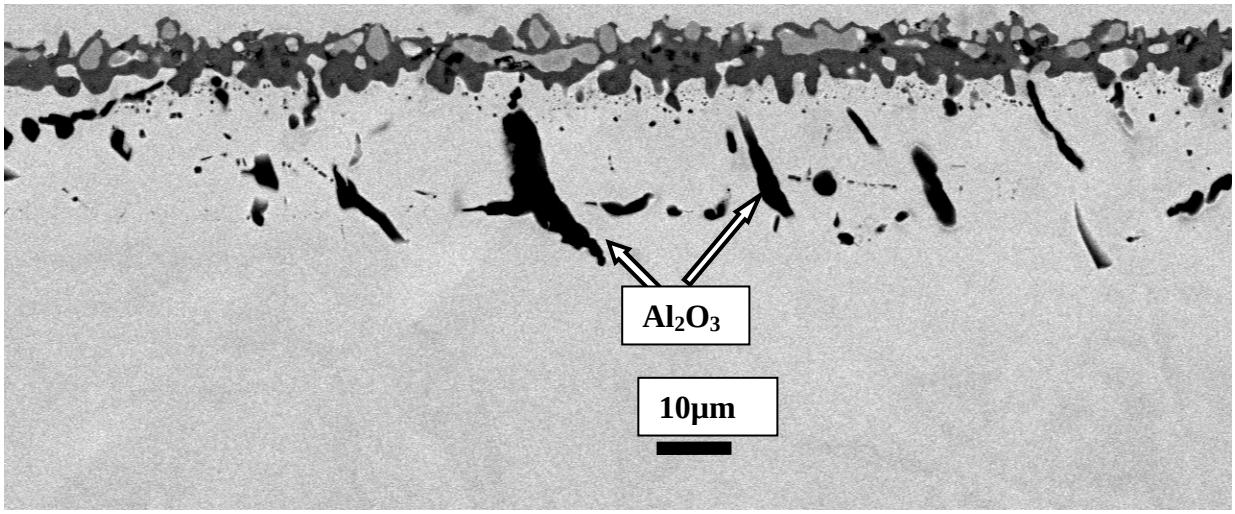

(b)

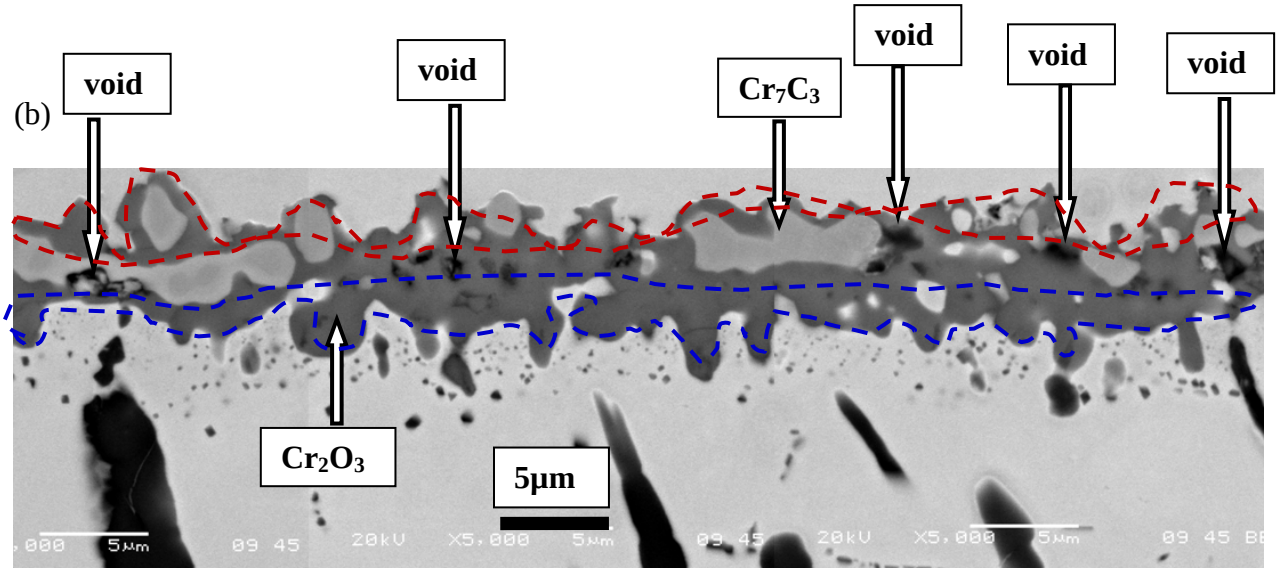

Figure 4.61(a) Low magnification and (b) high magnification BSE images of the sample exposed in environment 6 (CO/CO_2 = 1272) at 1000°C for 375h. The continuous Cr_2O_3 layer adjacent to the alloy is defined as inner layer (marked by blue dashed line). The Cr_2O_3 layer formed near the gas/scale is defined as outer Cr_2O_3 layer (marked with red dashed line).

(a)

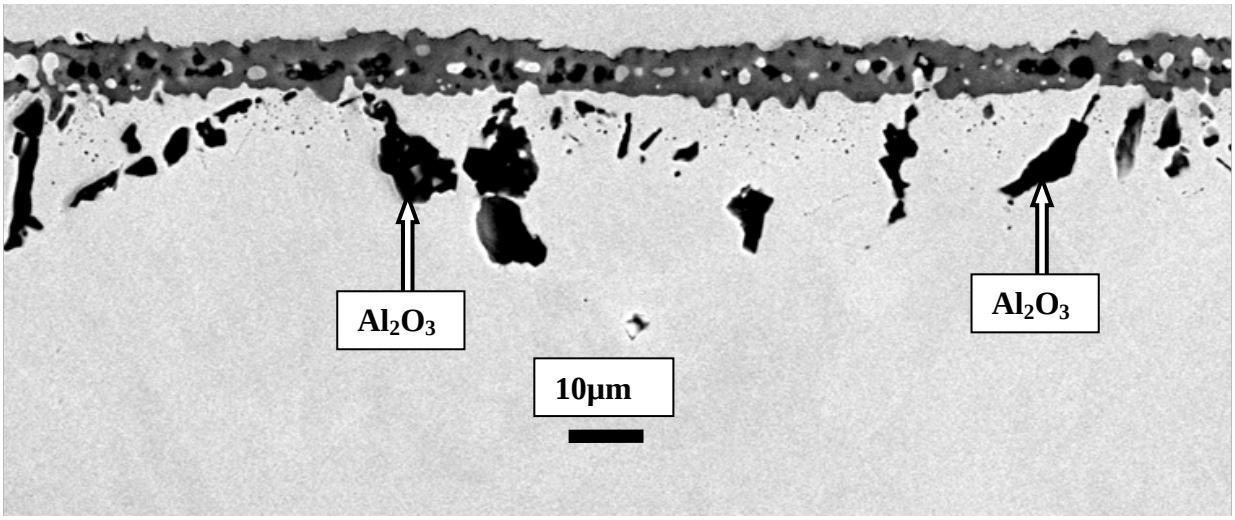

(b)

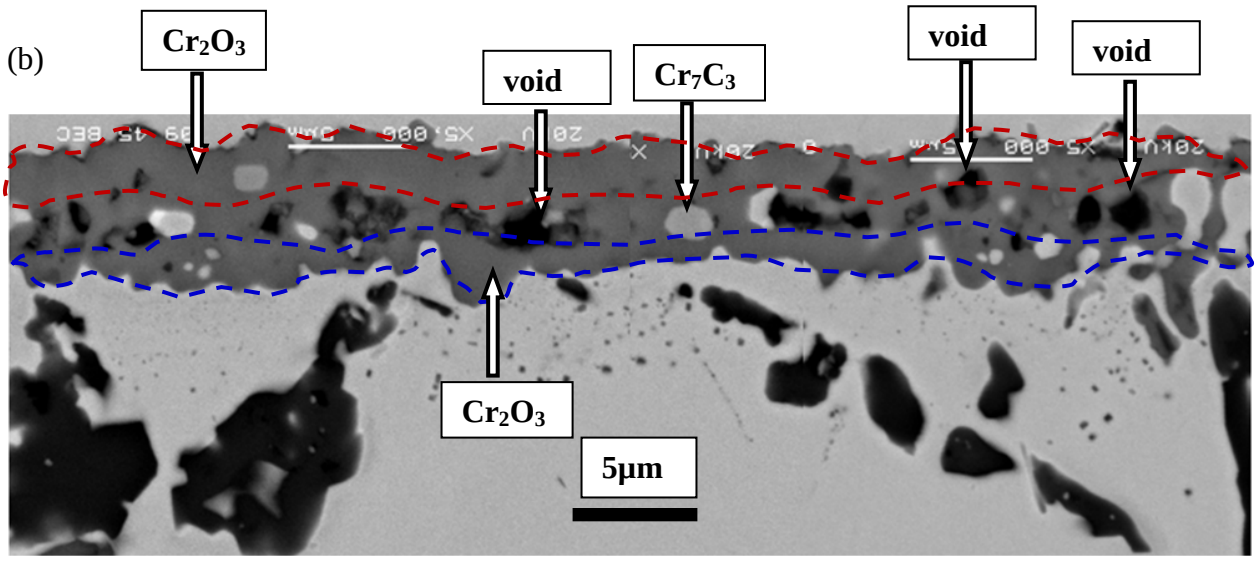

Figure 4.62 Low magnification BSE images of the sample exposed in environment 6 (CO/CO_2 = 1272) at 1000°C for 500h. The continuous Cr_2O_3 layer adjacent to the alloy is defined as inner layer (marked by blue dashed line). The Cr_2O_3 layer formed near the gas/scale is defined as outer Cr_2O_3 layer (marked with red dashed line).

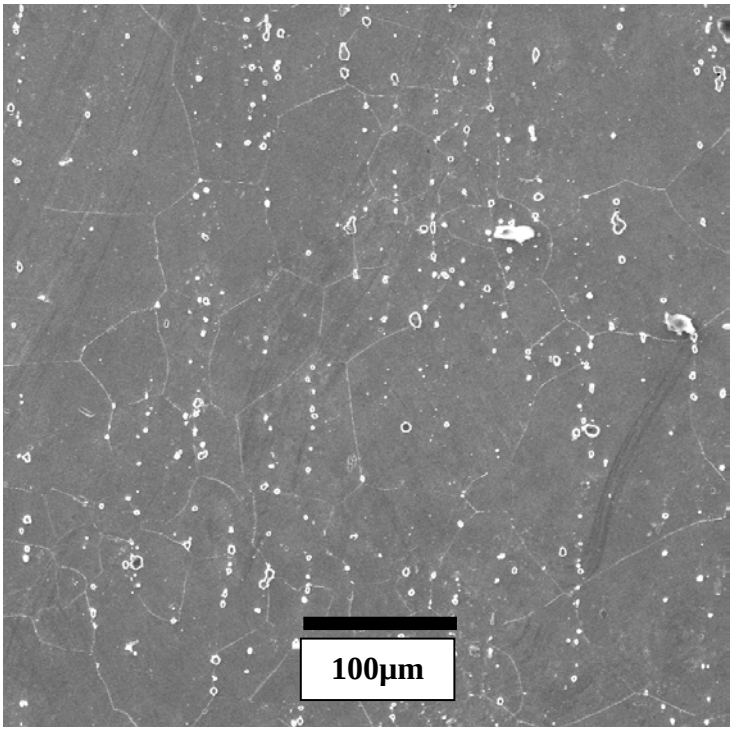

Figure 4.63 Bulk microstructure of the as received alloy 617. The white precipitates are $M_{23}C_6/M_6C$ carbides (where M is Cr, Mo).

(a)

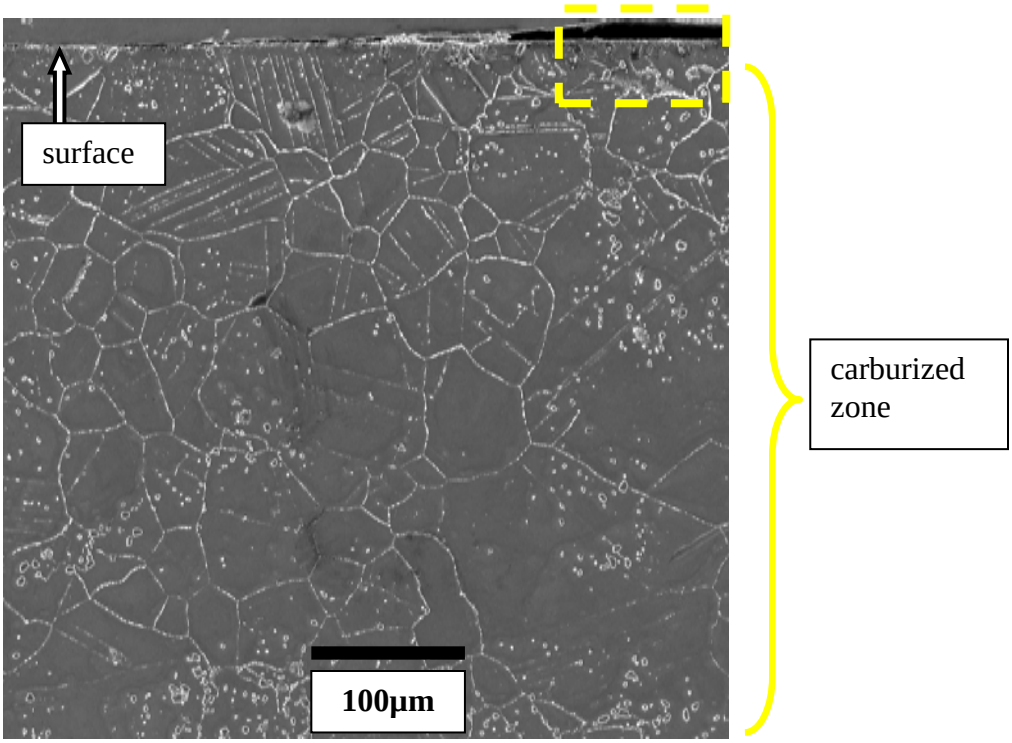

(b)

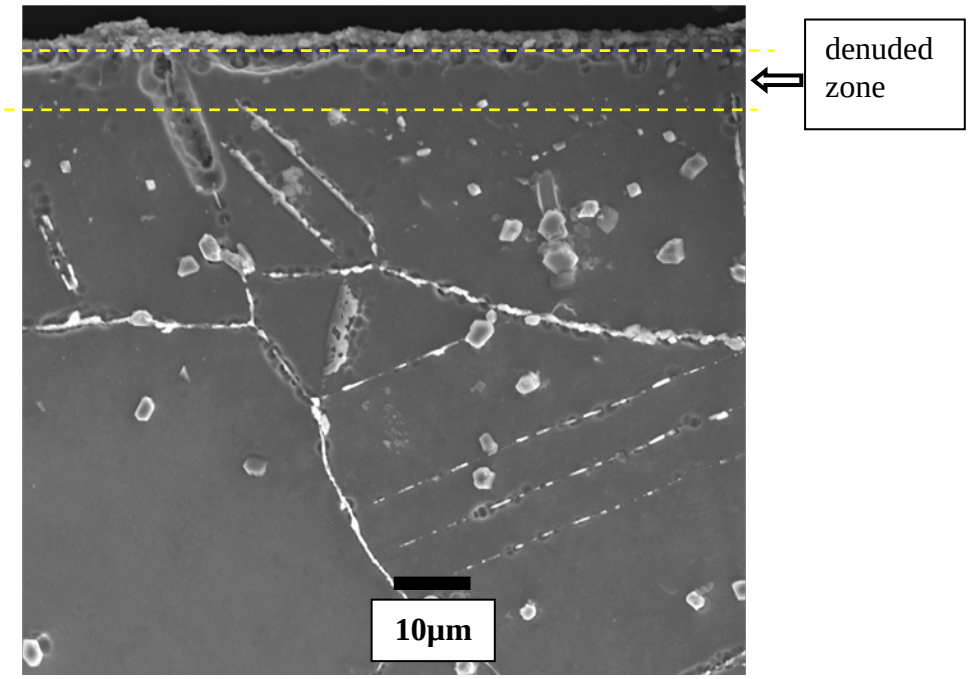

Figure 4.64(a). Bulk microstructure of the sample oxidized in environment 6 (CO/CO_2 = 1272) at 900°C for 100h. (b) high magnification image of the area boxed in (a).

(a)

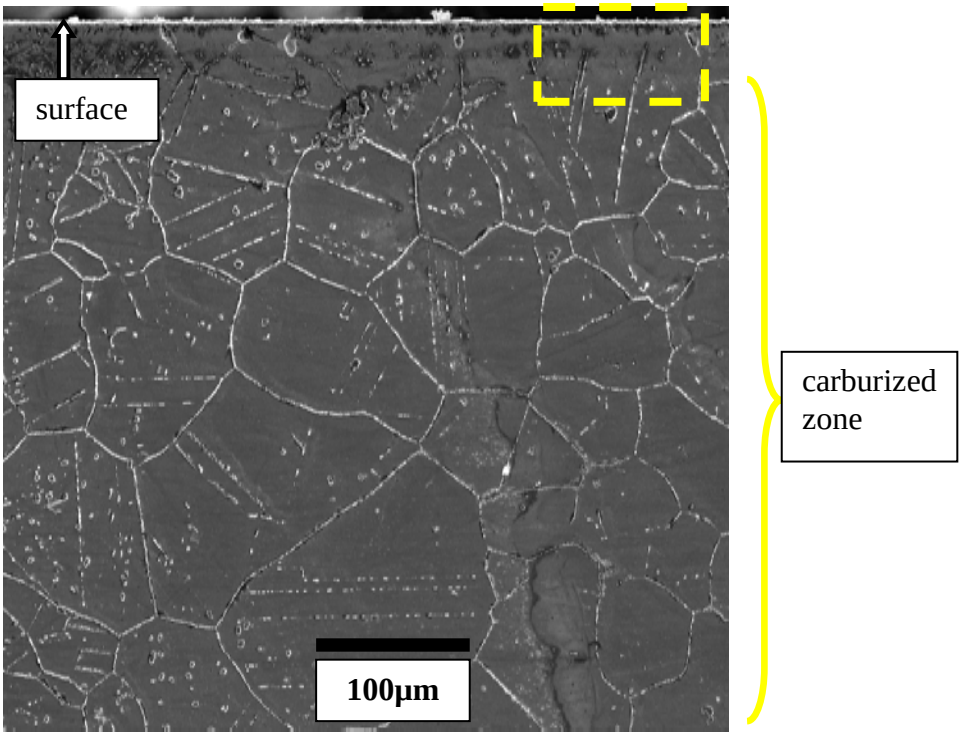

(b)

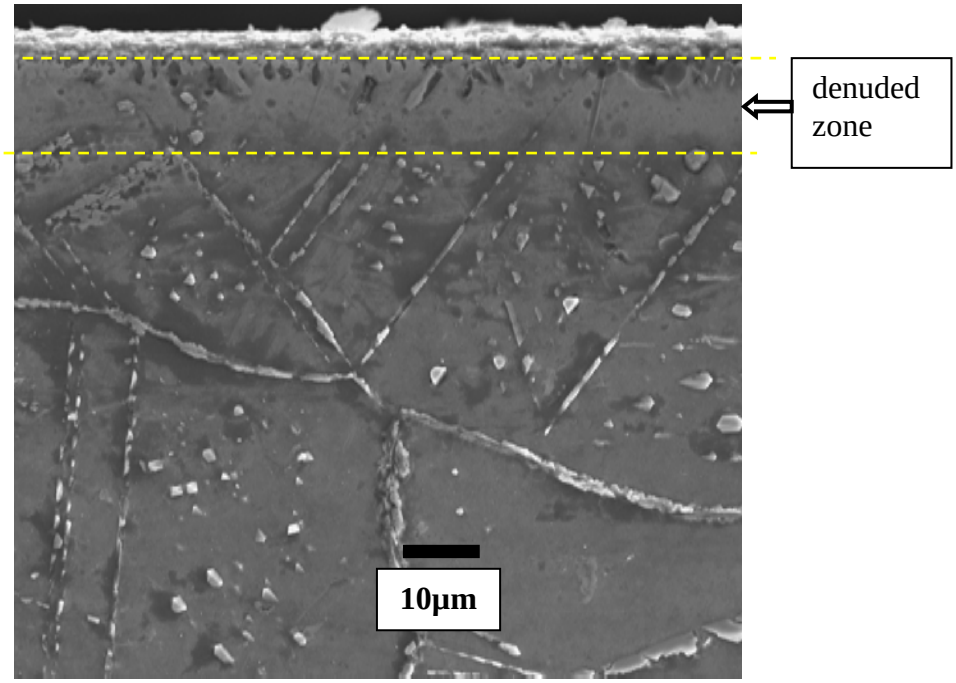

Figure 4.65(a). Bulk microstructure of the sample oxidized in environment 6 (CO/CO_2 = 1272) at 900°C for 375h, and (b) high magnification image of the area boxed in (a).

(a)

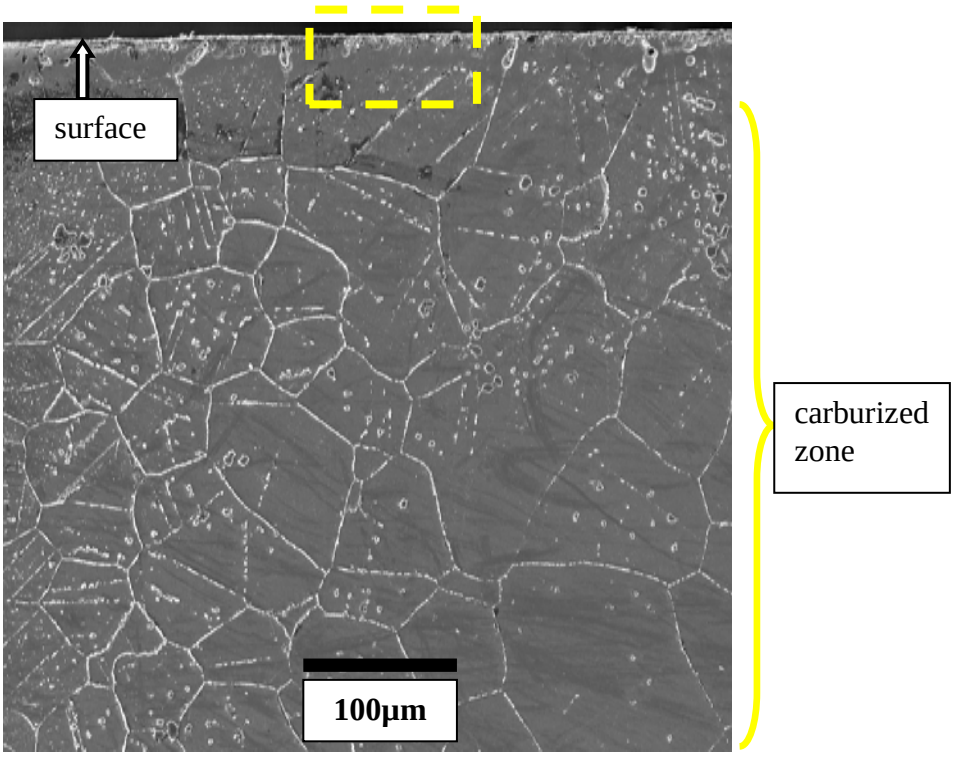

(b)

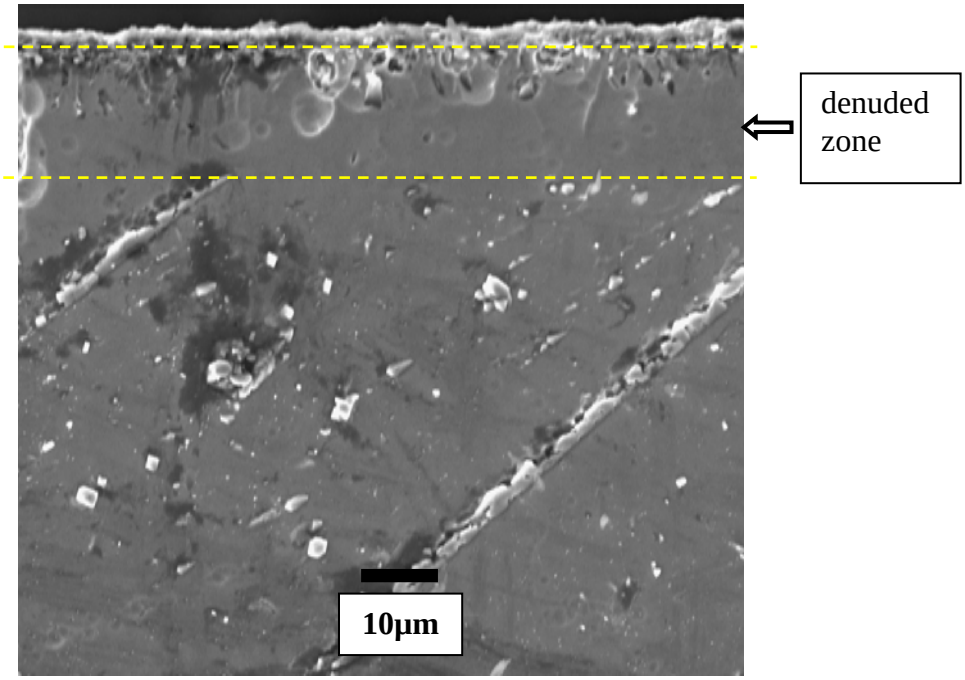

Figure 4.66(a). Bulk microstructure of the sample oxidized in environment 6 (CO/CO_2 = 1272) at 900°C for 500h, and (b) high magnification image of the area boxed in (a).

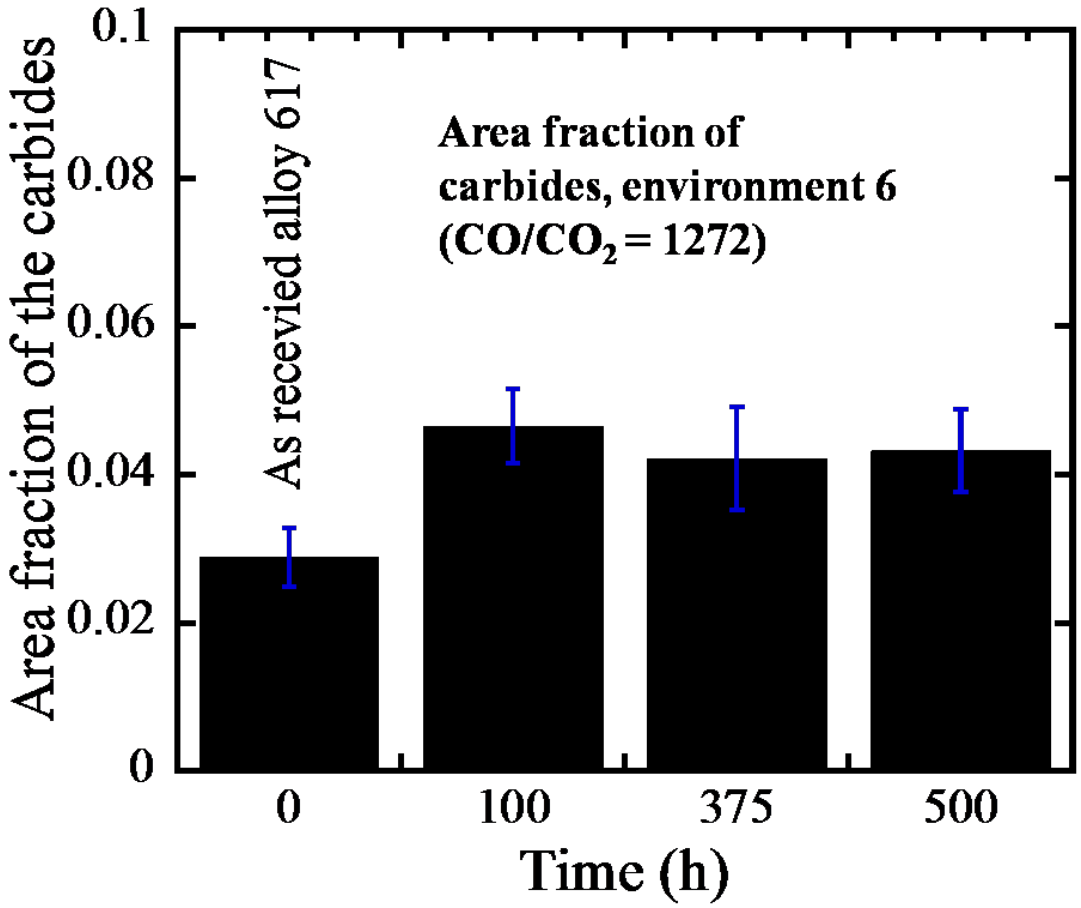

Figure 4.67 The measured area fraction of the $M_{23}C_6/M_6C$ carbides (where M is Cr, Mo) in the bulk of the alloy for as received alloy 617 and the samples oxidized in environment 6 (CO/CO_2 = 1272) for 100h, 375h and 500h at 900°C.

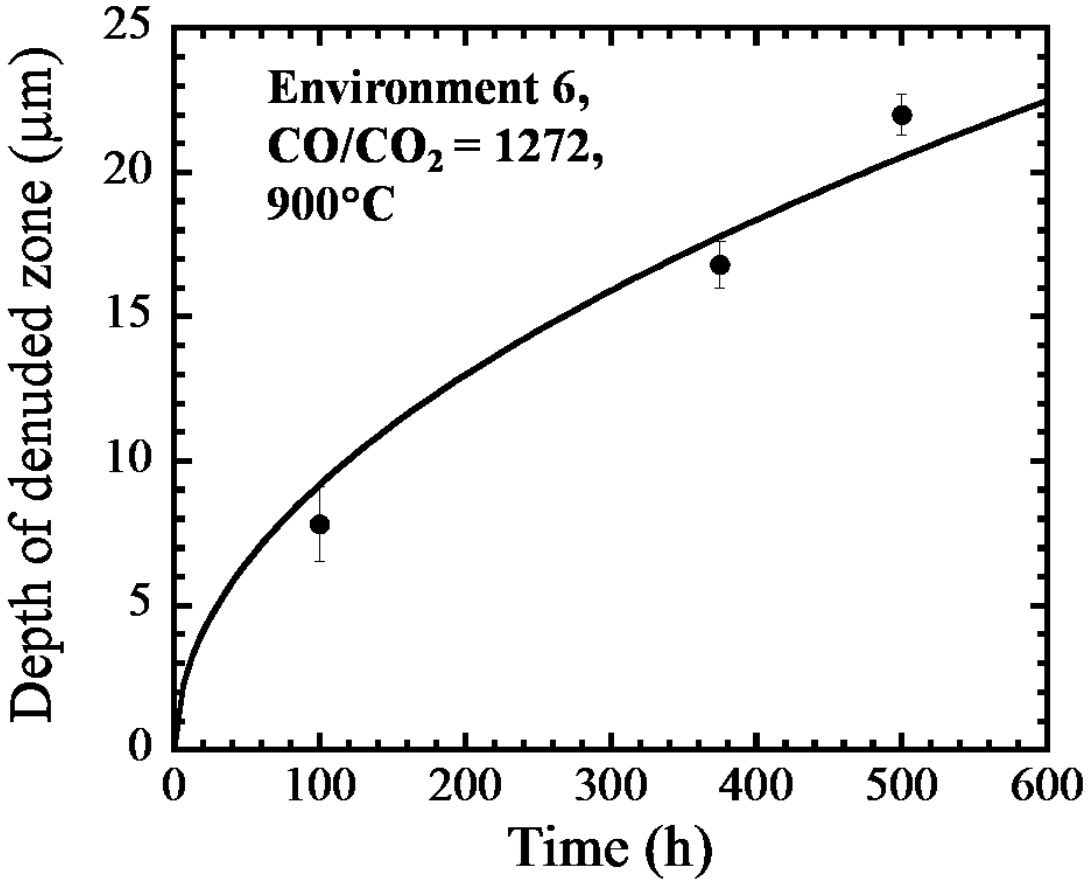

Figure 4.68 Plot of the depth of denuded zone vs. time for samples exposed in environment 6 ($CO/CO_2 = 1272$) at 900°C.

(a)

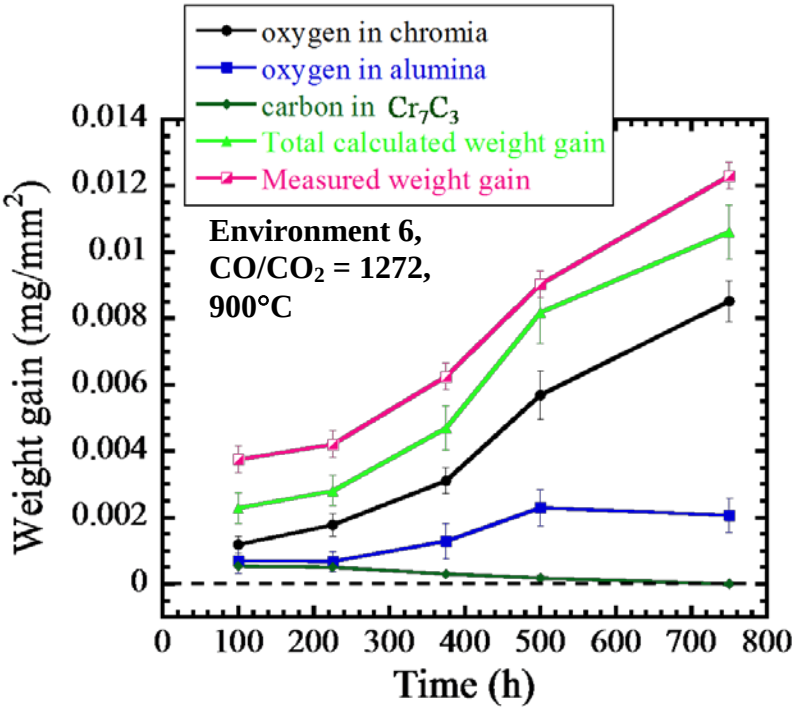

(b)

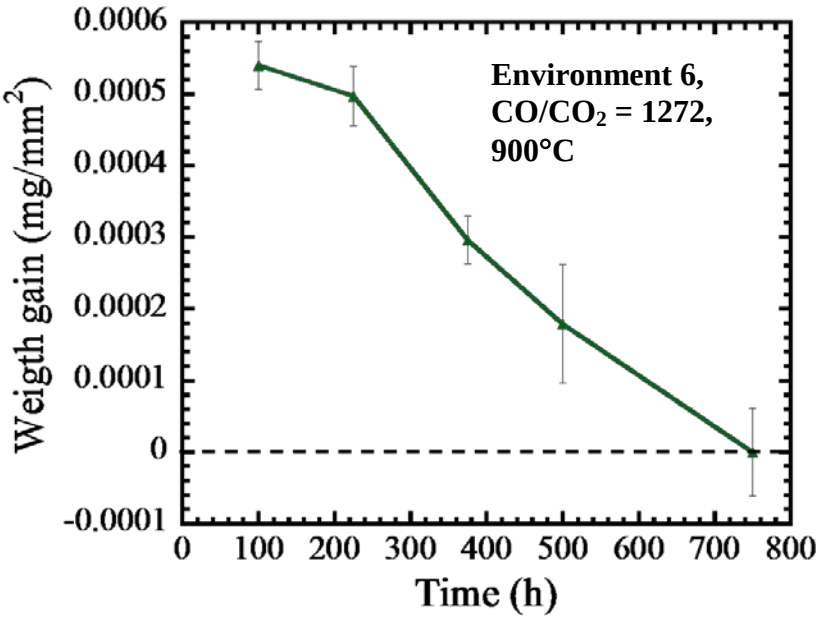

Figure 4.69 Plot of the calculated weight of oxygen in the form of Cr_2O_3 and Al_2O_3 and weight of carbon in the form of the surface Cr_7C_3 as a function of exposure duration. The weight of carbon in the form of surface carbides has been re-plotted in (b) for the clarity.

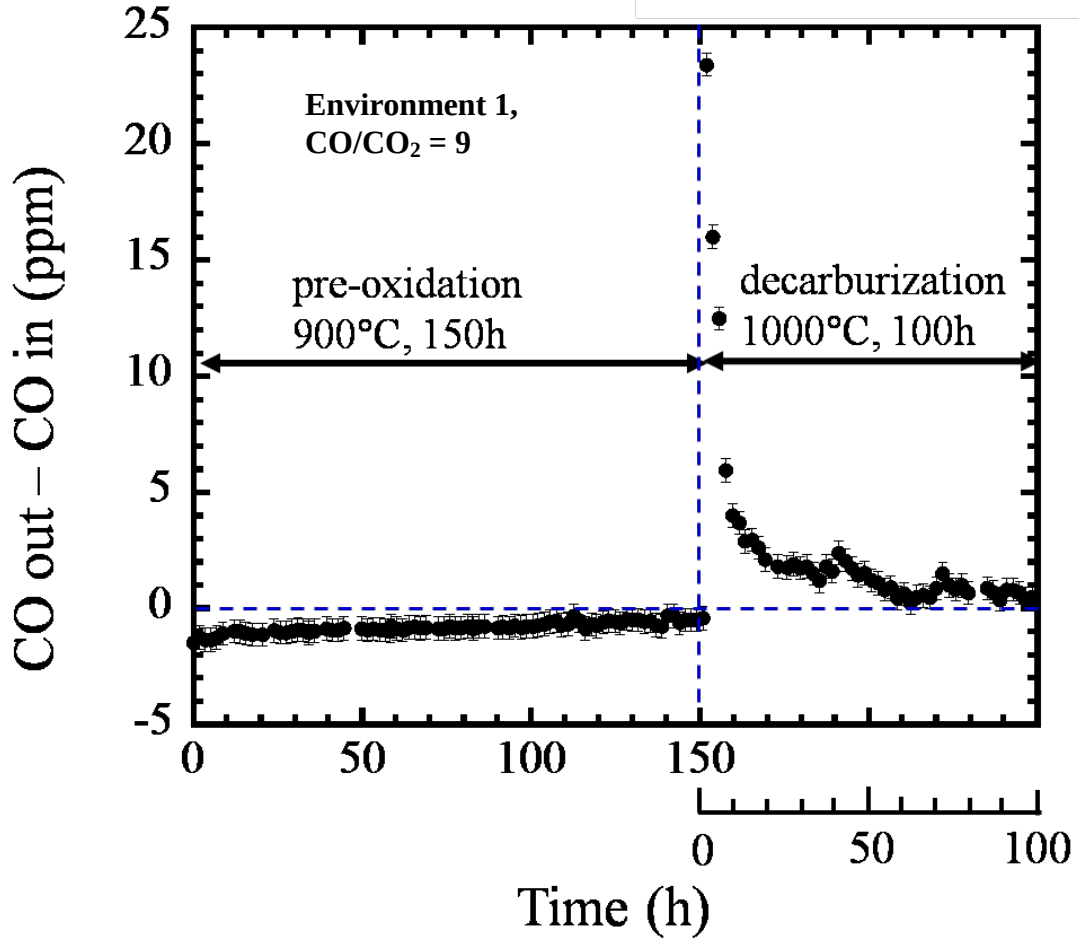

Figure 4.70 Plot of the difference in CO concentrations at the outlet and inlet as a function of exposure time during pre-oxidation step at 900°C and decarburization at 1000°C.

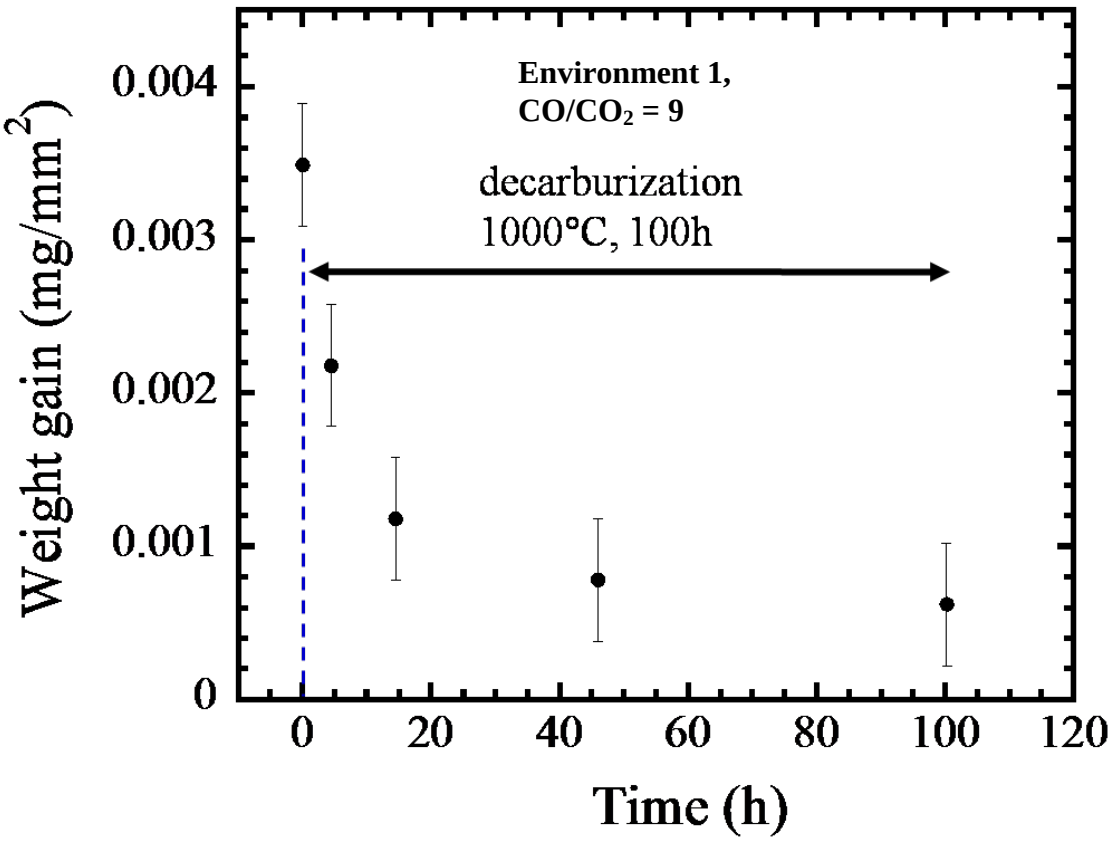

Figure 4.71 Change in the weight of the sample as a function of exposure duration during the decarburization step at 1000°C. The initial weight (at time = 0) shown is the weight gain in the sample after the 150h of pre-oxidation step at 900°C.

(a)

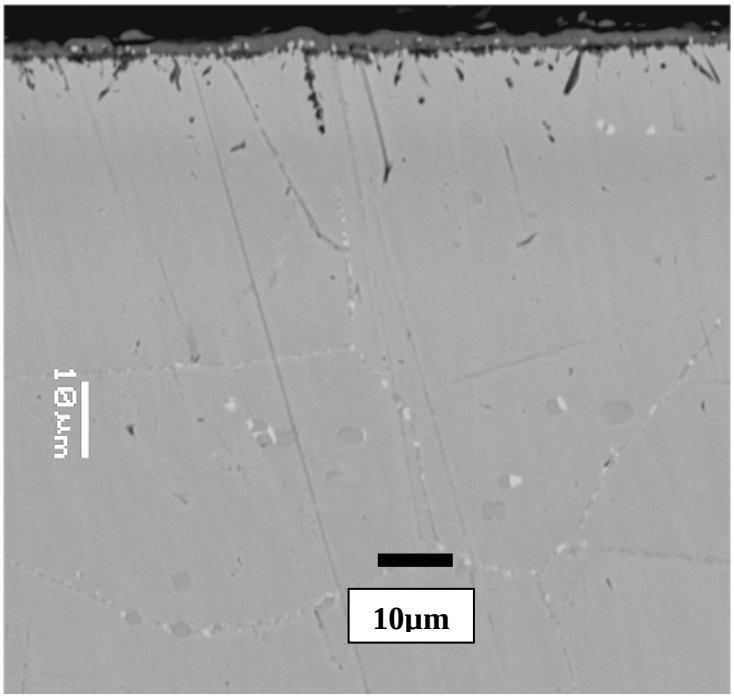

(b)

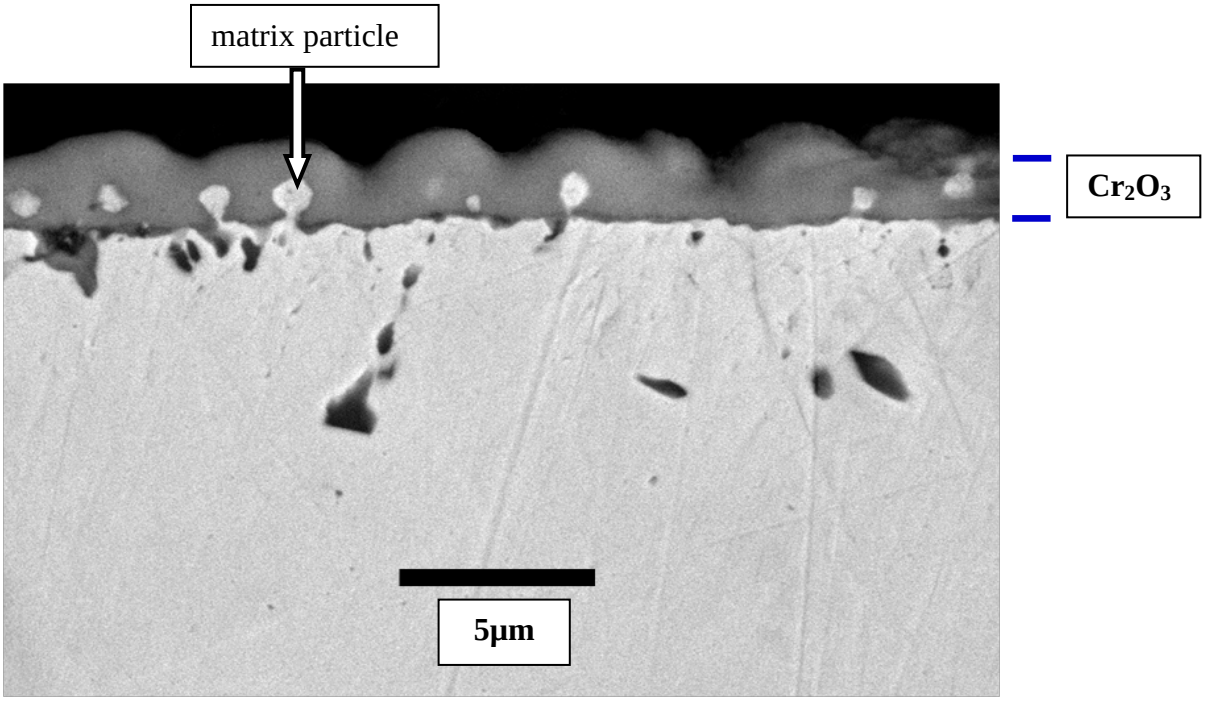

Figure 4.72 (a). Low magnification and (b) high magnification BSE image of the sample pre-oxidized at 900°C for 150 h. Environment 1 (CO/CO_2 = 9), pre-oxidation experiment.

(a)

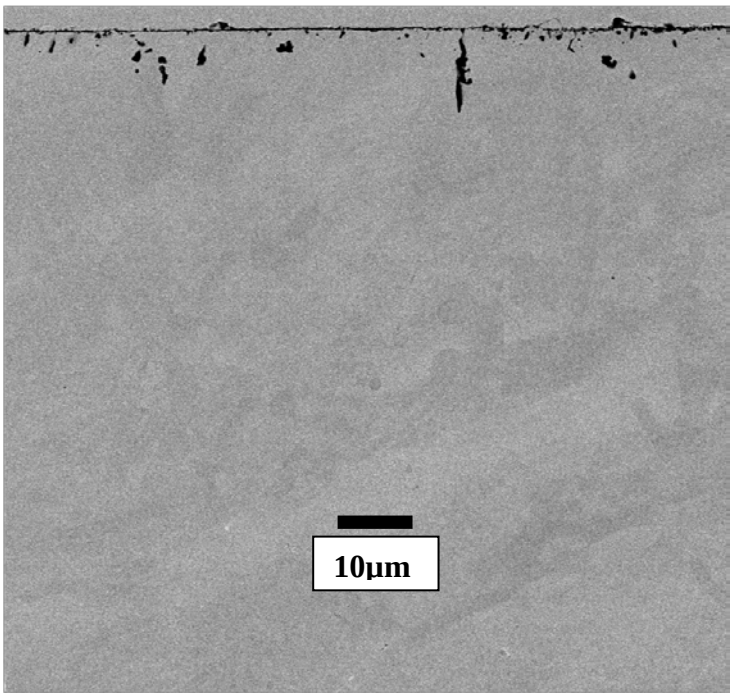

(b)

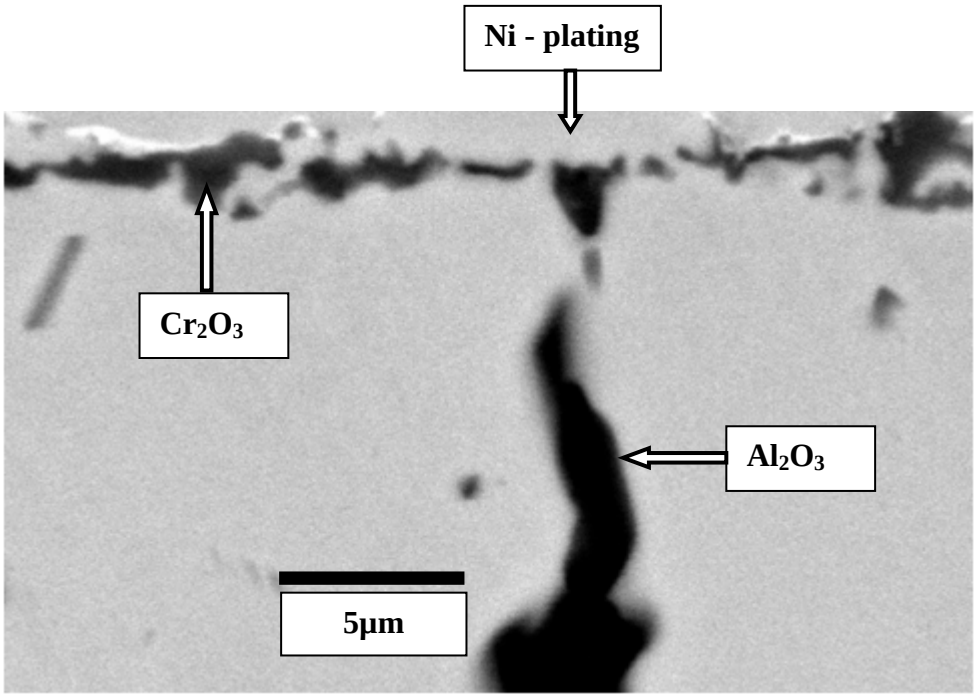

Figure 4.73 (a). Low and (b) high magnification BSE image of the sample after the 100h of decarburization step 1000°C. Environment 1 (CO/CO_2 = 9), pre-oxidation experiment.

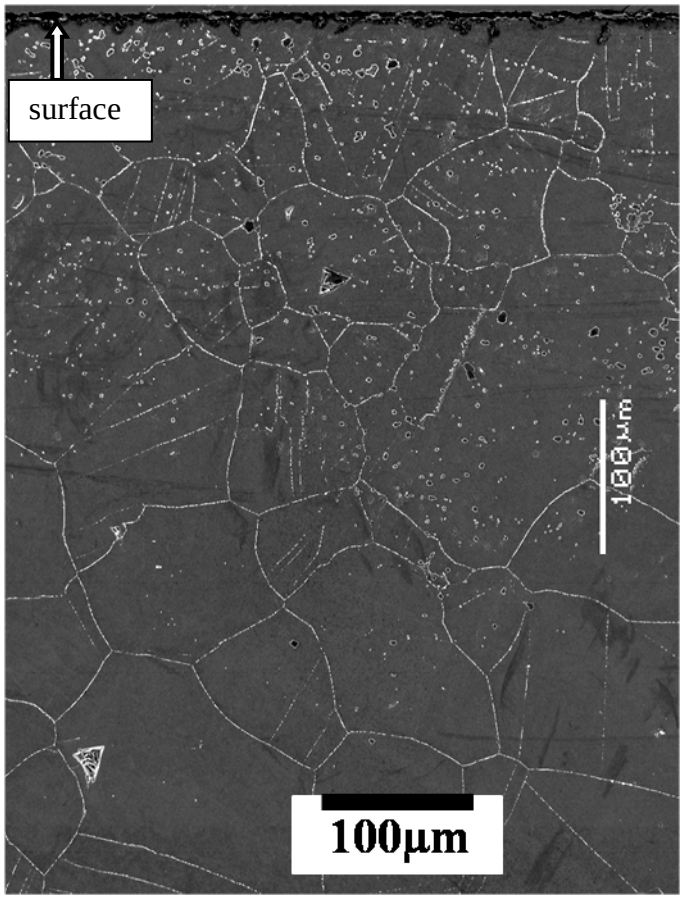

Figure 4.74 Secondary electron image of the sample pre-oxidized at 900°C for 150h. Environment 1 ($CO/CO_2 = 9$), pre-oxidation experiment.

(a)

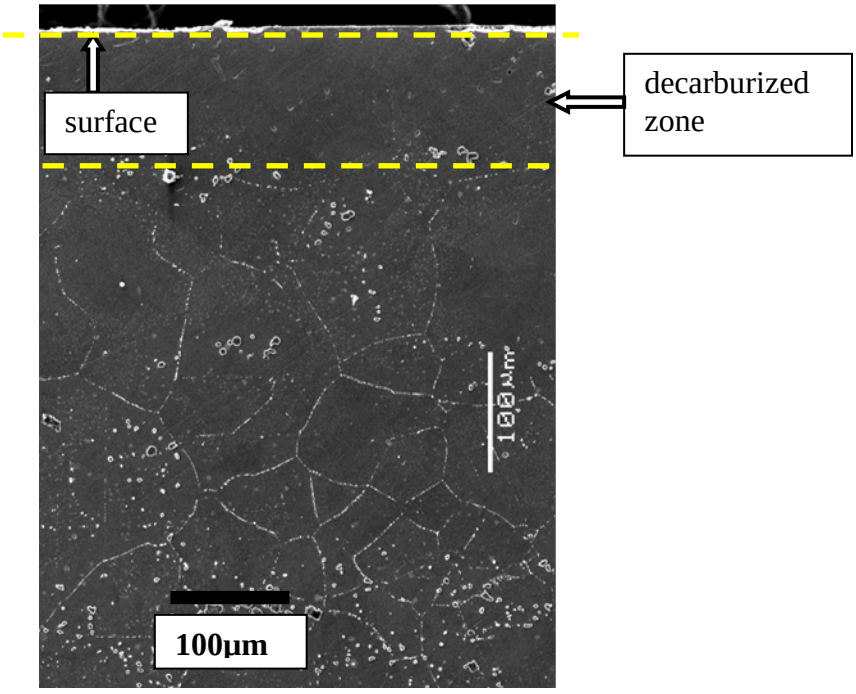

(b)

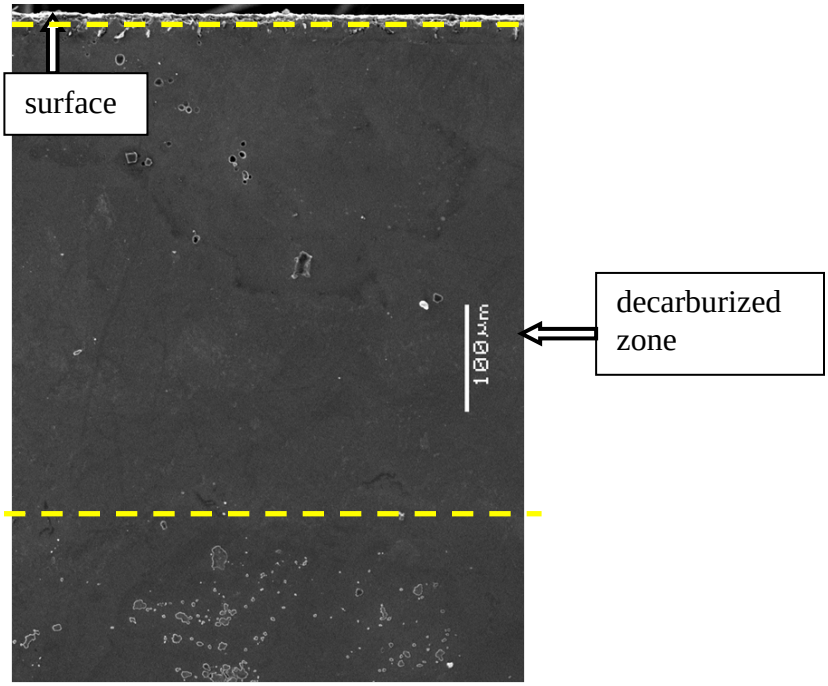

Figure 4.75 Bulk microstructure of the samples (a) decarburized for 15h at 1000°C, and (b) decarburized at 1000°C for 100 h. Environment 1 (CO/CO_2 = 9), pre-oxidation experiment.

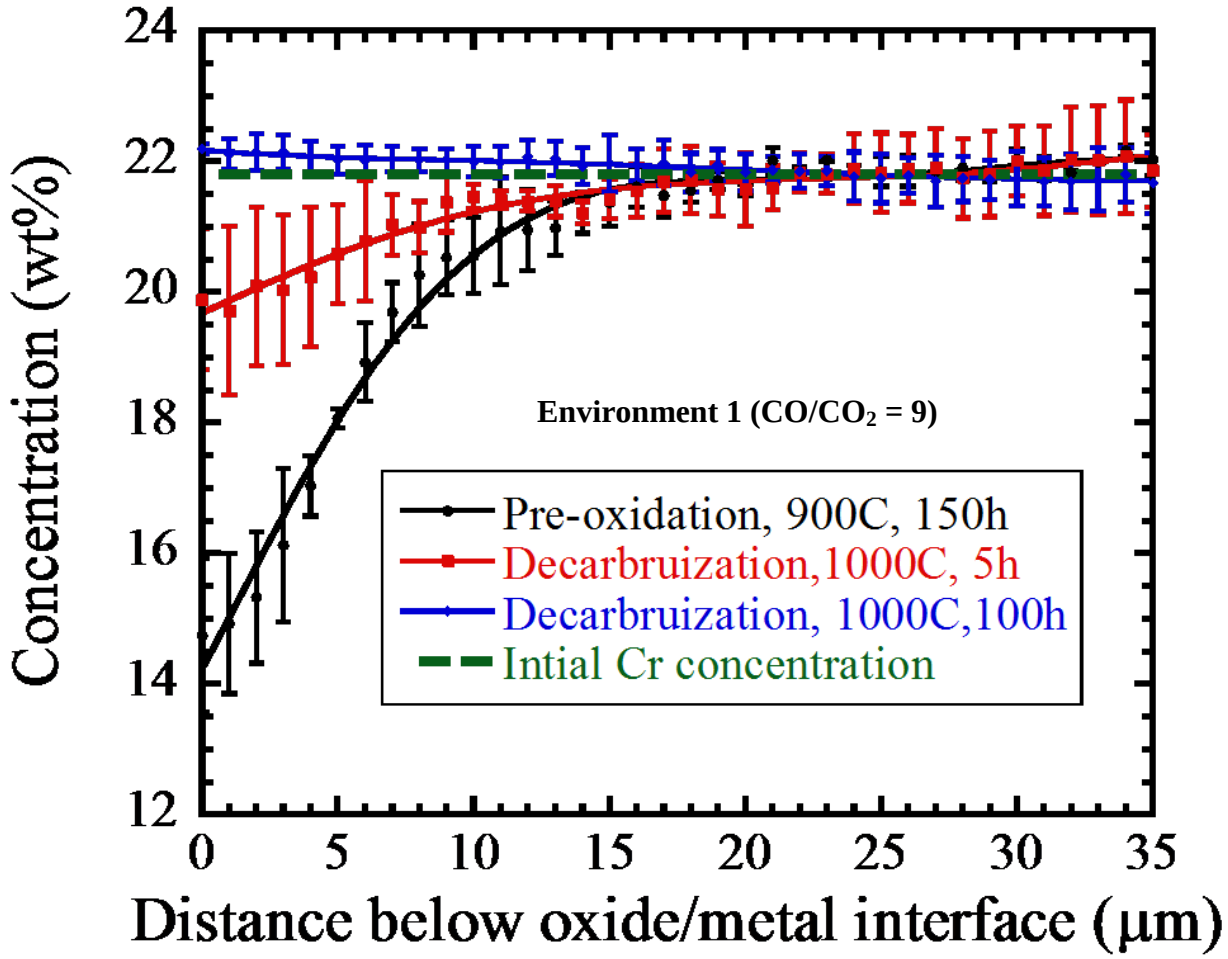

Figure 4.76 Concentration profile of Cr for samples pre-oxidized at 900°C for 150h and decarburized for 5h and 100h at 1000°C. The error bars are the standard deviations of the three line scans measured in each case. The initial concentration of Cr was 21.8% and is superimposed on the plot. Environment 1 ($CO/CO_2 = 9$), pre-oxidation experiment.

(a)

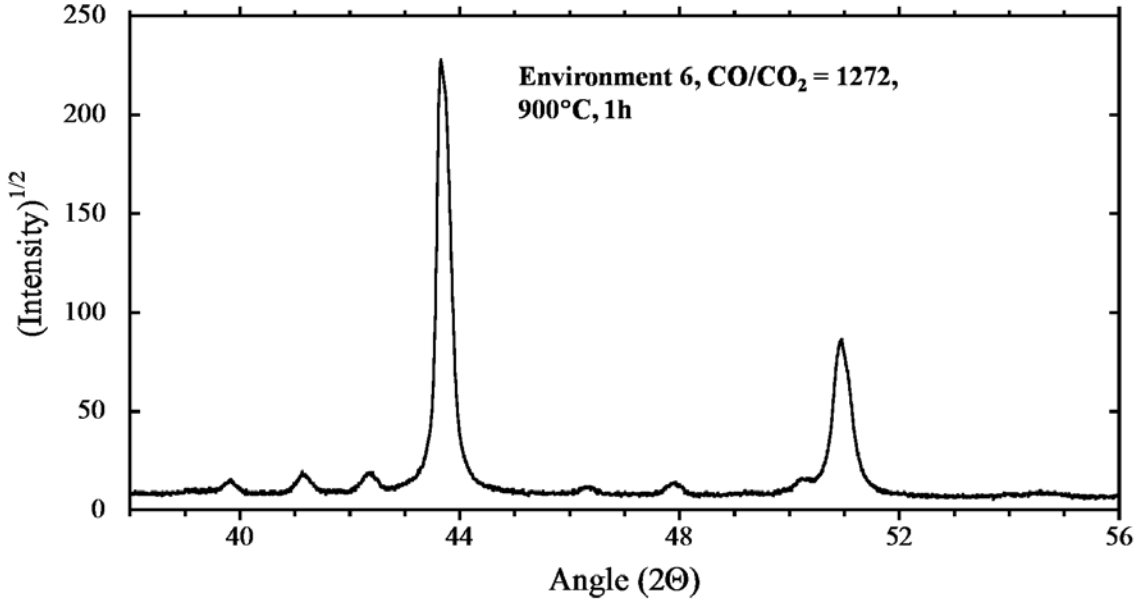

(b)

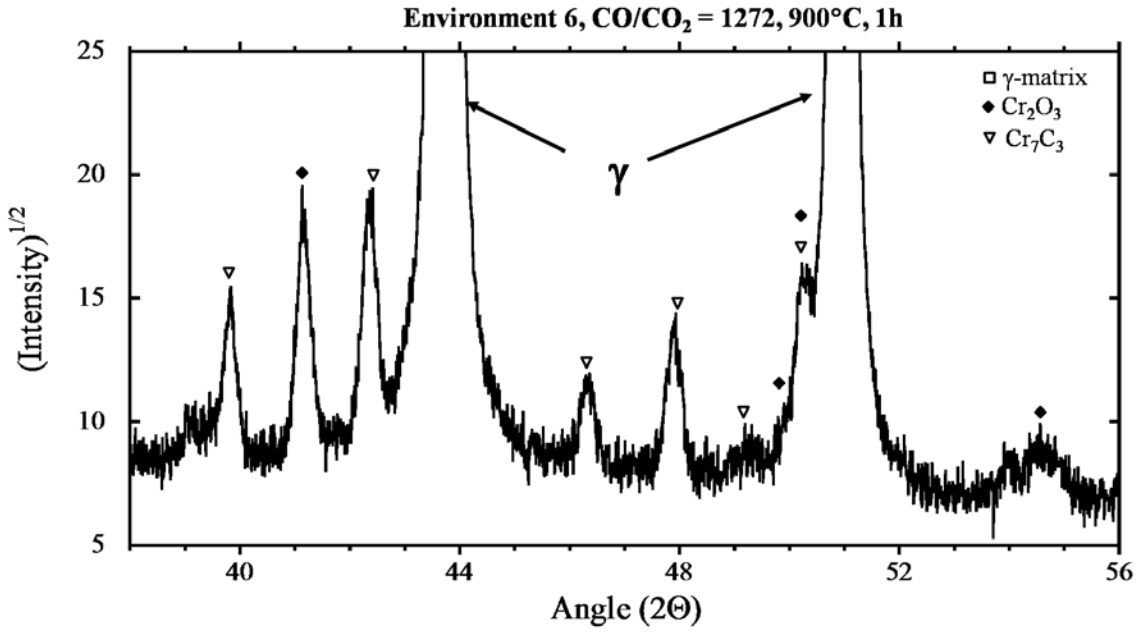

Figure 4.77 (a) XRD of the surface film formed after 1h of oxidation at 900°C in environment 6 (CO/CO_2 = 1272), (b) zoomed in portion of the XRD. Environment 6 (CO/CO_2 = 1272). The CuKα radiation with of wavelength of 1.540 A°was used to obtain the XRD pattern.

(a)

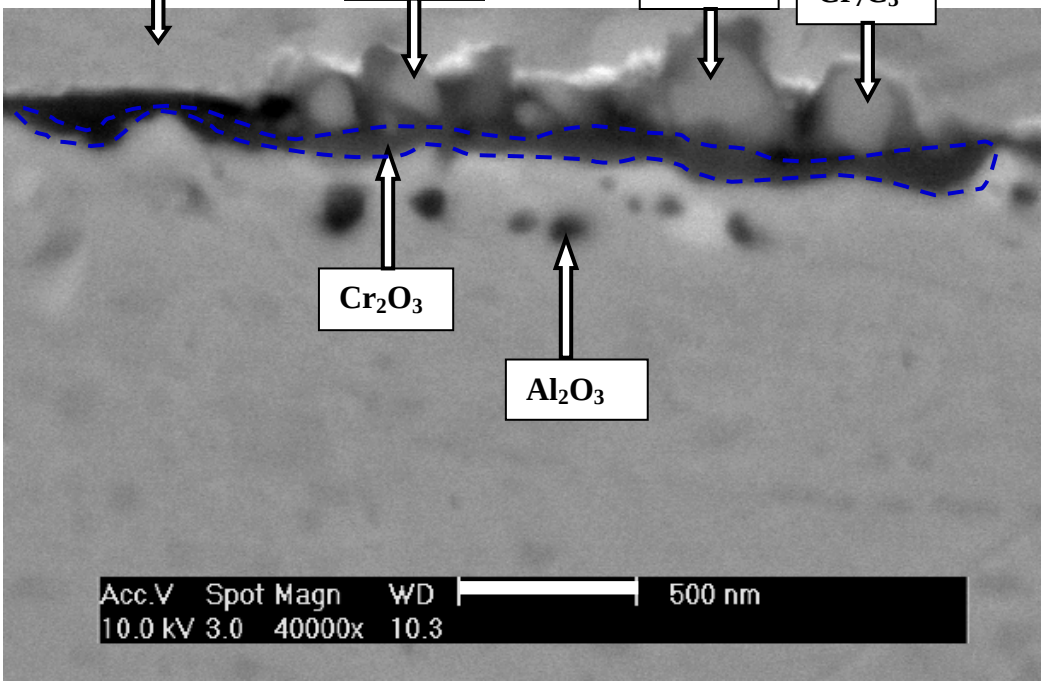

(b)

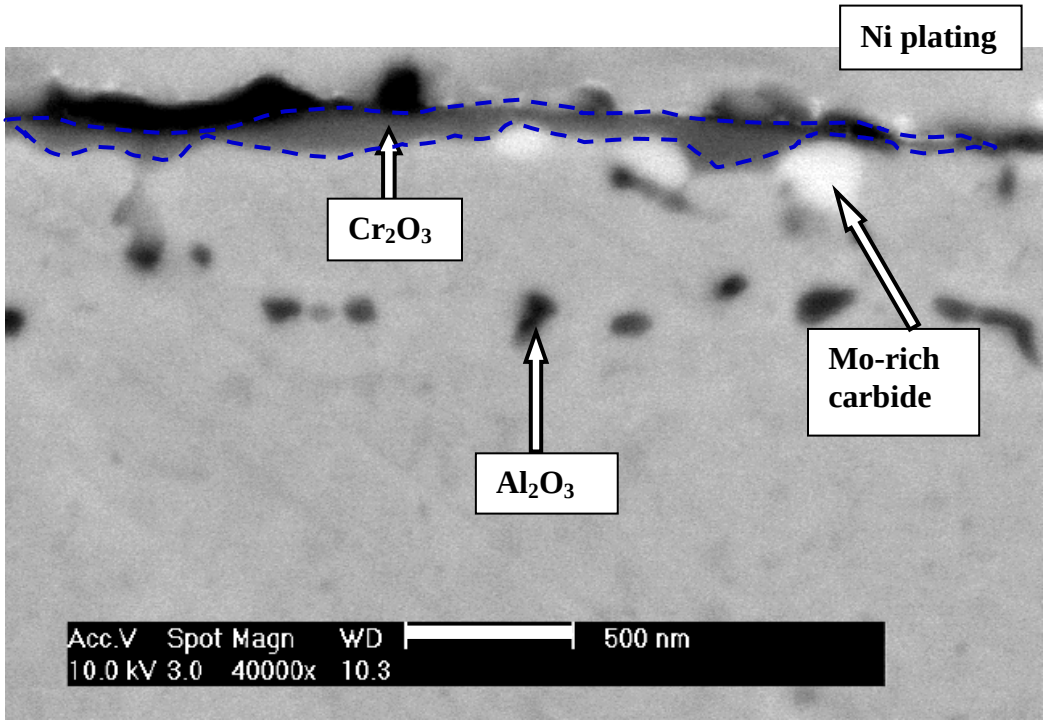

Figure 4.78 BSE image of the sample exposed in environment 6 (CO/CO_2 = 1272) for 1 h at 900°C. (a) and (b) show two different regions in the sample. The carbide density was non-uniform. Carbides are observed only in image (a). Inner Cr_2O_3 layer is outlined with blue dashed-line.

CHAPTER 5

DISCUSSION

This chapter is divided into four major sections. The first section establishes the chemical reactions that govern the carburization and decarburization of alloy 617 in a He-CO-CO_2 environment. The second section focuses on determination of the critical temperature for environment 1 (CO/CO_2 = 9) to 6 (CO/CO_2 = 1272). The third section describes the mechanism of decarburization of the alloy. The chemical reaction and the rate limiting step for the decarburization of the alloy will be discussed in this section. Lastly, the fourth section discusses the mechanism of carburization of the alloy in CO/CO_2 ratio environment of 1272. The mechanism of nucleation, growth, and dissolution of meta-stable surface carbide will be discussed in this section.

5.1 Establishment of reactions governing carburization and decarburization

The literature review presented in Chapter 2 showed that the oxidation of Ni-Cr base alloys in impure helium is strongly dependent on the CO concentration in the gas mixture, P_{CO}. A critical concentration of CO, P^*_{CO} is defined by the equilibrium reaction:[108]

$$2Cr + 3CO \leftrightarrow Cr_2O_3 + 3C_{solution}, \quad (5.1)$$

where $C_{solution}$ is the carbon in solid solution with the matrix. If $P_{CO} > P^*_{CO}$, the reaction in Eq. 5.1 proceeds in the forward direction and oxidizes and carburizes the alloy according to:

$$2Cr + 3CO \rightarrow Cr_2O_3 + 3C_{solution}. \quad (5.2a)$$

If $P_{CO} < P^*_{CO}$ then the reaction in Eq. 5.1 proceeds in reverse direction causing decarburization and oxide reduction according to:

$$2Cr + 3CO \leftarrow Cr_2O_3 + 3C_{solution}. \quad (5.2b)$$

The objective of this section is to establish the validity of the reactions in Eqs. 5.2a and 5.2b. The results of the pre-oxidation experiment presented in section 4.4 is best suited to accomplish this objective. In this experiment the samples were first pre-oxidized for 150h at 900°C in environment 1 (CO/CO_2 = 9) where P_{CO} (15ppm)> P^*_{CO} (5.5ppm)[108]. Thus, reaction 5.2a occurred and the sample was carburized. In the subsequent step the sample was exposed for 100h at 1000°C where P_{CO} (15ppm) < P^*_{CO} (~105ppm)[108]. Thus, the reaction 5.2b occurred and the sample was decarburized.

Section 5.1.1 evaluates the reaction in Eq. 5.2a and section 5.1.2 evaluates the reaction in Eq. 5.2b. Note that in environment 1 (CO/CO_2 = 9) two kinds of experiments were conducted: a pre-oxidation experiment in which the sample was first pre-oxidized at 900°C and then decarburized at 1000°C, and a second experiment in which the bare metal, as-received sample was oxidized between the temperature range of 850°C-1000°C. In this section the results analyzed pertain to the oxidation of pre-oxidized sample only.

5.1.1 Establishment of oxidation and carburization in the pre-oxidation experiment at 900°C (Eq. 5.2a)

It will be established that oxidation and carburization occurred according to Eq. 5.2a during pre-oxidation in environment 1 (CO/CO_2 = 9) at 900°C by showing that CO was consumed, resulting in formation of a surface film of chromia and internal carbides

due to carburization of the alloy. The formation of chromia will be verified by observation, and the amount of chromia formed will be verified quantitatively by establishing that the mass of oxygen consumed in the form of CO matches the mass of oxygen in the chromia. The formation of carbides due to internal carburization of the alloy will be established by comparing the bulk microstructure of the as-received sample and the sample pre-oxidized for 150h at 900°C.

Figure 4.70 showed the CO behavior at 900°C in environment 1 (CO/CO_2 = 9) in which a net consumption of CO occurred. The weight gain due to CO consumption was calculated from the area under the CO vs. time curve at 900°C in Fig. 4.70 using:

$$\text{Weight gain due to CO consumption } (\Delta W_{CO}) = \frac{I_{CO} \times \dot{V} \times M_{CO}}{V_m \times A}, \qquad (5.3)$$

where I_{CO} is the area under the CO vs. time curve (in mole-h), $\dot{V}$ is the flow rate of the gas mixture (in liter/h), M_{CO} is the molar weight of CO (28 g/mol), V_m is the molar volume of gas mixture (in liters/mol) ($V_m = \frac{R \times T}{P}$, R is universal gas constant, T is 298 K and P is 1 atm), and A is the surface area of the sample (in mm^2). Table 5.1 shows the details of the calculation.

The mass of oxygen consumed in the form of CO was calculated from the mass fraction of oxygen in CO of 0.57 (i.e., 16/28) and is tabulated in column 4 of the table 5.1. The thickness (1.5±0.4μm) of the chromia film in the pre-oxidized sample was measured from Fig. 4.72 and was presented in section 4.4. The mass of oxygen in the chromia is the film thickness (1.5 μm) times its density (5.2mg/mm^3) times the mass fraction of oxygen in chromia of 0.32 (i.e., 48/152), which is equal to 2.5 ±0.6 x 10^{-3}

mg/mm^2. This calculated mass of oxygen is shown in column 6 of the table 5.1. Note that this calculation neglects the mass of oxygen present in the form of internal oxide precipitates of alumina, which is not expected to introduce a large error as the area fraction of the alumina is negligible in comparison to the area fraction of chromia. As is evident from the columns 4 and 6 of the table 5.1 the mass of oxygen calculated from the gas-phase analysis (1.7×10^{-3} mg/mm^2) is in reasonably good agreement with the mass of oxygen in the chromia film ($2.5 \pm 0.6 \times 10^{-3}$ mg/mm^2), establishing that oxygen from the CO accounts for the oxygen in the chromia film according to the reaction given in Eq.5.2a.

Carburization is verified by the observation of increased carbide density in the alloy, since quantitative assessment of the carbide mass fraction from microstructure was not possible due to the small amount of carbide in the sample. The weight gain of carbon in the sample came from the mass fraction of carbon in CO of 0.43 (12/28). The increase in carbon was calculated to be 1.2×10^{-3} mg/mm^2 (column 5, table 5.1), which is ~30% of the initial carbon content (4.1×10^{-3} mg/mm^2) in the alloy. The weight gain of carbon in the sample was also calculated by subtracting the mass of oxygen in chromia film from the total weight gain in the sample of $3.5 \pm 0.3 \times 10^{-3}$ mg/mm^2 after pre-oxidation at 900°C, as shown in Fig. 4.71 and presented in section 4.4. The weight gain of carbon calculated from this approach is 1 ± 0.6 mg/mm^2 which is shown in column 7 of the table 5.1. As shown in this table the mass of carbon increase in the sample from this approach (column 7, table 5.1) is in reasonably good agreement with the increase in carbon due to consumption of CO (column 5, table 5.1). The increase in carbon content of the sample should result in an increased fraction of carbide in the bulk. Recall that the initial carbon

content (0.09wt%) in the alloy was higher than the solid solubility limit of ~0.01wt% at 900°C [from Pandat© Computherm LLC., Inc.] in the matrix, so carbides are expected. However, carburization will raise the carbon content still further and should cause an increased density of carbide precipitates. Qualitatively this can be verified by comparing the bulk microstructure of the as-received condition and the sample oxidized after exposure at 900°C (Fig. 5.1). In comparison to the as-received sample, the increased fractions of carbide in the oxidized sample, particularly along the twin boundaries near the alloy surface is most likely due to the carbon from the environment as per the reaction in Eq. 5.2a. This conclusion is supported by the fact that in the as-received sample the carbides were never observed along the twin boundaries, as shown in Fig. 5.1. Thus the increased fraction of carbide in the bulk provides further confirmation that the reaction in Eq.5.2a occurred at 900°C.

5.1.2 Establishment of decarburization during exposure at 1000°C (Eq. 5.2b)

This section will establish that the reaction in Eq. 5.2b occurred during exposure of the pre-oxidized sample to environment 1 (CO/CO_2 = 9) at 1000°C by showing that the chromia film was reduced and the alloy underwent decarburization, resulting in production of CO and Cr in the correct molar proportion. In the following subsections the reduction of chromia, the decarburization of the alloy, and production of CO and the redistribution of chromium are treated in separate sections.

Reduction of chromia

Reduction of chromia due to exposure at 1000°C in environment 1 (CO/CO_2 = 9) is established by comparing the chromia thickness after 150h of pre-oxidation at 900°C

and 100h of exposure at 1000°C. As presented in section 4.4, after 150h of pre-oxidation at 900°C the thickness of the chromia film measured from Fig. 4.72 was 1.5 ± 0.4μm, whereas after 100h of exposure at 1000°C the chromia film thickness measured from Fig. 4.73 was 0.1 ± 0.1μm. Reduction in chromia thickness shows that the chromia was consumed due to exposure at 1000°C. The mass of oxygen corresponding to this reduction in chromia is the reduction in film thickness (1.4μm) times the density of the chromia (5.21 mg/mm^3) times mass fraction of oxygen (0.32) which corresponds to 2.3 ± 0.8 x10^{-3} mg/mm^2 of oxygen.

Decarburization

The loss of carbon from the sample is verified qualitatively by comparing the bulk microstructure of the sample pre-oxidized for 150h at 900°C (Fig. 5.2a) and sample exposed at 1000°C (Fig. 5.2b, c). As observed in this figure, the fraction of the carbides in the sample exposed at 1000°C is less than that in the pre-oxidized sample. Further, a decarburization zone has formed near the alloy surface. The depth of this zone increased with time from ~100μm after 15h to ~450μm after 100h. The absence of carbides in decarburization zone suggests that the carbon level in this region dropped below the solubility limit. For simplicity if we take the $M_{23}C_6$ (where M is 90at%Cr, 10at%Mo) carbide to be $Cr_{23}C_6$, then the dissolution is given by:

$$Cr_{23}C_6 \rightarrow 23Cr + 6C_{solution}.$$

The dissolution of carbide in the carbide free zone is possible if either Cr concentration or carbon concentration decreases in comparison to the pre-oxidized sample. However, as shown in Fig.4.76, the Cr concentration increased during exposure at 1000°C and after

100hr, it is almost the same as that in the as-received alloy. Hence, it can be concluded that the decarburization zone formed mainly because carbon in this zone has decreased in comparison to the pre-oxidized sample. Thus this analysis confirms that the carbon necessary for the decarburization came from the sample itself.

Production of CO

This section establishes that as per the reaction in Eq. 5.2b, a net production of CO occurred. This will be accomplished by calculating the mass of CO evolved and comparing it with the decrease in mass of the sample measured by a microbalance.

The reaction in Eq. 5.2b will produce CO which can be verified by the evolution of CO measured by gas chromatograph in Fig. 4.70. The mass of carbon produced was calculated from the area under the curve in Fig. 4.70 and is plotted as a function of time in Fig. 5.3. For convenience, column 2 of table 5.2 lists the mass of CO produced for various exposure times. The production of CO will decrease the mass of the sample which was measured using a microbalance with a resolution of 0.01 mg and is shown in column 3 of this table. As is evident from the columns 2 and 3 of the table 5.2, the decrease in mass of the sample measured by microbalance (column 3, table 5.2) is in relatively good agreement with the mass of CO produced measured by gas chromatograph (column 2, table 5.2), suggesting that the decrease in mass of the sample during decarburization is due to evolution of CO by the sample. Thus, it is unlikely that processes such as chromia evaporation, oxide spallation etc. contributed to the measured mass loss.

Redistribution of Cr

This section first establishes that reduction of chromia resulted in an increased concentration of Cr near the alloy surface by comparing the concentration profile of Cr after pre-oxidation at 900°C and exposure at 1000°C. Next, it is established that the mass of dissolved Cr in the alloy agrees with the mass of Cr released by the reduction of chromia according to Eq. 5.2b.

Fig. 4.76 showed that after pre-oxidation at 900°C the outward diffusion of Cr atoms resulted in the formation of the surface chromia film which in turn depleted the Cr concentration near the surface. However, during subsequent exposure at 1000°C there was a partial and complete recovery in the Cr-profile after 5h and 100h, respectively. The recovery of Cr near the alloy surface implied that there was a net accumulation of Cr in the Cr-depleted zone, which is possible either by the diffusion of Cr from the bulk or from a source at the alloy surface. The Cr diffusion from the bulk of the sample to the alloy surface will further increase the depth of the Cr-depletion zone in the alloy and not recovery and hence this possibility is ruled out. Thus, it is concluded that the recovery of Cr in the Cr-depletion zone observed after pre-oxidation is due to replenishment of Cr from the reduction of chromia film by carbon, which released Cr that diffused back into the alloy and filled the Cr-depletion zone formed after pre-oxidation.

In order to establish that the mass of CO released from the sample and mass of Cr released due to reduction of chromia are in accordance with the reaction in Eq. 5.2b. The mass of Cr released from the chromia film and the mass of CO released from the sample after 5h and 100h were calculated from the reaction in Eq. 5.2b. The mass of Cr accumulated in the depleted zone was determined from Fig. 4.76 using Eq. 3.13 and is

given in column 4 of table 5.2. The mass of Cr accumulated in the depleted zone was then compared with the mass of Cr resulting from the production of the measured amount of CO in Eq. 5.2b and is given in column 5 of table 5.2. The comparison between the mass of Cr calculated from the two methods shows that there is good agreement between the two measures of Cr produced establishing that the redistribution of Cr is indeed due to the reduction of chromia. Thus, the changes in the masses of the reactants are accounted for by the changes in the masses of the products, confirming that the decarburization reaction described in Eq. 5.2b occurred during exposure of a pre-oxidized sample of alloy 617 to environment 1 ($CO/CO_2 = 9$) at 1000°C.

Another conclusion drawn from the Cr-concentration profile in Fig. 4.76 is that the volatilization of chromia in the present study is negligible, as the volatilization of chromia requires that Cr atoms leave the alloy, typically in the form of CrO_3 vapor [109]. Since the mass of Cr that "filled-in" the Cr-depleted zone fully accounts for the mass of Cr from the loss of the chromia film, there is no excess chromia that could have been volatilized. Further, the chemical analysis of the walls of the quartz tube under SEM/EDS did not show Cr-peak (Fig. 5.4), which supports the contention that chromia was not volatilized. Note that this result is not surprising, as volatilization of oxides at temperatures ≤1000°C is typically only important in water-rich environments, where high vapor pressure hydrated complexes, such as $CrO_2(OH)$, $CrO_2(OH)_2$ form[110, 111]. These oxides have been shown to be volatile at temperatures as low as 600°C in the case of chromia formed on stainless steel [112, 113]. However, the present study was performed in water vapor-free environments, where hydrated chromia complexes cannot form. Christ et al. [26], and Quadakkers et al. [108] also stated that the volatilization of

chromia is insignificant in impure helium even when it contains ppm levels of water vapor.

In summary, the analysis presented in this section established that, in agreement with the data in literature, reaction 5.1 is a reversible reaction[26, 93, 108]. At lower temperature (900°C) when $P_{CO} > P^*_{CO}$, CO was consumed by the alloy according to reaction 5.2a; resulting in chromia formation and carburization, which caused chromium depletion near the surface and increased chromium carbide formation in the bulk. Subsequent exposure at 1000°C, where $P_{CO} < P^*_{CO}$, resulted in decarburization and dissolution of carbides near the surface, and a reaction between carbon and chromia producing CO and refilling the Cr depleted zone.

5.2 Determination of the critical temperature range for reaction 5.1

The critical temperature is the temperature at which for a given CO concentration the reaction:

$$2Cr + 3CO \leftrightarrow Cr_2O_3 + 3C_{solution,} \quad (5.1)$$

is in equilibrium. Below the critical temperature the reaction in Eq. 5.1 proceeds to the right, so a net consumption of CO will occur, whereas at temperatures above the critical temperature the reaction in Eq. 5.1 proceeds to the left resulting in a net production of CO. This section is divided into four parts. The first part will determine the critical temperature range in environment 1 (CO/CO_2 = 9). The second part will determine the critical temperature in environments 2 (CO/CO_2 = 150) to 6 (CO/CO_2 = 1272). The third part will then compare the critical temperature range with the literature. The fourth part

will calculate the range of Cr-activity in alloy 617 from the critical temperature range established in the first part.

5.2.1Critical temperature in environment 1 ($CO/CO_2 = 9$)

This section will show that in environment 1 (ratio 9) a critical temperature exists that lies between 900°C and 950°C. The consumption/evolution behavior of CO and the bulk microstructure of the samples will be presented to support this conclusion. Note that in environment 1($CO/CO_2 = 9$) two kinds of experiments were conducted: pre-oxidizing experiment in which the sample was first pre-oxidized and then decarburized at 1000°C, and a second in which the bare metal as-received sample was oxidized between the temperature range of 850°C-1000°C. In this section the results analyzed pertain to the oxidation of as-received sample only.

The consumption/evolution behavior of CO and CO_2 was presented in section 4.1. The gas component that played the most important role was CO. This was noted by the change in the behavior of CO from net consumption at 900°C to net production at 950°C. Consumption of CO oxidized the sample according to reaction in Eq. 5.2a. Since the only source of carbon inside the reaction zone was the sample itself, the evolution of CO must be due to decarburization of the sample. The total mass of carbon produced in the form of CO was calculated from the area under the curve in Fig. 4.1 at 950°C and 1000^{o}C, respectively using Eq. 5.3 and is plotted as a function of time in Fig. 5.5. The initial weight of the carbon in the sample was 2.02 x 10^{-3} mg/mm^2 at 950°C and 3.9 x 10^{-3} mg/mm^2 at 1000°C (as the sample thickness at 950°C was ~half at 1000°C).

As shown in the Fig. 5.5 the sample was decarburized at both 950°C and 1000°C. Further complete decarburization of the sample occurred at both temperatures, i.e. all the carbon in the sample came out in the form of CO. The decarburization was complete in ~300h at 1000°C and ~250h at 950°C.

In order to further substantiate that in environment 1, the alloy undergoes oxidation at 900°C and complete decarburization between 950°C-1000°C, the bulk microstructures after 375h of oxidation at 900°C, 950°C, and 1000°C are shown in Fig. 5.6. As is evident from this figure, after 375 h of oxidation at 900°C, the microstructure has an increased fraction of carbide. The carbides have decorated the grain boundaries as well as the twin boundaries. However, at 950°C and 1000°C, exposure for the same amount of time resulted in the dissolution of carbides to the center of the samples. The gas-phase analysis in conjunction with the bulk microstructure confirmed that there was a change in oxidation mechanism between 900°C and 950°C, or in other words, there existed a critical temperature in environment 1 (CO/CO_2 = 9) that lies between 900°C and 950°C. Below this critical temperature the alloy undergoes oxidation and above this critical temperature the alloy decarburizes completely.

5.2.2 Critical temperature in environments 2 (CO/CO_2 =150) to 6 (CO/CO_2 =1272)

This section will show that in the tested temperature range of 850°C-1000°C a critical temperature did not exist in the any of the other environments (2:CO/CO_2 = 150 to 6:CO/CO_2 = 1272), i.e. the alloy did not decarburize in these environments. The

consumption/evolution behavior of CO and the bulk microstructure of the samples will be presented to support this conclusion.

The CO and CO_2 behaviors environments 2 (CO/CO_2 =150) to 6 (CO/CO_2 =1272) are shown in Figs. 4.2 to 4.6. A net consumption of CO from the beginning of the experiment was measured at each temperature. The consumption of CO will oxidize the sample according to the reaction in Eq. 5.2a. Further, the CO consumption dropped to nearly zero after 50-80h, which can be ascribed to the fact that a surface scale had formed that separated the metal from the gas, thereby decreasing the CO consumption. With continued exposure CO production was measured, which at least, in environment 5 (CO/CO_2 = 900) and environment 6 (CO/CO_2 = 1272) was higher than the repeatability error (3 to 5 ppm) of the gas chromatograph (GC). The reason for evolution of CO is the dissolution of surface carbide which will be discussed later in section 5.4 The important point to note here is that a critical temperature did not exist in the environments 2 (CO/CO_2 = 150) to 6(CO/CO_2 = 1272), i.e. the alloy did not decarburize in these environments.

Substantiation of the lack of decarburization in environments 2 (CO/CO_2 = 150) and 6 (CO/CO_2 = 1272) is provided by the micrographs of the alloy after 375h of oxidation at 1000°C shown in Fig. 5.7. For comparison, the bulk microstructure of the as-received alloy and the sample decarburized in environment 1 (CO/CO_2 = 9) for 375h at the same temperature is also provided. As is evident from this figure, except for a ~55μm denuded zone near the surface, the carbides are still present in the entire sample the alloy oxidized in environments 2 and 6, confirming that the alloy did not decarburize in these environment. The observed denuded zone is due to the outward diffusion of Cr forming

surface scale on the sample and thereby depleting the Cr in this zone and dissolving the carbides in the matrix.

Thus in summary the critical temperature that separates oxidation from decarburization is dependent on the CO concentration in the gas-mixture. In environment 1 (CO/CO_2 = 9) with CO concentration of 15 ppm it lies between 900°C and 950°C, whereas for environments 2 (CO/CO_2 = 150) to 6 (CO/CO_2 = 1272), it did not lie in the test temperature range of 850°C-1000°C.

5.2.3 Comparison of the critical temperature with literature

The influence of gas composition on critical temperature for alloy 617 was reviewed in section 2.4.5. It was concluded that critical temperature is a weak function of hydrogen, methane, water vapor, and depends mainly on the CO concentration in the helium. Since the critical temperature depends mainly on CO concentration, the critical temperature range in the present study can be compared against those in the literature with similar gas compositions. Fig. 5.8 is a compilation of the critical temperature determined in various studies for alloy 617. The detailed gas compositions of the studies cited in this figure were given in table 2.2. As shown in this figure, for 15 ppm of CO (relevant to environment 1: CO/CO_2 = 9) the critical temperatures among three independent studies ranges from 920°C to 926°C [86, 88, 108]. The critical temperature range in environment 1 (CO/CO_2 = 9) also with 15 ppm of CO is 900°C – 950°C, which encompasses the critical temperature range of 920°C to 926°C from literature. Thus the result from the present study is in good agreement with the literature and supports the

conclusion that critical temperature is dependent mainly on the CO concentration in helium.

Further, as is evident from this figure, the critical temperature increases with CO concentration and at ~105 ppm of CO it is 1000°C. The CO concentration in environments 2 (CO/CO_2 = 150) to environment 6 (CO/CO_2 = 1272) was ≥ 240ppm and according to the literature the critical temperature above which decarburization occurs should be >1000°C, which is also in agreement with the present study.

5.2.4 Calculation for activity of Cr in alloy 617:

This section first derives an equation correlating the critical temperature and activity of Cr in the alloy, then calculates a lower and upper bound on the activity of Cr using the fact that critical temperature in environment 1 lies in the range of 900°C-950°C.

Recall that at the critical temperature, T_{cr}, the reaction described in Eq. 5.1 is in equilibrium. If carbon is in the form of carbides of $M_{23}C_6$ (where M = 90at% Cr, 10at%Mo) in alloy 617 and we assume the carbide to contain only Cr as metal, $Cr_{23}C_6$, then at the critical temperature the following reaction must be in equilibrium:

$$2Cr_2O_3(s) + Cr_{23}C_6(s) \leftrightarrow 27Cr + 6CO(g) \qquad (2.14)$$

Hence, at the critical temperature, the change in Gibbs free energy for reaction in Eq. 2.14 is zero,

$$\Delta G_{2.14}\left(T = T_{cr}\right) = 0 \quad . \qquad (5.4)$$

Further, the change in Gibbs free energy of the reaction in Eq. 2.14 ($\Delta G_{2.14}$) can be expressed in terms of the standard change in Gibbs free energy ($\Delta G^{0}_{2.14}$), universal gas constant (R), and quotient (Q) as per:

$$\Delta G^{0}_{2.14}(T_{cr}) + RT_{cr} \ln Q = 0 \tag{5.5}$$

$$Q = \left(\frac{\left(P^{*}_{CO}\right)^{6} \left(a_{Cr}\right)^{27}}{a^{2}_{Cr_2O_3}\, a_{Cr_{23}C_6}} \right) \tag{5.6}$$

where a_i is the activity of Cr, Cr_2O_3, and $Cr_{23}C_6$, and P^{*}_{CO} is the CO concentration in the environment.

Substituting the value of Q from Eq. 5.6 in to Eq. 5.5, we get

$$\Delta G^{o}_{2.14} + RT_{cr} \ln \left(\frac{\left(P^{*}_{CO}\right)^{6} \left(a_{Cr}\right)^{27}}{a^{2}_{Cr_2O_3}\, a_{Cr_{23}C_6}} \right) = 0 \quad , \tag{5.7}$$

If we assume the activities of the oxide and carbide are unity then the Eq. 5.7 simplifies to:

$$\Delta G^{o}_{2.14} + RT_{cr} \ln \left(\left(P^{*}_{CO}\right)^{6} \left(a_{Cr}\right)^{27} \right) = 0 \quad . \tag{5.8}$$

The value for $\Delta G^{o}_{2.8}$ can be obtained from standard thermo-chemical tables [114]:

$$\Delta G^{o}_{2.14} = 198518 - 1003.2T_{cr} \text{(joule)} \qquad . \tag{5.9}$$

Combining Eqs. 5.9 and 5.8 and solving for T_{cr}, we get an expression for critical temperature as a function of a_{Cr} , universal gas constant R, and P^{*}_{CO} :

$$T_{Cr} = \frac{198518}{R\left(\ln\left(P^{*}_{CO}\right) + \frac{27}{6} \ln a_{Cr} \right) - 1003.2} \quad . \qquad (5.10)$$

In the present study the critical temperature range is 900°C - 950°C in environment 1 (CO/CO_2 = 9), and correspondingly a lower and upper bound of a_{Cr} can be estimated from the bounding temperatures. The lower bound of a_{Cr} corresponding to T_{cr} = 900°C is 0.57 and the upper bound of a_{Cr} corresponding to T_{cr} = 950°C is 0.77. Thus from the present study, the a_{Cr} in the alloy 617 lies between 0.57 and 0.77 in the temperature range of 900°C-950°C.

Quadakkers et al. [108], Christ et al. [26], and Cabet et al. [88] used similar approach showed the a_{Cr} for alloy 617 to be 0.65, 0.75, and 0.72, respectively in the temperature range of 900°C-1000°C. The mass-spectroscopic study by Gosse et al. [115] on alloy 617 showed that a_{Cr} was 0.65 at 900°C and 0.57 at 950°C. The range of a_{Cr} values in the present study is in good agreement with the a_{Cr} value of alloy 617 in the literature.

A similar range for a_{Cr} cannot be calculated for the environments 2 (CO/CO_2 = 150) to 6 (CO/CO_2 = 1272) as the critical temperature in these environments was >1000°C. However, a lower bound on a_{Cr} can be calculated assuming that the critical temperature for environment 2 (CO/CO_2 = 150) with CO concentration of 240 ppm is 1000°C. In this case, the a_{Cr} was calculated to be 0.56. This calculated value of a_{Cr} is also in good agreement with the literature.

In summary it can be concluded that in the temperature range of 900°C-1000°C the activity of Cr in alloy 617 lies between 0.57 and 0.77.

5.3 Decarburization Mechanism

This section describes the mechanism of decarburization of the as-received alloy in environment 1 (CO/CO_2 = 9). A hypothesis for the mechanism is provided first, followed by establishment of the key steps required to validate the hypothesis.

Figure 5.9 shows a schematic of the proposed mechanism of decarburization of the as-received alloy at 1000°C. Note that alumina does not interfere with decarburization directly and for simplicity is not included in the schematic, but it will be discussed later. As shown in this figure at time = 0, the system consists of alloy 617 (containing carbide in the matrix and on the grain boundaries) in contact with an environment consisting of 15 ppm CO and 1.5 ppm CO_2 at 1000°C with oxygen partial pressure of 9.6×10^{-17} atm and carbon potential of 9.8×10^{-7}. Since the carbon potential in the alloy (5.6×10^{-3}[88, 108]) is four orders of magnitude higher than that in the environment (9.8×10^{-7}), decarburization of the alloy occurs, which can be explained by following major steps:

(1) At time $t = t_1$, chromia forms on the alloy surface via reaction between Cr in the alloy and oxygen in the environment according to:

$$2Cr + 3/2O_2 \rightarrow Cr_2O_3, \quad (5.11a)$$

Chromia is immediately reduced by the carbon in the alloy resulting in metallic Cr which diffuses back into the alloy, and CO gas as per the reaction:

$$Cr_2O_3 + 3C_{solution} \rightarrow 2Cr + 3CO\uparrow. \quad (5.11b)$$

Reactions in Eqns 5.11a and b occur simultaneously and at the same rate, thus resulting in no accumulation of chromia on the alloy surface.

(2) The loss of carbon to CO destabilizes the carbide/matrix equilibrium in the subsurface zone and at time $t = t_2$, the carbide dissolution occurs as per:

$$M_{23}C_6 \rightarrow 23M + 6C_{solution}\ , \quad (5.12)$$

$$M_6C \rightarrow 6M + C_{solution}\ , \quad (5.13)$$

where M is Cr, Mo. The result is a decarburized zone in the subsurface area.

(3) The decarburized zone grows into the metal due to the outward diffusion of carbon, and after time = t_3, the carbon in the alloy is depleted and the reaction in Eq. 5.11b stops.

(4) Without carbon to reduce Cr_2O_3 (reaction in eqn 5.11b), a chromia film begins to accumulate after time = t_3, according to eqn 5.11a.

In the following subsections the four steps are discussed separately and evidence for their existence is provided.

Step (1) – Simultaneous formation and reduction of chromia

This section shows that a chromia film must have formed on the alloy exposed to environment 1 (CO/CO_2 = 9) at 1000°C from the beginning of the experiment, i.e. at time t > 0, but was not observed under SEM and XRD (as shown in Figs. 4.36 and 4.37), as it was reduced by the carbon in the alloy as soon as it formed resulting in a net production of CO gas.

Chromia can form on the alloy surface only if the oxygen partial pressure in the environment is higher than the Cr/chromia equilibrium oxygen pressure. The partial pressure of oxygen in environment 1 (CO/CO_2 = 9) at 1000°C is 9.6×10^{-17} atm, whereas the Cr/chromia equilibrium oxygen pressure is 2.3×10^{-22} atm. Thus, since the oxygen partial pressure in the environment is ~5 orders of magnitude higher than that of the minimum partial pressure of oxygen required for the formation of chromia, i.e. Cr/chromia equilibrium oxygen pressure, formation of chromia is thermodynamically favorable.

Following arguments support the hypothesis that, although it was not observed under SEM, chromia film formation is kinetically favored.

(i) As summarized in table 4.5 and presented in section 4.3.2.1, a stable chromia film did form in this environment at temperatures between 850°C -950°C (Fig. 4.28 to 4.30). Since oxidation of metal is a thermally activated process, the increase in temperature should result in an increased rate of chromia formation at higher temperatures.

(ii) At 1000°C, a stable chromia film formed in environment 6 (CO/CO_2 =1272). Both environment 1 (CO/CO_2 = 9, oxygen pressure = 9.6 x 10^{-17} atm, carbon potential = 9.8x10^{-7}) and environment 6 (CO/CO_2 = 1272, oxygen pressure = 4.9 x 10^{-21} atm, carbon potential = 1.7x10^{-2}) have oxygen potentials that are higher than the Cr/chromia equilibrium potential. The main difference is in the carbon potential. Chromia formation as per reaction in Eq. 5.11 depends only on the oxygen potential in the environment and not on the carbon potential. Since a chromia film formed in environment 6 (CO/CO_2 = 1272) at the same temperature, it is likely that a chromia film also formed in environment 1 (CO/CO_2 = 9).

(iii) The literature suggests that at 1000°C, alloy 617 is a stable chromia film former in both high oxygen partial pressure environment such as air [116], and low oxygen partial pressure environment such as Ar-H_2-H_2O with oxygen partial pressure varying in the range of 10^{-19} to 10^{-16} atm [117].

These arguments support the assertion that chromia formation on alloy 617 exposed to environment 1 (CO/CO_2 = 9) at 1000°C is both thermodynamically feasible, and kinetically favorable. It did not accumulate to measurable amounts because it was

reduced by the reaction in eqn. 5.11b. The combined effect of the two simultaneous reactions proceeding at the same rate was a net production of CO that was measured by gas chromatograph as shown in Fig. 4.1. Note that the occurrence of the reaction in eqn. 5.11b, i.e. reduction of chromia by the carbon in the alloy has already been established at the same temperature and environment in the section 5.1.2.

Two other possible reactions that impact the validity of this hypothesis need to be addressed. One is that the measured CO resulted from a gas reaction. The second is that chromia formed and was volatilized rather than reduced.

Evidence that the measured CO did not come simply from the gas reaction:

$$CO_2\,(g) \rightarrow CO(g) + 1/2O_2\,(g) \qquad (5.14)$$

is contained in the microstructure of the samples that were decarburized at 1000°C for 100h and 375h in environment 1 ($CO/CO_2 = 9$), and presented in section 4.3.2.2 and Fig. 4.43. If CO came from this simple gas reaction, then there will be no change in the carbon content in the alloy, and the dissolution of carbides would not occur. However, as observed in the Fig. 4.43 significant decarburization occurs resulting in carbide dissolution. So, the possibility of decarburization by gaseous reaction in Eq. 5.14 is ruled out.

If the volatilization of chromia occurred, then chromia should not have formed after 375h. It should have been volatilized throughout the 500h of exposure duration and the sample would not have undergone a rapid weight gain corresponding to chromia formation between 375h and 500h in Fig. 5.10. Further, after 100h of decarburization at 1000°C in this environment, the concentration profiles of elements Cr, Ni, Mo, and Co was essentially flat and same as the initial concentration in the alloy, as presented in

section 4.3.2.1 and shown in Fig. 4.38. The volatilization of chromia requires that Cr atoms leave the alloy, typically in the form of CrO_2 vapor [109], resulting in a chromium depleted zone near the surface. Since the concentration profiles of Cr show that the mass of Cr is conserved, volatilization could not have occurred. The analysis of the pre-oxidized experiment, where samples were first pre-oxidized at 900°C and decarburized at 1000°C (section 5.1.2) also confirms that volatilization of chromia was insignificant at 1000°C in environment 1 (CO/CO_2 = 9). Finally, if chromia was volatilized, it would have deposited on the tube walls at the exit from the furnace where the temperature was lower. Analysis of the tube walls by SEM/EDS revealed no evidence of chromium. Based on these arguments, it can be concluded that volatilization of chromia is insignificant at 1000°C in environment 1 (CO/CO_2 = 9).

Thus in summary it is established that decarburization of the as-received alloy in environment 1 (CO/CO_2 = 9) occurs via formation and immediate reduction of chromia as per the reactions in eqns. 5.11a and b, resulting in the net production of CO gas. The lack of a measurable amount of chromia on the alloy surface simply indicates that the reaction in eqns. 5.11a and 5.11b were occurring simultaneously and at the same rates. The rate limiting step was the formation of chromia (reaction 5.11a). The net result is decarburization and production of CO which was measured by the gas chromatograph.

Step 2- dissolution of carbide due to decarburization

As the carbon in the sample is lost due to decarburization the carbide/matrix equilibrium will be destabilized which will result in the dissolution of carbide. The comparative microstructure of the sample after 100h and 375h at 1000°C in Fig. 5.11

provides the microstructure evidence to support this step. With continued exposure, carbides from distances farther from the surface dissolve in the matrix resulting in a decarburization zone of ~100μm after 100 h and ~700μm after 375h, confirming the hypothesis made at step 2.

Step 3- The chromia reduction reaction in Eq. 5.11b stops

The chromia reduction reaction in Eq. 5.11b can occur only if the reactants (chromia and carbon) are present. As argued earlier (step 1) the chromia film forms throughout the 500h of exposure at 1000°C. However, the mass of carbon in the sample is finite and when the supply of carbon is exhausted due to decarburization or the activity of carbon in the alloys equals that in the environment, the reaction in Eq. 5.11b stops.

Fig. 5.12 plots the mass fraction of carbon remaining in the sample as a function of time for the as-received sample decarburized at 1000°C in environment 1 (CO/CO_2 = 9). The fraction of carbon remaining in the alloy is defined as the difference between the mass of carbon in the as-received sample and carbon lost due to decarburization; normalized by the mass of carbon in the as-received sample. The mass of carbon lost due to decarburization was calculated from the area under the CO evolution curve at 1000°C in Fig. 4.1 by using Eq. 5.3. As is evident from this figure the carbon in the sample was depleted in ~300h. Since there is no carbon in the sample, the decarburization cannot occur and the reaction in Eq. 5b will cease.

To further substantiate that the carbon in the sample got exhausted in ~300h, the bulk microstructure of the sample decarburized for 375h at 1000°C (slightly longer than 300h when decarburization stops according to Fig. 5.12) is shown in Fig. 5.11c. The

carbides have dissolved in the entire sample at 375h. The carbon content in the as-received alloy was 0.09wt%. The solid solubility limit of the alloy 617 at 1000°C is ~0.02wt% [Pandat® database from Computherm, LLC.], which means that out of total 0.09wt% carbon, at least 0.02wt% is in the solution and up to 0.07wt% is tied up with the carbides. The dissolution of carbides in the entire sample implies that at least 0.07wt% of carbon, which amounts to ~80% of the carbon in the as-received alloy, has diffused out in the form of CO. The result of the gas phase analysis shown in Fig. 5.12 is that all of the carbon has diffused out in ~300h. Thus, the microstructure analysis supports the conclusion of the gas-phase data that the carbon was depleted from the sample in ~300h and hence decarburization reaction in Eq. 5.2b stopped.

Step 4-growth of chromia film on the surface

At step 4 in Fig. 5.9, the carbon in the sample has exhausted and the chromia reduction reaction in Eq. 5.11b has stopped. However, the chromia formation as per the reaction in Eq. 5.11a can still continue as the thermodynamic and kinetic conditions in step 1 are still valid. The growth of chromia during continued exposure from 375h to 500h can be verified by the comparison between the SEM micrograph in Fig. 5.13. This figure, which was presented in section 4.3.2.1 shows that after the cessation of chromia reduction at ~300h, the chromia film has grown on the alloy surface.

To further substantiate the argument that chromia film grew on the sample after the chromia reduction reaction stopped, the CO production due to decarburization, i.e. CO out-CO in and the weight gain due to chromia growth is plotted as a function of time in Fig. 5.14. If we assume that total weight gain in the sample is due to oxygen in

alumina and chromia, then the weight gain due to chromia growth is total weight gain (shown in Fig.4.17) in the sample less the weight gain due to oxygen in alumina measured from the microstructure (shown in Figs. 4.39 and 4.40 and summarized in table 4.5). Further, the weight gain due to oxygen in alumina is the alumina film thickness times the density of alumina (4 mg/mm^3) times the weight fraction of oxygen in alumina of 0.47 (48/102). As is evident from this figure the weight gain corresponding to chromia growth occurs mainly after ~300h when the decarburization is complete and no net production of CO was measured by the gas chromatograph. This confirms that the chromia growth did not occur until the carbon in the sample was depleted.

5.3.2 Rate limiting step for decarburization of as-received alloy at 1000°C

The aim of this section is to determine the slowest of the four steps just described. It was concluded in the previous section (section 5.3.1) that the chromia formation reaction 5.11a and chromia reduction reaction 5.11b occur simultaneously (until ~300h). But, the microstructure examination under SEM (shown in Fig.4.36) and XRD (Fig. 4.37) did not show the presence of chromia film, which can mean only one thing, i.e. chromia was reduced as soon as it formed. Otherwise, we would have observed chromia film on the surface. So, it can be concluded that the chromia formation reaction is the rate limiting step during decarburization at 1000°C.

In order to substantiate this conclusion it needs to be established that the dissolution of carbide (step 2, section 5.3.1), and diffusion of carbon to the alloy are not rate limiting step.

It has been shown in the literature that the carbide dissolution between 1000°C-1200°C occurs very rapidly with 1-2 μm sized carbides (average size of carbides in the as-received alloy 617) dissolving in less than 1h [118], which is much less than the total decarburization time of ~300h shown in Fig. 5.12. Hence dissolution of the carbide cannot be the slowest process during decarburization.

In order to estimate if the diffusion of carbon to the alloy surface is the slowest step, a 1-dimensional diffusion analysis was done. It was assumed that the initial concentration of the carbon in the alloy is uniform throughout the cross-section and the activity of carbon at the surface is equal to that of the environment. In other words, the alloy and gas are in local equilibrium with each other. Further since activity of carbon in the environment is given by the CO/CO_2 ratio in the environment, which is fixed as the same gas composition was maintained throughout the experiment, the activity of carbon at the alloy surface will be fixed. Under this assumption, time taken for complete decarburization is given by[119]:

$$\frac{D_C \times t}{L^2} = 1, \qquad (5.15)$$

where D_C, t, and L are the diffusion coefficient of carbon in the alloy, time, and one half of the thickness of the sample. Taking the Dc at 1000^oC as 1.4×10^{-7} cm^2/sec[120], and L = 0.7mm, the total time, t, taken for complete decarburization is 9.7h, which is ~30 times less than the time calculated for complete decarburization of ~300h by gas chromatograph. Furthermore, the bulk microstructure of the sample decarburized after 100h (Fig.5.11b) does not support complete decarburization within 9.7h, as even after 100h of decarburization the carbides are observed in the microstructure. Thus, carbon diffusion is not rate limiting.

A further proof that the diffusion of carbon to the alloy surface is fast and is not the rate limiting step during decarburization of the as-received alloy at 1000°C or 950°C is given by the weight of carbon production vs. time plot in Fig. 5.5. As observed in this figure, the rate of carbon production, which is given by the slope of the curve, is constant. A constant rate of decarburization means that the decarburization is a reaction controlled process and not diffusion controlled process, as the diffusion controlled processes slow down with time$^{1/2}$.

Hence, since dissolution of carbide and diffusion of carbon to the alloy surface are fast, and chromia film was not observed on the sample (until ~300h), it is concluded that chromia formation reaction was the rate limiting step during decarburization of as-received alloy at 1000°C.

Now, let's consider the case of decarburization of as-received alloy at 950°C. It can be assumed that similar to decarburization at 1000°C, the decarburization at 950°C also occurs via a kinetic competition between the chromia formation and chromia reduction reactions, which occur simultaneously at the sample surface until the carbon in the sample is depleted, i.e. ~250h (Fig. 5.5). But, as shown in Fig. 4.32 a thin chromia film was observed at 950°C after 100h of oxidation, which means that at this temperature, the rate limiting step is the chromia reduction and not chromia formation.

In summary, it is shown in this section that the rate limiting step during decarburization at 1000°C is the chromia formation, whereas, the rate limiting step during decarburization at 950°C is the chromia reduction. In other words, the activation energy for chromia reduction reaction is higher than the chromia formation reaction.

5.3.3 Role of Aluminum in decarburization

It was noted in section 4.3.2.1 that an alumina film formed on the as-received sample decarburized in environment 1 (CO/CO_2 = 9) at 1000°C. Further, the oxide microstructure was non-uniform after 500h of oxidation (Fig. 4.40), in the sense that a protective film of alumina formed on part of the sample (region I in Fig.4.40), whereas on the rest of the sample non-protective film of alumina formed as internal oxidation occurred in this area (region II in Fig. 4.40). Similar non-uniformity in the oxide microstructure was also noticed by Christ et al. [106] during 150h decarburization of alloy 617 at 1000°C in impure helium containing He + 10ppm water vapor + 50 ppm hydrogen. This section first gives the possible explanation for formation of alumina film on alloy 617 at 1000°C, which is expected to undergo internal oxidation. The oxidation behavior of alloy 617 will be compared with the oxidation behavior of an equivalent ternary Ni-Cr-Al alloy using the "oxide map" and it will be shown that the low ambient oxygen partial pressure, most likely, promoted formation of alumina film in environment 1 (CO/CO_2= 9). The possible reasons for local heterogeneity in the surface microstructure will be stated next.

Typically, to predict the formation of surface and sub-surface oxide in Ni-Cr-Al alloys, "oxide map" (discussed in section 2.3) is used. These maps are not thermodynamically-derived but are rather based on experimental data, and the minimum concentration of Al necessary for formation of alumina film on a Ni-Cr-Al alloy can be read form this map. Figure 5.15 shows the oxide map for Ni-Cr-Al ternary alloys constructed by Pettit et al. [55] at 1000°C and oxygen partial pressure of 0.1 atm. If we neglect the Co and Mo content then the alloy 617 can be viewed as Ni-22Cr-1Al alloy.

Thus, according to the oxide map shown in Fig.5.15 alloy 617 should undergo internal oxidation as the initial concentration of Al in the alloy (1.1wt%) is lower than the critical concentration of Al (~3wt%). However, the microstructure results presented in section 4.3.2.1 and shown in Figs. 4.36 to 4.40 confirmed the formation of alumina nodules after 100h, which eventually grew into a thin film of alumina of thickness 0.6μm after 500h of oxidation. The oxygen partial pressure in environment 1 (ratio 9) was ~10^{-16} atm which is much less than the oxygen partial pressure of 0.1 atm for which the oxide map shown in Fig. 5.15 was constructed. Thus, the formation of alumina film in present case suggests that the critical concentration of Al at ~10^{-16} atm oxygen pressure is at least ~1.1 wt%, whereas at 0.1 atm oxygen pressure it is ~3wt% Al. In other words, the decrease in ambient oxygen pressure decreased the critical concentration of Al required for the formation of alumina film. A decrease in ambient oxygen partial pressure is expected to decrease the critical concentration of Al, as shown in the following. The critical concentration of Al required for formation of alumina, $N_{Al,min}$, is given by[121]:

$$N_{Al,min} = \left(g^* \frac{\Pi}{2\nu} \frac{V_{alloy}}{V_{AlO_{1.5}}} \frac{N_O^S D_O}{D_{Al}} \right)^{1/2}$$

where g* is a constant which varies between 0.3 and 0.5[122, 123], ν is 1.5 for alumina, V_{alloy} and $V_{AlO1.5}$ are the molar volumes of the alloy and the alumina, N_O^S is the solubility of oxygen in the alloy which is proportional to oxygen partial pressure in the environment (Sievert's law), D_O and D_{Al} are the diffusion coefficients of oxygen and Al in the alloy.

According to this equation, formation of alumina film is promoted if (i) the diffusion coefficient of Al relative to the diffusion coefficient of oxygen, i.e. D_{Al}/D_O ratio in the alloy is increased, and/or (ii) the solubility of oxygen in the alloy (N_O^S), which is

proportional to partial pressure of oxygen in the environment is lowered. The D_{Al}/D_O ratio should primarily depend on the temperature as the diffusion coefficient of elements in an alloy is a function of temperature and not the environment. So, formation of alumina film in environment 1 (CO/CO_2 = 9) with oxygen pressure of 10^{-16} atm and internal oxidation for equivalent Ni-Cr-Al ternary alloy in 0.1 atm is most likely due to lower oxygen partial pressure in the environment 1 (CO/CO_2 = 9) as compared to the oxide map which was constructed at 0.1 atm oxygen.

A few reasons, given below, can explain the development of non-uniform microstructure in the sample decarburized for 375h and 500h in environment 1 (ratio 9) at 1000°C:

(i) even after 500h of oxidation the oxidation behavior of the alloy was in pre-steady state. This is evident by the weight gain curve shown in Fig.5.10. It is quite possible that if the oxidation were to continue further the oxidation will reach a steady state and the oxide microstructure will be uniform.

(ii) local differences in surface preparation affected the protectiveness of the alumina film formed after 375h. This is proposed based on the microstructure observation that the alloy/oxide interface, where internal oxidation of Al and chromia growth occurred (region II, Fig. 5.16), was more convoluted in comparison to the alloy/oxide interface where a protective film of alumina (region I, Fig. 5.16) formed which inhibited the internal oxidation of Al. The effect of local differences in surface preparations leading to non-uniform surface oxidation was also observed by Pettit et al. [55] during oxidation of Ni-20Cr-3Al alloy (see Fig. 2.11).

5.4 Carburization mechanism

This section describes the mechanism of carburization of the as-received sample in environment 6 (CO/CO_2 =1272). A hypothesis of the mechanism is provided first followed by establishment of key steps required to validate the hypothesis.

Figure 5.17 is a schematic of the proposed mechanism of carburization. Note that carburization involved nucleation, growth, and dissolution of Cr_7C_3 carbides in the surface scale and are not influenced by the oxidation of Al that occurred internally in the sub-surface zone, and hence for clarity it is not included in the schematic. At time t = 0, the sample is brought into contact with an environment consisting of 1908 ppm CO and 1.5 ppm CO_2 at 900°C with oxygen partial pressure of $10^{-22.3}$ atm and carbon potential of 0.07. Since the carbon potential in the environment (0.07) is higher than in the alloy (0.004), the carburization of the alloy occurs, which can be explained by following major steps:

(1) Nucleation of chromia: During initial exposure duration (time t <1h), CO dissociates on the alloy surface. The carbon permeates in the alloy causing internal carburization, whereas oxygen gets adsorbed on the surface and nucleates chromia. So, in essence following reaction occurs:

$$2Cr + 3CO \rightarrow Cr_2O_3 + 3C_{solution} \qquad (5.2a)$$

(2a) Growth of chromia and nucleation of surface carbide: At time t = t_2, chromia nuclei grow into a thin film and the Cr_7C_3, hereafter referred as surface carbide, nucleates at the gas/scale interface via reaction between the outward diffusing Cr-cation and the carbon adsorbed on the chromia:

$$7Cr + 3C_{ad} \rightarrow Cr_7C_3 \quad . \qquad (5.16)$$

The microstructure results presented in section 4.5 suggests that the nucleation of the surface carbide starts at ~1h.

The oxygen diffuses inward forming chromia at the alloy/scale interface.

$$2Cr + 3O \rightarrow Cr_2O_3 \quad . \qquad (5.17)$$

(2b) Growth of surface carbide: The process outlined at step 2a continues and the surface carbide grows at the gas/scale interface into more or less a continuous carbide layer, whereas the chromia grows via inward diffusion of oxygen to the alloy/scale interface. According to the gas chromatograph result presented in section 4.1 and shown in Fig. 4.6, the growth of the surface carbide must have occurred in the first 50h-80h, as the consumption of the carburizing gas CO occurred only in this time interval.

(3) Surface carbide growth stops: After time $t = t_3$, the growth of surface carbide stopped as the activity of Cr at the gas/scale interface fell below the minimum activity of Cr required for the formation of carbide. Further a thin layer of chromia, referred to as the outer chromia layer, formed over the surface carbide layer via outward diffusion of chromium.

(4) Carbide dissolution: After time $t = t_4$, carbide dissolution occurs via a reaction between chromia and surface carbide as per:

$$C_7C_3 + Cr_2O_3 \rightarrow 3CO\uparrow + 9Cr. \qquad (5.18)$$

The product CO escapes to the environment via interconnected pores or cracks where it was detected by the gas chromatograph and the Cr diffuses to the gas/scale surface due to the Cr gradient in the surface scale, and is re-oxidized as per reaction in Eq. 5.11a.

$$2Cr + 3/2O_2 \rightarrow Cr_2O_3 \quad (5.11)$$

The dissolution of carbide must have occurred between 50h-80h to 750h at 900°C, as in this time interval a net evolution of CO was measured by the gas-chromatograph (Fig. 4.6). The results of the microstructure measurements of the carbon contained in the surface carbide, which was presented in section 4.3.3.2.2 (Fig.4.69) also showed that a continuous dissolution of the carbide occurred from 100h to 750h.

In the following sub-sections, the mechanism of surface oxidation/carburization will be explained based on the steps mentioned above:

Step 1: Nucleation of chromia on the surface

The short term experiment in which sample was oxidized for only 1h at 900°C in environment 6 (CO/CO_2 = 1272) showed that chromia forms on the alloy surface first, followed by nucleation of surface carbide over the chromia. The results of this experiment were presented in section 4.5 and were also tabulated in table 4.9 along with the results from the 750h long test at the same temperature, environment, and surface finish of the sample prior to oxidation. This section discusses the reasons for preferential nucleation of chromia at the alloy surface over carbides during earlier exposure duration.

At 900°C, the carbon potential ($10^{-1.2}$) and the oxygen potential (~10^{-22}atm) in the environment are higher than those for the following equilibrium potentials: Cr/Cr_7C_3 ($10^{-2.6}$), $Cr/Cr_{23}C_6$ ($10^{-2.4}$), and Cr/Cr_2O_3 (10^{-24} atm). Consequently Cr_2O_3, $Cr_{23}C_6$ or Cr_7C_3 could have formed on the alloy surface. However, the literature suggests that the permeability of carbon in Ni-Cr base alloys is, typically, 3 to 4 orders of magnitude

higher than that for oxygen (e.g. in case of Ni-20Cr alloy, the oxygen and carbon permeability at 900^{o}C, a_C = 1, and P_{O_2} = Ni/NiO equilibrium were 7.2x10^{-13} cm^2/sec [124]and 6.5x10^{-10} cm^2/sec[114]). Hence, the permeability of carbon will result in formation of internal $M_{23}C_6$ or M_6C (where M is Cr, Mo) carbide. Oxygen may be adsorbed on the alloy surface where chromia will be nucleated. So, in essence following reaction occurs:

$$2Cr + 3CO \rightarrow Cr_2O_3 + 3C_{solution} \quad (5.2a)$$

Note that the reaction in Eq. 5.2a is thermodynamically feasible as the CO concentration the environment (1908 ppm) is higher than the critical concentration of CO, P^*_{CO} value of 5.5 ppm[108]. Further the occurrence of this reaction at 900°C in environment 1 (CO/CO_2 = 9) was shown in section 5.1.The microstructure of the sample oxidized for 100h at 900°C is shown in Fig. 5.18. Comparing with the as-received microstructure it is evident that after exposure the area fraction of the internal carbides has increased. The increase in carbide fraction can occur due to ingress of carbon in the alloy from the environment or due to the supersaturation of carbon in the matrix of the as-received alloy, if any. It is expected that if the observed increase in carbide fraction is entirely due to ingress of carbon then there should be a gradient in carbide fraction with higher carbide fraction near the surface than in the bulk. However, the microstructure examination did not show any significant gradient of carbide fraction in the oxidized sample till the middle of the cross-section, which suggests that the observed increase in area fraction of carbides, in part, could have come from the supersaturation of carbon in the as-received matrix. However, this does not contradict the supposition that part of the increase in carbide fraction is due to ingress of carbon from the environment also,

because of the fact the diffusion distance of carbon in the alloy 617 at 900°C in 100h of oxidation is $\sqrt{D_C t}$ = 0.7mm (D_C = diffusion coefficient of carbon in the alloy = $1.4 \times 10^{-8} cm^2/s$ [120], t =100h) which is equal to the half of the sample thickness and the ingressed carbon could diffuse in the entire sample and distribute homogenously resulting in homogenous precipitation of carbide.

Thus, in summary, during early exposure duration chromia nucleates on the alloy surface in preference to carbide as the high permeability of the matrix for carbon causes inward diffusion, resulting in internal carburization.

Step 2: growth of chromia and surface carbide

This section first explains why the surface carbide can nucleate and grow and then validates the proposed mechanism by performing a mass balance on the diffusing species, namely Cr, carbon, and oxygen. It will be shown that the nucleation/growth of surface carbides occurs at the gas/scale interface via reaction between the outward diffusing Cr-cation and carbon preferentially adsorbed at chromia, whereas the growth of chromia occurs via inward diffusion of oxygen at the scale/alloy interface.

According to the Cr-stability diagram shown in Fig. 5.19, the carbon and oxygen potentials in environment 6 (CO/CO_2 = 1272) were such that chromia was the most stable phase in contact with the equilibrated gas-mixture. However as presented in section 4.3.3.2.1 a metastable surface carbide nucleated and grew over chromia at the gas/scale interface. The nucleation/growth of a metastable phase (surface carbide) over the stable phase (chromia) requires a kinetic factor that will favor the preferential nucleation of the metastable carbide [125].

In step 2a (after ~1h), the chromia nucleated in step 1 has grown into a film of thickness 0.07μm. The CO molecules which at step 1 were dissociating at the alloy surface will now dissociate over chromia. The dissociation of CO will release carbon and oxygen atoms which can be adsorbed onto chromia and can diffuse inward. However, the ^{14}C tracer technique experiment has shown that the solubility of carbon in chromia lattice and grain boundaries is negligible (<0.01 ppm at 1000°C[126]), which means that the adsorbed carbon cannot permeate through the chromia, but oxygen can [109]. Thus, the preferential adsorption of carbon on the chromia will locally raise the carbon potential, favoring the nucleation of surface carbide, Cr_7C_3. Further, since the oxygen can permeate through chromia it will diffuse inward forming chromia at the alloy/scale interface. Thus, in essence the situation at this step is just the reverse of step 1, in which carbon could permeate the alloy surface but oxygen could not.

In step 2b, the surface carbides coarsen at the gas/scale interface via outward diffusion of Cr cations, whereas, chromia grows at the alloy/scale interface via inward transport of oxygen. To substantiate this hypothesis a comparative microstructure of the samples carburized for 1 h and 100h are shown in Fig. 5.20. The carbide particles nucleated after 1h act as a reference point, and the increase in the thickness of inner chromia layer from 0.07±0.02μm after 1h to 0.3±0.06μm after 100h is possible only if the oxygen were to permeate through the oxide and form chromia at the alloy/scale interface. Further validation for the mechanism of nucleation/growth of surface carbide is provided below.

Two key analyses required to validate the mechanism of nucleation/growth of surface carbide proposed above are: (i) the mass of carbon in the surface carbide and the

mass of oxygen in the inner chromia layer (which forms via inward diffusion of oxygen) after 100h of exposure are comparable to each other, and (ii) the outward diffusion of Cr through the inner chromia is fast enough to account for the mass of Cr in the surface carbide observed in Fig. 5.20b. In other words, a mass balance on carbon contained in the surface carbide and the oxygen contained in the inner chromia layer; and mass balance of Cr diffused through the inner chromia layer and contained in the surface carbide layer is required. Note that the microstructure after exposure of 100h is chosen to validate the nucleation and growth of carbide step as this microstructure is closest to the 50h – 80h time at which according to gas-phase analysis the CO consumption occurred.

The mass of carbon in the surface carbide was estimated by measuring the area fraction of the carbide and was presented in section 4.3.3.3. After 100h of exposure at 900°C the mass of carbon in the surface carbide was $0.5\pm0.03 \times 10^{-3}$ mg/mm^2. As per the hypothesis, for one mole of carbon (i.e. for 12gm/mole) one mole of oxygen (16 gm/mole) diffuses inward to form chromia, the theoretical mass of oxygen in the inner chromia layer should be the mass of carbon in the surface carbide times the ratio 16/12, which is equal to $0.7\pm0.03 \times 10^{-3}$ mg/mm^2 of oxygen in inner chromia layer. This calculated mass of oxygen is in reasonably good agreement with the mass of oxygen in the chromia film of $1.0\pm0.27 \times 10^{-3}$ mg/mm^2 measured from the microstructure (table 4.13, section 4.3.3.3), suggesting that during nucleation/growth of surface carbide the inward diffusion of oxygen forms chromia at the scale/alloy interface, whereas the carbon forms surface carbide at the gas/scale interface.

To determine if the outward diffusion of Cr through inner chromia layer is fast enough to account for the mass of Cr in the surface carbide, an approximate diffusion

coefficient of Cr in the chromia was calculated. To do this, first the amount of Cr in the surface carbide needs to be calculated. The mass of Cr in the surface carbide is the mass of carbon in the surface carbide times the ratio 364/36, which is t he ratio of mass of Cr and carbon in the Cr_7C_3. The mass of carbon in surface carbide after 100h is $0.5\pm.03x10^{-3}$ mg/mm^2 (table 4.13), which gives the mass of Cr in surface carbide as ~5.0×10^{-3} mg/mm^2. Given the mass of the diffusing species, the average flux can be calculated using the formula [127, 128]:

$$j_{Cr} = \frac{M}{At} \tag{5.19}$$

Where j_{Cr} is the average flux of Cr atoms that diffused through chromia, M is the mass of Cr in the surface carbide (5.0×10^{-3} mg/mm^2), A is the cross-sectional area, and t is the elapsed time (100h). Using the Eq. 5.19, $1.4x10^{-8}$ $mgmm^{-2}sec^{-1}$ of Cr-flux would be required to form a more or less continuous surface carbide layer observed after 100h of carburization.

To compute an approximate diffusion coefficient of Cr in chromia, D_{Cr} we use Fick's first law [127, 129]:

$$j_{Cr} = -D_{Cr}\frac{dC_{Cr}}{dx} = -C_{Cr}\frac{D_{Cr}}{kT}\frac{d\mu_{Cr}}{dx} \tag{5.20}$$

where C_{Cr} is the average concentration of chromium atoms in chromia (in $mgmm^{-3}$), k is the Boltzman's constant, T is the temperature, and $d\mu_{Cr}/dx$ is the chemical potential gradient of Cr in chromia scale.

The chemical potential of Cr can be expressed as

$$\mu_{Cr} = \mu^{o}_{Cr} + kT\ln P_{Cr} \tag{5.21}$$

where P_{Cr} is the chromium vapor pressure. The chemical potential gradient of Cr in chromia is accordingly given by:

$$\frac{d\mu_{Cr}}{dx} = kT\frac{dlnP_{Cr}}{dx} \tag{5.22}$$

Substituting Eq. 5.22 in Eq. 5.20 the Cr-flux is then given by:

$$j_{Cr} = -C_{Cr}D_{Cr}\frac{dlnP_{Cr}}{dx} \tag{5.23}$$

In order to evaluate Eq. 5.23 the value of chromium diffusion coefficient, D_{Cr} as a function of P_{Cr} must be known. This requires the knowledge of the defect structure of chromia. It has been shown in the literature that chromium interstitial is the predominant point defect in chromia formed on pure Cr [130], Ni-30Cr alloy [129], and alloy 617 [117] in low oxygen partial pressure environment. With the assumption that the predominant defect in the scale is Cr-interstitial, the diffusion coefficient of Cr can be expressed as a function of partial pressure of Cr vapor [117, 129]:

$$D_{Cr} = D^{o}_{Cr}\,P_{Cr} \tag{5.25}$$

where D^{o}_{Cr} is the diffusion coefficient of Cr in chromia corresponding to one atmosphere pressure of chromium vapor, i.e. at P_{Cr} = 1 atm.

After substituting the value of D_{Cr} from Eq. 5.25 in Eq. 5.24, and rearranging we get,

$$D^{o}_{Cr} = \frac{j_{Cr}\,\Delta x}{C_{Cr}\left(P^{i}_{Cr} - P^{o}_{Cr}\right)} \tag{5.26}$$

Further, using the Eq. 5.25, the diffusion coefficient of Cr in chromia at the Cr-Cr_2O_3 phase boundary, D_{Cr} is given by

$$D_{Cr} = D^{o}_{Cr}\,P^{i}_{Cr} \tag{5.27}$$

Combining Eqns. 5.26 and 5.27 we get

$$D_{Cr} = \frac{j_{Cr}\,\Delta x}{C_{Cr}\left(1-\frac{P^{o}_{Cr}}{P^{i}_{Cr}}\right)} \tag{5.28}$$

In order to calculate the D_{Cr} the ratio $\frac{P^{o}_{Cr}}{P^{i}_{Cr}}$ needs to be calculated. The value of P^{i}_{Cr} is given by

$$P^{i}_{Cr} = a_{Cr} P^{*}_{Cr} \tag{5.29}$$

where a_{Cr} and P^{*}_{Cr} are the activity of Cr in the alloy and vapor pressure of chromium corresponding to Cr-Cr_2O_3 equilibrium at the temperature of interest, respectively. The value of P^{*}_{Cr} can be read from tables of thermodynamic data [131]. At 900°C it is equal to 1.7 x 10^{-12} atm. Further, at 900°C the activity of Cr in alloy 617 has been reported to be 0.65 using mass-spectroscopic method [115]. Thus, at 900°C, as per the Eq. 5.29 P^{i}_{Cr} is equal to 1.1x10^{-12} atm.

In order to calculate P^{o}_{Cr} at the gas/scale interface, it can be assumed that the Cr vapor, Cr_2O_3, and the gas are in local equilibrium, i.e. the following reaction is in equilibrium at the gas/scale interface

$$Cr(gas) + 3/2O_2 \leftrightarrow Cr_2O_3\ (solid) \tag{5.30}$$

Using the identity that at 900°C the equilibrium constant for the reaction in Eq. 5.30 is 4.8 x 10^{63} [131] and the oxygen partial pressure in the gas (CO/CO_2 = 1272; environment

6) is 5.3×10^{-23} atm, the P_{Cr}^{o} will be 7.3×10^{-16} atm, which is ~ 4 orders of magnitude lower than the P_{Cr}^{i} value of 1.7×10^{-12} atm, and hence the ratio $\frac{P_{Cr}^{o}}{P_{Cr}^{i}}$ is <<1.

Retuning back to the Eq. 5.28, since the ratio $\frac{P_{Cr}^{o}}{P_{Cr}^{i}}$ <<1, the D_{Cr} is

$$D_{Cr} \sim \frac{j_{Cr}\,\Delta x}{C_{Cr}} \tag{5.31}$$

The average concentration of Cr in the chromia (C_{Cr}) is the density of chromia (5.21 $mgmm^{-3}$) times the weight fraction of Cr in chromia (0.68), which is equal to 3.56 $mgmm^{-3}$. Substituting values of j_{Cr} (from Eq. 5.19 = 1.4×10^{-8} $mgmm^{-2}sec^{-1}$), C_{Cr} (3.56 $mgmm^{-3}$), and the Δx ($0.3 \pm 0.03 \mu m$ from table 4.9) in Eq. 5.31 the diffusion coefficient of Cr in chromia is calculated to be 1.2×10^{-14} cm^2/sec. Note that this calculated diffusion coefficient is an approximate value and a rather detailed analysis is required to calculate the accurate value of D_{Cr}.

The above calculated D_{Cr} has been plotted in Fig. 5.22 along with the bulk diffusion coefficient of Cr in chromia as a function of temperature from literature. The calculated D_{Cr} is in good agreement with the literature and is similar to the bulk diffusion coefficient of Cr in polycrystalline chromia measured using ^{51}Cr tracer technique by Lobing et al. ($1.0 \times 10^{-14} cm^2/sec$) [132] and Ignatov et al. ($3.2 \times 10^{-14} cm^2/sec$, interpolated) [133] confirming the hypothesis that the outward diffusion of Cr-cation resulted in the nucleation/growth of surface carbide.

Therefore, in summary, since the diffusional flux of Cr can account for the mass of Cr in the surface carbide and the mass of carbon in the surface carbide and oxygen in the inner chromia layer are in good agreement with each other, it is concluded that the

nucleation/growth of surface carbide occurs via outward diffusion of Cr-cation reacting with the carbon adsorbed over chromia at the gas/scale interface and the growth of chromia occurs via inward diffusion of oxygen at the alloy/scale interface.

Step 3: Growth of surface carbide stopped

The growth of the surface carbide did not occur throughout the exposure duration, rather as per the gas-phase result shown in Fig. 4.6 and the microstructure analysis results presented in section 4.3.3.3 and shown in Fig. 4.69 the growth of carbide stopped after approximately 50h to 80h of carburization. This section determines a critical activity of Cr below which the growth of surface carbide will stop in environment 6 (CO/CO_2 =1272) and the test temperature of 900°C.

The surface carbide forms at the scale/gas interface according to the reaction in Eq. 5.16. This reaction will stop if either the activity of carbon or activity of Cr at the scale/gas decreases below a minimum value required for carbide formation. Activity of carbon at the gas/scale interface is set by the activity of carbon in the gas, which is fixed by the CO/CO_2 ratio and was maintained throughout the experiment. So, the carbide growth must stop occur because the activity of Cr fell below a critical value at the reaction site. This critical value of activity of Cr can be extracted from the a_{Cr}-a_C diagram shown in Fig. 5.23a. The slanted line in this figure is the locus of combination of a_{Cr} and a_C at which the Cr/Cr_7C_3 equilibrium exists. In the region below the slanted line Cr is stable, whereas, above the line carbide is stable and on the line both Cr and Cr_7C_3 are stable. The activity of carbon or carbon potential of the gas in environment 6 (CO/CO_2 = 1272) at 900°C is shown by the horizontal arrow. For a carbon potential equivalent to

environment 6 (CO/CO_2 =1272), Cr_7C_3 cannot form if the activity of Cr is less than that at point "A" (a_{Cr} = 0.16) in Fig.5.23a. Thus, it is concluded that the activity of Cr at the gas/scale interface must be ≤ 0.16, which stopped the growth of the carbide.

The reason for decrease in activity of Cr at the scale/gas can be explained by the fact that the continued carburization will result in increased thickness of the inner chromia layer. Recall that it was shown in step 2 that the growth of surface carbide is accompanied by the growth of the inner chromia layer. As the thickness of the inner chromia layer increases, the diffusion distance for Cr required for surface carbide formation increases; consequently, its concentration and activity at the scale/gas interface will decrease.

The carbide growth stops at around 50h-80h, the microstructure image taken closest to this duration is 100h which had an inner chromia layer thickness of ~0.3±0.03μm. So it follows that at approximately 0.3 μm, the activity of Cr at the scale/gas interface falls below 0.16 at 900°C resulting in the cessation of growth of surface carbide.

Another observation at this time is that an outer layer of chromia grew over the carbide near the gas/scale interface, which can only occur via outward diffusion of Cr-cations. In other words the Cr-flux which was supporting the growth of surface carbide is now involved in formation of chromia at the gas/scale interface. The a_{Cr}- P_{O_2} diagram shown in Fig. 5.23b supports this observation. Corresponding to the activity of Cr at point "A" (a_{Cr} = 0.16) the oxygen potential in the environment is higher than Cr/chromia equilibrium oxygen pressure and the chromia is the stable phase which grows over carbide.

Step 4: Dissolution of the carbide and growth of chromia

The surface carbide was the meta-stable phase and over long exposure duration it dissolved leaving behind voids in the surface scale. This section discusses the possible reactions by which the surface carbides can dissolve. The localized change in the volume of the surface scale will be calculated to propose the reaction primarily responsible for carbide dissolution.

Two observations that can help to determine the dissolution mechanism of the carbides are: (i) CO evolution occurred, which was measured by gas chromatograph, as shown in Fig. 4.6, and (ii) dissolution of surface carbides resulted in the formation of voids in the surface scale (Fig. 4.54 to 4.56). The conclusion that the dissolution of carbide resulted in the formation of void was based on the results presented in section 4.3.3.2.1. The key results presented in that section that support this conclusion are:

- that the voids in the surface scale were almost always observed near the surface carbides,
- the location of the voids with respect to the alloy/scale interface was similar as the location of surface carbides with respect to the alloy/scale interface,
- the fraction of the voids in the surface scale increased with the increased dissolution of surface carbides, and
- often the voids were observed near the half dissolved carbide, for example Fig. 4.56.

The morphological evidence listed above clearly showed that the dissolution of the surface carbides resulted in the formation of voids in the surface scale.

There are only two reactions in He-CO-CO_2 gas mixture that can account for dissolution of surface carbide and evolution of CO at the same time:

$$Cr_7C_3 + Cr_2O_3 \rightarrow 3CO + 9Cr \quad (5.18)$$

$$4Cr_7C_3 + 27O_2 \rightarrow 14Cr_2O_3 + 12CO \quad (5.21)$$

The reaction in Eq. 5.18 states that the equilibrium phase chromia reduces the metastable surface carbide (Cr_7C_3) into pure Cr and CO gas, whereas the reaction in Eq.5.21 states that the metastable carbide are simply oxidized by the oxygen into the equilibrium phase, chromia.

In order to determine the primary reaction responsible for dissolution of surface carbide the volume change due to occurrence of each reaction is calculated below.

Calculation of the change in volume % due to reaction in eqns.5.18 and 5.21

Data used were taken from references[109, 134]:

Molar volume of Cr_7C_3 ($\Delta\Omega_{Cr_7C_3}$) = 57.98 cm^3

Molar volume of Cr (Ω_{Cr}) = 7.28 cm^3

Molar volume of Cr_2O_3 ($\Delta\Omega_{Cr_2O_3}$) = 29.23 cm^3

Volume change due to reaction in Eq. 5.18

Total volume of the reactant = $\Delta\Omega_{Cr_7C_3} + \Delta\Omega_{Cr_2O_3}$

= 87.21 cm^3

Total volume of the product which is in solid form = $9\Omega_{Cr}$ = 65.5 cm^3

% change in volume, $\%\frac{\Delta V}{V} = \frac{V_{product} - V_{reactant}}{V_{reactant}} \times 100$

= -25%

Thus in case of reaction in Eq. 5.18 there will be a net 25% decrease in the volume of the surface scale. In other words the product occupies less volume than the reactants hence occurrence of this reaction will result in formation of voids near the surface carbides.

Volume change due to reaction in Eq. 5.21

Volume of the reactant = $4\Omega_{Cr_7C_3}$ = 231.9 cm^3

Volume of the product = $14\Omega_{Cr_2O_3}$ = 409.22 cm^3

$$\% \text{ change in volume} = \% \frac{\Delta V}{V} = \frac{V_{product} - V_{reactant}}{V_{reactant}} \times 100$$

$$= +76\%$$

Thus in case of reaction in Eq. 5.21 there will be a net 76% increase in the volume of the surface scale. Since in this case the product occupies 76% more space than the reactant, occurrence of this reaction will create a compressive stress in the surface scale, which in turn should result into the buckling or breaking off of the film. Further, voids cannot form in the surface scale. However, buckling of the film was never observed under SEM (Figs. 4.52 to 4.56).

Thus the reaction in Eq. 5.18 will form voids near the surface carbide, which were consistently observed in the microstructure examination (Figs.4.54 to 4.56). The reaction in Eq. 5.21 cannot result in void formation. The reaction in Eq. 5.21 will lead to a compressive stress in the surface film which should result in the buckling/breaking off of the scale, which was not observed under SEM examination. Thus the analysis supports the conclusion that dissolution of carbide occurs primarily via reaction in Eq. 5.18.

One more aspect of the reaction in Eq. 5.18 that should be considered is as to what happens to the Cr that is produced by the reaction in Eq. 5.18. The SEM and TEM (in case of sample exposed for 850^{o}C for 225h) did not show any segregation of pure Cr at the carbide/oxide boundary. So, the reaction product Cr must be transported either to the bulk of the alloy or to the alloy/gas interface. The direction of diffusion of a species is governed by the activity gradient and an estimate on the Cr-activity gradient between the scale/alloy and the alloy/gas interface would have to be done to answer whether the produced Cr diffused towards the alloy/scale interface or the scale/gas interface.

The activity of Cr at the scale/gas interface can be estimated by assuming that the chromia/gas interface is in local equilibrium. This approximation is valid as the Cr-stability diagram predicts that chromia is the equilibrium phase in contact with the gas in environment 6 (CO/CO_2 =1272) at 900°C. The formation of chromia near the gas/scale interface suggests that the sample + gas system is close to the equilibrium state, i.e. equilibrium between the alloy surface and the environment has been established. At 900°C, the oxygen partial pressure in environment 6 (CO/CO_2 = 1272) is ~10^{-22} atm and the activity of Cr in equilibrium with this oxygen partial pressure and chromia can be calculated using the equilibrium of the reaction in Eq. 5.11. The calculated activity of Cr at the chromia/gas interface would be 0.052 in environment 6 (CO/CO_2 =1272) and the test temperature of 900°C.

The activity of Cr at the alloy/scale interface will depend on the Cr concentration at the alloy/scale interface. The Cr concentration at the alloy/scale interface after 100h of carburization at 900°C was 18wt%, as shown in Fig. 5.21. The equivalent activity of Cr at the alloy/scale interface can be approximated by the mass-spectroscopic study by

Gosse et al. [115], who determined the activity of Cr for alloy Ni-18wt%Cr-0.1wt%C to be 0.42 at 900°C. The alloy 617 oxidized after 100h also contains 18wt% Cr along with ~10wt%Mo and ~11.6%Co. The Mo and Co are expected to decrease the activity of Cr, however their effect is not expected to be large, e.g. at 900°C the mass-spectroscopic study showed the activity of Cr in Ni-22wt%Cr-0.1wt%C ternary alloy as 0.82[115], whereas the activity of Cr in alloy 617 with Ni-22wt%Cr-9.6wt%Mo-11.6wt%Co-0.1wt%C as 0.65[115], amounting to a decrease of 0.17 in activity of Cr due to addition of Mo and Co. As a first order approximation the activity of Cr at the alloy/scale interface with 18wt% Cr can be set to ~0.42 at 900°C. Now, since the activity of Cr at the scale/alloy (~0.42) interface is approximately one order of magnitude higher than at the scale/gas (~0.052) interface, the Cr released via reaction in Eq. 5.18 can only diffuse toward the gas/scale interface, where it will be oxidized back to chromia via the reaction in Eq. 5.11.

$$2Cr + 3/2O_2 \rightarrow Cr_2O_3. \quad (5.11)$$

Thus in summary the dissolution of the carbide occurs primarily via reaction in Eq. 5.18

$$Cr_7C_3 + Cr_2O_3 \rightarrow 3CO\uparrow + 9Cr, \quad (5.18)$$

followed by transport of CO to the environment and solid state diffusion of Cr to the gas/scale, where it is re-oxidized to chromia via reaction in Eq. 5.11,

$$2Cr + 3/2O_2 \rightarrow Cr_2O_3. \quad (5.11)$$

Table 5.1. Calculation for the weight of CO consumed in the pre-oxidation experiment (environment 1; $CO/CO_2 = 9$) at a temperature of 900°C for 150h (from Eq. 5.3).

Temperature, time (°C, h)	900, 150
area under the curve (mole-h) x 10^{-6}	124
mass of CO from gas phase analysis, ΔW_{CO} (mg/mm^2) $x10^{-3}$	2.9
mass of oxygen in CO (mg/mm^2) $x10^{-3}$= ΔW_{CO} x mass fraction of oxygen in CO of 0.57	1.7
mass of carbon in CO (mg/mm^2) $x10^{-3}$ =ΔW_{CO} x mass fraction of carbon in CO of 0.43	1.2
mass of oxygen in chromia film (mg/mm^2) $x10^{-3}$= film thickness x density of chromia x weight fraction of oxygen in chromia	2.5 ±0.6
weight gain due to carbon in the sample = total weight gain – weight of oxygen in chromia (mg/mm^2) x 10^{-3}	1±0.6

Table 5.2. Comparison between the measured loss in weight of the sample and calculated weight of CO from the area under the curve for exposure of pre-oxidized alloy to 1000°C for 100h in environment 1 ($CO/CO_2 = 9$) (shown in Fig. 4.70) .

Temperature (°C), Time (h)	1000, 5	1000,15	1000, 46	1000, 100
mass of CO produced calculated from area under the curve in Fig. 4.70 using Eq. 5.3 (mg/mm^2x10^{-3})	0.9	1.5	3	3.8
decrease in mass of the sample measured by microbalance ($mg/mm^2x\ 10^{-3}$)	1.3± 0.4	2.3± 0.4	2.7± 0.4	2.9± 0.4
mass of Cr accumulated in the Cr-depleted zone formed after pre-oxidation at 900°C using Eq. 3.13 ($mg/mm^2x\ 10^{-3}$)	1.99			3.9
mass of Cr equivalent to mass of CO recovered calculated as per the reaction in Eq. 5.2b, i.e. 1 mole of CO produces 2/3 mole of Cr ($mg/mm^2x\ 10^{-3}$)	1.6			3.6

(a)

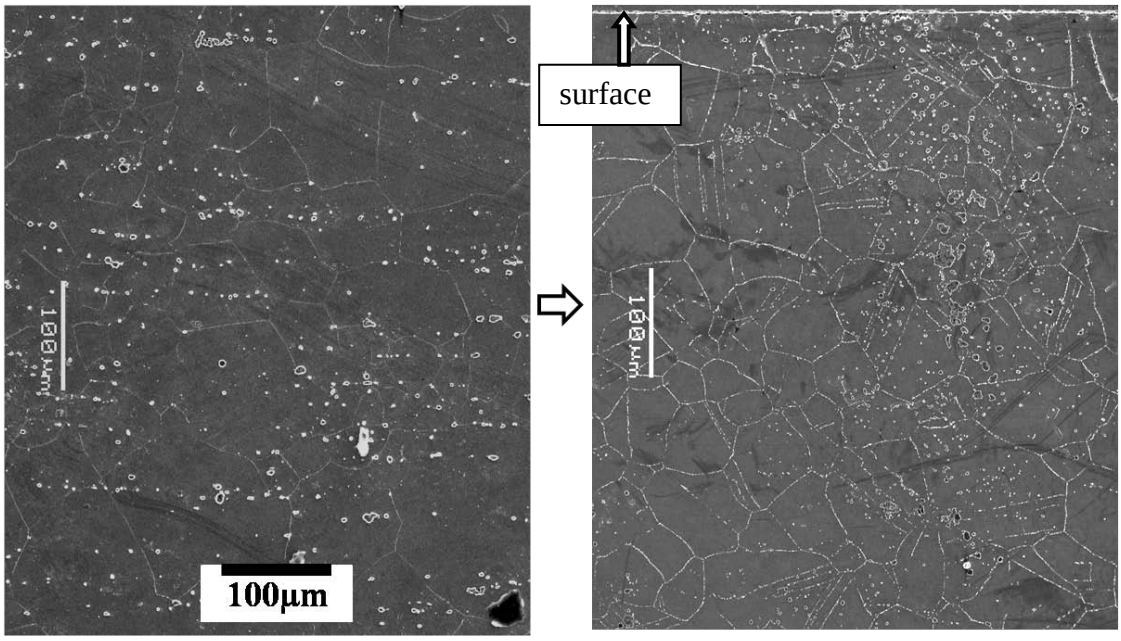

as-received alloy

pre-oxidized at 900°C for 150h in environment 1 (CO/CO_2 =9)

(b)

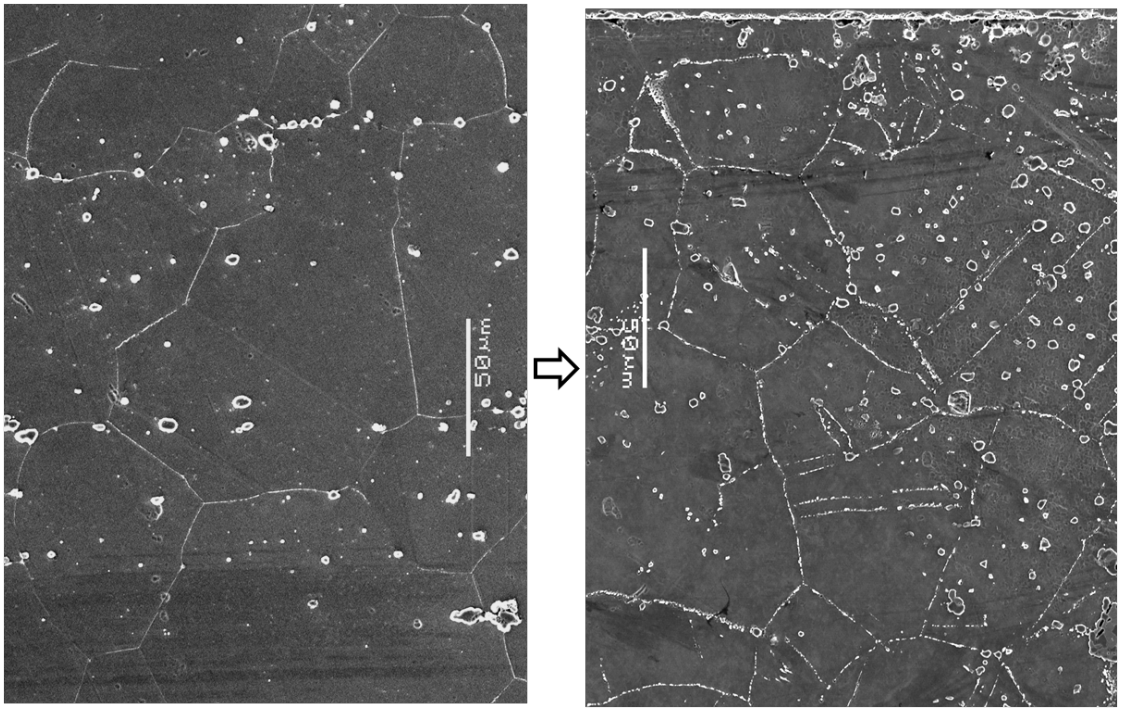

(c)

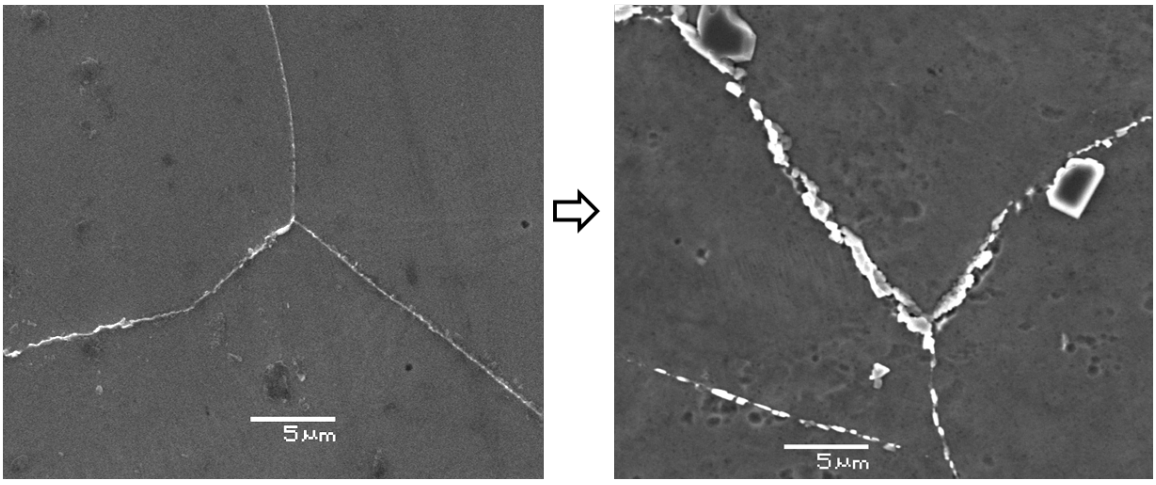

grain boundaries in as-received alloy

thicker carbide film in sample pre-oxidized at 900°C for 150h

Figure 5.1 Comparison between the bulk microstructures of the as received alloy, and sample pre-oxidized at 900°C for 150h in environment 1 (CO/CO_2 = 9). The area fraction of carbides in the oxidized sample is higher than as-received sample. Figs. (a) and (b) show the comparison between the carbide fraction near alloy surface. Fig. (c) shows the comparison between the thickness of carbide film along the grain boundary.

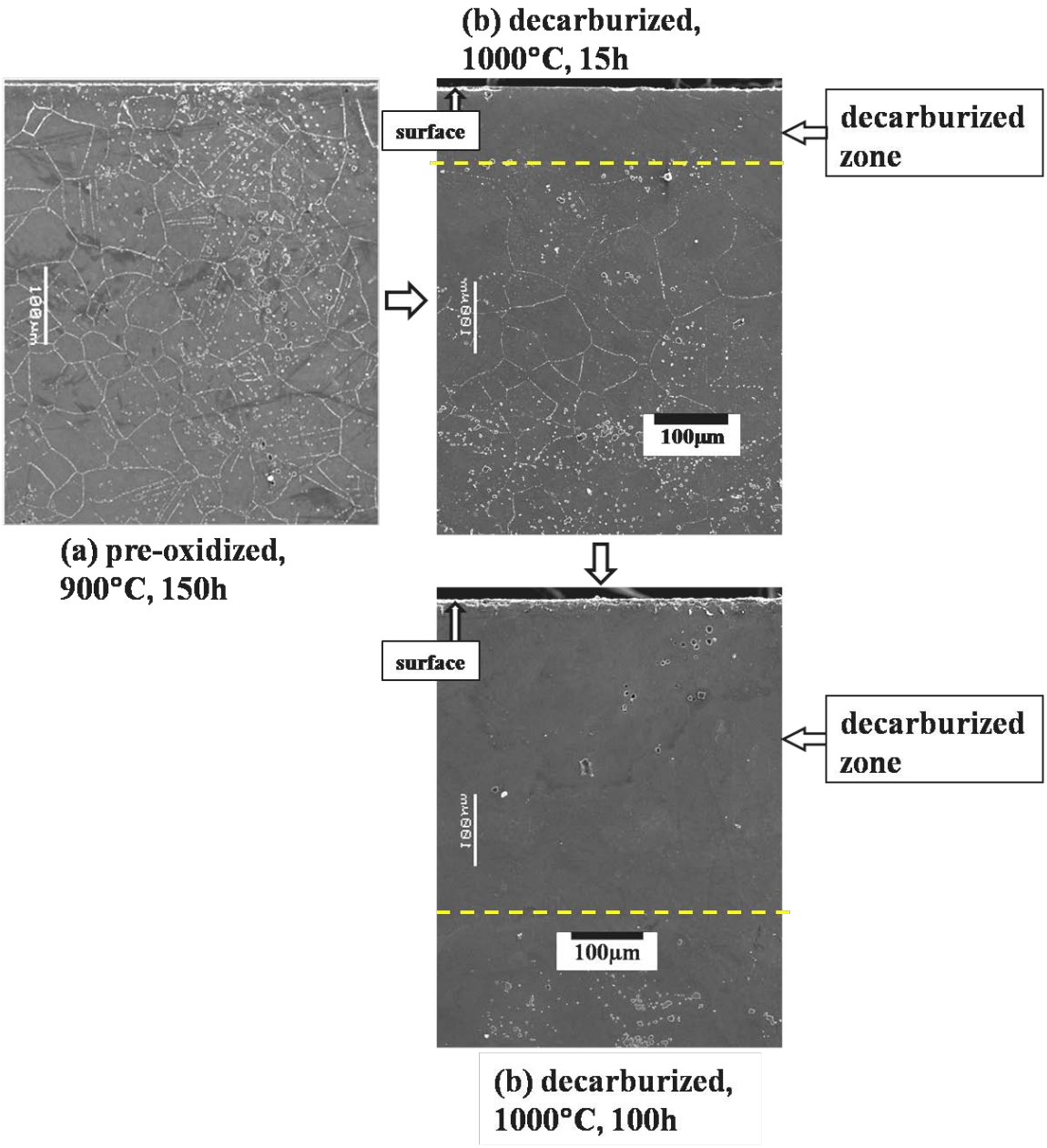

Figure 5.2 Bulk microstructures of (a) sample pre-oxidized at 900°C for 150h, (b) decarburized at 1000°C for 15h, and (c) decarburized at 1000°C for 100h. Environment 1 (CO/CO_2 = 9).

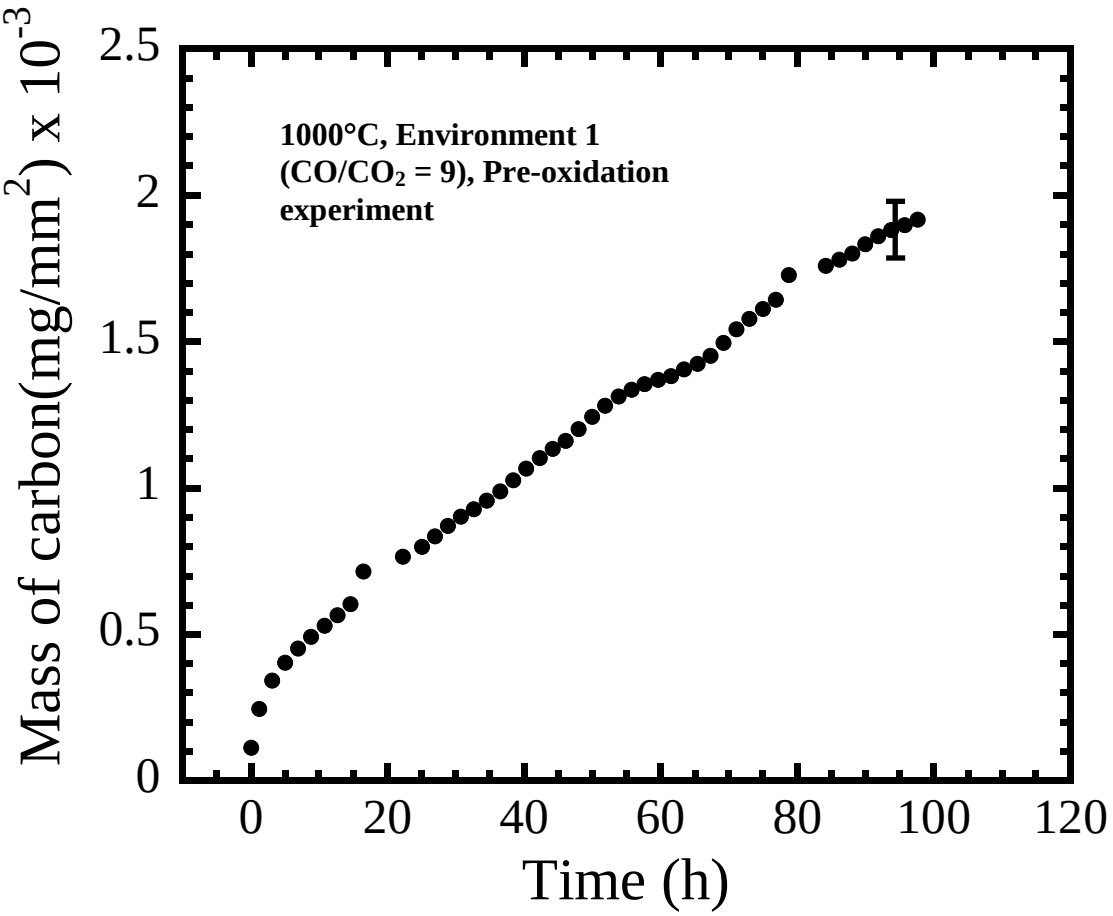

Figure 5.3 Mass of carbon released as CO from the sample during exposure at 1000°C. Note that this plot shows the result from the pre-oxidizing experiment, where sample was first pre-oxidized at 900°C and then decarburized at 1000°C. For clarity only one error bar is shown on the plot. The error corresponds to sum of 7.5% of error due to variation of CO concentration at the inlet and 6.5% due to variation in the flow rate of the gas mixture through the tube.

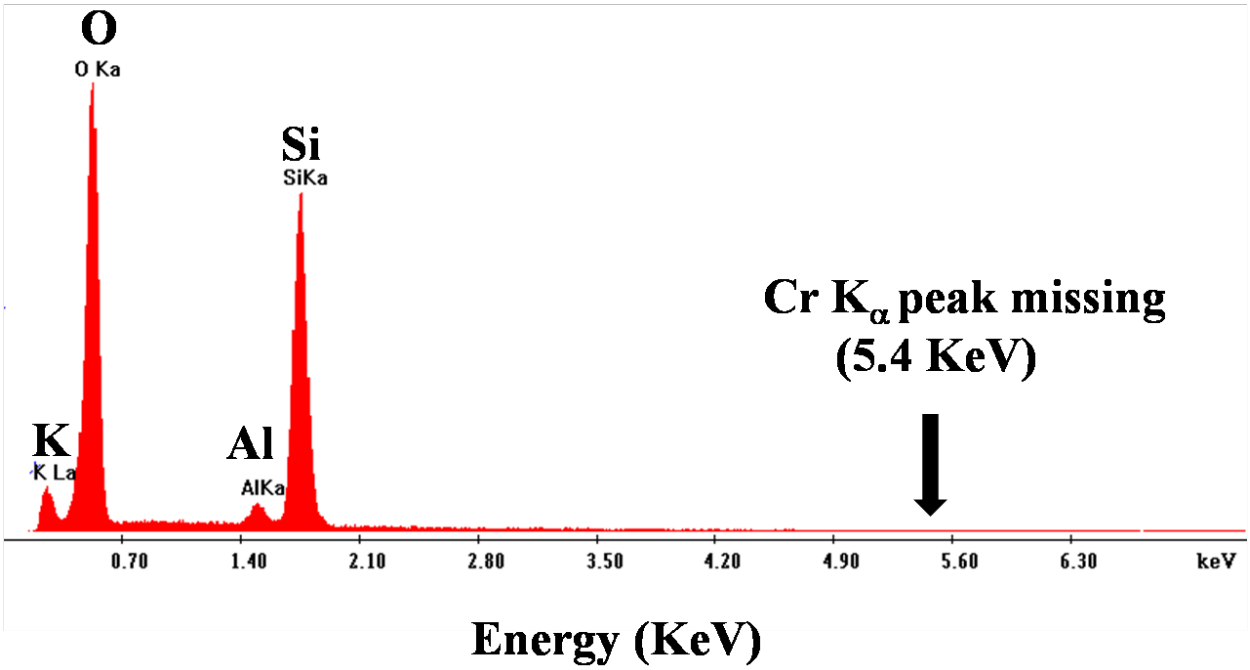

Figure 5.4 SEM/EDS spectrum of the quartz tube used in exposing samples in environment 1 (CO/CO_2 = 9) at 1000°C. Chromium peak was not observed suggesting that chromia was not volatile in the present case, otherwise, we will observe the Cr peak.

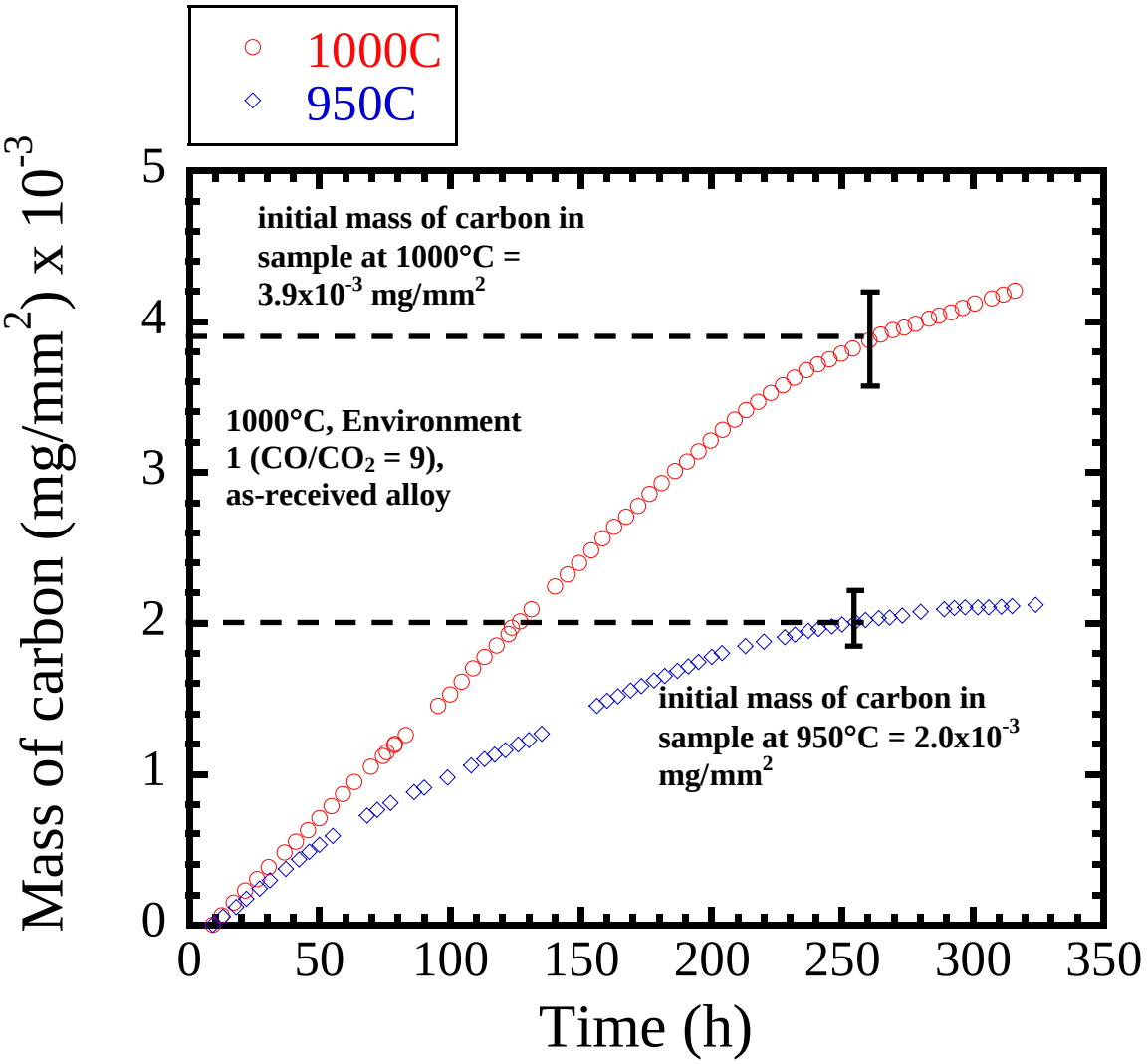

Figure 5.5 Mass of carbon released as CO during exposure of as-received sample at 950°C and 1000°C. For clarity only one error bar is shown on the plot. The error corresponds to sum of 7.5% of error due to variation of CO concentration at the inlet and 6.5% due to variation in the flow rate of the gas mixture through the tube.

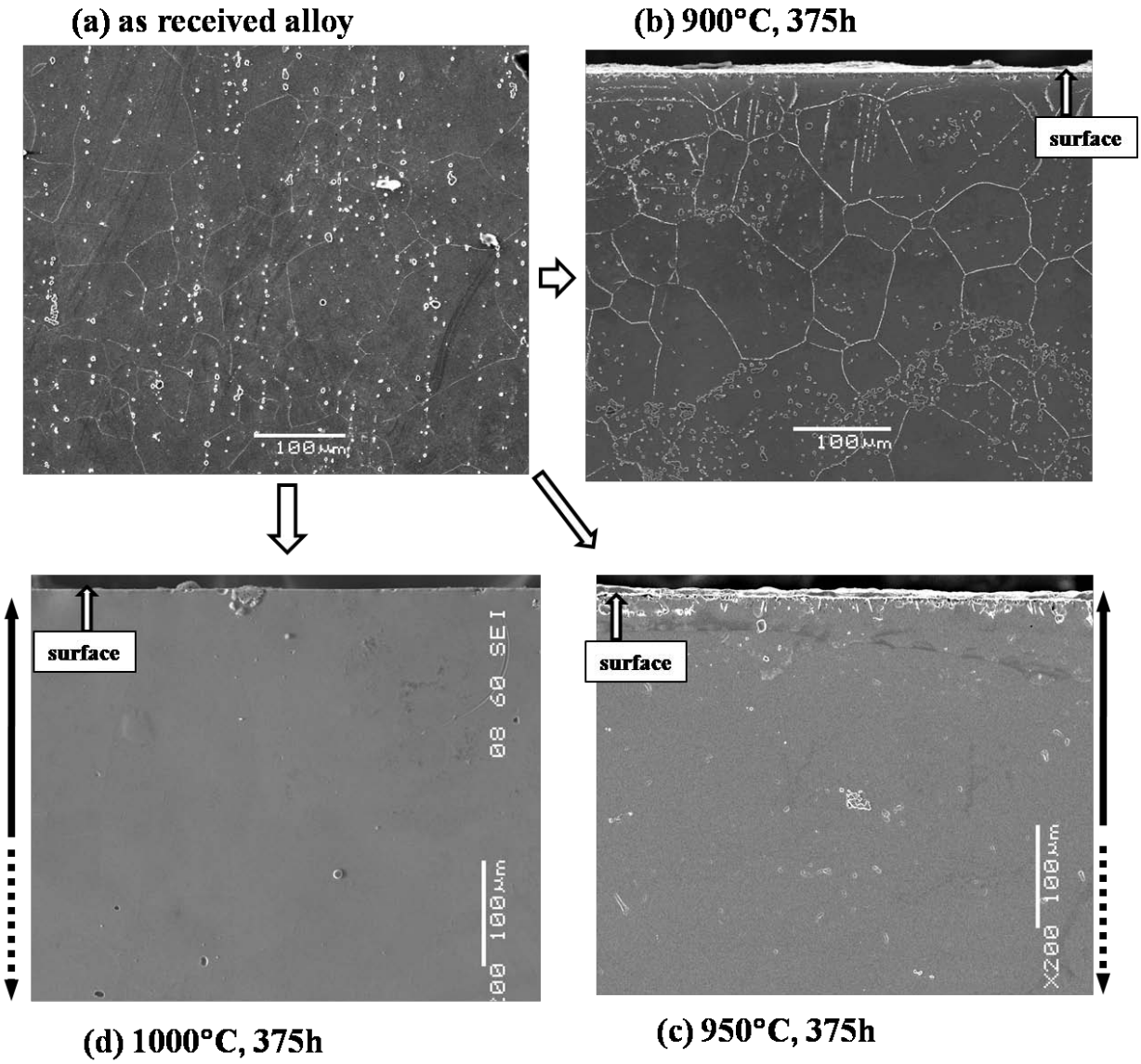

Figure 5.6 Bulk microstructures of (a) as received alloy 617, (b) sample oxidized at 900°C for 375h, (c) sample oxidized for 375h at 950°C, and (d) sample decarburized at 1000°C for 375h. Environment1 (CO/CO_2 = 9). The dashed arrow shows the decarburization zone where the carbides have dissolved in the matrix.

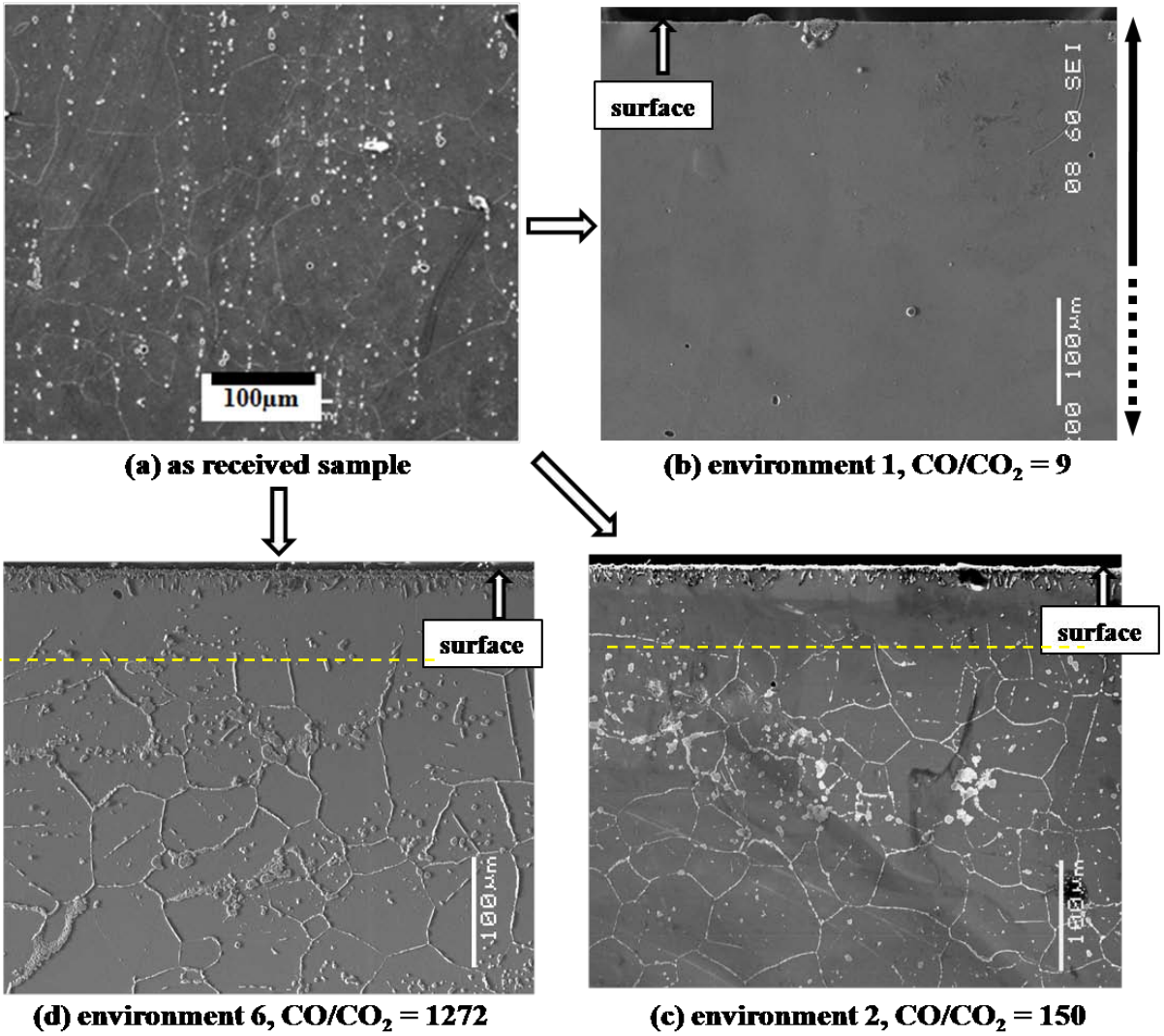

Figure 5.7 Bulk microstructure of (a) as-received alloy, (b) sample decarburized in environment 1 (CO/CO_2 = 9), carbides have dissolved in the entire cross-section, (c) sample oxidized in environment 2 (CO/CO_2 = 150), and (d) sample oxidized in environment 6 (CO/CO_2 = 1272). The yellow dashed line in Figs. (b) and (c) shows the denuded zone formed near the surface because Cr from this zone diffused outward forming surface scale. **Temperature =1000°C, time = 375h.**

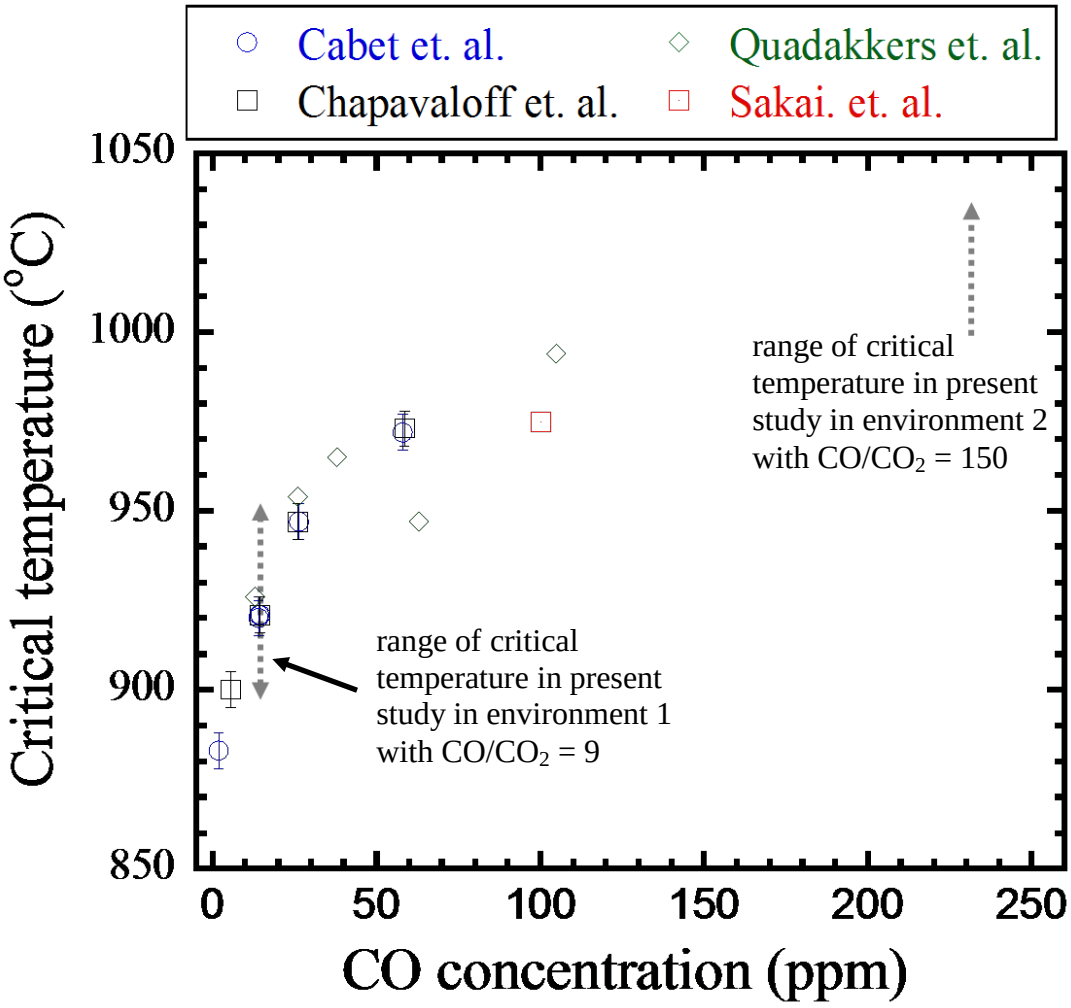

Figure 5.8 Plot of critical temperature as a function of CO concentration in impure helium for alloy 617. Data was borrowed from Cabet et al. [88], Quadakkers et al. [108], Chapavaloff et al. [86], and Sakai et al. [81]. Range of critical temperature from the present study are superimposed on this figure using broken arrows.

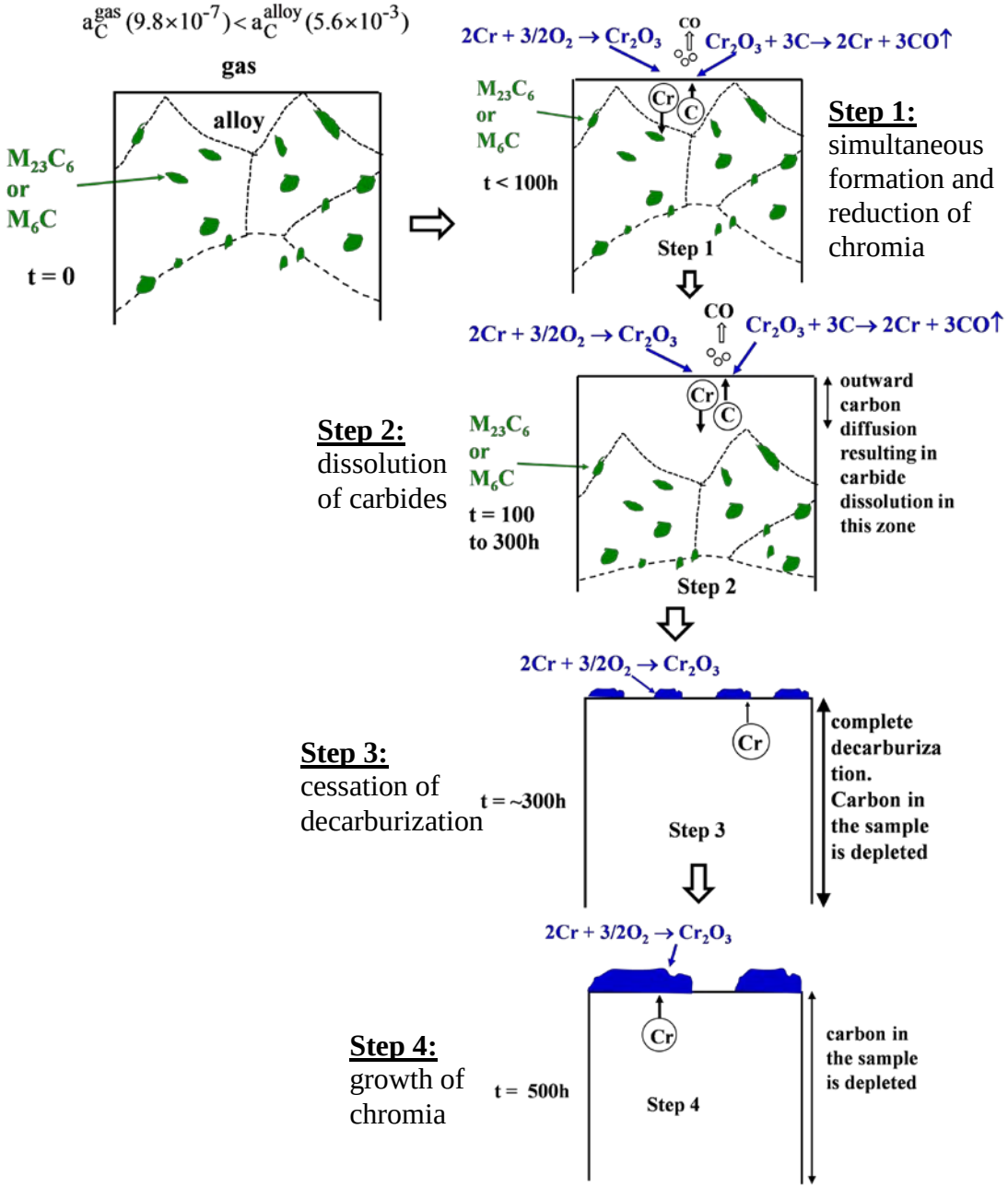

Figure 5.9 Schematic diagram showing the decarburization of the as received alloy at 1000°C in environment 1 (CO/CO_2 = 9) with 15 ppm of CO and 1.7 ppm CO_2 in helium.

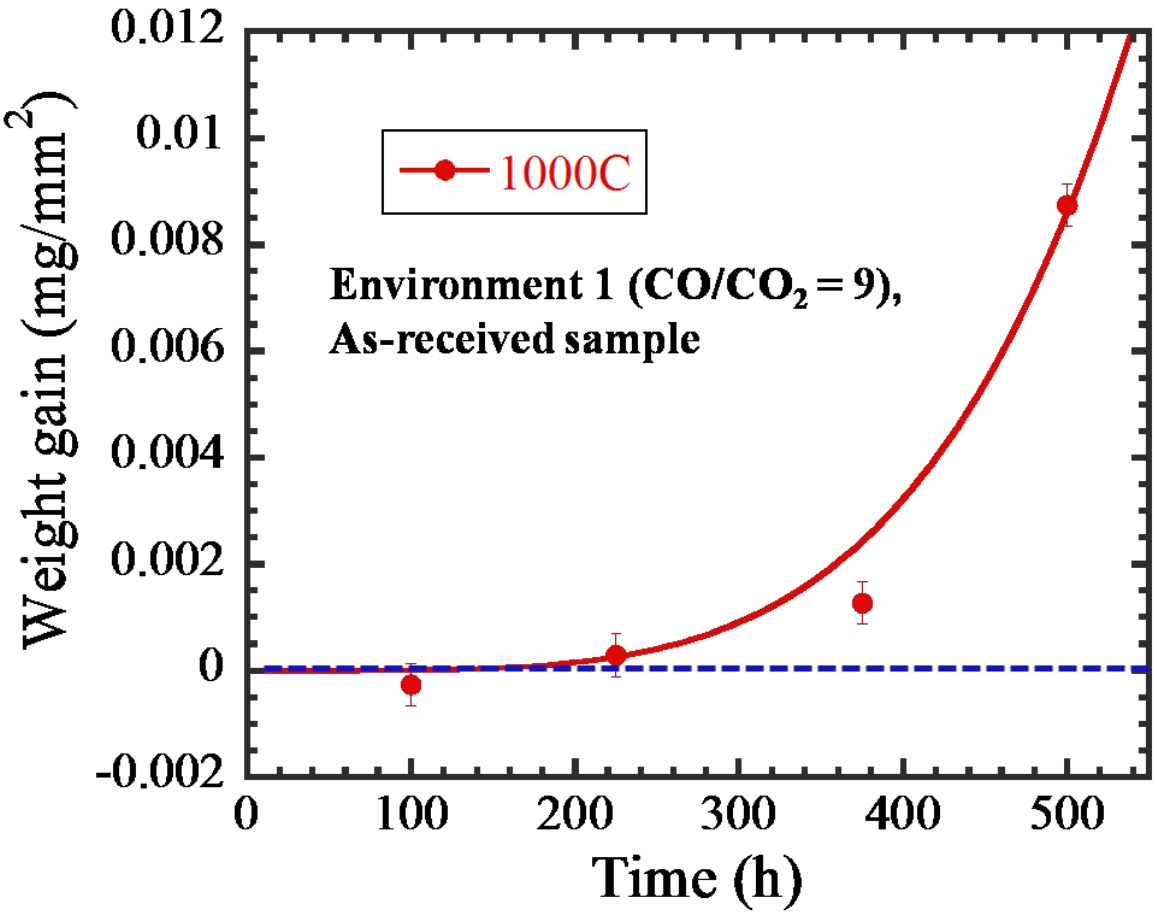

Figure 5.10 Weight gain vs. time for as-received sample exposed at 1000°C in environment 1 ($CO/CO_2 = 9$).

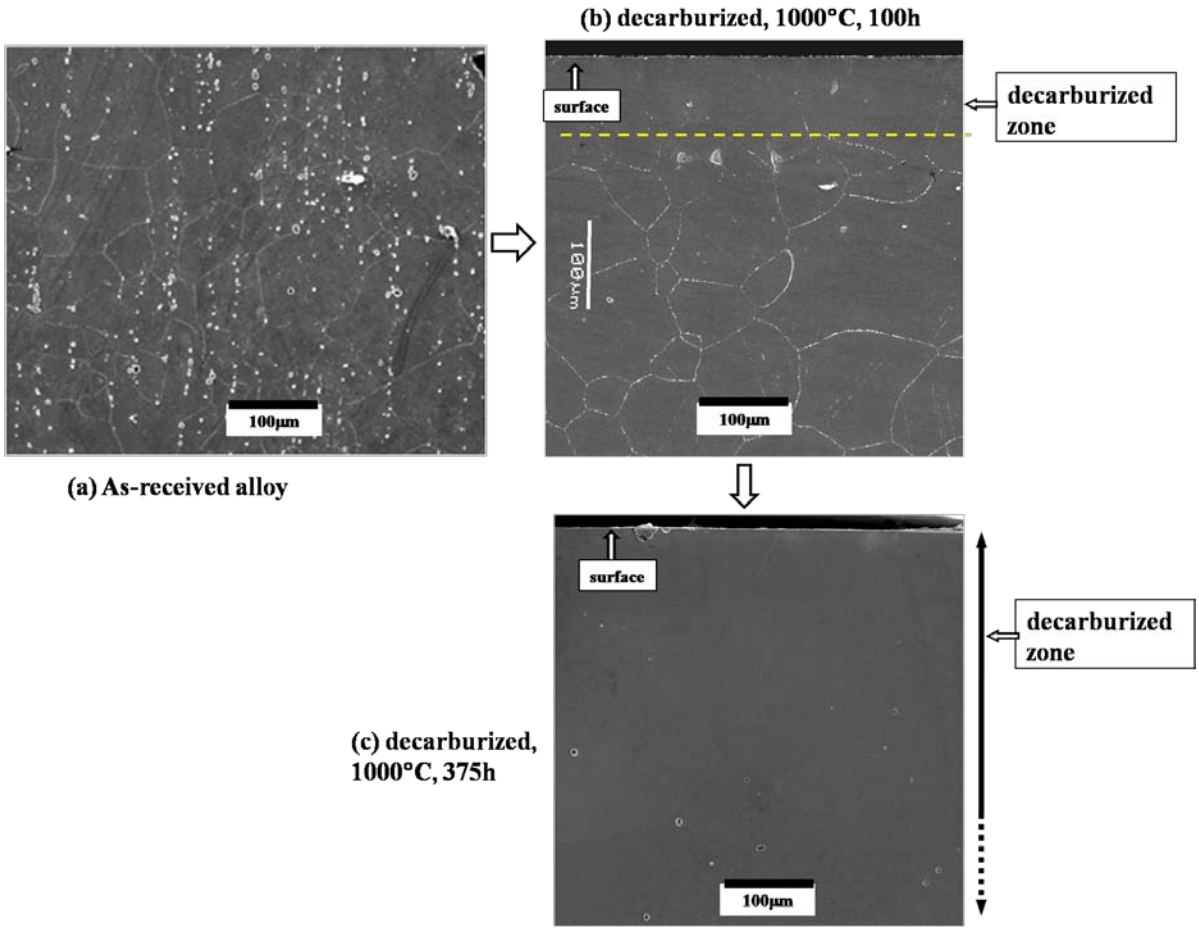

Figure5.11 Bulk microstructure of the (a) as-received alloy, and the bare metal as-received sample decarburized in environment 1 (CO/CO_2 = 9) at 1000°C (b) for 100h, and (c) for 375h.

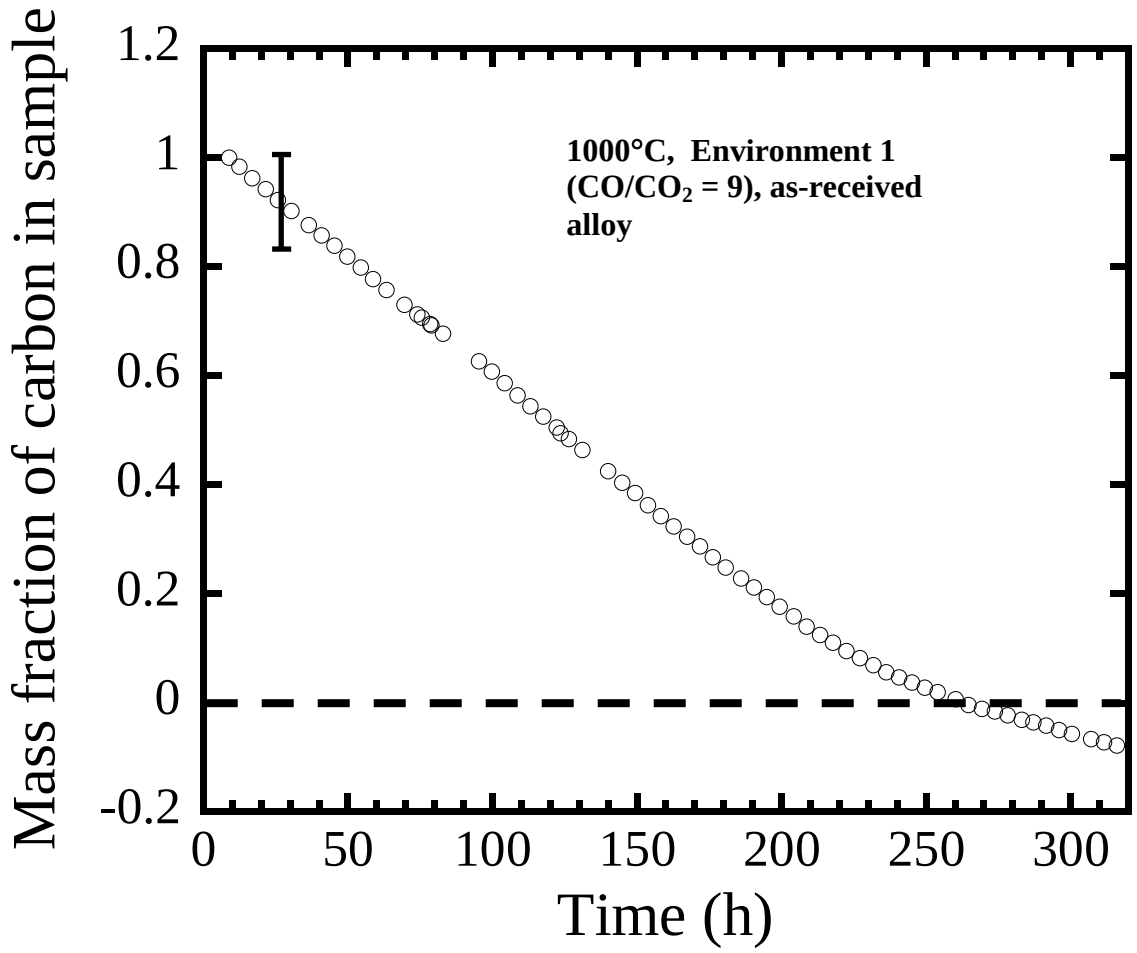

Figure 5.12 Plot of the mass fraction of carbon remaining in the sample as a function of time. The mass fraction of carbon remaining in the alloy was defined as the difference between the mass of carbon in the as-received sample and carbon lost due to decarburization, normalized by the mass of carbon in the as-received sample. For clarity only one error bar is shown on the plot. The error corresponds to sum of 7.5% of error due to variation of CO concentration at the inlet and 6.5% due to variation in the flow rate of the gas mixture through the tube.

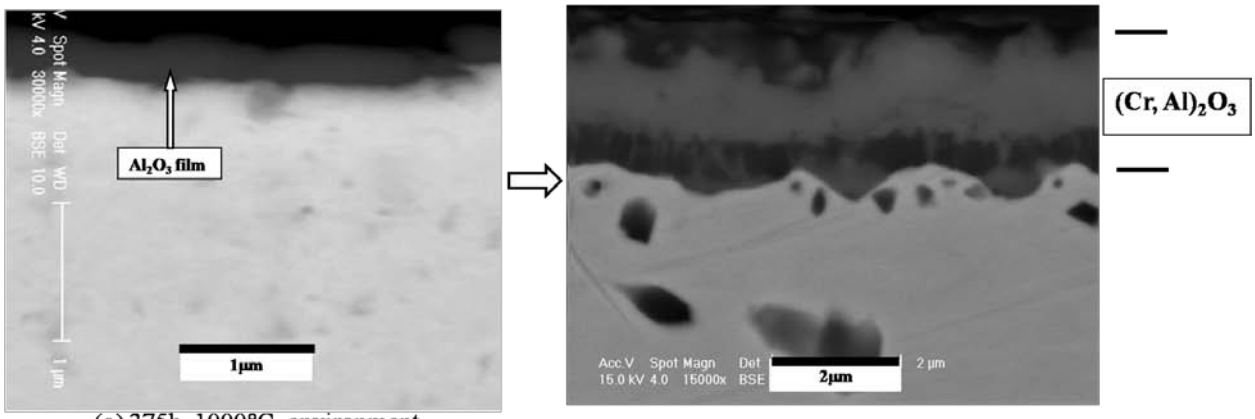

(a) 375h, 1000°C, environment 1 (CO/CO_2 = 9)

(b) 500h, 1000°C, environment 1 (CO/CO_2 = 9)

Figure 5.13 Surface microstructure of the sample decarburized in environment 1 (CO/CO_2 = 9) at 1000°C for (a) 375h and (b) 500h. A surface chromia film of 1.5±0.4µm has formed on the surface after 500h of oxidation.

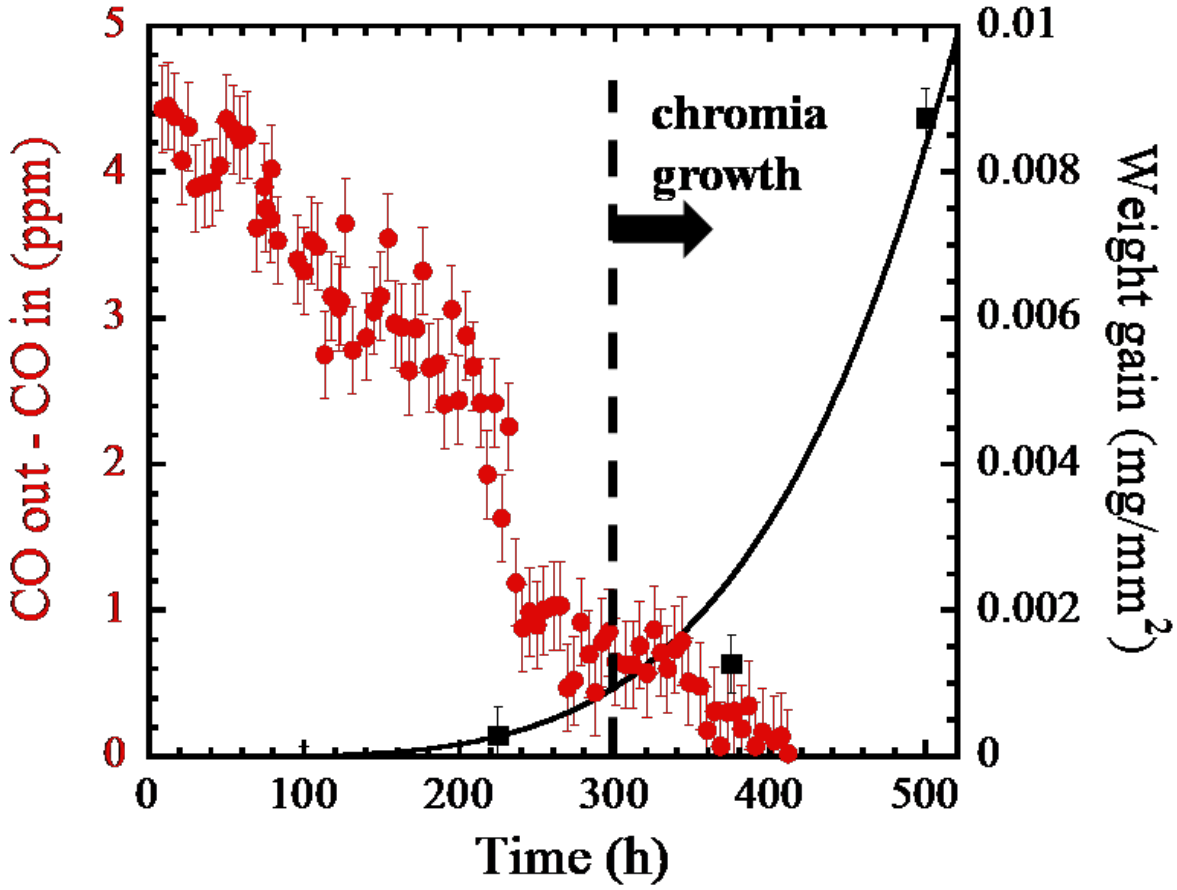

Figure 5.14 CO out – CO in and the weight gain due to oxygen in chromia as a function of time. The sample was decarburized in environment 1 ($CO/CO_2 = 9$) at 1000°C.

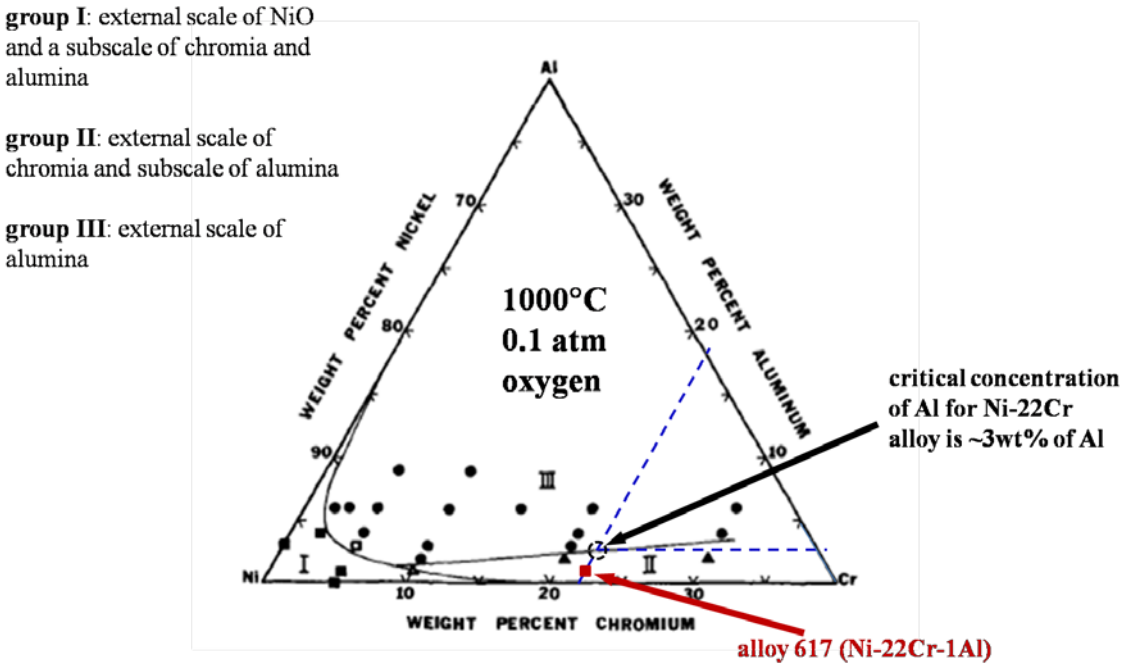

Figure 5.15 Oxide map for Ni-Cr-Al ternary alloy[55]. Alloy 617, if viewed as, Ni-22Cr-1Al alloy lies in group II and is expected to form internal oxidation of Al at 1000°C. For Ni-22Cr alloys the critical concentration of Al required to form alumina film is ~3wt%.

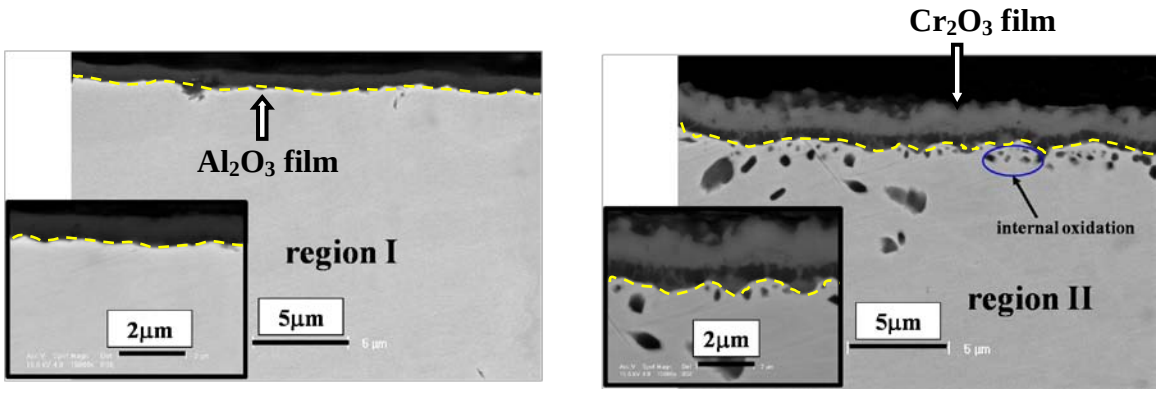

Figure 5.16 Alloy/oxide interface more convoluted in region II in comparison to region I. The sample was decarburized at 1000°C for 500h in environment 1 ($CO/CO_2 = 9$)

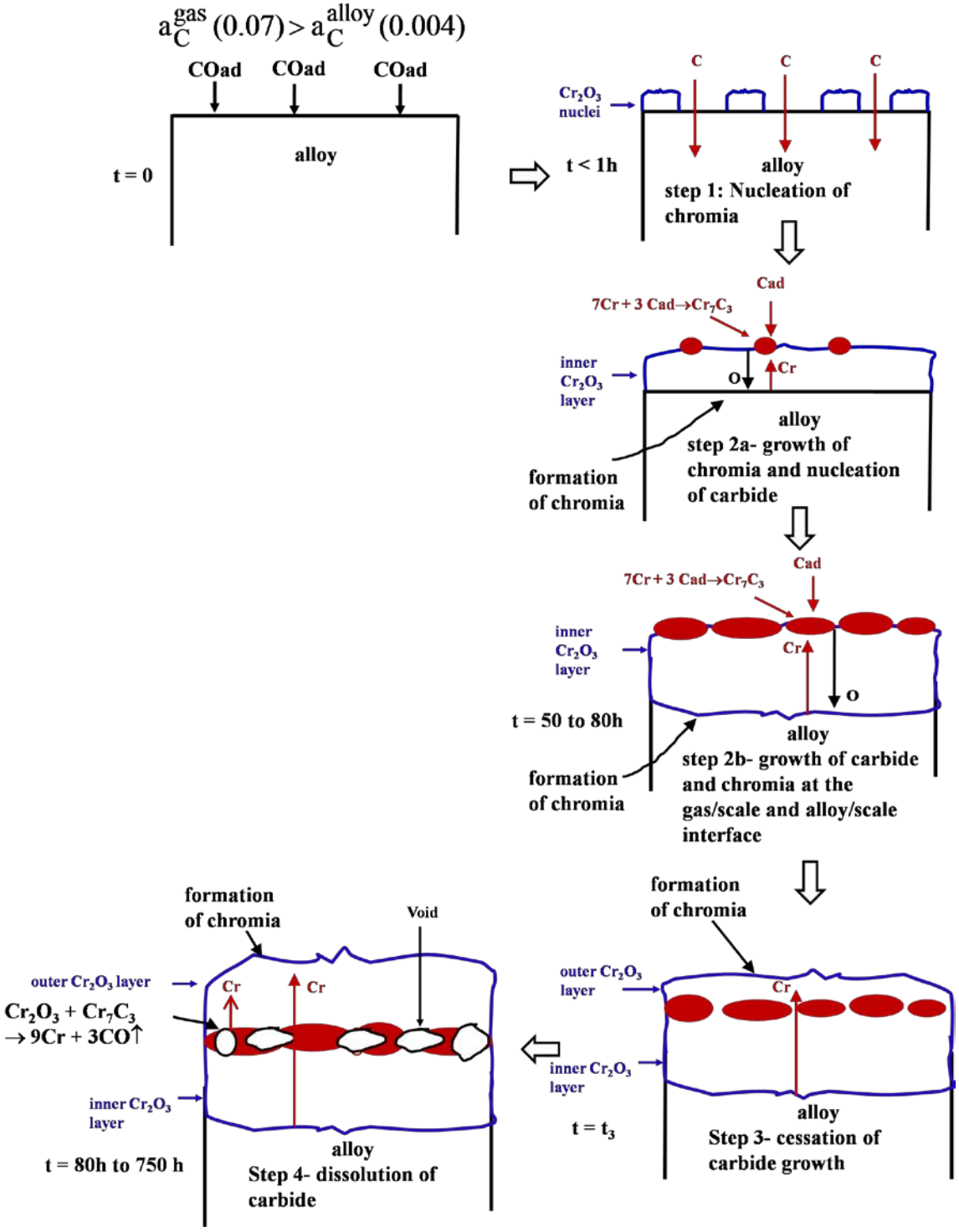

Figure 5.17 Schematic of mechanism of carburization of the as-received alloy in environment 6 (CO/CO_2 = 1272) at 900°C with CO = 1908 ppm and CO_2 = 1.5 ppm.

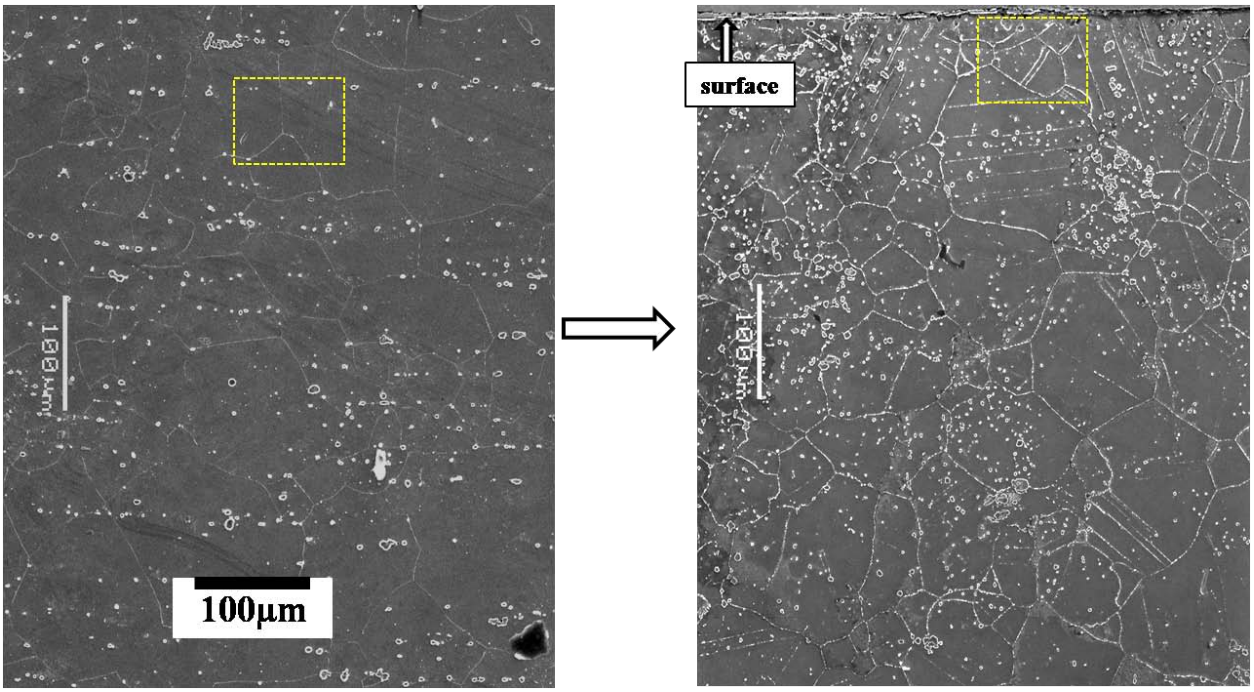

As received alloy

environment 6 (CO/CO_2 = 1272), 900°C, 100h

(c)

(d)

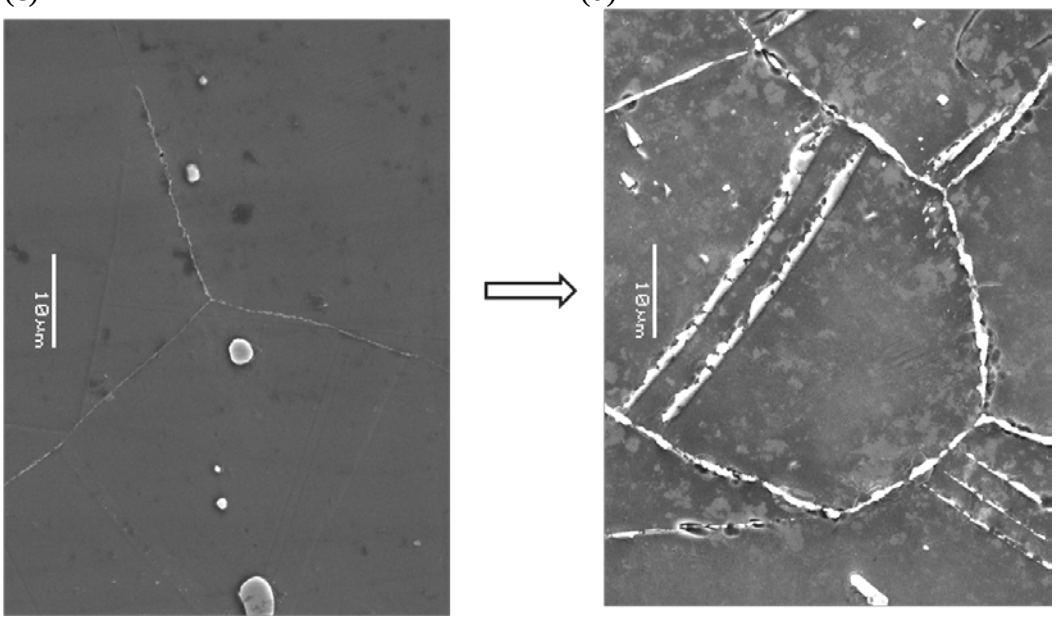

Figure 5.18 Bulk microstructure of the (a) as-received alloy, and (b) sample carburized in environment 6 (CO/CO_2 = 1272) at 900°C. Figs. (c) and (d) show the high magnification image of the area boxed in as received and carburized sample, respectively. Due to carburization thick film (0.3µm) of carbide has formed along the grain boundaries and twin boundaries.

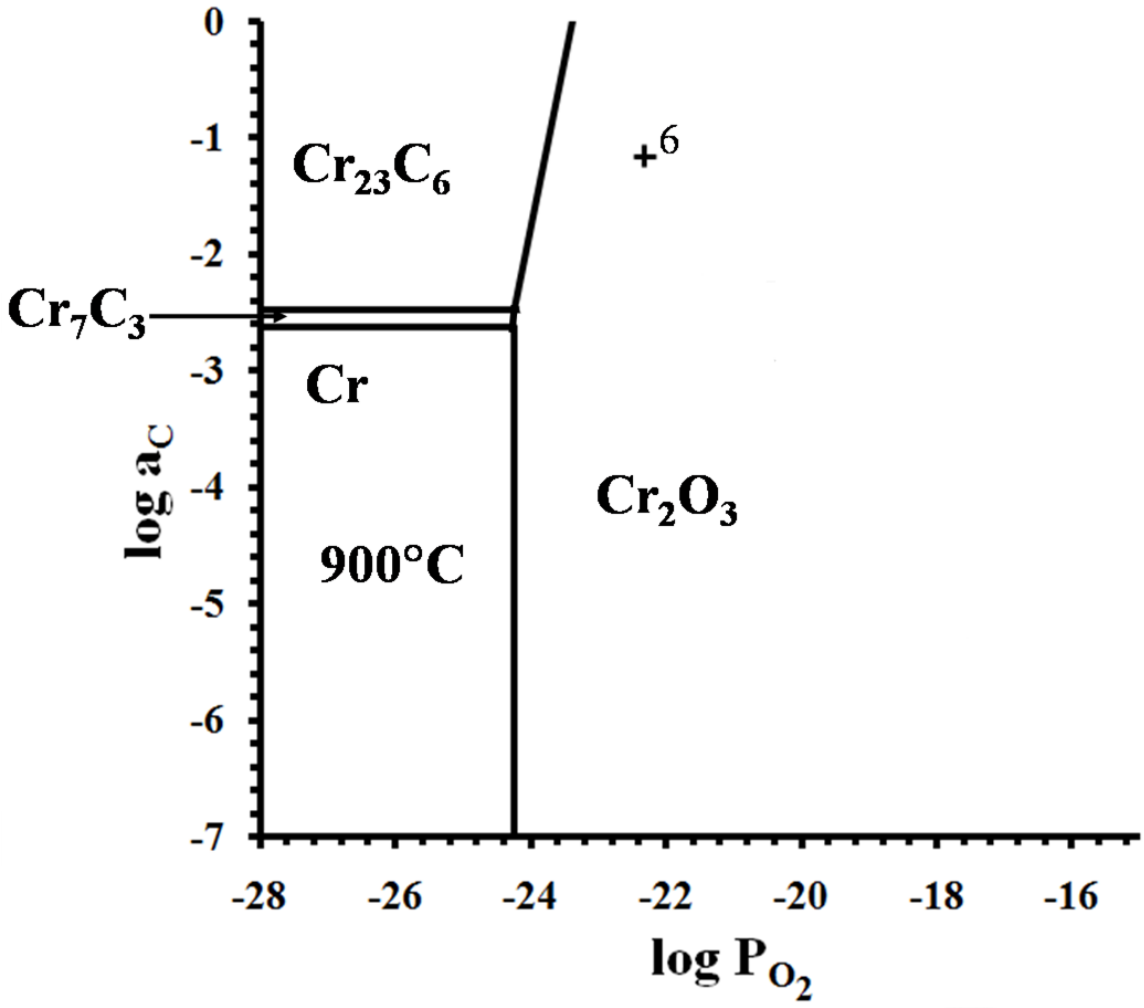

Figure 5.19 Carbon and oxygen potentials in the environment 6 (CO/CO_2 = 1272) superimposed on the Cr-stability diagram at 900°C.

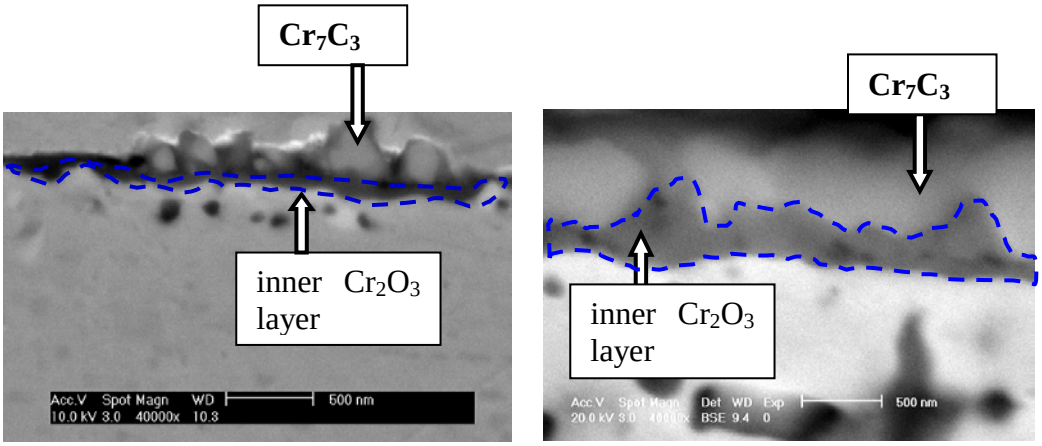

(a) 900°C, 1h (b) 900°C, 100h

Figure 5.20 Microstructure substantiation of the nucleation and growth mechanism of surface carbide. Environment 6, CO/CO_2 = 900°C.

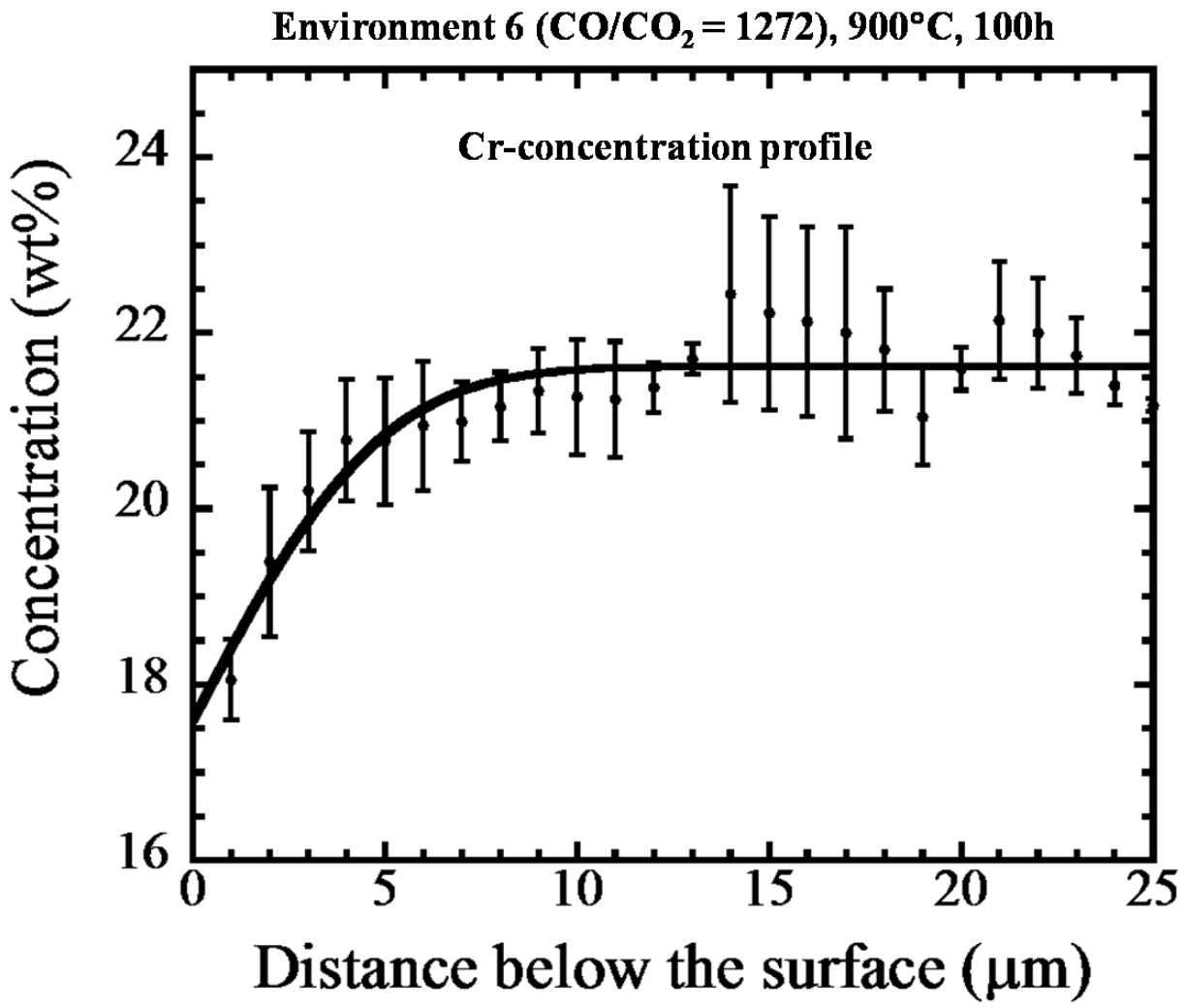

Figure 5.21 Concentration profile of Cr measured by EMPA. The sample was carburized in environment 6 (CO/CO_2 = 1272) for 100h at 900°C.

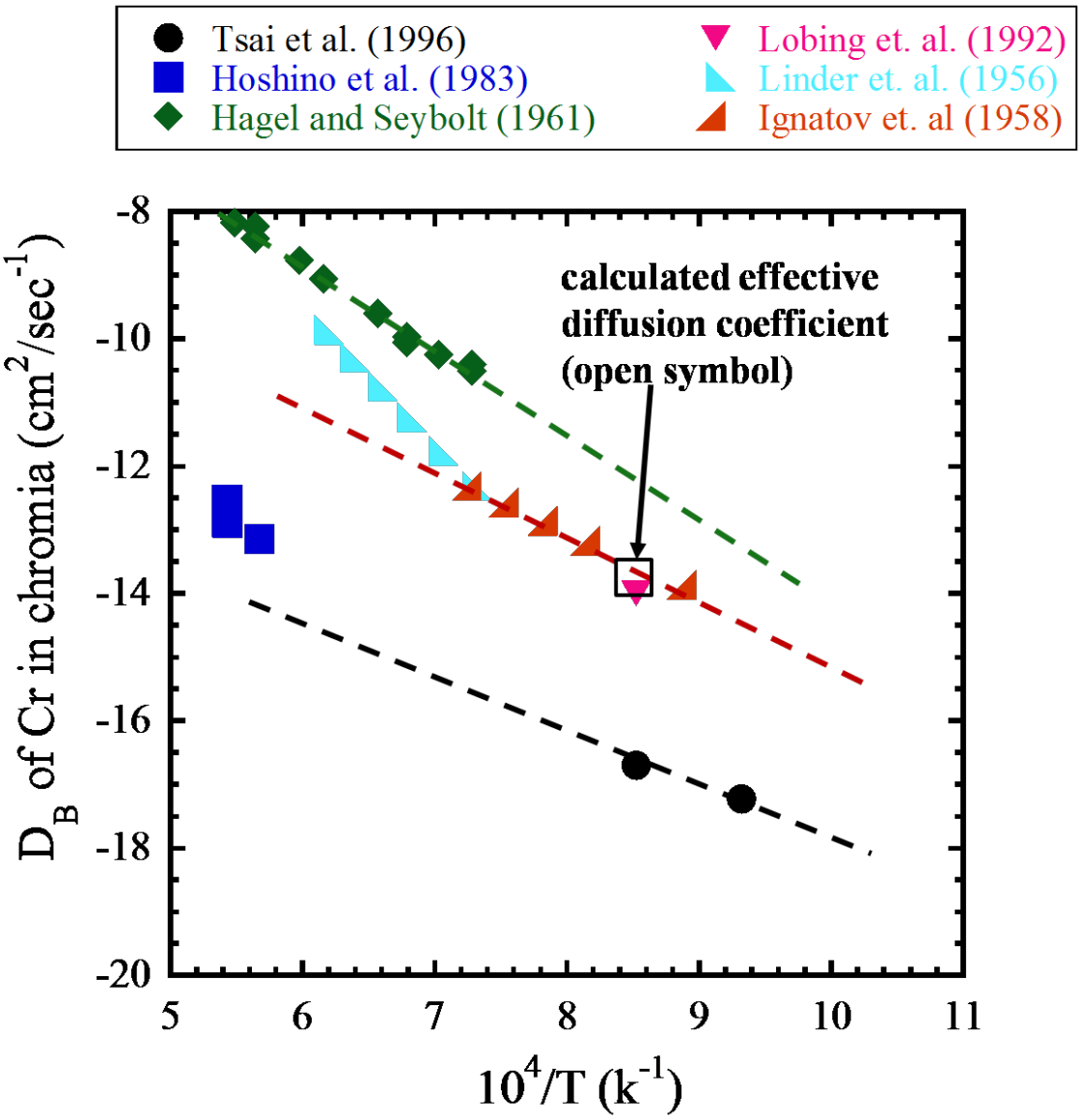

Figure 5.22 The calculated diffusion coefficient of Cr in chromia, D_{Cr} superimposed on the bulk diffusivity, D_B of Cr in chromia in the literature.

(a)

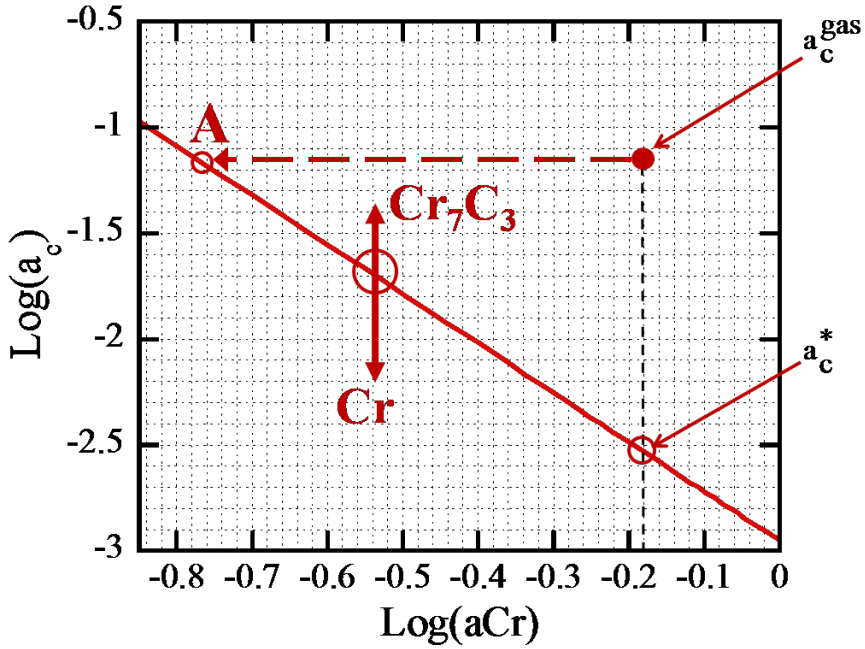

(b)

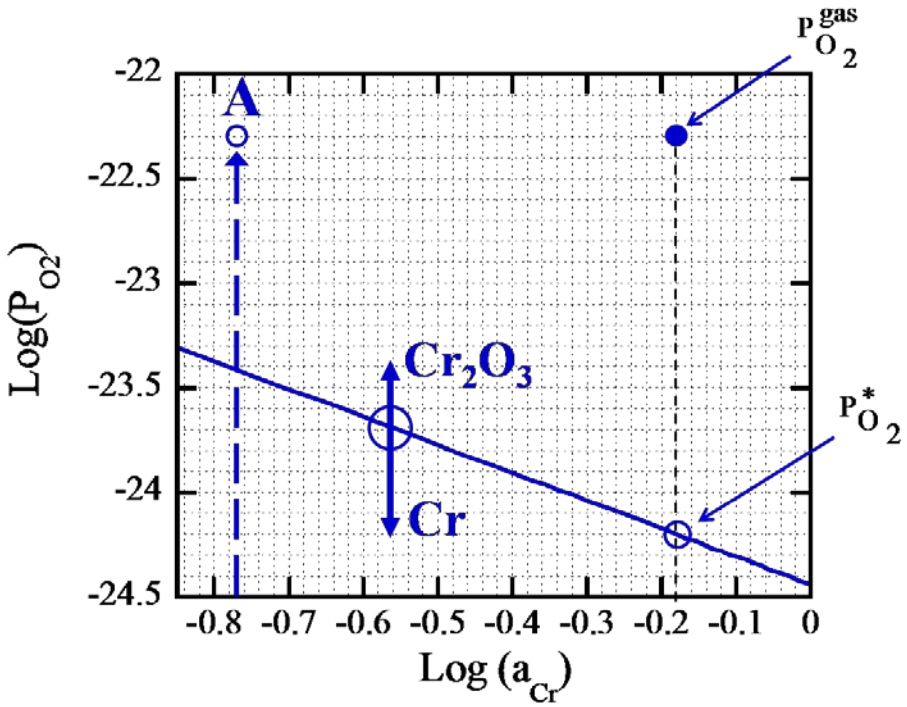

Figure 5.23 (a) Plots of (a) a_{Cr}-a_C at 900°C showing the a_{Cr} below which Cr_7C_3 cannot form (point A, a_{Cr} = 0.16) at the gas/scale interface where carbon potential is fixed by the CO/CO_2 ratio in the environment 6 (CO/CO_2 =1272), (b) a_{Cr}- P_{O_2} at 900°C diagram showing that the corresponding to the a_{Cr} = 0.16 (point A) in part (a), the chromia can form near the gas/scale interface

CHAPTER 6

CONCLUSIONS

The conclusions from the oxidation studies of alloy 617 in six He-CO-CO_2 environments between 850°C - 1000°C are the following:

1. There exists a critical temperature at which the reaction

$$2Cr + 3CO \leftrightarrow Cr_2O_3 + 3C_{solution}$$

is in equilibrium. Below the critical temperature the alloy reacted with CO resulting in formation of a stable chromia film and internal carburization as per the reaction:

$$2Cr + 3CO \rightarrow Cr_2O_3 + 3C_{solution},$$

whereas, above the critical temperature the chromia film was unstable and reacted with carbon in the alloy causing decarburization as per the reaction:

$$Cr_2O_3 + 3C_{solution} \rightarrow 2Cr + 3CO.$$

The mass balance performed on Cr and CO confirmed that the chromium metal produced during this reaction diffused back into the alloy, whereas, the carbon monoxide was transported out of the sample.

2. The critical temperature increased with the CO concentration in helium. In environment 1 (CO/CO_2 = 9) with CO concentration of 15 ppm the critical temperature was between 900°C and 950°C, whereas in environments 2 (CO/CO_2 = 150) to 6 (CO/CO_2 = 1272) with CO concentration higher than 240 ppm, it was greater than 1000°C.

3. The critical temperature can be used to calculate the activity of Cr in the alloy. For alloy 617, the activity of Cr is between 0.57 and 0.77.

4. Mechanism of decarburization (environment 1; $CO/CO_2 = 9$):

Above the critical temperature decarburization of the as-received sample occurred via two reactions occurring simultaneously on the alloy surface:

formation of chromia:

$$2Cr + 3/2O_2 \rightarrow Cr_2O_3$$

and reduction of chromia:

$$Cr_2O_3 + 3C_{solution} \rightarrow 2Cr + 3CO\ .$$

The formation of chromia film was rate limiting at 1000°C, which prevented the growth of a stable chromia film until the chromia reduction reaction stopped due to depletion of carbon in the sample. The depletion of carbon led to the dissolution of the carbides in the entire sample in ~300h, which is expected to reduce the creep-strength of the alloy, and, therefore limit its applicability in the heat exchanger.

5. Mechanism of carburization (environment 6; $CO/CO_2 = 1272$)

The carburization of the alloy resulted in the formation of an external chromia scale that contained discrete particles of Cr_7C_3. The carbide was a metastable phase and its nucleation was due to the preferential adsorption of carbon on the chromia surface. The Cr_7C_3 particles coarsened via outward diffusion of Cr cations through the chromia scale until the activity of Cr at the reaction site fell below the critical value of 0.16 at 900°C.

The time taken for this to occur was 50h to 80h at 900°C. Decrease in activity of Cr triggered the reaction

$$Cr_2O_3 + Cr_7C_3 \rightarrow 9Cr + 3CO.$$

The CO produced during this reaction was transported through the oxide cracks and pores and was released into the environment. Chromium diffused outward from the reaction site to the gas/scale interface where it was re-oxidized to Cr_2O_3 via the reaction:

$$2Cr + 3/2O_2 \rightarrow Cr_2O_3.$$

The porous surface scale formed in carburizing environment may not provide good oxidation resistance to the alloy during service.

CHAPTER 7

FUTURE WORK

The current research work focused on the role of specific impurities CO and CO_2 in helium gas mixtures on the degradation of alloy 617 by determining the mechanisms of decarburization and carburization. In order to appraise the degradation caused by other impurities, such as H_2O-H_2, CH_4-H_2, expected in the VHTR helium further research is warranted. Similar to the current investigation, a systematic study of the material degradation due to various impurity gaseous species is proposed, wherein alloy 617 will be exposed to varying levels of H_2O/H_2 and CH_4/H_2 ratios. The Cr-stability diagram will once again provide the thermodynamic basis for the design of experiments, in particular, the selection of the impurity ratios. Particular attention must be exercised in the case of H_2O-H_2 impurity environment since, in addition to oxidation, carburization and decarburization of alloys, the volatilization of chromia can be significant [110, 111]. Furthermore, the interaction between the carburizing species (CO and CH_4) and the oxidizing species (H_2O and CO_2) in helium, as well as their combined effect on the material degradation mechanism(s) needs elucidation. This 'synergy' between various impurity species can be achieved by combining the binary CO-CO_2, H_2O-H_2, and CH_4-H_2 gas mixtures, thus forming a complex multi-gas phase equilibrium that governs the impure-helium environment's oxygen and carbon potentials. *Quadakkers and co-workers* [27] have performed selected classical studies in this regard by varying the CO/H_2O and CH_4/H_2O ratios in helium. However, their study was limited to a selected gas

composition range: H_2O varied between 0.1 to1.5 ppm, CO between 15 to 100 ppm, and CH_4 varied between 10 and 20 ppm; in these conditions, the alloy microstructure degradation was not substantial. In order to completely determine the synergistic effects between the various impurities, the gas compositions should be varied systematically over wider range. Notwithstanding, their results are significant in terms of providing a set of guidelines on combining the binary gas mixtures and determining the competition between the carburizing and oxidizing species.

Another area of research with potential in improving the alloy stability in impure helium is the positive role of alumina on the surface and bulk stabilities of alloys with high Al content. Alumina is preferred due to its high thermodynamic stability, non-porous nature when it forms a continuous film, better adherence to the substrate, and slower growth kinetics than chromia. While higher Al alloys form undesirable γ' precipitates, alloys with Al ~ 3-3.5 wt% might just form a continuous and protective oxide film in impure helium that might provide barrier against diffusion. To optimize the Al content in alloy 617 a systematic study is necessary.

Finally, the structural integrity of the alloys in the VHTR is primarily determined by the degradation in creep strength of the alloy. Literature suggests that the impure helium environment has a greater effect on the alloy degradation in terms of reduction in the creep rupture strength compared to the atmospheric air [21, 22, 73]. Thus, in light of the degradation mechanisms proposed in the current work, it is imperative to determine the synergism between the microstructure degradation due to oxidation, carburization, and decarburization on the creep strength of the alloy.

Appendix I

This appendix contains the data from the EMPA measurements on the as-received sample exposed at 1000°C in environment 1 (CO/CO_2 = 9) for 100h. Three lines scans were done on this sample and the concentrations (in wt%) of Al, Ti, Cr, Fe, Co, Ni, Mo was noted.

Data for scan line 1

distance (μm)	Al	Ti	Cr	Fe	Co	Ni	Mo	Total
0	0.7	0.3	22.1	0.8	11.8	53.8	9.9	99.4
1	0.7	0.3	22.2	0.8	11.9	54.0	9.5	99.3
2	0.7	0.3	22.6	0.8	11.8	53.9	9.8	99.9
3	0.7	0.3	22.6	0.8	11.8	54.2	9.5	99.9
4	0.7	0.3	22.3	0.8	11.7	54.1	9.7	99.6
5	0.7	0.3	22.3	0.8	11.9	54.3	9.1	99.2
6	0.7	0.3	22.5	0.8	11.9	53.9	9.5	99.6
7	0.8	0.3	22.3	0.8	11.9	54.2	9.5	99.7
8	0.8	0.3	22.4	0.8	11.7	54.4	9.6	100.0
9	0.8	0.3	22.2	0.8	11.8	54.0	9.5	99.5
10	0.8	0.3	22.3	0.8	11.7	54.0	9.4	99.3
11	0.8	0.3	22.1	0.8	11.8	54.4	9.6	99.8
12	0.8	0.3	22.2	0.8	11.8	54.3	9.5	99.8
13	0.9	0.3	22.1	0.8	11.9	53.9	9.6	99.5
14	0.9	0.3	22.3	0.8	11.8	54.3	9.8	100.2
15	0.9	0.3	22.1	0.8	11.7	54.0	9.6	99.3
16	0.9	0.4	21.9	0.8	11.7	54.3	9.7	99.6
17	0.9	0.3	22.0	0.8	11.8	54.2	9.5	99.5
18	0.9	0.3	21.8	0.8	11.8	54.1	9.4	99.2
19	0.9	0.3	22.2	0.8	11.8	53.9	9.3	99.2
20	0.9	0.3	25.0	0.8	11.2	51.0	9.9	99.0
21	0.9	0.4	23.4	0.8	11.5	52.6	9.6	99.3
22	0.9	0.3	22.0	0.8	11.8	54.3	9.0	99.3
23	0.9	0.3	21.9	0.8	11.8	54.1	9.2	99.0
24	0.9	0.3	21.8	0.8	11.8	54.4	9.4	99.4
25	1.0	0.3	21.9	0.7	11.8	54.5	9.1	99.3
26	1.0	0.3	21.9	0.8	11.8	54.3	9.3	99.5
27	1.0	0.4	21.7	0.8	12.0	54.2	9.5	99.6
28	1.0	0.3	21.8	0.8	11.8	54.7	9.5	99.9
29	1.0	0.3	21.8	0.8	11.7	54.2	9.2	99.0
30	1.0	0.3	21.9	0.8	11.8	54.2	9.3	99.3
31	1.0	0.3	21.9	0.7	11.8	54.3	9.6	99.7

Data for line scan 2

distance (μm)	Ti	Cr	Fe	Co	Ni	Mo	Total
0	0.3	21.8	0.8	12.0	54.9	9.2	99.8
1	0.3	22.0	0.8	12.0	54.8	9.1	99.7
2	0.3	22.1	0.8	12.0	54.5	9.7	100.2
3	0.3	21.9	0.8	12.0	54.5	9.3	99.6
4	0.3	21.9	0.8	12.0	54.6	9.1	99.5
5	0.3	22.0	0.8	11.9	54.5	9.3	99.7
6	0.3	22.2	0.8	12.1	54.6	9.2	99.9
7	0.3	22.0	0.8	11.9	54.8	9.5	100.1
8	0.3	22.0	0.8	11.9	54.5	9.5	99.9
9	0.3	22.7	0.8	11.8	54.1	9.8	100.2
10	0.3	22.5	0.8	11.8	53.6	9.6	99.4
11	0.3	22.0	0.8	12.0	54.7	9.5	100.1
12	0.3	22.1	0.8	11.9	54.5	9.3	99.7
13	0.3	22.0	0.8	11.9	54.7	9.3	99.8
14	0.3	21.9	0.8	12.1	55.0	9.6	100.5
15	0.3	21.9	0.8	11.9	54.5	9.4	99.8
16	0.3	21.9	0.8	11.8	54.7	9.1	99.6
17	0.3	22.0	0.8	12.0	54.6	9.3	99.9
18	0.3	21.9	0.8	11.9	54.7	9.3	99.9
19	0.3	21.9	0.8	11.9	54.3	9.3	99.5
20	0.3	21.7	0.8	11.9	54.7	8.9	99.3
21	0.3	21.9	0.8	12.2	54.5	9.3	99.9
22	0.3	21.7	0.8	11.9	54.7	9.4	99.8
23	0.3	21.8	0.8	12.1	54.4	9.5	99.8
24	0.3	21.7	0.8	12.0	54.9	9.3	100.0
25	0.3	21.9	0.8	11.9	54.6	9.3	99.7
26	0.3	22.0	0.7	12.0	54.4	9.2	99.6
27	0.4	21.6	0.8	11.8	54.5	9.3	99.3
28	0.3	21.7	0.8	12.0	54.5	9.7	99.9
29	0.3	21.6	0.8	12.0	55.0	9.1	99.8
30	0.3	22.0	0.8	12.0	54.5	9.4	99.8
31	0.3	21.7	0.8	12.1	54.6	9.3	99.8
32	0.3	22.9	0.8	11.6	53.1	9.6	99.3

Data for line scan 3

distance (μm)	Al	Ti	Cr	Fe	Co	Ni	Mo
0.0	0.7	0.3	21.5	0.7	11.6	54.6	9.5
1.0	0.7	0.3	21.7	0.8	11.6	54.6	9.4
2.0	0.7	0.3	21.4	0.7	11.7	54.6	9.6
3.0	0.7	0.3	21.5	0.8	11.5	54.5	9.1
4.0	0.7	0.3	21.9	0.8	11.8	54.5	9.5
5.0	0.7	0.3	21.7	0.8	11.6	54.8	9.8
6.0	0.7	0.4	21.7	0.8	11.8	54.9	9.1
7.0	0.7	0.3	21.8	0.8	11.7	54.6	9.7
8.0	0.8	0.3	21.9	0.8	11.6	54.4	9.6
9.0	0.8	0.3	21.5	0.8	11.6	54.9	9.0
10.0	0.8	0.4	21.6	0.8	12.0	54.4	9.2
11.0	0.8	0.3	21.9	0.8	11.7	54.6	9.5
12.0	0.8	0.3	21.7	0.8	11.7	54.7	9.0
13.0	0.8	0.3	21.8	0.8	11.8	54.7	9.2
14.0	0.8	0.3	21.6	0.8	11.7	54.9	9.6
15.0	0.9	0.3	21.7	0.8	11.8	54.9	9.1
16.0	0.9	0.3	21.8	0.8	11.8	55.1	9.5
17.0	0.9	0.3	21.8	0.8	11.6	55.0	9.2
18.0	0.9	0.3	21.6	0.8	11.6	54.6	8.9
19.0	0.9	0.3	21.7	0.8	11.6	54.8	9.0
20.0	0.9	0.3	21.4	0.8	11.6	54.8	9.0
21.0	0.9	0.4	21.2	0.8	11.7	54.5	9.2
22.0	0.9	0.3	21.5	0.8	11.9	54.8	9.3
23.0	0.9	0.3	21.5	0.8	11.6	54.7	9.3
24.0	1.0	0.3	21.3	0.9	11.7	54.8	9.1
25.0	1.0	0.3	21.4	0.8	11.8	54.8	9.0
26.0	1.0	0.3	21.2	0.8	11.9	54.6	9.0
27.0	1.0	0.3	21.2	0.8	11.7	54.7	9.2
28.0	1.0	0.3	21.3	0.8	11.9	54.7	9.3
29.0	1.0	0.3	20.9	0.8	11.6	54.0	9.2
30.0	1.0	0.3	21.2	0.8	11.7	55.0	9.2
31.0	1.0	0.3	21.2	0.8	11.7	54.5	9.4
32.0	1.0	0.3	21.0	0.8	11.6	54.6	9.5
33.0	1.0	0.4	21.0	0.8	11.5	54.5	9.1
34.0	1.0	0.3	21.2	0.8	11.7	54.8	9.6
35.0	1.0	0.3	21.4	0.8	11.7	54.7	9.6

Appendix II

This appendix contains the data from the EMPA measurements on the sample pre-oxidized at (A) 900°C for 150h, (B) decarburized for 5h at 1000°C, and (C) decarburized for 100h at 1000°C in environment 1 (CO/CO_2 = 9). Three lines scans were done in each case and the concentrations (in wt%) of Al, Ti, Cr, Fe, Co, Ni, Mo was noted.

(A) EMPA measurements data on sample pre-oxidized for 150h at 900°C (scan 1)

distance (μm)	Al	Ti	Cr	Fe	Co	Ni	Mo	Total
0	5.6	0.0	13.9	0.9	11.7	54.0	11.2	96.8
1	4.0	0.0	14.3	0.9	12.1	55.8	11.6	98.1
2	5.9	0.0	14.6	0.9	11.9	54.1	11.1	97.9
3	7.9	0.1	15.1	0.9	11.9	52.9	10.1	98.3
4	0.2	0.1	16.6	0.9	12.5	57.9	10.5	98.0
5	0.3	0.1	17.9	0.9	12.2	57.4	10.0	98.2
6	0.4	0.2	18.9	0.8	12.2	56.5	9.3	97.7
7	0.5	0.2	19.7	0.8	12.0	56.1	9.2	97.9
8	0.6	0.2	20.5	0.8	12.0	55.5	9.3	98.2
9	0.6	0.2	20.7	0.8	11.9	55.3	8.9	97.8
10	0.7	0.2	20.9	0.8	11.9	55.2	8.8	97.8
11	0.8	0.2	21.2	0.8	11.9	55.1	8.8	98.2
12	0.8	0.2	21.2	0.8	11.8	55.0	8.7	98.0
13	0.8	0.2	21.1	0.8	11.7	54.8	8.8	97.7
15	0.8	0.3	21.2	0.8	11.6	54.7	9.0	97.8
16	0.9	0.3	21.4	0.8	11.7	54.5	8.9	97.8
17	0.9	0.3	21.7	0.8	11.7	54.4	9.3	98.5
18	0.9	0.3	21.6	0.8	11.6	54.3	8.9	97.8
19	0.9	0.3	21.6	0.8	11.7	54.1	9.0	97.8
20	0.9	0.3	21.6	0.8	11.7	54.2	8.9	97.8
21	0.9	0.3	21.6	0.8	11.7	54.4	9.0	98.1
22	1.0	0.3	21.9	0.8	11.7	53.7	9.0	97.7
23	1.0	0.3	21.8	0.8	11.6	53.7	9.2	97.8
24	1.0	0.3	22.1	0.8	11.6	53.6	9.0	97.7
25	1.0	0.3	21.9	0.8	11.6	53.8	9.1	97.9
26	1.0	0.3	21.6	0.8	11.7	54.0	9.1	97.8
27	1.0	0.3	21.6	0.8	11.6	53.7	9.4	97.8
28	1.1	0.3	21.9	0.8	11.6	53.8	9.1	98.0
29	1.0	0.3	22.1	0.8	11.6	53.8	9.1	98.1
30	1.0	0.3	21.9	0.8	11.6	53.7	8.8	97.5
31	1.0	0.3	22.2	0.8	11.6	53.4	9.3	98.0
32	1.0	0.3	22.0	0.8	11.7	53.6	9.2	98.1
33	1.0	0.3	21.8	0.8	11.7	54.1	9.2	98.3

line Scan 2

distance (μm)	Al	Ti	Cr	Fe	Co	Ni	Mo	Total
0	0.1	0.1	16.1	0.8	12.6	57.2	12.0	98.9
1	0.1	0.1	16.2	0.8	12.6	57.2	11.8	98.7
2	0.1	0.1	16.5	0.9	12.7	57.3	11.7	99.2
3	0.2	0.1	17.4	0.8	12.6	57.6	11.3	100.0
4	0.2	0.1	17.5	0.8	12.6	57.9	11.1	100.3
5	0.2	0.1	18.0	0.8	12.5	56.8	10.8	99.2
6	0.2	0.1	18.3	0.8	12.6	56.7	10.5	99.3
7	0.3	0.1	19.2	0.8	12.3	56.1	10.2	99.1
8	0.3	0.2	19.4	0.8	12.3	56.7	10.6	100.2
9	0.5	0.2	19.9	0.8	12.2	56.2	9.9	99.6
10	0.5	0.2	19.9	0.8	12.1	56.2	9.8	99.4
11	0.5	0.2	20.0	0.8	12.1	56.0	9.8	99.3
12	0.5	0.2	20.3	0.7	12.0	55.7	9.6	99.0
13	0.6	0.2	20.5	0.8	12.0	55.9	9.4	99.4
14	0.7	0.2	20.9	0.8	12.0	55.7	9.4	99.6
15	0.7	0.3	21.0	0.8	11.8	55.5	9.7	99.8
16	0.8	0.2	21.3	0.8	11.8	55.3	9.8	99.9
17	0.8	0.3	21.1	0.8	11.8	55.2	9.0	99.0
18	0.9	0.3	21.4	0.8	11.8	54.8	9.5	99.5
19	0.9	0.3	21.6	0.8	11.9	55.1	9.3	99.9
20	1.0	0.3	21.5	0.7	11.9	54.9	9.2	99.4
21	1.0	0.3	21.9	0.8	11.7	54.9	9.5	100.0
22	1.0	0.3	21.8	0.8	11.9	54.5	9.4	99.8
23	1.0	0.3	22.0	0.8	11.7	54.6	9.1	99.4
24	1.0	0.3	21.9	0.8	11.8	54.4	9.0	99.3
25	1.0	0.3	21.9	0.8	11.7	54.8	9.3	99.7
26	1.0	0.3	22.0	0.8	11.7	54.3	9.5	99.6
27	1.0	0.3	21.8	0.8	11.7	54.1	9.3	99.1
28	1.1	0.3	21.9	0.8	11.8	54.3	9.4	99.5
29	1.1	0.3	21.8	0.8	11.7	54.4	9.7	99.9
30	1.1	0.3	22.0	0.8	11.7	54.0	9.7	99.6
31	1.1	0.3	22.0	0.8	11.8	54.5	9.1	99.5
32	1.1	0.3	21.8	0.8	11.8	54.4	9.2	99.3
33	1.1	0.3	22.0	0.8	11.7	54.5	9.1	99.6
34	1.1	0.3	22.1	0.7	11.9	54.4	9.4	99.9
35	1.1	0.3	22.2	0.8	11.8	54.3	9.5	99.9
36	1.1	0.3	22.1	0.8	11.8	54.3	9.4	99.7
37	1.1	0.3	22.1	0.8	11.8	54.0	9.4	99.5
38	1.1	0.3	22.1	0.8	11.8	54.2	9.3	99.6
39	1.1	0.3	21.9	0.8	11.8	54.1	9.2	99.2
40	1.1	0.3	22.1	0.8	11.7	54.3	9.4	99.6
41	1.1	0.3	22.1	0.8	11.7	54.2	9.6	99.8
42	1.0	0.3	21.9	0.8	11.8	54.2	9.5	99.5
43	1.0	0.3	22.3	0.7	11.8	54.4	9.6	100.2

line scan 3

distance(μm)	Al	Ti	Cr	Fe	Co	Ni	Mo	Total
0	0.2	0.0	14.2	0.9	12.8	57.8	12.9	99.2
1	0.1	0.0	14.3	0.9	12.8	57.5	13.0	98.7
2	0.1	0.0	15.0	0.9	12.8	57.8	12.4	98.9
3	0.2	0.1	15.9	0.9	12.6	57.9	11.7	99.3
4	0.3	0.1	17.0	0.8	12.4	57.7	10.9	99.2
5	0.4	0.1	18.2	0.8	12.3	57.2	9.9	99.0
6	0.6	0.2	19.5	0.8	12.2	56.5	9.7	99.4
7	0.6	0.2	20.1	0.8	12.2	56.3	9.1	99.4
8	0.8	0.2	20.9	0.8	12.0	55.4	9.4	99.5
9	0.9	0.3	21.0	0.7	12.0	55.8	9.5	100.2
10	0.9	0.3	20.9	0.8	12.0	55.3	9.2	99.3
11	0.9	0.3	21.6	0.8	11.9	55.2	9.1	99.7
12	1.0	0.3	21.4	0.8	12.0	55.2	9.3	99.9
13	1.0	0.3	21.3	0.8	11.8	54.9	9.3	99.4
14	1.0	0.3	21.5	0.7	12.0	54.9	9.6	100.1
15	1.0	0.3	21.7	0.8	11.8	55.0	9.2	99.8
16	1.0	0.3	21.8	0.8	11.7	54.3	9.2	99.2
17	1.0	0.3	21.8	0.8	11.9	54.8	9.3	99.9
18	1.1	0.3	21.7	0.8	12.0	54.6	9.2	99.6
19	1.0	0.3	21.9	0.8	11.8	54.3	9.5	99.6
20	1.1	0.3	21.6	0.8	11.8	54.6	9.3	99.5
21	1.1	0.3	22.2	0.8	11.7	54.5	9.3	99.9
22	1.1	0.3	21.9	0.8	11.8	54.3	9.5	99.7
23	1.1	0.3	22.0	0.7	11.8	54.3	9.3	99.5
24	1.1	0.3	21.7	0.8	11.9	54.7	9.1	99.6
25	1.1	0.3	22.1	0.7	11.8	54.6	9.7	100.2
26	1.0	0.3	22.0	0.8	11.9	54.3	9.7	100.0
27	1.1	0.3	21.8	0.8	11.8	54.4	9.8	99.9
28	1.1	0.3	21.7	0.8	11.8	54.3	9.7	99.7
29	1.1	0.3	21.7	0.8	11.8	54.8	8.9	99.3
30	1.1	0.3	21.9	0.8	11.7	54.6	9.5	99.8
31	1.1	0.3	21.7	0.8	11.8	54.5	9.5	99.6
32	1.1	0.3	21.9	0.7	11.8	55.0	9.5	100.3
33	1.1	0.3	22.0	0.8	11.9	54.8	9.1	99.9
34	1.1	0.3	22.2	0.8	11.7	54.2	9.3	99.6
35	1.1	0.3	21.9	0.8	11.8	54.3	9.5	99.6
36	1.1	0.3	21.6	0.8	11.9	54.5	9.5	99.7
37	1.1	0.3	21.6	0.8	11.7	54.4	9.1	99.0
38	1.1	0.3	21.7	0.8	11.9	53.9	9.3	99.1
39	1.1	0.3	21.7	0.8	11.9	54.8	9.3	100.0
40	1.1	0.3	21.8	0.8	11.8	54.9	9.4	100.1
41	1.1	0.3	21.7	0.8	11.8	54.5	9.4	99.5
42	1.1	0.3	21.6	0.8	11.8	54.6	9.4	99.6
43	1.1	0.3	21.9	0.8	11.9	54.6	9.0	99.6
44	1.1	0.3	21.6	0.8	12.0	54.5	9.1	99.4
45	1.1	0.4	21.9	0.8	11.8	54.8	9.3	100.1

(B) EMPA data for sample decarburized for 5h at 1000°C; relevant to pre-oxidizing

Line scan 1

distance(μm)	Al	Ti	Cr	Fe	Co	Ni	Mo	Total
0	0.4	0.3	21.0	0.8	11.7	54.4	8.3	96.9
1	0.5	0.2	20.8	0.8	11.8	54.3	8.4	97.0
2	0.6	0.2	21.0	0.8	11.8	54.7	8.9	98.1
3	0.7	0.2	21.1	0.8	11.7	54.6	9.1	98.2
4	0.7	0.3	21.0	0.8	11.8	54.8	8.9	98.3
5	0.8	0.3	20.9	0.8	11.8	54.7	8.6	97.9
6	0.8	0.3	21.4	0.8	11.9	54.8	8.6	98.5
7	0.8	0.3	21.2	0.8	11.8	54.4	8.6	98.0
8	0.8	0.3	21.2	0.8	11.9	54.7	9.0	98.6
9	0.8	0.3	21.5	0.8	11.9	53.7	10.1	99.1
10	0.9	0.3	21.6	0.8	11.8	54.5	8.9	98.8
11	0.9	0.3	21.4	0.8	11.8	54.5	9.3	99.0
12	0.9	0.3	21.2	0.8	11.8	54.0	8.9	97.9
13	1.0	0.3	21.2	0.8	11.9	54.3	8.5	98.0
14	1.0	0.3	21.1	0.8	11.6	54.8	8.8	98.5
15	1.0	0.3	21.1	0.8	11.7	54.6	8.9	98.3
16	1.0	0.4	21.2	0.8	11.8	54.3	8.6	98.0
17	1.0	0.3	21.2	0.8	11.8	54.3	8.6	98.0
18	1.0	0.4	21.2	0.8	11.8	54.0	9.0	98.2
19	1.0	0.3	21.2	0.8	11.6	54.4	9.3	98.6
20	1.0	0.3	21.0	0.8	11.8	54.7	8.7	98.3
21	1.0	0.3	21.3	0.8	11.5	54.2	9.0	98.2
22	1.0	0.3	21.7	0.8	11.6	54.1	9.0	98.4
23	0.9	0.3	21.6	0.7	11.6	53.4	9.3	97.8
24	1.0	0.3	21.6	0.8	11.8	54.1	8.9	98.5
25	1.0	0.3	21.3	0.8	11.5	54.5	8.8	98.2
26	1.0	0.3	21.6	0.8	11.7	54.4	9.0	98.7
27	1.0	0.3	21.4	0.8	11.7	54.5	9.2	98.8
28	1.0	0.3	21.2	0.8	11.5	54.5	8.8	98.2
29	1.0	0.3	21.3	0.8	11.7	54.4	9.1	98.6
30	1.0	0.3	21.6	0.8	11.9	54.6	9.0	99.2
31	1.0	0.3	21.3	0.8	11.5	54.1	9.0	98.0
32	1.0	0.3	21.4	0.8	11.7	54.2	9.0	98.4
33	1.0	0.3	21.3	0.8	11.6	53.7	9.0	97.6
34	1.0	0.3	21.4	0.8	11.9	54.3	9.2	98.9
35	1.0	0.3	21.3	0.8	11.6	54.4	8.8	98.3
36	1.0	0.3	21.3	0.7	11.7	54.2	9.0	98.3
37	1.0	0.3	21.4	0.8	11.7	54.5	9.2	99.0
38	1.0	0.3	21.5	0.8	11.8	54.7	9.3	99.4
39	1.0	0.3	21.3	0.8	11.6	54.2	8.9	98.1
40	1.0	0.3	21.7	0.8	11.8	54.6	8.9	99.1
41	1.0	0.3	21.5	0.8	11.6	53.7	9.0	97.9

Line scan 2

distance(μm)	Al	Ti	Cr	Fe	Co	Ni	Mo	Total
0	0.3	0.0	18.8	0.8	11.6	53.1	12.7	97.4
1	0.1	0.0	18.3	0.9	11.8	54.7	12.2	98.0
2	0.2	0.0	18.7	0.9	11.8	55.1	11.8	98.6
3	0.3	0.1	18.8	0.8	12.0	55.4	10.8	98.2
4	0.3	0.1	19.0	0.8	12.0	55.1	10.8	98.1
5	0.4	0.1	19.7	0.8	12.0	55.4	10.5	99.0
6	0.5	0.2	19.7	0.8	12.0	55.0	10.2	98.5
7	0.5	0.2	20.5	0.8	11.9	54.9	10.1	98.8
8	0.6	0.2	20.5	0.8	11.7	54.8	10.1	98.7
9	0.6	0.2	20.9	0.8	11.8	54.9	10.3	99.4
10	0.6	0.2	21.3	0.8	11.8	55.0	9.5	99.3
11	0.7	0.2	21.3	0.7	11.8	54.7	10.2	99.6
12	0.6	0.2	21.4	0.8	11.6	54.7	9.2	98.5
13	0.8	0.2	21.4	0.8	11.8	54.0	9.4	98.2
14	1.4	0.2	21.1	0.7	11.2	52.4	10.1	97.2
15	0.8	0.2	21.7	0.7	11.6	53.4	9.8	98.3
16	0.9	0.2	22.0	0.8	11.6	54.4	10.2	100.1
17	0.9	0.2	22.2	0.8	11.6	53.9	9.9	99.6
18	0.9	0.3	22.2	0.8	11.5	54.3	9.8	99.9
19	1.0	0.3	22.0	0.7	11.6	54.1	9.6	99.3
20	1.0	0.3	22.1	0.8	11.6	54.1	9.7	99.5
21	1.0	0.3	22.0	0.7	11.6	53.9	10.0	99.4
22	1.0	0.3	22.2	0.8	11.5	53.9	9.6	99.3
23	1.0	0.3	22.2	0.8	11.8	53.4	10.0	99.4
24	1.0	0.3	22.5	0.8	11.7	53.3	9.9	99.5
25	1.0	0.3	22.5	0.8	11.6	53.1	10.0	99.2
26	1.0	0.3	22.5	0.7	11.5	53.0	10.1	99.1
27	1.1	0.3	22.6	0.7	11.6	53.1	10.1	99.4
28	1.0	0.3	22.4	0.8	11.4	53.1	9.7	98.7
29	1.1	0.3	22.6	0.8	11.6	53.2	9.8	99.2
30	1.1	0.3	22.6	0.8	11.6	53.2	9.9	99.4
31	1.0	0.3	22.6	0.8	11.6	53.3	9.6	99.2
32	1.0	0.3	22.9	0.8	11.6	53.3	10.0	99.9
33	1.0	0.3	22.9	0.7	11.6	53.5	10.1	100.1
34	1.0	0.3	23.0	0.7	11.5	52.9	9.8	99.4
35	1.1	0.3	22.5	0.8	11.5	53.4	9.7	99.2
36	1.1	0.3	22.5	0.8	11.7	53.9	9.7	100.0
37	1.1	0.3	22.0	0.8	11.6	54.0	9.4	99.2
38	1.1	0.3	22.0	0.8	11.8	54.5	9.4	99.8
39	1.1	0.3	22.2	0.8	11.7	53.4	9.9	99.3
40	1.0	0.3	26.3	0.8	11.3	50.8	10.0	100.3
41	1.1	0.3	22.4	0.7	11.7	53.8	9.6	99.7

Line scan 3

distance(μm)	Al	Ti	Cr	Fe	Co	Ni	Mo	Total
0	0.4	0.1	19.8	0.8	11.7	53.9	11.2	97.9
1	0.5	0.2	20.0	0.8	11.8	54.3	10.7	98.4
2	0.6	0.2	20.5	0.8	11.7	54.6	10.5	98.8
3	0.6	0.2	20.1	0.9	11.8	54.2	10.6	98.4
4	0.8	0.3	20.7	0.8	11.6	54.7	9.8	98.6
5	0.9	0.3	21.1	0.8	11.7	54.1	9.7	98.5
6	0.9	0.3	21.3	0.8	11.6	54.4	9.9	99.2
7	1.0	0.3	21.4	0.8	11.5	53.8	9.6	98.5
8	1.0	0.3	21.3	0.7	11.7	54.0	9.8	98.8
9	1.1	0.3	21.8	0.8	11.7	53.7	9.5	98.9
10	1.1	0.3	21.5	0.8	11.5	53.9	9.4	98.4
11	1.1	0.5	21.5	0.8	11.7	53.6	9.7	98.9
12	1.1	0.5	21.5	0.8	11.6	53.7	9.4	98.7
13	1.1	0.3	21.6	0.8	11.7	53.8	9.5	98.8
14	1.1	0.3	21.4	0.8	11.6	53.8	9.6	98.7
15	1.1	0.3	21.5	0.8	11.6	54.0	9.5	98.7
16	1.1	0.3	21.5	0.8	11.6	53.8	9.6	98.8
17	1.1	0.4	21.7	0.8	11.6	53.7	9.8	99.0
18	1.1	0.3	21.7	0.7	11.6	54.0	9.7	99.2
19	1.1	0.3	21.5	0.8	11.6	53.8	9.6	98.7
20	1.1	0.3	21.5	0.8	11.6	53.4	9.6	98.3
21	1.1	0.3	21.5	0.8	11.6	53.8	9.5	98.6
22	1.1	0.3	21.7	0.8	11.5	53.5	9.9	98.8
23	1.1	0.3	21.6	0.8	11.6	53.6	9.6	98.7
24	1.1	0.3	21.6	0.9	11.6	53.6	9.8	98.9
25	1.1	0.4	21.6	0.8	11.7	53.7	9.4	98.6
26	1.1	0.3	21.6	0.8	11.7	53.8	9.3	98.6
27	1.1	0.3	21.8	0.8	11.7	53.7	9.4	98.9
28	1.1	0.3	21.7	0.8	11.7	53.6	9.3	98.5
29	1.1	0.3	21.5	0.8	11.8	53.9	9.4	98.8
30	1.1	0.4	21.8	0.8	11.7	54.0	9.3	99.1
31	1.1	0.3	21.7	0.8	11.8	53.8	9.6	99.0
32	1.1	0.3	21.8	0.8	11.6	54.1	9.2	99.0
33	1.1	0.4	21.9	0.8	11.7	53.9	9.6	99.3
34	1.1	0.3	21.8	0.7	11.5	53.7	9.5	98.7
35	1.1	0.3	21.8	0.8	11.5	53.5	9.6	98.6
36	1.1	0.4	21.9	0.8	11.4	53.3	9.4	98.2
37	1.1	0.4	22.2	0.8	11.5	53.1	9.7	98.7
38	1.1	0.3	23.3	0.7	11.2	52.0	10.2	98.8
39	1.0	0.3	23.3	0.8	11.2	51.3	9.9	97.9
40	1.0	0.3	22.1	0.7	11.1	50.4	12.4	98.1
41	1.0	0.3	22.5	0.7	11.2	50.1	12.8	98.7

(C) EMPA data from sample decarburized for 100h at 1000°C, relevant to pre-oxidizing experiment

Line scan 1

distance(μm)	Al	Ti	Cr	Fe	Co	Ni	Mo	Total
0	0.4	0.1	22.2	0.8	11.6	52.7	10.3	98.0
1	0.4	0.1	22.1	0.8	11.4	53.3	9.7	97.9
2	0.4	0.1	22.4	0.8	11.5	53.2	9.8	98.4
3	0.5	0.2	22.1	0.8	11.3	52.9	9.8	97.5
4	0.5	0.2	22.0	0.8	11.5	53.3	9.8	98.0
5	0.5	0.2	21.7	0.8	11.6	53.0	9.8	97.7
6	0.5	0.2	21.7	0.8	11.6	53.4	9.8	97.9
7	0.6	0.2	21.8	0.8	11.4	53.3	9.8	97.9
8	0.6	0.2	21.8	0.8	11.5	53.8	9.6	98.3
9	0.6	0.2	21.8	0.8	11.4	53.7	9.6	98.1
10	0.6	0.2	21.9	0.8	11.4	53.5	9.7	98.2
11	0.7	0.2	21.7	0.8	11.5	53.9	9.7	98.6
12	0.7	0.3	22.1	0.8	11.6	54.2	9.7	99.3
13	0.7	0.3	21.9	0.8	11.4	53.9	9.6	98.5
14	0.7	0.2	21.7	0.8	11.5	54.0	9.8	98.8
15	0.8	0.3	21.7	0.8	11.5	53.9	9.4	98.3
16	0.8	0.3	21.8	0.8	11.6	54.0	9.2	98.5
17	0.8	0.3	21.7	0.8	11.5	54.0	9.6	98.7
18	0.8	0.3	21.6	0.8	11.6	54.4	9.7	99.2
19	0.8	0.3	21.8	0.8	11.6	54.2	9.3	98.8
20	0.9	0.3	21.7	0.8	11.6	54.5	9.7	99.4
21	0.9	0.3	21.8	0.8	11.5	54.1	9.2	98.5
22	0.9	0.3	21.7	0.8	11.6	54.6	9.7	99.6
23	0.9	0.3	21.6	0.8	11.6	54.5	9.7	99.4
24	0.9	0.3	21.4	0.8	11.7	54.6	9.6	99.2
25	0.9	0.3	21.4	0.8	11.5	54.5	9.6	98.9
26	0.9	0.3	21.6	0.8	11.6	54.1	9.3	98.7
27	0.9	0.3	21.2	0.8	11.6	54.4	9.4	98.6
28	0.9	0.3	21.5	0.8	11.7	54.7	9.4	99.3
29	1.0	0.3	21.6	0.8	11.6	54.5	9.2	98.9
30	1.0	0.3	21.4	0.8	11.6	54.1	9.1	98.2
31	1.0	0.3	21.3	0.8	11.5	54.2	9.3	98.3
32	1.0	0.3	21.3	0.8	11.5	54.6	9.2	98.6
33	1.0	0.3	21.2	0.8	11.5	54.0	9.3	98.1
34	1.0	0.3	21.5	0.8	11.7	54.3	9.7	99.2
35	1.0	0.3	21.5	0.8	11.6	54.2	9.4	98.8
36	1.0	0.3	21.6	0.8	11.7	54.6	9.4	99.3
37	1.0	0.3	21.5	0.8	11.4	54.6	9.6	99.2
38	1.0	0.3	21.3	0.8	11.7	54.2	9.6	99.0
39	1.0	0.3	21.4	0.8	11.4	54.6	9.2	98.7
40	1.0	0.3	21.4	0.8	11.6	54.7	9.7	99.5
41	1.0	0.3	21.5	0.8	11.7	54.4	9.6	99.4
42	1.0	0.3	21.4	0.7	11.6	54.1	9.6	98.9
43	1.0	0.3	21.3	0.8	11.6	54.4	9.7	99.1
44	1.0	0.3	21.2	0.8	11.6	54.6	9.3	98.8
45	1.0	0.3	21.4	0.7	11.6	54.2	9.7	99.0

46	1.1	0.3	21.3	0.8	11.7	54.1	9.3	98.5
47	1.0	0.3	21.2	0.8	11.5	54.3	9.5	98.6

Line scan 2

Distance (micron)	Al	Ti	Cr	Fe	Co	Ni	Mo	Total
0	0.4	0.1	22.3	0.8	11.4	52.9	10.1	98.1
1	0.4	0.2	22.1	0.8	11.5	52.9	9.8	97.7
2	0.5	0.2	22.1	0.8	11.5	53.2	10.1	98.3
3	0.5	0.2	22.0	0.8	11.6	53.3	10.0	98.4
4	0.5	0.2	21.9	0.8	11.5	53.4	10.1	98.4
5	0.5	0.2	21.9	0.8	11.6	53.7	9.9	98.6
6	0.6	0.2	21.9	0.8	11.4	53.6	9.7	98.1
7	0.6	0.3	21.9	0.8	11.6	54.0	10.0	99.1
8	0.6	0.2	21.9	0.8	11.4	53.9	9.8	98.6
9	0.7	0.2	21.9	0.8	11.5	54.2	9.4	98.7
10	0.7	0.2	21.7	0.8	11.5	53.6	9.7	98.1
11	0.7	0.2	21.8	0.8	11.6	54.0	9.6	98.8
12	0.7	0.2	21.6	0.8	11.6	54.1	9.6	98.7
13	0.7	0.2	21.7	0.8	11.6	54.2	9.4	98.7
14	0.7	0.3	21.6	0.8	11.5	54.7	9.5	99.1
15	0.8	0.3	21.4	0.8	11.5	54.2	9.6	98.5
16	0.8	0.3	21.6	0.8	11.4	54.1	9.3	98.3
17	0.8	0.3	21.5	0.8	11.7	54.4	9.5	98.9
18	0.8	0.3	21.4	0.8	11.5	54.3	9.3	98.4
19	0.8	0.3	21.6	0.8	11.5	54.2	9.6	98.8
20	0.9	0.3	21.5	0.8	11.5	54.3	9.3	98.5
21	0.9	0.3	21.6	0.8	11.5	54.6	9.7	99.3
22	0.9	0.3	21.5	0.8	11.5	54.4	9.4	98.7
23	0.9	0.3	21.6	0.8	11.5	54.2	9.4	98.7
24	0.9	0.3	21.4	0.8	11.5	54.4	9.2	98.5
25	0.9	0.3	21.3	0.8	11.5	54.3	9.7	98.8
26	1.0	0.3	21.4	0.8	11.5	54.2	9.2	98.3
27	0.9	0.3	21.3	0.8	11.7	54.4	9.5	99.0
28	0.9	0.3	21.3	0.8	11.5	54.5	9.3	98.7
29	1.0	0.3	21.3	0.8	11.6	54.5	9.2	98.7
30	1.0	0.3	21.2	0.8	11.5	54.3	9.4	98.5
31	1.0	0.3	21.3	0.8	11.6	54.2	9.3	98.6
32	1.0	0.3	21.2	0.8	11.6	54.3	9.2	98.4
33	1.0	0.3	21.4	0.8	11.5	54.1	9.6	98.7
34	1.0	0.3	21.4	0.8	11.4	54.5	9.5	98.9
35	1.0	0.3	21.1	0.8	11.6	54.4	9.1	98.3
36	1.0	0.3	21.3	0.8	11.5	54.2	9.6	98.7
37	1.0	0.3	21.2	0.8	11.6	54.3	9.4	98.6
38	1.0	0.3	21.3	0.8	11.7	54.3	9.5	98.8
39	1.0	0.3	21.4	0.8	11.7	54.5	9.6	99.2
40	1.0	0.3	21.3	0.8	11.6	54.3	9.5	98.8

BIBLIOGRAPHY

1. Hayner, G.O., et al., *Next generation nuclear plant materials research and development program plan*. 2006, Idaho National Laboratory: Idaho Falls.
2. *A technology roadmap for generation IV nuclear energy systems*. 2002, US DOE Nuclear Energy Research Advisory Committee.
3. Hoffelner, W., *Materials for the Very High Temperature Reactor: A versatile nuclear power station for combined cycle electricity and heat generation.* Chimia, 2005. **59**(12): p. 977-982.
4. Bennett, R., *Very high temperature reactor*. 2003, Idaho National Laboratory: Idaho Falls.
5. Harvego, E.A., *Evaluation of next generation nuclear power plant (NGNP) intermediate heat exchanger operating conditions*. 2006, Idaho National Laboratory: Idaho Falls.
6. Murty, K.L. and I. Charit, *Structure materials for Gen IV nuclear reactors: challenge and opportunities.* Journal of nuclear materials, 2008. **383**: p. 189-195.
7. Billot, P., D. Hittner, and P. Vasseur. *Outlines of the French R&D program for the development of high and very high temperature reactors*. In *3rd international topical meeting on high temperature reactor technology*. 2006. Johannesburg, South Africa.
8. Hosoi, Y. and S. Abe, *Effect of helium environment on the creep rupture properties of Inconel 617 at 1000^{o}C* Metallurgical Transactions A, 1975. **6A**(6): p. 1171-1178.
9. Ren, W. and R. Swindeman, *A review paper on aging effects in alloy 617 for Gen IV nuclear reactor applications.* Journal of pressure vessel and technology, 2009. **131**: p. 024002-1.
10. Natesan, K., A. Purohit, and S.W. Tam, *Materials behavior in HTGR environments*. 2003, Argonne National Laboratory: Argonne.
11. N., S., *Basic alloy system: fundamentals of strengthening. In: Superalloys II high temperature materials for aerospace and industrial power*. Wiley ed. 1987.
12. Nickel, H., F. Schubert, and H. Schuster, *Evaluation of alloys for advanced high-temperature reactor systems.* Nuclear Engineering and Design, 1984. **78**: p. 251-265.
13. Rahman, S., et al., *investigation of the secondary phases of alloy 617 by scanning kelvin probe force microscope.* Materials Letters, 2008. **62**: p. 2263-2266.
14. Hosier, J.C. and D.J. Tillack, Metals Engineering quarterly, 1972: p. 51-55.

15. Ohnami, M. and R. Imamura, *Effect of vacuum environment on creep rupture properties of Inconel 617 at 1000^{o}C.* Bulletin JSME, 1981. **24**(195): p. 1530-1536.
16. Whittenberger, J.D., *77 to 1200 K tensile properties of several wrought superalloys after long term 1093 K heat treatments in air and vacuum.* J. Mat. Eng. Perform., 1994. **3**: p. 91-103.
17. Whittenberger, J.D., *Effect of long term 1093 K exposure to air or vacuum on the structure of several wrought alloys.* J. Mat. Eng. Perform., 1993. **2**(5): p. 745-757.
18. H.M.Yun, et al., *The effect of high temperature reactor primary circuit helium on the formation and propagation of surface cracks in alloy 800H and Inconel 617.* Journal of Nuclear Materials, 1984. **125**: p. 1984.
19. Natesan, K. and P.S.Shankar, *Uniaxial creep response of alloy 800H in impure helium and in low oxygen potential environments for nuclear reactor applications.* Journal of Nuclear Materials, 2009. **394**: p. 46-51.
20. Cook, R.H., *Creep properties of Inconel 617 in air and helium at 800 to 1000^{o}C.* Nuclear Technology, 1984. **66**: p. 283-288.
21. P.S.Shankar and K. Natesan, *Effect of trace impurities in helium on the creep behavior of alloy 617 for very high temperature reactor application.* Journal of Nuclear Materials, 2007. **366**(1-2): p. 28-36.
22. Kurata, Y., Y. Ogawa, and T. Kondo, Creep and rupture behavior of a special grade hastelloy-X in simulated HTGR.
23. Kihara, S., et al., *Morphological changes of carbide during creep and their effects on creep properties of Inconel 617 at 1000^{o}C.* Metallurgical Transactions A, 1980. **11A**(6): p. 1019-1031.
24. Huchtemann, B., *The effect of alloy chemistry on creep behavior in a helium environment with low oxygen partial pressure.* Materials Science and Engineering, 1989. **A121**: p. 623.
25. Cabet, C., et al., *High temperature corrosion of structural materials under gas-cooled reactor helium.* Materials and Corrosion, 2006. **57**(2): p. 147-153.
26. Christ, H.J., et al., *Mechanisms of high temperature corrosion in helium containing small amounts of impurities II. corrosion of the Nickel-base alloy Inconel 617.* Oxidation of Metals, 1988. **30**(1-2): p. 27-51.
27. Quadakkers, W.J., *Corrosion of high temperature alloys in the primary circuit helium of gas cooled reactors. II. Experimental results.* Werkstoffe and Korrosion, 1985. **36**(8): p. 335-347.
28. Hirano, T., H. Araki, and H. Yoshida, *Carburization and decarburization of superalloys in the simulated HTGR helium.* Journal of nuclear materials, 1981. **97**: p. 272-280.
29. Mckee, D.W., *Corrosion behavior of experimental alloys in simulated HTGR helium at temperatures in the 750-1000^{o}C range.* Werkstoffe and Korrosion, 1983. **34**: p. 51-61.
30. Johnson, W.R. and L.D. Thompson, *Effects of methane concentration on the controlled-impurity helium corrosion behavior of selected HTGR structural materials*. December 1979, General Atomic Company.

31. Mutoh, I., et al., *Corrosion behavior of Ni-base superalloys at 1373 K in simulated HTGR impure helium gas environment.* Journal of nuclear materials, 1993. **207**: p. 212-220.
32. Brenner, K.G.E. and L.W. Graham, *The development and application of a unified corrosion model for high-temperature gas-cooled reactor systems.* Nuclear Technology, 1984. **66**: p. 40.
33. *Technical bulletin on Inconel 617 (publication number-SMC-029) (www.specialmetals.com).* March 2005.
34. Wilson, D.F., *Potential helium test environment for next generation nuclear plant material*. April 2005, Oak Ridge National Laboratory: Oak Ridge, TN.
35. Tillack, D.J., *Inconel 617-Data for use in design of gas-cooled and liquid-metal fast breeder reactors.* Special Metals, Inc., January, 1977.
36. Klarstrom, D.L., et al., *A new gas turbine combustor alloy,* in *International Gas Turbine Conference*. June 1984. paper no. 84-GT-70.
37. Ganesan, P., G.D. Smith, and D.H. Yates, *Performance of Inconel alloy 617 in actual and simulated gas turbine environments.* Materials and Manufacturing Processes, 1995. **10**(5): p. 925-938.
38. *"Inconel alloy 617". Special Metals Corp. Pub No. SMC-047, 2004*. 2004.
39. Bulletin, T., *Inconel alloy 617.* Special Metals Corporation (www.specialmetals.com), March 2005(SMC-029).
40. Erickson, G.L. *Superalloy developments for aerospace and industrial gas turbines*. in *Advanced Materials and coating for combustion turbine*. 1993. Pittsburg: ASM.
41. Yates, D.H., P. Ganesan, and G.D. Smith. *Recent advances in the enhancement of Inconel alloy 617 properties to meet the needs of gas turbine industry*. in *ASM 1993 Materials Congress*. 1993. Pittsburg, PA.
42. Mankins, W.L., J.C. Hosier, and T.H. Bassford, *Microstructure and phase stability of Inconel alloy 617.* Metallurgical Transactions, 1974. **5**(2579-2590).
43. Takahashi, T., et al., *Analysis of the phase in heat treated Inconel alloy 617.* Transactions of Iron and Steel Institute of Japan, 1978. **18**: p. 221-224.
44. Sims, T., N.S. Stoloff, and W.C. Hagel, *Superalloys II*. 1987, John Wiley and Sons. Inc.: New York.
45. Kimball, O.F., G.Y. Lai, and G.H. Reynolds, *Effects of thermal ageing on the microstructure and mechanical properties of a commercial Ni-Cr-Co-Mo alloy (Inconel 617).* Metallurgical Transactions A, 1976. **7A**: p. 1951-1952.
46. Smialek, J.L. and G.H. Meier, *High temperature oxidation,* in *Superalloys II*, C.T. Sims, N.S.Stoloff, and W.C.Hagel, Editors. 1987, John Wiley and Sons: New York. p. 293-326.
47. Caplan, D. and G.I. Sproule, *Effect of grain structure on the high-temperature oxidation of Cr.* Oxidation of Metals, 1975. **9**(5): p. 459-472.
48. Skeldon, M., J.M. Calvert, and D.G. Lees, *An investigation of the growth mechanism of Cr_2O_3 on pure chromium in 1 atm oxygen at 950^oC.* Oxidation of Metals, 1987. **28**(1-2): p. 109-125.
49. Graham, M.J., et al., *Anion transport in growing Cr_2O_3 and Al_2O_3 scales.* Materials science forum, 1989. **43**: p. 207-242.
50. Barnes, D.G., et al., Philosophical Magazine, 1973. **28**: p. 1303.

51. Lees, D.G. and J.M. Calvert, Corrosion Science, 1976. **16**: p. 767.
52. Zurek, J., et al., Materials Science and Engineering A, 2008. **477**: p. 259.
53. Stott, F.H., G.C. Wood, and J. Stringer, *The influence of alloying elements on the development and maintenance of protective scales.* Oxidation of Metals, 1995. **44**(1-2): p. 113-145.
54. Wallwork, G.R., *The oxidation of alloys.* Report of progress in Physics, 1976. **39**: p. 401-485.
55. C.S.Giggins and F.S.Pettit, *Oxidation of Ni-Cr-Al alloys between 1000^{o}C and 1200^{o}C.* Journal of Electrochemical Society, 1971. **118**(11): p. 1782-1790.
56. Wallwork, G.R. and A.Z. Hed, Oxidation of Metals, 1971. **3**: p. 171.
57. Kverns, I.A. and P. kofstad, Metallurgical Transactions, 1972. **3**: p. 1511.
58. Kofstad, P., *High temperature corrosion*. 1988, New York: Elsevier Applied Science. 396.
59. J.L.Smialek and G.H.Meier, *High temperature oxidation*, in *Superalloys II*, N.S.S. C.T. Sims, W. C. Hagel, Editor. 1987, John Wiley and sons: New York. p. 307.
60. Young, D.J., *High temperature corrosion and oxidation of metals*. Elsevier Corrosion Series: Elsevier.
61. Young, D.J., *High temperature and corrosion of metals*. 1st ed. Elsevier Corrosion Series, ed. T. Burstein. Vol. 1. 2008, New York: Elsevier. 147-151.
62. Birks, N., G.H. Meier, and F.S. Pettit, *Introduction to the high-temperature oxidation of metals*. 2 ed. 2006, Cambridge, UK: Cambridge University Press. 25.
63. Graham, L.W., Journal of Nuclear Materials, 1990. **171**: p. 76.
64. Krompholtz, K., J. Ebberink, and G. Menken. *Gas/metal interactions and depletion effects in helium-cooled process heat-HTRs*. in *Proc. 8th Int. congress on metallic corrosion*. 1981. Mainz, FGR.
65. Menken, G., et al. *Review of the gas metal interactions in HTR helium up to 950^{o}C*. In *Gas-Cooled Reactors Today*. 1982. London: Brtish Nuclear Energy Society.
66. Brenner, K.G.E. *Ternary diagrams for characterization of metallic corrosion in high temperature reactors*. In *Proc. Conf. on Gas-Cooled Reactors Today*. 1982. Bristol, UK.
67. Nieder, R. in *Proc. of Gas Cooled Reactors of Today*. 1982. London: British Nuclear Engineering Society.
68. Combrade, P. and D. Kaczowroski, *Review of the gas/Ni-base alloys interactions in HTR impure helium*. 2003, Framatome ANP: Paris, France. p. 1-26.
69. Graham, L.W. *Environmental conditions in HTRs and the selection and development of primary circuit materials*. In *IAEA symposium " Gas-cooled reactors with emphasis on advanced systems*. 1976. Vienna.
70. Krompholz, K., et al., *Fracture mechanics investigation on high-temperature gas-cooled reactor materials.* Nuclear Technology, 1984. **66**: p. 371.
71. H.J.Grabke and A. Schnaas. *Review on high temperature gaseous corrosion and mechanical performance in carburizing and oxidizing environment*. In *Proc. of Petten International Conference*. 1978. Petten, Netherlands: N-H.
72. Klower, J. and U. Heubner, *Carburization of nickel-based alloys and its effect on the mechanical properties.* Materials and Corrosion, 1985. **49**: p. 237-245.

73. Lee, K.S. and 1984, Creep rupture properties of hastelloy-x and Incoloy-800H in a simulated HTGH helium environment containing high levels of moisture.
74. Hsu, S.S., *The effect of fatigue, hold time, and creep on crack growth in high temperature environments: Ni-Cr-Co alloy.* Scripta Metallurgica et. Materialia, 1991. **25**(5): p. 1143.
75. Kondo, T. *Development and testing of alloys for primary circuit structures for VHTR.* In *IAEA Specialists meeting on High temperature metallic materials for application in gas-cooled reactors*. May 4-6, 1981. Vienna, Austria.
76. Quadakkers, W.J. and H. Schuster, *Corrosion of high temperature alloys in the primary circuit of high temperature gas cooled reactors.-Part I: theoretical background.* Werkstoffe and Korrosion, 1985. **36**: p. 141-150.
77. Quadakkers, W.J., *Corrosion of high temperature alloys in the primary circuit helium of high temperature gas cooled reactors. Part II: Experimental results.* Werkstoffe and Korrosion 1985. **36**: p. 335.
78. Brenner, K.G.E. *Ternary diagram for characterization of metallic corrosion in high temperature reactors*. In *Gas Cooled Reactors Today*. 1982. London: British Nuclear Energy Society.
79. Christ, H.-J., et al., *Mechanism of high-temperature corrosion in helium containing small amounts of impurities. I. theoretical and experimental characterization of the gas phase.* Oxidation of Metals, 1988. **30**(1-2): p. 1-26.
80. Christ, H.-J., et al., *High temperature corrosion of the nickel-based alloy inconel 617 in helium containing small amounts of impurities.* Materials Science and Engineering, 1987. **87**: p. 161-168.
81. Sakai, Y., et al., *Corrosion behavior of Inconel 617 in a simulated HTGR helium.* Transactions of national research institute for metals, 1985. **27**(1): p. 20-27.
82. Quadakkers, W.J., *High temperature corrosion in the service environments of a nuclear process heat plant.* Materials Science and Engineering, 1987. **87**: p. 107-112.
83. Constantineau, J.P., *Modified predominance diagram for gas-sold reactions.* Metallurgical and Materials Transactions B, 2000. **31B**: p. 1429-1437.
84. Gaskell, D.R., *Introduction to the thermodynamics of materials*. 5 ed. 2008, New York: Taylor & Francis. 404-410.
85. Christ, H.J., et al., *Mechanism of high temperature corrosion in helium containing small amounts of impurities. II. Corrosion of the nickel-base alloy Inconel 617.* Oxidation of Metals, 1988. **30**(1-2): p. 27.
86. Chapovaloff, J., D. Kaczorowski, and G. Girardin, *Parameters governing the reduction of oxide layers on Inconel 617 in impure VHTR He atmosphere.* Materials and Corrosion, 2008. **59**(7): p. 584.
87. Cabet, C. and F. Rouillard, *Corrosion of high temperature reactor structural materials.* Journal of Engineering for Gas Turbine and Power, 2009. **131**.
88. Cabet, C., et al., *High temperature reactivity of two chromium-containing alloys in impure helium.* Journal of Nuclear Materials, 2008. **375**: p. 173.
89. Kumar, D. and G.S. Was. *Mechanism of decarburization of alloy 617 at 1000^{o}C in helium containing CO and CO_2 impurities*. In *2008 MRS Fall Meeting*. 2008. Boston: MRS.

90. Rouillard, F., et al., *Oxide-layer formation and stability on a nickel-base alloy in impure helium at high temperatures.* Oxidation of Metals, 2007. **68**: p. 133-148.
91. Rouillard, F., et al., *Thermodynamic modeling of the destruction of the surface Cr2O3 on alloy 230 in the impure helium atmosphere of a gas-cooled reactor.* Materials science forum, 2008. **595-598**: p. 429-438.
92. Rouillard, F., et al., *Oxidation of a chromia-forming nickel base alloy at high temperature in mixed diluted CO/H2O atmosphere.* Corrosion Science, 2009. **51**: p. 752-760.
93. Rouillard, F., et al., *High temperature corrosion of a nickel base alloy by helium impurities.* Journal of Nuclear Materials, 2007. **362**: p. 248-252.
94. Christ, H.J., et al., *Mechanism of high temperature corrosion in helium containing small amounts of impurities-I. Theoretical and experimental characterization of the gas phase.* Oxidation of metals, 1988. **30**(1-2): p. 1-26.
95. Kimball, O.F. and D.E. Plumlee, *Gas/metal interaction studies in simulated HTGR helium.* 1985, General Electric, Inc.: Schenectady, NY, USA.
96. Wilson, D.F., *Potential helium test environment for the next generation nuclear plant materials*. 2005, Oak Ridge National Lab: Oak Ridge.
97. Cabet, C., et al., *High temperature reactivity of two-chromium containing alloys in impure helium.* Journal of Nuclear Materials, 2008. **37**: p. 173-184.
98. Voort, G.F.V., *Examination of some grain size measurement problems*, in *Metallography: past, present and future*, G.F.V. Voort, et al., Editors. 1993, American Society for Testing and Materials: Philadelphia. p. 266-294.
99. Cotell, C.M. and G.J. Yurek, *The influence of implanted yttrium on the mechanism of growth of Cr_2O_3 on Cr.* Journal of Electrochemical Society, 1987. **134**: p. 1871-1872.
100. Albertsen, J.Z., et al., *A model for high-temperature pitting corrosion of nickel-based alloys using internal precipitation of carbides, oxides, and graphites.* Metallurgical and Materials Transactions A, 2008. **39A**: p. 1258-1276.
101. Mitchell, D.F., R.J. Hussey, and M.J. Graham, *Oxygen transport in growing oxide films on chromium as studied by ^{18}O/SIMS.* Journal of vacuum science and technology A, 1984. **2**(2): p. 789-790.
102. Longo, D.M., J.M.Howe, and W.C.Johnson, *Development of a focused ion beam technique to minimize X-ray fluorescence during energy dispersive X-ray spectroscopy(EDS) of FIB specimens in the transmission electron microscope.* Ultramicroscopy, 1999. **80**(2): p. 69-84.
103. Williams, D.B. and C.B. Carter, *Transmission electron microscopy. I. Basics*. Vol. 1, New York: Springer Science + Business Media, LLC. 136.
104. Williams, D.B. and C.B. Carter, *Transmission electron microscope. II. Diffraction*. Vol. II, New York: Springer Science + Business Media, LLC. 271.
105. Tryon, B., *Multi-layered Ruthenium-containing bond coats for thermal barrier coatings*, in *Materials Science and Engineering*. 2005, University of Michigan: Ann Arbor. p. 34.
106. Christ, H.-J., et al., *Mechanisms of high-temperature corrosion in helium containing small amounts of impurities. II. corrosion in the nickel-base alloy Inconel 617.* Oxidation of Metals, 1988. **30**(1-2): p. 27-51.

107. Zimmermann, U. and H. Grimmer, *On the formation of n′ carbides during high tempearture corrosion of three nickel-based alloys in nuclear heat helium.* Materials Sceince and Engineering, 1987. **87**: p. 131-13.
108. Quadakkers, W.J., *Corrosion of high temperature alloys in the primary circuit helium of high temperature gas cooled reactors. Part II: Experimental results.* Werkstoffe and Korrosion, 1985. **36**: p. 335.
109. Zheng, X.G. and D.J. Young, *High-tempearture corrosion of Cr_2O_3-forming alloys in CO-CO_2-N_2 atmospheres.* Oxidation of Metals, 1994. **42**(3-4): p. 163-190.
110. Asteman, H., et al., Oxidation of Metals, 1999. **52**: p. 95.
111. Asteman, H., et al., Oxidation of Metals, 2000. **54**: p. 11.
112. Opila, E.J., et al., Journal of Physical Chemistry A, 2007. **111**: p. 1971.
113. Sigler, D.R., Oxidation of Metals, 1996. **46**: p. 335.
114. Young, D.J., *High temperature oxidation and corrosion of metals*. 1st ed. Elsevier Corrosion Series, ed. T. Berstein. Vol. 1. 2008, New York: Elsevier.
115. Gosse, S., et al., *Direct measurements of chromium activity in complex nickel base alloys by high temperature mass spectrometry.* Materials Science Forum, 2008. **595-598**: p. 975-985.
116. Kim, D., C. Jang, and W.S.Ryu, *Oxidation characteristics and oxide layer evolution of alloy 617 and haynes 230 at 900°C and 1100°C.* Oxidation of Metals, 2009. **71**: p. 271-293.
117. Christ, H.J., L. Berchtold, and H.G. Sockel, *Oxidation of Ni-base alloys in atmospheres with widely varying oxygen partial pressures.* Oxidation of Metals, 1986. **26**(1-2): p. 45-76.
118. Voice, W.E. and R.G. Faulkner, Metal Science, 1985(18): p. 411.
119. Willkinson, D.S., *Mass transport in solids and fluids*. 2000, Cambridge: University Press. 96.
120. Cermak, J. and H. Mehrer, *Tracer diffusion of 14C in austenitic Ni-Fe-Cr alloys.* Acta Metallurgica Materialia, 1994. **42**(4): p. 1345-1350.
121. Birks, N., G.H. Meier, and F.S. Pettit, *Introduction to the high-temperature oxidation of metals*. 2 ed. 2006, Cambridge: Cambridge University Press. 114.
122. Rapp, R.A., *Kinetics, microstructure and mechanisms of internal oxidation - its effect and prevention in high temperature ally oxidation.* Corrosion, 1965. **21**: p. 382-401.
123. Smeltzer, W.W. *Oxidation mechanism of metals and alloys*. In *Norman L. Peterson Memorial Symposium: Oxidation of Metals and Associated Mass Transport*. 1987: The Metallurgical symposium, Warrendale, PA.
124. Allen, A.T. and D.L. Douglass, *Internal carburization behavior of Ni-V, Ni-Cr and Ni-3Nb alloys.* Oxidation of Metals, 1999. **51**(3-4): p. 199-219.
125. Zheng, X.G. and D.J. Young, *Sulphide formation after pre-oxidation of chromia formers.* Corrosion Science, 1996. **38**(11): p. 1877-1897.
126. Wolf, I. and H.J.Grabke, *A study of the solubility and distribution of carbon in oxides.* Solid State Communications, 1985. **54**(1): p. 5-10.
127. Capell, B.M., *Intergranular stress corrosion cracking and selective internal oxidation of Ni-Cr-Fe alloys in hydrogenated steam*, in *Nuclear Engineering and Radiological Sciences*. 2005, University of Michigan: Ann Arbor.

128. Kofstad, P. and K.P. Lillerud, *Chromium transport through Cr2O3 scales. I. On lattice diffusion of chromium.* Oxidation of Metals, 1982. **17**(3-4): p. 177-194.
129. Ramanarayana, T.A., et al., *Transport through chromia films.* Solid State Ionics, 2000. **136-137**: p. 83-90.
130. Kofstad, P., *Defects and transport properties of metal oxides.* Oxidation of Metals, 1995. **44**(1-2): p. 3-25.
131. Barin, I., *Thermochemical data of pure substances*. 3rd ed. Vol. 1. 1995, Weinhein, Germany: VCH Verlagessescellschaft.
132. Lobing, R.E., et al., *Diffusion of cation in chromia layers grown in iron-base alloys.* Oxidation of Metals, 1992. **37**(1-2): p. 81-93.
133. Ignatov, D.V., I.N. Belkokurova, and I.N. Belyanin, *Tracer diffusivity of ^{51}Cr in Cr_2O_3 in 900-1100^oC range*, in *Metallurgy and Metal Research (all union scientific and technical conference on the use of radioactive and stable isotopes and radiation in the national economy and in science)*. 1958: Moscow. p. 326.
134. J.Z.Albertsen, et al., *A model for high-temperature pitting corrosion in Nickel-based alloys involving internal precipitation of carbides, oxides, and graphite.* Metallurgical and Materials Transactions A, 2008. **39A**: p. 1258-1276.